National Library of Canada
Bibliothèque nationale du Canada

Acquisitions and Bibliographic Services Branch
Direction des acquisitions et des services bibliographiques

395 Wellington Street
Ottawa, Ontario
K1A 0N4

395, rue Wellington
Ottawa (Ontario)
K1A 0N4

Your file Votre référence

Our file Notre référence

NOTICE

The quality of this microform is heavily dependent upon the quality of the original thesis submitted for microfilming. Every effort has been made to ensure the highest quality of reproduction possible.

If pages are missing, contact the university which granted the degree.

Some pages may have indistinct print especially if the original pages were typed with a poor typewriter ribbon or if the university sent us an inferior photocopy.

Reproduction in full or in part of this microform is governed by the Canadian Copyright Act, R.S.C. 1970, c. C-30, and subsequent amendments.

AVIS

La qualité de cette microforme dépend grandement de la qualité de la thèse soumise au microfilmage. Nous avons tout fait pour assurer une qualité supérieure de reproduction.

S'il manque des pages, veuillez communiquer avec l'université qui a conféré le grade.

La qualité d'impression de certaines pages peut laisser à désirer, surtout si les pages originales ont été dactylographiées à l'aide d'un ruban usé ou si l'université nous a fait parvenir une photocopie de qualité inférieure.

La reproduction, même partielle, de cette microforme est soumise à la Loi canadienne sur le droit d'auteur, SRC 1970, c. C-30, et ses amendements subséquents.

Canada

GENERAL SOLUTION FOR UNSTEADY ANNULAR FLOWS BETWEEN CONCENTRIC CYLINDERS AND ANNULAR FLOW-INDUCED INSTABILITIES

by

ABOLGHASEM MEKANIK

Department of Mechanical Engineering
McGill University
Montreal, Québec, Canada.

August, 1994

A Thesis submitted to the Faculty of Graduate Studies and Research
in partial fulfillment of the requirements for the degree of
Doctor of Philosophy.

© Abolghasem Mekanik, 1994

National Library of Canada

Bibliothèque nationale du Canada

Acquisitions and Bibliographic Services Branch

Direction des acquisitions et des services bibliographiques

395 Wellington Street
Ottawa, Ontario
K1A 0N4

395, rue Wellington
Ottawa (Ontario)
K1A 0N4

Your file Votre référence

Our file Notre référence

THE AUTHOR HAS GRANTED AN IRREVOCABLE NON-EXCLUSIVE LICENCE ALLOWING THE NATIONAL LIBRARY OF CANADA TO REPRODUCE, LOAN, DISTRIBUTE OR SELL COPIES OF HIS/HER THESIS BY ANY MEANS AND IN ANY FORM OR FORMAT, MAKING THIS THESIS AVAILABLE TO INTERESTED PERSONS.

L'AUTEUR A ACCORDE UNE LICENCE IRREVOCABLE ET NON EXCLUSIVE PERMETTANT A LA BIBLIOTHEQUE NATIONALE DU CANADA DE REPRODUIRE, PRETER, DISTRIBUER OU VENDRE DES COPIES DE SA THESE DE QUELQUE MANIERE ET SOUS QUELQUE FORME QUE CE SOIT POUR METTRE DES EXEMPLAIRES DE CETTE THESE A LA DISPOSITION DES PERSONNE INTERESSEES.

THE AUTHOR RETAINS OWNERSHIP OF THE COPYRIGHT IN HIS/HER THESIS. NEITHER THE THESIS NOR SUBSTANTIAL EXTRACTS FROM IT MAY BE PRINTED OR OTHERWISE REPRODUCED WITHOUT HIS/HER PERMISSION.

L'AUTEUR CONSERVE LA PROPRIETE DU DROIT D'AUTEUR QUI PROTEGE SA THESE. NI LA THESE NI DES EXTRAITS SUBSTANTIELS DE CELLE-CI NE DOIVENT ETRE IMPRIMES OU AUTREMENT REPRODUITS SANS SON AUTORISATION.

ISBN 0-612-05755-0

Canada

"In the Name of Allah, the Compassionate the Merciful"

To the Memory of my Parent

Abstract

The aim of this Thesis is to obtain time-accurate solutions of the Navier-Stokes equations for laminar incompressible unsteady flows generated by oscillating boundaries in an annular region made from two concentric cylinders. For this, a *time-dependent coordinate transformation* is first used to obtain a fixed computational domain. The resulting governing equations in the fixed domain are discretized in real time based on a three-time-level implicit scheme. A pseudo-time integration with artificial compressibility is then used to obtain the solution at a new real-time level. A factored ADI scheme is used to reduce the resulting coupled discretized equations in delta form to a set of decoupled scalar tridiagonal systems.

The method of solution has been applied to various 3-D unsteady flows in annular geometries, as well as to 2-D annular flows. The numerical results obtained are compared with those based on a mean position analysis, without transformation, for small-amplitude oscillations. This comparison shows that the *time-dependent coordinate transformation* is necessary to obtain accurate solutions for larger-amplitude oscillations.

The mean-position approach has also been applied to the analysis of axially variable annular configurations. The results obtained show more pressure recovery after a diffuser section with 6^o half-angle than in the case of 20^o half-angle.

A comprehensive experimental study was conducted to validate the theoretical results in the range of laminar flow. The results obtained were in good agreement with the numerical results, specially with those obtained by the *time-dependent coordinate transformation*. Experiments were also conducted for turbulent flow.

Based on the theoretical models developed, a computational method has been used to study fluid-structure interaction phenomena. It was applied to several cylindrical annular configurations in which one side of the annulus, the outer cylinder, is assumed to be flexibly supported, and thus to be susceptible to flow-induced instabilities. The structural and N-S equations were solved simultaneously by employing the

numerical method developed for the unsteady flow and a fourth-order Runge-Kutta scheme for the structural motion. The numerical results thus obtained have predicted the stability of the structure for different annular geometries. The structure having a uniform annular geometry was shown to be more damped, while the annular geometry with a backward facing step is less damped. The study of the structure for a uniform annular geometry in the case of rocking motion of the outer cylinder predicts an instability in the form of flutter of the outer cylinder.

Résumé

Pour obtenir les solutions précises en temps des équations de Navier-Stokes pour des écoulements instationnaires générés par des parois vibrantes dans la région comprise entre deux cylindres concentriques, on transforme d'abord les coordonnées dépendant du temps afin de réduire le problème à un domaine de calcul fixé dans le temps. Les équations ainsi obtenues dans le domaine fixé sont discrétisées en temps réel en utilisant une procédure implicite basée sur trois niveaux de temps. Une intégration en pseudo-temps avec une compressibilité artificielle, est utilisée pour réduire la solution à un nouveau niveau en temps réel. Un procédé de factorisation ADI est utilisé pour réduire les équations discrétisées couplées obtenues dans une forme delta en un system tridiagonal scalaire découplé.

Les solutions ont été appliquées aux espaces annulaires ainsi qu'à des ecoulements annulaires 2-D. Les résultats numériques obtenues sont comparées avec ceux basés sur l'analyse des positions moyennes, sans transformation, pour de petites amplitudes d'oscillation. Cette comparaison met en évidence que, la transformation des coordonnées dépendant du temps conduit à des solutions plus exactes pour de larges amplitude d'oscillations.

La méthode de position moyenne a été appliquée aux régions annulaires qui sont axiallement variables (avec décrochement cônique). Les résultats obtenus indiquent une plus importante récupération de pression après le décrochement cônique de demi-angle 6^o qu'après celui de demi-angle 20^o.

Une étude expérimentale détaillée a été développée pour valider les résultats théoriques concernant les écoulements laminaires. Les résultats expérimentaux s'accordent avec les résultats numériques, spécialement avec ceux obtenus avec la transformation des coordonnées dépendant du temps. La procédure expérimentale a été appliquée aux écoulements turbulents.

Basé sur les modèles théoriques utilisés, une méthode numérique a aussi été utilisée pour étudier les phénomènes d'interaction fluide-structure. Elle a été ap-

pliquée à plusieures configurations cylindriques annulaires. Pour ces configurations, le cylindre externe est maintenu de manière flexible et pourrait devenir instable sous l'éffet de l'écoulement. L'évolution du mouvement est suivie en temps pendant que les équations de N-S et de la structure sont résolues simultanément en employant pour l'équation de la structure la méthode de Runge-Kutta en quatre étapes. Les résultats numériques obtenus pour les oscillations libres du cylindre extérieur, ont permis de prévoir la stabilité de la structure pour différentes géometries annulaires. La configuration géométrique la plus stable est celle avec le cylindre interne uniforme, tandis que la moins stable est celle avec le cylindre à décrochement droit. L'étude de la structure pour le cas du cylindre interne uniforme, lorsque le cylindre extérieur est animé d'un mouvement de bascule a montré des instabilités de flottement caractérisées par un mouvement oscillatoire du cylindre externe.

Acknowledgement

The author would like to express his sincere appreciation and regard to professors D. Mateescu and M.P. Païdoussis, for their guidance and help in the course of this study. Without their experience and deep insight in the fields of computational fluid dynamics and flow-induced vibration, this work could not have been implemented successfully.

I wish to express my special thanks to my wife for her continuous encouragement and to all members of my family for their patience during the course of this research work. The author is grateful to and acknowledges the financial support of the Ministry of Culture and Higher Education of the Islamic Republic of Iran.

Finally, the author's gratitude extends to his good friend Scott Manktelow for the excellent work he did in fabricating the experimental apparatus and for his continuous help during the experimentation.

Contents

Nomenclature

Ordinary Symbols

a	Artificial sound velocity
A_n	Annular cross-sectional area
$A(x^*)$	Dummy function
$A(\theta,t)$	Dummy function
$B(x^*)$	Dummy function
$B(\theta,t)$	Dummy function
BU_j, BV_j	Dummy functions
$C(\theta,t)$	Dummy function
$D(x^*)$	Dummy function
$D(\theta,t)$	Dummy function
DU_j, DV_j	Dummy functions
$\mathcal{A}_1, \mathcal{A}_2, \mathcal{A}_3, \mathcal{A}_4$	Accelerations of the structure
c	Coefficient of damping of the structure per unit length
C	Coefficient of damping of oscillating cylinder
Cr	Courant number
C_d	Coefficient of Discharge for orifice plate
C_a, M_a, K_a	Dimensional added-damping, added-mass and added stiffness
e_r, e_p, e_u	Errors (uncertainties) in variables R, p and U
$\mathbf{E}$	Dummy symbol for velocity differencing
f	Frequency of oscillation of the moving cylinder, dummy function
F	Fluid force
F_1, F_2, F_3, F_4	Factors
$\mathcal{F}$	Nondimensional fluid dynamic forces
$\check{\mathcal{F}}$	Nondimensional fluid forces per unit length
$G(f_k)$	Fourier Transform at frequency f_k
$G(k)$	Discrete Fourier Transform at harmonic k

h	Nondimensional annular gap width
h_d	Nondimensional half height of the diffuser
H	Annular gap width
H_d	Dimensional half height of the diffuser
$\hat{i}, \hat{j}, \hat{k}$	Unit normal vectors
$\mathbf{I}$	Unit matrix
J	Mass-moment of inertia of the moving cylinder; or Jacobian of transformation
J_a	Dimensional added mass-moment of inertia of the moving cylinder
k	Stiffness coefficient of the structure per unit length
K	Stiffness coefficient of oscillating cylinder
l_1, l_2	Constants
L	Length of the oscillating outer cylinder
L_1, L_u	Length of upstream fixed portion
L_2, L_d	Length of downstream fixed portion
m	Mass of the moving cylinder per unit length
M	Mass of the moving cylinder
M_a	Mach number
M_o	Moment of the fluid forces about hinge point
$\mathbf{M}_x, \mathbf{M}_r, \mathbf{M}_\theta$	Matrices in x, r and θ directions (defined in Chapters 4-6)
N	Number of time steps
$N-S$	Navier-Stokes
p	Nondimensional pressure (defined in Chapter 2)
p^*	Dimensional pressure
q	Representative flow speed
q_1, q_2, q_0	Nondimensional added damping, added mass and added stiffness (defined in equation (9.25))
Q	Volumetric air flow rate

$\mathbf{Q}$	Dummy function
r	Nondimensional radial coordinate
r_1	Nondimensional radius of inner cylinder
r_2	Nondimensional radius of outer cylinder
r^*	Physical dimensional radial distance in diffuser geometry
r_{iu}, r_{id}	Nondimensional forms of R_{iu} and R_{id}
r_j^u, r_j^v	Computational radius at grid-point j
R	Dummy function
R_i	Dimensional radius of inner cylinder
R_o	Dimensional radius of outer cylinder
$R(\theta, t)$	Dummy function
R_{iu}	Inner cylinder radius at upstream for diffuser geometry
R_{id}	Inner cylinder radius at downstream for diffuser geometry
Re	Reynolds number, $\text{Re} = 2UH/\nu$
RU_j, RV_j	Physical radii at grid point j
S	Stokes number
$\mathbf{S}$	Matrix of the residuals of the momentum and continuity equations
t	Nondimensional time
$\bar{t}, t^*$	Dimensional time
T_1	Truncation error
u, v, w	Nondimensional perturbed fluid-velocity components in, respectively, axial, radial and tangential directions
U	Flow velocity
U_o	Mean axial fluid velocity
$\mathbf{U}_w$	Moving boundary velocity
$U(r)$	Nondimensional axial fluid velocity (defined by equation (4.64))
$U^*(r)$	Dimensional axial fluid velocity
v_w	Normal velocity at the wall

$\mathbf{V}$	Nondimensional fluid velocity vector
$\mathbf{V}^*$	Dimensional fluid velocity vector
$\mathbf{V}_o^*$	Dimensional uniform fluid velocity vector
$\mathcal{V}_1, \mathcal{V}_2, \mathcal{V}_3, \mathcal{V}_4$	Velocities of the structure in the intermediate time steps
w_w	Tangential velocity at the wall
x^*	Physical dimensional axial distance in diffuser geometry
x	Nondimensional axial distance in diffuser geometry, nondimensional axial coordinate
X	Hinge position
X, J, K	Number of grid points in axial, radial and circumferential directions
$\mathcal{X}_1, \mathcal{X}_2, \mathcal{X}_3, \mathcal{X}_4$	Amplitudes of the structure at intermediate time levels
y	y-coordinate (see Figure 7.5), displacement
$\dot{y}$	Velocity of the moving cylinder
$\ddot{y}$	Acceleration of the moving cylinder
Y	Expansion factor for the orifice plate

Greek Letters

α	Diffuser half-angle
β	$(2/3)\Delta t$
γ	Ratio of the orifice diameter to the pipe diameter
δ	Compressibility factor
δ_{ij}	Kronecker delta
Δ	Time difference, velocity difference, pressure difference, central difference operator
ϵ	Amplitude of displacement of the moving cylinder
$\epsilon(x^*)$	Diffuser coordinate at x^*
$\bar{\epsilon}_w$	Dimensional amplitude of displacement of the moving cylinder
$\dot{\epsilon}$	Velocity of the moving cylinder
$\ddot{\epsilon}$	Acceleration of the structure

η	Dummy variable
θ	Angular displacement of the moving cylinder, θ-coordinate
$\dot{\theta}$	Angular velocity of the structure
$\ddot{\theta}$	Angular acceleration of the structure
κ	Dummy function
λ	Wave velocity
μ	Dynamic viscosity of fluid, pseudo-time step
ν	Kinematic viscosity of fluid
ξ	Dummy function; or reduced mechanical damping
Π_{ij}	Stress tensor
ρ	Nondimensional density of fluid
ρ^*	Dimensional fluid density
ρ'	Artificial density
σ, σ_m	Nondimensional added-mass coefficients
τ	Pseudo-time
$\tau_{rr}, \tau_{rx}, \tau_{r\theta}$	Stress components
$\Phi(\theta, t)$	Dummy function
χ	Dummy function
Ψ	$[u, v, w, p]^T$
ω	Nondimensional frequency= $2S/\mathrm{Re}$
ω_n	Natural frequency of structure
Ω	Circular frequency of the oscillation
Ω_n	Dimensional frequency of structure
∇	Backward difference operator, nondimensional divergence operator
∇^*	Dimensional divergence operator

Subscripts

b	Moving boundary
d	Downstream, discharge, orifice diameter

D	Upstream of the orifice plate (for Reynolds number)
f	Fluid
i	Inner cylinder, in
i, j, k	i^{th}, j^{th} and k^{th} positions of the grid point
n	Annulus
o	Outer diameter, hinge point, out
s	Steady component of fluid pressure or velocity
u	Unsteady component of fluid pressure or velocity, upstream, axial direction
v	Radial direction
w	Circumferential direction, water

Superscripts

m	Pseudo-time level for the convergence of the solution
$n-1, n, n+1$	Three time-levels in three point backward implicit scheme
ru, rd	Above and below of a specific radial position
v, w	Radial positions where u, v or w is defined
$\theta f, \theta b$	Ahead and behind of a specific circumferential position
μ	Solution at pseudo-time level
$*$	Physical domain
$\pm, 1, 2, 3$	Forward or backward wave velocities
$\hat{}$	Pseudo-time integration
$\bar{}, \tilde{}$	Intermediate variables
$\dot{}$	Derivative with respect to time
$'$	Derivative with respect to x

List of Figures

List of Tables

Chapter 1

Introduction

In nature, when structures submerged in quiescent or flowing fluids oscillate, the surrounding fluid must participate in the motion; *i.e.*, we have a coupled fluid-structure motion and fluid-structure interaction. The result of this motion is sometimes pleasant, as in musical instruments, and sometimes annoying, disagreeable or destructive, as in the case for acoustical noise or damage to the structures. There are different mechanisms of fluid-structure coupling and interaction; where oscillatory motion is involved, this is sometimes called Flow-Induced Vibration or FIV.

Because of the possibly destructive nature of some of these phenomena, the study of this subject is of great interest for design. Although flow-induced vibrations are usually regarded as a secondary design consideration, at least until a failure occurs, it has become increasingly important in recent years because designers are using materials to their limit, causing structures to become progressively lighter, more flexible and more prone to vibration. Since 1939, an extensive research effort has been expended to find out the mechanisms involved in different kinds of flow-induced vibrations; the methods of predicting the onset of vibration and whether the system remains stable or becomes unstable have been discussed by Païdoussis (1980,1983,1987,1993), Chen (1987), Blevins (1990).

The fluid and the structure are coupled through the forces they exert on each other, as shown in Figure 1.1. In a very simple explanation, the fluid forces cause the structure to deform; as the structure deforms, the boundaries of the flow change, and the fluid forces therefore change. Furthermore, just as the fluid exerts a force on the structure, the structure exerts an equal but opposite force on the fluid; hence the name of fluid-structure interaction.

Depending on the geometry and direction of the flow relative to the structure, *e.g.*, flow within or over the structure, the induced vibrations are categorized into different types, such as cross flow-, axial (internal or external) flow-, and annular flow-induced vibrations. Each of these types of vibrations arises from distinct fluid dynamic phenomena that can be classified by the nature of the flow and the structure, as shown in Figure 1.2. The most important ones, for example in the case of cross flow are: (i) separation of the fluid and vortex shedding, (ii) turbulence buffeting, and (iii) fluid-elastic instabilities. As a practical examples of fluid-structure interactions, the vortex shedding mechanism is well known and has been experienced by any fast swimmer on his arms; or the internal tubular flow such as the large lateral force that must be exerted by one holding a fire-hose at high discharge rates, and the thrashing, snaking motions resulting when the fire-hose (or garden hose) is released.

As far as industrial applications are concerned, cylindrical structures subjected to either internal or external flows are found in many engineering constructions, particularly in the power-generating, chemical, and petrochemical industries; *e.g.*, in the form of piping of all kinds, marine risers, and chimneys; fuel pins, monitoring, and control rods in nuclear reactors; heat exchanger tube arrays and bundles of electrical conductors in transmission lines; and thin-walled shrouds and flow containment shells in nuclear reactors, aircraft engines, and jet pumps; to name but a few of the most familiar such systems.

The vibrations and instabilities associated with internal flow in tubular and external axial flow around cylindrical structures are of limited practical concern, despite their very considerable fundamental appeal. Most, but not all, engineering structures are sufficiently stiff, so that unusually high flow velocities would be required for these instabilities to occur. This, however, is not the case for instabilities associated with annular flows (Païdoussis 1987), where practical occurrences abound; a number of such cases are presented in Païdoussis (1980).

The present Thesis is concerned with the vibration of cylindrical structures in annular configurations, in still fluid or in axial flow in the annular passages. Some of the practical situations where annular-flow-induced instabilities have occurred in practice are: (i) control rods in guide tubes, fuel strings in coolant channels, and feedwater spargers, in various types of nuclear reactors; and (ii) certain types of jet pumps, pistons and valves. Figure 1.3 illustrates a jet pump, as an example of such applications. It should be mentioned that annular-flow-induced instabilities are sometimes referred to as leakage-flow-induced oscillations, or instabilities, which reflects the fact that in most cases of practical concern, the annular flow passage is quite narrow. Excellent reviews are given by Mulcahy (1983), Mateescu & Païdoussis (1985,1987)and Hobson & Jedwab (1990).

1.1 Previous Work on this and Related Problems

Cylindrical systems subjected to annular flow are notoriously prone to self-excited vibration, and consequently to damage through wear and fatigue, or outright fracture. Some work on stability of flexible cylinders in axisymmetrically confined flow was undertaken by Païdoussis and co-workers (1979,1981). Since then, the research effort on this topic, specifically applicable to narrow annuli was intensified and a number of interesting papers on the subject may be found in the proceedings of various symposia in this area, *e.g.*, Païdoussis *et al.* (1984,1988,1992).

The first attempts to generate an analytical viscous model for the cylindrical geometry are due to Hobson (1982) and Spurr & Hobson (1984). For the sake of simplicity, Hobson considered a rigid cylindrical body, hinged at one point and coaxially positioned in a flow-carrying duct, generally of nonuniform cross-sectional area; he showed that, at sufficiently high flow velocities, oscillatory instability can occur, via a negative damping mechanism. Moreover, the model was capable of dealing, in an approximate manner involving some degree of empiricism, with situations of sudden constriction or enlargement in the flow passage. The analysis was extended to predict the dynamical behaviour of an actual fuel assembly oscillating in a channel of arbitrary shape (Hobson 1984). Measurements of damping forces caused by flow between two concentric cylinders were made by Hobson (1991) in which he compared the experimental results with theory by making simple quasi-steady assumptions about the frictional forces acting on the cylinder. It was shown that damping of cylindrical structures due to annular flow arises from inlet or outlet effects and from frictional effects in the annulus, both effects increasing with flow velocity. Also, he found that the damping forces and pressure distribution along the annulus can be well predicted if simple assumptions about the unsteady flow in the annulus are made.

Several approaches have been used by different authors to obtain theoretical or experimental studies on fluid-structure interactions in very narrow annuli, or on so-called leakage flows. Among them is the study of Ashurts & Durst (1980) on flow-induced vibrations associated with shear-layer-induced flow oscillations in a symmetric, two-dimensional, plane test section with a sudden expansion. Parkin & Watson (1984) describe a physical model for explaining flow-induced vibration observed in 6^o and 30^o annular diffusers, where the centre-body forming the diffuser can move radially. Their model is based on experimental evidence and accounts for both fluid behaviour and structural response. This type of behaviour has relevance to the on-load refuelling of advanced gas cooled reactors. Spur & Hobson (1984) conducted some experiments in which they measured the unsteady forces caused by the flow down an annulus formed between a fixed outer cylinder and a vibrating centre-body and compared the results with those predicted using a linear small perturbation analysis. It was found that the forces are particularly sensitive to the amount of pressure recovery which takes place when the annulus is terminated in an annular diffuser, and that high pressure recovery leads to forces on the centre-body which are in phase with centre-body velocity and therefore likely to lead to coupled fluid-structure self-excited vibrations.

Mulcahy (1988) obtained closed-form solutions for the flow damping (velocity-dependent) and stiffness (displacement-dependent) forces acting on the vibrating walls of a one-dimensional leakage-flow channel. He also checked the effect on stability of pressure drop and of nonuniform geometries by using a constriction at the entrance of the annulus or varying the annular geometry via smoothly converging or diverging widths. The final conclusion was that the minimum conditions necessary for dynamic and static (divergence) instability are (i) a pressure loss at the upstream end of the annulus and (ii) a divergent channel with a finite-length throat region.

Hobson & Jedwab (1990) studied the effect of eccentricity on the unsteady forces on the centre-body of an annular diffuser. They carried out experiments and measured the forces on the fixed or forced vibrating centre-body at different frequencies and amplitudes within an annular diffuser. They found that periodic instability can be initiated by increasing the forced vibration amplitude above a frequency-dependent threshold.

Inada & Hayama (1990) theoretically and experimentally analyzed the viscous fluid-dynamic forces and the moments acting on the walls of a one-dimensional, narrow, tapered passage when one wall is vibrating in single or coupled translational and rotational modes. The fluid dynamic mass, damping and stiffness matrices are determined, with the help of which the mechanism of instability generated by the flow through the narrow passage is examined.

A more rigorous, purely analytical potential-flow model was formulated by Mateescu & Païdoussis (1985), once again for a rigid-body (the "centre-body") hinged at one point and coaxially positioned in a flow-carrying conduit; free motions of the centre-body were constrained by a rotational spring and a rotational dashpot at the hinge point. The cross-sectional areas of the body and the conduit were generally axially (and axisymmetrically) variable, but changes were smooth—precluding sudden constrictions or enlargements, but nevertheless allowing for a diffuser-type flow passage or a convergent one. In this inviscid analysis it was found that there is a critical location of the hinge: if the hinge is situated downstream of that location, then the system may lose stability at sufficiently high flow velocity when the negative fluid-dynamic damping, associated with motions of the centre-body, overcomes the mechanical damping; the necessary flow velocity becoming progressively smaller as the hinge is moved farther downstream. The fluid-dynamic forces become larger as the annular passage becomes narrower, destabilizing the system. It was also found that a divergent flow passage (diffuser) destabilizes the system, whereas a convergent one stabilizes it, as compared to the cylindrical geometry, which agrees with Hobson's (1982) finding.

This rigid-body model was then extended to take into account, in an approximate manner, viscous effects (Mateescu & Païdoussis 1987). One of the principal findings of this work was that viscous effects stabilize the system, and that they become more important as the annulus becomes narrower, which is reasonable on physical grounds. In this analysis an approximate solution of the Navier-Stokes equations was obtained, in which viscosity related modification of the unsteady pressure is obtained. Subsequently, the fluid dynamic pressures acting on the centre-body having a rocking motion were measured and compared with the theoretical ones (Mateescu *et al.* 1988). Good agreement between the two was found. To include the effects of turbulence, albeit approximately, the potential solution was combined with a turbulent model based on a power law for the velocity profile that fits the logarithmic form fairly well (Mateescu *et al.* 1989).

In another investigation in which a flexible, as opposed to a flexibly mounted, structure was used, the dynamical behaviour of the system of a cylinder beam with fixed ends subjected to axial flow in a narrow annulus was studied (Païdoussis *et al.* 1990). It was found that, as the annular gap becomes narrower, the system loses stability by divergence at smaller flow velocities, provided the gap size is such that inviscid fluid effects are dominant. For very narrow annuli, where viscous forces dominate, however, this trend is reversed, and further narrowing of the gap has a stabilizing effect on the system.

In an early investigation, the stability of coaxial shells with annular flow was conducted by Païdoussis *et al.* (1984) and it was found that, for annular flow, the critical flow velocity is lowered as the annulus is made narrower. If both shells are flexible, the instability threshold is lower than if the outer cylinder is rigid, the system losing stability first in the antisymmetric modes. This model was subsequently extended by Païdoussis *et al.* (1985) to take into account the steady viscous effects due to the surface traction and pressurization (to overcome frictional pressure drop); it was found that pressurization in the flow within the inner shell tends to stabilize the system, as is physically reasonable. Similarly, pressurization in the annular flow is destabilizing, if the outer shell is rigid. On the other hand, pressurization in the annular flow when both shells are flexible could either stabilize or destabilize the system, depending on the system parameters; this becomes clear when it is realized that in this case the effect on the inner shell is destabilizing, whereas it is stabilizing on the outer shell, and that motions of the two are coupled.

Further development in this area has been achieved by the use of computational models which involve simultaneous numerical integration of the Navier-Stokes equations for laminar flow, and the equation of motion of the structure (Païdoussis *et al.* 1992). To this end, a forced vibration of the outer (or inner) cylinder in an annular configuration was considered in which the Navier-Stokes equations were linearized and solved in the annulus for small amplitude oscillation of the cylinder, using primitive variables Mateescu *et al.* (1991,1994), and a spectral collocation method (see Canuto *et al.* (1987)) for unsteady annular flow in concentric and eccentric annuli, again for small amplitude oscillation of the moving boundary (Mateescu *et al.* 1994).

Mateescu and his coworkers used a method in which the primitive variables were considered. Further explanation of their work will be given in the subsequent paragraphs and chapters. An intensive review regarding the methods using primitive variables to solve Navier-Stokes equations can be found in Rogers & Kwak (1990). Most such methods can be classified into three groups. The first of these, and historically one of the most commonly used primitive variables schemes, *is the pressure Poisson method*, as first introduced by Harlow & Welch (1965). In this method, the velocity field is advanced in time using the momentum equations. Then a Poisson equation in pressure, which is formed from the momentum equations, is solved for the pressure at the current time level, such that the continuity equation be satisfied at the next time level. In this method, the velocity and pressure are indirectly coupled. The second group of methods can be classified as *fractional step methods.* This idea was first introduced by Chorin (1968), and is characterized by first solving for an intermediate velocity from the momentum equations, and then solving for the pressure field that will map the intermediate velocity into a divergence-free velocity. Computing the pressure field is usually accomplished by solving a Poisson equation in pressure, which can be very time-costly. The third method is that of *artificial compressibility*, which was used with much success by Mateescu and co-workers, and which will be used in the present analysis. This third method was also first introduced by Chorin (1967) for use in obtaining the steady-state solutions to the incompressible N-S equations. Several authors have recently used this method successfully in computing time-accurate problems. Merkle & Athavale (1987) presented solutions using this approach in 2-D generalized coordinates. Soh & Goodrich (1988) have also used this method to present solutions for a Cartesian mesh in 2-D. In the artificial compressibility formulation, a pseudo-time derivative of pressure is added to the continuity equation, which directly couples the pressure and velocity. The equations are advanced in physical time by iterating until a divergence-free velocity is obtained at the new physical time level.

Similarity exists between this formulation and the fractional step method of Chorin (1968), because his mapping of the intermediate velocity field to the divergence-free velocity is based on the artificial compressibility approach. However, the artificial compressibility method is different in that it provides a direct coupling between the pressure and velocity as they are advanced in time.

In the work done by Rogers & Kwak (1990), once again the artificial compressibility approach is used to solve 2-D N-S equations using an upwind differencing scheme based on flux-difference splitting, to compute the convective terms. In another work, Rosenfeld *et al.* (1991) used a fractional step method for solving the time-dependent 3-D incompressible N-S equations in generalized coordinate systems. They used the finite volume method, with a staggered mesh to discretize the governing equations, and solved the momentum equations by an approximate factorization method.

The approach used by Mateescu *et al.* (1991,1994) which is based on three-point-backward time discretization provides more accurate pressure results than the Crank-Nicolson scheme used by Soh & Goodrich (1988). This is why in the present work the former is adopted. In this approach, the solution to the momentum equations results in an unsteady pressure which is free of spurious oscillation; furthermore, the equations are cast in delta form *after* the introduction of the pseudo-time relaxation, allowing one to solve the implicit semi-discretized equations by the Alternating Direction Implicit (ADI) method along the exact same lines as in the method of artificial compressibility applied to the solution of steady-flow problems (Soh 1987) by using any of the existing space discretization schemes.

The present work has generalized the earlier work by Mateescu and co-workers (i) by taking more fully into account the nonlinearities in the N-S equations, (ii) by applying the boundary conditions on the moving boundary, rather than at its mean position —both of special interest for larger-amplitude oscillations— and (iii) by extending it to deal with nonuniform annular geometries (Mekanik *et al.* 1993, Mateescu *et al.* 1994). To carry out all these aims, the governing N-S equations should be transformed in time and space, *i.e.*, the physical domain of integration should be transformed into a computational domain, for both the uniform annular geometry and the nonuniform ones. There are different methods to treat moving-boundary problems.

The moving-boundary problems (MBPs) are a class of problems which can be found in many engineering and scientific fields. Numerous papers can be found in the literature which propose different methods for solving this class of problems. In practice, MBPs have several applications, such as ice making, freezing of food, diffusion of oxygen in body tissue, casting, melting (change of phase), crystal growth, etc. For each application a specific method of grid adaptation or generation is used, the purpose of which, in general, is to obtain accurate values for the field variables.

Early methods for solving moving boundary problems used body- or boundary-fitted curvilinear coordinate systems and adaptive grids in which at each time step a new grid was obtained through some grid-generation technique (algebraic, partial differential; elliptic, hyperbolic, or parabolic), *vide* Thompson *et al.* (1985). Thames *et al.* (1977) developed body-fitted coordinate systems to implement numerical solutions for viscous and potential flows about arbitrary two-dimensional bodies. Their solution is based on a technique of automatic numerical generation of a curvilinear coordinate system having a coordinate line coincident with the body contour, regardless of its shape. Thompson *et al.* (1977) presented a code for the numerical generation of boundary-fitted curvilinear coordinate systems. In this code, the coordinate lines are coincident with all boundaries of general multiconnected, two-dimensional regions containing any number of arbitrarily shaped bodies. No restrictions are placed on the shape of the boundaries, which may even be time-dependent. This approach provides a rectangular computational field with a square mesh; no interpolation is required, regardless of the shape of the physical boundaries, regardless of the spacing of the curvilinear coordinate lines in the physical field, and regardless of the movement of the coordinate system in the physical plane. Rai & Anderson (1982) introduced a new technique that provides a simple way of moving the mesh points in physical space in order to reduce the error in the computed asymptotic solution relative to that using a fixed mesh. Their adaptive grid technique has application in complex fluid flow problems involving many dependent variables, curved stationary and moving boundaries, and systems of partial differential equations. Kansa (1988) set forth an explicit moving-grid technique in which a moving frame is found in which the conservation equations appear stationary in a least-squares sense. In this moving frame, which was used to solve shock-wave problems, it is possible to drastically reduce or eliminate the temporal truncation errors. Finally, Shyy (1988) used an adaptive grid method to solve complex fluid flow problems such as uniform channel flow. An application of a moving-finite-element, instead of moving-grid, method can be found in Djomehri & George (1988). They used this method to solve the moving-boundary Stefan (heat transfer between water and ice) problems. Although these methods provide solutions for these problems, they are not efficient in terms of computation time and cost.

Several other methods were developed in which these deficiencies were somehow removed from the solution of the problems. Ogawa & Ishiguro (1987) proposed a new method for computing flow fields with arbitrary moving boundaries, which is in the same line as the previous class of grid-generation methods. According to their formulation, the computational coordinates fitted to the body move in space, contrary to the usual computational procedures. Thomas & Lombard (1979) formulate a differential "geometric conservation law" that governs the spatial volume element under an arbitrary mapping. Their method remedies the difficulties with maintenance of global conservation and with computation of local volume elements under time-dependent mapping that results from boundary motion. Warsi (1981) worked out the solution of the N-S equations in conservative-law form in general nonsteady coordinate systems in a simple and direct fashion, by manipulating some standard vectors and tensors. Demirdžić & Peric (1990) present a method that can be used for both the Lagrangian and Eulerian solution of the N-S equations in a domain of arbitrary shape, bounded by boundaries which move in any prescribed time-varying fashion. Yeoh *et al.* (1990) used a boundary-fitted coordinate system to predict the shape and the movement of the solid-liquid interface in the course of a numerical study of 3-D natural convection with phase change.

From all of the forgoing, it is obvious that an efficient way of handling this type of problem should be adopted. In this respect, immobilization of the domain of integration was found to be a reasonable choice in solving moving-boundary problems, at least to an acceptable extent. To immobilize the grids, a time-dependent transformation must be used by which the governing equations and boundary conditions are transformed from the moving physical domain into a stationary computational domain (Thompson *et al.* 1974). Based on this type of transformation several problems have been solved in the last two decades. To mention just a few cases, Duda *et al.* (1975) present a technique for the analysis of unsteady, two-dimensional diffusive heat- or mass-transfer problems characterized by moving irregular boundaries. The technique includes an immobilization transformation and a numerical scheme for the solution of the transformed equations. Saitoh (1978) developed a numerical method for multidimensional freezing problems in an arbitrary domain, using a boundary-fixing method. Hsu *et al.* (1981) set forth a methodology for the numerical solution of transient two-dimensional diffusion-type problems (*e.g.*, heat conduction) in which one of the boundaries of the solution domain moves with time. The moving boundary is immobilized by a coordinate transformation, but the transformed coordinates are, in general, not orthogonal. Faghri *et al.* (1984) used a nonorthogonal, algebraic coordinate transformation to obtain a rectangular solution domain for solving convection-diffusion problems. This transformation avoids the task of numerically generating boundary-fitted coordinates. Finally, Ralph & Pedley (1988) worked out a numerical solution for the N-S equations in a channel with a moving indentation, which is close to the situation we have in the present work, using a time-dependent coordinate transformation to resolve the boundary-condition difficulties arising from the presence of the moving wall. With boundary immobilization, while the problem becomes more complicated, it is ensured that the computational domain remains a fixed rectangle.

It is important to note that time-dependent coordinate transformations of the partial derivatives of the governing equations introduces cross-derivative terms, which is a characteristic of nonorthogonality of the grids. This, however, does not introduce errors in the accuracy of the final solution of the problem if the grid skewness is not large, as explained in Thompson *et al.* (1982) and verified by Braaten & Shyy (1986), who also proved that grid skewness only affects the convergence of the numerical solution. Therefore, in the present work the time- dependent transformation is used to obtain a rectangular computational domain with an orthogonal grid, even though the grid in the physical domain is nonorthogonal and skewed. Since boundary motions in the problems considered in this work are such that the criteria set forth by Thompson and co-workers for skewness of the grid are maintained (see Chapter 6), it is not necessary to be concerned about grid skewness in the solutions obtained.

1.2 The Contents of this Thesis

The scope of the research program undertaken in the present work is four-fold. First, to use the method of artificial compressibility to perform the time-accurate integration of the unsteady incompressible Navier-Stokes equations in annular regions for fluid flow in the laminar regime, taking into account the large motion of the oscillating boundary (Mekanik *et al.* 1993); this method will be used for all unsteady problems treated in this Thesis. Second, to apply this method to nonuniform annular geometries, again for large amplitudes motion of the moving boundary. Third, to investigate experimentally the forced vibration of the annular problems with different geometries (uniform, with backstep, and with diffuser-shaped annuli) by measurement of the unsteady pressure resulting from boundary oscillation in quiescent or flowing fluid in the annulus, and to compare the results with what was obtained from the theoretical (numerical) study. Experimental results for turbulent fluid flows were also obtained with an eye towards future extension of this work into the turbulent flow regime.

Fourth, to theoretically couple the N-S equations and the equation of motion of the moving body (in this study the outer cylinder), to determine the linear stability of the structure for large-amplitude oscillation. It should be remarked that for all cases mentioned, the small-amplitude (mean-position) analysis is also utilized, so as to compare the theoretical small- and large-amplitude results, and the numerical with experimental results, to the extent possible, and to eventually be able to conclude that beyond a certain amplitude the small-amplitude solution is not reliable.

In Chapter 2, the physical problems with the special geometries that can be found in practice and the related variable physical parameters influencing the solutions under consideration are defined. This is followed by introducing the unsteady flow equations (*i.e.*, the Navier-Stokes and continuity equations) in cylindrical coordinates. Finally, the fluid forces resulting from the solution of the flow equations are derived and the dynamical equation of motion of the structure, which is coupled with the fluid equations through the fluid forces, is presented.

Chapter 3 covers the numerical formulation for unsteady annular flows with small amplitudes of oscillation. This includes real time-discretization of the flow equations, The introducing of the method of artificial compressibility, and the pseudo-time formulation of the resulting equations. The equations obtained are discretized in space by using a staggered grid and solved in delta form, which is efficient in terms of computer time, using the (ADI) scheme.

In Chapter 4 the validation of the method of solution introduced in the previous chapter for 2-D and 3-D steady annular flow problems is discussed. Then, the cases of 2-D and 3-D unsteady annular flows are treated and the related problems are discussed both for uniform and nonuniform (backstep) annular geometries. For both geometries, the uncoupled translational and rotational motions of the moving outer cylinder are considered. The results obtained for small-amplitude oscillations are discussed and the effects of different parameters such as flow velocity, amplitudes and frequencies of oscillation, the annular gap width, and the length of upstream and downstream fixed portions of the vibrating cylinder on the results are presented.

Chapter 5 is devoted to the solution of the fluid flow equations for nonuniform geometries (diffuser shapes). This is due to the fact that, during the solution procedure of this type of annular geometries, one will obtain nonorthogonal highly skewed computational grids in the annular space in the axial direction which will have a negative effect on the accuracy of the solution. To overcome this problem, a special space transformation is used to obtain physical as well as computational orthogonal grids. The same procedure used for the time- and space-discretizations of the N-S equations employed in Chapter 3 is also applied here to discretize these equations in the transformed domain. It should be remarked that, for the special case of a diffuser-shaped annulus, the small amplitude (mean-position) analysis is used because of numerical difficulties, due to both the time-dependent and space transformations. The numerical results obtained for this geometry are presented and discussed in terms of different physical parameters affecting the solution. These factors include the amplitude (small amplitude only, the large-amplitude solution and results will be presented in Chapter 6 for uniform and backstep geometries) and frequency of oscillation, diffuser angle, annular gap width, fluid velocity, and the length of the oscillating cylinder as well as the lengths of upstream and downstream fixed portions.

Chapter 6 is devoted to the solution of the Navier-Stokes equations using a time-dependent coordinate transformation, and includes the development of the transformation equations and derivation of the partial derivatives in the transformed computational domain. Then, the transformed N-S equations are formed and the equations are discretized in real- and pseudo-times. Spatial discretizations are implemented on the same lines used in Chapter 4. The discretized equations are then solved using the ADI scheme. There follows a discussion of grid skewness in the physical domain, which is unavoidable due to the motion of the cylinder, although in the computational domain the grids are not skewed. The numerical results are presented and the mean-position analysis is compared with the time-dependent analysis.

Chapter 7 describes several ways of testing the convergence and accuracy of the results *vis-à-vis* the effects of important parameters, such as the number of real time-steps, the length of the system under consideration and the mesh, to name but a few, on the numerical results and the accuracy of the numerical model used by comparing the numerical and analytical results for a benchmark problem.

Chapter 8 is exclusively devoted to the experimental investigations. In this chapter, the main apparatus with its specifications and characteristics, the ancillary equipment, the instruments and the measuring devices are described. The preliminary experimental work, such as preparation of the apparatus and calibration of the related devices, is explained. A complete description of the experimental procedure is given for the two cases of translational and rocking motion of the outer cylinder. Although the main objective of the theoretical and experimental work in this Thesis is to study the fluid flow and its interaction with the structure in the laminar-flow regime, the available equipment and facilities permit experimentation in the turbulent regime. A complete set of measurements for different Reynolds numbers, including those in the turbulence range, were obtained and the results for various geometries are presented. The theoretical results obtained by both theoretical methods are compared with the experimental results, and the validity of the results obtained by time-dependent coordinate transformation is discussed. Finally, a discussion of the related experimental errors conclude the work of this chapter.

In Chapter 9, fluid-structure interaction is considered, in which the Navier-Stokes equations for 2-D and 3-D, either for the small-amplitude (mean position) solution or the large-amplitude (time-dependent transformation) solution, are coupled with the dynamical linear equation of motion of the system through either predictor-corrector scheme or a fourth-order Runge-Kutta scheme. The coupled equations are then solved numerically and the stability of the vibrating outer cylinder is discussed in terms of its displacement versus time, regarding different factors influencing it, such as the flow velocity, fluid viscosity, Reynolds number, annular shape (uniform or nonuniform), and amplitude of oscillation. The stability analysis also includes the different motions of the outer cylinder such as translational or rocking motion.

Chapter 10 completes the Thesis with a summary of the important findings, conclusions regarding the originality of the work done in this research and some suggestions and recommendations for future work.

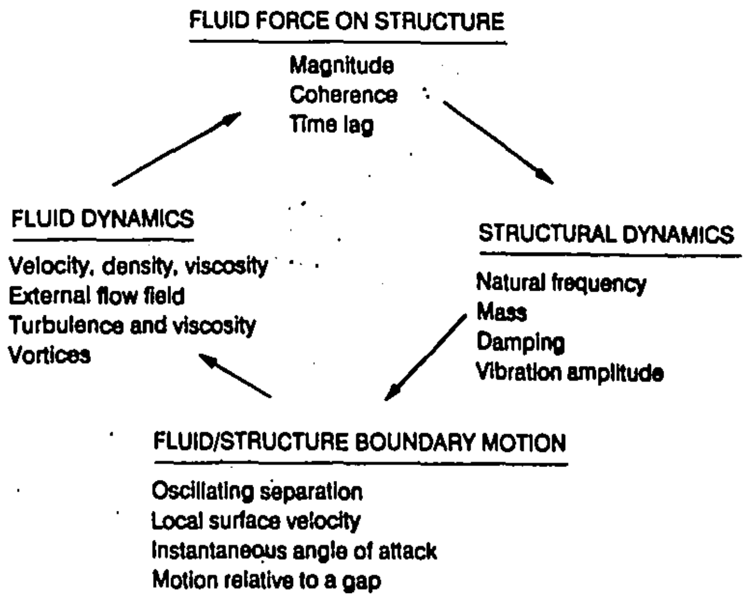

Figure 1.1: Feedback between fluid and structure (reprinted from Blevins 1990).

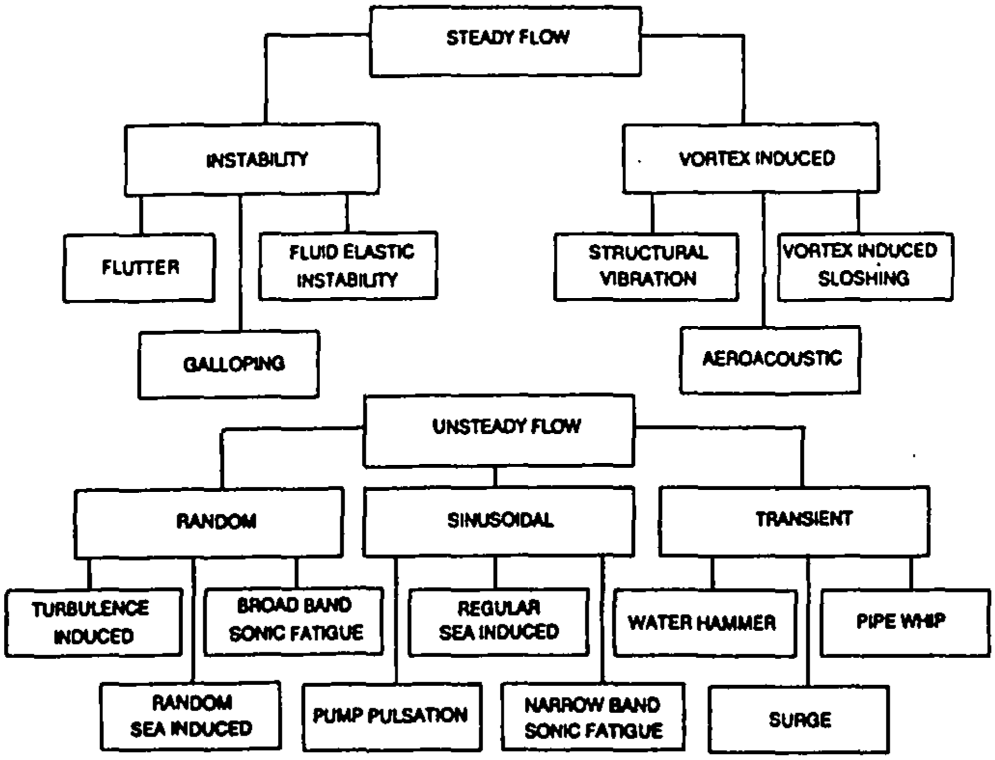

Figure 1.2: A classification of flow-induced vibrations (reprinted from Blevins 1990).

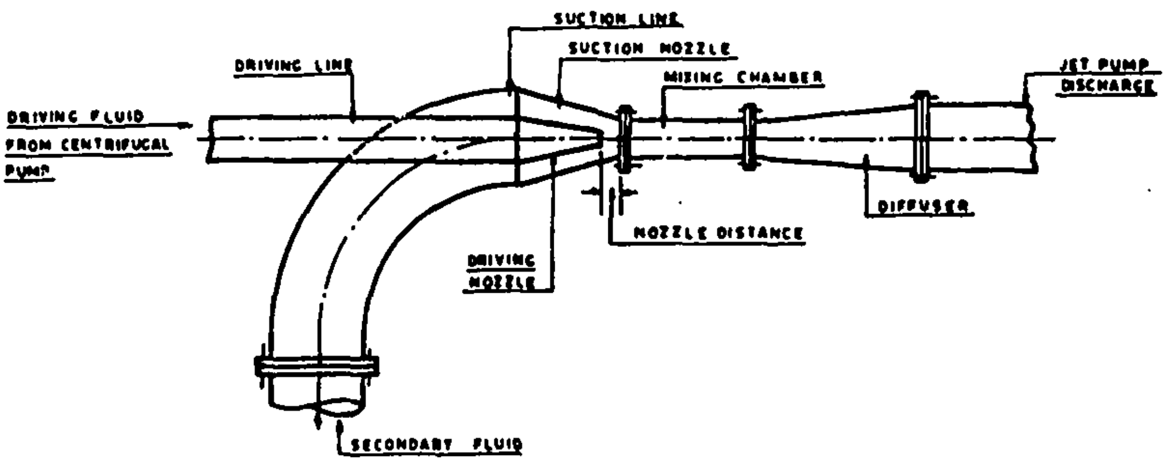

Figure 1.3: An example of a system subjected to annular-flow-induced vibration.

Chapter 2

Problem Formulation

2.1 Introduction

The importance of the problem was discussed in the previous chapter. In this chapter the key elements of the formulation of the problem are introduced, which are at the heart of the research presented in this Thesis. This is the set of basic equations of fluid motion in their unsteady form, which eventually lead to the estimation of the fluid-dynamic forces acting on a cylinder in an annular configuration.

The annular configurations considered consist of a centre-body concentrically located in a cylindrical conduit, as shown in Figure 2.1. For an axially uniform configuration, the radius of the inner cylinder is r_1 and the annular space between the two cylinders is H; thus, the radius of the outer cylinder is $r_2 = r_1 + H$. The centre-body is immersed in either quiescent fluid or a steady laminar flow. It is generally the outer cylinder which is forced to execute oscillatory motion. These types of annular geometry have applications in many engineering applications, such as the one shown in Figure 2.2, illustrating the core of an advanced gas cooled reactor during the refuelling process. To model such a physical configuration numerically, each one of the geometries of Figure 2.1 is redrawn in a special form in Figure 2.3. In this figure several new parameters are introduced which are part of the final mathematical model. It should be remarked that, exclusively in this analysis, the inner cylinder is fixed and the outer one is forced to oscillate.

The total length of the outer cylinder is divided into three parts. The upstream and downstream parts of variable lengths L_1 and L_2 are kept stationary. The central portion of the cylinder, L, executes oscillatory motions, either translational or rocking around a fixed hinge as shown in Figure 2.4.

The radii of the cylinders, r_1 and r_2, as well as the length of the oscillating cylinder are variable. The annular widths downstream of the backstep or diffuser sections are assumed to be appropriately larger than the corresponding upstream section; moreover, the angle of the diffuser section is variable. Different values are used for the flow velocity U including $U = 0$, the amplitude ϵ, and the frequency of oscillation f of the central part of the outer cylinder. Although during oscillation there arise physical discontinuities between the fixed upstream and downstream portions and the central portion as shown in Figure 2.3, the derivatives of the flow variables are taken to be continuous and hence no singularities arise due to these discontinuities. Also, since there always are certain gaps between these fixed and moving parts, for the computation it is assumed that no fluid leaks from these gaps. Since the equations of fluid motion, as will be described in the next section, are in non-dimensional form, the solutions obtained for these equations are applicable to incompressible-fluid flow in the laminar regime.

The final goal in this Thesis is the stability analysis of the systems described above. To this end, these systems are assumed to be affected by the fluid dynamic forces that result from the flow in the annulus and interact with the structure. These oscillating structures have certain characteristics such as mass, damping and stiffness. In the stability analysis, one looks for the changes caused by the presence of quiescent or flowing fluid. As will be seen, the stability of the structure depends most importantly on the fluid dynamic damping, although the fluid changes the characteristics of the structure in other ways, *e.g.* by increasing the effective mass of the whole system or affecting the effective stiffness of the structure. In this Thesis, the stability analysis is applied to the system shown in Figure 2.4.

The outer cylinder oscillates either in translational motion in the y direction or in rocking motion about the fixed point, as shown in Figure 2.4. The cylinder is rigid but is flexibly supported, with support stiffness K and damping C. For the purpose of evaluating the effect of fluid damping on the structure, the structural damping is neglected. For the system shown in Figure 2.4 it is assumed that the outer cylinder is displaced by a distance ϵ and then released. Due to the oscillation of the cylinder, fluid forces are generated which interact with the structure; the final result of this fluid-structure interaction is the dynamical behaviour of the cylinder (*i.e.*, whether it remains stable or becomes unstable), which is exclusively the topic of Chapter 9. However, before this goal is reached, the fluid forces should be determined by solving the unsteady N-S equations in the annular region. As a first step toward this aim, the fluid flow equations for incompressible fluids are introduced in the following section.

2.2 Basic Equations of Unsteady Flows

In unsteady flows, the three velocity components and the pressure are functions of space and time. These four unknowns can be determined from the governing equations, *i.e.*, the continuity equation (conservation of mass) and the Navier-Stokes equations (conservation of momentum).

In this analysis the viscosity and density are assumed to remain constant. Thus, the continuity and N-S equations, without body forces, are expressed in dimensional form as

$$\nabla^* \cdot \mathbf{V}^* = 0, \tag{2.1}$$

$$\frac{\partial \mathbf{V}^*}{\partial t^*} + \nabla^* \cdot (\mathbf{V}^*\mathbf{V}^*) = -\frac{1}{\rho^*}\nabla^* p^* + \nu \nabla^{*2}\mathbf{V}^*, \tag{2.2}$$

respectively, where $\mathbf{V}^*$ is the velocity vector, t^* is the time, ρ^* is the density, ν is the kinematic viscosity, and p^* is the pressure.

In order to generalize the present problem, it is convenient to define the following non-dimensional parameters:

$$\mathbf{V} = \frac{\mathbf{V}^*}{V_o^*}, \quad p = \frac{p^*}{\rho^* V_o^{*2}}, \quad \nabla = H\nabla^*, \quad \mathrm{Re} = \frac{HV_o^*}{\nu}, \quad t = \frac{t^* V_o^*}{H},$$

where V_o^* is the reference velocity, and H is the annular gap width.

Using these parameters, one can write equations (2.1) and (2.2) as

$$\nabla \cdot \mathbf{V} = \mathbf{0}, \tag{2.3}$$

$$\frac{\partial \mathbf{V}}{\partial t} + \nabla \cdot (\mathbf{V}\mathbf{V}) = -\nabla p + \frac{1}{\mathrm{Re}}\nabla^2 \mathbf{V}, \tag{2.4}$$

and in compact form equation (2.4) is written as

$$\frac{\partial \mathbf{V}}{\partial t} + \mathbf{Q}(\mathbf{V}, p) = \mathbf{0}, \tag{2.5}$$

where in cylindrical coordinates $\mathbf{Q}(\mathbf{V},p) = [Q_u(u,v,w,p), Q_v(u,v,w,p), Q_w(u,v,w,p)]^T$. The continuity equation and the components of $\mathbf{Q}(\mathbf{V},p)$ are given by

$$\nabla \cdot \mathbf{V} = \frac{\partial u}{\partial x} + \frac{1}{r}\frac{\partial (rv)}{\partial r} + \frac{1}{r}\frac{\partial w}{\partial \theta}, \tag{2.6}$$

$$\begin{aligned} Q_u(u,v,w,p) &= \frac{\partial (uu)}{\partial x} + \frac{1}{r}\frac{\partial (rvu)}{\partial r} + \frac{1}{r}\frac{\partial (wu)}{\partial \theta} + \frac{\partial p}{\partial x} \\ &- \frac{1}{\mathrm{Re}}\left[\frac{\partial^2 u}{\partial x^2} + \frac{1}{r}\frac{\partial}{\partial r}\left(r\frac{\partial u}{\partial r}\right) + \frac{1}{r^2}\frac{\partial^2 u}{\partial \theta^2}\right], \end{aligned} \tag{2.7}$$

$$\begin{aligned} Q_v(u,v,w,p) &= \frac{\partial (uv)}{\partial x} + \frac{1}{r}\frac{\partial (rvv)}{\partial r} + \frac{1}{r}\frac{\partial (wv)}{\partial \theta} - \frac{w^2}{r} + \frac{\partial p}{\partial r} \\ &- \frac{1}{\mathrm{Re}}\left[\frac{\partial^2 v}{\partial x^2} + \frac{1}{r}\frac{\partial}{\partial r}\left(r\frac{\partial v}{\partial r}\right) + \frac{1}{r^2}\frac{\partial^2 v}{\partial \theta^2} - \frac{2}{r^2}\frac{\partial w}{\partial \theta} - \frac{v}{r^2}\right], \end{aligned} \tag{2.8}$$

$$\begin{aligned} Q_w(u,v,w,p) &= \frac{\partial (uw)}{\partial x} + \frac{1}{r}\frac{\partial (rvw)}{\partial r} + \frac{1}{r}\frac{\partial (ww)}{\partial \theta} + \frac{vw}{r} + \frac{1}{r}\frac{\partial p}{\partial \theta} \\ &- \frac{1}{\mathrm{Re}}\left[\frac{\partial^2 w}{\partial x^2} + \frac{1}{r}\frac{\partial}{\partial r}\left(r\frac{\partial w}{\partial r}\right) + \frac{1}{r^2}\frac{\partial^2 w}{\partial \theta^2} + \frac{2}{r^2}\frac{\partial v}{\partial \theta} - \frac{w}{r^2}\right], \end{aligned} \tag{2.9}$$

in which u, v and w are the axial, radial and circumferential non-dimensional velocity components ($\mathbf{V} = \hat{i}u + \hat{e}_r v + \hat{e}_\theta w$).

Equations (2.3) and (2.4) are subject to initial and boundary conditions, which may be stated as follows:

$$v = 0, \qquad w = 0, \qquad \text{at } t = 0, \text{ in the annulus}$$

$$\mathbf{V} = 0, \qquad \text{on the inner cylinder} \tag{2.10}$$

$$\mathbf{V} = 0, \qquad \text{on the fixed portions of the outer cylinder} \tag{2.11}$$

and

$$\mathbf{V} = \mathbf{V}_b, \qquad \text{on the moving boundary}, \tag{2.12}$$

where $\mathbf{V}_b$ is the boundary velocity.

Also, depending on the method of solution, the boundary conditions are imposed either at the mean position of the outer cylinder (for small-amplitude oscillations; see Chapter 4), or at its true time-dependent position (as shown in Figure 2.5) for larger-amplitude oscillations (see Chapter 6).

Therefore, the boundary conditions associated with the geometry of Figure 2.5 are given on the fixed inner cylinder $R = R_i$ as

$$\left.\begin{aligned} v_w(R_i,\theta,t) &= 0 \\ w_w(R_i,\theta,t) &= 0 \end{aligned}\right\}, \tag{2.13}$$

and on the moving outer cylinder $R_o = R_i + \Phi(\theta,t)$ according to Figures 2.5(b) and 6.2

$$\left.\begin{aligned} v_w(R_o,\theta,t) &= [d\epsilon(t)/dt]\cos\theta \\ w_w(R_o,\theta,t) &= -[d\epsilon(t)/dt]\sin\theta \end{aligned}\right\}, \tag{2.14}$$

with no velocity in the axial direction (positive θ is in the counterclockwise direction). The known displacement of cylinder ϵ, which is a function of time, provides the necessary velocities $[v_w, w_w]^T$ at different time steps.

2.3 Dynamics of the Structure as a Result of Fluid Forces

The fluid-dynamic forces, which are expressed in terms of inertial, damping and stiffness components are evaluated based on the viscous-flow analysis developed in the following chapters. The steady and unsteady fluid-dynamic forces are obtained by integrating the pressure and skin friction around the cylinder. These forces, which will be obtained in later chapters, are necessary for the evaluation of stability if one of the two elements of the annulus (the centre-body or the outer cylinder) is flexible or flexibly mounted.

The resultant forces acting on the structure per unit length, including the unsteady components, can be calculated by using the following stress equation in tensor form

$$\prod_{ij} = -p\delta_{ij} + \mu\left(\frac{\partial u_i}{\partial x_j} + \frac{\partial u_j}{\partial x_i}\right), \tag{2.15}$$

where $\partial u_i/\partial x_j$ represents the partial derivative of the velocity component in the i direction with respect to the j coordinate, μ is the dynamic viscosity, and δ_{ij} denotes the Kronecker delta.

The steady viscous forces, which are dependent on the gradients of the motion with respect to the axial direction, are derived from the longitudinal frictional force and from the pressurization of the flow to overcome the pressure drop. In this analysis, since these factors do not affect the problem, the steady forces will not be considered.

The unsteady viscous forces arise from normal and tangential friction forces containing the effect of the viscous pressure distribution along the circumference in a direction normal to the wall. Thus, the unsteady forces acting on the outer cylinder per unit length due to its oscillatory motion can be obtained by multiplying equation (2.15) by the unit vector normal to the outer cylinder and integrating the result:

$$F(t) = \int_0^{2\pi} \left(\tau_{rr}\,|_{r=R_o} \cos\theta - \tau_{r\theta}\,|_{r=R_o} \sin\theta\right) R_o\, d\theta\,, \tag{2.16}$$

where $\tau_{rr} = \prod_{11}$, and $\tau_{r\theta} = \prod_{12}$. The stress components in terms of the gradients of the radial and circumferential components of the unsteady-flow velocity and pressure are written as

$$\tau_{rr}(r,\theta,t) \quad = \quad -p + 2\mu\frac{\partial v}{\partial r}\,, \tag{2.17}$$

$$\tau_{r\theta}(r,\theta,t) = \mu\left(\frac{1}{r}\frac{\partial v}{\partial \theta} + \frac{\partial w}{\partial r} - \frac{w}{r}\right). \tag{2.18}$$

The forces obtained from equation (2.16) are used in the equation of motion of the structure to analyze the dynamics and stability of the system. Hence, one can write

$$M\ddot{y} + C\dot{y} + Ky = F(t), \tag{2.19}$$

when translational motion of the cylinder is considered, where M, C and K are, respectively, the mass, damping and stiffness of the cylinder (see Figure 2.4).

In the case of rocking motion, the equation of motion of the cylinder about the hinge point shown in Figure 2.4 is written as

$$J\ddot{\theta} + C\dot{\theta} + K\theta = M_o(t), \tag{2.20}$$

where $M_o(t)$ is the moment of the fluid forces about the fixed hinge point, J is the moment of inertia of the cylinder about the hinge axis and θ is the angular displacement of the cylinder.

These equations are solved by a special method (Chapter 9) and the results obtained determine whether the structure, which has been set in motion and interacts with the fluid during its motion, remains stable or becomes unstable, as determined by whether its displacement decreases or increases with time. In the case of negative fluid damping, the system becomes unstable in an oscillatory manner (dynamic instability). In addition to this, however, if the total (mechanical and fluid-induced) stiffness of the system becomes negative, then the system loses stability by divergence (static instability), irrespective of the damping.

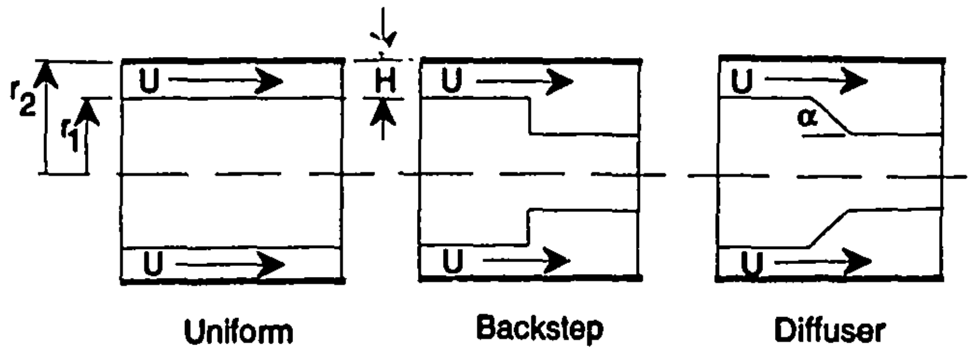

Figure 2.1: Schematic diagram of the uniform and non-uniform annular flow geometries.

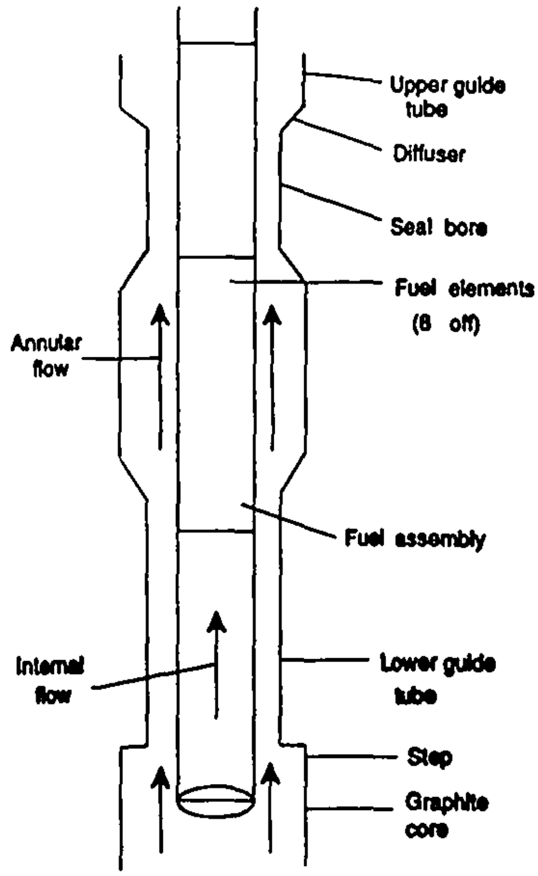

Figure 2.2: Schematic diagram of a small part of the Core of an Advanced Gas Cooled Reactor during refuelling.

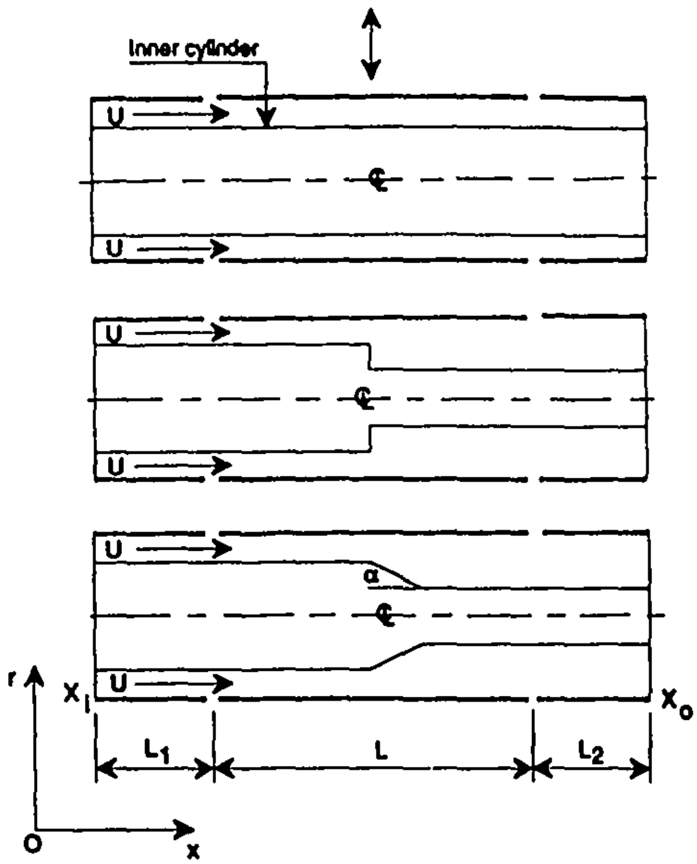

Figure 2.3: Schematic diagram of annular flow configuration in which the central part of the outer cylinder is forced to oscillate.

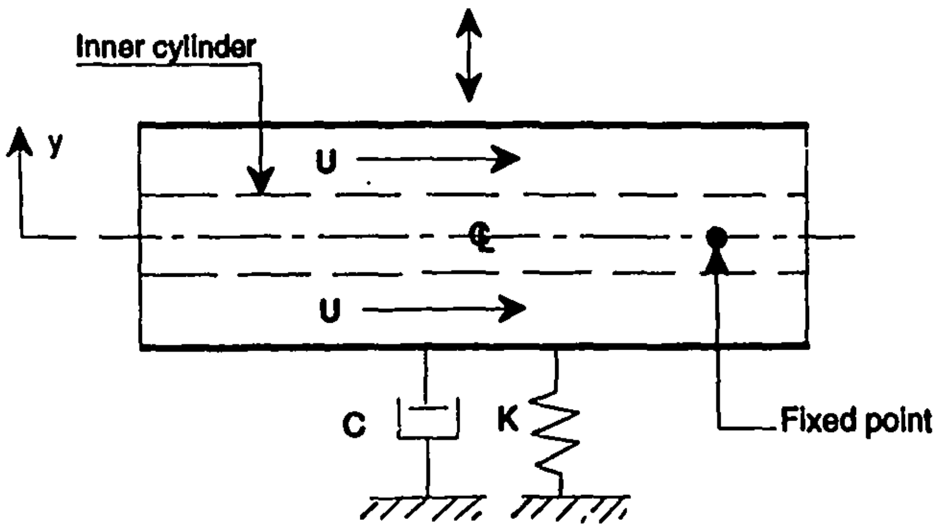

Figure 2.4: Schematic diagram showing the system considered for stability analysis.

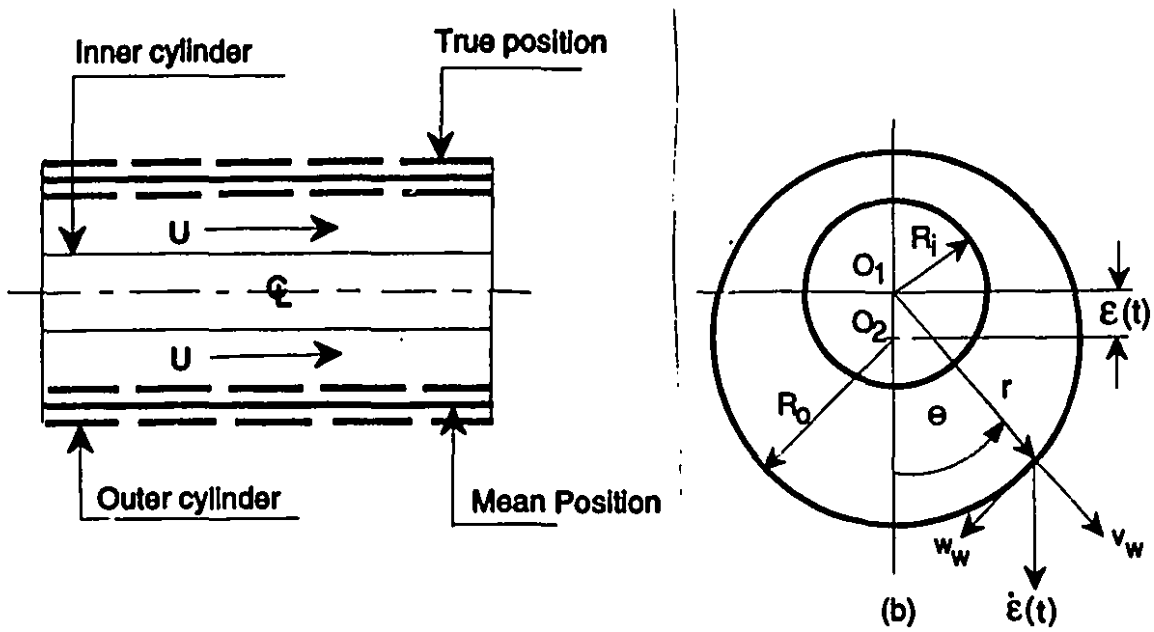

Figure 2.5: (a) Schematic diagram indicating the mean and the true maximum and minimum positions of the outer cylinder during oscillations. (b) Cross-sectional view of the annular space during oscillation (exaggerated amplitude). The boundary conditions are applied either at the mean position or at the moving boundary.

Chapter 3

Numerical Formulation for Unsteady Annular Flows with Low-Amplitude Oscillation

3.1 Introduction

The equations governing the unsteady fluid flow were introduced in Chapter 2. These equations are solved in steady or unsteady form depending on the requirement of the particular problem under consideration. In both cases, when the numerical solution is sought, these equations are discretized spatially and, for unsteady fluid flow, in time as well.

To implement the numerical solution of the Navier-Stokes (N-S) equations, the method employed for time and space discretizations of the equations to obtain a time-accurate solution with the aid of artificial compressibility is explained in this chapter. The auxiliary equations used in pseudo-time to couple the continuity and momentum equations are derived, by which the solution proceeds to the next real-time step. To solve the pseudo-time equations, the method of factorization is used leading to the linear equations which can be solved by the ADI scheme (to be presented in what follows).

3.2 Time-discretization of the Navier-Stokes Equations

To discretize the time derivative which appears in the momentum equation, the three-point backward implicit time-discretization scheme used by Mateescu et al. (1991) is utilized. This scheme provides the accurate unsteady pressure, free of spurious numerically induced oscillations, in contrast to the Crank-Nicolson discretization scheme used for example by Soh and Goodrich (1988).

The method of artificial compressibility, which was introduced by Chorin (1967), is also applied, in order to obtain the solution for the incompressible nonlinear N-S equations for unsteady flow problems. Let us examine the reasons for requiring the use of this method. For incompressible flows there are various possibilities for the formulation of the problem. These include primitive-variable, stream-function/vorticity, and vorticity/velocity methods. The primitive-variable approach offers the fewest complications in extending two-dimensional calculations to three dimensions. The primary difficulty with this approach is the specification of boundary conditions on pressure which, nevertheless, can be eliminated by the specific numerical models utilized. In our analysis the primitive-variable approach was recognized to be more feasible and adaptable to our physical problems. On the other hand, we determined to obtain time-accurate solutions of these equations by marching in time, which will be used later in our special method for stability analysis. To carry out this task, the continuity and momentum equations must somehow be coupled through the pressure terms. The role of artificial compressibility is to perform this task, *i.e.*, to introduce the necessary coupling.

According to Chorin's method of artificial compressibility , the magnitude of the change in the pressure at a given point in the field is directly proportional to the magnitude of the divergence of the velocity field and inversely proportional to the artificial compressibility factor.

The artificial compressibility factor comes from the artificial equation of state, *i.e.*, $p\delta = \rho'$, where p is the pressure at a point , ρ' is the artificial density, and δ is the artificial compressibility factor. Using the artificial compressibility in the continuity equation implies that the density is a function of "pseudo-time". The important thing to note is that the artificial continuity equation is cast so that the density becomes asymptotically constant with respect to time, at the end of the pseudo-time iterations when the real continuity equation for an incompressible fluid is satisfied.

Before the artificial compressibilty is introduced into the equations of fluid motion, the N-S equations must be discretized in real-time. Hence, we first write equation (2.5) as

$$\frac{\partial \mathbf{V}}{\partial t} + \mathbf{Q}(\mathbf{V}, p) = \mathbf{0} . \tag{3.1}$$

Introducing the three-point backward implicit time differencing scheme results in

$$\frac{3\mathbf{V}^{n+1} - 4\mathbf{V}^{n} + \mathbf{V}^{n-1}}{2\Delta t} + \mathbf{Q}^{n+1} = 0 , \tag{3.2}$$

where $\mathbf{Q}^{n+1} = \mathbf{Q}(\mathbf{V}^{n+1}, p^{n+1})$. From this discretization the value of $\mathbf{V}$ at time $t^{n+1} = (n+1)\Delta t$ is obtained, given the solution for previous values at time levels t^{n} and t^{n-1}. Equation (3.2) together with the continuity equation which must be satisfied at all times can be written (Mateescu *et al.* 1991) as

$$\mathbf{V}^{n+1} + \beta \mathbf{Q}^{n+1} = \mathbf{E}^{n} , \tag{3.3}$$

$$\nabla \cdot \mathbf{V}^{n+1} = 0 , \tag{3.4}$$

where

$$\beta = \frac{2}{3}\Delta t , \quad \mathbf{E}^{n} = \frac{1}{3}(4\mathbf{V}^{n} - \mathbf{V}^{n-1}).$$

The time integration procedure requires the initial conditions for $\mathbf{V}$ and p throughout the fluid domain and the boundary conditions at the entrance and exit of the domain, as well as at the fluid-structure interface as discussed in the previous chapter and as will be addressed in Chapters 4-6 where the details of integration for each problem are explained. Equations (3.3) and (3.4), which are a non-homogeneous system of nonlinear equations, can be solved for $\mathbf{V}^{n+1}$ and p^{n+1}, $n = 1, ..., N-1$.

3.3 Pseudo-time Integration Based on Artificial Compressibility

Equations (3.3) and (3.4) can be solved numerically by an iterative relaxation technique if we introduce a continuous auxiliary system in pseudo-time (Soh and Goodrich 1988) as

$$\frac{\partial \hat{\mathbf{V}}}{\partial \tau} + \hat{\mathbf{V}} + \beta \hat{\mathbf{Q}} = \mathbf{E}^n, \tag{3.5}$$

$$\delta \frac{\partial \hat{p}}{\partial \tau} + \nabla \cdot \hat{\mathbf{V}} = 0, \tag{3.6}$$

where τ is the *pseudo-time* , and δ is the artificial compressibility coefficient; here the hat denotes a transient value in pseudo-time. The time τ is called here *pseudo-time*, to be distinguished from the *physical time t*. From equations (3.5) and (3.6) we can see that $\hat{\mathbf{V}}$ and $\hat{p}$ become $\hat{\mathbf{V}}^{n+1}$ and $\hat{p}^{n+1}$, respectively, as the steady state is reached asymptotically in pseudo-time. Consequently, the solution of the system (3.3) and (3.4) is equivalent to the steady solution of the system (3.5) and (3.6). As we see in (3.6), the divergence-free velocity field is not obtained until the steady state is reached. Therefore, the system (3.5) and (3.6) has no physical meaning until the numerical solution converges in pseudo-time. Since the pseudo-time τ is purely artificial, the time increment $\Delta\tau$ can be taken as large as possible to expedite the convergence to the steady state, within the limit of the numerical stability condition based on the Courant number (see the discussions in Chapter 4 and Mateescu *et al.* 1994, Part 1) .

For the pseudo-time semi-discretization, an implicit Euler scheme in delta form is used, namely

$$\Delta \mathbf{V} + \Delta\tau \hat{\mathbf{V}}^{\mu+1} + \beta \Delta\tau \hat{\mathbf{Q}}^{\mu+1} = \Delta\tau \mathbf{E}^n, \tag{3.7}$$

$$\Delta p + \frac{\Delta\tau}{\delta} \nabla \cdot \hat{\mathbf{V}}^{\mu+1} = 0, \tag{3.8}$$

where μ indicates the solution at the pseudo-time level $\tau^\mu = \mu\Delta\tau$. The terms $\Delta\mathbf{V}$ and Δp are given by $\hat{\mathbf{V}}^{\mu+1} - \hat{\mathbf{V}}^\mu$ and $\hat{p}^{\mu+1} - \hat{p}^\mu$, respectively, and $\hat{\mathbf{Q}}^{\mu+1} = \mathbf{Q}(\hat{\mathbf{V}}^{\mu+1}, \hat{p}^{\mu+1})$

is calculated at each pseudo-time step, while the non-homogeneous term $\mathbf{E}^n$, which is also calculated at the beginning of the pseudo-time relaxation, is kept constant throughout.

When the solution converges, at $\mu = m$, the pseudo-time derivatives $\Delta\mathbf{V}$ and Δp become zero, giving $\hat{\mathbf{V}}^{m+1} = \hat{\mathbf{V}}^m$ and $\hat{p}^{m+1} = \hat{p}^m$, and equations (3.5) and (3.6) reduce to (3.3) and (3.4), at which point $\hat{\mathbf{V}}^{m+1} \equiv \hat{\mathbf{V}}^{n+1}$ and $\hat{p}^{m+1} \equiv \hat{p}^{n+1}$, where $n+1$ is the new *real* time step.

Introducing $\Delta\mathbf{Q} = \hat{\mathbf{Q}}^{\mu+1} - \hat{\mathbf{Q}}^{\mu}$ into the equations (3.7) and (3.8), to be consistent with the $\hat{\mathbf{V}}$ and $\hat{p}$ variables in delta form, and rearranging the terms in the equations, the final momentum and continuity equations in matrix delta form are expressed as

$$
\begin{aligned}
(\mathbf{I} + \Delta\tau)\Delta\mathbf{V} + \beta\Delta\tau\Delta\mathbf{Q} &= \Delta\tau(\mathbf{E}^n - \hat{\mathbf{V}}^{\mu} - \beta\hat{\mathbf{Q}}^{\mu}), && (3.9)\\
\Delta p + \frac{\Delta\tau}{\delta}\nabla\cdot(\Delta\mathbf{V}) &= -\frac{\Delta\tau}{\delta}\nabla\cdot\hat{\mathbf{V}}^{\mu}, && (3.10)
\end{aligned}
$$

which is an implicit system of equations, nonlinearly coupled by the term $\Delta\mathbf{Q}$. Equations (3.9) and (3.10) can be written in global matrix form as

$$
[\mathbf{I} + \beta\Delta\tau(\mathbf{M}_x + \mathbf{M}_r + \mathbf{M}_\theta)]\,\Delta\Psi = \Delta\tau\mathbf{S}\,, \tag{3.11}
$$

in which the matrices $\mathbf{M}_x, \mathbf{M}_r$, and $\mathbf{M}_\theta$ contain the spatial derivatives with respect to x, r, and θ of the variable $\Delta\Psi = [\Delta u, \Delta v, \Delta w, \Delta p]^T$. The vector $\mathbf{S}$ is given by

$$
\mathbf{S} = \begin{bmatrix} \mathbf{E}^n - \hat{\mathbf{V}}^{\mu} - \beta\,\hat{\mathbf{Q}}^{\mu} \\ -(1/\delta)\,\nabla\cdot\hat{\mathbf{V}}^{\mu} \end{bmatrix}. \tag{3.12}
$$

3.4 Spatial Discretization on a Staggered Mesh

3.4.1 Grid Generation

The numerical solution of partial differential equations requires some discretization of the field into a collection of points or elemental volumes (cells). The differential equations are approximated by a set of algebraic equations on this collection of points and volumes, and this system of algebraic equations is then solved to produce a set of discrete values which approximates the solution of the partial differential system over the field. The discretization of the field requires some organization for the solution thereon to be efficient, *i.e.*, it must be possible to readily identify the points or cells neighbouring the computation site. Furthermore, the discretization must conform to the boundaries of the region in such a way that the boundary conditions can be accurately represented. This organization is provided by a coordinate system, and the need for alignment with the boundary is reflected in the routine choice of Cartesian coordinates for rectangular regions, polar(or cylindrical) coordinates for circular regions, etc.

The use of coordinate line intersections to define the grid points provides an organizational structure which allows all computation to be done on a fixed square grid when the partial differential equations of interest have been transformed so that the curvilinear coordinates replace the Cartesian coordinates as the independent variables. The boundaries may also be in motion, either as specified externally, which is the case in this Thesis, or in response to the developing physical solution. In any case, the numerically generated grid allows all computation to be done on a fixed square grid in the computational field which is always rectangular by construction. In this chapter, a fixed grid related to the mean position of the moving boundary is used by contrast with the analysis based on a *time-dependent coordinate transformation*, which will be explained in Chapter 6, in which the moving physical domain is transformed into a fixed rectangular computational domain with an orthogonal mesh.

The finite difference method was used to discretize the spatial differential operators which are centrally differenced on a staggered grid. On curvilinear coordinate systems the definition of order of a difference representation is integrally tied to a point distribution function. The order is determined by the error behaviour as the spacing varies with the points fixed in a certain distribution, either by increasing the number of points or by changing a parameter in the distribution.

The hyperbolic tangent and hyperbolic sine (stretching) functions are used to obtain the best possible spatial resolution and concentrate more points in regions of higher velocity gradients, for example, near solid walls. The hyperbolic tangent was used to concentrate grid points normal to solid walls, while the hyperbolic sine was used in flow problems involving a preferred flow direction, to distribute the points in that direction. These distribution functions provide best accuracy for the difference representation of differential operators (Vinokur 1983).

The hyperbolic tangent stretching function is constructed using the following equations:

$$r_j = r_0 + (r_j - r_0)\kappa(\eta) \; , \tag{3.13}$$

where

$$\kappa(\eta) = \frac{1}{2}\left\{1 + \frac{\tanh(\gamma(\frac{\eta}{j} - \frac{1}{2}))}{\tanh(\frac{\gamma}{2})}\right\} , \tag{3.14}$$

and the points are then located by taking integer values of η, *i.e.*, $\eta = 0, 1, 2, \ldots\ldots, j$.

In the x-direction, which corresponds to the mean flow direction, we use the hyperbolic sine distribution function, which reads

$$x_i = x_0 + (x_I - x_0)\chi(\xi) \; , \tag{3.15}$$

where

$$\chi(\xi) = \frac{\sinh(\gamma\frac{\xi}{I})}{\sinh\gamma} \; . \tag{3.16}$$

The points are again located by taking integer values of $\xi, \xi = 0, 1, 2, \ldots., I$. Indeed, the fluid equations are now considered to be solved on a normalized domain with coordinates ξ/I, $0 \le \xi/I \le 1$, and η/J, $0 \le \eta/J \le 1$, instead of on the original physical domain with coordinates x, $x_0 \le x \le x_I$ and r, $r_0 \le r \le r_j$ and with coordinate θ, $0 \le \theta \le \pi$ uniformly distributed along circumferential direction.

3.4.2 Spatial Differential Operators Based on a Staggered Grid

By taking into account all the aforementioned considerations, and noting that the problem of generating a curvilinear coordinate system can be formulated as a problem of generating values of the Cartesian coordinates in the interior of the rectangular transformed region from specified values on the boundaries, in the present analysis, for central differences, the first and second derivatives are evaluated as (see Figure 3.1)

$$\left.\frac{df}{dx}\right|_{x=x_i} = \frac{f_{i+1} - f_{i-1}}{x_{i+1} - x_{i-1}} , \tag{3.17}$$

$$\begin{aligned}
\left.\frac{d^2f}{dx^2}\right|_{x=x_i} &= \left[\frac{d}{dx}\left(\frac{df}{dx}\right)\right]_{x=x_i} \\
&= \frac{1}{x_{i+1/2} - x_{i-1/2}}\left[\left(\frac{df}{dx}\right)_{x_{i+1/2}} - \left(\frac{df}{dx}\right)_{x_{i-1/2}}\right] \\
&= \frac{1}{x_{i+1/2} - x_{i-1/2}}\left[\frac{f_{i+1} - f_i}{x_{i+1} - x_i} - \frac{f_i - f_{i-1}}{x_i - x_{i-1}}\right] .
\end{aligned} \tag{3.18}$$

In the present analysis it was decided to use a staggered grid (such as that used by Harlow & Welch 1965) instead of using a collocated one, for which the accuracy of the solution deteriorates (see Patankar 1980). A sample of the staggered grid used in the 2-D analysis of the problems is shown in Figure 3.2. In addition to the benefit obtained, the staggered grid provides the possibility of simplifying the boundary conditions for pressure. Thus, in the present analysis, using the staggered grid frees the solution from the pressure to be described at the solid walls and reduces the number of boundary conditions for the problem.

This advantage has, however, its own price. A computer program based on a staggered grid must carry all the indexing and geometric information about the locations of the velocity components and the pressure (especially in 2-D and 3-D problems) and must perform certain interpolations as have been done in this analysis and are described in the next section and subsequent chapters and appendices. But the benefits of the staggered grid are well worth the additional trouble.

By considering Figure 3.2, the central Δ and backward ∇ difference operators are defined for 2-D problems as

$$\begin{aligned}
\Delta r_j^w &= r_j^v - r_{j-1}^v , & \Delta r_j^v &= r_{j+1}^w - r_j^w , \\
\nabla r_j^w &= r_j^w - r_{j-1}^w , & \nabla r_j^v &= r_j^v - r_j^w .
\end{aligned} \tag{3.19}$$

It is apparent that in this staggered grid the velocity components v and w are defined at different grid points, namely at (r_j^v, θ_k^v) and (r_j^w, θ_k^w) for $v_{j,k}$ and $w_{j,k}$, which are also different from the grid point where the pressure $p_{j,k}$ is defined, *i.e.*, (r_j^w, θ_k^v). The r- and θ-momentum equations and the continuity equation are differenced about the points where $v_{j,k}, w_{j,k}$ and $p_{j,k}$ are defined, respectively. Now the linear interpolation of the velocity components using the difference operators (3.19) is implemented here for certain velocity components

$$v_v^{ru} = \frac{\nabla r_{j+1}^v \, v_{j,k} + \nabla r_{j+1}^w \, v_{j+1,k}}{\Delta r_{j+1}^w} \quad , \qquad v_v^{rd} = \frac{\nabla r_j^v \, v_{j-1,k} + \nabla r_j^w \, v_{j,k}}{\Delta r_j^w} ,$$
$$v_v^{\theta f} = \frac{v_{j,k} + v_{j,k+1}}{2} \quad , \qquad v_v^{\theta b} = \frac{v_{j,k} + v_{j,k-1}}{2} , \tag{3.20}$$

in which ru and rd stand for "upper" and "lower" from a certain radial position, while θf and θb stand for "forward" and "backward" of a certain circumferential position; the derivation of the other components will be illustrated in Appendix A. Meanwhile, the same difference operators will be used to evaluate Δv and Δw appearing in factored forms of equations (2.6-2.9) when they are cast in delta forms which will be given in the section 3.5.

In this analysis, the grid has uniform spacing $\Delta\theta$ in the circumferential direction θ and is stretched in the radial direction in order to cluster more points near the cylinder walls. Furthermore, the evaluation of the viscous derivative term $(1/r)(\partial/\partial r)(r\partial w/\partial r)$, as appears, for example, in equation (2.9), near the outer or inner cylinder wall requires special treatment, as explained in Chapter 4 for 2-D problems.

Now we are well prepared to write the N-S equations in difference form, using equations (3.19) and (3.20) and the equations presented in Appendix A. The discretization of equations (2.6), (2.8) and (2.9), for example for 2-D problems, is thus given by the following relations:

$$(\nabla \cdot \mathbf{V})_{j,k} = \frac{r_j^v \, v_{j,k} - r_{j-1}^v \, v_{j-1,k}}{r_j^w \, \Delta r_j^w} + \frac{w_{j,k} - w_{j,k-1}}{r_j^w \, \Delta\theta} , \tag{3.21}$$

$$
\begin{aligned}
(Q_v)_{j,k} &= \frac{1}{r_j^v\,\Delta r_j^v}\Bigg[r_{j+1}^w\,(v_v^{ru})^2 - r_j^w\,(v_v^{rd})^2 \\
&- \frac{1}{\mathrm{Re}}\left\{\frac{r_{j+1}^w}{\Delta r_{j+1}^w}\,(v_{j+1,k}-v_{j,k}) - \frac{r_j^w}{\Delta r_j^w}\,(v_{j,k}-v_{j-1,k})\right\}\Bigg] \\
&+ \frac{p_{j+1,k}-p_{j,k}}{\Delta r_j^v} + \frac{1}{r_j^v}\left[\frac{w_v^{\theta f}\,v_v^{\theta f} - w_v^{\theta b}\,v_v^{\theta b}}{\Delta\theta} - (w_v)^2\right] \qquad (3.22) \\
&- \frac{1}{\mathrm{Re}\,(r_j^v)^2}\left[\frac{v_{j,k+1}+v_{j,k-1}-2\,v_{j,k}}{(\Delta\theta)^2} - 2\,\frac{w_v^{\theta f}-w_v^{\theta b}}{\Delta\theta} - v_{j,k}\right],
\end{aligned}
$$

$$
\begin{aligned}
(Q_w)_{j,k} &= \frac{1}{r_j^w\,\Delta r_j^w}\Bigg[r_j^v\,v_w^{ru}w_w^{ru} - r_{j-1}^v\,v_w^{rd}w_w^{rd} \\
&- \frac{1}{\mathrm{Re}}\left\{\frac{r_j^v}{\Delta r_j^v}\,(w_{j+1,k}-w_{j,k}) - \frac{r_{j-1}^v}{\Delta r_{j-1}^v}\,(w_{j,k}-w_{j-1,k})\right\}\Bigg] \\
&+ \frac{1}{r_j^w}\left[\frac{(w_w^{\theta f})^2-(w_w^{\theta b})^2+p_{j,k+1}-p_{j,k}}{\Delta\theta} + v_w\,w_{j,k}\right] \qquad (3.23) \\
&- \frac{1}{\mathrm{Re}\,(r_j^w)^2}\left[\frac{w_{j,k+1}+w_{j,k-1}-2\,w_{j,k}}{(\Delta\theta)^2} + 2\,\frac{v_w^{\theta f}-v_w^{\theta b}}{\Delta\theta} - w_{j,k}\right].
\end{aligned}
$$

The superscripts $ru, rd, \theta f$ and θb specify the upper and lower as well as forward and backward components of the interpolated velocities as in (3.20) and similar equations. The terms v_w and w_v need special interpolations and are given in Appendix A.

3.5 Method of Solution Based on the ADI Scheme

Now we apply an approximate factorization (Hoffman 1989) to (3.11), thereby rewriting the implicit left-hand side of the equation as

$$
\left[\mathbf{I}+\beta\Delta\tau(\mathbf{M}_x+\mathbf{M}_r+\mathbf{M}_\theta)\right]\Delta\Psi = (\mathbf{I}+\beta\Delta\tau\mathbf{M}_x)(\mathbf{I}+\beta\Delta\tau\mathbf{M}_r)(\mathbf{I}+\beta\Delta\tau\mathbf{M}_\theta)\Delta\Psi = \Delta\tau\mathbf{S}\,. \qquad (3.24)
$$

The nonlinear term in equation (3.9) appears as $\Delta\mathbf{Q}$. This term is linearized by simply lagging the velocity component (Anderson *et al.* 1984) which, along with the

$\Delta \mathbf{V}$ components, in pseudo-time variation form are expressed as

$$\Delta \mathbf{V} = \begin{bmatrix} \Delta u \\ \Delta v \\ \Delta w \end{bmatrix} = \begin{bmatrix} \hat{u}^{\mu+1} - \hat{u}^{\mu} \\ \hat{v}^{\mu+1} - \hat{v}^{\mu} \\ \hat{w}^{\mu+1} - \hat{w}^{\mu} \end{bmatrix},$$

$$\Delta \mathbf{Q} = \begin{bmatrix} \Delta Q_u \\ \Delta Q_v \\ \Delta Q_w \end{bmatrix} = \begin{bmatrix} \hat{Q}_u^{\mu+1} - \hat{Q}_u^{\mu} \\ \hat{Q}_v^{\mu+1} - \hat{Q}_v^{\mu} \\ \hat{Q}_w^{\mu+1} - \hat{Q}_w^{\mu} \end{bmatrix},$$

with, for example, ΔQ_u in cylindrical coordinates given by

$$\begin{aligned} \Delta Q_u \equiv & \frac{\partial(\hat{u}^{\mu}\Delta u)}{\partial x} + \frac{1}{r}\frac{\partial(r\hat{v}\Delta u)}{\partial r} + \frac{1}{r}\frac{\partial(\hat{w}\Delta u)}{\partial \theta} + \frac{\partial(\Delta p)}{\partial x} \\ & - \frac{1}{\mathrm{Re}}\left[\frac{\partial^2(\Delta u)}{\partial x^2} + \frac{1}{r}\frac{\partial}{\partial r}\left(r\frac{\partial(\Delta u)}{\partial r}\right) + \frac{1}{r^2}\frac{\partial^2(\Delta u)}{\partial \theta^2}\right], \end{aligned} \tag{3.25}$$

which is first-order accurate, consistent with the order of accuracy of the Euler pseudo-time semi-discretization discussed previously.

An alternating direction implicit (ADI) scheme (Peaceman & Rachford 1955) is used in this analysis in order to separate the numerical integration of the linear system of equations (3.24). This is done by introducing the intermediate variables $\overline{\Delta\Psi} = [\overline{\Delta u}, \overline{\Delta v}, \overline{\Delta w}, \overline{\Delta p}]^T$ and $\widetilde{\Delta\Psi} = [\widetilde{\Delta u}, \widetilde{\Delta v}, \widetilde{\Delta w}, \widetilde{\Delta p}]^T$, thereby leading to

$$(\mathbf{I} + \beta\,\Delta\tau \mathbf{M}_r)\,\widetilde{\Delta\Psi} = \Delta\tau\,\mathbf{S}, \tag{3.26}$$

$$(\mathbf{I} + \beta\,\Delta\tau \mathbf{M}_\theta)\,\overline{\Delta\Psi} = \widetilde{\Delta\Psi}, \tag{3.27}$$

$$(\mathbf{I} + \beta\,\Delta\tau \mathbf{M}_x)\,\Delta\Psi = \overline{\Delta\Psi}. \tag{3.28}$$

In, for example equation (3.26), the variables $\widetilde{\Delta u}, \widetilde{\Delta v}, \widetilde{\Delta w}$, and $\widetilde{\Delta p}$ are decoupled as well as the corresponding variables in equations (3.27) and (3.28). Then, for each variable $(\Delta u, \Delta v, \Delta w)$ and for each direction (x, r, θ) the solving reduces to a tridiagonal systems of equations. Since central differences are used to discretize the spatial differential operators, only the resulting tridiagonal systems of equations need to be solved, which is computationally efficient. The procedure for solving the specific problems by using the matrix equations (3.26-3.28) in 3-D or the simplified form in

2-D for different annular geometries will be explained in the related chapters.

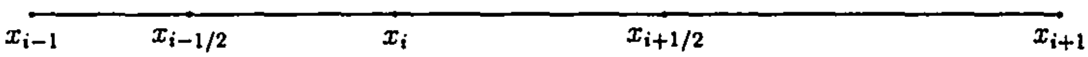

Figure 3.1: Portion of a one-dimensional stretched grid.

$$
\begin{array}{llllllll}
r^v_{j+1} & — & \diamond v_{j+1,k-1} & & \diamond v_{j+1,k} & & \diamond v_{j+1,k+1} & \\
r^w_{j+1} & — & \bigcirc p_{j+1,k-1} & \square w_{j+1,k-1} & \bigcirc p_{j+1,k} & \square w_{j+1,k} & \bigcirc p_{j+1,k+1} & \square w_{j+1,k+1} \\
r^v_{j} & — & \diamond v_{j,k-1} & & \diamond v_{j,k} & & \diamond v_{j,k+1} & \\
r^w_{j} & — & \bigcirc p_{j,k-1} & \square w_{j,k-1} & \bigcirc p_{j,k} & \square w_{j,k} & \bigcirc p_{j,k+1} & \square w_{j,k+1} \\
r^v_{j-1} & — & \diamond v_{j-1,k-1} & & \diamond v_{j-1,k} & & \diamond v_{j-1,k+1} & \\
r^w_{j-1} & — & \bigcirc p_{j-1,k-1} & \square w_{j-1,k-1} & \bigcirc p_{j-1,k} & \square w_{j-1,k} & \bigcirc p_{j-1,k+1} & \square w_{j-1,k+1} \\
 & & | & | & | & | & | & | \\
 & & \theta^v_{k-1} & \theta^w_{k-1} & \theta^v_{k} & \theta^w_{k} & \theta^v_{k+1} & \theta^w_{k+1}
\end{array}
$$

Figure 3.2: Schematic representation of the 2-D staggered grid used to discretize the non-linear unsteady annular flow equations.

Chapter 4

2-D and 3-D Unsteady Annular Flow Solutions: Method Validation

To solve the unsteady Navier-Stokes (N-S) equations one needs to have an initial condition. Here we use the steady state solution. This steady solution is obtained by neglecting the first time-dependent term, *i.e.*, $\partial \mathrm{V}/\partial t$ in equations (2.2) and (2.4). In the present analysis the N-S equations without body forces and the continuity equation are solved numerically.

It has been shown (Mateescu *et al.* 1991) that the three-point backward time-discretization along with the pseudo-time iterative relaxation method using artificial compressibility can be used to solve certain problems in steady and unsteady flows. Available analytical solutions are limited to cases where the annular passage is narrow (Mateescu & Païdoussis 1985), which also limits the amplitude of oscillation to be small, such that the ratio of the amplitude of oscillation to the annular gap width remains small; or the annular passage is narrow and uniform (Mateescu & Païdoussis 1987, 1989).

For both steady and unsteady equations the numerical solution procedure is the same regarding the spatial discretization and pseudo-time relaxation. Usually the numerical solution for each model is compared with either an existing analytical one or experimental results, if available, so as to validate the accuracy of the solution or the applicability of the model to the specific problem at hand.

In the study of viscous incompressible flow, it is necessary to obtain the velocity vector $\mathbf{V}$ and the pressure p as functions of space and time. However, the complete general solution for the N-S equations is still not possible because of analytical difficulties and the lack of appropriate numerical models.

There are various approaches for working out the solution of the N-S and continuity equations in general, and in the present analysis in annular geometries. In the first approach, assuming small-amplitude periodic motions of the structure, one imposes a periodic motion on the confined fluid and decomposes the velocity into steady and unsteady components,

$$\mathbf{V}(x,r,\theta,t) = \mathbf{V}_s(x,r,\theta) + \mathbf{V}_u(x,r,\theta,t)\ ; \tag{4.1}$$

the pressure is also expressed as the sum of steady and unsteady terms,

$$p(x,r,\theta,t) = p_s(x,r,\theta) + p_u(x,r,\theta,t). \tag{4.2}$$

The equations for steady viscous flow are

$$(\mathbf{V}_s\cdot\nabla)\mathbf{V}_s = -\frac{1}{\rho}\nabla p_s + \nu\nabla^2\mathbf{V}_s\,, \qquad \nabla\cdot\mathbf{V}_s = 0\,. \tag{4.3, 4.4}$$

The system of equations in both steady and unsteady flows is solved subject to appropriate boundary and initial conditions, one of which is the impermeability condition at the surface of the oscillating structure.

For the steady-flow solution, equations (2.3) and (2.5) read

$$\mathbf{Q}(\mathbf{V},p) = \mathbf{0}\,, \qquad \nabla\cdot\mathbf{V} = 0\,, \tag{4.5, 4.6}$$

where the term $\mathbf{Q}(\mathbf{V},p)$ is expressed as

$$\mathbf{Q}(\mathbf{V},p) = \nabla\cdot\mathbf{V}\mathbf{V} + \nabla p - \frac{1}{\mathrm{Re}}\nabla^2\mathbf{V}\,. \tag{4.7}$$

The pseudo-time analogy of equations (4.5) and (4.6) for steady flow then becomes

$$\frac{\partial\hat{\mathbf{V}}}{\partial\tau} + \hat{\mathbf{Q}}(\mathbf{V},p) = \mathbf{0}\,, \qquad \delta\frac{\partial\hat{p}}{\partial\tau} + \nabla\cdot\hat{\mathbf{V}} = 0\,; \tag{4.8, 4.9}$$

by applying the implicit Euler scheme for semi-discretization and finally recasting the equations in the form of equations (3.7) and (3.8) results in

$$\Delta \mathbf{V} + \Delta\tau\Delta\mathbf{Q} = -\Delta\tau\hat{\mathbf{Q}}^{\mu}, \tag{4.10}$$

$$\Delta p + \frac{\Delta\tau}{\delta}\nabla\cdot(\Delta\mathbf{V}) = -\frac{\Delta\tau}{\delta}\nabla\cdot\hat{\mathbf{V}}^{\mu}, \tag{4.11}$$

in which equation (4.10) is more simplified due to the fact that $\beta = 1$; the vector equation (3.12) reduces to

$$\mathbf{S} = \begin{bmatrix} -\hat{\mathbf{Q}}^{\mu} \\ -(1/\delta)\,\nabla\cdot\hat{\mathbf{V}}^{\mu} \end{bmatrix}.$$

Since the procedure for discretizing the equations and solving the problem, especially in the pseudo-time integration of the equations, is identical for steady and unsteady annular flows, only the solution for the unsteady flow is described. As a matter of fact, the steady solution of the N-S equations is the unsteady solution for just one real time step and several pseudo-time steps; in this case the moving boundary remains stationary.

In this analysis the major differences between the steady and unsteady solutions, besides the boundary movement, is the method of selecting the artificial compressibility factors and pseudo-time steps. For steady solutions of the N-S equations, the selection of the artificial compressibility factor δ and pseudo-time step $\Delta\tau$ is done as explained by Chorin (1967) and Soh (1987). To begin, we note that the reason for introducing artificial compressibility is to allow the flow field to converge quickly to an incompressible solution. Based on equation (3.6), we remark that the pressure change at a point with respect to artificial time is large if δ is small; for steady flows, δ is related to the speed of propagation of a pressure disturbance by $a = 1/\delta^{1/2}$, where a is the artificial sound velocity in the fluid. The method of artificial compressibility requires that the speed of fluid particles be less than the speed of sound or $M_a < 1$, where M_a is the artificial Mach number defined by $M_a = U_{max}/a$. The solution will not converge if the artificial Mach number is near zero, because a disturbance propagates through too large a portion of the flow field if a is too large; but if the Mach number is close to unity, the pressure disturbance propagates only slightly faster than the maximum velocity and the magnitude of the disturbance is small.

The selection of δ depends on whether the flow is steady or unsteady. In the steady flow problem, as explained in Soh (1987), the value of δ depends on the characteristics of the square matrices of the following equation:

$$\frac{\partial}{\partial t}\begin{bmatrix} u \\ v \\ p \end{bmatrix} + \begin{bmatrix} 2u & 0 & 1 \\ v & u & 0 \\ 1/\delta & 0 & 0 \end{bmatrix} \frac{\partial}{\partial x}\begin{bmatrix} u \\ v \\ p \end{bmatrix} + \begin{bmatrix} v & u & 0 \\ 0 & 2v & 1 \\ 0 & 1/\delta & 0 \end{bmatrix} \frac{\partial}{\partial y}\begin{bmatrix} u \\ v \\ p \end{bmatrix} = 0\,, \tag{4.12}$$

where $\beta = 1$ and the characteristics of both square matrices are $\lambda_1 = (u^2+v^2)^{1/2}$, $\lambda_{2,3} = (u^2+v^2)^{1/2} \pm (u^2+v^2+1/\delta)^{1/2}$, which indicates that two right-running waves at the inlet and one left-running wave at the exit propagate into the computational domain. This necessitates that a certain number of boundary conditions to be imposed at the inlet and exit, namely u and v at the inlet and p at the outlet; p is given by the following equation

$$p_{I,j} - p_{I,2} = -\int_{y_2^*}^{y_j^*} \left[\frac{\partial(uv)}{\partial x} + \frac{\partial(vv)}{\partial y} - \frac{1}{Re}\left(\frac{\partial^2 v}{\partial x^2} + \frac{\partial^2 v}{\partial y^2}\right)\right]_{x=x_I^*} dy\,, \tag{4.13}$$

see Soh (1987).

We choose δ in such a way that the magnitudes of the eigenvalues are of the same order as

$$\begin{aligned} \lambda_2 &\sim (u^2+v^2)^{1/2} + (u^2+v^2+1/\delta)^{1/2}\,, \\ \lambda_3 &\sim \left|(u^2+v^2)^{1/2} - (u^2+v^2+1/\delta)^{1/2}\right|\,. \end{aligned} \tag{4.14}$$

According to this analysis, from equation (4.14) we conclude that these eigenvalues have the same order if δ is selected to be

$$\delta = \frac{1}{3q^2}\,, \tag{4.15}$$

where $q^2 = u^2+v^2$ is some representative flow speed. Now, the pseudo-time increment, $\Delta\tau$, can be expressed as

$$\Delta\tau = \frac{\mathrm{Cr}\Delta x}{\lambda}\,, \tag{4.16}$$

where Δx is a typical mesh spacing and Cr is the Courant number, which is a criterion for the convergence of the numerical solution. This number can be chosen appropriately to accelerate convergence.

For unsteady-flow problems, similar to the case of steady ones, we first need to determine the artificial compressibility factor δ and the pseudo-time step $\Delta\tau$. To that end, the matrix equation (4.12) will be used with certain modifications. First, due to unsteadiness of the flow field the real time t in terms of $\beta = 2\Delta t/3$ will appear in the equations. Second, to have an idea of the appropriate value of δ, it is not necessary to solve the two-dimensional inviscid matrix equation (4.12). A one-dimensional model problem from (3.5) and (3.6) will provide (Soh and Goodrich 1988)

$$\frac{\partial}{\partial\tau}\left\{\begin{array}{c}\hat{u}\\ \hat{p}\end{array}\right\} + \left[\begin{array}{cc}2\beta\hat{u} & \beta\\ 1/\delta & 0\end{array}\right]\frac{\partial}{\partial x}\left\{\begin{array}{c}\hat{u}\\ \hat{p}\end{array}\right\} = 0\,, \tag{4.17}$$

where nonderivative and nonhomogeneous terms are dropped for simplicity. The eigenvalues of the square matrix in (4.17) are

$$\lambda_{\pm} = \beta\hat{u} \pm (\beta^2\hat{u}^2 + \beta/\delta)^{1/2}\,. \tag{4.18}$$

They are real and distinct, so that the system (4.17) with artificial compressibility is hyperbolic in pseudo-time, and subsonic in the sense that the eigenvalues are of opposite sign.

Since an eigenvalue of the system (4.17) is a wave propagation velocity, the λ's in (4.18) as explained before may be interpreted as waves travelling with and against the fluid flow with a sound-like velocity, $(\beta^2\hat{u}^2 + \beta/\delta)^{1/2}$, relative to the local fluid flow. The local flow velocity in (4.18) is $\beta\hat{u}$ instead of $\hat{u}$, because that system was derived in pseudo-time by using a three-point backward time discretization. The choice of a value for δ is optimal if the magnitudes of the eigenvalues are close to each other (of the same order), as stated for the steady-flow problems by

$$\beta\hat{u} \sim \beta\hat{u} + (\beta^2\hat{u}^2 + \beta/\delta)^{1/2} \sim (\beta^2\hat{u}^2 + \beta/\delta)^{1/2} - \beta\hat{u}\,.$$

A good compromise can be reached if we take δ to be $1/(3\beta\hat{u}^2)$, so that the ratio of the largest to the smallest eigenvalues becomes only 3 (Soh 1987). Again, since the flow model defined by (4.17) is similar to a subsonic compressible flow, it can be characterized by an artificial Mach number $M_a = q\sqrt{\beta\delta} = q\sqrt{2\delta\Delta t/3} \approx \sqrt{1/3}$, in which q represents a characteristic flow speed as defined previously and $\beta = 2\Delta t/3$. Thus, in the present analysis for unsteady flows, δ is given by

$$\delta = \frac{1}{2q^2\Delta t}, \tag{4.19}$$

where Δt is the real physical time-step.

The choice of q is highly heuristic, especially for a fluid flow with no preferred direction. However, equation (4.19) provides a plausible guideline for the artificial compressibility. The estimation of the pseudo-time step $\Delta\tau$ will follow the same argument as in the case of steady-flow problems and it is based on relation (4.16) with $\lambda = \lambda_+$. For optimal values of δ and $\Delta\tau$, a physical understanding or qualitative estimation of the flow field under consideration as well as numerical experiments are needed.

4.1 2-D Unsteady Annular Flow Solutions

The time-accurate method of solution of the unsteady incompressible N-S equations equations was developed in Chapter 3. To obtain a numerical solution to these equations in 2-D annular flows, the governing equations (3.26-3.28) are reduced substantially, *i.e.*, all derivatives with respect to x are equal to zero.

In addition, we assume that the inner cylinder remains fixed and the outer cylinder undergoes transverse oscillations while its axis always remains parallel to the axis of the inner cylinder; the dynamics of fluid flow induced by the movement of the outer cylinder does not need to be necessarily dependent on axial flow. Therefore, the equation of axial momentum is not solved and only the momentum equations in the r and θ directions and the continuity equation need to be considered. Furthermore, the equations are solved on a two-dimensional mesh spanning the radial and circumferential coordinate directions. As far as the boundary conditions are concerned, due to the two-dimensionality of the solution, there is no need to impose boundary conditions at the inlet or outlet. Since the geometry of the confined fluid changes with time as the outer cylinder undergoes oscillation, the method of solution should be suitable for problems with a variable computational domain. An excellent survey for various methods used for variable computational domains is given by Thompson *et al.* (1982). In this chapter, the boundary conditions are imposed at the mean position of the oscillating boundaries, which, as we shall see later, is appropriate for the case of small-amplitude oscillations.

The geometry of the two-dimensional unsteady annular flow system is shown in Figure 4.1 in which the mean position of the outer cylinder is indicated by a solid line.

During the oscillation of the outer cylinder we assume that the boundary will move with velocity $\mathbf{U}_w(t)$, and the vertical displacement of the outer cylinder is given by $\epsilon(t)$. The boundary conditions associated with this geometry are given by equations (2.13) and (2.14).

4.1.1 Differential Form of the Non-linear Navier-Stokes Equations

In the two-dimensional flow field illustrated in Figure 4.1(a), we write the matrices $\mathbf{M}_r$ and $\mathbf{M}_\theta$ as

$$\mathbf{M}_r = \begin{bmatrix} M + 1/\beta + 1/(\mathrm{Re}\, r^2) & -\hat{w}^\mu/r & \partial/\partial r \\ 0 & M + \hat{v}^\mu/r + 1/(\mathrm{Re}\, r^2) & 0 \\ (1/\beta\delta\, r)(\partial/\partial r)(r) & 0 & 0 \end{bmatrix},$$

$$\mathbf{M}_\theta = \begin{bmatrix} N & (2/\mathrm{Re}\, r^2)\partial/\partial\theta & 0 \\ -(2/\mathrm{Re}\, r^2)\partial/\partial\theta & N + 1/\beta & (1/r)\partial/\partial\theta \\ 0 & (1/\beta\delta\, r)\partial/\partial\theta & 0 \end{bmatrix},$$

where

$$M\varphi = \frac{\partial(r\hat{v}^\mu\varphi)}{r\,\partial r} - \frac{1}{\mathrm{Re}}\frac{\partial}{r\,\partial r}\left(r\frac{\partial\varphi}{\partial r}\right),$$

$$N\varphi = \frac{\partial(\hat{w}^\mu\varphi)}{r\,\partial\theta} - \frac{1}{\mathrm{Re}}\frac{\partial^2\varphi}{r^2\,\partial\theta^2},$$

and the components of $\mathbf{Q}(\mathbf{V},p)$ in the radial and circumferential directions and the continuity equation are given by

$$
\begin{aligned}
Q_v(v,w,p) &= \frac{1}{r}\frac{\partial(rvv)}{\partial r} + \frac{1}{r}\frac{\partial(wv)}{\partial \theta} - \frac{w^2}{r} + \frac{\partial p}{\partial r} \\
&- \frac{1}{\mathrm{Re}}\left[\frac{1}{r}\frac{\partial}{\partial r}\left(r\frac{\partial v}{\partial r}\right) + \frac{1}{r^2}\frac{\partial^2 v}{\partial \theta^2} - \frac{2}{r^2}\frac{\partial w}{\partial \theta} - \frac{v}{r^2}\right] ,
\end{aligned} \tag{4.20}
$$

$$
\begin{aligned}
Q_w(v,w,p) &= \frac{1}{r}\frac{\partial(rvw)}{\partial r} + \frac{1}{r}\frac{\partial(ww)}{\partial \theta} + \frac{vw}{r} + \frac{1}{r}\frac{\partial p}{\partial \theta} \\
&- \frac{1}{\mathrm{Re}}\left[\frac{1}{r}\frac{\partial}{\partial r}\left(r\frac{\partial w}{\partial r}\right) + \frac{1}{r^2}\frac{\partial^2 w}{\partial \theta^2} + \frac{2}{r^2}\frac{\partial v}{\partial \theta} - \frac{w}{r^2}\right] ,
\end{aligned} \tag{4.21}
$$

$$
\nabla \cdot \mathbf{V} = \frac{1}{r}\frac{\partial(rv)}{\partial r} + \frac{1}{r}\frac{\partial w}{\partial \theta} . \tag{4.22}
$$

The matrix equations (3.26) and (3.27) in different sweeps are then written as

$$
(\mathbf{I} + \beta\,\Delta\tau \mathbf{M}_r)\,\overline{\Delta\Psi} = \Delta\tau \mathbf{S} , \tag{4.23}
$$

$$
(\mathbf{I} + \beta\,\Delta\tau \mathbf{M}_\theta)\,\Delta\Psi = \overline{\Delta\Psi} , \tag{4.24}
$$

where, in this case, $\Delta\Psi = [\Delta v, \Delta w, \Delta p]^T$ and $\overline{\Delta\Psi} = [\overline{\Delta v}, \overline{\Delta w}, \overline{\Delta p}]^T$.

Hence, for 2-D problems the momentum and continuity equations to be discretized are limited to two matrix equations in the $r-$ and $\theta-$ directions, *i.e.*, the equations (4.23-4.24).

In the r-sweep, the equations become

$$
\begin{aligned}
(1+\Delta\tau)\,\overline{\Delta v} &+ \beta\,\Delta\tau \left[\frac{\partial(r\,\hat{v}^\mu\,\overline{\Delta v})}{r\,\partial r} + \frac{\partial(\overline{\Delta p})}{\partial r} - \frac{\hat{w}^\mu \overline{\Delta w}}{r}\right. \\
&- \left.\frac{1}{\mathrm{Re}}\left\{\frac{\partial}{r\,\partial r}\left(r\,\frac{\partial(\overline{\Delta v})}{\partial r}\right) - \frac{\overline{\Delta v}}{r^2}\right\}\right] \\
&= \Delta\tau(E_v^n - \hat{v}^\mu - \beta\hat{Q}_v^\mu) ,
\end{aligned} \tag{4.25}
$$

$$
\begin{aligned}
\overline{\Delta w} &+ \beta\,\Delta\tau \left[\frac{\partial(r\,\hat{v}^\mu\,\overline{\Delta w})}{r\,\partial r} + \frac{\hat{v}^\mu \overline{\Delta w}}{r} - \frac{1}{\mathrm{Re}}\frac{\partial}{r\,\partial r}\left(r\,\frac{\partial(\overline{\Delta w})}{\partial r}\right) + \frac{\overline{\Delta w}}{\mathrm{Re} r^2}\right] \\
&= \Delta\tau(E_w^n - \hat{w}^\mu - \beta\hat{Q}_w^\mu) ,
\end{aligned} \tag{4.26}
$$

$$\overline{\Delta p} + \frac{\Delta\tau}{\delta}\frac{\partial(r\,\overline{\Delta v})}{r\,\partial r} = -\frac{\Delta\tau}{\delta}\,\nabla\cdot\hat{\mathbf{V}}^{\mu}\ ; \tag{4.27}$$

and in the θ-sweep

$$\Delta v \quad + \quad \beta\,\Delta\tau\left[\frac{\partial(\hat{w}^{\mu}\Delta v)}{r\,\partial\theta} - \frac{1}{\mathrm{Re}}\frac{\partial^2(\Delta v)}{r^2\,\partial\theta^2}\right] = \overline{\Delta v} - \frac{2}{\mathrm{Re}r^2}\frac{\partial(\Delta w)}{\partial\theta}\ , \tag{4.28}$$

$$(1+\Delta\tau)\,\Delta w \quad + \quad \beta\,\Delta\tau\left[\frac{\partial(\hat{w}^{\mu}\Delta w)}{r\,\partial\theta} + \frac{\partial(\Delta p)}{r\,\partial\theta} - \frac{1}{\mathrm{Re}}\frac{\partial^2(\Delta w)}{r^2\,\partial\theta^2}\right]$$

$$= \quad \overline{\Delta w} + \frac{2}{\mathrm{Re}r^2}\frac{\partial(\Delta v)}{\partial\theta}\ , \tag{4.29}$$

$$\Delta p + \frac{\Delta\tau}{\delta}\frac{\partial(\Delta w)}{r\,\partial\theta} = \overline{\Delta p}\ , \tag{4.30}$$

where $\hat{\mathbf{Q}}^{\mu}_{v} = \mathbf{Q}_v(\hat{v}^{\mu},\hat{w}^{\mu},\hat{p}^{\mu}), \hat{\mathbf{Q}}^{\mu}_{w} = \mathbf{Q}_w(\hat{v}^{\mu},\hat{w}^{\mu},\hat{p}^{\mu})$. The variables $\hat{v}^{\mu+1} = \hat{v}^{\mu} + \Delta v, \hat{w}^{\mu+1} = \hat{w}^{\mu} + \Delta w, \hat{p}^{\mu+1} = \hat{p}^{\mu} + \Delta p$ are thus obtained by solving equations (4.25-4.30). The solution proceeds to the next pseudo-time iteration step until convergence, which is reached when Δv, Δw, and Δp are equal to zero.

One can notice that equations (4.25) and (4.27) in the r-sweep and equations (4.29) and (4.30) in the θ-sweep are coupled. A decoupling procedure is used to eliminate $\overline{\Delta p}$ and Δp from equations (4.25) and (4.29) with the aid of the continuity equation (4.27) and equation (4.30), respectively. This is done in conjunction with the discretization of equations (4.25)-(4.30) in the r- and θ-directions. This finally leads to a set of scalar tridiagonal equations, corresponding to equations (4.25), (4.26), (4.28) and (4.29), which are solved for $\overline{\Delta v}$, $\overline{\Delta w}$, Δv and Δw. Then, $\overline{\Delta p}$ and Δp can easilly be calculated from equations (4.27) and (4.30). Details of the discretizations are given in Appendix A and the discretized tridiagonal forms of the equations are described in the following paragraphs.

The $r-$momentum equation (4.25) in the r-sweep, after being coupled with the continuity equation and in discretized form, is given by

$$\overline{\Delta v}_{j-1,k}\left[\frac{\beta\Delta\tau}{r^v\Delta r^v_j}\left\{-r^w_j v^{rd}_v\frac{\nabla r^v_j}{\Delta r^w_j} - \frac{r^w_j}{\mathrm{Re}\Delta r^w_j}\right\} - \frac{\beta\Delta\tau^2 r^v_{j-1}}{\delta r^w_j\Delta r^w_j\Delta r^v_j}\right]$$

$$
\begin{aligned}
&+\overline{\Delta v}_{j,k}\left[1.0+\Delta\tau+\frac{\beta\Delta\tau}{r_j^v\Delta r_j^v}\left\{r_{j+1}^w v_v^{ru}\frac{\nabla r_{j+1}^v}{\Delta r_{j+1}^w}-r_j^w v_v^{rd}\frac{\nabla r_j^w}{\Delta r_j^w}\right.\right.\\
&\left.\left.+\frac{1}{\mathrm{Re}}\left(\frac{r_{j+1}^w}{\Delta r_{j+1}^w}+\frac{r_j^w}{\Delta r_j^w}+\frac{\Delta r_j^v}{r_j^v}\right)+\frac{\Delta\tau r_j^{v2}}{\delta r_j^w\Delta r_j^w}+\frac{\Delta\tau r_j^{v2}}{\delta r_{j+1}^w\Delta r_{j+1}^w}\right\}\right]\\
&+\overline{\Delta v}_{j+1,k}\left[\frac{\beta\Delta\tau}{r_j^v\Delta r_j^v}\left(r_{j+1}^w v_v^{ru}\frac{\nabla r_{j+1}^w}{\Delta r_{j+1}^w}-\frac{r_{j+1}^w}{\mathrm{Re}\Delta r_{j+1}^w}\right)-\frac{\beta\Delta\tau^2 r_{j+1}^v}{\delta r_{j+1}^w\Delta r_{j+1}^w\Delta r_j^v}\right]\\
&=\Delta\tau\left(E_v^n-\hat{v}^\mu-\beta\hat{Q}_v^\mu\right)_{j,k}+\frac{\beta\Delta\tau^2}{\delta\Delta r_j^v}\left(\nabla\cdot\mathbf{V}_{j+1,k}-\nabla\cdot\mathbf{V}_{j,k}\right). \qquad (4.31)
\end{aligned}
$$

For a given θ coordinate, θ_k, setting up equation (4.31) for each j, $2\leq j\leq J-2$, where j is the grid index in the $r-$direction, gives a *tridiagonal system of equations* which must be solved for $\overline{\Delta v}_{j,k}$. Note that $j=J-1$ corresponds, for example, to a solid wall (Soh 1987). This computation is done for each θ_k, $3\leq k\leq K-1$, where k is the grid index in the $\theta-$direction. Hence, $\overline{\Delta v}_{j,k}$ is calculated for all j and k, except at the boundaries where we have them as the boundary conditions. The reason that at θ_2 the calculation is not implemented is the usage of a staggered grid plus the symmetry of the problem with regard to the plane of oscillation, which will is explained in Appendix A. The left-hand side of equation (4.31) contains the terms that come from using central differences for the viscous derivatives. These derivatives are evaluated using non-central differencing near the solid walls as explained in the following paragraphs. We note that $\overline{\Delta p}_{j,k}$ is obtained from the continuity equation after $\overline{\Delta v}_{j,k}$ is determined.

The θ-momentum equation in the r-sweep and in discretized form is written as

$$
\begin{aligned}
&\overline{\Delta w}_{j-1,k}\left\{\frac{\beta\Delta\tau}{r_j^w\Delta r_j^w}\left[-r_{j-1}^v v_w^{rd}\frac{\nabla r_j^w}{\Delta r_{j-1}^v}-\frac{r_{j-1}^v}{\mathrm{Re}\Delta r_{j-1}^v}\right]\right\}\\
&+\overline{\Delta w}_{j,k}\left\{1.0+\frac{\beta\Delta\tau v_w}{r_j^w}+\frac{\beta\Delta\tau}{r_j^w\Delta r_j^w}\left[r_j^v v_w^{ru}\frac{\nabla r_{j+1}^w}{\Delta r_j^v}-r_{j-1}^v v_w^{rd}\frac{\nabla r_{j-1}^v}{\Delta r_{j-1}^v}\right.\right.\\
&\left.\left.+\frac{1}{\mathrm{Re}}\left(\frac{r_j^v}{\Delta r_j^v}+\frac{r_{j-1}^v}{\Delta r_{j-1}^v}\right)\right]+\frac{\beta\Delta\tau}{\mathrm{Re}r_j^{w2}}\right\}\\
&+\overline{\Delta w}_{j+1,k}\left\{\frac{\beta\Delta\tau}{r_j^w\Delta r_j^w}\left[r_j^v v_w^{ru}\frac{\nabla r_j^v}{\Delta r_j^v}-\frac{r_j^v}{\mathrm{Re}\Delta r_j^v}\right]\right\}\\
&=\Delta\tau\left(E_w^n-\hat{w}^\mu-\beta\hat{Q}_w^\mu\right)_{j,k}. \qquad (4.32)
\end{aligned}
$$

Once again this is a tridiagonal system of equations to be solved for $\overline{\Delta w}_{j,k}$. Therefore, equation (4.32) is set up for each j and k in the domain of integration which includes $2 \leq j \leq J-1$ and $2 \leq \theta \leq K-2$.

The r-momentum equation in the θ-sweep in discretized form reads

$$\Delta v_{j,k-1}\left\{\frac{\beta\Delta\tau}{r_j^v\Delta\theta}\left[-w_v^{\theta b}\left(\frac{1}{2}\right)-\frac{1}{\mathrm{Re}\, r_j^v\Delta\theta}\right]\right\}$$
$$+\Delta v_{j,k}\left\{1+\frac{\beta\Delta\tau}{r_j^v\Delta\theta}\left[w_v^{\theta f}\left(\frac{1}{2}\right)-w_v^{\theta b}\left(\frac{1}{2}\right)+\frac{2}{\mathrm{Re}\, r_j^v\Delta\theta}\right]\right\}$$
$$+\Delta v_{j,k+1}\left\{\frac{\beta\Delta\tau}{r_j^v\Delta\theta}\left[w_v^{\theta f}\left(\frac{1}{2}\right)-\frac{1}{\mathrm{Re}\, r_j^v\Delta\theta}\right]\right\}=\overline{\Delta v}_{j,k}-\frac{2(\Delta w_{j,k+1}-\Delta w_{j,k})}{\mathrm{Re}\, r_j^{v2}\Delta\theta}\,. \quad (4.33)$$

Equation (4.33) is set up for $2 \leq j \leq J-2$ and $3 \leq k \leq K-1$. We recall that the corresponding variables at $j = J-1$ come from the wall boundary conditions.

The θ-momentum equation in the θ-sweep and in discretized form is derived as

$$\Delta w_{j,k-1}\left\{\frac{\beta\Delta\tau}{r_j^w\Delta\theta}\left[-w_w^{\theta b}\left(\frac{1}{2}\right)-\frac{\Delta\tau}{\delta}\frac{1}{r_j^w\Delta\theta}-\frac{1}{\mathrm{Re}\, r_j^w\Delta\theta}\right]\right\}$$
$$+\Delta w_{j,k}\left\{1+\Delta\tau+\frac{\beta\Delta\tau}{r_j^w\Delta\theta}\left[w_w^{\theta f}\left(\frac{1}{2}\right)-w_w^{\theta b}\left(\frac{1}{2}\right)+\frac{2}{\mathrm{Re}\, r_j^w\Delta\theta}+\frac{\Delta\tau}{\delta}\frac{2}{r_j^w\Delta\theta}\right]\right\}$$
$$+\Delta w_{j,k+1}\left\{\frac{\beta\Delta\tau}{r_j^w\Delta\theta}\left[w_w^{\theta f}\left(\frac{1}{2}\right)-\frac{\Delta\tau}{\delta}\frac{1}{r_j^w\Delta\theta}-\frac{1}{\mathrm{Re}\, r_j^w\Delta\theta}\right]\right\}$$
$$=\overline{\Delta w}_{j,k}-\frac{\beta\Delta\tau}{r_j^w\Delta\theta}\left(\overline{\Delta p}_{j,k+1}-\overline{\Delta p}_{j,k}\right)+\frac{2(\Delta v_{j,k+1}-\Delta v_{j,k})}{\mathrm{Re}\, r_j^{v2}\Delta\theta}\,. \quad (4.34)$$

Equation (4.34), after being solved by the tridiagonal matrix solver, will be the last equation used in both r- and θ-sweeps with the final result of circumferential velocity difference, Δw. The pressure difference Δp is recovered from the continuity equation. To implement the solution, equation (4.34) is set up for $2 \leq j \leq J-1$ and $3 \leq k \leq K-2$. The magnitudes of the variables at the grid points other than those cited above are obtained by using the boundary values or symmetry conditions explained in the following paragraphs. At this point we recall that after the increments Δv, Δw, and Δp are obtained in each pseudo-time step, the perturbed flow field parameters v, w, and p are updated before the next real time step starts as

$$v^{\mu+1}=v^{\mu}+\Delta v\,, \qquad w^{\mu+1}=w^{\mu}+\Delta w\,, \qquad p^{\mu+1}=p^{\mu}+\Delta p\,,$$

and at the next real time step all these increments have already become zero indicating that the continuity equation (2.3) is satisfied; thus

$$\hat{\mathbf{V}}^{m+1} \equiv \hat{\mathbf{V}}^{n+1} \qquad \text{and} \qquad \hat{p}^{m+1} \equiv \hat{p}^{n+1} ,$$

as explained in Chapter 3.

In order to initiate the time-integration procedure, initial conditions must be provided for $\mathbf{V}^1$, $\mathbf{V}^0$ and p^1, p^0 throughout the fluid domain, which indicates that the solution is known at previous time levels t^1 and t^0. The initial conditions required to start the pseudo-time integration are taken to be ϵ^{n+1} on the moving boundary and $\mathbf{V}^n$, and p^n inside the fluid field, *i.e.*,

$$\hat{\epsilon}^{\mu}\Big|_{\mu=1} = \epsilon^{n+1} , \qquad \hat{\mathbf{V}}^{\mu}\Big|_{\mu=1} = \mathbf{V}^{n} , \qquad \hat{p}^{\mu}\Big|_{\mu=1} = p^{n} , \tag{4.35}$$

where on the boundary of the fluid domain the known displacement ϵ_w^{n+1} and velocity $\mathbf{U}_w^{n+1}$ of the walls at the advanced time level t^{n+1} are set as boundary conditions and kept unchanged until the steady state has been reached in pseudo-time. The wall displacement ϵ_w^{n+1} and velocity $\mathbf{U}_w^{n+1}$ serve as driving terms to advance the solution to time level $(n+1)\Delta t$, along with the nonhomogeneous term $\mathbf{E}^n$, which is also calculated at the beginning of the pseudo-time relaxation and kept constant throughout. In the case of 2-D problems Δv and Δw are zero on a solid wall, even when the wall has non-zero velocity. This is because the velocities v_w^{n+1} and w_w^{n+1} of the wall at t^{n+1} are imposed as boundary conditions and remain fixed during the pseudo-time relaxation.

The annular-flow geometries under consideration throughout this analysis are composed of two bodies of revolution which are concentric and where the space between them is filled with fluid. In addition, the vibration of either body is considered to be constrained only in one plane, the plane of oscillation; therefore, the flow variables v and p for 2-D problems are assumed to be even functions of θ, and w is an odd function of θ; *i.e.*, with respect to the plane of symmetry at $\theta = 0$ and $\theta = \pi$ (see Figure A.1)

$$v_{j,2} = v_{j,3} , \qquad w_{j,1} = -w_{j,3} , \qquad p_{j,2} = p_{j,3} ,$$

$$v_{j,k-1} = v_{j,k}\,, \qquad w_{j,k-2} = -w_{j,k}\,, \qquad p_{j,k-1} = p_{j,k}\,,$$

where k is the index in the θ-direction.

As far as the movement of the solid walls is concerned, on the inner cylinder the displacement $\epsilon(t)$ is zero, while on the outer cylinder in the plane of symmetry it is given by (see Figure 4.1)

$$\bar{\epsilon}_w(t) = -\bar{\epsilon}_w \cos \Omega \bar{t}\,, \tag{4.36}$$

with the velocity of the wall expressed by

$$\dot{\bar{\epsilon}}_w(t) = \bar{\epsilon}_w \Omega \sin \Omega \bar{t}\,, \tag{4.37}$$

where $\bar{\epsilon}$ is the amplitude and Ω is the circular trequency of the oscillation.

The evaluation of the viscous derivative term $(1/r)(\partial/\partial r)(r\partial\hat{w}/\partial r)$ near the boundaries of the outer or inner cylinder requires special treatment. Indeed, by looking at Figure 4.2, which clarifies the evaluation of viscous derivative in the x-r plane and will be used later in this chapter, in the staggered grid a wall parallel with the x-coordinate passes through the points where for example $v_{i,1}$ are defined, and similarly a wall parallel with the r-coordinate passes through the points where $u_{1,j}$ are defined. Hence, the numerical evaluation of the viscous derivatives would require points defined outside the physical boundaries. To handle this problem, we use non-central differencing to compute the aforementioned derivatives and other similar ones.

With reference to Figure 4.3 the viscous derivative $(1/r)(\partial/\partial r)(r\partial\hat{w}/\partial r)$ near the inner cylinder wall is evaluated by

$$\frac{\partial}{r\,\partial r}\left(r\,\frac{\partial \hat{w}}{\partial r}\right)_{r=r_2^w} = \frac{1}{r_2^w\,\Delta r_2^w}\left[r_2^v\left(\frac{\hat{w}_{3,k}-\hat{w}_{2,k}}{\Delta r_2^v}\right) - r_1^v\left(\frac{\frac{8}{3}\,\hat{w}_{w,k} - 3\,\hat{w}_{2,k} + \frac{1}{3}\,\hat{w}_{3,k}}{\frac{8}{3}\,r_1^v - 3\,r_2^w + \frac{1}{3}\,r_3^w}\right)\right]\,, \tag{4.38}$$

where $\hat{w}_{w,k}$ is the wall velocity boundary condition.

A similar procedure applies for the evaluation of the same derivatives near the outer cylinder wall or near a vertical wall in the plane of constant x such as in a region of discontinuity in the annular space; for instance, at the vertical face of a step.

Introducing equations (4.38) into our discretized equations will result in slightly modified equations (Beam and Warming 1978). We recall that Δv and Δw are zero on a solid wall, even when the wall has non-zero velocities; this is because the velocity $\hat{w}_{w,k}$ is imposed as a boundary condition and remains fixed during the pseudo-time relaxation. The initial conditions also set the perturbations equal to zero, before starting the vibration of the outer cylinder, and integration of the equation is implemented until a periodic state in the solution is achieved, which takes at least three harmonic cycles.

For 2-D problems, since there is no fluid velocity U, the Reynolds number, which is defined in terms of the mean-flow velocity U, has no meaning; hence we choose ΩH to be the characteristic velocity, and the Reynolds number in the N-S equations becomes the Stokes number, which is therefore related to the frequency of the system, or Re $\equiv$ S $= \Omega H^2/\nu$, where Ω is the circular frequency of oscillation.

4.2 3-D Unsteady Flow Solution for Uniform and Nonuniform Annular Configurations

In this section, the analysis of the 3-D annular configuration with axial flow is performed by solving the full nonlinear Navier-Stokes and continuity equations for small amplitude oscillation (mean-position analysis) in 3-D. Therefore, all derivatives with respect to x are kept, and the governing equations now are equations (3.26)-(3.28). The mesh used in this analysis will be a 3-D mesh spanning in the x, r and θ directions. Since the flow is along the x-axis, the boundary conditions at the inlet and outlet of the annular space and the initial conditions are required.

The geometry of the 3-D unsteady annular flow is shown in Figure 4.4 in which the mean position of the outer cylinder is indicated by a solid line and the direction of flow is shown by the velocity vector **U**. Once again, the moving boundary of the fluid (outer cylinder) has velocity $\mathbf{U}_w(t)$ and the vertical displacement of the center of the outer cylinder is given by $\epsilon(t)$ for translational motion and by $\epsilon(t,x)$ for rocking motion. The velocities of the boundary v_w and w_w for the case of translational motion are given by equations (2.14). For rocking motion, the velocities v_w and w_w are linearly calculated with respect to the hinge position, as shown in Figure 4.5, and they are given by equations

$$v_w = \dot{\epsilon}(t,x)\cos\theta\,, \qquad w_w = -\dot{\epsilon}(t,x)\sin\theta\,, \tag{4.39, 4.40}$$

where $\dot{\epsilon}(t,x) = d\epsilon(t,x)/dt$, and $\epsilon(t,x)$ is given by

$$\epsilon(t,x) = -\frac{\epsilon(t)}{l_2}x + \frac{\epsilon(t)(l_1+l_2)}{l_2}\,; \tag{4.41}$$

$\epsilon(t)$ is given by equation (4.36), and l_1 and l_2 are constant, as shown in Figure 4.5.

4.2.1 Differential Form of the Non-linear Navier-Stokes and Continuity Equations

In three-dimensional flow fields, equations (3.26-3.28) must be employed; they are given here for reference as

$$(\mathbf{I}+\beta\,\Delta\tau\mathbf{M}_r)\,\widetilde{\Delta\mathbf{f}} = \Delta\tau\;\mathbf{S}\,, \quad (\mathbf{I}+\beta\,\Delta\tau\mathbf{M}_\theta)\,\overline{\Delta\mathbf{f}} = \widetilde{\Delta\mathbf{f}}\,, \quad (\mathbf{I}+\beta\,\Delta\tau\mathbf{M}_x)\,\Delta\mathbf{f} = \overline{\Delta\mathbf{f}}\,,$$

where $\mathbf{S}$ is given by (3.12) and $\Delta\Psi$ is the velocity vector defined in Chapter 3. Then the matrices $\mathbf{M}_x$, $\mathbf{M}_r$, and $\mathbf{M}_\theta$ are

$$\mathbf{M}_x = \begin{bmatrix} L+1/\beta & 0 & 0 & \partial/\partial x \\ 0 & L & 0 & 0 \\ 0 & 0 & L & 0 \\ (1/\beta\delta)\partial/\partial x & 0 & 0 & 0 \end{bmatrix},$$

$$\mathbf{M}_r = \begin{bmatrix} M & 0 & 0 & 0 \\ 0 & M+1/\beta+1/(\mathrm{Re}\,r^2) & -\hat{w}^\mu/r & \partial/\partial r \\ 0 & 0 & M+\hat{v}^\mu/r+1/(\mathrm{Re}\,r^2) & 0 \\ 0 & (1/\beta\delta\,r)(\partial/\partial r)(r) & 0 & 0 \end{bmatrix},$$

$$
\mathbf{M}_\theta = \begin{bmatrix} N & 0 & 0 & 0 \\ 0 & N & (2/\mathrm{Re}\, r^2)\partial/\partial\theta & 0 \\ 0 & -(2/\mathrm{Re}\, r^2)\partial/\partial\theta & N + 1/\beta & (1/r)\partial/\partial\theta \\ 0 & 0 & (1/\beta\delta\, r)\partial/\partial\theta & 0 \end{bmatrix},
$$

where

$$
\begin{aligned}
L\varphi &= \frac{\partial(\hat{u}^\mu \varphi)}{\partial x} - \frac{1}{\mathrm{Re}}\frac{\partial^2 \varphi}{\partial x^2}, \\
M\varphi &= \frac{\partial(r\hat{v}^\mu \varphi)}{r\,\partial r} - \frac{1}{\mathrm{Re}}\frac{\partial}{r\,\partial r}\left(r\frac{\partial \varphi}{\partial r}\right), \\
N\varphi &= \frac{\partial(\hat{w}^\mu \varphi)}{r\,\partial \theta} - \frac{1}{\mathrm{Re}}\frac{\partial^2 \varphi}{r^2\,\partial \theta^2}.
\end{aligned}
$$

The nonlinear Navier-Stokes and continuity equations in terms of Q_u, Q_v, Q_w, and $\nabla \cdot \mathbf{V}$ which will be used in different sweeps, in delta-form equations, as the known explicit terms in pseudo-time, are

$$
\begin{aligned}
Q_u(u,v,w,p) &= \frac{\partial(uu)}{\partial x} + \frac{1}{r}\frac{\partial(rvu)}{\partial r} + \frac{1}{r}\frac{\partial(wu)}{\partial \theta} + \frac{\partial p}{\partial x} \\
&- \frac{1}{\mathrm{Re}}\left[\frac{\partial^2 u}{\partial x^2} + \frac{1}{r}\frac{\partial}{\partial r}\left(r\frac{\partial u}{\partial r}\right) + \frac{1}{r^2}\frac{\partial^2 u}{\partial \theta^2}\right],
\end{aligned} \tag{4.42}
$$

$$
\begin{aligned}
Q_v(u,v,w,p) &= \frac{\partial(uv)}{\partial x} + \frac{1}{r}\frac{\partial(rvv)}{\partial r} + \frac{1}{r}\frac{\partial(wv)}{\partial \theta} - \frac{w^2}{r} + \frac{\partial p}{\partial r} \\
&- \frac{1}{\mathrm{Re}}\left[\frac{\partial^2 v}{\partial x^2} + \frac{1}{r}\frac{\partial}{\partial r}\left(r\frac{\partial v}{\partial r}\right) + \frac{1}{r^2}\frac{\partial^2 v}{\partial \theta^2} - \frac{2}{r^2}\frac{\partial w}{\partial \theta} - \frac{v}{r^2}\right],
\end{aligned} \tag{4.43}
$$

$$
\begin{aligned}
Q_w(u,v,w,p) &= \frac{\partial(uw)}{\partial x} + \frac{1}{r}\frac{\partial(rvw)}{\partial r} + \frac{1}{r}\frac{\partial(ww)}{\partial \theta} + \frac{vw}{r} + \frac{1}{r}\frac{\partial p}{\partial \theta} \\
&- \frac{1}{\mathrm{Re}}\left[\frac{\partial^2 w}{\partial x^2} + \frac{1}{r}\frac{\partial}{\partial r}\left(r\frac{\partial w}{\partial r}\right) + \frac{1}{r^2}\frac{\partial^2 w}{\partial \theta^2} + \frac{2}{r^2}\frac{\partial v}{\partial \theta} - \frac{w}{r^2}\right],
\end{aligned} \tag{4.44}
$$

$$
\nabla \cdot \mathbf{V} = \frac{\partial u}{\partial x} + \frac{1}{r}\frac{\partial(rv)}{\partial r} + \frac{1}{r}\frac{\partial w}{\partial \theta}. \tag{4.45}
$$

The implicit left-hand sides of the matrix equations (3.26-3.28) are then written as:

in the r-sweep:

$$\widetilde{\Delta u} + \beta\,\Delta\tau\,\left[\frac{\partial(r\,\hat{v}^{\mu}\widetilde{\Delta u})}{r\,\partial r} - \frac{1}{\mathrm{Re}}\frac{\partial}{r\,\partial r}\left(r\,\frac{\partial(\widetilde{\Delta u})}{\partial r}\right)\right]$$

$$= \Delta\tau\,(E_u^n - \hat{u}^{\mu} - \beta\,\hat{Q}_u^{\mu})\,, \tag{4.46}$$

$$(1+\Delta\tau)\,\widetilde{\Delta v} + \beta\,\Delta\tau\,\left[\frac{\partial(r\,\hat{v}^{\mu}\,\widetilde{\Delta v})}{r\,\partial r} + \frac{\partial(\widetilde{\Delta p})}{\partial r} - \frac{\hat{w}^{\mu}\widetilde{\Delta w}}{r}\right.$$

$$\left. - \frac{1}{\mathrm{Re}}\left\{\frac{\partial}{r\,\partial r}\left(r\,\frac{\partial(\widetilde{\Delta v})}{\partial r}\right) - \frac{\widetilde{\Delta v}}{r^2}\right\}\right]$$

$$= \Delta\tau\,(E_v^n - \hat{v}^{\mu} - \beta\,\hat{Q}_v^{\mu})\,, \tag{4.47}$$

$$\widetilde{\Delta w} + \beta\,\Delta\tau\,\left[\frac{\partial(r\,\hat{v}^{\mu}\,\widetilde{\Delta w})}{r\,\partial r} + \frac{\hat{v}^{\mu}\widetilde{\Delta w}}{r} - \frac{1}{\mathrm{Re}}\frac{\partial}{r\,\partial r}\left(r\,\frac{\partial(\widetilde{\Delta w})}{\partial r}\right) + \frac{\widetilde{\Delta w}}{\mathrm{Re}r^2}\right]$$

$$= \Delta\tau\,(E_w^n - \hat{w}^{\mu} - \beta\,\hat{Q}_w^{\mu})\,, \tag{4.48}$$

$$\widetilde{\Delta p} + \frac{\Delta\tau}{\delta}\frac{\partial(r\,\widetilde{\Delta v})}{r\,\partial r} = -\frac{\Delta\tau}{\delta}\,\nabla\cdot\hat{\mathbf{V}}^{\mu}\,; \tag{4.49}$$

then, in the θ-sweep:

$$\overline{\Delta u} + \beta\,\Delta\tau\,\left[\frac{\partial(\hat{w}^{\mu}\overline{\Delta u})}{r\,\partial\theta} - \frac{1}{\mathrm{Re}}\frac{\partial^2(\overline{\Delta u})}{r^2\,\partial\theta^2}\right] = \widetilde{\Delta u}\,, \tag{4.50}$$

$$\overline{\Delta v} + \beta\,\Delta\tau\,\left[\frac{\partial(\hat{w}^{\mu}\overline{\Delta v})}{r\,\partial\theta} - \frac{1}{\mathrm{Re}}\frac{\partial^2(\overline{\Delta v})}{r^2\,\partial\theta^2}\right] = \widetilde{\Delta v} - \frac{2}{\mathrm{Re}}\frac{\partial(\overline{\Delta w})}{r^2\partial\theta}\,, \tag{4.51}$$

$$(1+\Delta\tau)\,\overline{\Delta w} + \beta\,\Delta\tau\,\left[\frac{\partial(\hat{w}^{\mu}\overline{\Delta w})}{r\,\partial\theta} + \frac{\partial(\overline{\Delta p})}{r\,\partial\theta} - \frac{1}{\mathrm{Re}}\frac{\partial^2(\overline{\Delta w})}{r^2\partial\theta^2}\right]$$

$$= \widetilde{\Delta w} + \frac{2}{\mathrm{Re}}\frac{\partial(\overline{\Delta v})}{r^2\partial\theta}\,, \tag{4.52}$$

$$\overline{\Delta p} + \frac{\Delta\tau}{\delta}\frac{\partial(\Delta w)}{r\,\partial\theta} = \widetilde{\Delta p}\,; \tag{4.53}$$

and finally in the x-sweep:

$$(1+\Delta\tau)\,\Delta u + \beta\,\Delta\tau\,\left[\frac{\partial(\hat{u}^{\mu}\Delta u)}{\partial x} + \frac{\partial(\Delta p)}{\partial x} - \frac{1}{\mathrm{Re}}\frac{\partial^2(\Delta u)}{\partial x^2}\right] = \overline{\Delta u}\,, \tag{4.54}$$

$$\Delta v \quad + \quad \beta\,\Delta\tau\,\left[\frac{\partial(\hat{u}^{\mu}\Delta v)}{\partial x} - \frac{1}{\mathrm{Re}}\frac{\partial^2(\Delta v)}{\partial x^2}\right] = \overline{\Delta v}\,, \tag{4.55}$$

$$\Delta w \quad + \quad \beta\,\Delta\tau\,\left[\frac{\partial(\hat{u}^{\mu}\Delta w)}{\partial x} - \frac{1}{\mathrm{Re}}\frac{\partial^2(\Delta w)}{\partial x^2}\right] = \overline{\Delta w}\,, \tag{4.56}$$

$$\Delta p + \frac{\Delta\tau}{\delta}\frac{\partial(\Delta u)}{\partial x} = \overline{\Delta p}\,. \tag{4.57}$$

As we see in equation (3.9), there are undifferentiated terms arising from $\Delta\tau\Delta\mathbf{V}$ which we have included in $\mathbf{M}_x$, $\mathbf{M}_r$ and $\mathbf{M}_\theta$. These terms are not the only undifferentiated terms appearing in our matrices, rather the terms which arise in cylindrical coordinates; the terms $-\hat{w}\Delta w/r$ and $\Delta v/r^2\mathrm{Re}$ in the r-momentum equation, $\hat{v}\Delta w/r$ and $\Delta w/r^2\mathrm{Re}$ in the θ-momentum equation are also undifferentiated terms. In addition to these terms, there are some off-diagonal terms $-\hat{w}/r$, $(2/\mathrm{Re}r^2)\partial/\partial\theta$ and $[-(2/\mathrm{Re}r^2)\partial/\partial\theta]$ in the $\mathbf{M}_r$ and $\mathbf{M}_\theta$ matrices that will contribute coupling between the velocity components Δv and Δw in the r- and θ-momentum equations. This coupling indicates that the scalar tridiagonal systems of equations cannot be obtained anymore when using the factored ADI scheme and eliminating the pressure with the aid of the continuity equation. There is, however, a scalar tridiagonal solution for this problem, based on equations (4.46-4.57), which affects (i) neither the overall accuracy of the solution, because these terms are in Δ-form and ultimately become zero; at the end of the pseudo-time integration, (ii) nor do they affect significantly the overall implicit coupling and convergence rate of the pseudo-time iteration procedure. Indeed, when convergence has been reached in pseudo-time, it necessitates that $\Delta\mathbf{V}$ be zero, thus all the terms that have been dropped would then be zero in any case, as are those that are kept. The accuracy in the results is ensured by the terms $\hat{Q}^{\mu}_{u}$, $\hat{Q}^{\mu}_{v}$, and $\hat{Q}^{\mu}_{w}$ which are on the right-hand sides of equations (4.46-4.48), and which are always calculated in their full form. In the present procedure, to reduce the problem to decoupled tridiagonal systems, the off-diagonal terms are lagged and transferred to the right-hand side, as shown in the equations (4.51,4.52). In this manner, the pseudo-relaxation procedure will reflect better the complete equations of fluid motion.

All the quantities in equations (4.46-4.57) are evaluated at the pseudo-time μ and the values of u, v, w, and p are updated at the end of each pseudo-time as

$$\hat{u}^{\mu+1} = \hat{u}^{\mu} + \Delta u\,, \qquad \hat{v}^{\mu+1} = \hat{v}^{\mu} + \Delta v\,, \qquad \hat{w}^{\mu+1} = \hat{w}^{\mu} + \Delta w\,, \qquad \hat{p}^{\mu+1} = \hat{p}^{\mu} + \Delta p\,,$$

and the solution progresses in pseudo-time till convergence is reached where $u^{n+1} \equiv \hat{u}^{m+1}$, $v^{n+1} \equiv \hat{v}^{m+1}$, $w^{n+1} \equiv \hat{v}^{m+1}$, and $p^{n+1} \equiv \hat{p}^{m+1}$, in which $n+1$ is the next real-time step and m is the iteration number. The detailed numerical procedure and the initial and boundary conditions required for the integration will be explained in subsequent sections and in Appendix A.

In section 3.4.1 it was stated that a satisfactory grid generation and grid point distribution are the major requirements for the numerical solution to be accomplished successfully in terms of accuracy and stability. Based on the reasons explained in Chapter 3, the grid generation in this section would follow the same procedure used for 2-D analysis, with the exception that the grid points are now distributed in the axial direction as well. The distribution functions used for grid point location are given by equation (3.13) for the radial direction and (3.15) for the axial direction. These distribution functions provide a good distribution of the grid points in the domain of integration, as shown by Vinokur (1983) and Thompson (1985), and as discussed in Chapter 3.

A typical staggered grid-point distribution in 3-D is shown in Figure 4.6 and in isometric view in Figure 4.7. These diagrams are the result of superposition of two sets of grid point distribution: one shown in Figure 4.8 and the other shown in Figure 4.9, which are in the x-r and r-θ directions, respectively. Since u's and w's have identical r-positions, then $r_j^u = r_j^w$...etc. As we see in Figures 4.6 and 4.7, the pressure p is always located at the centre of a cell and is surrounded by either u and v or by v and w, implying that the grid is also staggered in the θ-direction. The grid is stretched in the x- and r-directions, but not in the θ-direction.

Due to the specific location defined for w, a two-dimensional mesh, *e.g.*, Figure 4.8, is sufficient for numerical calculations because the solution starts, for example for v, in the r-sweep, then it is followed by the θ-sweep and finally by the x-sweep. The same trend for sweeps is used for w and u. Figure 4.7 can be used to visualize the elimination of the pressure term from the momentum equation by using the continuity equation. For instance, $p_{i,j,k}$ is between $u_{i,j,k}$ and $u_{i-1,j,k}$ in the x-direction, between $v_{i,j,k}$ and $v_{i,j-1,k}$ in the r-direction, and between $w_{i,j,k}$ and $w_{i,j,k-1}$ in the θ-direction. Therefore, the r-momentum equation (4.47) is coupled with the continuity equation (4.49) to determine v; the θ-momentum equation (4.52) is coupled with (4.53) to determine w; and, ultimately, the x-momentum equation (4.54) is coupled with (4.57) to determine u.

As explained in Chapter 3, the central Δ and backward ∇ difference operators in the r-direction are given by equation (3.19) and in the x-direction they are written as

$$\begin{aligned} \Delta x_i^u &= x_{i+1}^v - x_i^v , \qquad \Delta x_i^v = \Delta x_i^u - x_{i-1}^u , \\ \nabla x_i^u &= x_i^u - x_i^v , \qquad \nabla x_i^v = x_i^v - x_{i-1}^u . \end{aligned} \tag{4.58}$$

Again in a staggered grid, $u_{i,j,k}$, $v_{i,j,k}$, $w_{i,j,k}$ and $p_{i,j,k}$ are defined, respectively, at $(x_i^u, r_j^u, \theta_k^v)$, $(x_i^v, r_j^v, \theta_k^v)$, $(x_i^v, r_j^u, \theta_k^w)$, and $(x_i^v, r_j^u, \theta_k^v)$ and the x-, r-, θ-momentum and continuity equations are differenced about these points, respectively. As was the case in 2-D analysis, the linear interpolations of the velocity components using the difference operators (3.19) and (4.58) are given here for some of the velocity components

$$\begin{aligned} u_u^{xf} &= \frac{\nabla x_{i+1}^u\, u_{i,j,k} + \nabla x_{i+1}^v\, u_{i+1,j,k}}{\Delta x_{i+1}^v} , \qquad u_u^{xb} = \frac{\nabla x_i^u\, u_{i-1,j,k} + \nabla x_i^v\, u_{i,j,k}}{\Delta x_i^v} , \\ v_v^{xf} &= \frac{\nabla x_{i+1}^v\, v_{i,j,k} + \nabla x_i^u\, v_{i+1,j,k}}{\Delta x_i^u} , \qquad v_v^{xb} = \frac{\nabla x_i^v\, v_{i-1,j,k} + \nabla x_{i-1}^u\, v_{i,j,k}}{\Delta x_{i-1}^u} , \\ w_w^{xf} &= \frac{\nabla x_{i+1}^v\, w_{i,j,k} + \nabla x_i^u\, w_{i+1,j,k}}{\Delta x_i^u} , \qquad w_w^{xb} = \frac{\nabla x_i^v\, w_{i-1,j,k} + \nabla x_{i-1}^u\, w_{i,j,k}}{\Delta x_{i-1}^u} ; \end{aligned} \tag{4.59}$$

the equations for the other components are given in Appendix A. The same difference operators will be used to evaluate Δu, Δv and Δw appearing in equations (4.46)-(4.57). The evaluation of the viscous derivative terms near the outer or inner cylinder walls has to be done as was demonstrated for 2-D analysis. These viscous derivative terms are $\partial^2\hat{v}/\partial x^2$, $\partial^2\hat{w}/\partial x^2$, $(1/r)(\partial/\partial r)(r\partial\hat{u}/\partial r)$ and $(1/r)(\partial/\partial r)(r\partial\hat{w}/\partial r)$. They are calculated by the following equations:

$$\left.\frac{\partial^2\hat{v}}{\partial x^2}\right|_{x=x_2^v} = \frac{1}{\Delta x_2^v}\left[\left(\frac{\hat{v}_{(3,j)}-\hat{v}_{(2,j)}}{\Delta x_2^u}\right)-\left(\frac{\frac{8}{3}\,\hat{v}_{(w,j)}-3\,\hat{v}_{(2,j)}+\frac{1}{3}\,\hat{v}_{(3,j)}}{\frac{8}{3}\,x_1^u-3\,x_2^v+\frac{1}{3}\,x_3^v}\right)\right], \tag{4.60}$$

$$\left.\frac{\partial^2\hat{w}}{\partial x^2}\right|_{x=x_2^v} = \frac{1}{\Delta x_2^v}\left[\left(\frac{\hat{w}_{(3,j)}-\hat{w}_{(2,j)}}{\Delta x_2^u}\right)-\left(\frac{\frac{8}{3}\,\hat{w}_{(w,j)}-3\,\hat{w}_{(2,j)}+\frac{1}{3}\,\hat{w}_{(3,j)}}{\frac{8}{3}\,x_1^u-3\,x_2^v+\frac{1}{3}\,x_3^v}\right)\right], \tag{4.61}$$

$$\frac{\partial}{r\,\partial r}\left(r\,\frac{\partial\hat{u}}{\partial r}\right)_{r=r_2^u} = \frac{1}{r_2^u\,\Delta r_2^u}\left[r_2^v\left(\frac{\hat{u}_{(i,3)}-\hat{u}_{(i,2)}}{\Delta r_2^v}\right)-r_1^v\left(\frac{\frac{8}{3}\,\hat{u}_{(i,w)}-3\,\hat{u}_{(i,2)}+\frac{1}{3}\,\hat{u}_{(i,3)}}{\frac{8}{3}\,r_1^v-3\,r_2^u+\frac{1}{3}\,r_3^u}\right)\right], \tag{4.62}$$

$$\frac{\partial}{r\,\partial r}\left(r\,\frac{\partial\hat{w}}{\partial r}\right)_{r=r_2^u} = \frac{1}{r_2^u\,\Delta r_2^u}\left[r_2^v\left(\frac{\hat{w}_{(i,3)}-\hat{w}_{(i,2)}}{\Delta r_2^v}\right)-r_1^v\left(\frac{\frac{8}{3}\,\hat{w}_{(i,w)}-3\,\hat{w}_{(i,2)}+\frac{1}{3}\,\hat{w}_{(i,3)}}{\frac{8}{3}\,r_1^v-3\,r_2^u+\frac{1}{3}\,r_3^u}\right)\right]. \tag{4.63}$$

A similar procedure applies for the evaluation of the same derivatives near the outer cylinder wall or near a vertical wall in a plane of constant x; for instance, in a region of discontinuity in the annular space, at the vertical face of a backstep.

We recall that Δu, Δv and Δw are zero on a solid wall even when the wall has non-zero velocities. This is because the velocities $\hat{u}_{i,w}$, $\hat{v}_{w,j}$, $\hat{w}_{i,w}$ and $\hat{w}_{w,j}$ are imposed as boundary conditions and remain fixed during the pseudo-time relaxation. Finally, it should be emphasized that the boundary conditions imposed on all equations to be solved were such that all perturbations in the flow quantities must be equal to zero at both the inlet and outlet of the domain, including velocity components and pressure. The initial conditions were to set the perturbations equal to zero before starting the vibration of the outer cylinder, and integration of the equation is implemented until a periodic solution is achieved, which takes at least 3 harmonic cycles.

The solution to equations (4.46)-(4.57) will be obtained after they are discretized, using equations (3.19), (4.58), (4.59) and similar ones described in Appendix A. Thus, equations (4.42-4.45) are discretized first in the forms given by equations (A.25), (A.31), (A.37) and (A.44). Then, equations (4.46)-(4.57) are discretized, which provide equations (A.45-A.56). These equations are used to solve the appropriate problem as described for 2-D analysis. The details of discretization are given in Appendix A.

After the discretization is done, the solution procedure continues by the same method as that used for 2-D problems: briefly, it starts by using the discretized form of equations (4.42)-(4.45) in the discretized form of matrix equation (3.12) to have the known explicit right-hand sides for the discretized form of (4.46)-(4.49). These equations are then solved in different r-, θ- and x-sweeps to obtain Δv, Δw, Δu, respectively, and finally Δp, by solving several sets of tridiagonal systems of equations.

As far as the different sweeps are concerned, at a given pseudo-time step τ^{μ}, equations (4.46)-(4.49) are set up for i, $2 \le i \le I-1$, for j, $2 \le j \le J-1$, and finally for k, $3 \le k \le K-1$, and they are solved for $\widetilde{\Delta v}$, $\widetilde{\Delta w}$, $\widetilde{\Delta u}$ and $\widetilde{\Delta p}$. Equations (4.50)-(4.53) are solved to obtain $\overline{\Delta v}$, $\overline{\Delta w}$, $\overline{\Delta u}$ and $\overline{\Delta p}$. The last four equations (4.54)-(4.57) are solved in the same range of grid points to find Δv, Δw, Δu and Δp. At the points on the boundaries the values of u, v, w and p in all sweeps are either given as boundary conditions or by interpolating and /or extrapolating from the points inside the domain of integration or by using the fictitious points outside the domain or by setting equal to zero, as the case requires, and in the same way as for 2-D analysis. Use is made of the symmetry of the problem with respect to the plane of oscillation ($\theta = 0$ and $\theta = \pi$), *i.e.*, the values of u, v, w, and p at the grid points other than those mentioned previously are obtained from the following equations:

$$u_{i,j,2} = u_{i,j,3}\,, \qquad v_{i,j,2} = v_{i,j,3}\,, \qquad w_{i,j,1} = -w_{i,j,3}\,, \qquad p_{i,j,2} = p_{i,j,3}\,,$$

$$u_{i,j,k-1} = u_{i,j,k}\,, \qquad v_{i,j,k-1} = v_{i,j,k}\,, \qquad w_{i,j,k-2} = -w_{i,j,k}\,, \qquad p_{i,j,k-1} = p_{i,j,k}\,.$$

In 3-D annular flow problems, the initial direction of flow is taken to be along the x-axis. Therefore, the initial values for velocity and pressure should be defined at the inlet and outlet of the domain, as well as on the fixed and moving boundaries. The values for u, v and p are imposed at the inlet and outlet according to what has already been described for 2-D analysis (for v and p) to start the pseudo-time solution. To get the 3-D solution we must first have a steady solution for flow in the annular space before getting into the time-accurate solution procedure. This velocity profile in the steady flow is given by the following nondimensional equation:

$$U(r) = \frac{U^*(r)}{U_o} = \frac{2\left[1-(r/r_1)^2+(n^2-1)\ln(r/r_1)/(\ln n)\right]}{n^2+1-(n^2-1)/(\ln n)}, \tag{4.64}$$

where $U^*(r)$ and U_o are the dimensional axial and mean axial velocities in the annulus, respectively, $n = r_2/r_1$; we also set $v = w = 0$ for all grid points at the inlet. The initial conditions inside the domain are given by $\hat{\mathbf{V}}^\mu = \mathbf{V}^n$ and $\hat{p}^\mu = p^n$ at the first pseudo-time step and on the boundaries as the velocity of the walls, $\mathbf{U}_w^{n+1}$, which is kept constant. The velocities at the outlet of the annular space are obtained by extrapolating the known values of the flow variables from inside the domain as given by the following equations (Anderson *et al.* 1984):

$$u_{I,j,k} = \left(1+\frac{\Delta x_I^v}{\Delta x_{I-1}^v}\right) u_{I-1,j,k} - \frac{\Delta x_I^v}{\Delta x_{I-1}^v} u_{I-2,j,k}, \tag{4.65}$$

$$v_{I,j,k} = \left(1+\frac{\Delta x_{I-1}^u}{\Delta x_{I-2}^u}\right) v_{I-1,j,k} - \frac{\Delta x_{I-1}^u}{\Delta x_{I-2}^u} v_{I-2,j,k}, \tag{4.66}$$

$$w_{I,j,k} = \left(1+\frac{\Delta x_{I-1}^u}{\Delta x_{I-2}^u}\right) w_{I-1,j,k} - \frac{\Delta x_{I-1}^u}{\Delta x_{I-2}^u} w_{I-2,j,k}. \tag{4.67}$$

The pressure at the outlet is set equal to zero, nevertheless it can be calculated from the integration of the normal momentum equation (Soh 1987) as

$$p_{I,j,k} - p_{I,2,k} = -\int_{r_2^u}^{r_j^u} \left[\frac{\partial(uv)}{\partial x} + \frac{1}{r}\frac{\partial(rvv)}{\partial r} + \frac{1}{r}\frac{\partial(wv)}{\partial\theta} - \frac{w^2}{r}\right.$$
$$\left.\left. - \frac{1}{\mathrm{Re}}\left[\frac{\partial^2 v}{\partial x^2} + \frac{1}{r}\frac{\partial}{\partial r}\left(r\frac{\partial v}{\partial r}\right) + \frac{1}{r^2}\frac{\partial^2 v}{\partial\theta^2} - \frac{2}{r^2}\frac{\partial w}{\partial\theta} - \frac{v}{r^2}\right]\right]\right|_{x=x_I^v} dr\,. \tag{4.68}$$

4.2.2 Solution of 2-D and 3-D Annular Flow Problems and Numerical Results

2-D Unsteady Flow Results

To solve the Navier-Stokes and continuity equations in 2-D annular configurations with small-amplitude oscillations of the outer cylinder, we need to generate a 2-D mesh. This is done by choosing appropriate inner and outer radii, the stretching function, and the number of grid points in the r- and θ-directions. To reproduce the results obtained by Bélanger (1991), the numerical computations have been performed on a nondimensional mesh with inner radius $r_i = 9$ and outer radius $r_o = 10$ for a Stokes number $S = 300$, which defines the vibrational characteristics of the system. The results are shown in Figures 4.10-4.13, in which all quantities are dimensionless. Each cycle of the periodic motion was divided into 19 time steps. Initial conditions for velocity and pressure in the fluid domain were zero and equations (4.31)-(4.34) were solved until a periodic state was reached, which for a stable solution takes at least 3 cycles. The mesh used was a 2-D mesh as shown in Figure 3.2, spanning the circumferential direction between $\theta = 0$ and $\theta = \pi$, and uniform in that direction. The stretching function used in the r-direction was a hyperbolic tangent function, as shown in equation (3.14). This mesh is composed of 24×24 grid points, where Δr_{min} is equal to 0.020 when $S = 300$.

Figures 4.10-4.13 contain the curves representing the solutions for each of 5 instants t^n within the harmonic cycle. The five instants are obtained from $t^n = 2\pi n/N, n = 7, 9, 11, 13$ and 15 for the circumferential velocity component w, and $n = 3, 5, 7, 9$ and 11 for the results involving the pressure p; N is the number of time steps, taken to be 19. Figure 4.10(a) presents the radial profiles of pressure taken at $\theta = 3.75^o$ and Figure 4.10(b) presents the radial profiles of w at an azimuth of $\theta = 45^o$. Figure 4.11(a,b) presents circumferential profiles of the pressure p and velocity component w, taken at $r = 9.75$. As pointed out previously, the results obtained for small-amplitude oscillations are similar to those obtained by Bélanger, although in his decoupling procedure of the discretized equations he neglected the off-diagonal terms. Thus, a comparison between the results of the present analysis and Bélanger results for 3-D unsteady flow will be made in the paragraph dealing with 3-D analysis. In Chapter 6, a comparison will be made between the 2-D and 3-D results of this chapter and those obtained for large-amplitude oscillations. Aspects of convergence and other numerical features are discussed in Chapter 7.

To obtain the amplitude and the phase angle with respect to the displacement of the outer cylinder, or the real and imaginary parts of the velocity components and pressure, a Fourier Transform was used which is defined by the following equation (Cooley *et al.* 1969)

$$G(f_k) = \frac{1}{T}\int_{-T/2}^{T/2} g(t)e^{-j2\pi f_k t}dt\,, \tag{4.69}$$

where $f_k = kf_1$, *i.e.* the k^{th} harmonic of f_1 and $g(t)$ is a periodic function with period T. In discrete form, equation (4.69) is written as

$$G(k) = \frac{1}{N}\sum_{n=0}^{N-1} g(n)e^{-j\frac{2\pi kn}{N}}\,, \tag{4.70}$$

which is used in this analysis, where $g(n)$ represents p, u, v, or w. Hence, Figure 4.12(a,b) presents the pressure amplitude and phase angle at different Reynolds and Stokes numbers and for the potential flow solution. Figure 4.13(a,b) presents the real and imaginary components of the pressure obtained for the same range of Reynolds and Stokes numbers (where Re$= 2S = 2\omega H^2/\nu$ for the 2-D annular configuration). For these results the inner and outer cylinder radii are $r_i = 4$ and $r_o = 5$, respectively. The nondimensional amplitude of oscillation is $\epsilon = 0.1$. The mesh used has 12×15 grid points in (r, θ)-plane. The pressure results obtained are at $r = 4.965$ and $\theta = 7.5^o$.

3-D Unsteady Flow Results

To solve the N-S and continuity equations in 3-D annular configurations, we construct 3-D meshes as shown in Figure 4.7. The numerical computations have been implemented for two sets of geometry. The first set is for small lengths of fixed upstream and downstream portions, as shown in Figure 2.3. The second set was devoted to larger lengths of these parts, to investigate the effect of fixed boundary conditions on the perturbed fluid variables and on the propagation of the perturbed pressure outside the domain of translational or rocking motion. The nondimensional annular gap width was also changed from $r_i = 9$ and $r_o = 10$ to $r_i = 4.785$ and $r_o = 5.785$, to obtain results for both narrow and wide annular gaps; in the experimental apparatus used in this research to investigate the unsteady pressure produced by the forced vibration of the outer cylinder, the radii are $r_i = 4.785$ and $r_o = 5.785$, as will be discussed in Chapter 8.

Two different meshes were used for the 3-D analysis. The first one is $65 \times 12 \times 15$, spanning the axial, radial and circumferential directions. This mesh is used when we set $L = 100, L_1 = 20$, and $L_2 = 20$ (see Figure 2.3). A second mesh has $89 \times 12 \times 15$ grid points in the computational domain, and it is used when $L = 100, L_1 = 60$, and $L_2 = 60$. The stretching function used in the r-direction was the same as in 2-D analysis but in the axial direction the hyperbolic sine distribution function was utilized instead of the hyperbolic tangent one; while in the θ-direction a uniform distribution of grid points was used. Equations (4.46-4.57) were solved in this 3-D computational domain until a periodic state was reached, as in the 2-D solution.

Due to the staggered nature of the grid points, the pressure cannot be calculated at $\theta = 0$ and $\theta = \pi$. At these and other locations, which are affected by the staggered grids, the pressure and other variables which are neither calculated nor defined explicitly can be computed by interpolating between the adjacent node values. Also, on the boundaries no values are required to be supplied for the pressure. As before, the computation can be done for different Reynolds and Stokes numbers, always in the laminar regime. For quiescent fluid, in this analysis, in order to be able to obtain a solution, one needs to supply the Reynolds number in the computational program. This can be done by selecting the Stokes number (based on the frequency of oscillation, annular gap width and fluid viscosity), and using the relations

$$\mathrm{Re} = \frac{2UH}{\nu}, \qquad S = \frac{\Omega H^2}{\nu},$$

from which the nondimensional frequency ω can also be written as $\omega = \Omega H/U = 2S/\mathrm{Re}$.

In 3-D, as in 2-D, the time step $\Delta t = T/N$ with $N = 19$ was used. For all of the problems treated in this Thesis the compressibility factor δ and pseudo-time step $\Delta\tau$ were chosen based on equations (4.15), (4.16) and (4.19). Initial guesses were used for q and the Courant number, Cr, which is also based on the criteria supplied by Chorin (1967), Soh (1987) and Soh and Goodrich (1988), and finally implementing numerical experiments by correcting the values of δ and $\Delta\tau$ using appropriate correction factors. In all computations, convergence was reached and the iterations were stopped in pseudo-time when the rms values of the numerical residuals of the momentum and continuity equations were all less than 10^{-4}, which is low enough to ensure that the governing equations of fluid motion are satisfied for each real-time step. The residuals are the numerical evaluation of the right-hand sides of equations (3.9) and (3.10) at the grid points —actually, equation (3.9) must be divided by $\Delta\tau$ and equation (3.10) by $\Delta\tau/\delta$.

Figure 4.14(a,b) presents the unsteady pressure amplitude and phase angle versus the axial length of the cylinder obtained for 3-D solution of a uniform annular passage, at $r = 9.965$ and $\theta = 7.5^o$. In Figure 4.14, a comparison is made between the present results and Bélanger's results. They are almost the same, nevertheless the discrepancies are most likely due to carrying out the complete solution of the N-S equations in the present analysis *vis-à-vis* the Bélanger approach in which the simplified N-S equations were considered. Figure 4.15(a,b) presents the circumferential velocity w and its phase angle obtained at $X = 50$ and $\theta = 45^o$. Figure 4.16 (a,b) demonstrates the effect of amplitude of oscillation on the pressure; for small amplitude oscillations it can be seen that the amplitude of the pressure increases almost linearly with the amplitude of oscillation. In Figure 4.16(b) it is seen that the phase angle increases (in the negative sense) for $\epsilon = 0.2$, but decreases as the amplitude increases, which indicates that it appraoches the results of the potential-flow solution at higher amplitudes, while for small amplitudes the change in phase angle is less pronounced.

Figure 4.17 gives a set of solutions obtained at different Reynolds numbers. It is shown that this model can easilly handle higher flow rates, simply by keeping the off-diagonal terms and performing minor modifications in the numerical solutions; in contrast, the solution obtained by Bélanger was for a maximum Reynolds number of Re = 250. This figure demonstrates that, as the Reynolds number is increased, the pressure amplitudes are decreased, and at Re = 1000 and Re = 1500 the pressure amplitudes become almost identical. Figure 4.18 presents the phase angle for pressure at various Reynolds numbers. The same conclusion as before can be reached for this figure regarding the effect of increasing the flow velocity on the phase angle.

Figure 4.19 presents the circumferential velocity w for different Reynolds numbers. This figure shows that the fully developed laminar-shape velocity profile for w at lower Reynolds numbers tends to a shape similar to that of turbulent flows with increasing Re. This is interesting from the point of view of shear force calculations on the cylinder, *i.e.*, larger shear forces are created at higher Reynolds numbers. Figure 4.20 presents the phase angle for w at various Reynolds numbers and it is seen that the phase angle curves retain the same shape as Reynolds number is increased, tending to a parabolic shape at high Reynolds numbers.

Figure 4.21 shows the effect of the extension of the fixed downstream and upstream portions of the computational domain on the numerical results. At lower amplitudes of oscillation, *i.e.* $\epsilon = 0.1$, it is clear that the perturbation pressure at the upstream end approaches zero as it does at the downstream end (compare with Figure 4.14(a)). But at higher-amplitude oscillations, even the axial extensions of the fixed boundaries do not help, in this mean-position approach (for low-amplitude oscillations), to reduce the unsteady pressure to zero outside the oscillating portion, as seen in Figure 4.21 for $\epsilon = 0.2$ and $\epsilon = 0.3$. The curves for phase angle in Figure 4.21 indicate how the results depend on the extension of the boundaries as compared to Figure 4.16(b).

Figure 4.14-4.21 are for an annulus with $r_i = 9$ and $r_o = 10$. To investigate the effect of annular gap width and also to be able to compare the theoretical results with the experimental ones, the following figures were obtained for $r_i = 4.785$ and $r_o = 5.785$. Figure 4.22 is similar to Figure 4.16 but for this different geometry; here it is apparent that the pressure amplitude decreases due to the increase in annular gap width. The results for phase angle in Figure 4.22(b) are more realistic than those in Figure 4.16(b). Figure 4.23 is similar to 4.21, *i.e.*, it is for extended upstream and downstream portions, but is for this new geometry. The ripples shown in pressure amplitudes are due to the discontinuities at the moving and fixed parts of the cylinders. The same conclusion reached for Figure 4.21 applies to Figure 4.23.

Figure 4.24 presents pressure amplitudes at much higher frequencies and demonstrates the effects on the pressure of (a) different amplitudes of oscillation and (b) various frequencies, still for a quiescent fluid subjected to oscillation of the outer cylinder. Finally, Figure 4.25 presents the same results as those of Figure 4.24 but for fluid flow with Re = 2900. It should be remembered that the results obtained were subjected to the constraint of small-amplitude oscillation and it is apparent from the figures that for this model to produce acceptable results the amplitude of oscillation must be $\epsilon \leq 0.1$ for narrow annular gaps —a conclusion which was also reached by Bélanger (1991)— and $\epsilon \leq 0.05375$ for wide annular gaps.

For the nonuniform annular geometries, such as a geometry with a backstep, the N-S and continuity equations are solved on the 3-D mesh shown in Figure 4.26 in the (r, x)-plane and similar meshes for different θ-planes. From this diagram, it is seen that around the discontinuities at the upstream and downstream portions of the moving cylinder and around the step, as well as close to the cylinder wall and centreline of the annulus, the grid points are clustered, by using the stretching functions described before, so as to ensure the accuracy of the results. For this non-uniform annular space, several meshes have been used which are classified in Table 4.1.

Figures 4.27 and 4.28 present the results obtained with the short axial length of the vibrating cylinder and narrow annular gap (to reproduce the Bélanger results). Mesh type A was used for these calculations. In these figures, the unsteady pressure

	Axial	Radial	Circumferential	r_i	r_o	Δx_{min}	Δr_{min}	L	L_1	L_2
A	71	14	15	8	10	0.2	0.105	40	20	20
B	97	14	15	8	10	0.2	0.105	40	60	60
C	103	14	15	3.785	5.785	0.2	0.105	100	20	20
D	99	14	15	3.785	5.785	0.1	0.105	100	60	60

Table 4.1: Different meshes used for numerical computations involving backstep.

p and circumferential velocity w with their respective phase angles were presented. From Figure 4.27 it is clear that the unsteady pressure drops off after the backstep due to the enlargement in the annular gap width, resulting in a reduction in the magnitude of the perturbation velocities. Also, the pressure perturbation approaches zero far downstream but not at the upstream end. The pressure phase curve also shows a different behaviour as compared to Figure 4.14(b).

Figure 4.29 presents the unsteady pressure magnitude and phase angle for three different amplitudes of oscillation. It is seen that the phase angle remains almost the same while the amplitude increases appropriately. This was not the case for the uniform annular geometry (compare with Figure 4.16(b)). Figure 4.30 demonstrates the effect of extending the fixed upstream and downstream portions on the results (cf. Figure 4.29), as was done in uniform annular cases. In this case it is seen that, when using longer lengths for these portions which is shown in Table 4.1 for mesh type B, the unsteady pressure approaches to its lowest possible values. The results of Figure 4.31 were obtained using mesh type C for a wider annular gap. There are some differences between these results and those of Figure 4.30, due to changes made in the size of the annular space and in the length of the vibrating cylinder. Figure 4.32 presents the effect of using longer lengths for the fixed portions. The results show that for this geometry and with the defined parameters, using longer cylinders would not help too much in reducing the unsteady pressure to zero in the fixed-boundary domains. For Figure 4.32 and subsequent ones, mesh type D was used.

Figures 4.33 and 4.34 are similar to Figures 4.24 and 4.25 and present the effect of amplitude or frequency on the pressure for quiescent or flowing fluids in an annular space with backstep. Some wiggles are seen in the pressure results of Figure 4.34 which are obviously due to fluctuations of the pressure at higher Reynolds numbers (producing vortices) after the step. This pressure loss and recovery which is partly due to the oscillation of the outer cylinder is believed to be the main factor causing vibration of the systems involving non-uniform annular passages; this will be discussed in more detail in Chapter 9.

For uniform annular space with the outer cylinder in rocking motion, Figures 4.35-4.37 present the unsteady pressure and phase angle for quiescent and flowing fluids at high frequency of oscilation of the outer cylinder. In this type of motion, a similar mesh as used for uniform annular space analysis was utilized, and the extended fixed portions were used, *i.e*, $L = 100$, $L_1 = 60$, and $L_2 = 60$, while $r_i = 4.785$ and $r_o = 5.785$. The hinge about which the rocking motion takes place is located at $X = 81.0$. It should be emphasized that, due to the small-amplitude-motion assumption, the effects of the amplitude of oscillation on the moving boundary were neglected, even though at the upstream of the vibrating cylinder the amplitude of oscillation is larger than that in the fictitious shaker position. Also, the boundary conditions for the velocity on the vibrating wall were obtained using equations (4.39)-(4.41). Once again, Figure 4.37 demonstrates that the assumption of small-amplitude oscillation, will be valid when $\epsilon \leq 0.05375$ in the mean-position analysis.

Figures 4.38 and 4.39 present the unsteady pressure and phase angle for non-uniform geometry (backstep) when the outer cylinder is in rocking motion. Here, the hinge is located at $X = 82.0$ and the results are for quiescent and flowing fluids. The effects of having a step are clearly shown in Figure 4.39 when there is a fluid flow.

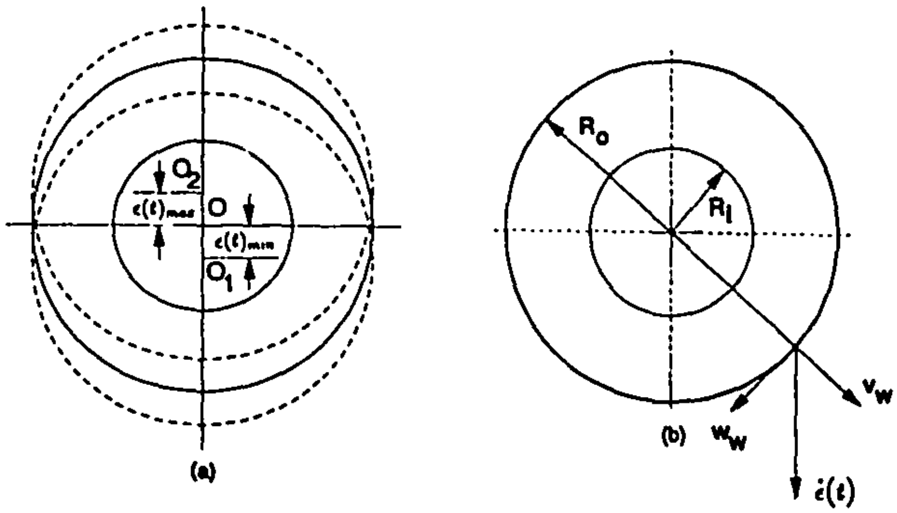

Figure 4.1: Schematic diagram of 2-D annulus (a) Oscillation of the outer cylinder (b) The velocity components on the outer cylinder.

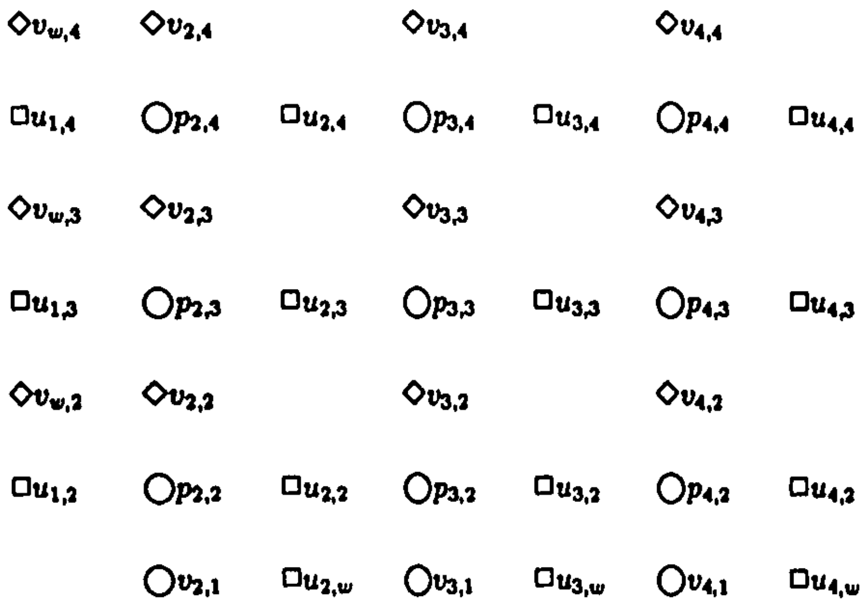

Figure 4.2: Schematic representation of the grid points near the walls, for evaluation of viscous derivatives, where the quantities $u_{i,w}$ and $v_{w,j}$ are defined.

$\diamond v_{3,k-1}$		$\diamond v_{3,k}$		$\diamond v_{3,k+1}$	
$\bigcirc p_{3,k-1}$	$\square w_{3,k-1}$	$\bigcirc p_{3,k}$	$\square w_{3,k}$	$\bigcirc p_{3,k+1}$	$\square w_{3,k+1}$
$\diamond v_{2,k-1}$		$\diamond v_{2,k}$		$\diamond v_{2,k+1}$	
$\bigcirc p_{2,k-1}$	$\square w_{2,k-1}$	$\bigcirc p_{2,k}$	$\square w_{2,k}$	$\bigcirc p_{2,k+1}$	$\square w_{2,k+1}$
$\bigcirc v_{1,k-1}$	$\square w_{w,k-1}$	$\bigcirc v_{1,k}$	$\square w_{w,k}$	$\bigcirc v_{1,k+1}$	$\square w_{w,k+1}$

Figure 4.3: Schematic representation of the grid points, for the evaluation of viscous derivatives near the inner cylinder wall where the quantity $w_{w,k}$ has been defined.

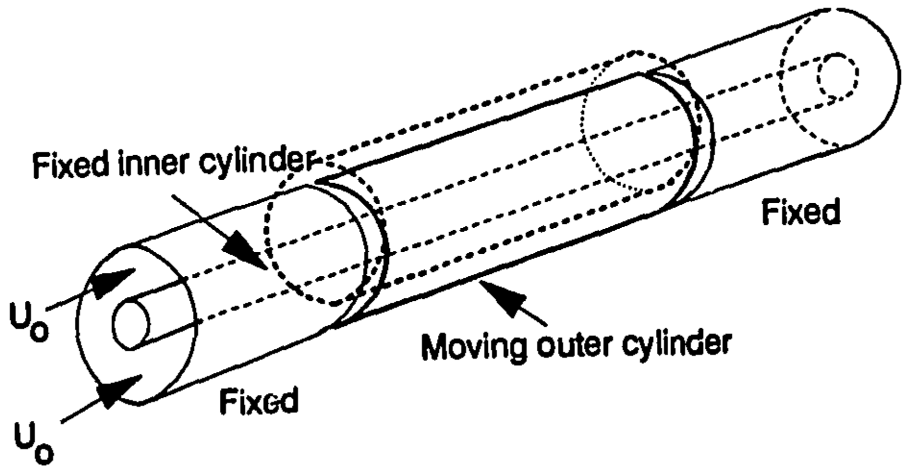

Figure 4.4: Schematic representation of annular flow geometry in three dimensions.

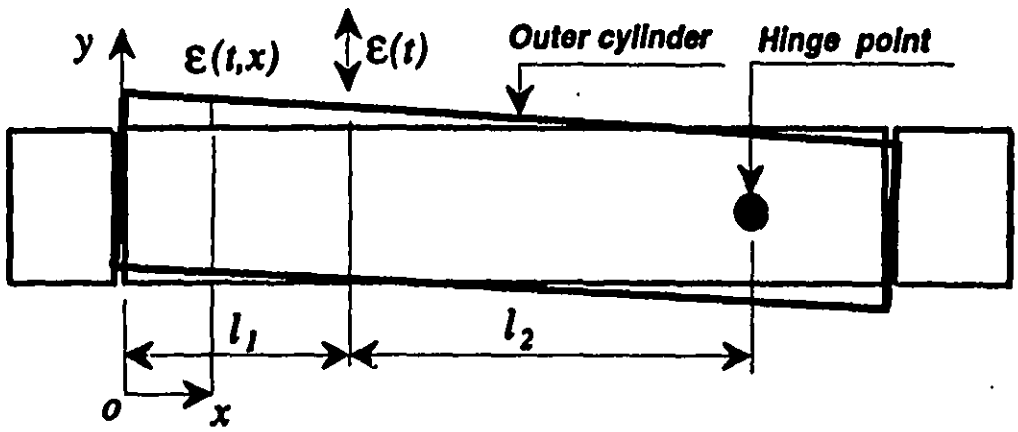

Figure 4.5: Schematic representation of the geometry of outer cylinder during rocking motion for boundary velocity calculation.

r^v_{j+1} —	$\diamond\hat{v}_{i-1,j+1,k}$		$\diamond\hat{v}_{i,j+1,k}$		$\diamond\hat{v}_{i+1,j+1,k}$	
r^u_{j+1} —	$\bigcirc$ $\hat{\psi}_{i-1,j+1,k}$ $p_{i-1,j+1,k}$	$\square\hat{u}_{i-1,j+1,k}$	$\bigcirc$ $\hat{\psi}_{i,j+1,k}$ $p_{i,j+1,k}$	$\square\hat{u}_{i,j+1,k}$	$\bigcirc$ $\hat{\psi}_{i+1,j+1,k}$ $p_{i+1,j+1,k}$	$\square\hat{u}_{i+1,j+1,k}$
r^v_j —	$\diamond\hat{v}_{i-1,j,k}$		$\diamond\hat{v}_{i,j,k}$		$\diamond\hat{v}_{i+1,j,k}$	
r^u_j —	$\bigcirc$ $\hat{\psi}_{i-1,j,k}$ $p_{i-1,j,k}$	$\square\hat{u}_{i-1,j,k}$	$\bigcirc$ $\hat{\psi}_{i,j,k}$ $p_{i,j,k}$	$\square\hat{u}_{i,j,k}$	$\bigcirc$ $\hat{\psi}_{i+1,j,k}$ $p_{i+1,j,k}$	$\square\hat{u}_{i+1,j,k}$
r^v_{j-1} —	$\diamond\hat{v}_{i-1,j-1,k}$		$\diamond\hat{v}_{i,j-1,k}$		$\diamond\hat{v}_{i+1,j-1,k}$	
r^u_{j-1} —	$\bigcirc$ $\hat{\psi}_{i-1,j-1,k}$ $p_{i-1,j-1,k}$	$\square\hat{u}_{i-1,j-1,k}$	$\bigcirc$ $\hat{\psi}_{i,j-1,k}$ $p_{i,j-1,k}$	$\square\hat{u}_{i,j-1,k}$	$\bigcirc$ $\hat{\psi}_{i+1,j-1,k}$ $p_{i+1,j-1,k}$	$\square\hat{u}_{i+1,j-1,k}$
	x^v_{i-1}	x^u_{i-1}	x^v_i	x^u_i	x^v_{i+1}	x^u_{i+1}

Figure 4.6: Schematic representation of the staggered grid used in the spatial discretization of the three-dimensional nonlinear equations.

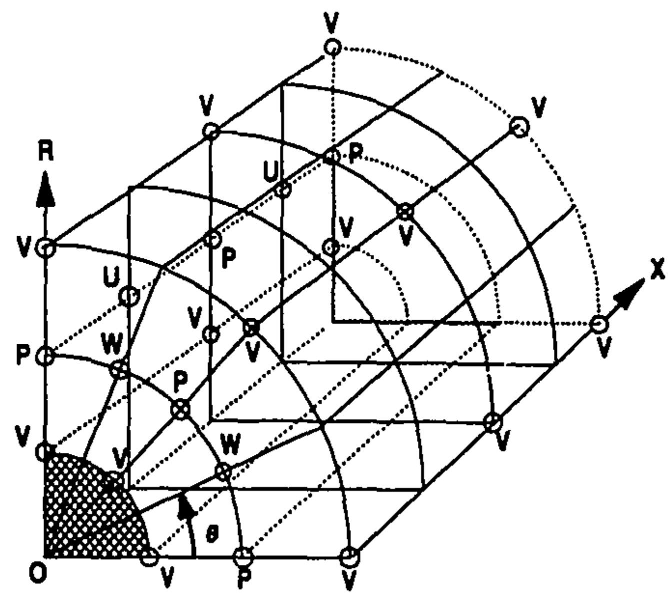

Figure 4.7: Isometric view of the grid-point distribution in the 3-D analysis.

$$
\begin{array}{llllllll}
r^v_{j+1} & - & \Diamond v_{i-1,j+1} & & \Diamond v_{i,j+1} & & \Diamond v_{i+1,j+1} & \\
r^u_{j+1} & - & \bigcirc p_{i-1,j+1} & \square u_{i-1,j+1} & \bigcirc p_{i,j+1} & \square u_{i,j+1} & \bigcirc p_{i+1,j+1} & \square u_{i+1,j+1} \\
r^v_{j} & - & \Diamond v_{i-1,j} & & \Diamond v_{i,j} & & \Diamond v_{i+1,j} & \\
r^u_{j} & - & \bigcirc p_{i-1,j} & \square u_{i-1,j} & \bigcirc p_{i,j} & \square u_{i,j} & \bigcirc p_{i+1,j} & \square u_{i+1,j} \\
r^v_{j-1} & - & \Diamond v_{i-1,j-1} & & \Diamond v_{i,j-1} & & \Diamond v_{i+1,j-1} & \\
r^u_{j-1} & - & \bigcirc p_{i-1,j-1} & \square u_{i-1,j-1} & \bigcirc p_{i,j-1} & \square u_{i,j-1} & \bigcirc p_{i+1,j-1} & \square u_{i+1,j-1} \\
 & & | & | & | & | & | & | \\
 & & x^v_{i-1} & x^u_{i-1} & x^v_{i} & x^u_{i} & x^v_{i+1} & x^u_{i+1}
\end{array}
$$

Figure 4.8: Schematic representation of the staggered grid used in the spatial differentiation in the r and x directions.

$$
\begin{array}{llllllll}
r^v_{j+1} & - & \Diamond v_{j+1,k-1} & & \Diamond v_{j+1,k} & & \Diamond v_{j+1,k+1} & \\
r^w_{j+1} & - & \bigcirc p_{j+1,k-1} & \square w_{j+1,k-1} & \bigcirc p_{j+1,k} & \square w_{j+1,k} & \bigcirc p_{j+1,k+1} & \square w_{j+1,k+1} \\
r^v_{j} & - & \Diamond v_{j,k-1} & & \Diamond v_{j,k} & & \Diamond v_{j,k+1} & \\
r^w_{j} & - & \bigcirc p_{j,k-1} & \square w_{j,k-1} & \bigcirc p_{j,k} & \square w_{j,k} & \bigcirc p_{j,k+1} & \square w_{j,k+1} \\
r^v_{j-1} & - & \Diamond v_{j-1,k-1} & & \Diamond v_{j-1,k} & & \Diamond v_{j-1,k+1} & \\
r^w_{j-1} & - & \bigcirc p_{j-1,k-1} & \square w_{j-1,k-1} & \bigcirc p_{j-1,k} & \square w_{j-1,k} & \bigcirc p_{j-1,k+1} & \square w_{j-1,k+1} \\
 & & | & | & | & | & | & | \\
 & & \theta^v_{k-1} & \theta^w_{k-1} & \theta^v_{k} & \theta^w_{k} & \theta^v_{k+1} & \theta^w_{k+1}
\end{array}
$$

Figure 4.9: Schematic representation of the staggered grid used in the spatial differentiation in the r and θ directions.

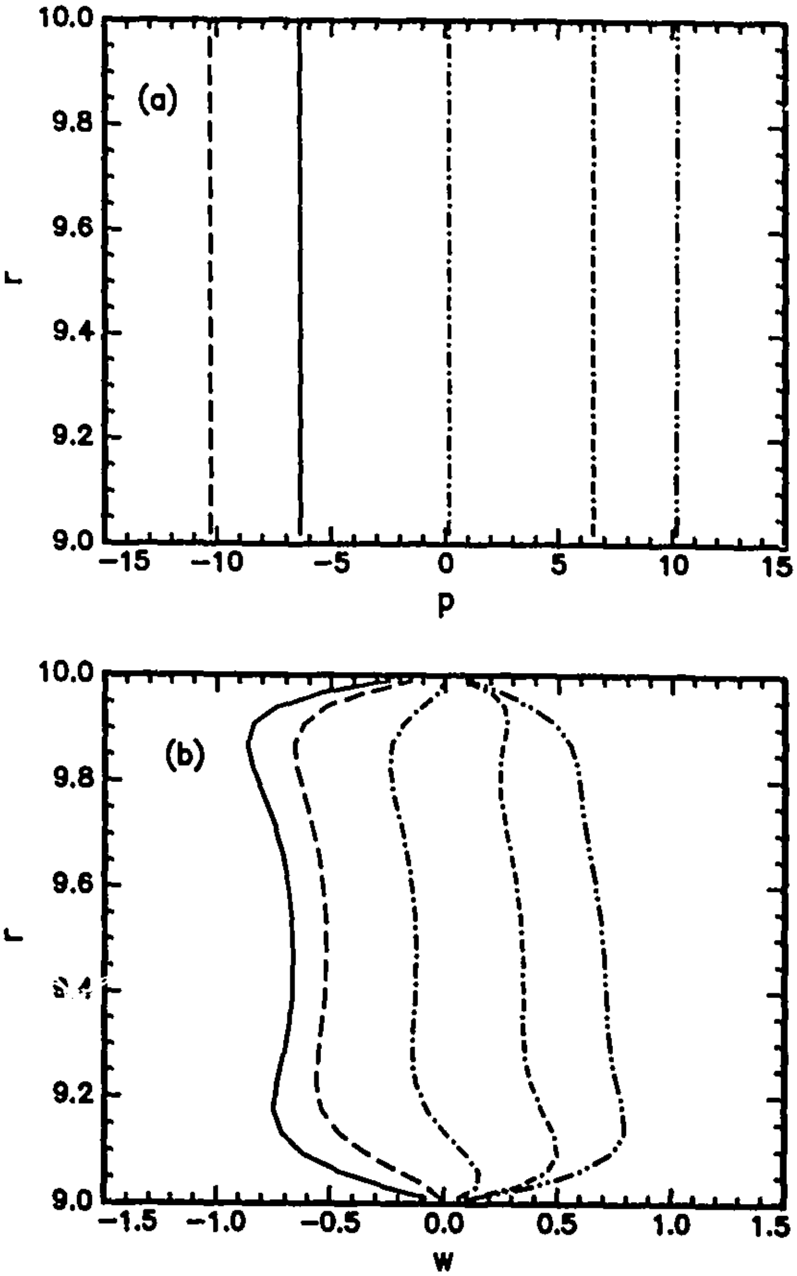

Figure 4.10: Radial profiles of pressure p at $\theta = 3.75^o$ and radial profiles of circumferential velocity w at $\theta = 45^o$ for $S = 300$ at 5 instants t^n within the harmonic cycle.

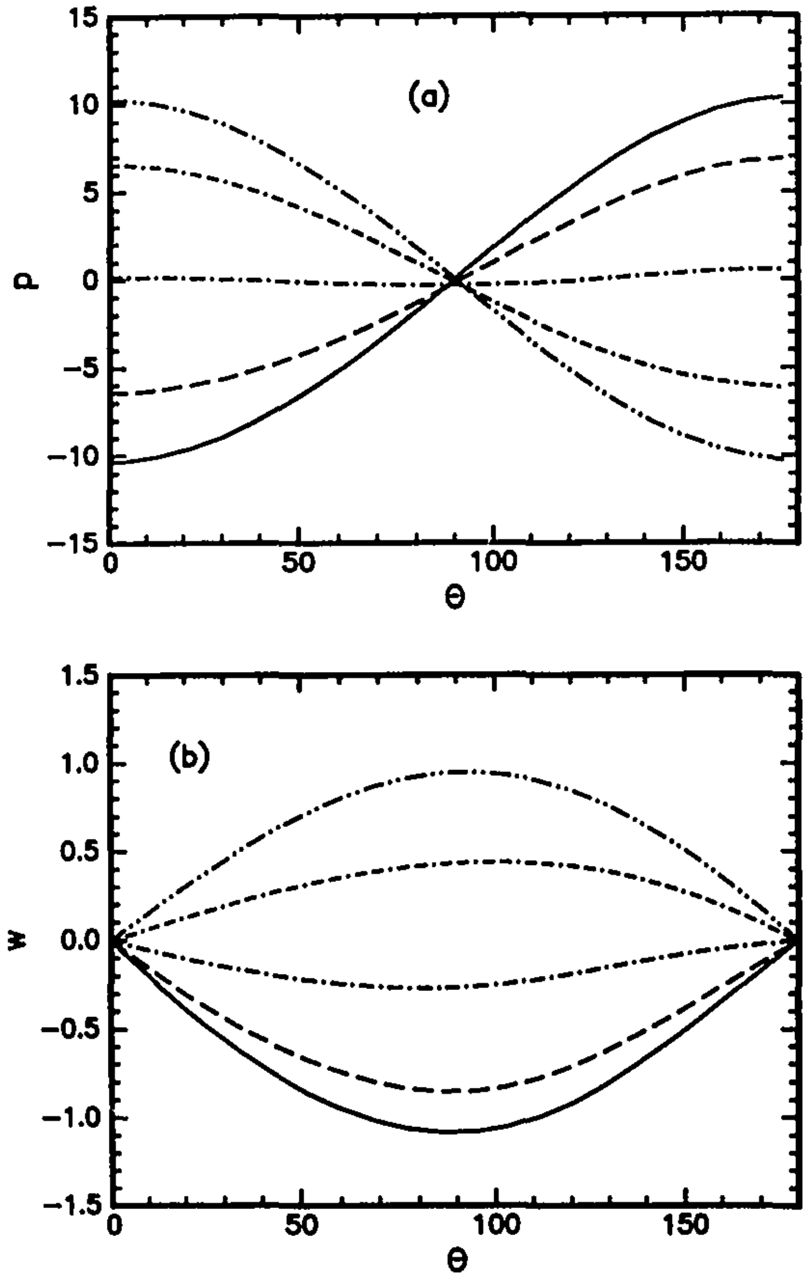

Figure 4.11: Circumferential profiles of pressure p and circumferential profiles of the circumferential velocity component w at $r = 9.75$ for $S = 300$ at 5 instants t^n within the harmonic cycle.

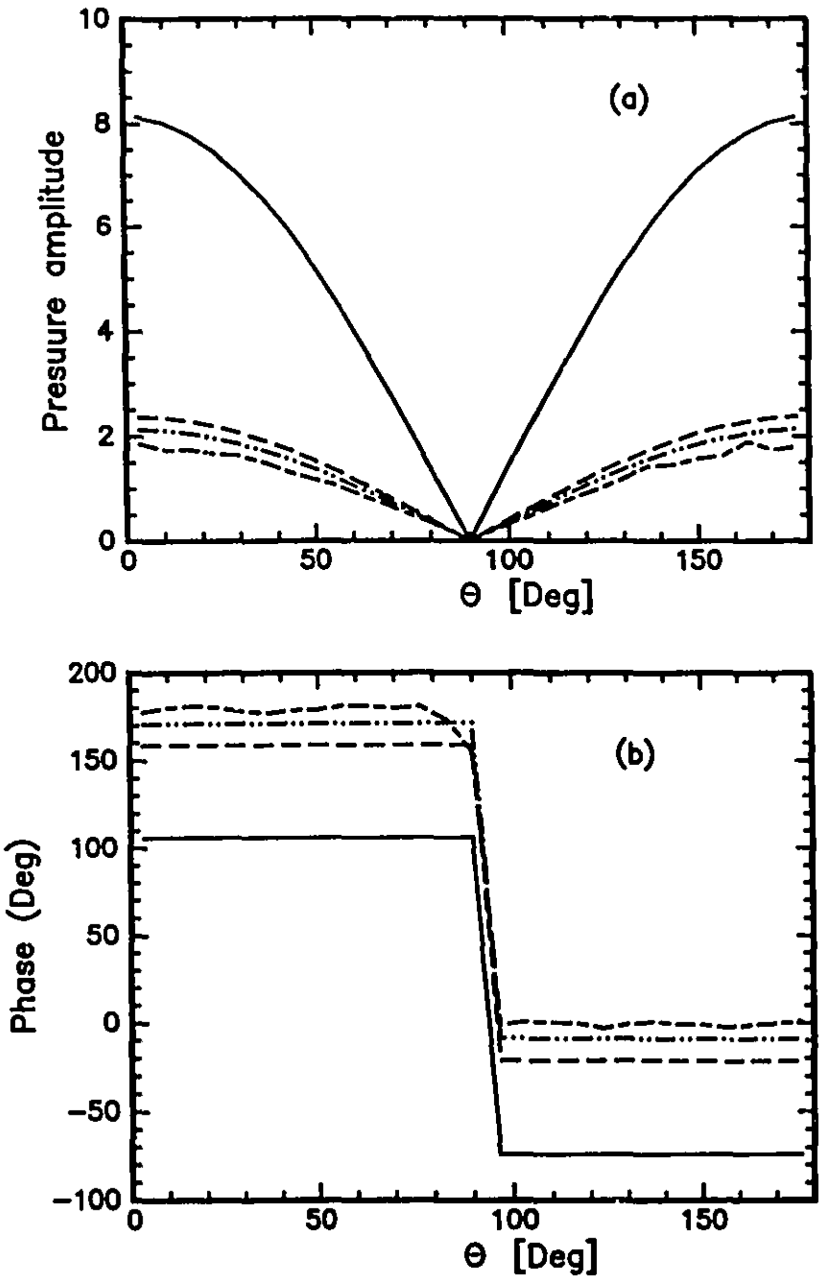

Figure 4.12: Nondimensional unsteady pressure amplitude (a) and phase angle (b) at $r = 4.965$ for: —,Re $= 6.25, S = 3.125$; – – –,Re $= 62.5, S = 31.25$; – · · – ··, Re $=$ $250, S = 125$; - - -,potential flow.

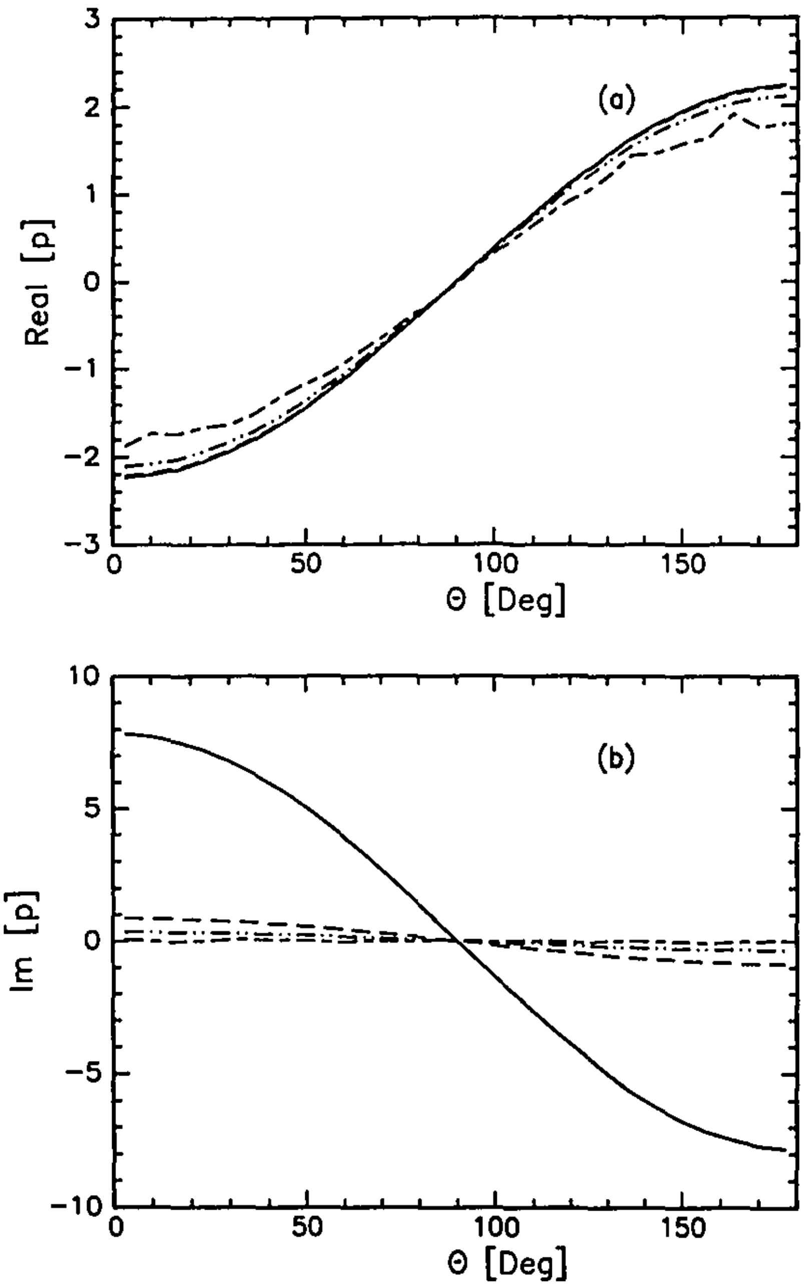

Figure 4.13: Real and imaginary parts of the nondimensional unsteady pressure obtained at $r = 4.965$ for: —,Re $= 6.25, S = 3.125$; – – –,Re $= 62.5, S = 31.25$; – · · – ··, Re $= 250, S = 125$; - - -,potential flow.

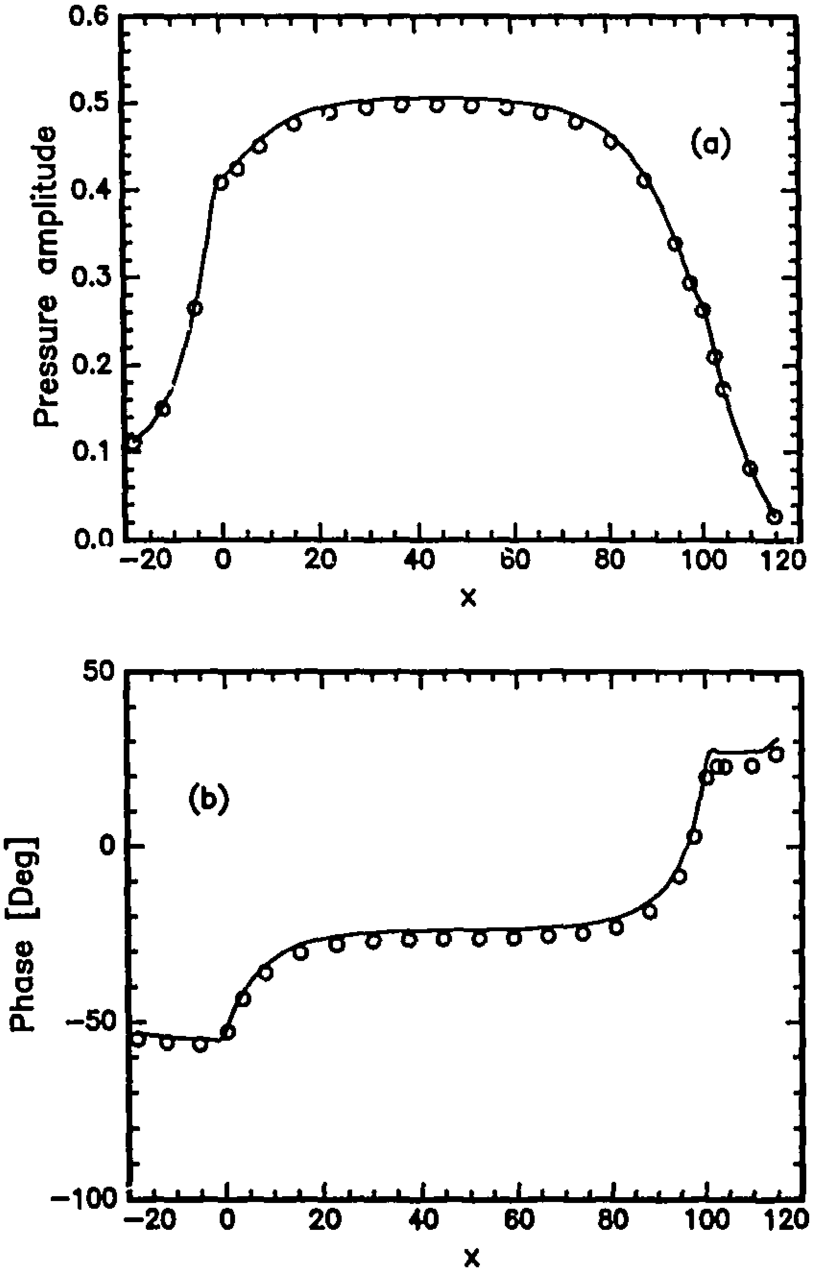

Figure 4.14: The unsteady pressure (a) and phase angle (b) for Re = 250, $\omega = 0.2$, $r_i = 9$, $r_o = 10$ at $r = 9.965$, $\theta = 7.5^{\circ}$ and $\epsilon = 0.1$. Comparison between: —,present analysis; o, Bélanger (1991).

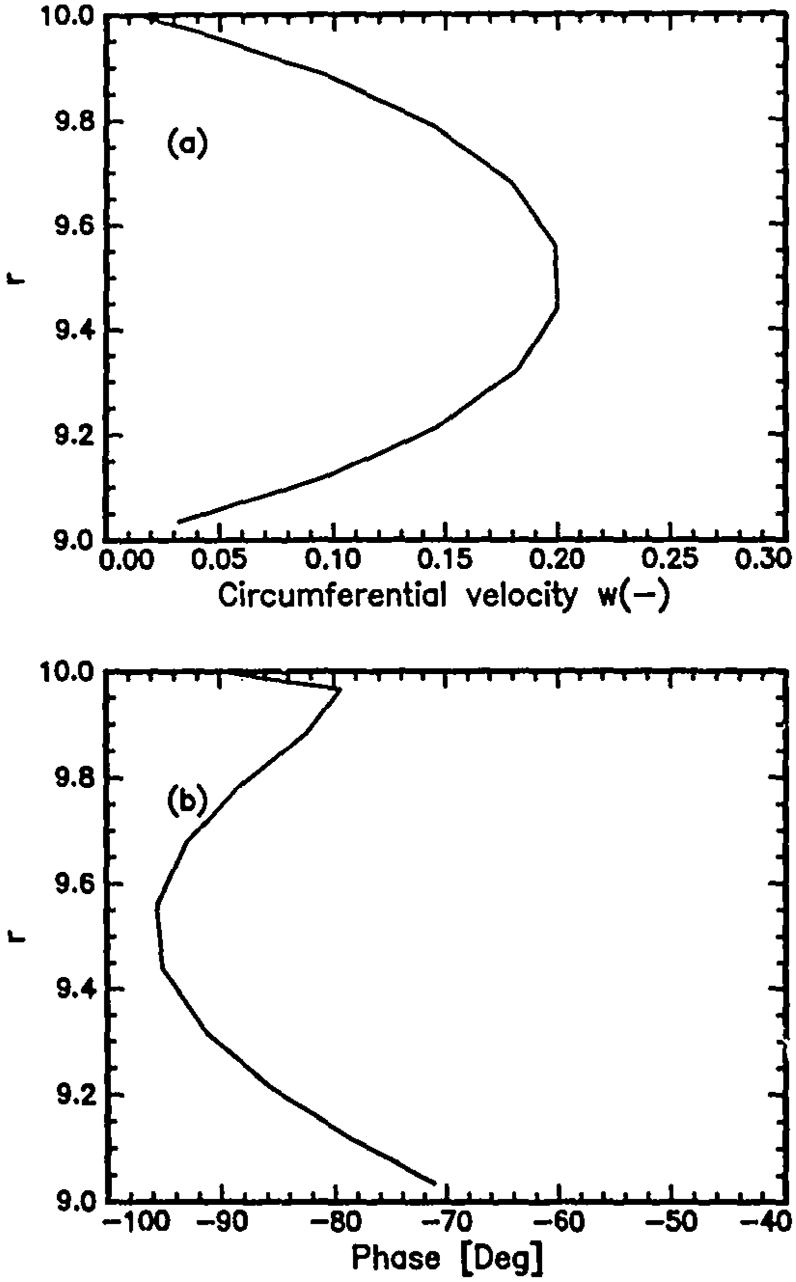

Figure 4.15: (a) The circumferential velocity w and (b) phase angle with respect to the displacement of the outer cylinder in annular gap for Re $= 250$, $\omega = 0.2$, $r_i = 9$, $r_o = 10$, and $\epsilon = 0.1$ at $X = 50$, $\theta = 45°$.

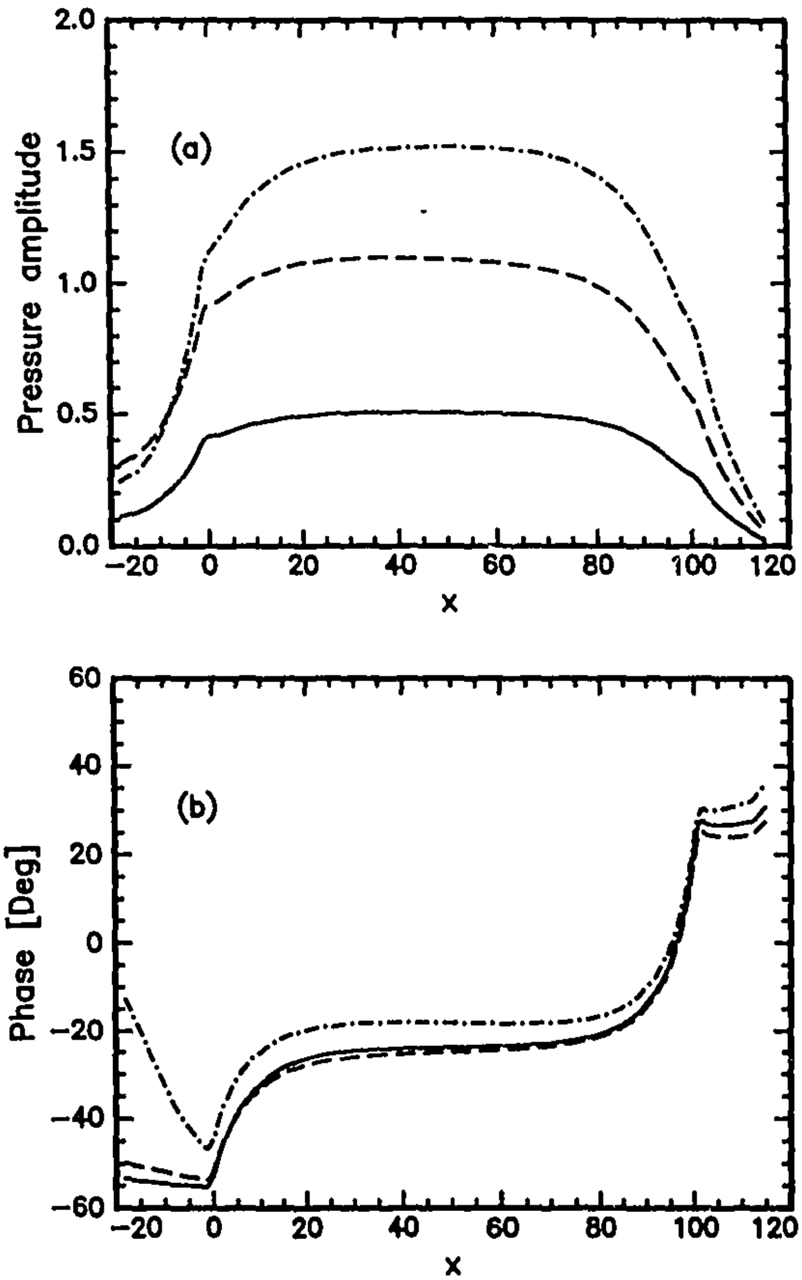

Figure 4.16: (a) The unsteady pressure amplitude and (b) phase angle with respect to the displacement of the outer cylinder versus axial length of the cylinder for Re = 250, $\omega = 0.2$, $r_i = 9$, $r_o = 10$ at $r = 9.965$ and $\theta = 7.5^o$: —,$\epsilon = 0.1$; – – –,$\epsilon = 0.2$; – · –,$\epsilon = 0.3$.

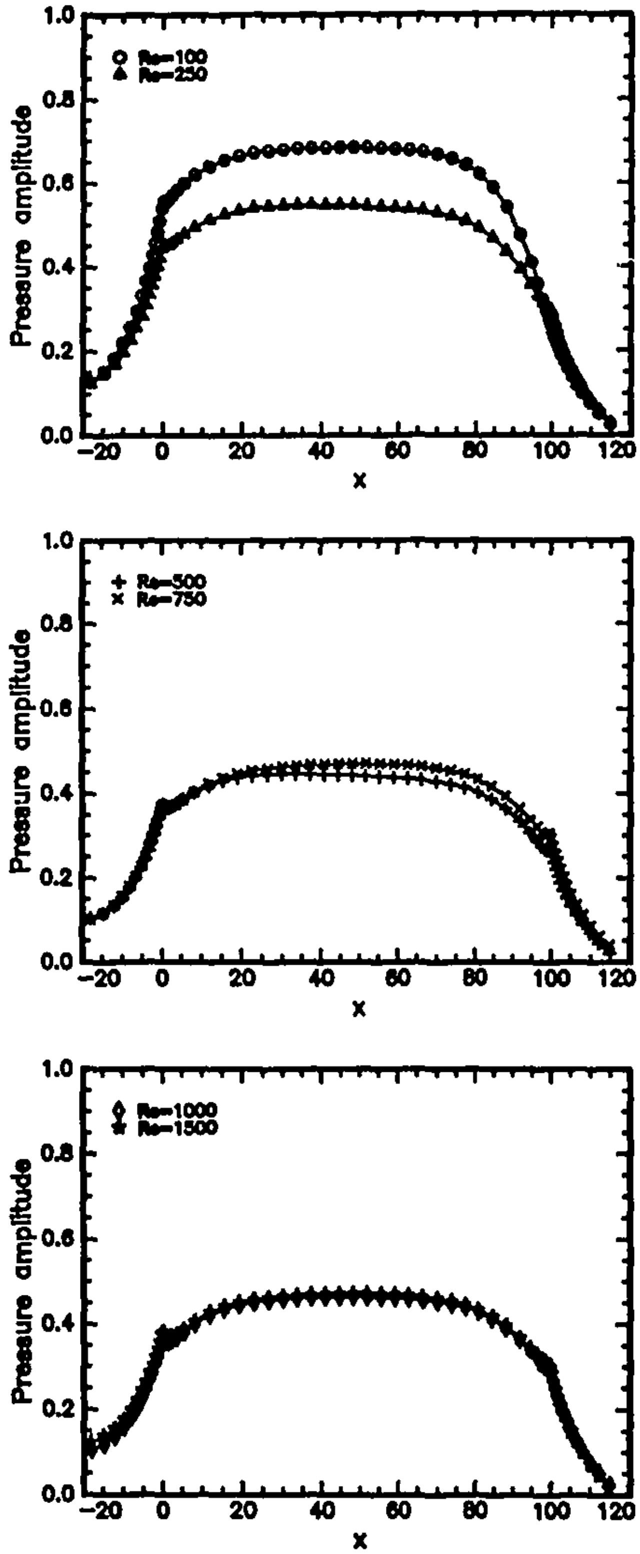

Figure 4.17: Unsteady pressure versus axial length of the cylinder at different Reynolds numbers for $\omega = 0.2$, $r_i = 9$, $r_o = 10$ at $r = 9.965$, $\epsilon = 0.1$ and $\theta = 7.5^o$.

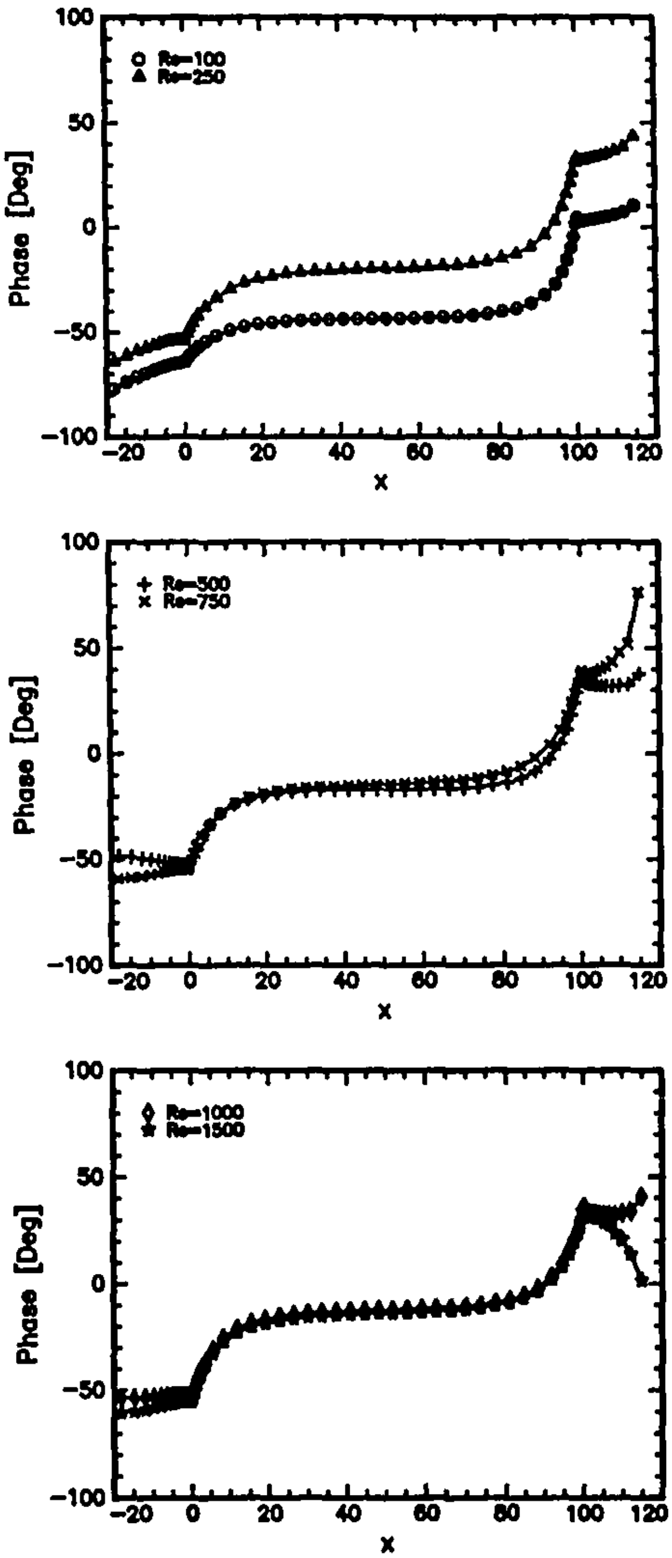

Figure 4.18: Phase angle for pressure versus axial length of the cylinder at different Reynolds numbers for $\omega = 0.2$, $r_i = 9$, $r_o = 10$ at $r = 9.965$, $\epsilon = 0.1$ and $\theta = 7.5^o$.

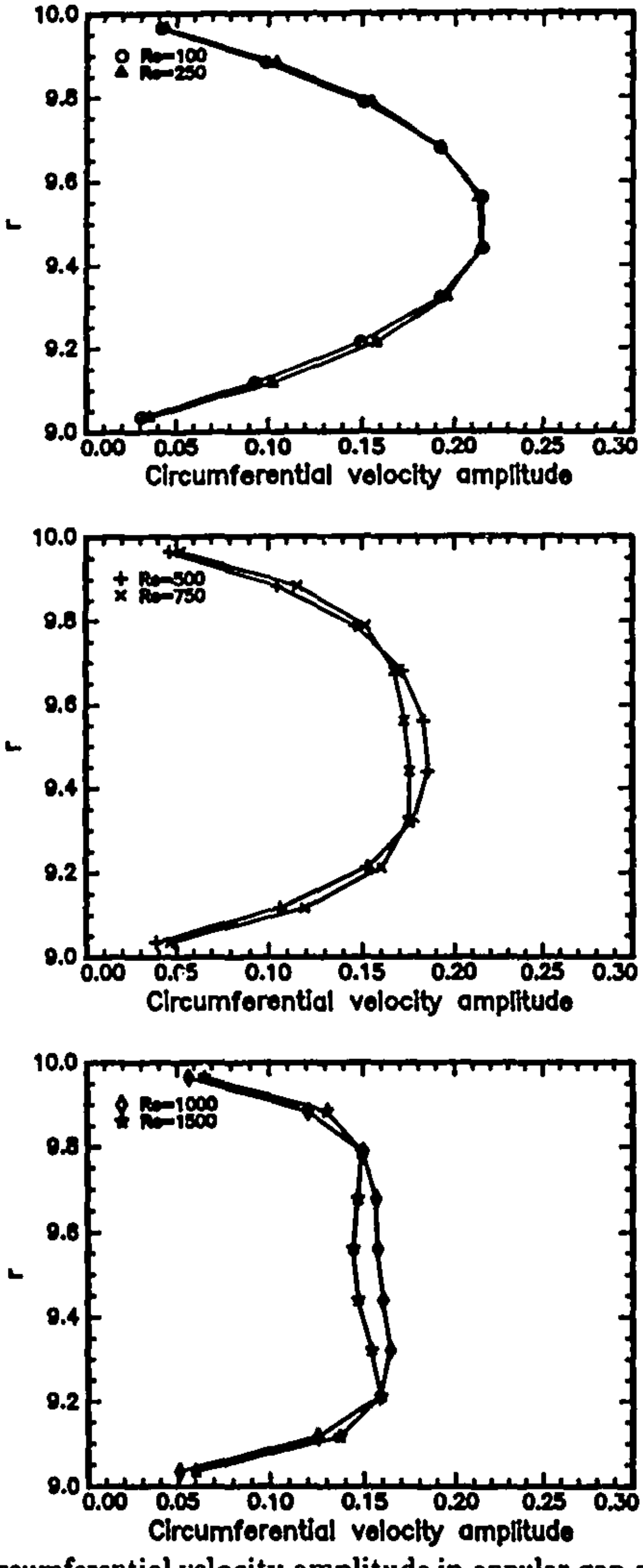

Figure 4.19: Circumferential velocity amplitude in annular gap at different Reynolds numbers for $\omega = 0.2$, $r_i = 9$, $r_o = 10$, $\epsilon = 0.1$, and at $X = 50$, $\theta = 45°$.

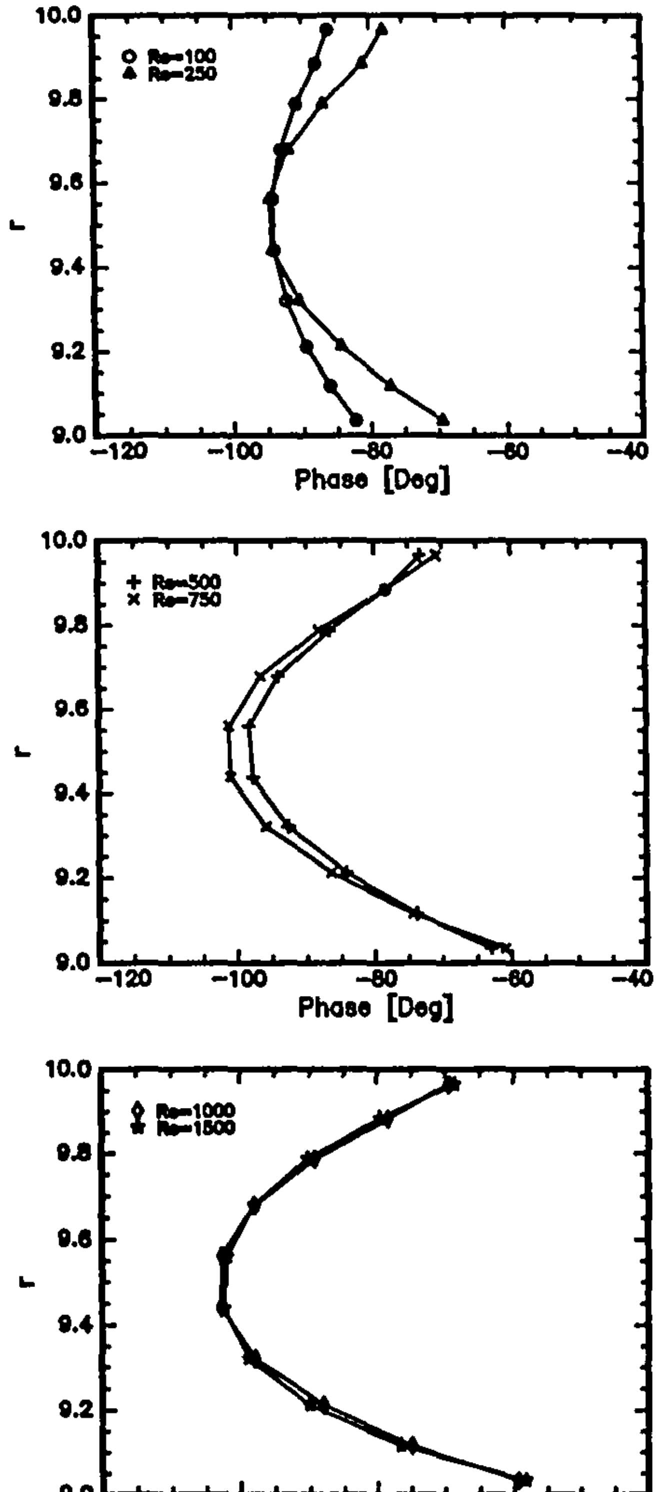

Figure 4.20: Phase angle for w in annular gap at different Reynolds numbers for $\omega = 0.2$, $r_i = 9$, $r_o = 10$, $\epsilon = 0.1$, and at $X = 50$, $\theta = 45^o$.

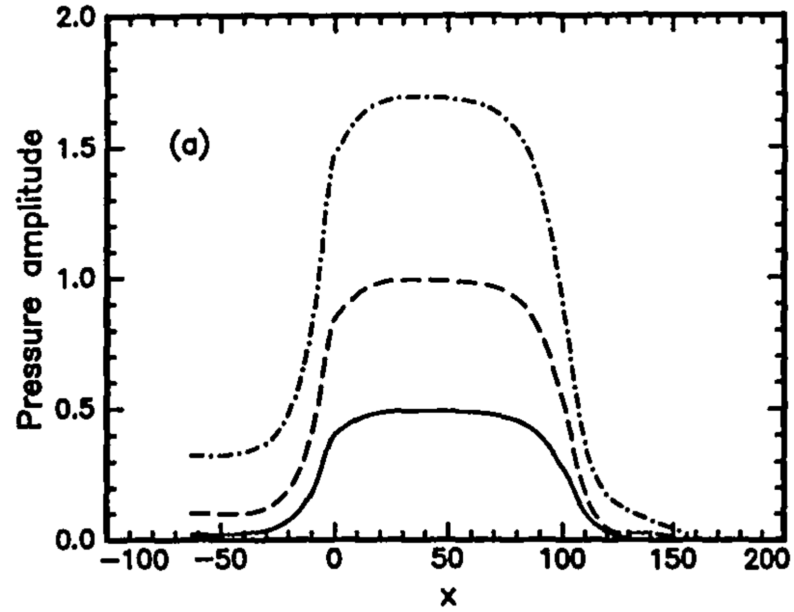

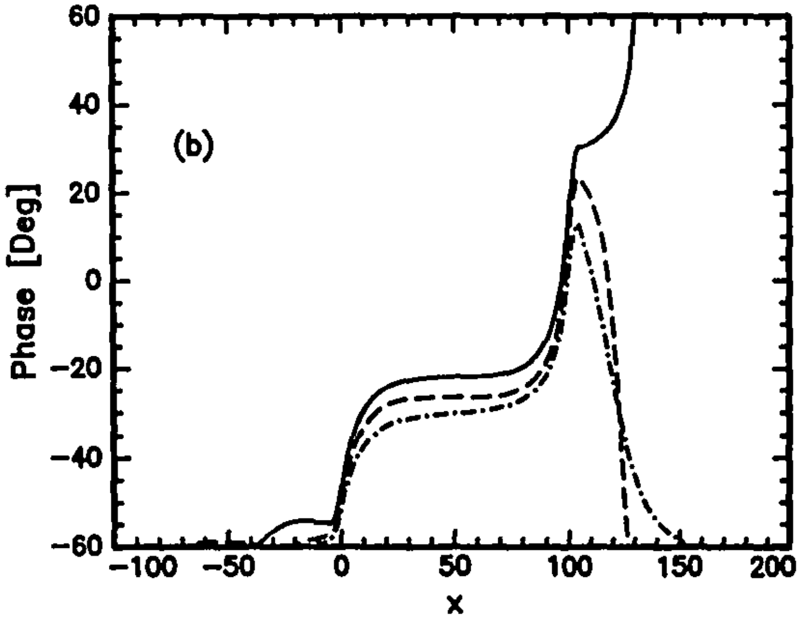

Figure 4.21: The effect of extension of the fixed upstream and downstream portions on (a) unsteady pressure amplitude and on (b) phase angle for Re = 250, $\omega = 0.2$, $r_i = 9$, $r_o = 10$ at $r = 9.965$ and $\theta = 7.5°$: —, $\epsilon = 0.1$; – – –, $\epsilon = 0.2$; – · –, $\epsilon = 0.3$.

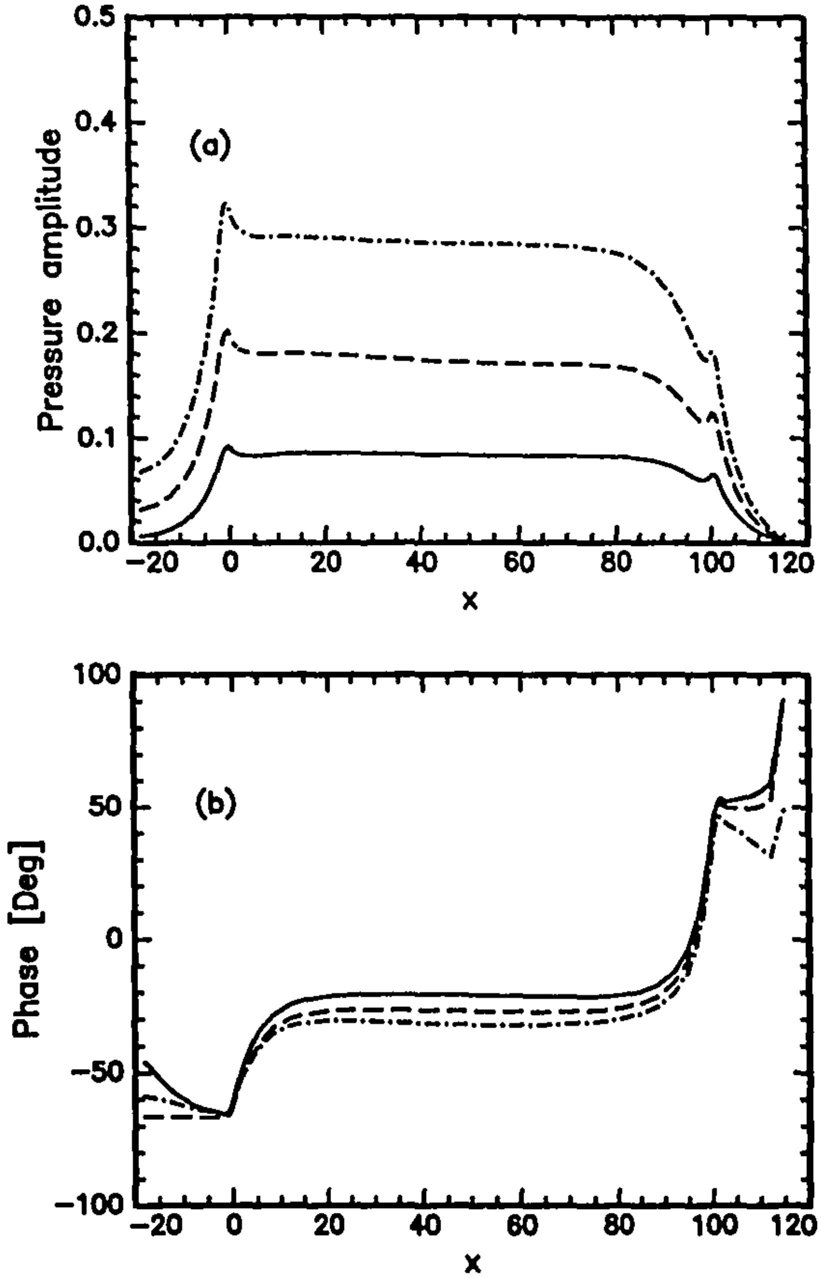

Figure 4.22: The effect of annular gap width on (a) unsteady pressure amplitude and on (b) phase angle for Re = 250, $\omega = 0.2$, $r_i = 4.785$, $r_o = 5.785$ at $r = 5.727$ and $\theta = 7.5^o$: —,$\epsilon = 0.05375$; – – –,$\epsilon = 0.1075$; – · –, $\epsilon = 0.16125$.

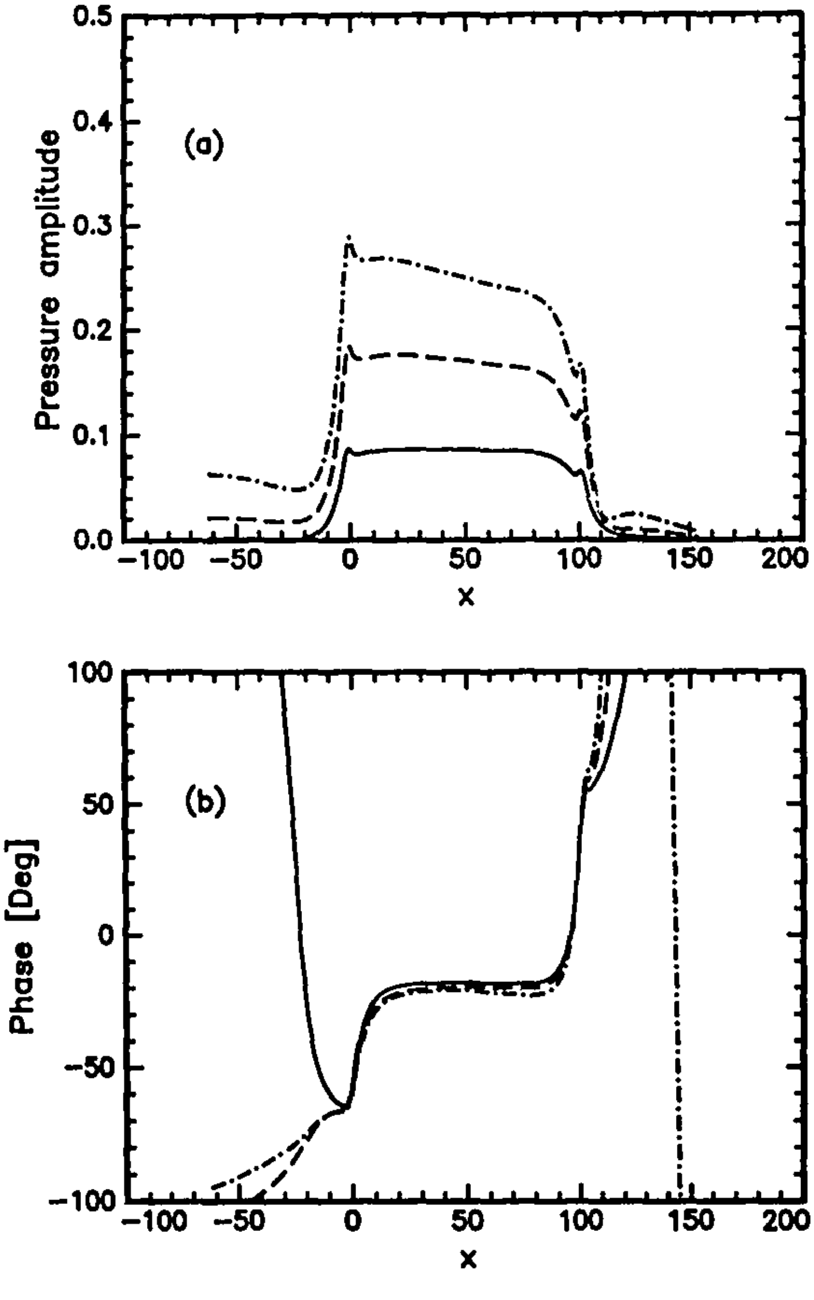

Figure 4.23: The effect of extension of the fixed upstream and downstream portions on (a) unsteady pressure amplitude and on (b) phase angle for Re = 250, $\omega = 0.2$, $r_i = 4.785$, $r_o = 5.785$ at $r = 5.727$ and $\theta = 7.5°$: —, $\epsilon = 0.05375$; – – –, $\epsilon = 0.1075$; – · –, $\epsilon = 0.16125$.

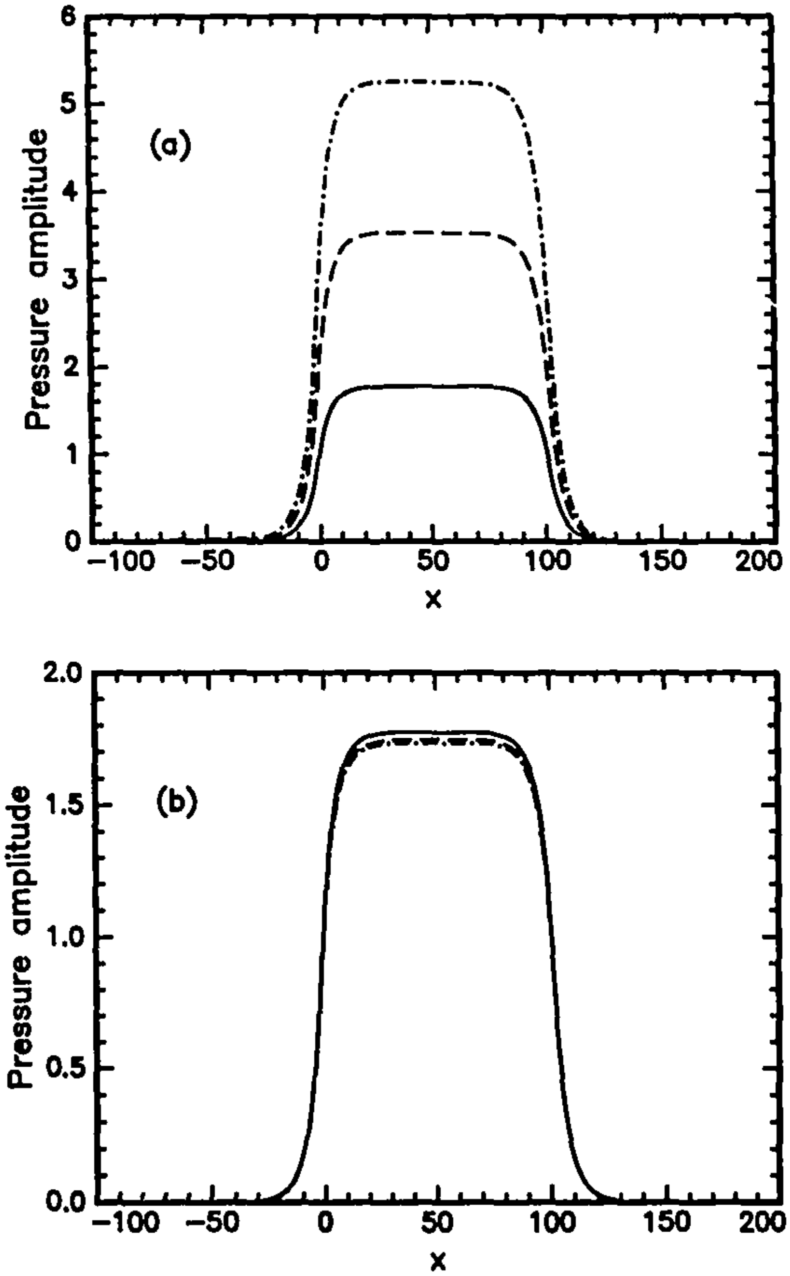

Figure 4.24: The effect of the oscillation amplitude on the unsteady pressure amplitude (a): —,$\epsilon = 0.05375$; – – –,$\epsilon = 0.1075$; – · –,$\epsilon = 0.16125$ at $f = 20$ Hz and the effect of frequency of oscillation on the unsteady pressure amplitude (b): —,$f = 20$ Hz; – – –, $f = 30.4$ Hz; – · –, $f = 40$ Hz at $\epsilon = 0.05375$ both for $U = 0$.

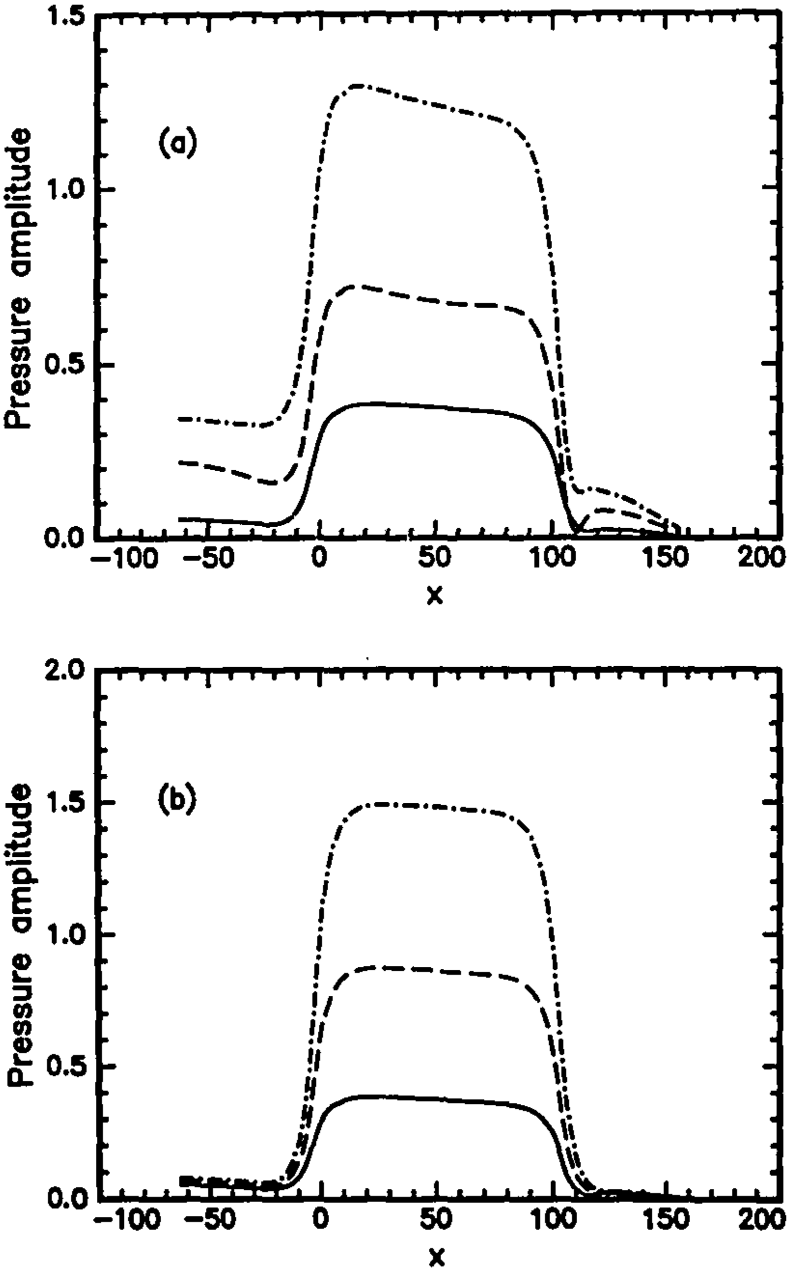

Figure 4.25: The effect of the oscillation amplitude on the unsteady pressure amplitude (a): —,ϵ = 0.05375; – – –,ϵ = 0.1075; – · –,ϵ = 0.16125 at f = 20 Hz and the effect of frequency of oscillation on the unsteady pressure amplitude (b): —,f = 20 Hz; – – –,f = 30.4 Hz; and – · –,f = 40 Hz at ϵ = 0.05375 both for Re = 2900.

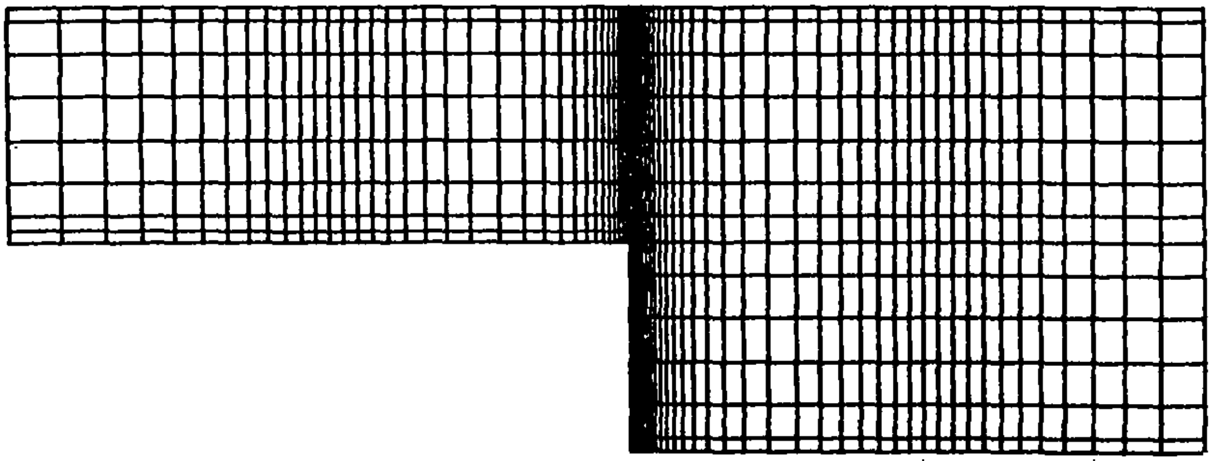

Figure 4.26: Mesh used in numerical computation for backstep geometry.

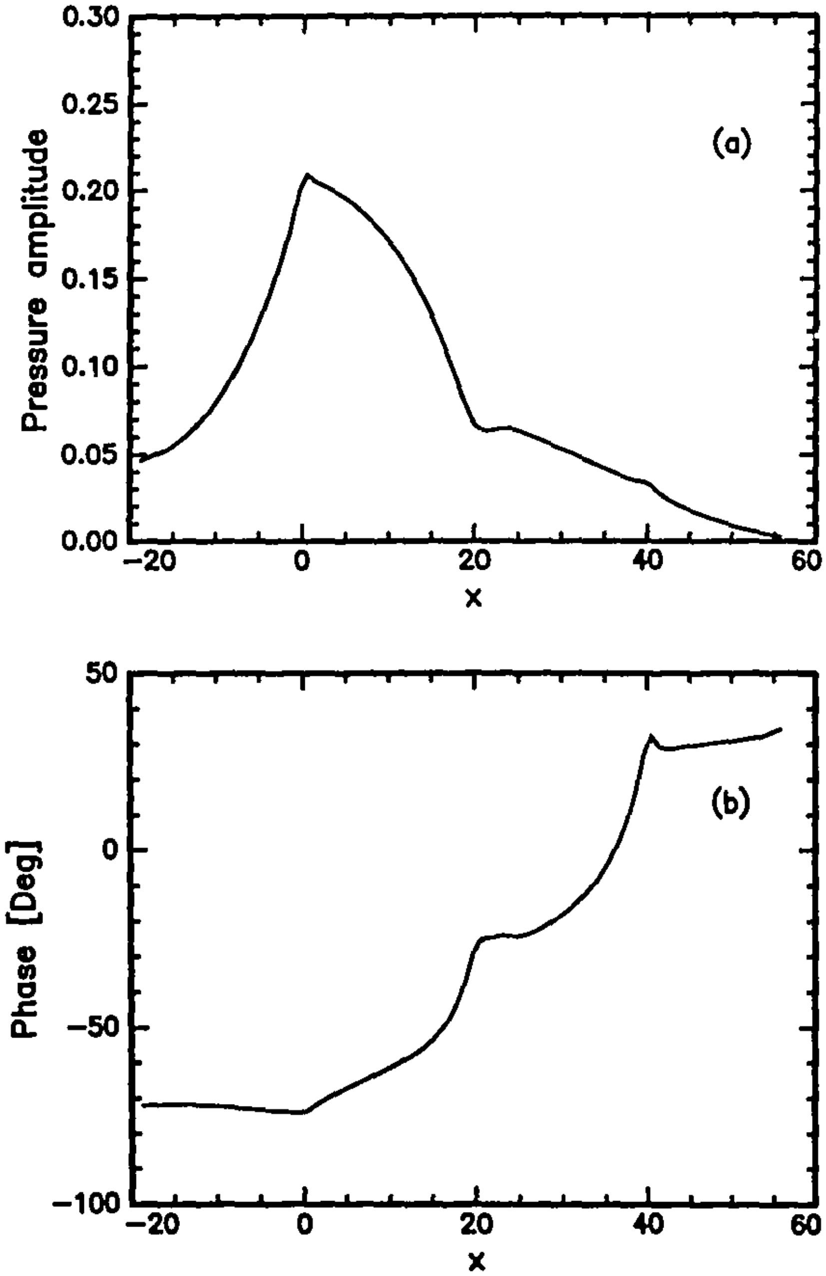

Figure 4.27: (a) The unsteady pressure amplitude and (b) phase angle for backstep geometry and Re $= 100$, $\omega = 0.1$, $r_i = 8$, $r_o = 10$, $L = 40$, $L_1 = L_2 = 20$ at $r = 9.942$, $\theta = 7.5^o$ and $\epsilon = 0.1$.

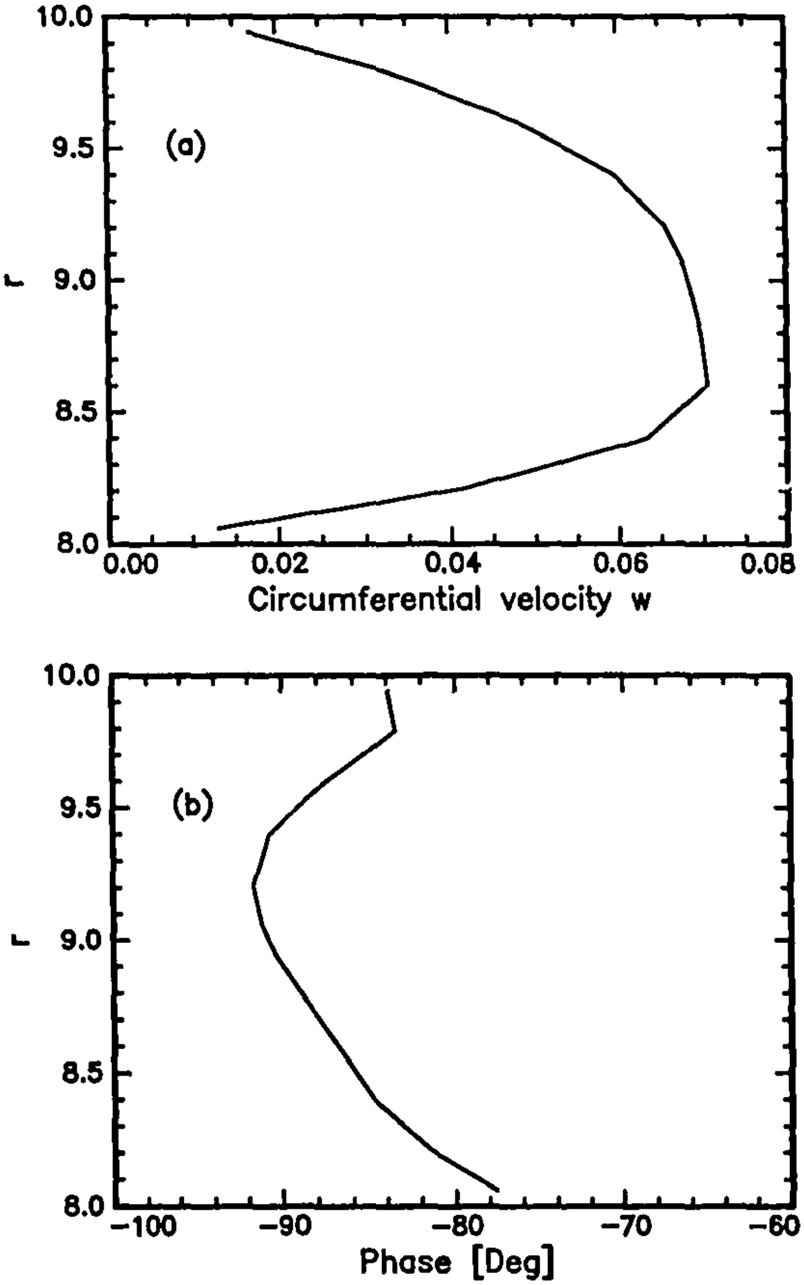

Figure 4.28: (a) The circumferential velocity amplitude w and (b) phase angle with respect to the displacement of outer cylinder in annular gap with backstep for Re = 100, $\omega = 0.1$, $r_i = 8$, $r_o = 10$, and $\epsilon = 0.1$ at $X = 20$, $\theta = 45^o$.

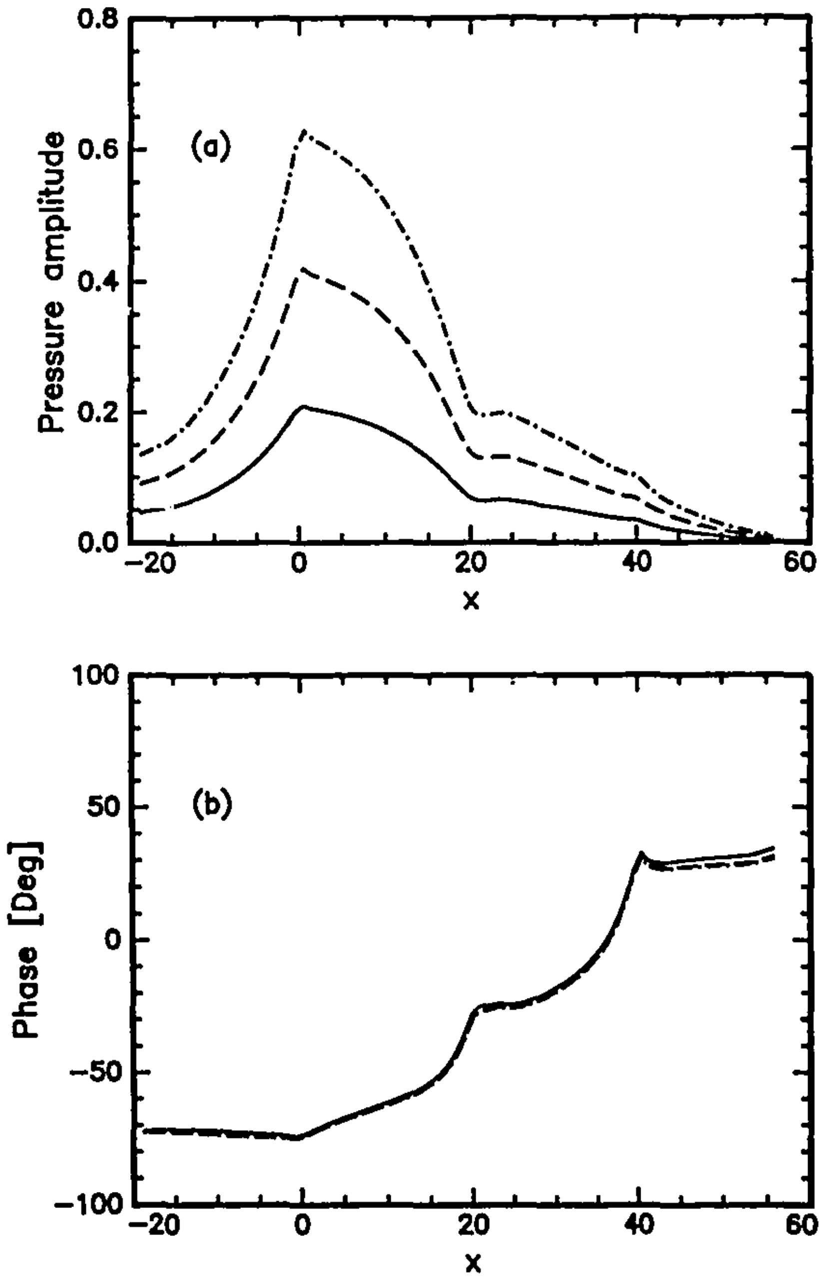

Figure 4.29: (a) The unsteady pressure amplitude and (b) phase angle with respect to the displacement of outer cylinder versus axial length of the cylinder with backstep for Re = 100, $\omega = 0.1$, $r_i = 8$, $r_o = 10$, $L = 40$, $L_1 = L_2 = 20$ at $r = 9.942$ and $\theta = 7.5^o$: —,$\epsilon = 0.1$; – – –,$\epsilon = 0.2$; – · –,$\epsilon = 0.3$.

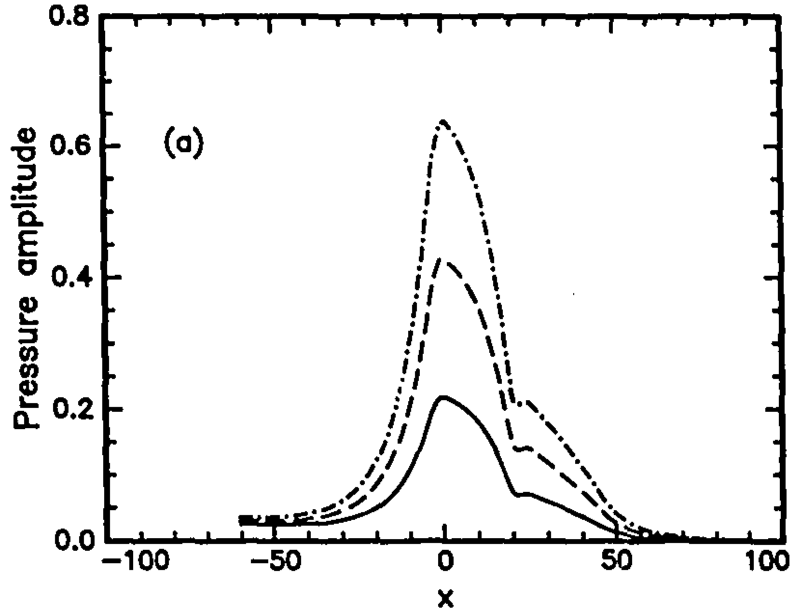

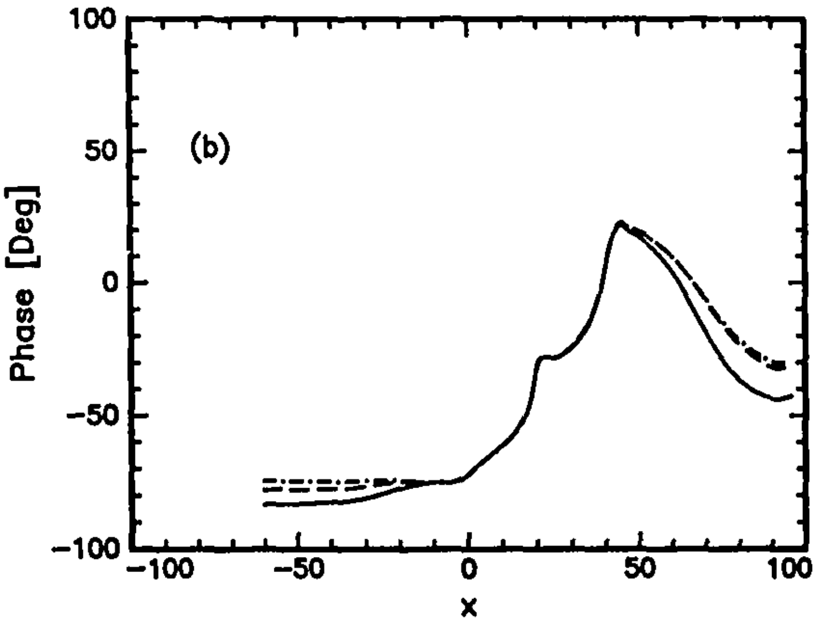

Figure 4.30: The effect of extension of the fixed upstream and downstream portions on (a) unsteady pressure amplitude and on (b) phase angle; backstep geometry for Re = 100, $\omega = 0.1$, $r_i = 8$, $r_o = 10$, $L = 40$, $L_1 = L_2 = 60$ at $r = 9.942$ and $\theta = 7.5°$: —,$\epsilon = 0.1$; - - -,$\epsilon = 0.2$; — · —,$\epsilon = 0.3$.

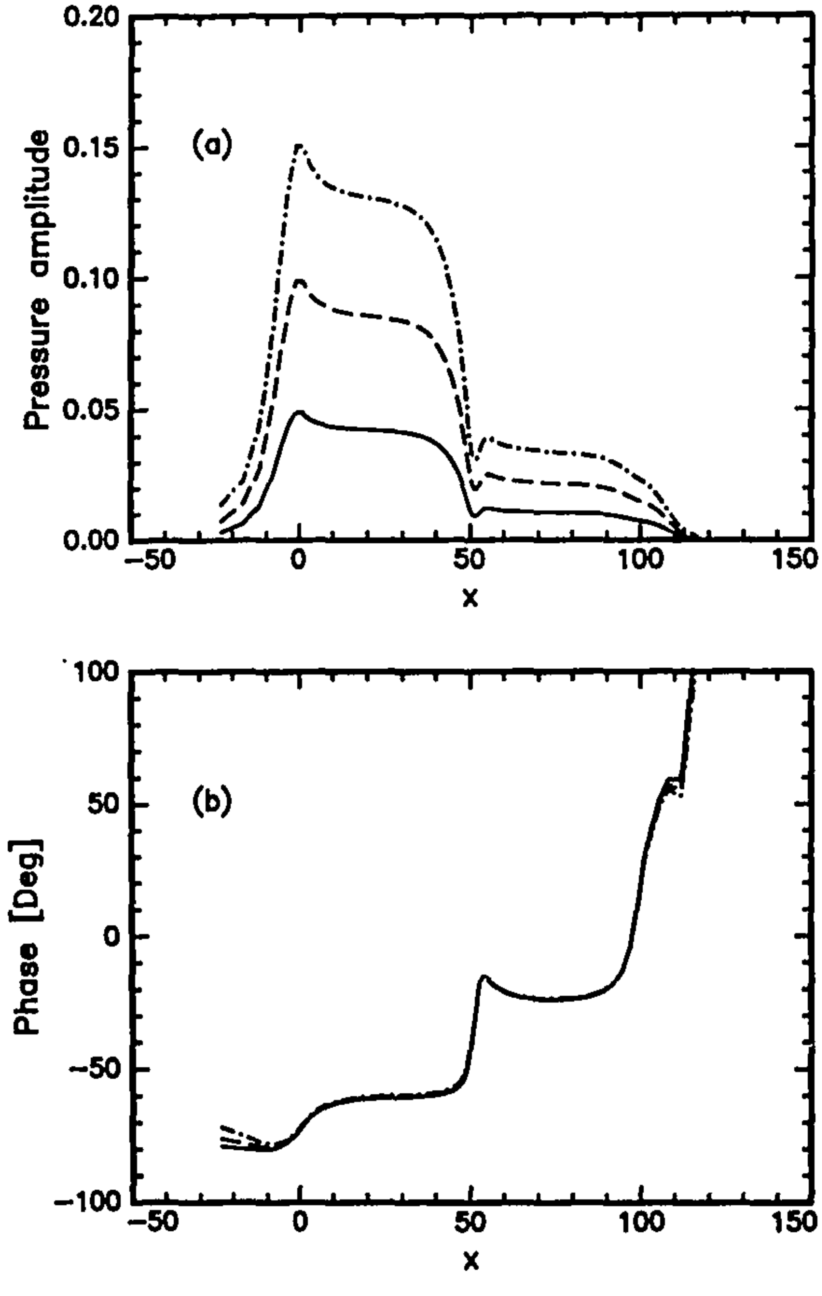

Figure 4.31: The effect of annular gap width on (a) unsteady pressure amplitude and on (b) phase angle; backstep geometry for Re $= 100$, $\omega = 0.1$, $r_i = 3.785$, $r_o = 5.785$, $L = 100$, $L_1 = L_2 = 20$ at $r = 5.727$ and $\theta = 7.5^{\circ}$: —,$\epsilon = 0.05375$; – – –,$\epsilon = 0.1075$; – · –,$\epsilon = 0.16125$.

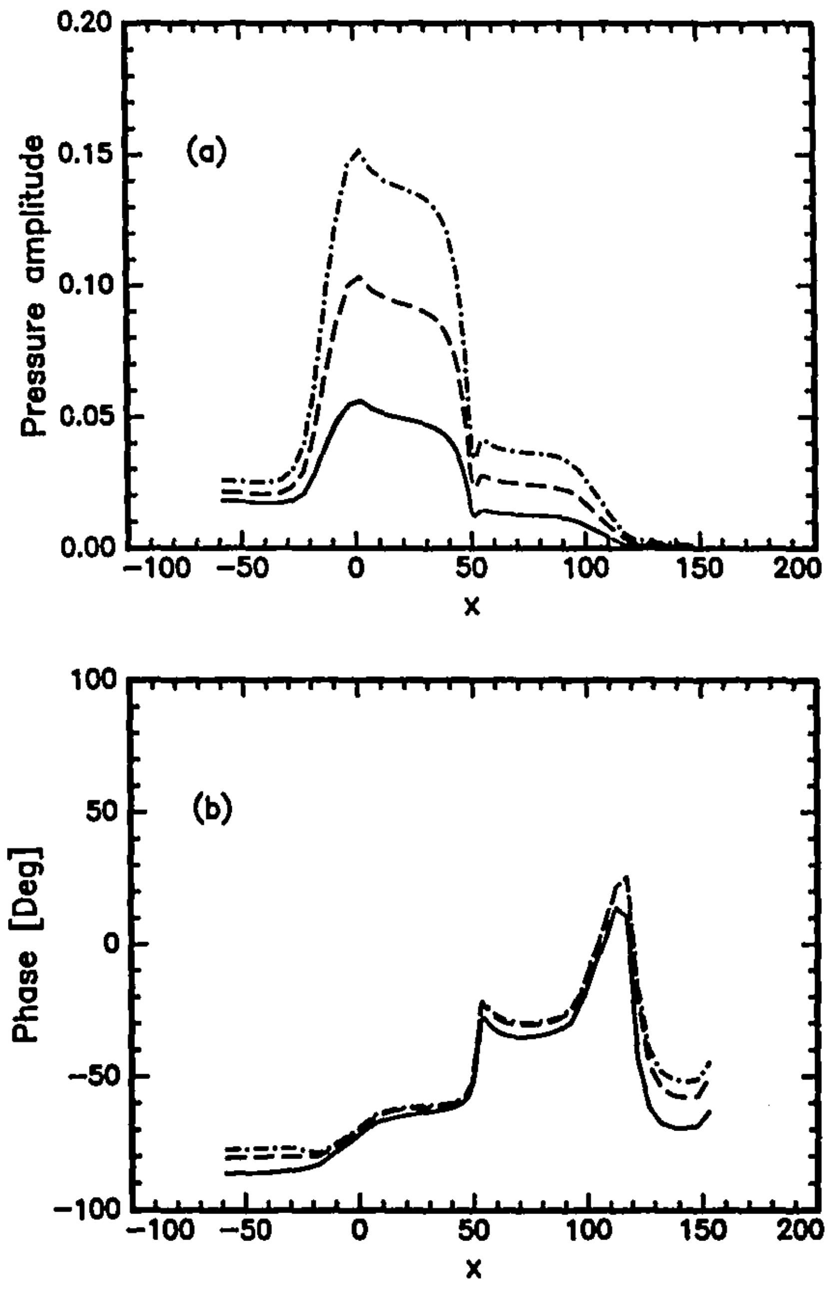

Figure 4.32: The effect of extension of the fixed upstream and downstream portions on (a) unsteady pressure amplitude and on (b) phase angle; backstep geometry for Re $= 100$, $\omega = 0.1$, $r_i = 3.785$, $r_o = 5.785$, $L = 100$, $L_1 = L_2 = 60$ at $r = 5.727$ and $\theta = 7.5^o$: —,$\epsilon = 0.05375$; – – –,$\epsilon = 0.1075$; – · –,$\epsilon = 0.16125$.

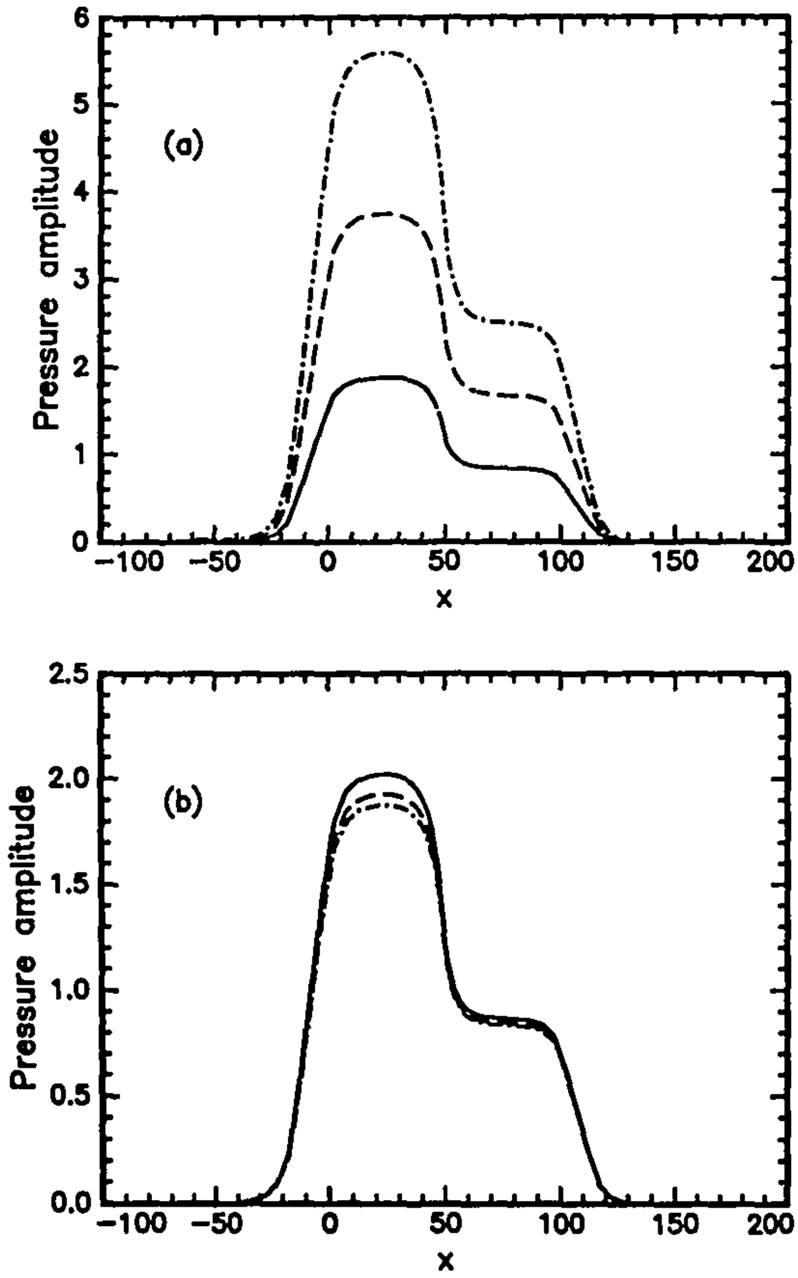

Figure 4.33: The effect of amplitude of oscillation on pressure amplitude (a): — ,$\epsilon = 0.05375$; – – –,$\epsilon = 0.1075$; – · –,$\epsilon = 0.16125$ at $f = 4.5$ Hz and the effect of frequency of oscillation on pressure amplitude (b): —,$f = 1.5$ Hz, – – –,$f = 3$ Hz; – · –,$f = 4.5$ Hz at $\epsilon = 0.05375$ both for backstep geometry and $U = 0$; $L = 100$, $L_1 = L_2 = 60$.

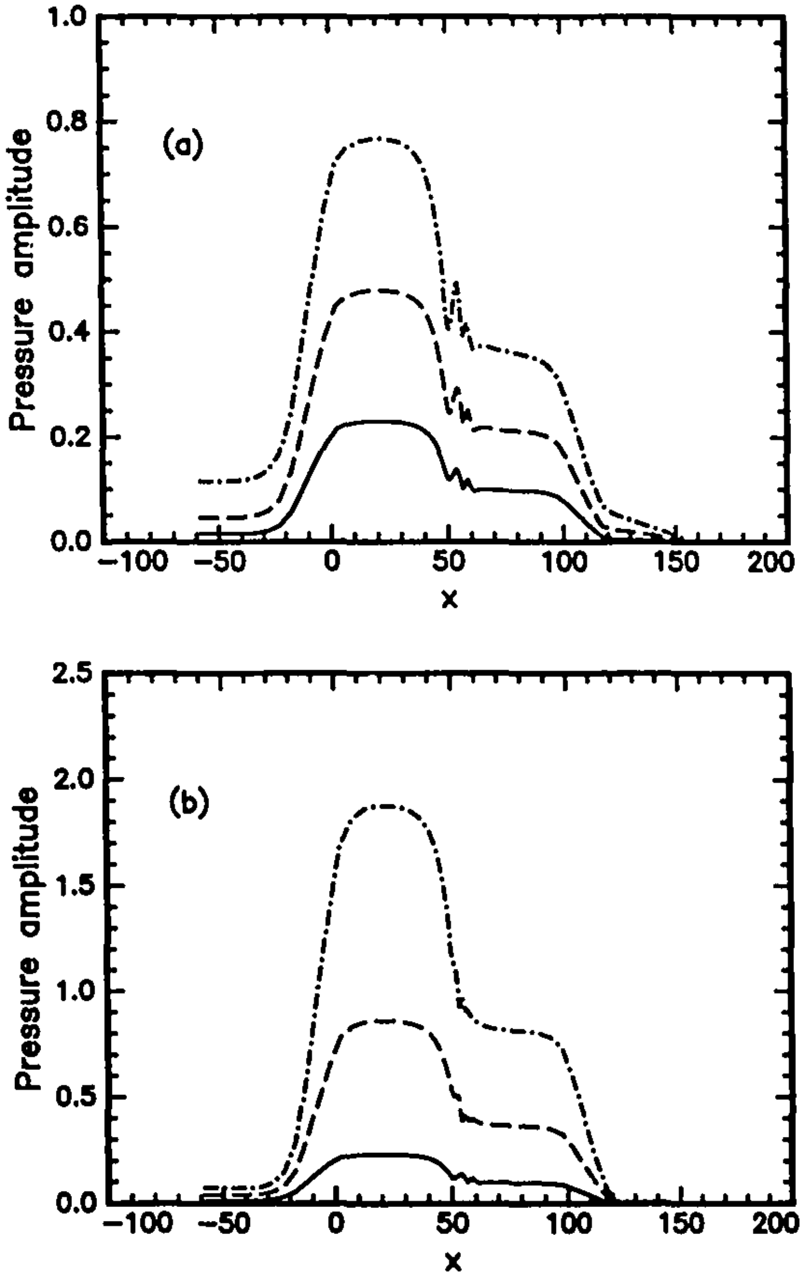

Figure 4.34: The effect of amplitude of oscillation on pressure amplitude (a): — ,$\epsilon = 0.05375$; – – –,$\epsilon = 0.1075$; – · –,$\epsilon = 0.16125$ at $f = 1.5$ Hz and the effect of frequency of oscillation on pressure amplitude (b): —,$f = 1.5$ Hz; – – –,$f = 3$ Hz; – · –,$f = 4.5$ Hz at $\epsilon = 0.05375$ both for backstep geometry and Re = 300; $L = 100$, $L_1 = L_2 = 60$.

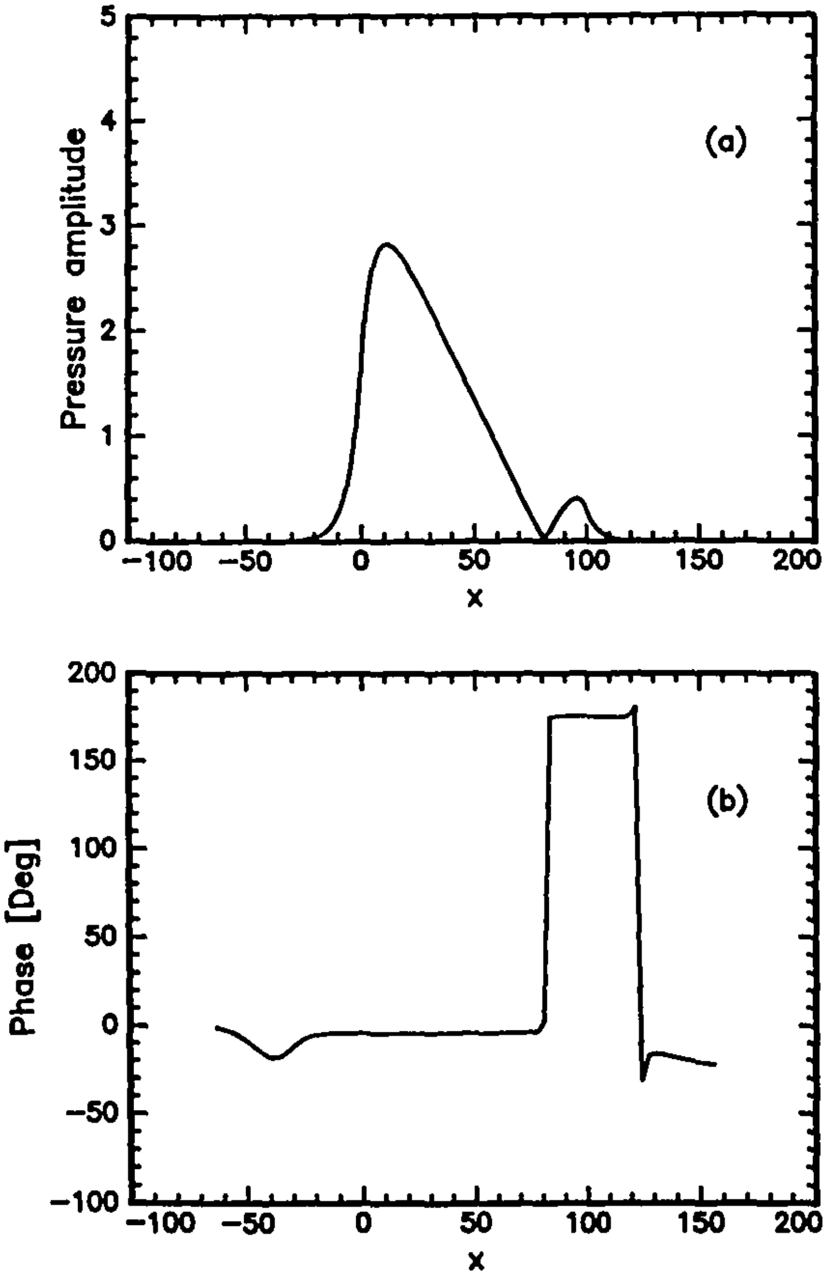

Figure 4.35: (a) The unsteady pressure amplitude and (b) phase angle in uniform annular space during rocking motion of outer cylinder for $U = 0$, $\omega = 1.0$ ($f = 20$ Hz), $r_i = 4.785$, $r_o = 5.785$, $L = 100$, $L_1 = L_2 = 60$ and $\epsilon = 0.1075$ (at shaker position; see text). Hinge location at $X = 81.0$.

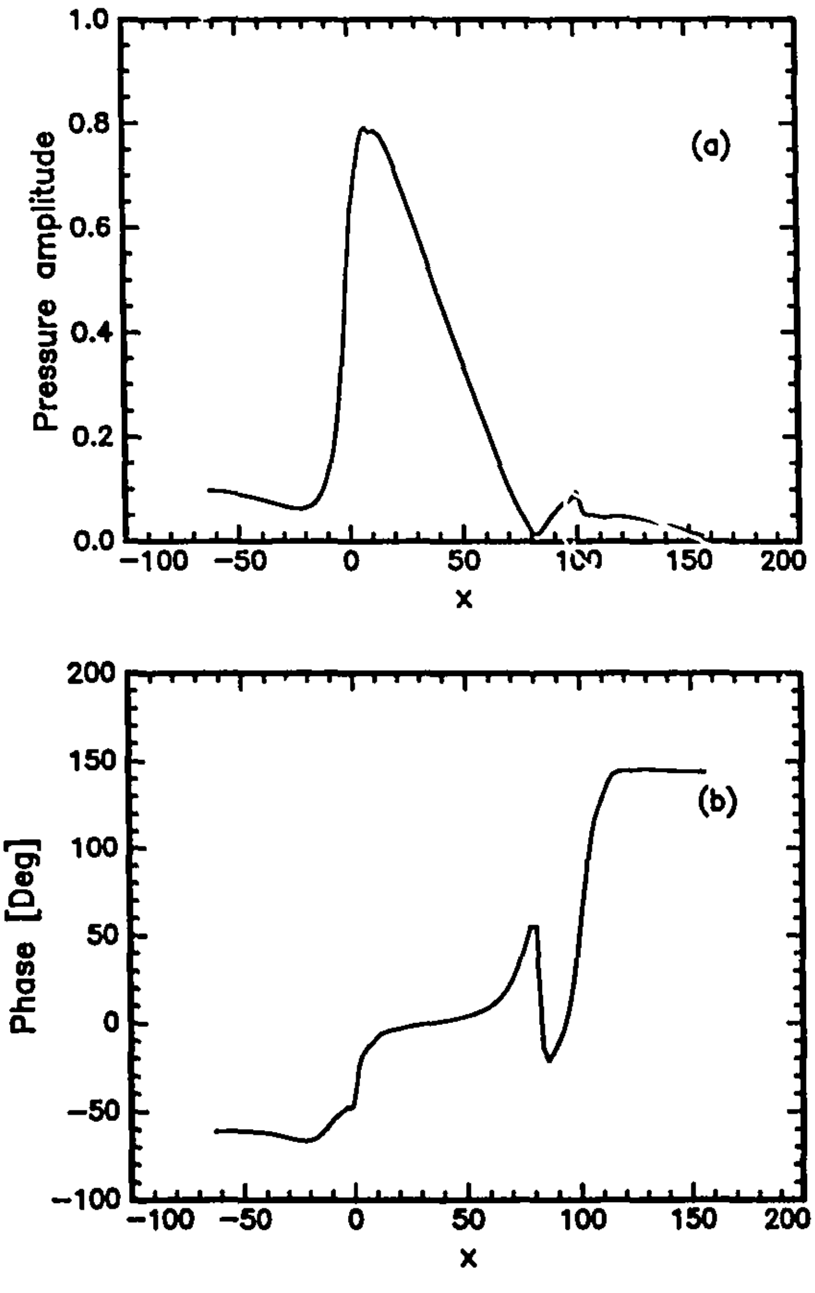

Figure 4.36: (a) The uusteady pressure amplitude and (b) phase angle in uniform annular space during rocking motion of outer cylinder for Re = 2900, $\omega = 0.231$ (f = 20 Hz), $r_i = 4.785$, $r_o = 5.785$, $L = 100$, $L_1 = L_2 = 60$ and $\epsilon = 0.1075$ (at shaker position; see text). Hinge location at $X = 81.0$.

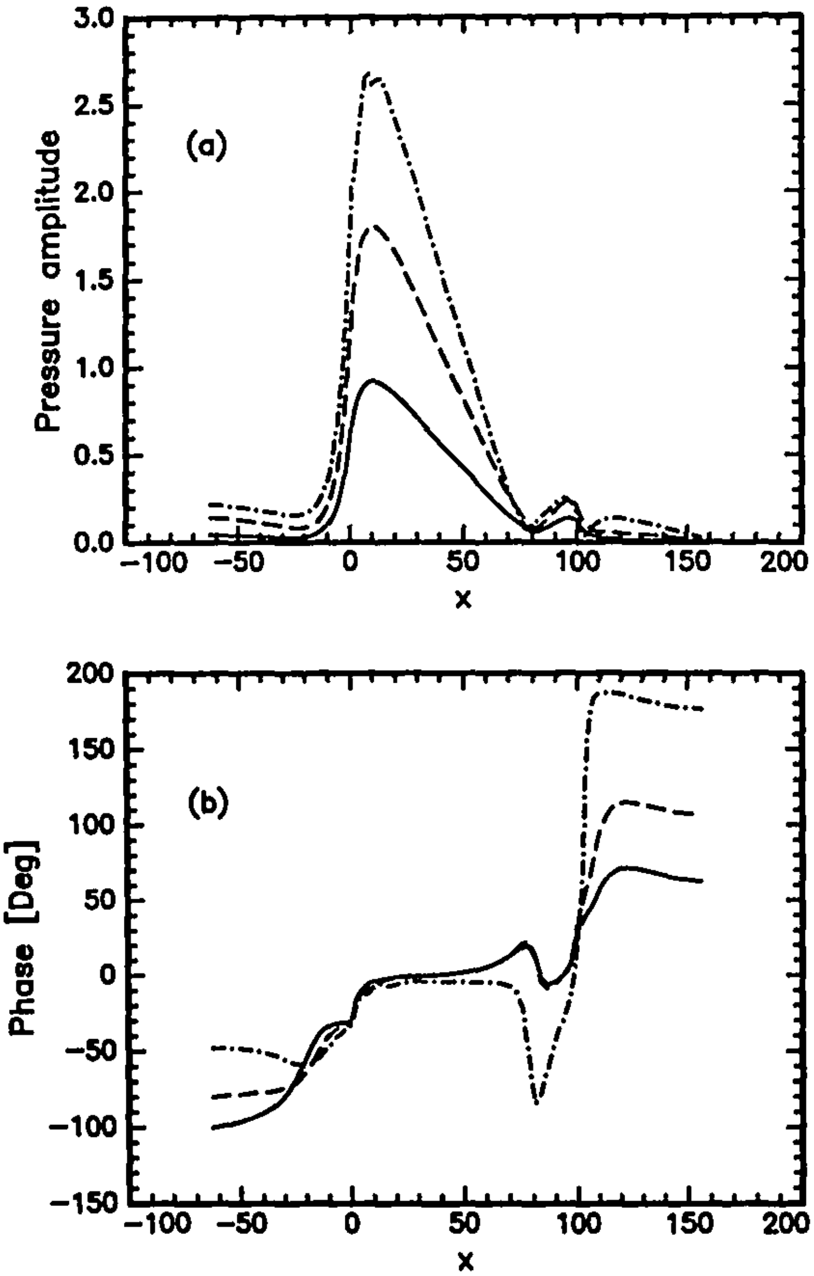

Figure 4.37: (a) The unsteady pressure amplitude and (b) phase angle in uniform annular space during rocking motion of outer cylinder for Re = 2900, ω = 0.703 (f = 30.4 Hz), r_i = 4.785, r_o = 5.785, L = 100, $L_1 = L_2$ = 60: —,ϵ = 0.05735; – – –,ϵ = 0.1075; – · –,ϵ = 0.16125 (at shaker position; see text). Hinge location at X = 81.0.

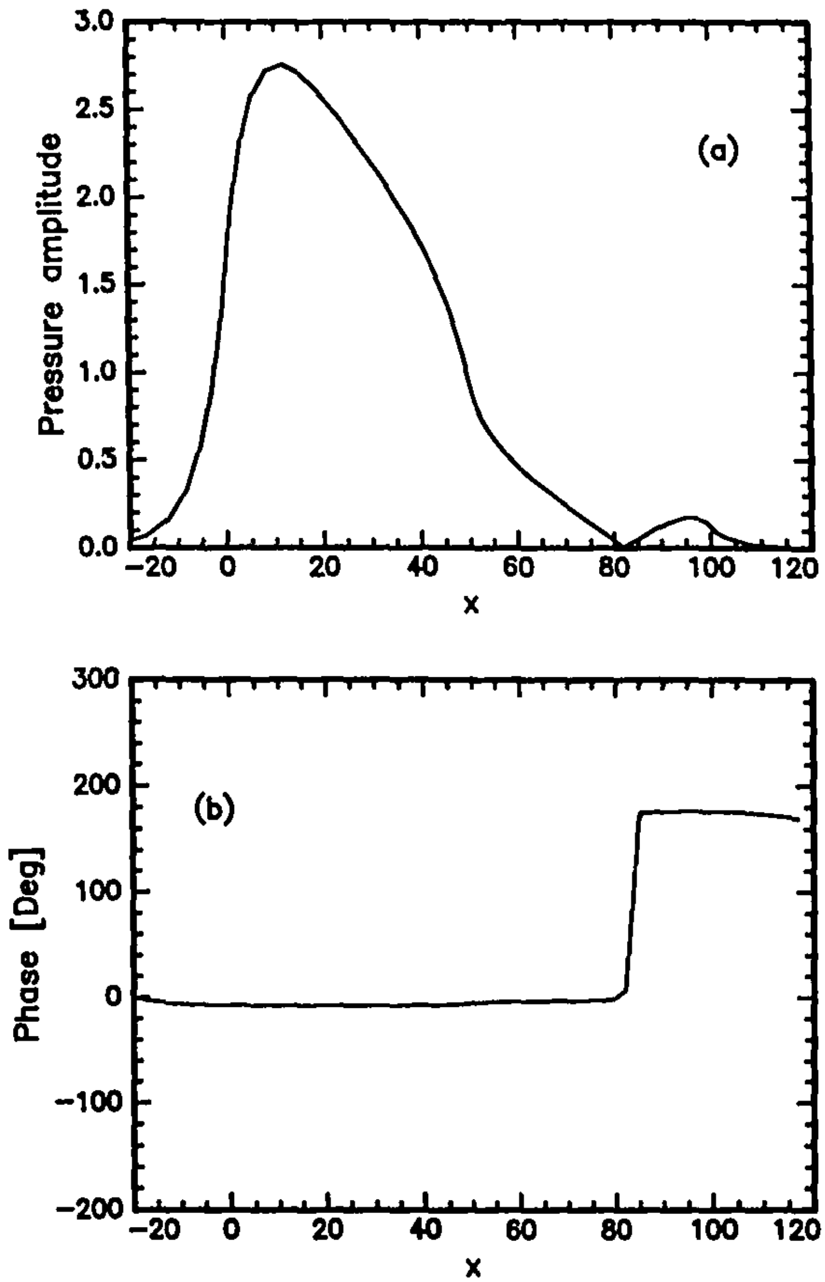

Figure 4.38: (a) The unsteady pressure amplitude and (b) phase angle in annular geometry with backstep during rocking motion of outer cylinder for $U = 0$, $\omega = 1.0$ ($f = 6$ Hz), $r_i = 4.785$, $r_o = 5.785$, $L = 100$, $L_1 = L_2 = 20$ and $\epsilon = 0.1075$ (at shaker position; see text). Hinge location at $X = 82.0$.

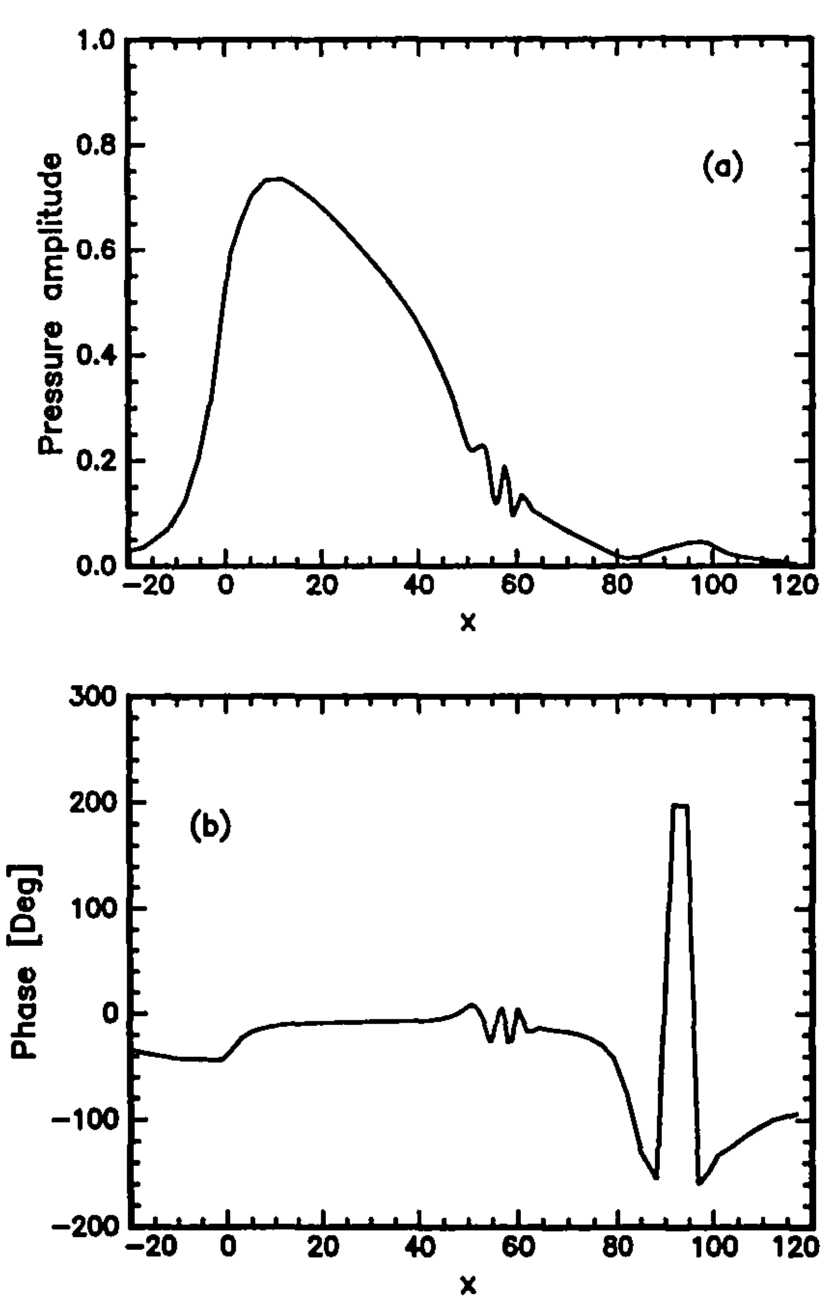

Figure 4.39: (a) The unsteady pressure amplitude and (b) phase angle in annular geometry with backstep during rocking motion of outer cylinder for Re = 400, $\omega = 0.5$ ($f = 3$ Hz), $r_i = 4.785$, $r_o = 5.785$, $L = 100$, $L_1 = L_2 = 20$ and $\epsilon = 0.1075$ (at shaker position; see text). Hinge location at $X = 82.0$.

Chapter 5

Three-Dimensional Solution for Axially Variable Annular Configurations

One of the important geometries which have been considered for a long time by investigators as a major instability-producing system is the annular geometry with a diffuser section. Examples are the self-excited vibrations of jet pumps used in boiling water reactors (similar to that shown in Figure 1.3) and in the AGR flow control device called gag bomb. Several investigations have been done on this type of geometry to discover the underlying mechanism leading to instability of such systems.

There is a theoretical link between pressure recovery in the diffuser and reduced stability which has also been established experimentally by Hobson (1984). He developed a closed-form analytical expression for the negative aerodynamic damping for this type of geometry. In his theoretical model, he included skin friction in the analysis and proved that a diffuser can promote instability. He confirmed this conclusion by measuring experimentally the aerodynamic forces acting on a cylinder oscillating in a diffuser.

Spurr & Hobson (1984) have conducted a series of tests with the annulus terminated in a diffuser with half-angles of $0°, 2°, 4°$, and $6°$, and hence with a variable amount of pressure recovery; such geometries can be found in some nuclear reactors . It must be remarked in Figure 2.2 that the gas flow between channel and assembly can cause potential damaging vibration of the long, slender fuel assembly in a number of ways, but it is recognized that the flow in the annular diffusing section immediately above the seal bore provides the main source of excitation. It is predicted that the seal bore aerodynamics give rise to negative fluid damping whilst a reduction in pressure recovery promotes stability. It has been shown that this mechanism is typical of the diffuser with 6^o half-angle.

Because of the importance of annular-flow-induced vibrations and instabilities in systems with diffuser geometries, a special chapter is devoted to this topic. Hence, in this chapter, the numerical solution of the N-S and continuity equations is obtained for concentric cylinders with two different diffuser half-angles, namely, 6^o and 20^o. In the following sections the procedure is described for solving the flow equations on an orthogonal grid rather than on skewed grid. The method of solution after coordinate transformation is similar to the method described in Chapter 4.

5.1 Geometrical Configuration

The nonuniform annular space considered here consists of two concentric cylinders in which the inner one has a diffuser shape as shown in Figure 5.1. In this figure, H_d is the diffuser height which is equal to half of the annular gap, *i.e.*, $H_d = H = R_o - R_{iu}$. As mentioned before, the diffuser angle was chosen to be either $\alpha = 6^o$ or $\alpha = 20^o$. The characteristic length H and characteristic velocity U at the upstream of the diffuser are used to non-dimensionalize the fluid flow equations. In this analysis, as in the analysis for uniform annuli, the outer cylinder is composed of three parts: the central part has length L and oscillates harmonically with frequency Ω, or in non-dimensional form $\omega = \Omega H/U$; two fixed parts are situated upstream and downstream of the central part with lengths L_u and L_d. The equivalent non-dimensional forms of R_o, R_{iu} and R_{id} are given by $R_o/H = r_o, R_{iu}/H = r_{iu}$ and $R_{id}/H = r_{id} = r_o - 1 - h_d$ respectively, where $h_d = H_d/H$.

5.2 Coordinate Transformation for Axially Variable Annular Configurations

To solve flow equations for nonuniform geometries one can use the mesh shown in Figure 4.26, which is a schematic representation of the mesh used for backward-facing step, spanning the r- and x-directions. The major step taken for the solution of the flow equations in the diffuser-shaped annular spaces is the space transformation to reduce the problem to the case of a backward facing step. This is required to solve the problem on an orthogonal grid, rather than on a non-orthogonal one which could arise due to the presence of the diffuser shape. This annular space transformation, while complicating the problem by adding more terms to the equations, especially the cross-derivative terms which are the characteristics of non-orthogonality, nevertheless ensures that the derivatives are calculated on an orthogonal mesh.

In order to generalize the problem, it is necessary to transform the annular space (r^*, x^*) in the physical domain of Figure 5.2(a) into the rectangular computational domain (r, x) shown in Figure 5.2(b).

For this purpose, it is convenient to define the nondimensional transformation equations as

$$r = \frac{Rr^* - R_{iu}\epsilon(x^*)}{R - \epsilon(x^*)}, \tag{5.1}$$

$$t = t^*, \qquad x = x^*, \qquad \theta = \theta^*, \qquad H_d = R = R_{iu} - R_{id}, \qquad X = x_2^* - x_1^*, \tag{5.2}$$

where $\epsilon(x^*) = H_d(x_2^* - x^*)/X$, and the stared quantities indicate the physical domain. This transformation is only for the region where the diffuser section is located, *i.e.*, for $x_1^* \leq x^* \leq x_2^*$ in Figure 5.2(a).

All functions having continuous partial derivatives in the physical cylindrical domain can be expressed in the form of functions in the computational domain by the chain rule. Thus, one can write

$$\frac{\partial}{\partial x^*} = \frac{\partial r}{\partial x^*}\frac{\partial}{\partial r} + \frac{\partial}{\partial x}, \quad \frac{\partial}{\partial r^*} = \frac{\partial r}{\partial r^*}\frac{\partial}{\partial r}, \quad \frac{\partial}{\partial \theta^*} = \frac{\partial}{\partial \theta}, \quad \frac{\partial}{\partial t^*} = \frac{\partial}{\partial t}. \tag{5.3 - 5.6}$$

Using equations (5.3-5.6), the radial-direction derivatives of a function g in the physical domain, in terms of the independent variables in the computational domain, can be written as

$$\frac{\partial g}{\partial r^*} = \frac{\partial r}{\partial r^*}\frac{\partial g}{\partial r} = A(x^*)\frac{\partial g}{\partial r}, \tag{5.7}$$

$$\frac{\partial^2 g}{\partial r^{*2}} = \left(\frac{\partial r}{\partial r^*}\right)^2 \frac{\partial^2 g}{\partial r^2} = A^2(x^*)\frac{\partial^2 g}{\partial r^2}, \tag{5.8}$$

where the Jacobian of the transformation is given by

$$A(x^*) = \frac{\partial r}{\partial r^*} = \frac{R}{R - \epsilon(x^*)}. \tag{5.9}$$

Since $g = g(x, r)$, then

$$\frac{\partial r}{\partial x^*} = \frac{\partial r}{\partial \epsilon}\frac{\partial \epsilon}{\partial x^*} = A(x^*)\epsilon'(x^*)\left[\frac{r^* - R_{iu}}{R - \epsilon(x^*)}\right] = D(x^*), \tag{5.10}$$

$$\frac{\partial^2 r}{\partial x^{*2}} = 2\epsilon'(x^*)\left\{\frac{Rr^* - R_{iu}R}{[R - \epsilon(x^*)]^3}\right\} = B(x^*), \tag{5.11}$$

where $B(x^*)$ may be re-written as

$$B(x^*) = 2A(x^*)\epsilon'^2(x^*)\left\{\frac{r^* - R_{iu}}{[R - \epsilon(x^*)]^2}\right\}, \tag{5.12}$$

and $\epsilon'(x^*) = -H/X$.

The axial-direction partial derivatives of g can, equivalently, be expressed in terms of the independent variables of the computational domain as

$$\frac{\partial g}{\partial x^*} = \frac{\partial r}{\partial x^*}\frac{\partial g}{\partial r} + \frac{\partial g}{\partial x} = D(x^*)\frac{\partial g}{\partial r} + \frac{\partial g}{\partial x}, \tag{5.13}$$

$$\frac{\partial^2 g}{\partial x^{*2}} = B(x^*)\frac{\partial g}{\partial r} + D^2(x^*)\frac{\partial^2 g}{\partial r^2} + \frac{\partial^2 g}{\partial x^2} + 2D(x^*)\frac{\partial^2 g}{\partial r \partial x}. \tag{5.14}$$

In this manner, the partial differential equations in the physical domain for concentric nonuniform annular diffusers can be discretized accurately in an orthogonal computational domain with the finite-difference method.

5.3 Transformed Form of the Navier-Stokes Equations in the Computational Domain

In this section the differential forms of the N-S and continuity equations are expressed in terms of transformed coordinates x, r and θ, by using the relations (5.7-5.14). In three-dimensional flow fields, the matrices $\mathbf{M}_x, \mathbf{M}_r$, and $\mathbf{M}_\theta$ for the nonuniform (diffuser) region are expressed as

$$\mathbf{M}_x = \begin{bmatrix} L + 1/\beta & 0 & 0 & \partial/\partial x \\ 0 & L & 0 & 0 \\ 0 & 0 & L & 0 \\ 1/(\beta\delta)\partial/\partial x & 0 & 0 & 0 \end{bmatrix},$$

$$\mathbf{M}_r = \begin{bmatrix} M & 0 & 0 & D\partial/\partial r \\ 0 & M + 1/\beta + 1/(\mathrm{Re}\, r^{*2}) & -w/r^* & A\partial/\partial r \\ 0 & 0 & M + v/r^* + 1/(\mathrm{Re}\, r^{*2}) & 0 \\ D/(\beta\delta)\partial/\partial r & A/(\beta\delta\, r^*)(\partial/\partial r)(r^*) & 0 & 0 \end{bmatrix},$$

$$\mathbf{M}_\theta = \begin{bmatrix} N & 0 & 0 & 0 \\ 0 & N & 2/(\mathrm{Re}\, r^{*2})\partial/\partial\theta & 0 \\ 0 & -2/(\mathrm{Re}\, r^{*2})\partial/\partial\theta & N + 1/\beta & (1/r^*)\partial/\partial\theta \\ 0 & 0 & 1/(\beta\delta\, r^*)\partial/\partial\theta & 0 \end{bmatrix};$$

$$L\varphi = \frac{\partial(\hat{u}^\mu\varphi)}{\partial x} - \frac{1}{\mathrm{Re}}\frac{\partial^2\varphi}{\partial x^2},$$

$$M\varphi = D\frac{\partial(\hat{u}^\mu\varphi)}{\partial r} + \frac{A}{r^*}\frac{\partial}{\partial r}(r^*\hat{v}^\mu\varphi) - \frac{1}{\mathrm{Re}}\left[\frac{A}{r^*}\frac{\partial}{\partial r}\left(Ar^*\frac{\partial\varphi}{\partial r}\right)\right.$$

$$\left. + B\frac{\partial\varphi}{\partial r} + D^2\frac{\partial^2\varphi}{\partial r^2} + 2D\frac{\partial^2\varphi}{\partial r\partial x}\right],$$

$$N\varphi = \frac{1}{r^*}\frac{\partial}{\partial\theta}(\hat{w}^\mu\varphi) - \frac{1}{\mathrm{Re} r^{*2}}\frac{\partial^2\varphi}{\partial\theta^2};$$

the components of $\mathbf{Q}(\mathbf{V},p)$ are given as

$$Q_u(u,v,w,p) = \frac{\partial(uu)}{\partial x} + D\frac{\partial(uu)}{\partial r} + \frac{A}{r^*}\frac{\partial}{\partial r}(r^* vu) + \frac{1}{r^*}\frac{\partial(wu)}{\partial\theta} + \frac{\partial p}{\partial x} + D\frac{\partial p}{\partial r}$$

$$-\frac{1}{\mathrm{Re}}\left[\frac{\partial^2 u}{\partial x^2} + \frac{A}{r^*}\frac{\partial}{\partial r}\left(Ar^*\frac{\partial u}{\partial r}\right) + \frac{1}{r^{*2}}\frac{\partial^2 u}{\partial\theta^2} + B\frac{\partial u}{\partial r} + D^2\frac{\partial^2 u}{\partial r^2} + 2D\frac{\partial^2 u}{\partial r\partial x}\right], \quad (5.15)$$

$$Q_v(u,v,w,p) = \frac{\partial(uv)}{\partial x} + D\frac{\partial(uv)}{\partial r} + \frac{A}{r^*}\frac{\partial}{\partial r}(r^* vv) + \frac{1}{r^*}\frac{\partial(wv)}{\partial\theta} - \frac{w^2}{r^*} + A\frac{\partial p}{\partial r}$$

$$-\frac{1}{\mathrm{Re}}\left[\frac{\partial^2 v}{\partial x^2} + \frac{A}{r^*}\frac{\partial}{\partial r}\left(Ar^*\frac{\partial v}{\partial r}\right) + \frac{1}{r^{*2}}\frac{\partial^2 v}{\partial\theta^2} - \frac{2}{r^{*2}}\frac{\partial w}{\partial\theta} - \frac{v}{r^{*2}}\right.$$

$$\left. + B\frac{\partial v}{\partial r} + D^2\frac{\partial^2 v}{\partial r^2} + 2D\frac{\partial^2 v}{\partial r\partial x}\right], \quad (5.16)$$

$$Q_w(u,v,w,p) = \frac{\partial(uw)}{\partial x} + D\frac{\partial(uw)}{\partial r} + \frac{A}{r^*}\frac{\partial}{\partial r}(r^* vw) + \frac{1}{r^*}\frac{\partial(ww)}{\partial\theta} + \frac{vw}{r^*} + \frac{1}{r^*}\frac{\partial p}{\partial\theta}$$

$$-\frac{1}{\mathrm{Re}}\left[\frac{\partial^2 w}{\partial x^2} + \frac{A}{r^*}\frac{\partial}{\partial r}\left(Ar^*\frac{\partial w}{\partial r}\right) + \frac{1}{r^{*2}}\frac{\partial^2 w}{\partial\theta^2} + \frac{2}{r^{*2}}\frac{\partial v}{\partial\theta} - \frac{w}{r^{*2}}\right.$$

$$\left. + B\frac{\partial w}{\partial r} + D^2\frac{\partial^2 w}{\partial r^2} + 2D\frac{\partial^2 w}{\partial r\partial x}\right], \quad (5.17)$$

$$\nabla\cdot\mathbf{V} = \frac{\partial u}{\partial x} + D\frac{\partial u}{\partial r} + \frac{A}{r^*}\frac{\partial(r^* v)}{\partial r} + \frac{1}{r^*}\frac{\partial w}{\partial\theta}, \quad (5.18)$$

where the coefficients A, B, and D stand for $A(x^*), B(x^*)$, and $D(x^*)$, respectively.

5.4 Temporal and Spatial Discretizations

The temporal discretization is the same as explained in Chapter 3; the spatial discretization is described in this chapter, and is along the same lines as that used in Chapter 4, but with minor changes and more terms appearing in the equations. Before discretizing the equations we must cast them in delta form used in different sweeps. Thus, the matrix equations (3.26-3.28) in different sweeps are then expressed as

In the r−sweep:

$$\widetilde{\Delta u} + \beta\Delta\tau\left[\frac{A}{r^*}\frac{\partial}{\partial r}\left(r^*\hat{v}^\mu\widetilde{\Delta u}\right) + D\frac{\partial}{\partial r}\left(\hat{u}^\mu\widetilde{\Delta u}\right) + D\frac{\partial\left(\widetilde{\Delta p}\right)}{\partial r}\right.$$

$$
-\frac{1}{\mathrm{Re}}\left\{\frac{A}{r^*}\frac{\partial}{\partial r}\left(Ar^*\frac{\partial\left(\widetilde{\Delta u}\right)}{\partial r}\right)+D^2\frac{\partial^2\left(\widetilde{\Delta u}\right)}{\partial r^2}+B\frac{\partial\left(\widetilde{\Delta u}\right)}{\partial r}+2D\frac{\partial^2\left(\widetilde{\Delta u}\right)}{\partial r\partial x}\right\}\Bigg]
$$

$$
=\Delta\tau\left(E_u{}^n-\hat{u}^\mu-\beta\hat{Q}_u^\mu\right), \tag{5.19}
$$

$$
(1+\Delta\tau)\,\widetilde{\Delta v}+\beta\Delta\tau\left[\frac{A}{r^*}\frac{\partial}{\partial r}\left(r^*\hat{v}^\mu\widetilde{\Delta v}\right)+D\frac{\partial}{\partial r}\left(\hat{u}^\mu\widetilde{\Delta v}\right)+A\frac{\partial\left(\widetilde{\Delta p}\right)}{\partial r}-\frac{\hat{w}^\mu\widetilde{\Delta w}}{r}\right.
$$

$$
-\frac{1}{\mathrm{Re}}\left\{\frac{A}{r^*}\frac{\partial}{\partial r}\left(Ar^*\frac{\partial\left(\widetilde{\Delta v}\right)}{\partial r}\right)+D^2\frac{\partial^2\left(\widetilde{\Delta v}\right)}{\partial r^2}+B\frac{\partial\left(\widetilde{\Delta v}\right)}{\partial r}+2D\frac{\partial^2\left(\widetilde{\Delta v}\right)}{\partial r\partial x}-\frac{\widetilde{\Delta v}}{r^{*2}}\right\}\Bigg]
$$

$$
=\Delta\tau\left(E_v{}^n-\hat{v}^\mu-\beta\hat{Q}_v^\mu\right), \tag{5.20}
$$

$$
\widetilde{\Delta w}+\beta\Delta\tau\left[\frac{A}{r^*}\frac{\partial}{\partial r}\left(r^*\hat{v}^\mu\widetilde{\Delta w}\right)+D\frac{\partial}{\partial r}\left(\hat{u}^\mu\widetilde{\Delta w}\right)\right.
$$

$$
-\frac{1}{\mathrm{Re}}\left\{\frac{A}{r^*}\frac{\partial}{\partial r}\left(Ar^*\frac{\partial\left(\widetilde{\Delta w}\right)}{\partial r}\right)+D^2\frac{\partial^2\left(\widetilde{\Delta w}\right)}{\partial r^2}+B\frac{\partial\left(\widetilde{\Delta w}\right)}{\partial r}+2D\frac{\partial^2\left(\widetilde{\Delta w}\right)}{\partial r\partial x}\right\}\Bigg]
$$

$$
=\Delta\tau\left(E_w{}^n-\hat{w}^\mu-\beta\hat{Q}_w^\mu\right), \tag{5.21}
$$

$$
\widetilde{\Delta p}+\frac{A\Delta\tau}{r^*\delta}\frac{\partial}{\partial r}\left(r^*\widetilde{\Delta v}\right)+\frac{D\Delta\tau}{\delta}\frac{\partial\left(\widetilde{\Delta u}\right)}{\partial r}=-\frac{\Delta\tau}{\delta}\nabla.\hat{\mathbf{V}}^\mu; \tag{5.22}
$$

in the $\theta-$sweep:

$$
\overline{\Delta u}+\beta\Delta\tau\left[\frac{1}{r^*}\frac{\partial\left(\hat{w}^\mu\overline{\Delta u}\right)}{\partial\theta}-\frac{1}{\mathrm{Re}r^{*2}}\frac{\partial\left(\overline{\Delta u}\right)}{\partial\theta^2}\right]=\widetilde{\Delta u}, \tag{5.23}
$$

$$
\overline{\Delta v}+\beta\Delta\tau\left[\frac{1}{r^*}\frac{\partial\left(\hat{w}^\mu\overline{\Delta v}\right)}{\partial\theta}-\frac{1}{\mathrm{Re}r^{*2}}\frac{\partial\left(\overline{\Delta v}\right)}{\partial\theta^2}\right]=\widetilde{\Delta v}-\frac{2}{\mathrm{Re}}\frac{\partial(\overline{\Delta w})}{r^2\partial\theta}, \tag{5.24}
$$

$$
(1+\Delta\tau)\,\overline{\Delta w}+\beta\Delta\tau\left[\frac{1}{r^*}\frac{\partial\left(\hat{w}^\mu\overline{\Delta w}\right)}{\partial\theta}+\frac{1}{r^*}\frac{\partial\left(\overline{\Delta p}\right)}{\partial\theta}+\frac{\hat{v}^\mu\overline{\Delta w}}{r^*}\right.
$$

$$
\left.-\frac{1}{\mathrm{Re}}\left\{\frac{1}{r^{*2}}\frac{\partial^2\left(\overline{\Delta w}\right)}{\partial\theta^2}-\frac{\overline{\Delta w}}{r^{*2}}\right\}\right]=\widetilde{\Delta w}+\frac{2}{\mathrm{Re}}\frac{\partial(\overline{\Delta v})}{r^2\partial\theta}, \tag{5.25}
$$

$$
\overline{\Delta p}+\frac{\Delta\tau}{\delta}\frac{\partial\left(\overline{\Delta w}\right)}{r^*\partial\theta}=\widetilde{\Delta p}; \tag{5.26}
$$

and finally in the $x-$sweep:

$$
(1+\Delta\tau)\,\Delta u+\beta\Delta\tau\left[\frac{\partial\left(\hat{u}^\mu\overline{\Delta u}\right)}{\partial x}+\frac{\partial\left(\overline{\Delta p}\right)}{\partial x}-\frac{1}{\mathrm{Re}}\frac{\partial^2(\Delta u)}{\partial x^2}\right]=\overline{\Delta u}, \tag{5.27}
$$

$$\Delta v + \beta\Delta\tau\left[\frac{\partial\left(\hat{u}^{\mu}\overline{\Delta v}\right)}{\partial x} - \frac{1}{\mathrm{Re}}\frac{\partial^2(\Delta v)}{\partial x^2}\right] = \overline{\Delta v}\,, \tag{5.28}$$

$$\Delta w + \beta\Delta\tau\left[\frac{\partial\left(\hat{u}^{\mu}\overline{\Delta w}\right)}{\partial x} - \frac{1}{\mathrm{Re}}\frac{\partial^2(\Delta w)}{\partial x^2}\right] = \overline{\Delta w}\,, \tag{5.29}$$

$$\Delta p + \frac{\Delta\tau}{\delta}\frac{\partial(\Delta u)}{\partial x} = \overline{\Delta p}\,. \tag{5.30}$$

The solution to equations (5.19-5.30) will follow the same procedure used for small-amplitude-oscillation method described in Chapter 4 for 2-D and 3-D analyses. In general, in this 3-D analysis the terms Q^{μ}_{u}, Q^{μ}_{v} and Q^{μ}_{w} will be calculated, and then the variables $\hat{u}^{\mu+1}$, $\hat{v}^{\mu+1}$, $\hat{w}^{\mu+1}$ and $\hat{p}^{\mu+1}$ are obtained by solving (5.19-5.30).

To perform the discretization of the equations so as to solve the full non-linear N-S equations in the transformed domain, one needs to construct the staggered mesh and to define the interpolates in the physical domain as was done in Chapter 4. Once again, the grid points are stretched in the x and r directions, but not in the θ direction, in order to cluster more points near the solid walls or in regions of steep gradients in the flow domain, e.g. in the vicinity of the step or near the change in the contour of the diffuser section (see Figures 4.26 and 5.2). The velocity components v, w and the pressure p have identical x position, while u, w and p have identical r position in the grid scheme. The momentum and continuity equations are differenced about the points where $\hat{u}_{i,j,k}, \hat{v}_{i,j,k}, \hat{w}_{i,j,k}$ and $\hat{p}_{i,j,k}$ are defined.

In the following discretized equations, the rearranged form of the transformation equation (5.1) to define r^* in the physical domain is

$$r^* = r\frac{[R - \epsilon(x^*)] + R_{iu}\epsilon(x^*)}{R}\,. \tag{5.31}$$

This equation is used to define the following equations at each computational point $r^u = r^w$ and r^v in the staggered mesh:

$$RU_j = \frac{r^u_j\,\{R - \epsilon(x) + R_{iu}\epsilon(x)\}}{R} \quad , \quad RV_j = \frac{r^v_j\,\{R - \epsilon(x) + R_{iu}\epsilon(x)\}}{R}\,, \tag{5.32, 5.33}$$

$$DU_j = A(x)\epsilon'(x)\left[\frac{RU_j - R_{iu}}{R - \epsilon(x)}\right] \quad , \quad DV_j = A(x)\epsilon'(x)\left[\frac{RV_j - R_{iu}}{R - \epsilon(x)}\right]\,, \tag{5.34, 5.35}$$

$$BU_j = \frac{2\epsilon'(x)DU_j}{R-\epsilon(x)} \quad , \quad BV_j = \frac{2\epsilon'(x)DV_j}{R-\epsilon(x)} \,. \tag{5.36, 5.37}$$

Then, the continuity equation (5.18) is discretized as

$$-\frac{\Delta\tau}{\delta}(\nabla\cdot\mathbf{V})_{i,j,k} = -\frac{\Delta\tau}{\delta}\left[\frac{(u_{i,j,k}-u_{i-1,j,k})}{\Delta x_i^u} + \frac{A\,(RV_jv_{i,j,k}-RV_{j-1}v_{i,j-1,k})}{RU_j\Delta r_j^u}\right.$$
$$\left. + \frac{DV_{j-1}\,(u_{i,j,k}-u_{i,j-1,k})}{\Delta r_{j-1}^v} + \frac{(w_{i,j,k}-w_{i,j,k-1})}{RU_j\Delta\theta}\right] , \tag{5.38}$$

and the r-momentim equation (5.20) is descretized to implement the radial sweep for $v_{i,j,k}$ as

$$(1+\Delta\tau)\,\widetilde{\Delta v}_{i,j,k} + \frac{\beta\Delta\tau}{RV_j\Delta r_j^v}\left[A\left(RU_{j+1}v_v^{ru}\widetilde{\Delta v}_v^{ru} - RU_jv_v^{rd}\widetilde{\Delta v}_v^{rd}\right)\right]$$
$$+\frac{\beta\Delta\tau DV_j\left(u_v^{ru}\widetilde{\Delta v}_v^{ru} - u_v^{rd}\widetilde{\Delta v}_v^{rd}\right)}{\Delta r_j^v} + \frac{A\beta\Delta\tau}{\Delta r_j^v}\left(\widetilde{\Delta p}_{i,j+1,k} - \widetilde{\Delta p}_{i,j,k}\right)$$
$$-\frac{A^2\beta\Delta\tau}{\mathrm{Re}RV_j\Delta r_j^v}\left[\frac{RU_{j+1}\left(\widetilde{\Delta v}_{i,j+1,k}-\widetilde{\Delta v}_{i,j,k}\right)}{\Delta r_{j+1}^u} - \frac{RU_j\left(\widetilde{\Delta v}_{i,j,k}-\widetilde{\Delta v}_{i,j-1,k}\right)}{\Delta r_j^u}\right]$$
$$-\frac{DV_j^2\beta\Delta\tau}{\mathrm{Re}\Delta r_j^v}\left[\frac{\left(\widetilde{\Delta v}_{i,j+1,k}-\widetilde{\Delta v}_{i,j,k}\right)}{\Delta r_{j+1}^u} - \frac{\left(\widetilde{\Delta v}_{i,j,k}-\widetilde{\Delta v}_{i,j-1,k}\right)}{\Delta r_j^u}\right]$$
$$-\frac{DV_j\beta\Delta\tau}{\mathrm{Re}\Delta x_{i-1}^u}\left[\frac{\left(\widetilde{\Delta v}_{i,j,k}-\widetilde{\Delta v}_{i,j-1,k}\right)}{\Delta r_j^u} - \frac{\left(\widetilde{\Delta v}_{i,j,k-1}-\widetilde{\Delta v}_{i,j-1,k-1}\right)}{\Delta r_j^u}\right]$$
$$-\frac{BU_j\beta\Delta\tau}{\mathrm{Re}\Delta r_{j-1}^u}\left(\widetilde{\Delta v}_{i,j,k}-\widetilde{\Delta v}_{i,j-1,k}\right) + \frac{\beta\Delta\tau\widetilde{\Delta v}_{i,j,k}}{\mathrm{Re}RV_j^2}$$
$$= \Delta\tau\,(E_v{}^n - v^\mu - \beta Q_v^\mu)_{i,j,k}\,. \tag{5.39}$$

The terms $\widetilde{\Delta v}_v^{ru}, \widetilde{\Delta v}_v^{rd}, v_v^{ru}$ and v_v^{rd} appearing in this equation, as well as other similar terms in the following equations, are obtained from the appropriate relations as explained in Chapter 4 and Appendix A. The term $\widetilde{\Delta p}_{i,j,k}$ is obtained from the continuity equation (5.22) as

$$\widetilde{\Delta p}_{i,j,k} = -\frac{\Delta\tau}{\delta}\nabla\cdot\mathbf{V}_{i,j,k} - \frac{A\Delta\tau}{\delta RU_j\Delta r_j^u}\left(RV_j\widetilde{\Delta v}_{i,j,k} - RV_{j-1}\widetilde{\Delta v}_{i,j-1,k}\right)$$

$$- \frac{DV_{j-1}\Delta\tau}{\delta\Delta r^v_{j-1}} \left(\widetilde{\Delta u}_{i,j,k} - \widetilde{\Delta u}_{i,j-1,k}\right) , \tag{5.40}$$

with a similar expression for $\widetilde{\Delta p}$ at $J = j + 1$.

The component $-\beta\Delta\tau Q_v$ of the vector **Q** in equation (5.16) is discretized as

$$\begin{aligned}
(-\beta\Delta\tau Q_v)_{i,j,k} = &-\frac{\beta\Delta\tau}{\Delta x^v_i}\left[u^{xf}_v v^{xf}_v - u^{xb}_v v^{xb}_v - \frac{1}{\mathrm{Re}}\left\{\frac{v_{i+1,j,k} - v_{i,j,k}}{\Delta x^u_i} - \frac{v_{i,j,k} - v_{i-1,j,k}}{\Delta x^u_{i-1}}\right\}\right] \\
&-\frac{\beta\Delta\tau DV_j}{\Delta r^v_j}\left(u^{ru}_v v^{ru}_v - u^{rd}_v v^{rd}_v\right) - \frac{\beta\Delta\tau}{RV_j\Delta r^v_j}\Big[A\cdot RU_{j+1}v^{ru2}_v - A\cdot RU_j v^{rd2}_v \\
&-\frac{A^2}{\mathrm{Re}}\left\{\frac{RU_{j+1}}{\Delta r^u_{j+1}}(v_{i,j+1,k} - v_{i,j,k}) - \frac{RU_j}{\Delta r^u_j}(v_{i,j,k} - v_{i,j-1,k})\right\}\Big] - \frac{A\beta\Delta\tau}{\Delta r^v_j}(p_{i,j+1,k} - p_{i,j,k}) \\
&-\frac{\beta\Delta\tau}{RV_j}\left(\frac{w^{\theta f}_v v^{\theta f}_v - w^{\theta b}_v v^{\theta b}_v}{\Delta\theta} - {w_v}^2\right) + \frac{\beta\Delta\tau}{\mathrm{Re}}\Big[\frac{BU_j\left(v_{i,j,k} - v_{i,j-1,k}\right)}{\Delta r^u_j} \\
&+\frac{DV^2_j}{\Delta r^v_j}\left(\frac{v_{i,j+1,k} - v_{i,j,k}}{\Delta r^u_{j+1}} - \frac{v_{i,j,k} - v_{i,j-1,k}}{\Delta r^u_j}\right) \\
&+\frac{DV_j}{\Delta x^v_i}\left(\frac{v_{i,j,k} - v_{i,j-1,k}}{\Delta r^u_j} - \frac{v_{i-1,j,k} - v_{i-1,j-1,k}}{\Delta r^u_j}\right) \\
&+\frac{1}{RV^2_j}\left(\frac{v_{i,j,k+1} + v_{i,j,k-1} - 2v_{i,j,k}}{\Delta\theta^2} - 2\frac{w^{\theta f}_v - w^{\theta b}_v}{\Delta\theta} - v_{i,j,k}\right)\Big] ,
\end{aligned} \tag{5.41}$$

where w_v is given in Appendix A. Now, the discretized r-momentum equation (5.24) in the θ-sweep, incorporating the result of (5.39), provides

$$\begin{aligned}
\overline{\Delta v}_{i,j,k} \ + \ &\frac{\beta\Delta\tau}{RV_j\Delta\theta}\Big[w^{\theta f}_v \overline{\Delta v}^{\theta f}_v - w^{\theta b}_v \overline{\Delta v}^{\theta b}_v \\
- \ &\frac{1}{\mathrm{Re}}\left(\frac{\overline{\Delta v}_{i,j,k+1} + \overline{\Delta v}_{i,j,k-1} - 2\overline{\Delta v}_{i,j,k}}{RV_j\Delta\theta}\right)\Big] = \widetilde{\Delta v}_{i,j,k} ,
\end{aligned} \tag{5.42}$$

and the discretization of r-momentum equation (5.28) in the x-sweep, using the results of equation (5.42), yields

$$\begin{aligned}
\Delta v_{i,j,k} \ + \ &\frac{\beta\Delta\tau}{\Delta x^v_i}\Big\{u^{xf}_v \Delta v^{xf}_v - u^{xb}_v \Delta v^{xb}_v \\
- \ &\frac{1}{\mathrm{Re}}\left[\frac{\Delta v_{i+1,j,k} - \Delta v_{i,j,k}}{\Delta x^u_i} - \frac{\Delta v_{i,j,k} - \Delta v_{i-1,j,k}}{\Delta x^u_{i-1}}\right]\Big\} = \overline{\Delta v}_{i,j,k} .
\end{aligned} \tag{5.43}$$

The same procedure is applied to discretize the r-, θ-, x-momentum and continuity equations (5.21, 5.25, 5.26, 5.29) and (5.19, 5.23, 5.27, 5.30), respectively. The discretized equations are

$$\widetilde{\Delta w}_{i,j,k} + \frac{\beta\Delta\tau}{RU_j\Delta r_j^v}\left[A\left(RV_j v_w^{ru}\widetilde{\Delta w}_w^{ru} - RV_{j-1}v_w^{rd}\widetilde{\Delta w}_w^{rd}\right)\right]$$

$$-\frac{A^2\beta\Delta\tau}{\mathrm{Re}RU_j\Delta r_j^v}\left[\frac{RV_j\left(\widetilde{\Delta w}_{i,j+1,k} - \widetilde{\Delta w}_{i,j,k}\right)}{\Delta r_j^v} - \frac{RV_{j-1}\left(\widetilde{\Delta w}_{i,j,k} - \widetilde{\Delta w}_{i,j-1,k}\right)}{\Delta r_{j-1}^v}\right]$$

$$+\frac{DU_j}{\Delta r_j^u}\left(u_w^{ru}\widetilde{\Delta w}_w^{ru} - u_w^{rd}\widetilde{\Delta w}_w^{rd}\right) - \frac{DU_j\beta\Delta\tau}{\mathrm{Re}\Delta x_i^v}\left(\frac{\widetilde{\Delta w}_{i,j,k} - \widetilde{\Delta w}_{i,j-1,k}}{\Delta r_j^v} - \frac{\widetilde{\Delta w}_{i-1,j,k} - \widetilde{\Delta w}_{i-1,j-1,k}}{\Delta r_{j-1}^v}\right)$$

$$-\frac{BV_{j-1}\beta\Delta\tau}{\mathrm{Re}\Delta r_{j-1}^v}\left(\widetilde{\Delta w}_{i,j,k} - \widetilde{\Delta w}_{i,j-1,k}\right) = \Delta\tau\left(E_w^n - w^\mu - \beta Q_w^\mu\right)_{i,j,k}\,. \tag{5.44}$$

Similarly, the $-\beta\Delta\tau Q_w$ component is given by

$$(-\beta\Delta\tau Q_w)_{i,j,k} = -\frac{\beta\Delta\tau}{\Delta x_i^v}\left[u_w^{xf}w_w^{xf} - u_w^{xb}w_w^{xb} - \frac{1}{\mathrm{Re}}\left(\frac{w_{i+1,j,k} - w_{i,j,k}}{\Delta x_i^u} - \frac{w_{i,j,k} - w_{i-1,j,k}}{\Delta x_{i-1}^u}\right)\right]$$

$$-\frac{\beta\Delta\tau DU_j}{\Delta r_j^u}\left(u_w^{ru}w_w^{ru} - u_w^{rd}w_w^{rd}\right) - \frac{\beta\Delta\tau}{RU_j\Delta r_j^u}\Bigg[A\cdot RV_j v_w^{ru}w_w^{ru} - A\cdot RV_{j-1}v_w^{rd}w_w^{rd}$$

$$\left.-\frac{A^2}{\mathrm{Re}}\left\{\frac{RV_j}{\Delta r_j^v}\left(w_{i,j+1,k} - w_{i,j,k}\right) - \frac{RV_{j-1}}{\Delta r_{j-1}^v}\left(w_{i,j,k} - w_{i,j-1,k}\right)\right\}\right]$$

$$-\frac{\beta\Delta\tau}{RU_j}\left[\frac{w_w^{\theta f^2} - w_w^{\theta b^2} + p_{i,j,k+1} - p_{i,j,k}}{\Delta\theta} + v_w w_{i,j,k}\right]$$

$$+\frac{\beta\Delta\tau}{\mathrm{Re}}\Bigg\{\frac{BV_{j-1}}{\Delta r_{j-1}^v}\left(w_{i,j,k} - w_{i,j-1,k}\right) + \frac{DU_j^2}{\Delta x_j^u}\left(\frac{w_{i,j+1,k} - w_{i,j,k}}{\Delta r_j^v} - \frac{w_{i,j,k} - w_{i,j-1,k}}{\Delta r_{j-1}^v}\right)$$

$$+\frac{DU_j}{\Delta x_i^v}\left(\frac{w_{i,j,k} - w_{i,j-1,k}}{\Delta r_{j-1}^v} - \frac{w_{i-1,j,k} - w_{i-1,j-1,k}}{\Delta r_{j-1}^v}\right)$$

$$\left.\frac{1}{RU_j^2}\left[\frac{w_{i,j,k+1} + w_{i,j,k-1} - 2w_{i,j,k}}{\Delta\theta^2} + 2\frac{v_w^{\theta f} - v_w^{\theta b}}{\Delta\theta} - w_{i,j,k}\right]\right\}\,, \tag{5.45}$$

where v_w is given in Appendix A. The discretized θ momentum and continuity equations (5.25) and (5.26) in the θ-sweep are obtained as

$$(1+\Delta\tau)\overline{\Delta w}_{i,j,k} \;+\; \frac{\beta\Delta\tau}{RU_j\Delta\theta}\left[w_w^{\theta f}\overline{\Delta w}_w^{\theta f} - w_w^{\theta b}\overline{\Delta w}_w^{\theta b} - \frac{\overline{\Delta w}_{i,j,k+1} + \overline{\Delta w}_{i,j,k-1} - 2\overline{\Delta w}_{i,j,k}}{\mathrm{Re}RU_j\Delta\theta}\right]$$

$$+\;\frac{\beta\Delta\tau}{RU_j}\left[+\frac{\overline{\Delta p}_{i,j,k+1} - \overline{\Delta p}_{i,j,k}}{\Delta\theta}\right] = \widetilde{\Delta w}_{i,j,k}\,, \tag{5.46}$$

$$\overline{\Delta p}_{i,j,k} = \widetilde{\Delta p}_{i,j,k} - \frac{\Delta\tau}{\delta}\frac{\overline{\Delta w}_{i,j,k} - \overline{\Delta w}_{i,j,k-1}}{RU_j \Delta\theta}\,. \tag{5.47}$$

The discretized θ-momentum equation (5.29) in the x-sweep is written as

$$\Delta w_{i,j,k} + \frac{\beta\Delta\tau}{\Delta x_i^v}\Big\{u_w^{xf}\Delta w_w^{xf} - u_w^{xb}\Delta w_w^{xb} - \frac{1}{\text{Re}}\left[\frac{\Delta w_{i+1,j,k} - \Delta w_{i,j,k}}{\Delta x_i^u} - \frac{\Delta w_{i,j,k} - \Delta w_{i,j-1,k}}{\Delta x_{i-1}^u}\right]\Big\} = \overline{\Delta w}_{i,j,k}\,, \tag{5.48}$$

which completes the discretization of the θ-momentum equation in all sweeps. Now, the discretized x-momentum equation (5.19) in the r-sweep is given by

$$\begin{aligned}
&\widetilde{\Delta u}_{i,j,k} + \frac{\beta\Delta\tau}{RU_j\Delta r_j^u}\left[A\left(RV_j v_u^{ru}\widetilde{\Delta u}_u^{ru} - RV_{j-1}v_u^{rd}\widetilde{\Delta u}_u^{rd}\right)\right] \\
&\frac{DU_j}{\Delta r_j^u}\left(u_u^{ru}\widetilde{\Delta u}_u^{ru} - u_u^{rd}\widetilde{\Delta u}_u^{rd}\right) + \frac{\beta\Delta\tau DV_j}{\Delta r_j^v}\left(\widetilde{\Delta p}_{i,j+1,k} - \widetilde{\Delta p}_{i,j,k}\right) \\
&-\frac{A^2\beta\Delta\tau}{\text{Re}RU_j\Delta r_j^u}\left[\frac{RV_j}{\Delta r_j^v}\left(\widetilde{\Delta u}_{i,j+1,k} - \widetilde{\Delta u}_{i,j,k}\right) - \frac{RV_{j-1}}{\Delta r_{j-1}^v}\left(\widetilde{\Delta u}_{i,j,k} - \widetilde{\Delta u}_{i,j-1,k}\right)\right] \\
&-\frac{DU_j^2\beta\Delta\tau}{\text{Re}\Delta r_j^u}\left(\frac{\widetilde{\Delta u}_{i,j+1,k} - \widetilde{\Delta u}_{i,j,k}}{\Delta r_j^v} - \frac{\widetilde{\Delta u}_{i,j,k} - \widetilde{\Delta u}_{i,j-1,k}}{\Delta r_{j-1}^v}\right) \\
&-\frac{DU_j\beta\Delta\tau}{\text{Re}\Delta x_i^v}\left(\frac{\widetilde{\Delta u}_{i,j,k} - \widetilde{\Delta u}_{i,j-1,k}}{\Delta r_{j-1}^v} - \frac{\widetilde{\Delta u}_{i-1,j,k} - \widetilde{\Delta u}_{i-1,j-1,k}}{\Delta r_{j-1}^v}\right) \\
&-\frac{BV_{j-1}\beta\Delta\tau}{\text{Re}\Delta r_{j-1}^v}\left(\widetilde{\Delta u}_{i,j,k} - \widetilde{\Delta u}_{i,j-1,k}\right) = \Delta\tau\left(E_u^n - u^\mu - \beta Q_u^\mu\right)_{i,j,k}\,,
\end{aligned} \tag{5.49}$$

with $-\beta\Delta\tau Q_u$ given by

$$\begin{aligned}
(-\beta\Delta\tau Q_u)_{i,j,k} = &-\frac{\beta\Delta\tau}{\Delta x_i^v}\Big\{u_u^{xf}u_u^{xf} - u_u^{xb}u_u^{xb} + p_{i+1,j,k} - p_{i,j,k} \\
&-\frac{1}{\text{Re}}\left[\frac{u_{i+1,j,k} - u_{i,j,k}}{\Delta x_{i+1}^v} - \frac{u_{i,j,k} - u_{i-1,j,k}}{\Delta x_i^v}\right]\Big\} - \frac{DU_j\beta\Delta\tau}{\Delta r_j^u}\left(u_u^{ru2} - u_u^{rd2}\right) \\
&-\frac{\beta\Delta\tau}{RU_j\Delta r_j^u}\Big\{A\left(RV_j v_u^{ru}u_u^{ru} - RV_{j-1}v_u^{rd}u_u^{rd}\right) \\
&-\frac{A^2}{\text{Re}}\left[\frac{RV_j}{\Delta r_j^v}\left(u_{i,j+1,k} - u_{i,j,k}\right) - \frac{RV_{j-1}}{\Delta r_{j-1}^v}\left(u_{i,j,k} - u_{i,j-1,k}\right)\right]\Big\} \\
&-\frac{\beta\Delta\tau}{RU_j}\left(\frac{w_u^{\theta f}u_u^{\theta f} - w_u^{\theta b}u_u^{\theta b}}{\Delta\theta}\right) - \frac{DV_j\beta\Delta\tau}{\Delta r_j^v}(p_{i,j+1,k} - p_{i,j,k})
\end{aligned}$$

$$+\frac{\beta\Delta\tau}{\mathrm{Re}}\left[\frac{(BV_{j-1}}{\Delta r^{v}_{j-1}}(u_{i,j,k}-u_{i,j-1,k})+\frac{DU^2_j}{\Delta r^v_j}\left(\frac{u_{i,j+1,k}-u_{i,j,k}}{\Delta r^v_j}-\frac{u_{i,j,k}-u_{i,j-1,k}}{\Delta r^v_{j-1}}\right)\right.$$

$$\left.+\frac{(u_{i,j,k+1}+u_{i,j,k-1}-2u_{i,j,k})}{RU^2_j\Delta\theta^2}+\frac{DU_j}{\Delta x^v_i}\left(\frac{u_{i,j,k}-u_{i,j-1,k}}{\Delta r^v_{j-1}}-\frac{u_{i-1,j,k}-u_{i-1,j-1,k}}{\Delta r^v_{j-1}}\right)\right]. \tag{5.50}$$

The discretized x-momentum equation (5.23) in the θ-sweep is then written as

$$\overline{\Delta u}_{i,j,k} + \frac{\beta\Delta\tau}{RU_j\Delta\theta}\left[w^{\theta f}_u\overline{\Delta u}^{\theta f}_u - w^{\theta b}_u\overline{\Delta u}^{\theta b}_u\right.$$

$$\left.- \frac{1}{\mathrm{Re}}\left(\frac{\overline{\Delta u}_{i,j,k+1}+\overline{\Delta u}_{i,j,k-1}-2\overline{\Delta u}_{i,j,k}}{RU_j\Delta\theta}\right)\right] = \widetilde{\Delta u}_{i,j,k}, \tag{5.51}$$

and the discretized x-momentum and continuity equations (5.27) and (5.30) in the x-sweep are given by

$$(1+\Delta\tau)\,\Delta u_{i,j,k}+\frac{\beta\Delta\tau}{\Delta x^v_i}\left[u^{xf}_u\Delta u^{xf}_u - u^{xb}_u\Delta u^{xb}_u\right.$$

$$\left.-\frac{1}{\mathrm{Re}}\left(\frac{\Delta u_{i+1,j,k}-\Delta u_{i,j,k}}{\Delta x^v_{i+1}}-\frac{\Delta u_{i,j,k}-\Delta u_{i,j-1,k}}{\Delta x^v_i}\right)+\Delta p_{i+1,j,k}-\Delta p_{i,j,k}\right] = \overline{\Delta u}_{i,j,k}, \tag{5.52}$$

$$\Delta p_{i,j,k} = \overline{\Delta p}_{i,j,k} - \frac{\Delta\tau}{\delta}\cdot\frac{1}{\Delta x^v_i}\left(\Delta u_{i,j,k}-\Delta u_{i-1,j,k}\right). \tag{5.53}$$

We recall that the terms containing ∇ and Δ, as given in the previous equations and also in Appendix A, indicate the central and backward difference operators applied to the grid-point coordinates and 34 interpolates, such as $v^{ru}_v, v^{rd}_v, w^{ru}_v, w^{rd}_v$...etc., they are evaluated by the relations given in Appendix A.

5.5 Method of Solution (Based on ADI Scheme)

The equations (5.39), (5.42)-(5.44), (5.46), (5.48), (5.49), (5.51) and (5.52) are now ready to be written in *tridiagonal* forms and the solution of these equations proceeds by starting the calculation of the right-hand sides of equations (5.19)-(5.22) using relations (5.38), (5.41), (5.45) and (5.50). In the r-sweep, $\widetilde{\Delta v}$ is obtained from equation (5.39) after eliminating $\widetilde{\Delta p}$ with the aid of equation (5.40). The terms $\overline{\Delta v}$ and

Δv are obtained from equations (5.42) and (5.43) in the θ- and x-sweeps respectively. The same procedure is applied in determining $\widetilde{\Delta w}$ from equation (5.44), $\overline{\Delta w}$ from equation (5.46) with the aid of equation (5.47) to eliminate $\overline{\Delta p}$, and finally Δw from equation (5.48). Also, $\widetilde{\Delta u}$ is determined from equation (5.49), $\overline{\Delta u}$ is obtained from equation (5.51) and Δu is calculated using equation (5.52) with the aid of equation (5.53) as a coupling equation. The pressure difference Δp is obtained, ultimately, after Δu is determined. In all these calculations, it is obvious that several times the scalar tridiagonal systems of equations must be inverted as explained in Chapter 4.

The boundary conditions for velocity imposed at the inlet, $x = -L_u$, is a developed laminar-flow profile, which is given by equation (4.64), and the boundary values for v and w at the inlet and outlet are set equal to zero. The applied pressures at the inlet and outlet of the domain are the same as those used for uniform and backstep geometries. The extrapolation of the velocities at the outlet to second-order accuracy from inside the flow domain is done in the same way as is explained in section 4.2, and the boundary values for the velocity and pressure on the solid stationary and moving walls are the same as before. As initial conditions, to start the time-marching solution, the steady-flow solution obtained without any oscillation of the outer cylinder is given and then the harmonic motion of the cylinder is started. Here too, the N-S equations are integrated for at least 3 harmonic cycles, until a periodic solution is obtained. As far as the domain of integration in the different sweeps is concerned, the details of the numerical solution are the same as before, except that, similar to the case of the backstep geometry, in the r-sweep the domain of integration is divided into two parts. The first part extends from r_{iu} to r_j, before the diffuser section, and from r_{id} to r_j after this section, where $j = J - 1$ is the index for grid points in the r-direction and in the vicinity of the outer cylinder (see Figure 5.1).

It is remarked that some parts of the terms arising from the cross-derivatives $\partial^2/\partial r\partial x$ are evaluated in the explicit right-hand sides of the equations (5.39), (5.44) and (5.49) to restore the implicit nature of the tridiagonal systems of equations, and hence affecting the accuracy of the results and the convergence rate of the numerical solution.

5.6 3-D Unsteady Flow Solutions for Diffuser Geometries

In this section, the numerical results are presented for $\alpha = 6^o$ and 20^o. To have a comparison with the numerical results obtained for the backstep geometry, although they are not directly related, the numerical computations have been implemented on two non-dimensional meshes: for the first one, the inner cylinder radius is $r_{id} = 8$, the outer cylinder radius is $r_o = 10$, and $r_{iu} = 9$; in the second mesh, $r_{id} = 3.785$, $r_o = 5.785$ and $r_{iu} = 4.785$. The span of the meshes in the x-direction is also variable, to investigate the effects of shorter and longer lengths of vibrating outer cylinder, as well as the effects of shorter and longer lengths of the upstream and downstream fixed parts, on the results. Hence, Table 4.1 of Chapter 4 will also be used in this chapter.

The results, all for Re = 100 and $\omega = 0.1$, are shown in Figures 5.3-5.11 in which all quantities are dimensionless. Figure 5.3 presents the unsteady pressure amplitude and phase angle with respect to the displacement of the outer cylinder at the circumferential angle $\theta = 7.5^o$ for an amplitude of oscillation $\epsilon = 0.1$, using mesh type A (defined in Table 4.1). The comparison between this figure and Figure 4.27 shows that replacing the backstep with a diffuser with $\alpha = 6^o$ increases the amount of the unsteady pressure after the discontinuity, and that the phase angle is flatter for this diffuser geometry. Figure 5.4 shows the circumferential velocity w and the phase angle obtained using mesh type A, at axial location $X = 20$ and circumferential position $\theta = 45^o$. In this figure, as well as in all the figures drawn over the diffuser surface, the lower parts of the curves terminate on the diffuser surface, which starts at $r = 8.625$ for the mesh of type A.

Figure 5.5 presents the unsteady pressure and phase angle for three different oscillation amplitudes of the outer cylinder, and should be compared to the results of Figure 4.29. The upstream portions of the unsteady pressure in Figures 4.29 and 5.5 are almost the same, but in the downstream portion of the annulus the pressure recovery is noticeable in the diffuser geometry *vis-à-vis* the backstep geometry. It is remarked in Figure 5.5 that the phase angles are almost independent of the vibration amplitudes. Figure 5.6 demonstrates the effect of extending the upstream and downstream fixed portions on the results, using a mesh of type B. This figure should be compared with Figure 5.5 to highlight how important the extension of the upstream fixed portion is in reducing the perturbation at the upstream end of the vibrating outer cylinder. Once again, the pressure recovery is noticeable downstream of the diffuser in comparison to Figure 4.30 for the backstep geometry. In Figure 5.6 the phase angles are almost the same.

Figure 5.7 presents the effect of using a larger annular gap on the unsteady pressure and phase angle, using mesh type C. It is clear that due to having a larger annular gap, the pressure recovery is not as pronounced as in Figure 5.6, and the unsteady pressure is proportional in value to that of Figure 4.31 for the backstep geometry, but the phase angles are different and smaller (in the positive sense) the amplitude of oscillation increases. Figure 5.8 shows the effect of the extension of the upstream and downstream fixed portions on the results, using a larger annular gap and using mesh type D, at different oscillation amplitudes. It is interesting to note that the unsteady pressures after the diffuser section almost coincide for larger amplitudes of oscillation. Also, at higher amplitude the pressure perturbation does not tend to zero at the upstream portion of the moving cylinder, which might be due to the pressure buildup at the diffuser section. The phase angle results have a completely different behaviour *vis-à-vis* the phase angle shown in Figure 4.32 for the backstep geometry. All these interesting results indicate how important are the effect of the annular gap width and the length of the fixed portions on the solution of the N-S equations for different geometries.

The unsteady pressure and the phase angle shown in Figure 5.9 have been obtained for a diffuser angle $\alpha = 20^o$ and can be compared to those for $\alpha = 6^o$ of Figure 5.8. In spite of the minor discrepancies, this result is comparable with the results of Figure 4.32, which indicates that the behaviour of the diffuser system with $\alpha = 20^o$ is similar to that of a system with a backstep geometry; the pressure recovery is not as pronounced as in the case of diffuser with $\alpha = 6^o$ (see Figure 5.8). Incidentally, the phase angle shows the same trend as in Figure 4.32(b) *vis-à-vis* the results shown in Figure 5.8(b).

A comparison between the unsteady pressure and phase angle for three different geometries is made in Figures 5.10 and 5.11 for two amplitudes of oscillation. There are several points to be noticed in these figures. First, the upstream fixed portion influences the results much more in the case of a diffuser than in the case of the backstep geometry. Second, the pressure recovery is much more pronounced for a diffuser with $\alpha = 6^o$ than for either $\alpha = 20^o$ or the backstep geometry. In fact, the unsteady pressure downstream of the diffuser ($\alpha = 20^o$) is reduced more than is the case downstream of the backstep. As is seen, the pressure perturbations for all these geometries approach zero at the exit from the annulus ($X = 150$). The results of the phase angle for three geometries also present different trends. The phase angle for the diffuser with $\alpha = 6^o$ is almost flat, while the phase angle result for the diffuser with $\alpha = 20^o$ is much different, although at the upstream end of both the step and the two diffuser sections the phase angles vary in almost the same range, contrary to the downstream portions.

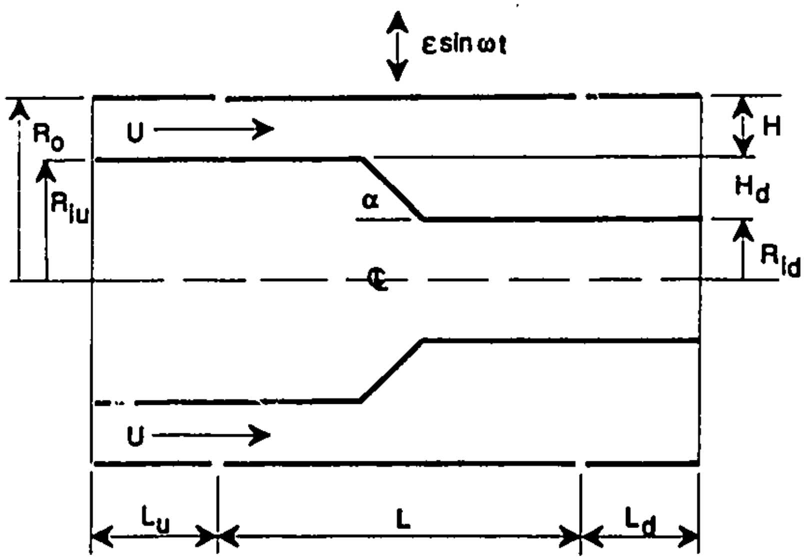

Figure 5.1: Schematic diagram of diffuser shaped annular flow.

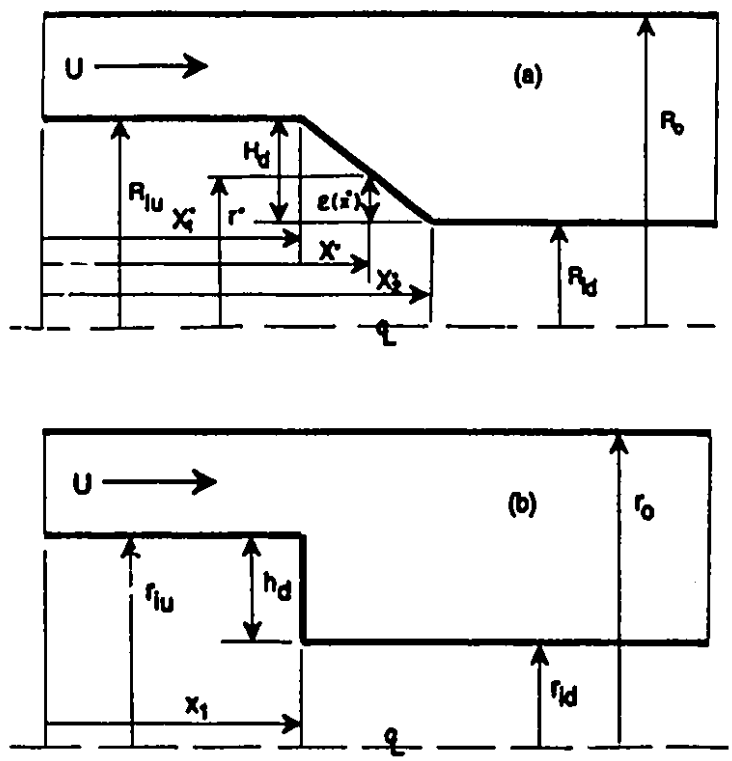

Figure 5.2: Schematic diagram of (a) physical and (b) computational domains after coordinate transformation.

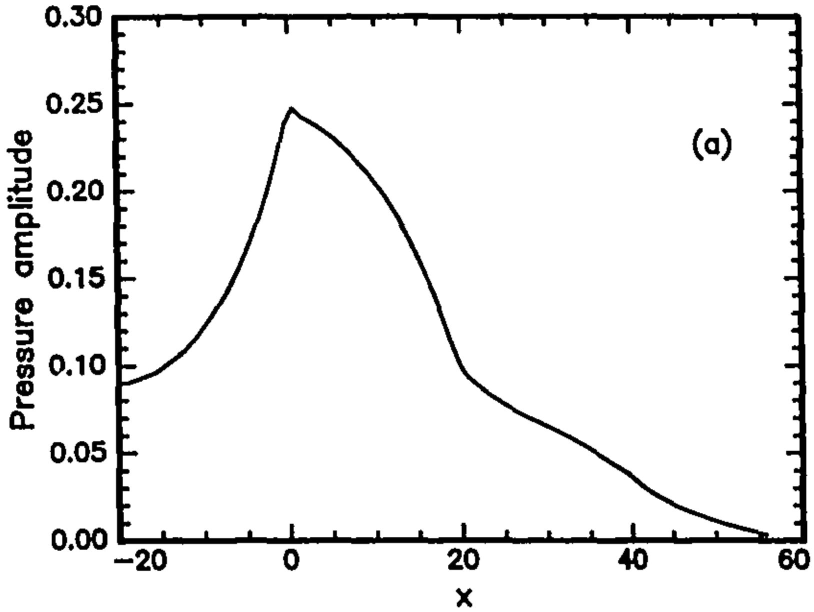

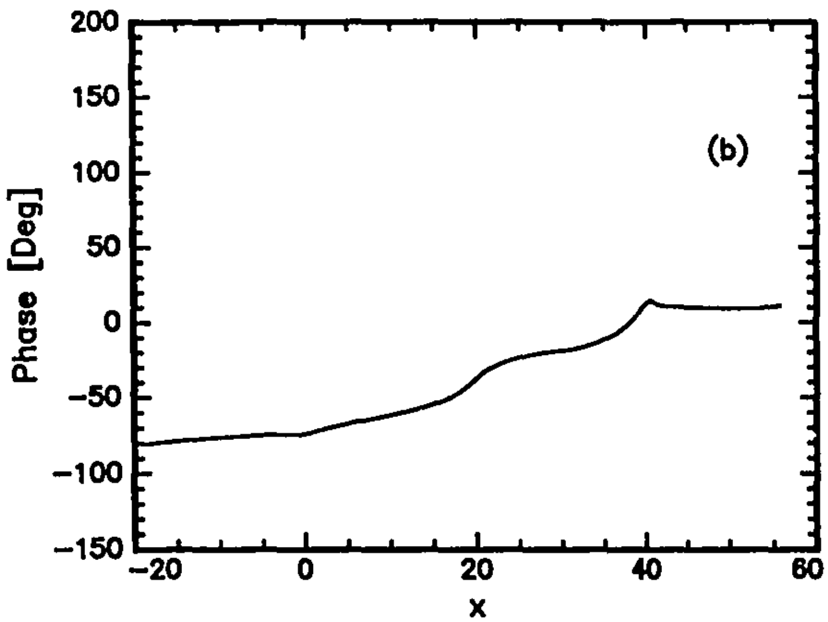

Figure 5.3: (a) The unsteady pressure and (b) phase angle for Re = 100, $\omega = 0.1$, $r_{id} = 8$, $r_o = 10$, at $r = 9.942$, $\theta = 7.5^o$, for $\alpha = 6^o$ and $\epsilon = 0.1$.

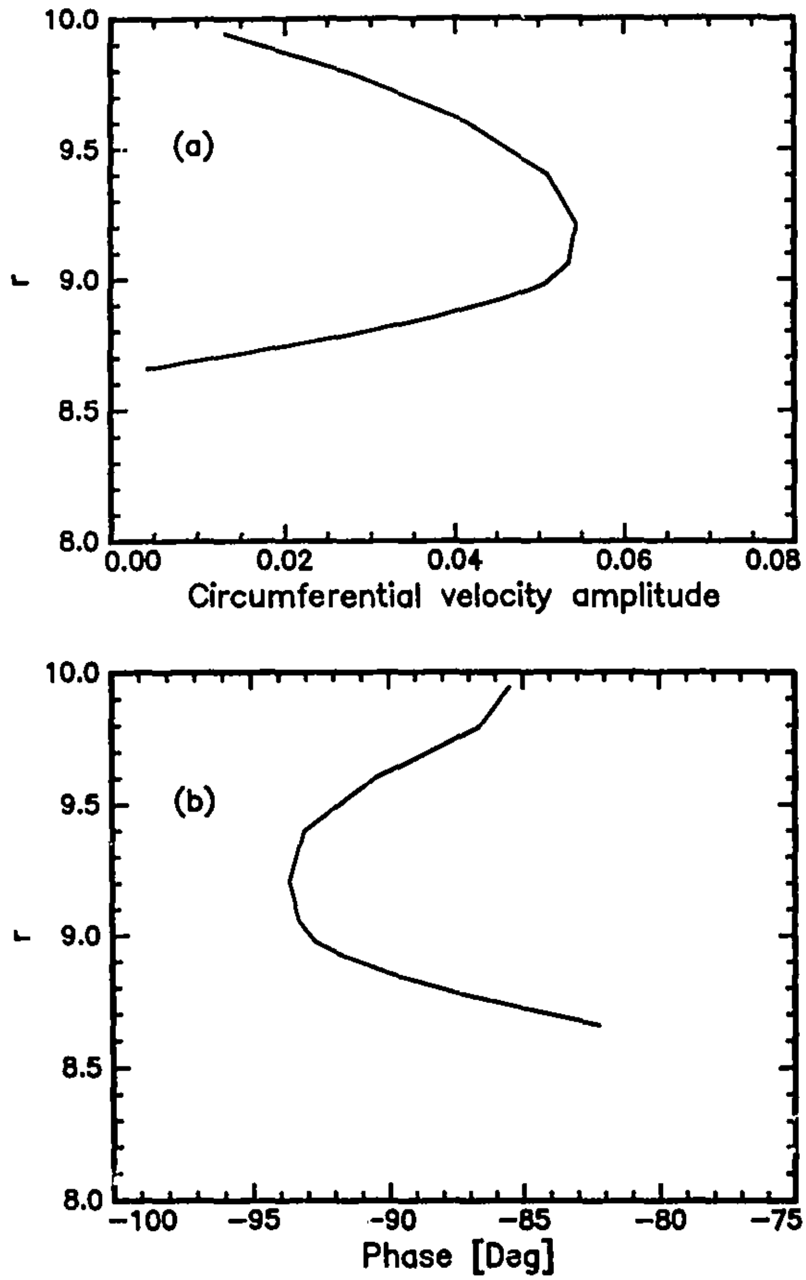

Figure 5.4: (a) The circumferential velocity w and (b) phase angle in annular gap for Re $= 100$, $\omega = 0.1$, $r_{id} = 8$, $r_o = 10$, $\alpha = 6^o$ and $\epsilon = 0.1$ at $X = 20$, $\theta = 45^o$.

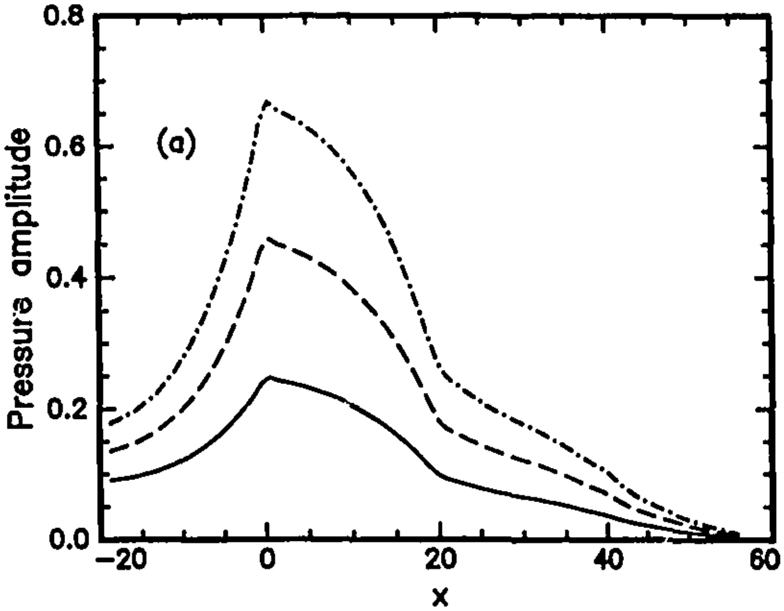

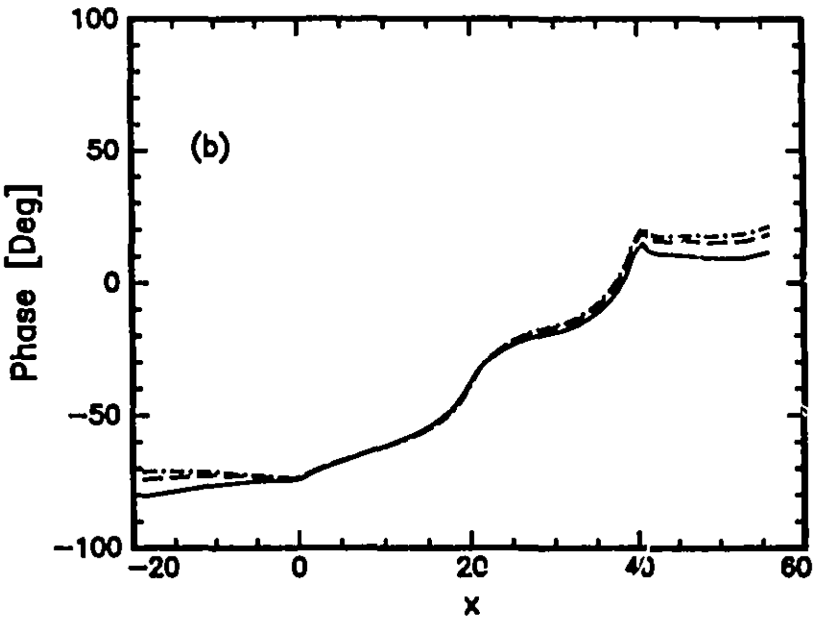

Figure 5.5: (a) The unsteady pressure and (b) phase angle versus axial length of the cylinder for Re = 100, $\omega = 0.1$, $r_{id} = 8$, $r_o = 10$, $\alpha = 6^o$ at $r = 9.942$ and $\theta = 7.5^o$: —,$\epsilon = 0.1$; – – –,$\epsilon = 0.2$; – · –,$\epsilon = 0.3$.

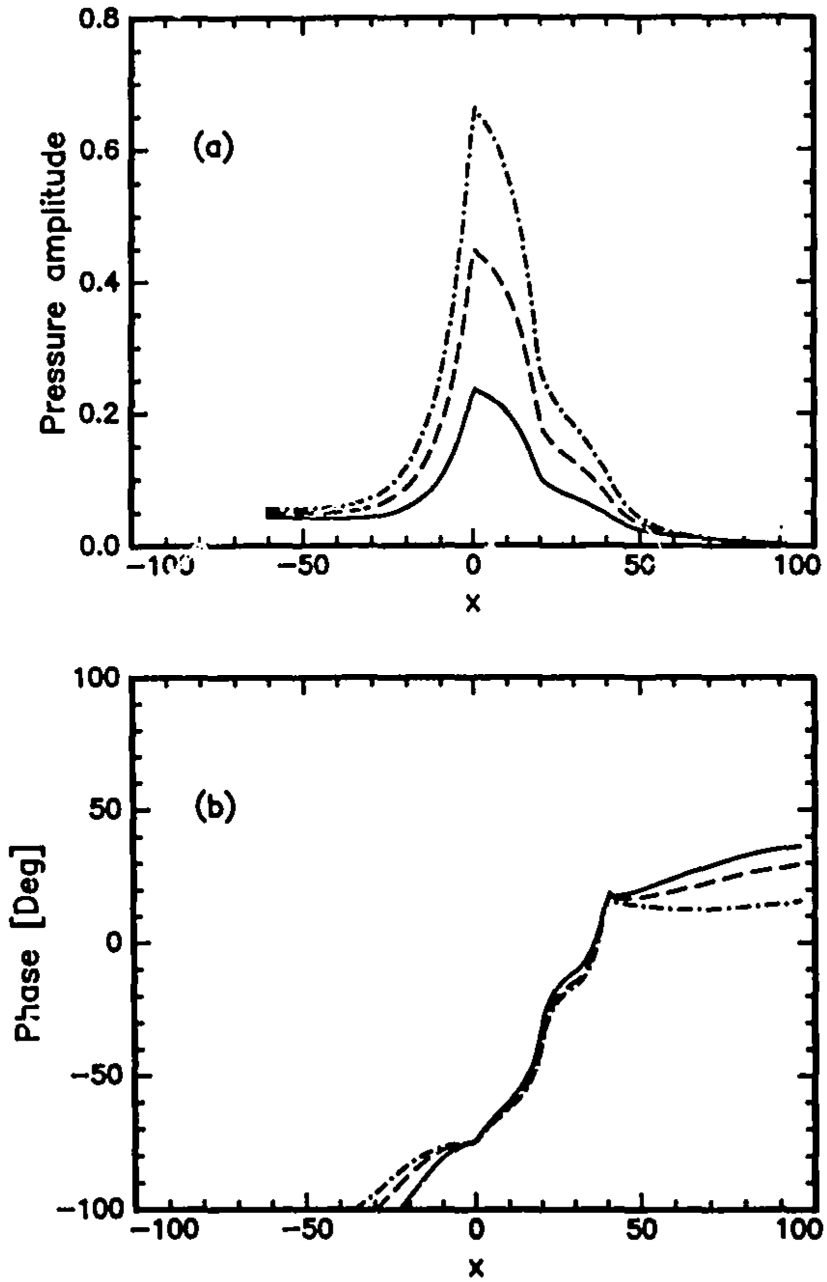

Figure 5.6: The effect of the extension of the fixed upstream and downstream portions on (a) the unsteady pressure and (b) the phase angle, for Re = 100, $\omega = 0.1$, $r_{id} = 8$, $r_o = 10$, $\alpha = 6^o$ at $r = 9.942$ and $\theta = 7.5^o$: —,$\epsilon = 0.1$; – – –,$\epsilon = 0.2$; – · –,$\epsilon = 0.3$.

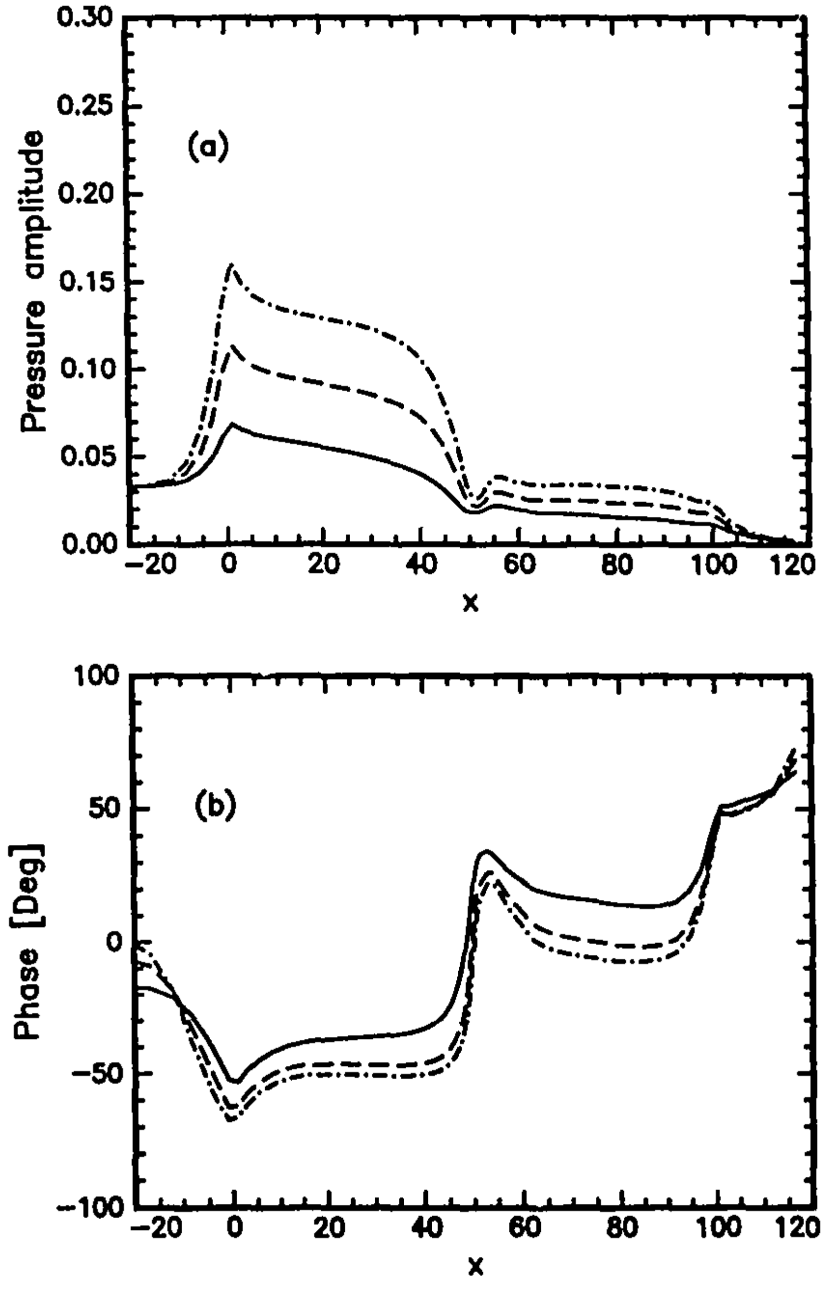

Figure 5.7: The effect of the annular gap width on (a) the unsteady pressure and (b) the phase angle, for Re = 100, $\omega = 0.1$, $r_{id} = 3.785$, $r_o = 5.785$, $\alpha = 6^o$ at $r = 5.727$ and $\theta = 7.5^o$: —,$\epsilon = 0.05375$; – – –,$\epsilon = 0.1075$; – · –,$\epsilon = 0.16125$.

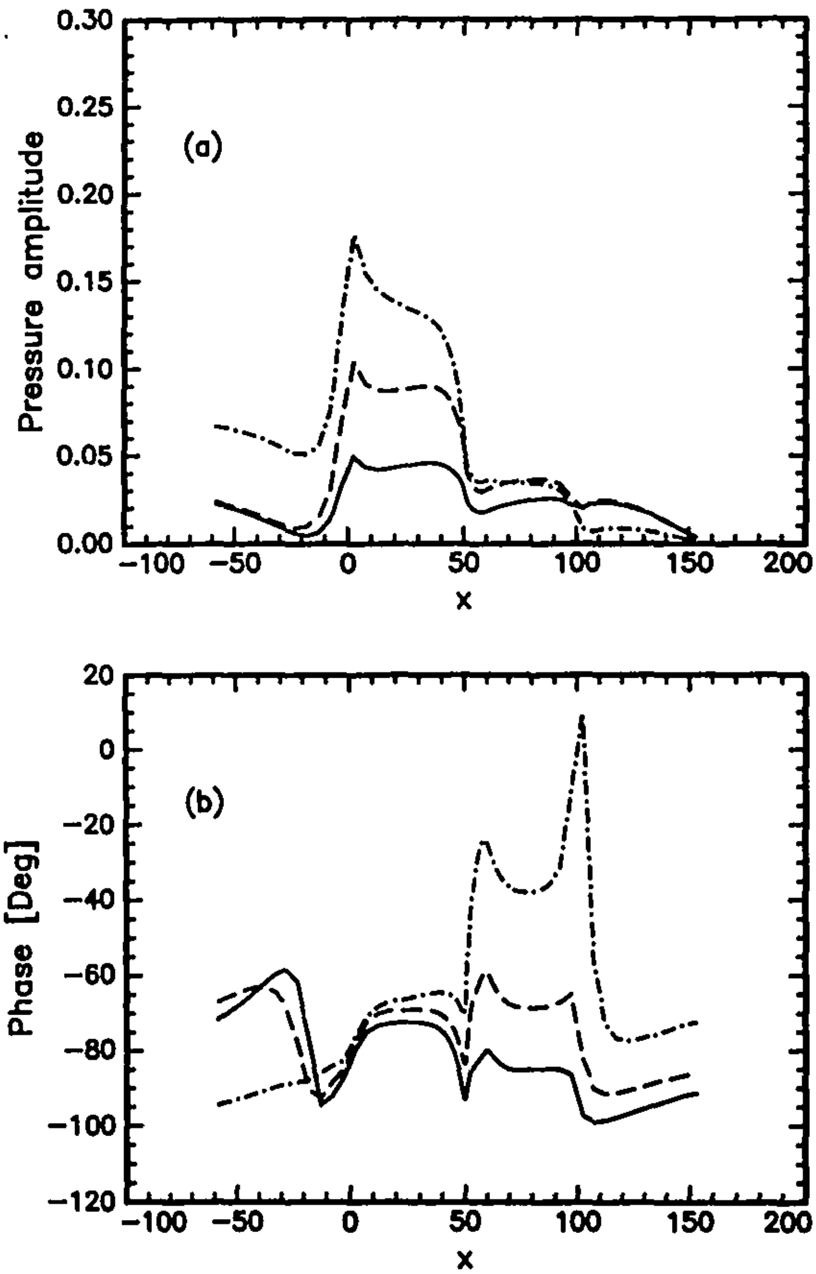

Figure 5.3: The effect of the extension of the fixed upstream and downstream portions on (a) the unsteady pressure and (b) the phase angle, for Re $=$ 100, $\omega = 0.1$, $r_{id} = 3.785$, $r_o = 5.785$, $\alpha = 6^o$ at $r = 5.727$ and $\theta = 7.5^o$: —,$\epsilon = 0.05375$; $- - -$,$\epsilon = 0.1075$; $- \cdot -$,$\epsilon = 0.16125$.

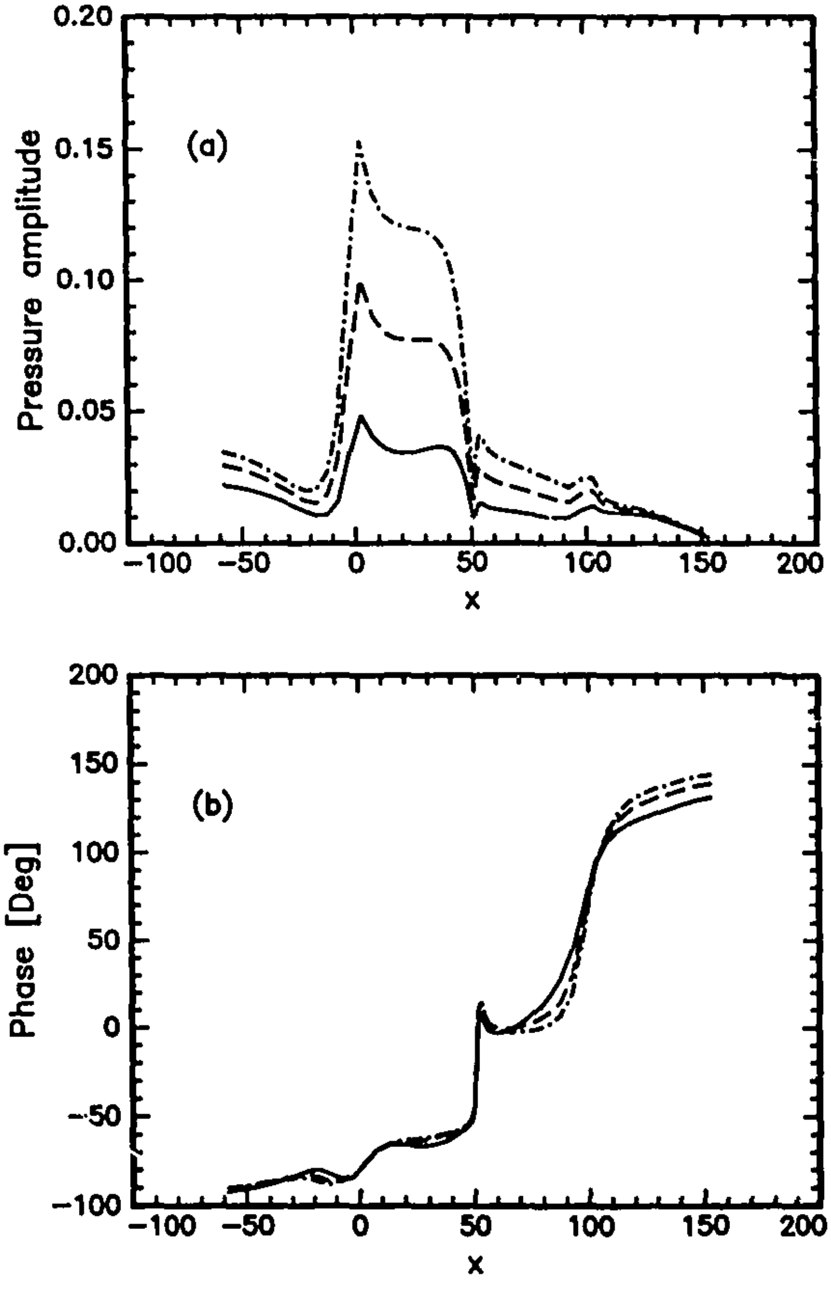

Figure 5.9: The effect of the extension of the fixed upstream and downstream portions on (a) the unsteady pressure and (b) the phase angle, for Re = 100, ω = 0.1, r_{id} = 3.785, r_o = 5.785, α = 20° at r = 5.727 and θ = 7.5°: —, ϵ = 0.05375; − − −, ϵ = 0.1075; − · −, ϵ = 0.16125.

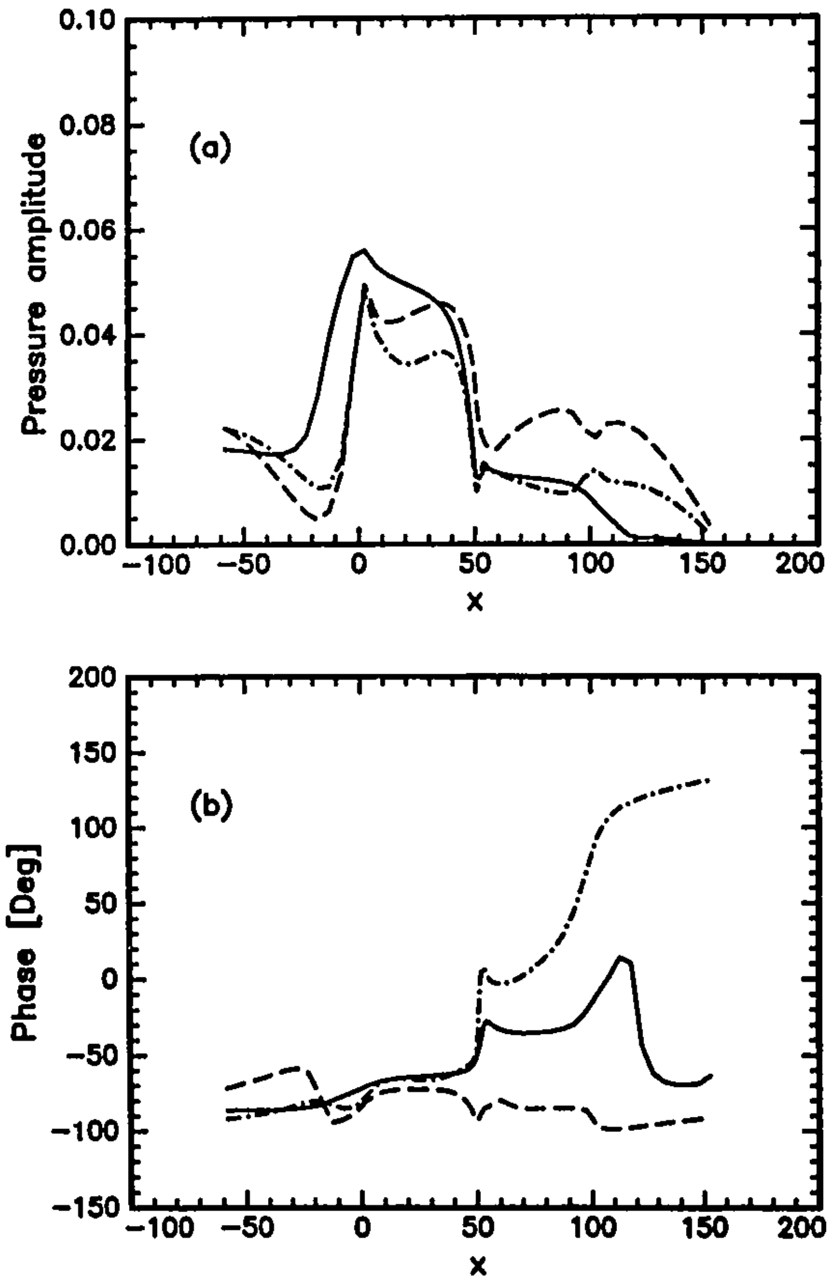

Figure 5.10: (a) Unsteady pressure and (b) phase angle for Re = 100, ω = 0.1, r_{id} = 3.785, r_o = 5.785, ϵ = 0.05375 at r = 5.727, θ = 7.5°, comparison between the results obtained for: —,backstep; – – –,diffuser with $\alpha = 6°$; – · –,diffuser with $\alpha = 20°$.

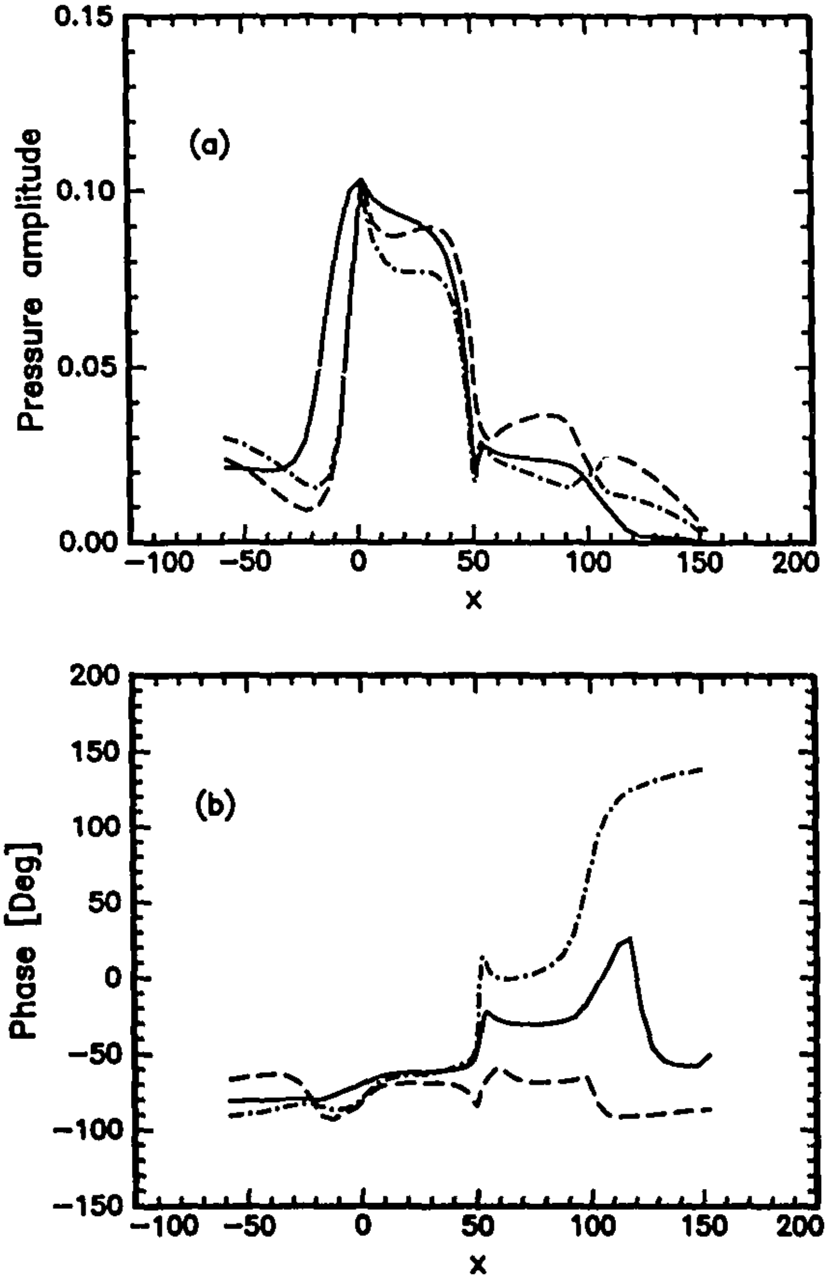

Figure 5.11: (a) Unsteady pressure and (b) phase angle for Re = 100, $\omega = 0.1$, $r_{id} = 3.785$, $r_o = 5.785$, $\epsilon = 0.1075$ at $r = 5.727$, $\theta = 7.5^o$, comparison between the results obtained for: —,backstep; – – –,diffuser with $\alpha = 6^o$; – · –,diffuser with $\alpha = 20^o$.

Chapter 6

Numerical Formulation Based on Time-Dependent Coordinate Transformation for Larger Amplitude Oscillation

One of the most important parts of this Thesis is covered in this chapter. Thus, the overall method of solution for a multidimensional problem, namely that of two nearly concentric cylinders with a moving outer cylinder, Figure (6.1), will be examined based on a time-dependent coordinate transformation, which is better suited for large-amplitude oscillations. The method will be applied to uniform as well as nonuniform (backstep) geometries for the case of translational motion of the outer cylinder, and the results obtained will be compared to similar results from Chapter 4, which were obtained by a mean-position analysis.

6.1 Time-dependent Coordinate Transformation

A coordinate system may need to be *time-dependent* because the boundaries move, either forced or in response to influences of the physical problem, or because the system is adjusted so as to concentrate lines in developing regions of large gradients. The simplest procedure is to regenerate the coordinate system at each time step using the new boundary locations from the physical solution at the previous time step; thus, the solution for the new coordinates at each time step is done separately from the physical solution at that step. Alternatively, the equations for the coordinate system can be added to the overall set of equations, and the entire set solved simultaneously at each time step.

In any case, with the partial time derivatives (at variable r^* and θ^*) in the physical solution equations replaced by partial time derivatives at fixed values of the curvilinear coordinates, the grid in the transformed plane is fixed even though the coordinate system in the physical plane is in motion. This introduces time derivatives of the Cartesian coordinates into the transformed physical solution equations, in the role of additional convective terms (Thompson *et al.* 1982).

With the method of transformation applied to our problems in this Thesis, it is possible to perform all the computation on the fixed rectangular grid in the transformed computational region *without any interpolation*, no matter how the grid points move in the physical domain as time progresses.

The computational coordinate system is generated as the solution of algebraic equations (3.13) and (3.15) with the values of coordinates (r^*, θ^*) specified on the boundaries in the physical domain, one of these coordinates being specified to be constant on the boundaries and the other being distributed as desired along the boundaries in order to concentrate grid points in certain regions. The transformed coordinates define a rectangular domain, the extent of which is determined by the range of the values r and θ. Now, if the same boundary values of r^* and θ^* are redistributed in the physical domain, perhaps because the boundaries in the physical domain have actually moved or because it is desirable to change the concentration of grid points around the boundaries, and a suitable algebraic system is solved for the transformed coordinates with these new boundary conditions, new transformation functions can be produced with still the same range of values in r and θ and hence in the same rectangular field in the transformed domain. The grid points in the rectangular transformed domain remain stationary, and the effect of moving of the coordinate system in the physical domain is then just to change the values of the physical coordinates (r^*, θ^*) at the fixed grid points in the rectangular transformed domain.

Mathematically what has transpired is that the original problem, consisting say of N partial differential equations of any type with appropriate, possibly steady, boundary conditions specified on moving general boundaries, has been transformed into a system of N partial differential equations and M ($M = 3$ for 3-D problems) algebraic equations for the natural coordinates with boundary conditions that are now *time-dependent* but specified on steady rectangular boundaries. The physical coordinate system has thus, in effect, been eliminated from the problem, at the expense of adding M algebraic equations to the original system (Thompson *et al.* 1974), plus the complexity of the equations as a result of the transformation of the governing partial differential equations. In our analysis, the transformation has its own merits, such as that we are no longer restricted to small-amplitude oscillations, in addition to obtaining more accurate results for small-amplitude oscillations by the *time-dependent coordinate transformation.*

For steady and unsteady flows in nearly concentric annular configurations, any fluid dynamic properties are variables dependent on the axial, radial and circumferential coordinates, x, r and θ, shown in Figure 6.1(a), as well as on time when the flow is unsteady. In this figure, R_i and R_o denote the inner and outer cylinder radii, $\epsilon(\theta, t)$ is the annular gap, and $\epsilon(t)$ is the instantaneous displacement when the outer cylinder is in translational motion.

In order to generalize the problem, it is necessary to transform the annular space (r^*, θ^*) between the eccentric cylinders in the physical domain of Figure 6.1(a) into the rectangular computational domain (r, θ) as shown in Figure 6.1(b). For this purpose it is convenient to define the non-dimensional transformation equations as

$$r = \frac{r^* - R_i}{[R_o^2 - \epsilon^2(t)\sin^2\theta^*]^{1/2} - R_i + \epsilon(\theta^*, t^*)}, \tag{6.1}$$

$$\theta = \theta^*, \qquad x = x^*, \qquad t = t^*, \tag{6.2}$$

where

$$\epsilon(\theta^*, t^*) = \epsilon(t^*)\cos\theta^* , \tag{6.3}$$

in which the starred quantities indicate the physical domain.

All functions having continuous partial derivatives in the physical cylindrical domain can be expressed in the form of functions in the computational domain by the chain rule. Hence, one obtains the following relations

$$\frac{\partial}{\partial x^*} = \frac{\partial}{\partial x} \quad , \quad \frac{\partial}{\partial r^*} = \frac{\partial r}{\partial r^*}\frac{\partial}{\partial r} ,$$

$$\frac{\partial}{\partial \theta^*} = \frac{\partial r}{\partial \theta^*}\frac{\partial}{\partial r} + \frac{\partial}{\partial \theta} \quad , \quad \frac{\partial}{\partial t^*} = \frac{\partial r}{\partial t^*}\frac{\partial}{\partial r} + \frac{\partial}{\partial t} .$$

Using equation (6.1), the derivatives in the radial direction of a function f in the physical domain, in terms of the independent variables in the computational domain, can be written as

$$\frac{\partial f}{\partial r^*} = \frac{\partial r}{\partial r^*}\frac{\partial f}{\partial r} = A(\theta, t)\frac{\partial f}{\partial r} , \tag{6.4}$$

$$\frac{\partial^2 f}{\partial r^{*2}} = \left(\frac{\partial r}{\partial r^*}\right)^2 \frac{\partial^2 f}{\partial r^2} = A^2(\theta, t)\frac{\partial^2 f}{\partial r^2} , \tag{6.5}$$

where

$$A(\theta, t) = \frac{\partial r}{\partial r^*} = \frac{1}{\Phi(\theta, t)} ,$$

and

$$\Phi(\theta, t) = R(\theta, t) - R_i + \epsilon(\theta, t) \ , \qquad R(\theta, t) = [R_o^2 - \epsilon^2(t)\sin^2\theta]^{1/2} .$$

Since in the problems under consideration the fluid dynamic property is $f = f(r, \theta)$, and the nondimensional coordinate is $r = r(r^*, \theta^*) = r(r^*, \theta)$, then

$$\frac{\partial r}{\partial \theta^*} = \frac{\partial r}{\partial \epsilon}\frac{\partial \epsilon}{\partial \theta^*} = \frac{(r^* - R_i)F_3\epsilon(t)\sin\theta}{[R(\theta, t) - R_i + \epsilon(\theta, t)]^2} = rB(\theta, t) , \tag{6.6}$$

$$\frac{\partial^2 r}{\partial \theta^{*2}} = \frac{(r^* - R_i)\left\{[(F_1 + F_2)\epsilon(t)\sin\theta + F_3\epsilon(t)\cos\theta]\Phi(\theta, t)^{1/2} - 2F_3F_4\epsilon(t)\sin\theta\right\}}{\Phi(\theta, t)^3}$$

$$= rD(\theta, t) , \tag{6.7}$$

where

$$B(\theta,t) = \frac{F_3\epsilon(t)\sin\theta}{\Phi(\theta,t)} = A(\theta,t)F_3\epsilon(t)\sin\theta\,,$$

$$D(\theta,t) = A(\theta,t)^2\left\{[(F_1+F_2)\epsilon(t)\sin\theta + F_3\epsilon(t)\cos\theta]\Phi(\theta,t)^{1/2} - 2F_3F_4\epsilon(t)\sin\theta\right\},$$

and

$$\begin{aligned}
F_1 &= -\epsilon(t)[\cos\theta\tan\theta + \sin\theta(1/\cos^2\theta)](1/R(\theta,t))\,,\\
F_2 &= -\epsilon^3(t)\sin^3\theta(1/R(\theta,t)^3)\,,\\
F_3 &= -\epsilon(t)\sin\theta\tan\theta(1/R(\theta,t)) + 1\,,\\
F_4 &= -\epsilon^2(t)\sin\theta\cos\theta(1/R(\theta,t)) - \epsilon(t)\sin\theta\,.
\end{aligned}$$

The partial derivatives of the fluid-dynamic property in the circumferential direction can, equivalently, be expressed in terms of the independent variables of the computational domain as

$$\frac{\partial f}{\partial\theta^*} = rB(\theta,t)\frac{\partial f}{\partial r} + \frac{\partial f}{\partial\theta}\,, \tag{6.8}$$

$$\frac{\partial^2 f}{\partial\theta^{*2}} = r\left[B^2(\theta,t) + D(\theta,t)\right]\frac{\partial f}{\partial r} + r^2B^2(\theta,t)\frac{\partial^2 f}{\partial r^2} + \frac{\partial^2 f}{\partial\theta^2} + 2rB(\theta,t)\frac{\partial^2 f}{\partial r\partial\theta}\,. \tag{6.9}$$

Since we now consider moving-boundary problems, the partial derivative of the fluid-dynamic property f with respect to time should be transformed as

$$\frac{\partial f}{\partial t^*} = \frac{\partial r}{\partial t^*}\frac{\partial f}{\partial r} + \frac{\partial f}{\partial t} = -\frac{F_3\dot\epsilon(t)\cos\theta}{\Phi^2(\theta,t)}\frac{\partial f}{\partial r} + \frac{\partial f}{\partial t} = rC(\theta,t)\frac{\partial f}{\partial r} + \frac{\partial f}{\partial t}\,, \tag{6.10}$$

where we have used

$$\frac{\partial r}{\partial t^*} = \frac{\partial r}{\partial\epsilon}\frac{\partial\epsilon}{\partial t^*}\,, \qquad \dot\epsilon(t) = \frac{d\epsilon(t)}{dt}\,,$$

and

$$C(\theta,t) = -A(\theta,t)F_3\dot\epsilon(t)\cos\theta\,.$$

In this manner, the partial differential equations defined in the physical domain for concentric cylinders, with the outer one in motion, can be discretized accurately in the computational domain with the finite-difference method. This transformation can now be applied to non-steady problems for cylindrical configurations with unsteady viscous flows in the axial direction or without axial flow, which will be studied later in this chapter.

6.2 Transformed Form of the Navier-Stokes Equations in the Computational Domain

In this section, the differential forms of the N-S and continuity equations are expressed in terms of transformed coordinates x, r and θ, using the relations (6.4-6.5) and (6.8-6.10) and Figure 6.2. The equivalent forms of the relations (2.3) and (2.5) in the transformed domain can be written as

$$\nabla \cdot \mathbf{V} = \frac{\partial u}{\partial x} + \frac{1}{r^*}\left[A\frac{\partial r^* v}{\partial r} + rB\frac{\partial w}{\partial r} + \frac{\partial w}{\partial \theta}\right] = 0\,, \tag{6.11}$$

$$\frac{\partial \mathbf{V}}{\partial t} + rC\frac{\partial \mathbf{V}}{\partial r} + \mathbf{Q}(\mathbf{V},p) = \mathbf{0}\,, \tag{6.12}$$

and the vector $\mathbf{Q}(\mathbf{V},p) = [Q_u(u,v,w,p), Q_v(u,v,w,p), Q_w(u,v,w,p)]^T$ includes the convective derivatives, pressure and viscous terms as

$$\begin{aligned} Q_u(u,v,w,p) &= \frac{\partial (uu)}{\partial x} + \frac{A}{r^*}\frac{\partial}{\partial r}(r^* vu) + \frac{1}{r^*}\frac{\partial (wu)}{\partial \theta} + \frac{\partial p}{\partial x} + rC\frac{\partial u}{\partial r} + \frac{rB}{r^*}\frac{\partial (wu)}{\partial r} \\ &-\frac{1}{\mathrm{Re}}\left[\frac{\partial^2 u}{\partial x^2} + \frac{A}{r^*}\frac{\partial}{\partial r}\left(Ar^*\frac{\partial u}{\partial r}\right) + \frac{1}{r^{*2}}\frac{\partial^2 u}{\partial \theta^2} + \frac{(rD + rB^2)}{r^{*2}}\frac{\partial u}{\partial r} + \frac{r^2B^2}{r^{*2}}\frac{\partial^2 u}{\partial r^2} + \frac{2rB}{r^{*2}}\frac{\partial^2 u}{\partial r \partial \theta}\right], \end{aligned} \tag{6.13}$$

$$\begin{aligned} Q_v(u,v,w,p) &= \frac{\partial (uv)}{\partial x} + \frac{A}{r^*}\frac{\partial}{\partial r}(r^* vv) + \frac{1}{r^*}\frac{\partial (wv)}{\partial \theta} - \frac{w^2}{r^*} + A\frac{\partial p}{\partial r} + rC\frac{\partial v}{\partial r} + \frac{rB}{r^*}\frac{\partial}{\partial r}(wv) \\ &-\frac{1}{\mathrm{Re}}\left[\frac{\partial^2 v}{\partial x^2} + \frac{A}{r^*}\frac{\partial}{\partial r}\left(Ar^*\frac{\partial v}{\partial r}\right) + \frac{1}{r^{*2}}\frac{\partial^2 v}{\partial \theta^2} - \frac{2}{r^{*2}}\frac{\partial w}{\partial \theta} - \frac{v}{r^{*2}}\right. \\ &\left. + \frac{(rD + rB^2)}{r^{*2}}\frac{\partial v}{\partial r} + \frac{r^2B^2}{r^{*2}}\frac{\partial^2 v}{\partial r^2} - \frac{2rB}{r^{*2}}\frac{\partial w}{\partial r} + \frac{2rB}{r^{*2}}\frac{\partial^2 v}{\partial r \partial \theta}\right], \end{aligned} \tag{6.14}$$

$$\begin{aligned} Q_w(u,v,w,p) &= \frac{\partial (uw)}{\partial x} + \frac{A}{r^*}\frac{\partial}{\partial r}(r^* vw) + \frac{1}{r^*}\frac{\partial (ww)}{\partial \theta} + \frac{vw}{r^*} + \frac{1}{r^*}\frac{\partial p}{\partial \theta} + rC\frac{\partial w}{\partial r} + \frac{rB}{r^*}\frac{\partial}{\partial r}(ww) \\ &+ \frac{rB}{r^*}\frac{\partial p}{\partial r} - \frac{1}{\mathrm{Re}}\left[\frac{\partial^2 w}{\partial x^2} + \frac{A}{r^*}\frac{\partial}{\partial r}\left(Ar^*\frac{\partial w}{\partial r}\right) + \frac{1}{r^{*2}}\frac{\partial^2 w}{\partial \theta^2} + \frac{2}{r^{*2}}\frac{\partial v}{\partial \theta} - \frac{w}{r^{*2}}\right. \\ &\left. + \frac{(rD + rB^2)}{r^{*2}}\frac{\partial w}{\partial r} + \frac{r^2B^2}{r^{*2}}\frac{\partial^2 w}{\partial r^2} + \frac{2rB}{r^{*2}}\frac{\partial v}{\partial r} + \frac{2rB}{r^{*2}}\frac{\partial^2 w}{\partial r \partial \theta}\right]. \end{aligned} \tag{6.15}$$

6.3 Real-Time and Pseudo-Time Discretizations

The discretization of the Navier-Stokes and continuity equations in real- and pseudo-time follow the same procedure as that in Chapter 3, namely, three time levels are used for real-time (similar to equation (3.2)) and a simple Euler scheme is used for pseudo-time discretizations (similar to equations (3.7) and (3.8)). The central difference is used for spatial discretization as explained in Section 3.4.

In the three-dimensional flow field, once again, we use equations (3.26-3.28) and write the matrices $\mathbf{M}_x$, $\mathbf{M}_r$, and $\mathbf{M}_\theta$ for the *transformed domain* as

$$\mathbf{M}_x = \begin{bmatrix} L + 1/\beta & 0 & 0 & \partial/\partial x \\ 0 & L & 0 & 0 \\ 0 & 0 & L & 0 \\ 1/(\beta\delta)\partial/\partial x & 0 & 0 & 0 \end{bmatrix},$$

$$\mathbf{M}_r = \begin{bmatrix} M & 0 & 0 & 0 \\ 0 & M + 1/\beta + 1/(\mathrm{Re}\, r^{*2}) & 2rB/(\mathrm{Re}\, r^{*2})\partial/\partial r - w/r^* & A\partial/\partial r \\ 0 & -2rB/(\mathrm{Re}\, r^{*2})\partial/\partial r & M + v/r^* + 1/(\mathrm{Re}\, r^{*2}) & rB/(r^*)\partial/\partial r \\ 0 & 1/(\beta\delta)\,(1/r^* + A\partial/\partial r) & rB/(\beta\delta\, r^*)(\partial/\partial r) & 0 \end{bmatrix},$$

$$\mathbf{M}_\theta = \begin{bmatrix} N & 0 & 0 & 0 \\ 0 & N & 2/(\mathrm{Re}\, r^{*2})\partial/\partial\theta & 0 \\ 0 & -2/(\mathrm{Re}\, r^{*2})\partial/\partial\theta & N + 1/\beta & (1/r^*)\partial/\partial\theta \\ 0 & 0 & 1/(\beta\delta\, r^*)\partial/\partial\theta & 0 \end{bmatrix},$$

in which

$$L\varphi = \frac{\partial(\hat{u}^\mu\varphi)}{\partial x} - \frac{1}{\mathrm{Re}}\frac{\partial^2\varphi}{\partial x^2},$$

$$M\varphi = \left(rC - \frac{rD}{\mathrm{Re} r^{*2}} - \frac{rB^2}{\mathrm{Re} r^{*2}}\right)\frac{\partial\varphi}{\partial r} + \frac{A}{r^*}\frac{\partial}{\partial r}(r^*\hat{v}^\mu\varphi) + \frac{rB}{r^*}\frac{\partial}{\partial r}(\hat{w}^\mu\varphi)$$

$$-\frac{1}{\mathrm{Re}}\left[\frac{A}{r^*}\frac{\partial}{\partial r}\left(Ar^*\frac{\partial\varphi}{\partial r}\right) + \frac{r^2B^2}{r^{*2}}\frac{\partial^2\varphi}{\partial r^2} + \frac{2rB}{r^{*2}}\frac{\partial^2\varphi}{\partial r\partial\theta}\right],$$

$$N\varphi = \frac{1}{r^*}\frac{\partial}{\partial\theta}(\hat{w}^\mu\varphi) - \frac{1}{\mathrm{Re} r^{*2}}\frac{\partial^2\varphi}{\partial\theta^2},$$

where the coefficients A, B, C, and D stand for $A(\theta,t)$, $B(\theta,t)$, $C(\theta,t)$, and $D(\theta,t)$, respectively.

Thus, the N-S and continuity equations in Δ form can be written in different sweeps as

In the r-sweep

$$\widetilde{\Delta u}+\beta\Delta\tau\left[\frac{A}{r^*}\frac{\partial}{\partial r}\left(r^*\hat{v}^\mu\widetilde{\Delta u}\right)+\frac{rB}{r^*}\frac{\partial}{\partial r}\left(\hat{w}^\mu\widetilde{\Delta u}\right)+rC\frac{\partial\left(\widetilde{\Delta u}\right)}{\partial r}\right.$$

$$\left.-\frac{1}{\mathrm{Re}}\left\{\frac{A}{r^*}\frac{\partial}{\partial r}\left(Ar^*\frac{\partial\left(\widetilde{\Delta u}\right)}{\partial r}\right)+\frac{r^2B^2}{r^{*2}}\frac{\partial^2\left(\widetilde{\Delta u}\right)}{\partial r^2}+\frac{rD+rB^2}{r^{*2}}\frac{\partial\left(\widetilde{\Delta u}\right)}{\partial r}+\frac{2rB}{r^{*2}}\frac{\partial^2\left(\widetilde{\Delta u}\right)}{\partial r\partial\theta}\right\}\right]$$

$$=\Delta\tau\left(E_u{}^n-\hat{u}^\mu-\beta\hat{Q}_u^\mu\right)\,, \tag{6.16}$$

$$(1+\Delta\tau)\,\widetilde{\Delta v}+\beta\Delta\tau\left[\frac{A}{r^*}\frac{\partial}{\partial r}\left(r^*\hat{v}^\mu\widetilde{\Delta v}\right)+\frac{rB}{r^*}\frac{\partial}{\partial r}\left(\hat{w}^\mu\widetilde{\Delta v}\right)+rC\frac{\partial\left(\widetilde{\Delta v}\right)}{\partial r}+A\frac{\partial\left(\widetilde{\Delta p}\right)}{\partial r}\right.$$

$$-\frac{1}{\mathrm{Re}}\left\{\frac{A}{r^*}\frac{\partial}{\partial r}\left(Ar^*\frac{\partial\left(\widetilde{\Delta v}\right)}{\partial r}\right)+\frac{r^2B^2}{r^{*2}}\frac{\partial^2\left(\widetilde{\Delta v}\right)}{\partial r^2}+\frac{rD+rB^2}{r^{*2}}\frac{\partial\left(\widetilde{\Delta v}\right)}{\partial r}+\frac{2rB}{r^{*2}}\frac{\partial^2\left(\widetilde{\Delta v}\right)}{\partial r\partial\theta}\right.$$

$$\left.\left.-\frac{2rB}{r^{*2}}\frac{\partial\left(\widetilde{\Delta w}\right)}{\partial r}-\frac{\widetilde{\Delta v}}{r^{*2}}\right\}\right]=\Delta\tau\left(E_v{}^n-\hat{v}^\mu-\beta\hat{Q}_v^\mu\right)\,, \tag{6.17}$$

$$\widetilde{\Delta w}+\beta\Delta\tau\left[\frac{A}{r^*}\frac{\partial}{\partial r}\left(r^*\hat{v}^\mu\widetilde{\Delta w}\right)+\frac{rB}{r^*}\frac{\partial}{\partial r}\left(\hat{w}^\mu\widetilde{\Delta w}\right)+rC\frac{\partial\left(\widetilde{\Delta w}\right)}{\partial r}+\frac{rB}{r^*}\frac{\partial\left(\widetilde{\Delta p}\right)}{\partial r}+\frac{v\widetilde{\Delta w}}{r^*}\right.$$

$$-\frac{1}{\mathrm{Re}}\left\{\frac{A}{r^*}\frac{\partial}{\partial r}\left(Ar^*\frac{\partial\left(\widetilde{\Delta w}\right)}{\partial r}\right)+\frac{r^2B^2}{r^{*2}}\frac{\partial^2\left(\widetilde{\Delta w}\right)}{\partial r^2}+\frac{rD+rB^2}{r^{*2}}\frac{\partial\left(\widetilde{\Delta w}\right)}{\partial r}\right.$$

$$\left.\left.+\frac{2rB}{r^{*2}}\frac{\partial^2\left(\widetilde{\Delta w}\right)}{\partial r\partial\theta}+\frac{2rB}{r^{*2}}\frac{\partial\left(\widetilde{\Delta v}\right)}{\partial r}-\frac{\widetilde{\Delta w}}{r^{*2}}\right\}\right]=\Delta\tau\left(E_w{}^n-\hat{w}^\mu-\beta\hat{Q}_w^\mu\right)\,. \tag{6.18}$$

$$\widetilde{\Delta p}+\frac{A\Delta\tau}{r^*\delta}\frac{\partial}{\partial r}\left(r^*\widetilde{\Delta v}\right)+\frac{rB\Delta\tau}{r^*\delta}\frac{\partial\left(\widetilde{\Delta w}\right)}{\partial r}=-\frac{\Delta\tau}{\delta}\nabla\cdot\hat{\mathbf{V}}^\mu\,; \tag{6.19}$$

in the θ−sweep

$$\overline{\Delta u}+\beta\Delta\tau\left[\frac{1}{r^*}\frac{\partial\left(\hat{w}^\mu\overline{\Delta u}\right)}{\partial\theta}-\frac{1}{\mathrm{Re}r^{*2}}\frac{\partial\left(\overline{\Delta u}\right)}{\partial\theta^2}\right]=\widetilde{\Delta u}\,, \tag{6.20}$$

$$\overline{\Delta v} + \beta\Delta\tau \left[\frac{1}{r^*} \frac{\partial\left(\hat{w}^\mu \overline{\Delta v}\right)}{\partial\theta} - \frac{1}{\mathrm{Re} r^{*2}} \frac{\partial\left(\overline{\Delta v}\right)}{\partial\theta^2} \right] = \widetilde{\Delta v}, \tag{6.21}$$

$$(1+\Delta\tau)\,\overline{\Delta w} + \beta\Delta\tau \left[\frac{1}{r^*} \frac{\partial\left(\hat{w}^\mu \overline{\Delta w}\right)}{\partial\theta} + \frac{1}{r^*} \frac{\partial\left(\overline{\Delta p}\right)}{\partial\theta} \right.$$

$$\left. - \frac{1}{\mathrm{Re}} \frac{1}{r^{*2}} \frac{\partial^2\left(\overline{\Delta w}\right)}{\partial\theta^2} \right] = \widetilde{\Delta w}, \tag{6.22}$$

$$\overline{\Delta p} + \frac{\Delta\tau}{\delta} \frac{\partial\left(\overline{\Delta w}\right)}{r^*\partial\theta} = \widetilde{\Delta p}. \tag{6.23}$$

and finally in the $x-$sweep

$$(1+\Delta\tau)\,\Delta u + \beta\Delta\tau \left[\frac{\partial\left(\hat{u}^\mu \Delta u\right)}{\partial x} + \frac{\partial\left(\Delta p\right)}{\partial x} - \frac{1}{Re} \frac{\partial^2\left(\Delta u\right)}{\partial x^2} \right] = \overline{\Delta u}, \tag{6.24}$$

$$\Delta v + \beta\Delta\tau \left[\frac{\partial\left(\hat{u}^\mu \Delta v\right)}{\partial x} - \frac{1}{Re} \frac{\partial^2\left(\Delta v\right)}{\partial x^2} \right] = \overline{\Delta v}, \tag{6.25}$$

$$\Delta w + \beta\Delta\tau \left[\frac{\partial\left(\hat{u}^\mu \Delta w\right)}{\partial x} - \frac{1}{Re} \frac{\partial^2\left(\Delta w\right)}{\partial x^2} \right] = \overline{\Delta w}, \tag{6.26}$$

$$\Delta p + \frac{\Delta\tau}{\delta} \frac{\partial\left(\Delta u\right)}{\partial x} = \overline{\Delta p}; \tag{6.27}$$

in the general case, $Q_u^\mu = Q_u(\hat{u}^\mu, \hat{v}^\mu, \hat{w}^\mu, \hat{p}^\mu)$, $Q_v^\mu = Q_v(\hat{u}^\mu, \hat{v}^\mu, \hat{w}^\mu, \hat{p}^\mu)$, and $Q_w^\mu = Q_w(\hat{u}^\mu, \hat{v}^\mu, \hat{w}^\mu, \hat{p}^\mu)$. The variables $\hat{u}^{\mu+1} = \hat{u}^\mu + \Delta u$, $\hat{v}^{\mu+1} = \hat{v}^\mu + \Delta v$, $\hat{w}^{\mu+1} = \hat{w}^\mu + \Delta w$ and $\hat{p}^{\mu+1} = \hat{p}^\mu + \Delta p$ are thus obtained by solving equations (6.16)-(6.27). The solution in pseudo-time step (iteration) continues until convergence is reached, where the terms $\partial\hat{\mathbf{V}}/\partial\tau$ and $\partial\hat{p}/\partial\tau$ become zero, thereby the differences Δu, Δv, Δw, and Δp are equal to zero.

6.4 Spatial Discretization on Staggered Grids

To perform the discretization of the equations in order to solve the full nonlinear Navier-Stokes equations in the transformed domain one needs to construct a staggered mesh and to define the interpolates. The staggered mesh is made in 3-D, by combining two 2-D meshes, Figure 4.8 and 4.9, as shown in Chapter 4; this constitutes a grid scheme spanning the x, r and θ directions. The grid points are stretched in the x and r directions, but not in the θ direction, as explained in previous chapters, in order to concentrate points near solid walls or in regions of larger gradients in the flow domain geometry, such as in the vicinity of a step or near changes in the contour of diffuser sections, see Figures 4.26 and 5.2. The velocity components v, w and the pressure p have identical x position, while u, w, and p have identical r position in the grid scheme. The momentum and continuity equations are differenced about the points where $\hat{u}_{i,j,k}$, $\hat{v}_{i,j,k}$, $\hat{w}_{i,j,k}$, and $\hat{p}_{i,j,k}$ are defined.

The discretization of the equations (6.16)-(6.27) and the numerical solution, which is similar to those described in Chapters 4 and 5, are given in Appendix B. It was shown that the differential equations in the transformed domain are more complicated than in the physical one due to the extra convective and diffusive terms in addition to the cross-derivative terms, which reflect the non-orthogonal nature of the coordinates, all of them arising from the transformation. During the solution procedure, the cross derivative terms destroy the tridiagonal aspect of the system of equations to be solved; hence these terms are evaluated explicitly. The amount of computer memory and time due to these added terms as well as their effects on the convergence of the solution have been considered to be tolerable with respect to the solution using the mean-position (no time-dependent coordinate transformation) analysis. This comparison will be made later in Chapter 7.

6.4.1 Importance of Grid Skewness on the Results

Before solving the differential equations of fluid motion, the grid system must be investigated carefully for grid *skewness*. In determining the grid points, a few constraints must be imposed. First, the mapping must be one-to-one; *i.e.*, grid lines of the same family cannot cross each other. Second, from the numerical point of view, a smooth grid distribution with minimum *skewness*, with orthogonality or near-orthogonality, and a concentration of grid points in regions where high gradients occur are all required.

The grid system generated by the grid-generation methods may not be satisfactory for some applications due to large *skewness* of the grid lines, especially when they occur at the surface. The difficulty is encountered when normal gradients of flow properties are required. To overcome this deficiency, a forcing function is used which will enforce orthogonality of grid lines at the surface. The resulting grid system simplifies the computation of the normal gradients and increases their accuracy. Although the overall orthogonality of the grid lines is important, it has been proved that the non-orthogonal curvilinear coordinates do not affect the accuracy of the results; rather, only the convergence of the solution will be influenced by the *skewness* of the grid lines.

To investigate this statement, if the metric coefficient is evaluated numerically, one obtains

$$f_x = \frac{f_{i+1} - f_{i-1}}{x_{i+1} - x_{i-1}} + T_1 \,,$$

where T_1 is the truncation error. A Taylor series expansion in x about the central point then shows the leading terms of the truncation error T_1 to be (Thompson *et al.* 1982)

$$-\frac{1}{6}x_\xi^2 f_{xxx} - \frac{1}{2}x_{\xi\xi} f_{xx} \,, \tag{6.28}$$

where x_ξ and $x_{\xi\xi}$ are the central difference representaions of these respective derivatives,

$$x_\xi = \frac{1}{2}(x_{i+1} - x_{i-1}), \qquad x_{\xi\xi} = x_{i+1} - 2x_i + x_{i-1} \,. \tag{6.29}$$

The representation of f_x is truly second order, only if $x_{\xi\xi} \simeq x_\xi^2$. If the system is not orthogonal (*e.g.*, skewed), then the same type of 1-D analysis yields the following additional term in the truncation error:

$$-\frac{1}{2}(\cot\theta)^2 x_{\xi\xi} f_{yy} - (\cot\theta) x_{\xi\xi} f_{xy} \,, \tag{6.30}$$

where θ is the angle between the coordinate lines. Thus for second-order accuracy it is necessary that

$$x_{\xi\xi}\cot\theta \simeq x_\xi^2 \,.$$

If the intersection angle is less than 45°, then the requirement would already be met if $x_{\xi\xi} \simeq x_\xi^2$ as required above. For this reason, departure from orthogonality of up to 45° can be considered tolerable (Thompson *et al.* 1982).

Braaten and Shyy (1986), have shown that the effects of the local mesh skewness on the convergence behaviour are not very strong. Based on their results, it seems that, unless both the skewness measure of the individual mesh and the smoothness of the neighbouring meshes are excessive, considerable skewness of the individual cell does not noticeably affect the numerical accuracy. They showed that the effects of larger local mesh skewness on the overall calculated accuracy of the N-S equations are tolerable, which supports the assessment of Thompson *et al.* (1982). Shyy (1985), however, has shown that the use of excessively skewed meshes is not tolerable, since it destabilizes the line-iterative procedure. With the findings of Braaten & Shyy (1986) and Shyy (1985), it appears that the mesh skewness, especially in the boundary region, is likely to significantly affect the numerical stability and convergence behaviour of the numerical scheme rather than the numerical accuracy. Indeed Shyy has put in evidence that a desirable mesh distribution from the view-point of solution accuracy is not necessarily non-skewed throughout the whole domain.

In this Thesis, the fluid equations are written in cylindrical coordinates ,which are orthogonal, and are solved in a rectangular transformed domain in which the coordinate lines are obviously orthogonal. Some non-orthogonality is seen in the physical domain shown in Figure 6.3, where for the maximum amplitude of the outer cylinder (maximum eccentricity of the outer cylinder with respect to the reference inner cylinder) the departure from orthogonality for the angles between the coordinate lines is less than 5°, which is much smaller than the 45° assessed as the limit by Thompson *et al.*; this is even smaller for smaller amplitudes of oscillation.

For this reason, the physical flow variables, *i.e.*, physical u, v, w and p, not the transformed ones such as covariant or contravariant velocity components, have been used in the transformed partial differential equations, and hence there is no need to do the inverse transform of the numerical results to obtain the real physical flow variables.

6.5 Method of Solution Based on ADI Scheme

In order to start the time-integration procedure, initial conditions must be provided for **V** and p throughout the fluid domain which is given by equation (4.35). The known displacement ϵ_w^{n+1} and velocity $\mathbf{U}_w^{n+1}$ of the walls at the advanced time level t^{n+1} are set as boundary conditions and kept unchanged until the steady state has been reached in pseudo-time. As explained in Chapter 4, the wall displacement ϵ_w^{n+1} is not important for the mean-position analysis and it mainly serves in the evaluation of the velocity of the moving boundary U_{mb}, but in the *time-dependent transformation* analysis the displacement plays a major role and appears almost everywhere in the transformed equations. Both ϵ_w^{n+1} and $\mathbf{U}_w^{n+1}$ serve as driving terms to advance the solution to time level $(n+1)\Delta t$, along with the term $\mathbf{E}^n$, which is calculated at the beginning of pseudo-time relaxation and kept constant throughout.

The previous inflow and outflow boundary conditions for the velocity and pressure are also applied to the *time-dependent coordinate transformation* analysis. The evaluation of the viscous derivative terms near the solid walls using non-central differencing, the extrapolation of the fluid velocities from within the domain of integration, the symmetry boundary conditions with respect to the plane of oscillation for u, v, w and p, follow the same line explained for the case of mean-position analysis. As far as the movement of the solid walls is concerned, one notes that on the inner cylinder the displacement $\bar{\epsilon}_w(\bar{t})$ is zero, while on the outer cylinder in the plane of symmetry it is given by

$$\bar{\epsilon}_w(\bar{t}) = -\bar{\epsilon}_w \cos \Omega \bar{t}\,,$$

with the velocity of the wall expressed by

$$\dot{\bar{\epsilon}}_w(\bar{t}) = \bar{\epsilon}_w \Omega \sin \Omega \bar{t}\,,$$

where $\bar{\epsilon}$ is the dimensional amplitude of oscillation, Ω is the circular frequency of oscillation and $\bar{t}$ is the dimensional time respectively. Hence, the nondimensional components of the velocities of the fixed and moving walls in the radial and circumferential directions are given by equations (2.13) and (2.14).

Now, the solution to the equations (6.16)-(6.27) can be obtained since they are cast in discretized forms using the relations (3.19), (4.58), (4.59) and similar ones expressed in Appendix A. Thus, the right-hand sides of equations (6.16)-(6.19) are computed using the relations (B.3), (B.7), (B.14) and (B.21). The domain of integration in each sweep and at a given pseudo-time step, τ^{μ}, in which equations (6.16)-(6.27) are set up spans for $2 \leq i \leq I-1$, $2 \leq j \leq J-1$, and $3 \leq k \leq K-1$. These equations are solved for $\Delta u, \Delta v, \Delta w$, and Δp. In the r-sweep, $\widetilde{\Delta v}$ is obtained from (B.8) after eliminating $\widetilde{\Delta p}$ with the aid of (6.19). The terms $\overline{\Delta v}$ and Δv are obtained from equations (B.10) and (B.12) in the θ- and x-sweep, respectively. The same procedure is applied in determining $\widetilde{\Delta w}$ from (B.15), $\overline{\Delta w}$ from (B.17) with the aid of equation (6.23) to eliminate $\overline{\Delta p}$, and finally Δw from (B.19). Also, $\widetilde{\Delta u}$ is determined from (B.22), $\overline{\Delta u}$ is obtained from (B.24) and Δu is determined from (B.26) with the aid of (6.27) as a coupling equation. The pressure difference Δp is obtained, ultimately, after Δu is determined. In all these calculations it is obvious that several times the scalar tridiagonal systems of equations must be inverted as explained in Chapters 4 and 5.

6.6 Two-Dimensional Solutions for Larger-Amplitude Oscillations

In the case of 2-D solutions for larger-amplitude oscillations, the same mesh as used in Chapter 4 for 2-D analysis with small-amplitude oscillations is utilized. This is done by choosing the appropriate inner and outer radii to be used in the transformation equation (6.1), which gives the grid points spanning the r- and θ-directions with $0 \leq r \leq 1$ and $0 \leq \theta \leq \pi$. To compare the results obtained for larger amplitudes with those in Chapter 4, the numerical computation has been implemented on a non-dimensional mesh with physical inner and outer radii $R_i = 4.5$ and $R_o = 5.0$, corresponding to $r_i = 0$ and $r_o = 1$ in the computational domain, and for oscillatory Reynolds number $S = 300$.

The results are shown in Figures 6.4-6.7 in which, as in Chapter 4, all quantities are dimensionless. In this analysis, the number of time steps is 19 and equations (6.16)-(6.19) are solved for each real-time step using equations (6.11), (6.14), and (6.15) for 2-D (*i.e.*, all derivatives with respect to x are equal to zero in all the aforementioned equations) to evaluate their right-hand sides. Questions of convergence and accuracy are discussed in Chapter 7. It is found that 3 harmonic cycles are sufficient for a stable solution after which a periodic state is reached with no changes in the computed results. It should be remarked that, even in the case of large-amplitude oscillation, after coordinate transformation the grid points are clustered near the solid walls as well as in the centre of the annulus to ensure an accurate solution in these regions in which the higher velocity gradients exist. As before, the stretching function in the r-direction is a hyperbolic tangent and the mesh is composed of 24×24 grid points.

Figure 6.4(a,b) contains the curves representing the solutions for each of 5 instants t^n within the harmonic cycle. The five instants are obtained from $t^n = 2\pi n/N$. $n = 7, 9, 11, 13$, and 15 for circumferential velocity w, and $n = 3, 5, 7, 9$, and 11 for the results involving the pressure p and $N = 19$. Figure 6.4(a) presents the radial profiles of the pressure taken at $\theta = 3.75°$. In this figure, the results obtained for small-amplitude oscillations are presented for comparison. The magnitude of the pressure at each t and for the mean position analysis is completely different from those obtained using time-dependent transformation analysis. Using the Discrete Fourier Transform (equation (4.70)) to calculate the amplitude of the pressure shows that for this small amplitude oscillation ($\epsilon = 0.1$) the unsteady pressure results for two solutions are not too different, as shown in Figures 6.5(a) and 6.6(a).

Figure 6.4(b) presents the radial profiles of w at an azimuth of $\theta = 45^{\circ}$ for five instants of time together with the results for small-amplitude analysis (Figure 4.10(b)). The difference between the corresponding values of w for the two methods of solution is noticeable. In fact, the solution obtained for w with time-dependent coordinate transformation almost corresponds to Bélanger's (1991) results which were obtained using the linearized first harmonic solution. Figure 6.5 presents the real and imaginary parts of the unsteady pressure at four different amplitudes of oscillation. The results for the real parts do not present significant differences, but for the imaginary parts the difference between the results obtained by the two methods of solution is remarkable. The first thing to note is that for $\epsilon = 0.01$ both Figures 6.5(a) and 6.5(b) show that the real values and the imaginary values as obtained from the two methods are the same. This highlights the fact that the mean position analysis is quite valid for $\epsilon \leq 0.01$. As the amplitude of oscillation increases, however, the differences between the results become larger. As a matter of fact, for the small-amplitude oscillation, the results vary linearly which is the characteristic of this method in which nonlinearity in the solution does not show up due to the boundary being limited in its movement. Contrary to this simple method, the larger amplitude solution demonstrates that the imaginary values increase nonlinearly with the amplitudes of oscillation as shown in Figure 6.5(b).

Figure 6.6 presents the real and imaginary parts of the unsteady pressure versus the azimuth θ for different oscillation amplitudes. In this figure, the real and imaginary parts obtained from the two methods of solution at $\epsilon = 0.05$ are almost the same, which indicates that we are not very far from small amplitude motion, in contrast to the corresponding values at larger amplitudes oscillation. Figure 6.7 presents the real and imaginary parts of the circumferential velocity w for different oscillation amplitudes. As far as the effect of oscillation amplitudes are concerned, the explanation given for Figure 6.6 applies here also, *i.e.*, one can see the correspondence between the real values as well as the imaginary values for the two methods of solution at $\epsilon = 0.05$.

6.7 Three-Dimensional Solutions for Larger Amplitude Oscillation

6.7.1 Uniform Annular Geometry

To solve the N-S and continuity equations in 3-D, the three-dimensional mesh shown in Figure 4.7 is used. The numerical computations have been performed for two sets of geometries to obtain results comparable with those obtained through mean position analysis presented in Chapter 4. The first set is for small lengths of the fixed upstream and downstream portions, while the second set is for larger lengths of these portions, in order to investigate the effect of the length of these portions in diminishing the perturbation pressure at the extremities. The effect of the gap width is also investigated by using two different annular spaces: (a) $r_i = 9$, $r_o = 10$ and (b) $r_i = 4.785$, $r_o = 5.785$, corresponding to smaller and larger annular spaces, respectively. The same meshes used for the 3-D analysis in Chapter 4 were used here, with the same type of stretching functions in the r- and x-directions. Equations (6.16)-(6.27) were solved in this 3-D domain until a periodic state was reached, as was done in Chapter 4.

As before, the computations were conducted for different Reynolds numbers, including the case of quiescent fluid, for which the definition of the Reynolds number has been given in Chapter 4. The basic parameters affecting the solution of the problems and the criteria for convergence (such as the values of the real-time Δt, compressibility factor δ, pseudo-time $\Delta\tau$, Courant number Cr, etc.) follow the same lines as in Chapter 4. In the time-dependent-transformation analysis, as a first step, the amplitude and the velocity of the moving boundary are calculated using equations (4.36) and (4.37) and are kept constant throughout the pseudo-time relaxation. The other initial and boundary conditions are given or calculated following the same procedure described in the previous chapters.

Figure 6.8(a,b) presents the unsteady pressure amplitude and phase angle versus the axial length of the cylinder for both mean-position and time-dependent-transformation analyses. For the smaller fixed portions at the extremities of the moving cylinder, this result shows about 14% and 40% increase in the pressure amplitude and phase respectively. As one notices, the perturbation pressure does not vanish at the upstream end. The reasons for having this problem, as well as the appropriate procedure to avoid it are explained briefly at the end of this chapter and in more details in Chapter 7. Figure 6.9(a,b) demonstrates the effect of larger-amplitude oscillation on the circumferential velocity w and on its phase angle. It is seen that the amplitude of w does not vary too much, but a substantial change in its phase angle is noted. It must be mentioned that in Figure 6.9 the annular space h shown is in the computational domain, $0 \leq h \leq 1$, which is related to the computational domain $9 \leq h \leq 10$ in the mean-position analysis; this relation is simple and obvious if one notes that the non-dimensional annular gap is always $h = 1$, and hence one can present the results for both methods on the same diagram.

Figure 6.10 by comparison to Figure 6.8 shows the effect of extension of the fixed portions on the unsteady pressure and its phase angle. It is interesting to note how the inflow and outflow boundary conditions influence the results compared to those shown in Figure 6.8. In this case, the amplitude of unsteady pressure obtained from time-dependent transformation approach is not higher; rather it has turned out to become even smaller than that obtained from the mean-position analysis. Also, the pressure perturbation at the far upstream extremity approaches much lower values (although it has not become zero) than the corresponding values in Figure 6.8. Similarities exist between the values and behaviour of the phase angle results of Figure 6.10 with those of Figure 6.8 for the moving part of the cylinder, $0 \leq X \leq 100$.

Figure 6.11 presents the comparison between the results obtained using both methods of solution but for higher frequency of oscillation ($f = 20$ Hz) and in quiescent fluid. In Figure 6.11(a), although the fixed portions at the extremities of the moving cylinder have larger lengths, the time-dependent solution demonstrates an increase of 6% in the pressure amplitude which is due to the larger value of the oscillation frequency. Figure 6.11(b) presents, as usual, lower values for the phase angle, as compared to the one obtained by the mean-position analysis.

Figure 6.12 presents the effect of annular gap width on the results when the fluid flows in the annulus with Re= 2900 and the frequency of oscillation is $f = 20$ Hz. Once again, the mean values for the unsteady pressure obtained from both approaches are almost the same; also, the effect on the phase angle is similar to that in previous figures.

Finally, to demonstrate that the time-dependent-coordinate solution is more reliable at much higher amplitudes of oscillation than the mean-position approach, Figure 6.13 has been drawn for $\epsilon = 0.5$ using the smaller annular gap ($r_i = 9$ and $r_o = 10$). It is seen that not only does the frequency of oscillation make substantial changes in the pressure results (see Figure 6.11), but the amplitude of oscillation produces large differences in the pressure, as shown in Figure 6.13. Also the phase angles are very much closer to each other, as compared for example with Figure 6.10(b), and its value tends toward zero.

6.7.2 3-D Solution for Non-Uniform Annular (Backstep) Geometry

The method of solution for larger-amplitude oscillation applied to non-uniform annular geometry (case of backstep) is similar to that discussed in previous chapters; the mesh used is shown in Figure 4.26, with its description given in Chapter 4. Also, Table 4.1 was utilized to obtain the appropriate results for each specific mesh.

Figure 6.14 presents the unsteady pressure and phase angle for both approaches using mesh type C with $r_{id} = 8$ and $r_o = 10$. As expected, there are some differences in the results, *i.e.*, there is an overall increase in the value of pressure in comparison to that obtained through the mean-position analysis. Also, the phase angle (after the step geometry) tends more toward zero than the corresponding value obtained by the mean-position approach.

Figure 6.15 presents the circumferential velocity w and its phase angle obtained at $X = 50.816$. $\theta = 45^o$ and for $\epsilon = 0.2$ using mesh type C. Figure 6.16 demonstrates the effect of the length of vibrating cylinder ($L = 40$) on the pressure and on its phase angle. This figure should be compared with Figure 6.14 with $L = 100$, even though the amplitudes of oscillation differ. It is seen that reducing the length L will affect the pressure results after the step. It is obvious that the results shown in Figure 6.14 are more reliable, since the step is farther from the extremities.

Figure 6.17 was drawn for three different amplitudes of oscillation and is similar to Figure 4.29, except that the phase-angle results have different shapes but still coincide for different amplitudes. For this figure mesh type A was used. Figure 6.18 demonstrates the effect of extension of the fixed upstream and downstream portions on the results with $\epsilon = 0.3$ and using mesh type B. It is clear, that the pressure perturbations approach to their lower possible values but in the case of time-dependent analysis the perturbation tends toward zero before building up at larger distances. Figure 6.18(b) presents larger values for the phase angle (in positive sense) after the step obtained by the time-dependent analysis than that obtained from mean position analysis. Lastly, Figure 6.19 presents the unsteady pressure and phase angle for quiescent fluid at higher frequencies of oscillation ($f = 1.5$ Hz) for three amplitudes of oscillation using mesh type C. The phase-angle curves for all three amplitudes remain almost flat, similar to each other and the values of the phase angles approach zero.

Up to now, due to economical reasons (time and space on the computer), the effect of extension of the fixed portions on the unsteady pressure was studied for the maximum length $L_1 = L_2 = 60$. As one notices, in the figures presented, the perturbations at the upstream end do not vanish. There are numerical reasons for this problem, which will be discussed in the next chapter. But, by selecting a larger length for the fixed portions, this perturbation can be forced to approach its minimum possible value in those sections, as will be shown in the next chapter. Also, using larger fixed portions will increase the pressure amplitude in the oscillating domain, *i.e.*, we will have better agreement between the theoretical results obtained by the two methods of solution and the experimental results (see Figure 7.4 and figures presented in Chapter 8).

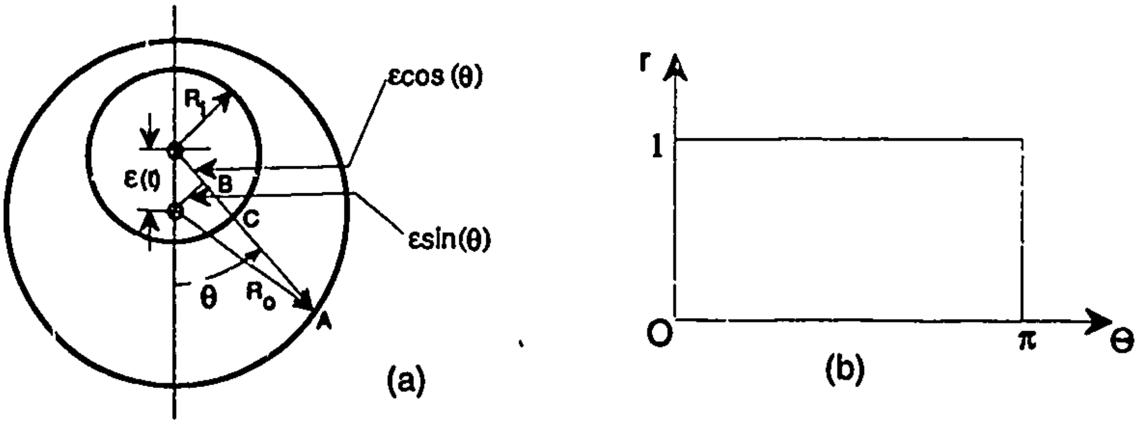

Figure 6.1: Physical and transformed computational domains for two nearly concentric cylinders with moving outer cylinder.

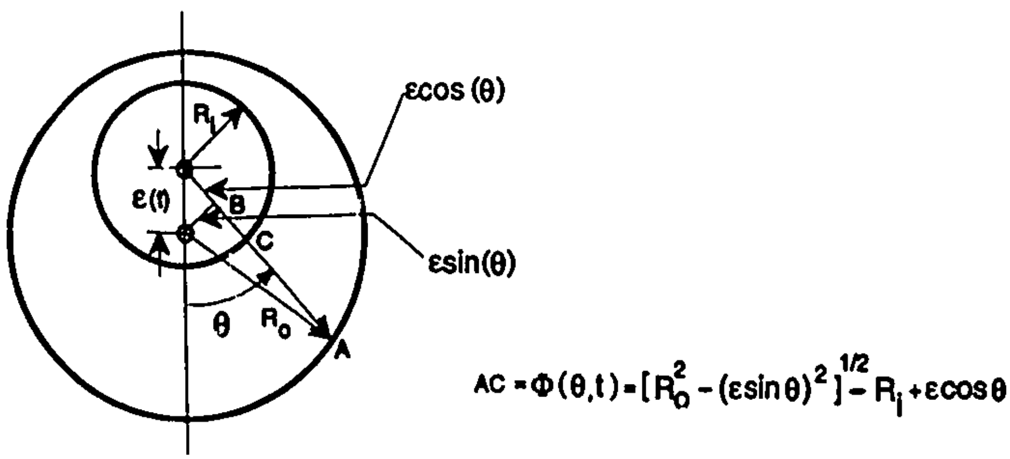

Figure 6.2: Schematic representation of two cylinders during oscillation of the outer cylinder for the evaluation of $\Phi(\theta, t)$.

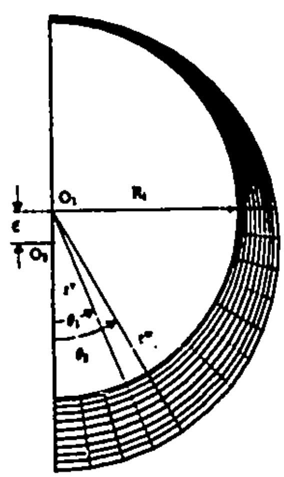

Figure 6.3: Grid point distribution in physical domain.

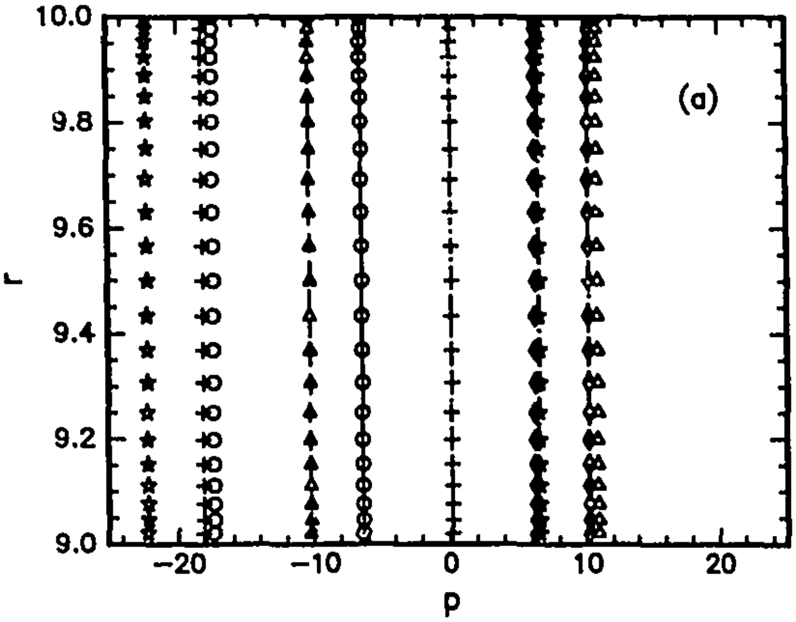

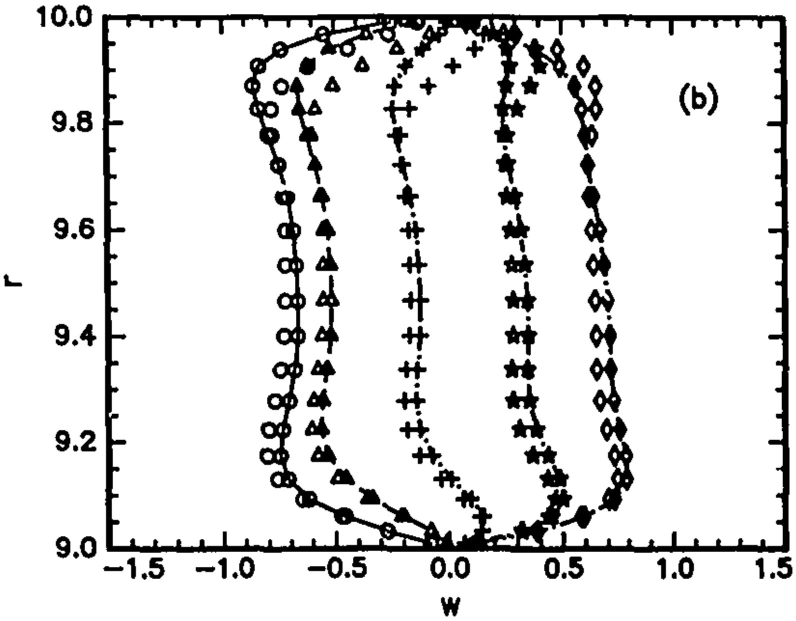

Figure 6.4: (a) Radial profiles of pressure p at $\theta = 3.75^o$ and (b) radial profiles of circumferential velocity w at $\theta = 45^o$ for $S = 300$, $R_o/R_i = 1.25$, $\epsilon = 0.1$ at 5 instants t^n within the harmonic cycle; –o–,mean-position analysis; o,time-dependent-transformation analysis; the rest are similar (*i.e.*, symbols with lines for the mean-position analysis, and symbols for the time-dependent-transformation analysis).

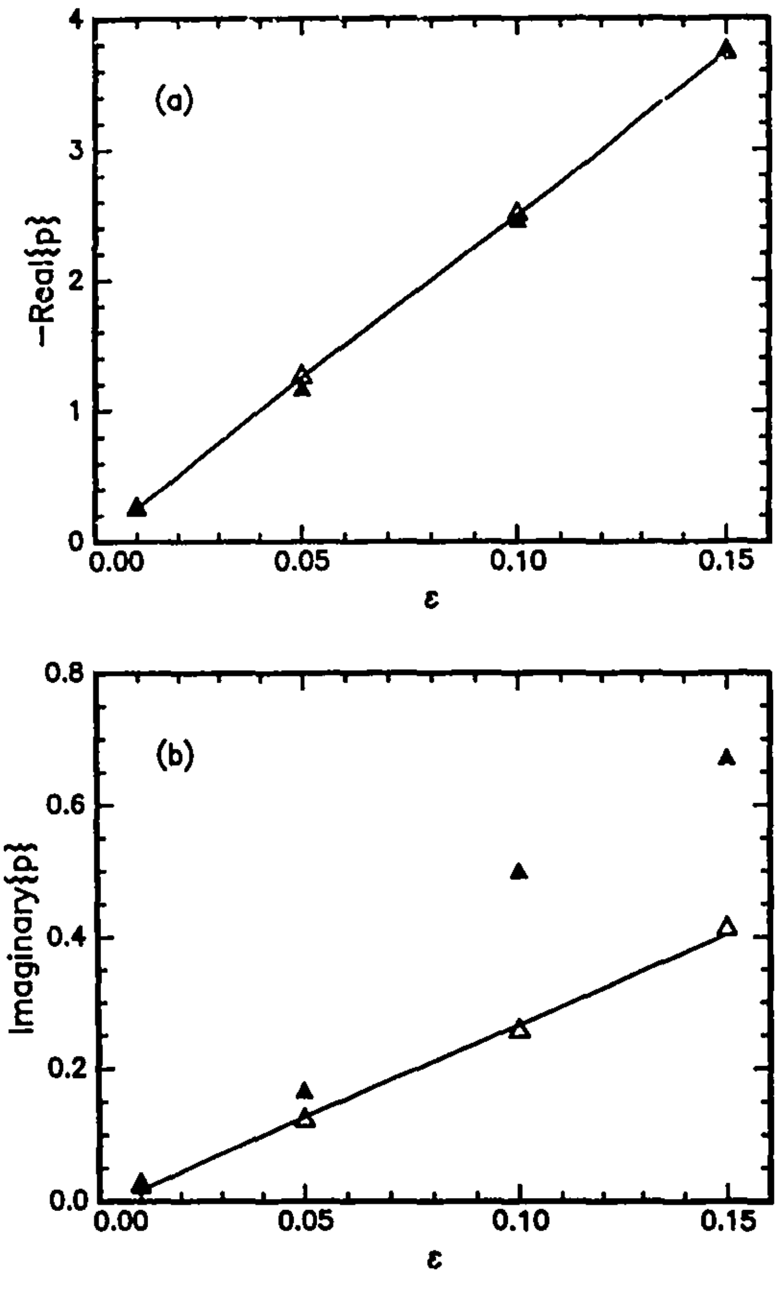

Figure 6.5: Variation with the oscillation amplitude, ϵ, of the real and imaginary components of the unsteady pressure, p, on the oscillating cylinder at $\theta = 7.5^o$; Δ time-dependent-coordinate transformation analysis, -Δ-mean position analysis.

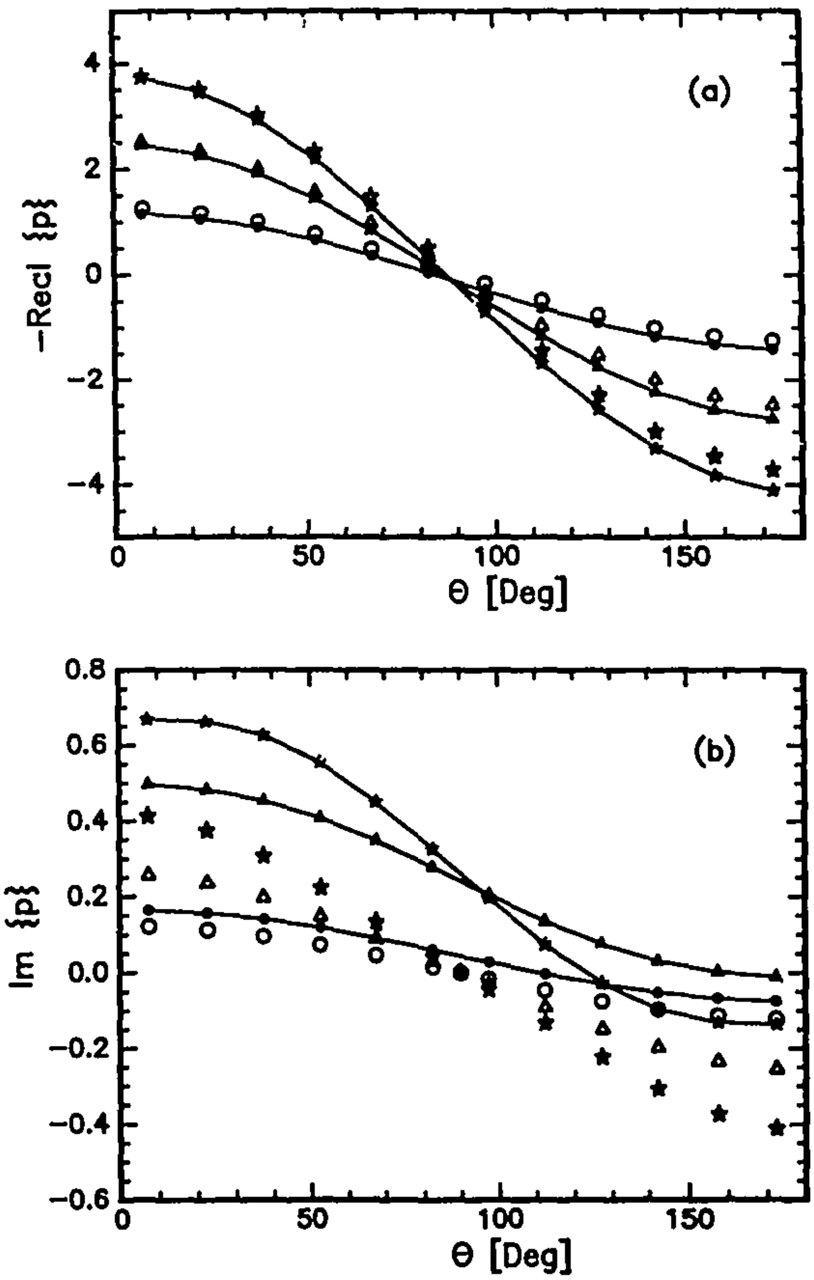

Figure 6.6: Azimuthal (θ-) variation of the real and imaginary components of the unsteady pressure, p, on the oscillating cylinder for three values of the amplitude of oscillation, ϵ; o, $\epsilon = 0.05$; Δ, $\epsilon = 0.1$; $*$, $\epsilon = 0.15$. o,mean-position analysis; -•-,time-dependent-transformation analysis; the rest are similar.

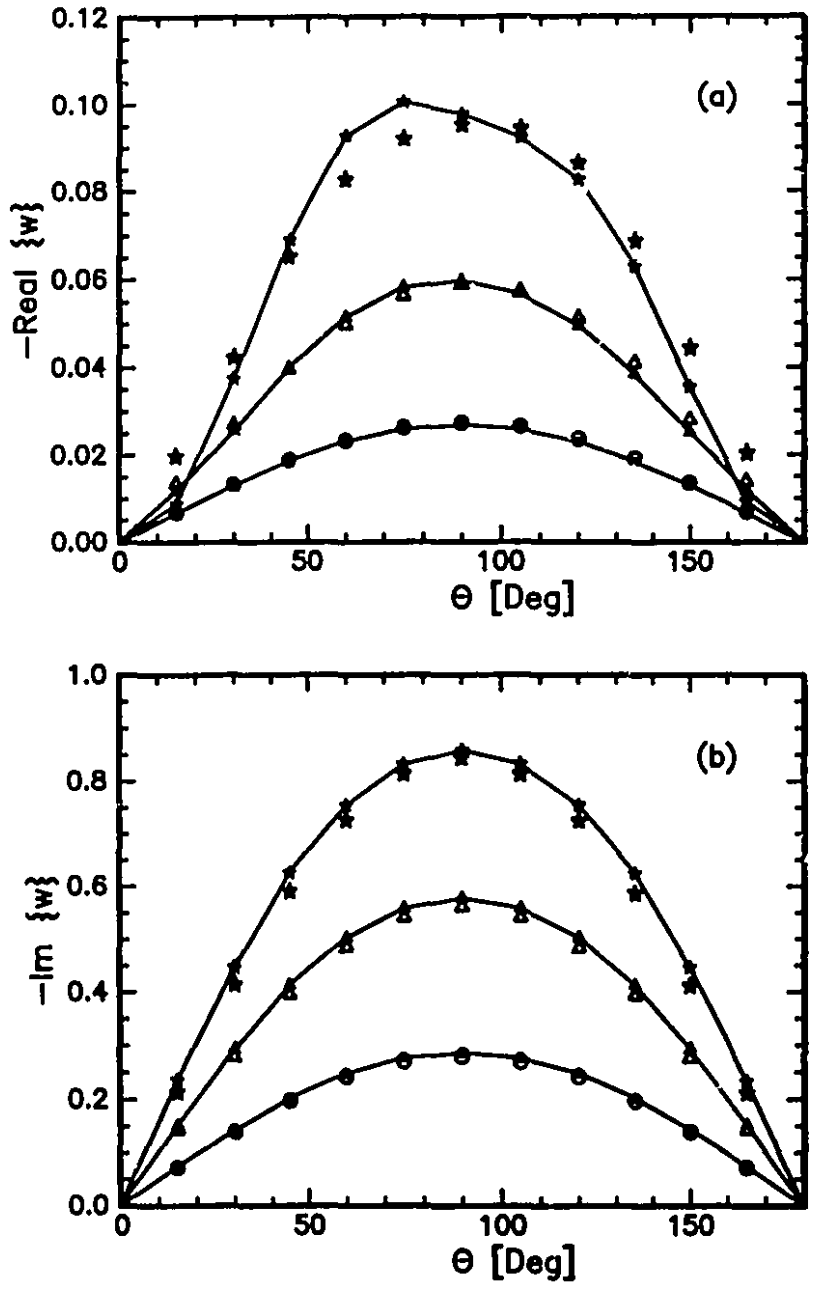

Figure 6.7: Azimuthal (θ-) variation of the real and imaginary components of circumferential velocity, w, at mid gap, for three values of ϵ; o, $\epsilon = 0.05$; Δ, $\epsilon = 0.1$; $*$, $\epsilon = 0.15$. o,mean-position analysis; -•-,time-dependent-transformation analysis; the rest are similar.

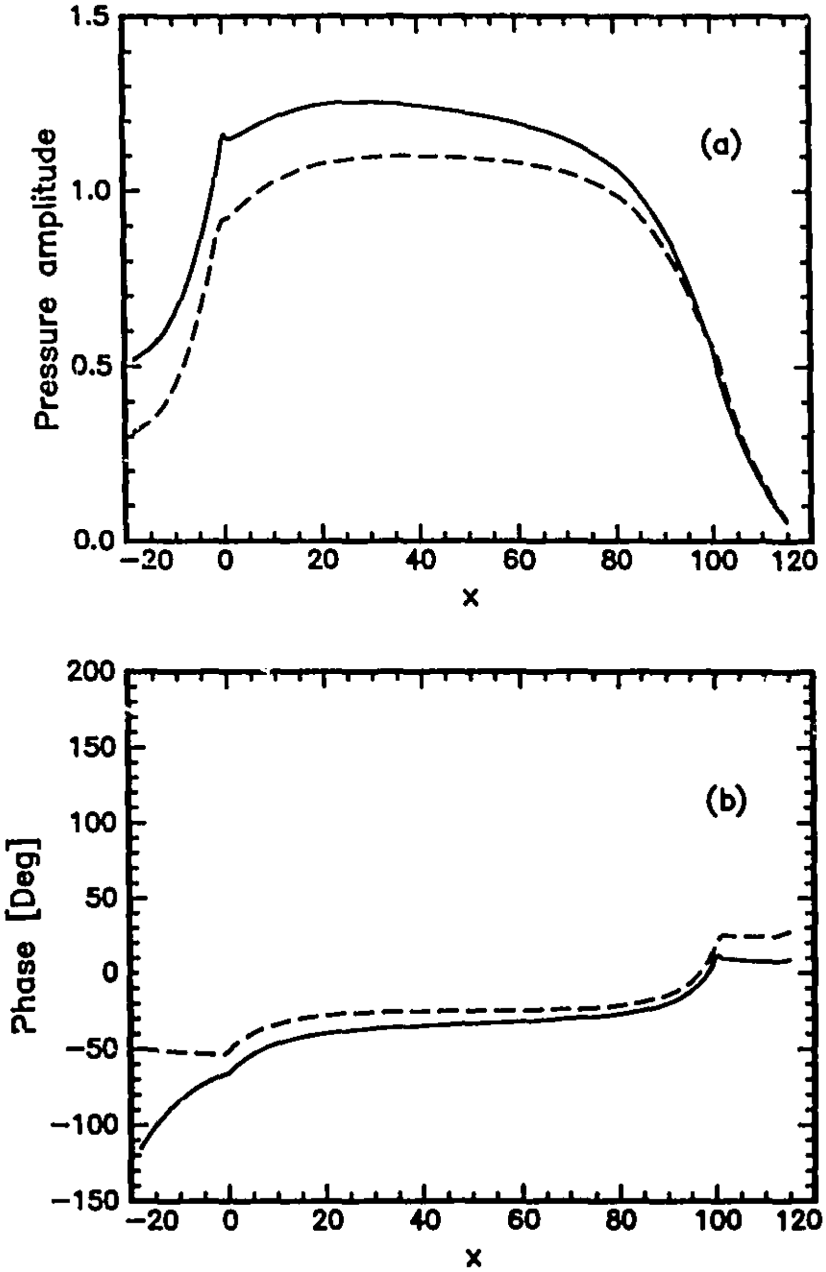

Figure 6.8: (a) Unsteady pressure and (b) phase angle for Re= 250, $\omega = 0.2$, $r_i = 9$, $r_o = 10$, $L_u = L_d = 20$, at $r = 9.965$, $\theta = 7.5^o$, with $\epsilon = 0.2$; —time-dependent-transformation analysis, - - -mean-position analysis.

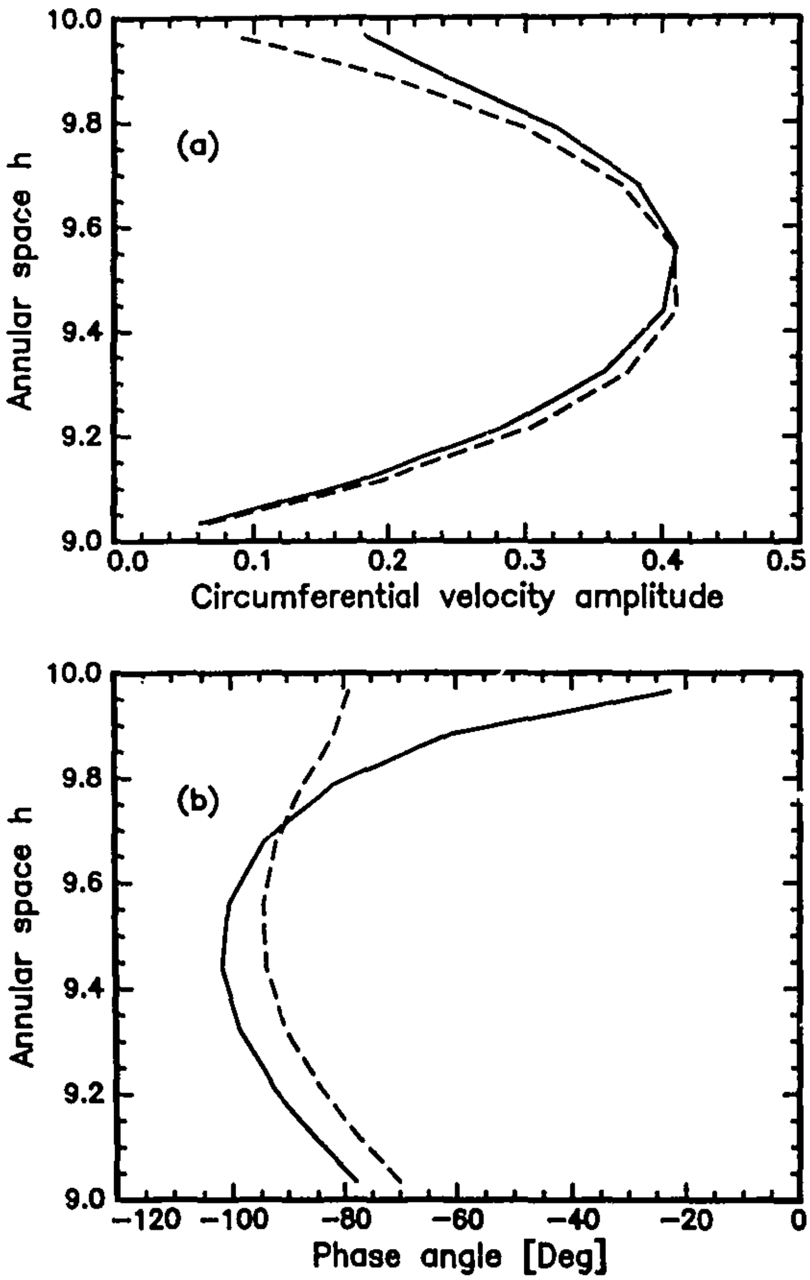

Figure 6.9: (a) Magnitude of circumferential velocity w and (b) phase angle with respect to the displacement of outer cylinder at mid gap, for Re= 250, $\omega = 0.2$, $r_i = 9$, $r_o = 10$, $L_u = L_d = 20$, and $\epsilon = 0.2$ at $X = 50$, $\theta = 45°$; —time-dependent-transformation analysis, - - -mean-position analysis.

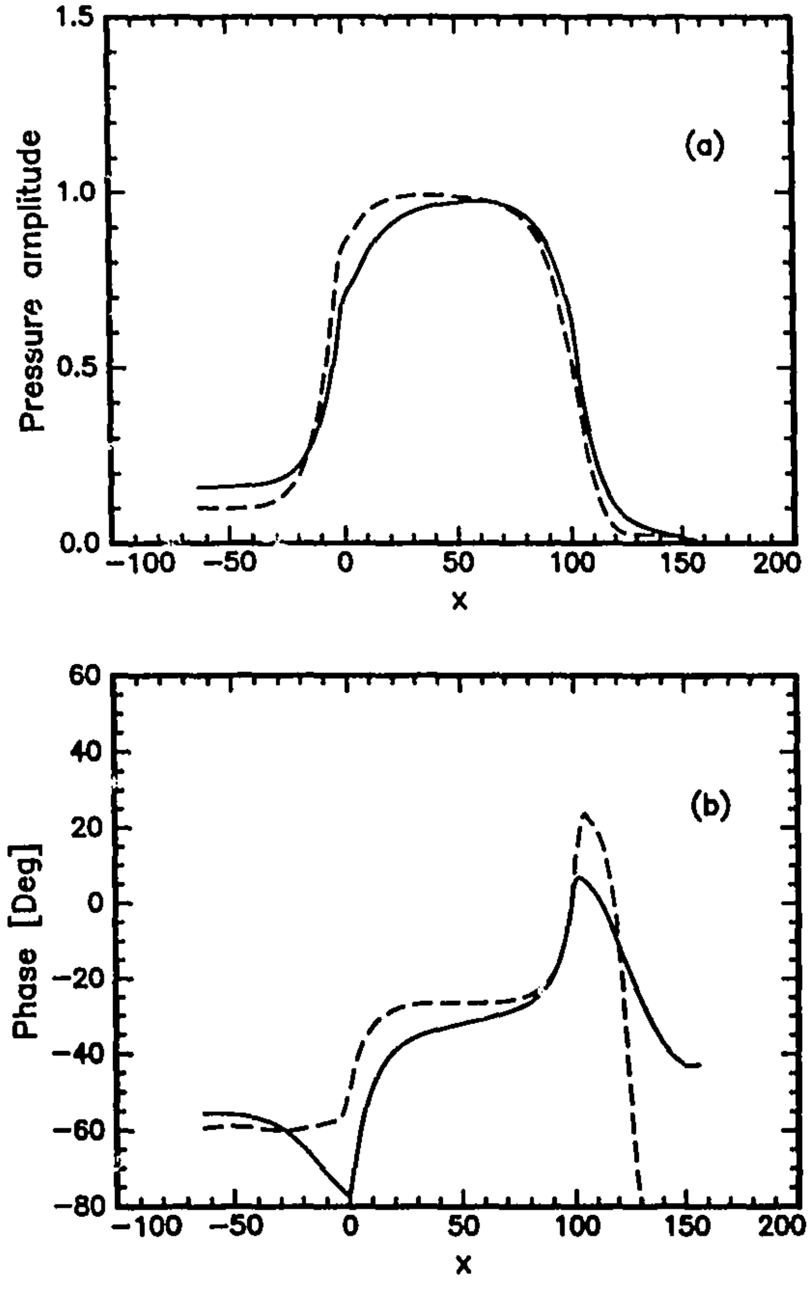

Figure 6.10: (a) Magnitude of unsteady pressure and (b) phase angle for Re= 250, $\omega = 0.2$, $r_i = 9$, $r_o = 10$, $L_u = L_d = 60$, at $r = 9.965$, $\theta = 7.5^\circ$, with $\epsilon = 0.2$; —time-dependent-transformation analysis, - - -mean-position analysis.

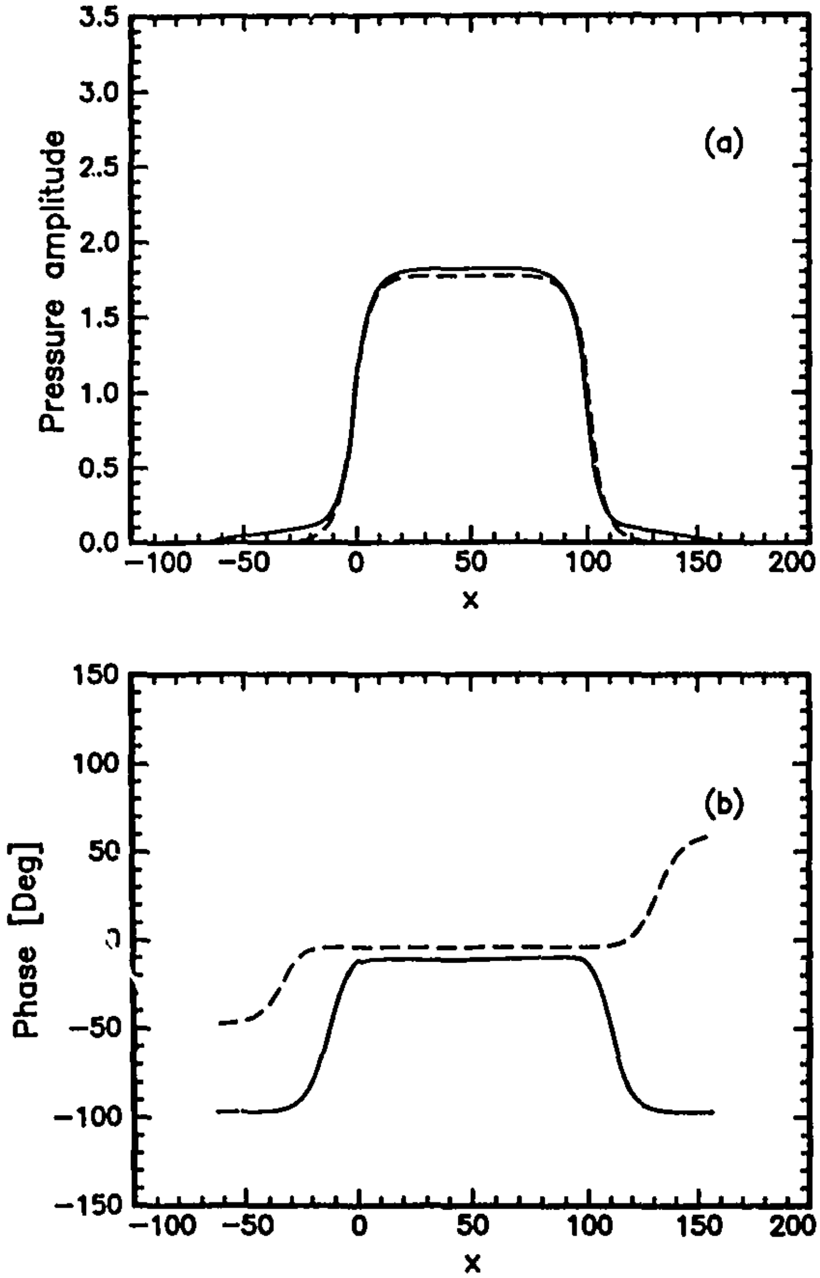

Figure 6.11: (a) Magnitude of unsteady pressure and (b) phase angle for quiescent fluid with $\omega = 1$ ($f = 20$ Hz), $r_i = 4.785$, $r_o = 5.785$, $\epsilon = 0.05375$, $L_u = L_d = 60$, at $r = 5.727$, $\theta = 7.5°$; —time-dependent-transformation analysis, - - -mean-position analysis.

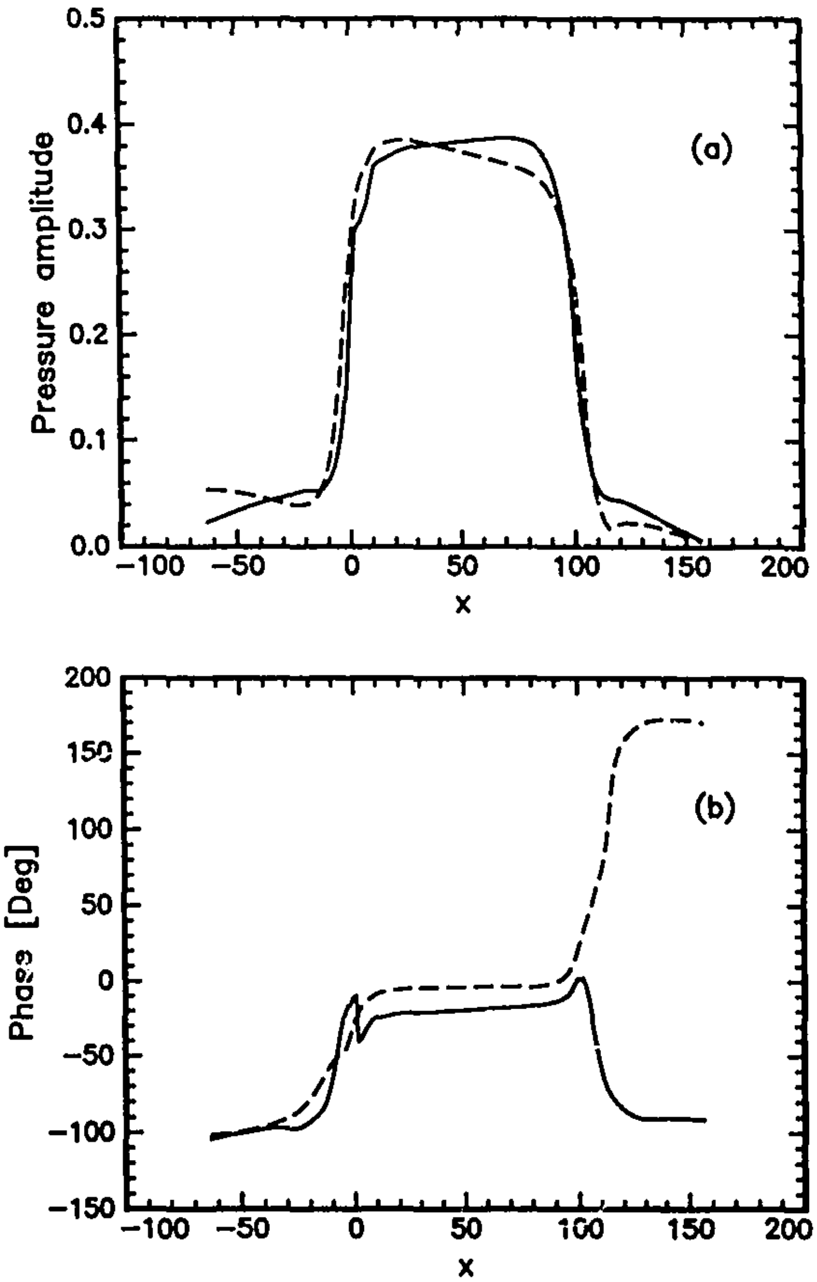

Figure 6.12: (a) Magnitude of unsteady pressure and (b) phase angle for Re = 2900, $\omega = 0.463$ ($f = 20$ Hz), $r_i = 4.785$, $r_o = 5.785$, $\epsilon = 0.05375$, $L_u = L_d = 60$, at $r = 5.727$, $\theta = 7.5^o$; —time-dependent-transformation analysis, - - -mean-position analysis.

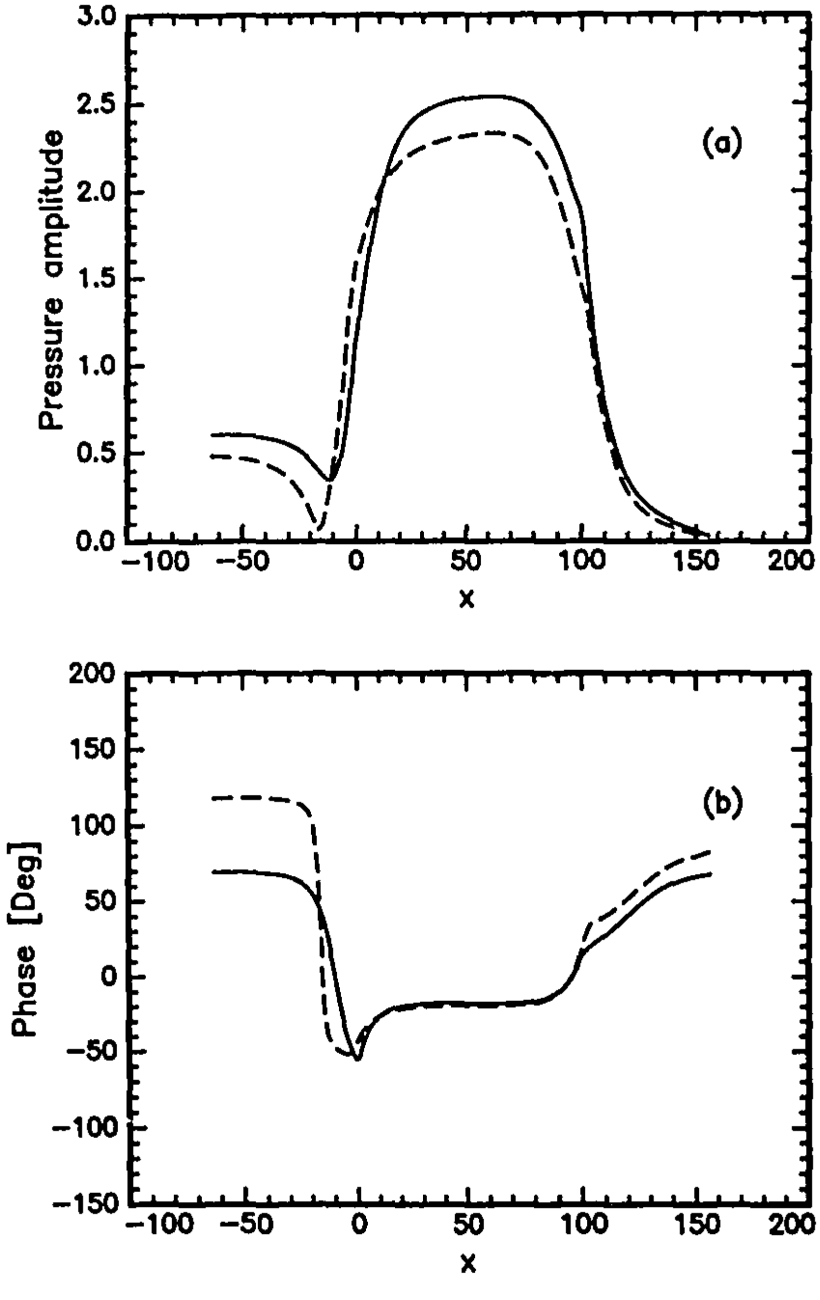

Figure 6.13: (a) Magnitude of unsteady pressure and (b) phase angle for Re = 250, $\omega = 0.2$, $r_i = 9$, $r_o = 10$, $\epsilon = 0.5$, $L_u = L_d = 60$, at $r = 9.965$, $\theta = 7.5°$; —time-dependent-transformation analysis, - - -mean-position analysis .

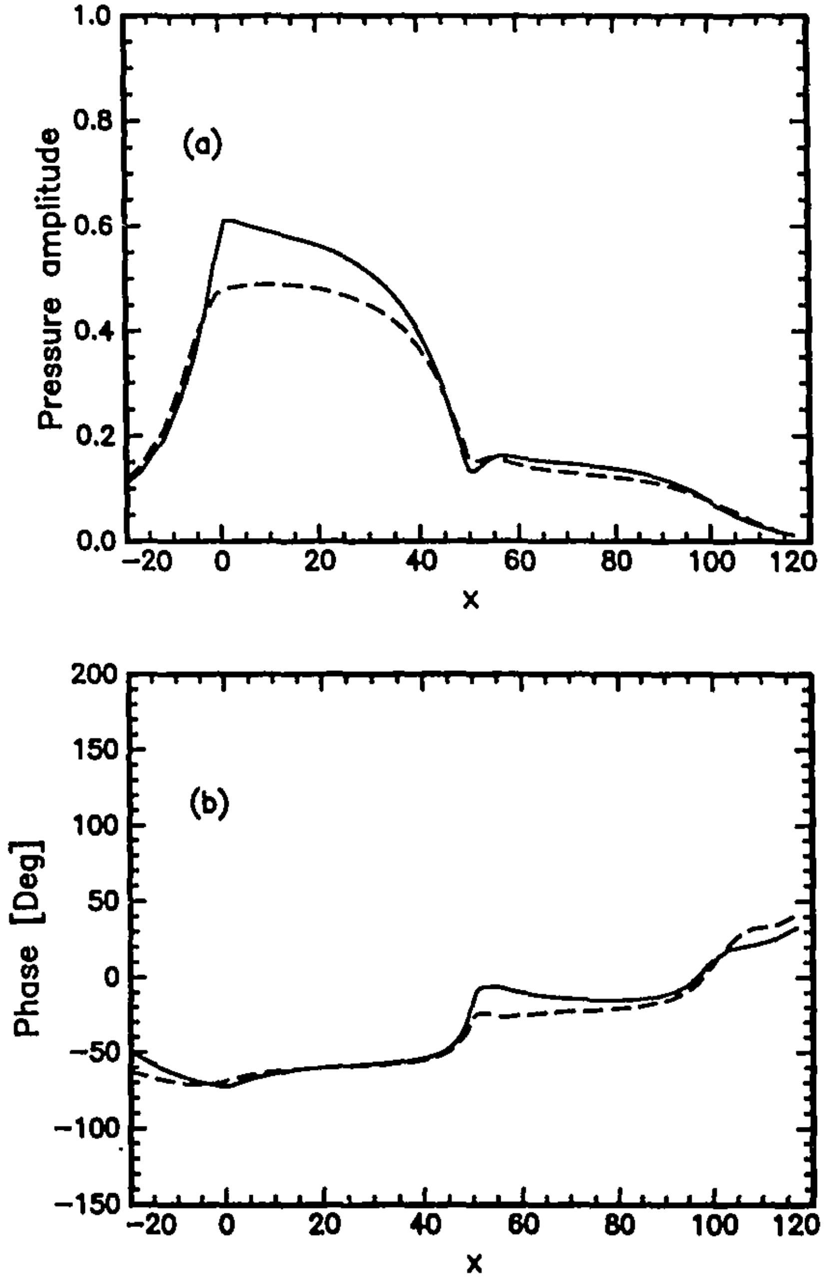

Figure 6.14: (a) The unsteady pressure and (b) phase angle in annulus with backstep geometry for Re = 100, $\omega = 0.1$, $r_{id} = 8$, $r_o = 10$, $L = 100$, $L_u = L_d = 20$, at $r = 9.942$, $\theta = 7.5^o$, with $\epsilon = 0.2$; —time-dependent-transformation analysis, - - -mean-position analysis.

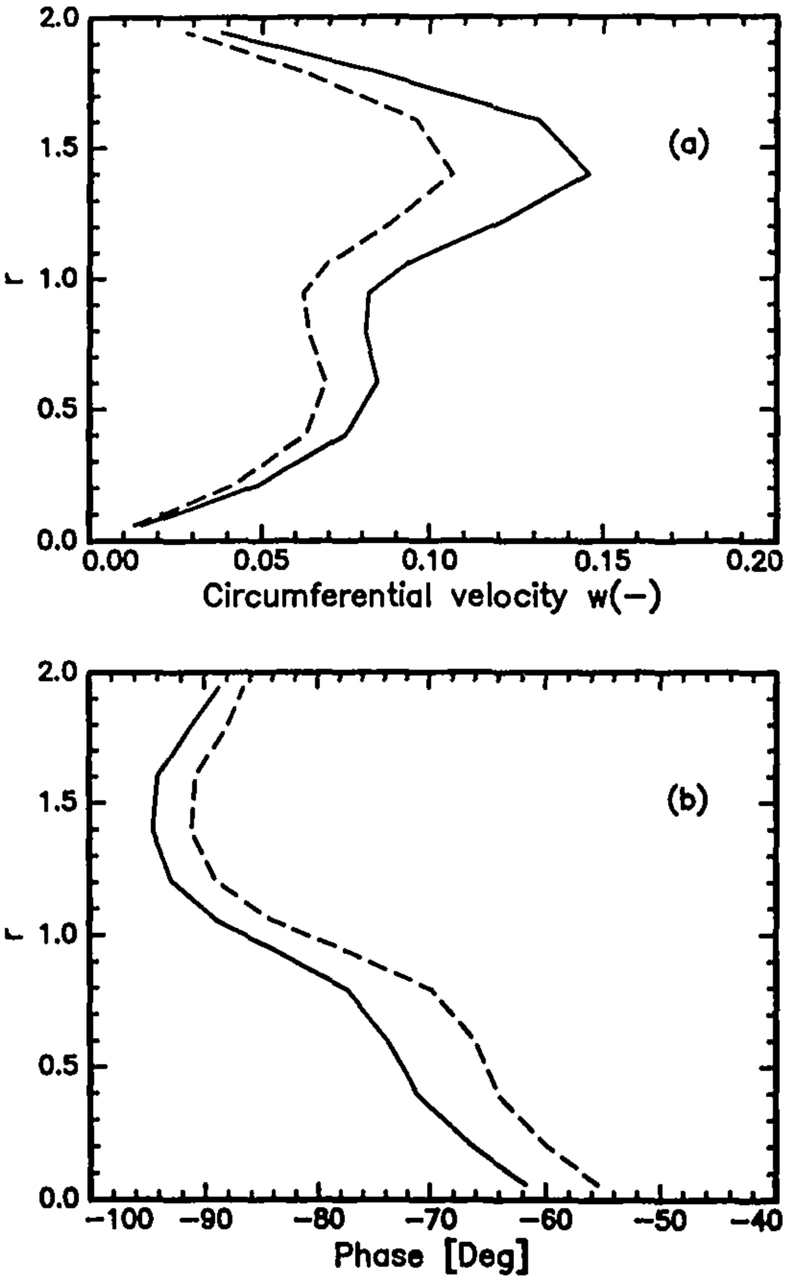

Figure 6.15: (a) Magnitude of circumferential velocity w and (b) phase angle at mid gap, in annulus with backstep geometry for Re = 100, $\omega = 0.1$, $r_{id} = 8$, $r_o = 10$, $L = 100$, $L_u = L_d = 20$, and $\epsilon = 0.2$ at $X = 50.816$, $\theta = 45°$; —time-dependent-transformation analysis, - - -mean-position analysis.

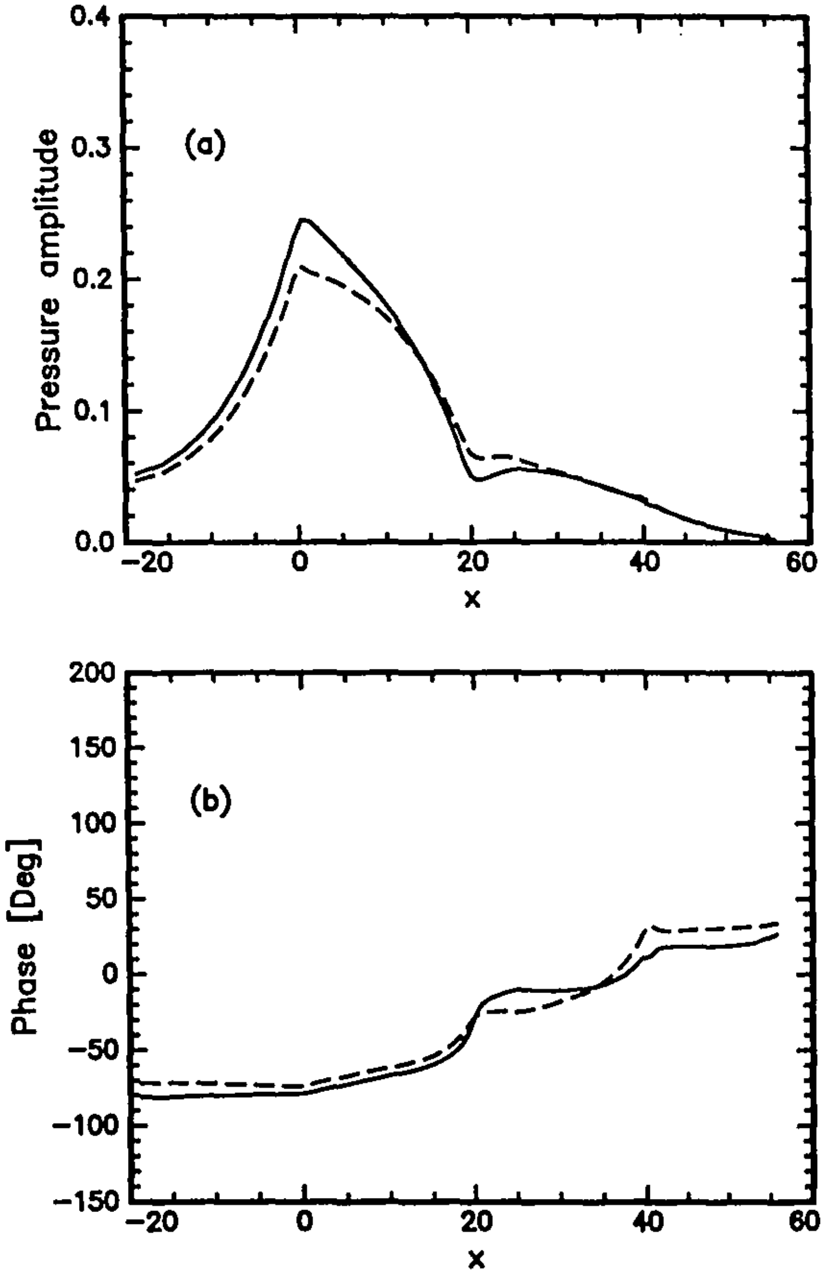

Figure 6.16: (a) The unsteady pressure and (b) phase angle in annulus with backstep geometry for Re = 100, $\omega = 0.1$, $r_{id} = 8$, $r_o = 10$, $L = 40$, $L_u = L_d = 20$, at $r = 9.942$, $\theta = 7.5^o$, with $\epsilon = 0.1$; —time-dependent-transformation analysis, - - -mean-position analysis.

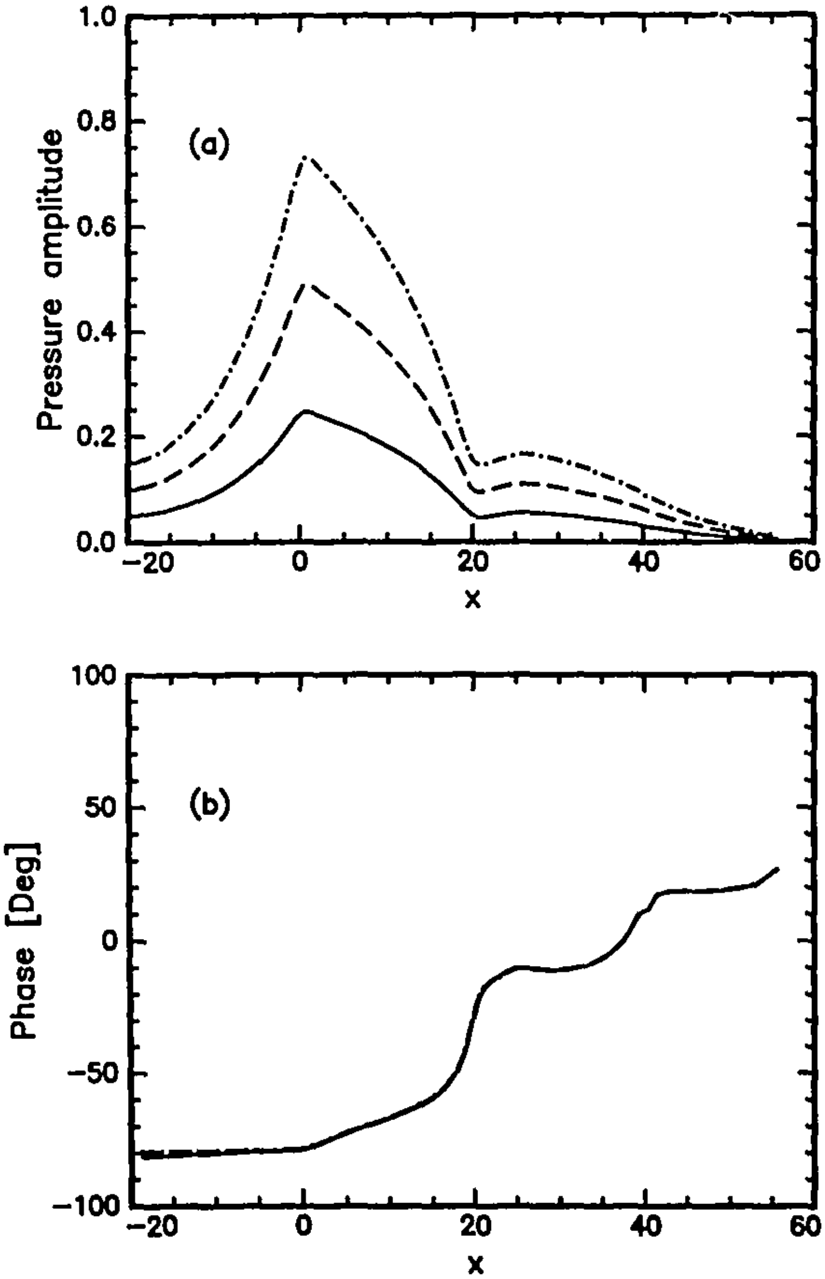

Figure 6.17: (a) The unsteady pressure and (b) phase angle in annulus with backstep geometry for Re = 100, ω = 0.1, r_{id} = 8, r_o = 10, L = 40, L_u = L_d = 20, at $r = 9.942$, $\theta = 7.5^o$; —$\epsilon = 0.1$, - - -$\epsilon = 0.2$, and —·—$\epsilon = 0.3$.

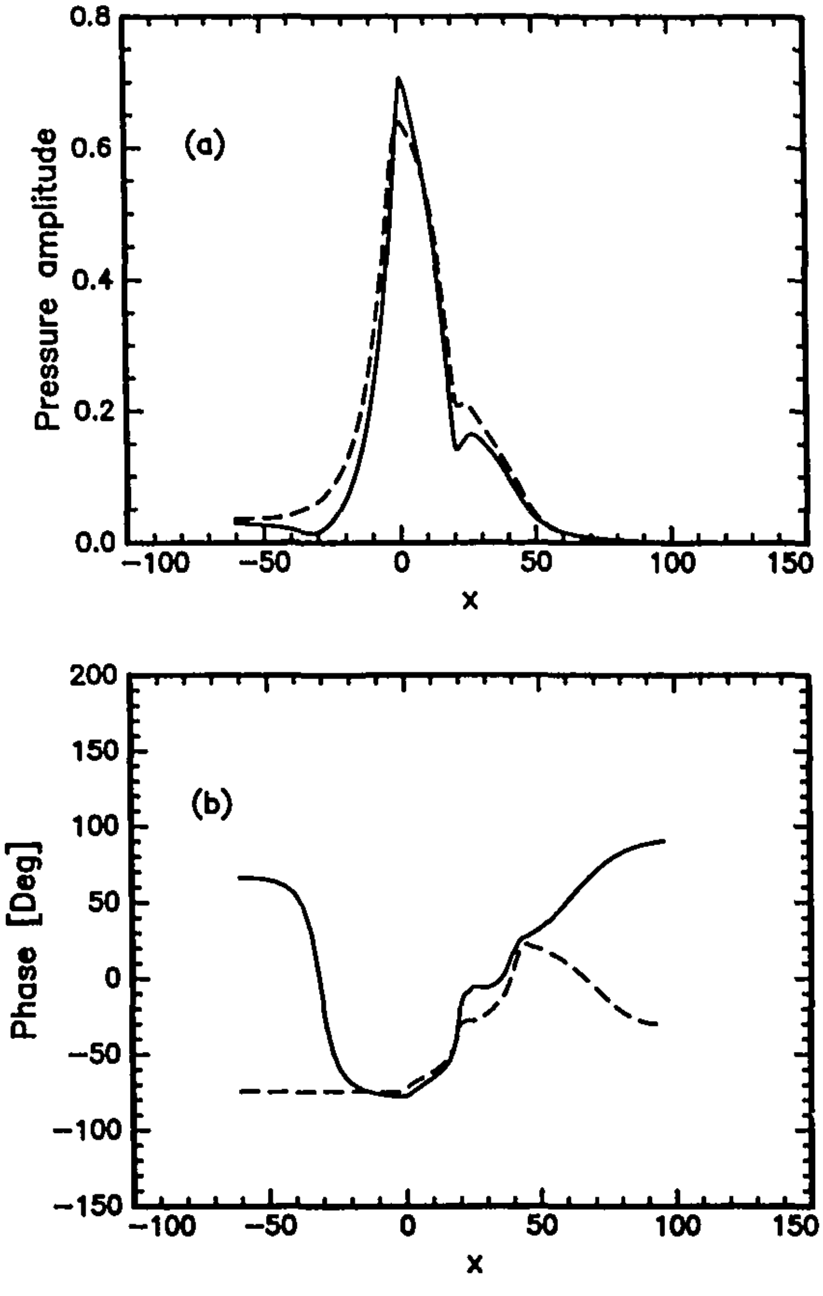

Figure 6.18: (a) The unsteady pressure and (b) phase angle in annulus with backstep geometry for Re = 100, $\omega = 0.1$, $r_{id} = 8$, $r_o = 10$, $L = 40$, $L_u = L_d = 60$, at $r = 9.942$, $\theta = 7.5^o$, with $\epsilon = 0.3$; —time-dependent-transformation analysis, - - -mean-position analysis.

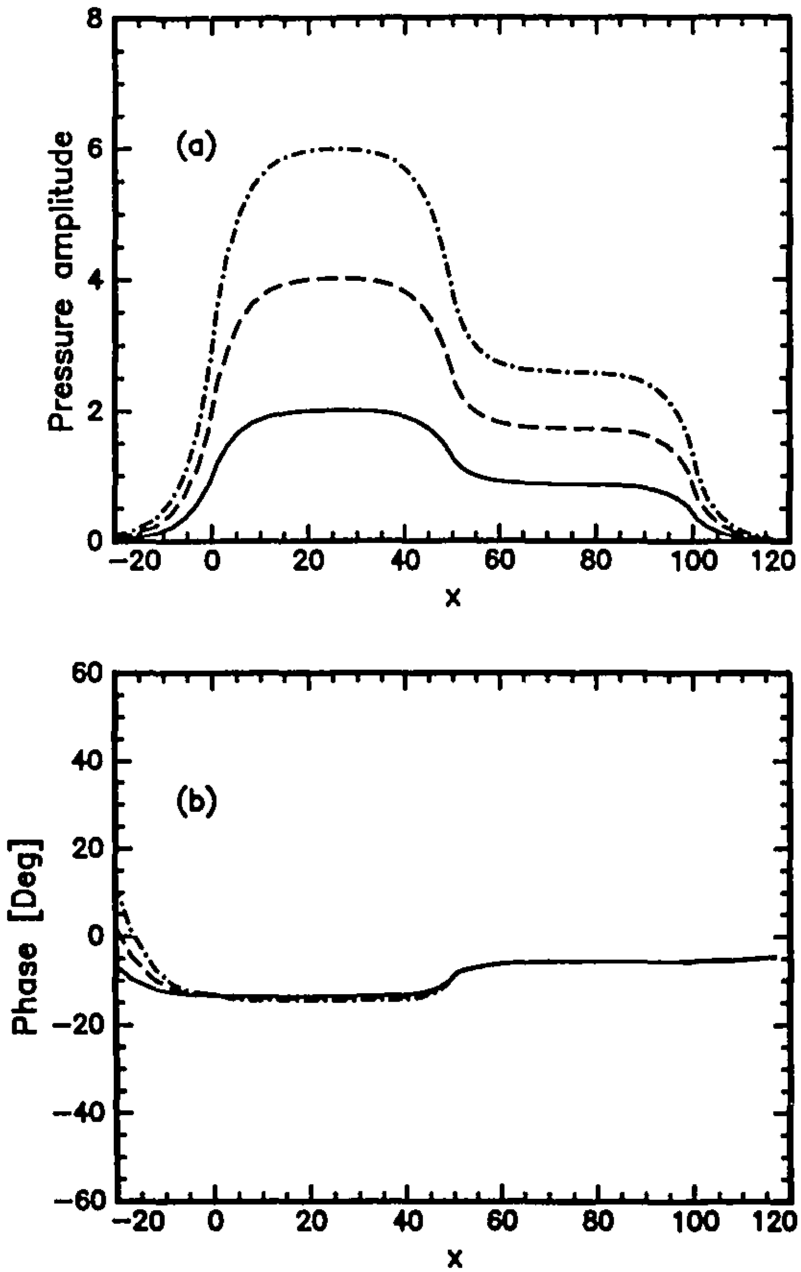

Figure 6.19: (a) The unsteady pressure and (b) phase angle in annulus with backstep geometry for Re = 100, $\omega = 1$ (f = 1.5 Hz), $r_{id} = 3.785$, $r_o = 5.785$, $L = 100$, $L_u = L_d = 20$, at $r = 5.727$, $\theta = 7.5°$; —$\epsilon = 0.05375$, - - -$\epsilon = 0.1$, and —·—$\epsilon = 0.16125$.

Chapter 7

Convergence Tests and Accuracy of the Numerical Model

To make sure that the numerical approach used works properly, the numerical results presented in the previous chapters must be compared with either analytical or experimental results for the specific problems treated in this Thesis.

Unfortunately, due to the complexity of the Navier-Stokes equations which are fully nonlinear, no complete analytical solution exists for these equations, even for the simple laminar annular flows considered in this Thesis. The analytical solutions available in the literature are either potential flow solutions or approximate viscous flow solutions which lack the accuracy required as compared to the complete solution for the N-S equations. This is why in this Thesis the experimental investigation was selected as the main measure for validating the numerical results. It is shown in Chapter 8 that the experimental results obtained confirm the numerical results. But, still one needs to check by other means to what extent these results are reliable.

To ensure that the model used in this Thesis is accurate enough for different important factors such as the spacing of the grid points in the different meshes used and also in terms of various values of the time difference Δt, a number of convergence tests have been conducted. In addition the validation of the method of solution was checked by comparing the analytical solution for a bench-mark problem of oscillating plate in a confined fluid with the numerical solution obtained for such a problem by using the method presented in this Thesis.

To this end, a uniform annular space was chosen as the "test case", and the solutions were obtained for 2- and 3-D annular flows. In what follows, for the 2-D analysis, the number of grid points in the r- and/or θ-direction is changed to investigate the effect of the number of grid points in both directions on the numerical results. Calculations here, as for all parts of this Thesis, were carried out on a 486 PC, 50 MHz for the 2-D analysis; on 286 PC computer equipped with an Alacron board, to increase the speed of computation, for the 3-D analysis. In the 3-D analysis, due to the limitations of computer space and also the CPU time for the finer meshes, only one mesh, *i.e.*, $65 \times 12 \times 15$ in the x-, r- and θ-directions was used while the number of time-steps, N, were changed from $N = 10$ to $N = 70$ in order to check the convergence and accuracy of the solutions *vis-à-vis* the number of Δt. To perform the same convergence test in 2-D analysis, the mesh chosen was 12×15 in the r- and θ-directions with the same range of N as in the 3-D analysis. Also, the amplitude of oscillation $\epsilon = 0.1$, the Reynolds number Re $= 62.5$, and the Stokes number $S = 31.25$ for 2-D tests; Re $= 250$ and $S = 25$ for 3-D tests.

The effect of the number of grid points for 2-D analysis is shown in Table 7.1. The results presented in this table are for Re $= 62.5$, $S = 31.25$ and $\epsilon = 0.1$. The first part of the table shows the effect of increasing the number of grid points in the r-direction, J, while keeping the number of grid points in the θ-direction constant at $K = 15$: the second part of the table shows the effect of increasing K while keeping $J = 20$. Table 7.1 indicates that there is about a 0.2% difference between the results of the unsteady pressure amplitude for the mesh that consists of 12×15 grid points in r- and θ-directions *vis-à-vis* the meshes having 30×15 or 20×30 grid points in those directions. Thus, the mesh with 12×15 grid points was used throughout, since it provides accurate results as well as faster computation.

In the course of this study, the major factors which could be used to investigate the accuracy of the results, especially in the 2-D analysis, were the real and imaginary parts of the unsteady pressure obtained, which are compared with the results obtained by Mateescu *et al.* 1994, using spectral collocation method. The results of their approaches compared with the present results are shown in Table 7.2. The reliability of the results of the present method has also been checked against the results obtained for the unsteady forces by Chen *et al.* 1976, and by Mateescu *et al.* 1994, as shown in Table 7.3. The results shown in Table 7.3 are the real and imaginary parts of the unsteady force acting on the moving cylinder. These parameters which are related to the added-mass and added damping of the fluid, have been obtained as a closed form solution confirmed by experiment (Chen *et al.* 1976). As one can see, the agreement between the present results based on the full nonlinear solution of the N-S equations and the other, earlier results based on approximate solutions is good.

Another important factor affecting the stability and convergence of the numerical solution is the number of iteration steps taken between each sequential real-time step. A sample of such convergence criteria which consists of the rms values of the residual of the momentum and continuity equations is shown in Table 7.4 for the 2-D analysis and in Table 7.5 for the 3-D approach. For the 2-D analysis, the maximum CPU time is 35 seconds for three harmonic cycles to obtain a steady-state solution and for the 3-D analysis the CPU time is 45 minutes for the same number of harmonic cycles on the computers mentioned previously, when we consider the number of time-steps $N = 19$. The number of iterations shown in Table 7.4 and 7.5 indicate how fast the solution converges which obviously also depends on the selection of the compressibility factor δ and the pseudo-time step $\Delta\tau$. Based on these results, the calculations presented in this Thesis were done for $N = 19$ for the 2-D and 3-D analyses.

One of the major factors influencing the accuracy and the speed of convergence of the solution is the real-time step Δt. This factor can be chosen in such a way as to (i) achieve convergence, and (ii) to obtain acceptable results, which compare well with the results cited in the literature as well as experimental results; at the same time, keeping with constraints imposed by computer limitations, in terms of space and CPU time of the fastest PC computers available to us. Thus, a comparison is made between the amplitude of the unsteady pressure obtained for different values of N (number of time steps), which is shown in Table 7.6 and Figure 7.1(a) for the 2-D analysis. From Figure 7.1(a), it is clear that as the number of time steps increases, the unsteady pressure amplitude approaches its minimum value and then increases for larger N. However, the difference between the values obtained with $N = 19$ and $N = 70$ is less than 10%.

It must also be mentioned that the convergence tests as mentioned above were also carried out for the time-dependent-coordinate-transformation analysis; the same conclusions as discussed above were reached for the selection of the number of time steps as well as the effect of the mesh size on the results. The major difference is that, when Δt decreases the amount of time for the computation and the space on the computer increase significantly, which are not justified when the difference between the results for $N = 19$ and $N = 70$ is less than 4% for this analysis, as shown in Figure 7.1(b).

Once again, a comparison of the pressures for different numbers of time-steps indicates a better realiability of the results obtained by the time-dependent-coordinate-transformation approach *vis-à-vis* the mean-position analysis.

Also, by looking at Table 7.7 which shows the rms values of the residual of the momentum and continuity equations for a larger number of time steps, $N = 70$, one notices that the number of iterations for all sequences of the real-time steps are reduced appreciably for $N = 70$, as compared to that for $N = 19$ of Table 7.4. This shows that the numerical model converges faster for the mean-position analysis as the time step Δt becomes smaller, which is obvious from the point of view of the data transfer between two real times t^n and t^{n+1}.

For the two analyses, a smaller value for Δt has its own drawback, *i.e.*, it necessitates a larger number of computations and hence implies larger round-off errors, in addition to the increases in time and memory on the computer. For the reasons mentioned and by considering Table 7.2, the number of Δt, *i.e.*, N, which gives accurate results comparable with the theoretical and experimental results (see Chapter 8) and yet remains economically feasible was chosen to be $N = 19$.

Table 7.8 is similar to Table 7.5 but it is for the 3-D analysis with $N = 70$. Once again, the rms values shown here indicate the faster computation, but by looking at Table 7.9 and Figure 7.2(a) one notices that the minimum value occurs around $15 \leq N \leq 30$. Once again, the difference between the pressure values for $N = 19$ and $N = 70$ is about 2%. In the case of a time-dependent-coordinate transformation for the 3-D analysis, the results of the convergence test are shown in Table 7.10 and Figure 7.2(b), with the discrepancy between p_{19} and p_{70} less than 3%. Thus, we have chosen $N = 19$ for the 3-D analysis too.

Finally, to be able to compare the present theoretical results based on the full nonlinear N-S equations with Bélanger's (1991) results, as shown in Figure 4.14, the number of time steps must be $N = 19$.

In another attempt to check the accuracy of the numerical solution, the length of the fixed upstream and downstream portions was increased for just one of the several cases studied (*i.e.*, for the uniform annular geometry) to see the effect of more extended portions on the unsteady pressure obtained and on the values of the pressure perturbation outside the domain of oscillation. It is recalled from Chapters 4 and 6 that for no flow, the perturbation goes to zero at both fixed ends (see for example Figures 4.24, 4.33, 4.35, 4.38, 6.11 and 6.19). But in the case of flow, the perturbations have not vanished, specially at the upstream portions, in almost all cases studied. The following describes this problem and the way it can be solved.

In a confined flow, such as the annular flow under consideration, we have used a staggered grid to solve the N-S equations. As explained in Chapter 4, using a staggered grid we must impose two boundary conditions at the inlet, such as the velocities, and one at the outlet, such as the pressure. At the inlet the pressure is calculated automatically by the numerical calculations, and there we have no control over this variable once the outlet pressure has been specified (for instance, zero). This is the drawback of using a staggered grid. The calculation of the dependent variables starts from grid points $I = 2$ to $N - 1$, where N is the last grid point in the x-direction. Once the unsteady pressure generated by the oscillating cylinder, in the vicinity of the upstream section, propagates outside of the domain of oscillation it does not change until it vanishes by viscous dissipation which would exist if we have the unsteady velocities along the fixed portions. But if we look at Figure 7.3, the velocity perturbations v and w, from which the shear stresses are calculated, are zero along the fixed portions and u approaches its steady value imposed as an initial condition for the unsteady solution; hence, no viscous dissipation exists and the pressure waves which are shown in the figures presented in this Thesis remain unchanged once they are calculated from the continuity and momentum equations in the x-direction. These perturbations, which are partly numerical, can be reduced to an acceptable level through the use of appropriate lengths for the fixed portions and an appropriate mesh spacing in the x-direction. The results of this study are shown in Figure 7.4 which were obtained for Re = 250, $S = 25$, $\epsilon = 0.1$, $L_1 = L_2 = 20$, 60, 100, 200 and 300.

Figure 7.4 demonstrates that the problem of pressure-wave propagation can be solved by choosing as long a length for the fixed portions as possible. Thus, increasing the length of the fixed portions affects the unsteady pressure reduction over the fixed portions as well as the unsteady pressure in the oscillating domain. It must be stressed that for all the results presented in the Thesis, the accuracy of the results, the amount of time for computation and the space available on the computer were all factors determining the solutions that could be obtained; they are conflicting factors and were selected by compromise.

Finally and equally important, the accuracy of the model utilized in this analysis was also checked by comparing the results obtained analytically for a 2-D unsteady problem (as a benchmark problem) with the numerical results obtained for the same problem. The unsteady problem selected is the unsteady flow between oscillating plates. We consider two infinite plates, parallel with each other and aligned with the x-coordinate. They are separated by a distance H. The top plate is fixed while the bottom one has a harmonic oscillatory motion of frequency Ω:

$$\overline{u}(\overline{y},\overline{t})\big|_{y=0} = \Omega H \sin \Omega \overline{t} \ ,$$

$$\overline{u}(\overline{y},\overline{t})\big|_{y=H} = 0 \ ,$$

where barred quantities are dimensional. H and ΩH serve as characteristic length and velocity to non-dimensionalize the equations, and Stokes number $S = \Omega H^2/\nu$.

The analytical solution for this problem is given by

$$u(y,t) = \mathrm{Im}\left\{F(y)e^{it}\right\} \ , \qquad\qquad F(y) = \frac{\sinh \beta(1-y)}{\sinh \beta} \ ,$$

where Im denotes the imaginary part, $i = \sqrt{-1}$ and $\beta = \sqrt{iS}$.

The comparison between the analytical and numerical results is shown in Figure 7.5, where the solid lines indicate the analytical solution and symbols indicate the numerical solution. Figure 7.5 compares analytical and numerical results for $S = 1000$, number of grid points in y-direction $J = 26$ and number of time step $N = 19$. The results shown are for three instants of time $t^n = 2\pi n/19\omega$, $n = 1, 2, 10$. The discrepancies between the two sets of results close to the oscillating plate are due to the different types of meshes used. For the numerical computation, the stretched grid in the y-direction was used; while for the analytical solution, a uniform grid was used. Overall agreement between the analytical and numerical solutions is good.

Number of grid points	Real (p)	Imaginary (p)	Amplitude (p)
12 × 15	-2.22505	0.97697	2.43008
14 × 15	-2.22871	0.96784	2.42978
16 × 15	-2.22713	0.96783	2.42833
20 × 15	-2.22548	0.96844	2.42706
30 × 15	-2.22418	0.96782	2.42563
20 × 12	-2.23173	0.97148	2.43401
20 × 14	-2.23270	0.96915	2.43397
20 × 16	-2.23100	0.96916	2.43242
20 × 20	-2.22931	0.96917	2.43087
20 × 30	-2.22744	0.96957	2.42931

Table 7.1: Real, and Imaginary components of the pressure and the pressure amplitude obtained for various meshes; 2-D analysis for $\epsilon = 0.1$, Re $= 62.5$, $\omega = 1$ and at $r = 4.965$, $\theta = 7.5^o$.

Oscillatory	Present analysis		Mateescu *et al.* 1994	
Reynolds No.	Real	Imaginary	Real	Imaginary
31.25	5.57	2.42	5.52	2.17
3.125	6.19	19.36	5.59	19.60

Table 7.2: Real and imaginary parts of the unsteady pressure for different Reynolds numbers; 2-D analysis with $R_o/R_i = 1.25$, $\omega = 1$ and at $r = 4.965$, $\theta = 7.5^o$. The oscillatory Reynolds number 3.125 is equivalent to 50 in the analyses of Mateescu and Chen.

		Present solution		Mateescu *et al.* 1994		Chen *et al.* 1976	
R_o/R_i	S	Real{F}	-Im{F}	Real{F}	-Im{F}	Real{F}	-Im{F}
1.5	31.25	3.00	0.662	3.112	0.668	3.10	0.68
1.25	312.5	4.82	0.59	5.016	0.546	4.90	0.54

Table 7.3: The real and imaginary parts of the unsteady fluid-dynamic force obtained by the present solution, compared with those by Mateescu *et al.* 1994 and Chen *et al.* 1976. The oscillatory Reynolds number 31.25 is equivalent to 500 in the analyses of Mateescu and Chen.

n	k	rms (v)	rms (w)	rms (p)
3	34	0.9023E-04	0.2699E-04	0.4187E-05
4	39	0.5641E-04	0.1225E-04	0.9571E-06
5	38	0.8536E-04	0.1954E-04	0.3702E-06
6	37	0.8653E-04	0.1999E-04	0.1900E-06
7	35	0.8636E-04	0.1971E-04	0.8098E-07
8	33	0.5661E-04	0.1062E-04	0.1045E-05
9	32	0.7357E-04	0.2424E-04	0.3544E-05
10	38	0.9711E-04	0.2342E-04	0.1501E-06
11	39	0.7494E-04	0.1714E-04	0.3467E-06
12	39	0.7714E-04	0.1747E-04	0.4742E-06
13	39	0.7122E-04	0.1596E-04	0.5508E-06
14	38	0.9928E-04	0.2293E-04	0.3404E-06
15	38	0.7018E-04	0.1586E-04	0.3869E-06
16	36	0.9302E-04	0.2171E-04	0.8635E-07
17	34	0.6890E-04	0.1454E-04	0.3085E-06
18	32	0.7031E-04	0.1601E-04	0.2258E-05
19	38	0.8331E-04	0.2025E-04	0.2002E-06
20	39	0.7065E-04	0.1630E-04	0.2686E-06
21	39	0.7711E-04	0.1754E-04	0.4162E-06

Table 7.4: Number, k, of pseudo-time steps required for convergence at time level t^n, and rms values of residuals at convergence. The computations were performed at Re = 62.5, $S = 31.25$ and $N = 19$ for 2-D analysis.

n	k	rms (u)	rms (v)	rms (w)	rms (p)
3	78	0.1915E-04	0.5826E-04	0.8271E-04	0.9929E-04
4	53	0.2846E-04	0.6101E-04	0.8163E-04	0.9715E-04
5	50	0.2577E-04	0.6077E-04	0.8274E-04	0.9871E-04
6	46	0.2633E-04	0.5904E-04	0.7985E-04	0.9664E-04
7	50	0.2383E-04	0.5610E-04	0.7723E-04	0.9619E-04
8	50	0.2188E-04	0.5556E-04	0.7750E-04	0.9839E-04
9	48	0.1988E-04	0.5523E-04	0.7746E-04	0.9818E-04
10	43	0.1831E-04	0.5656E-04	0.7888E-04	0.9829E-04
11	36	0.1727E-04	0.5972E-04	0.7874E-04	0.9740E-04
12	30	0.2408E-04	0.7343E-04	0.7754E-04	0.9619E-04
13	34	0.3315E-04	0.7031E-04	0.7846E-04	0.9906E-04
14	43	0.2972E-04	0.6066E-04	0.7715E-04	0.9764E-04
15	46	0.2641E-04	0.6016E-04	0.7961E-04	0.9679E-04
16	48	0.2548E-04	0.6111E-04	0.8239E-04	0.9829E-04
17	50	0.2329E-04	0.5751E-04	0.7924E-04	0.9703E-04
18	49	0.2191E-04	0.5591E-04	0.7806E-04	0.9871E-04
19	46	0.1983E-04	0.5540E-04	0.7752E-04	0.9764E-04
20	39	0.1826E-04	0.5993E-04	0.8138E-04	0.9904E-04
21	32	0.1862E-04	0.6912E-04	0.8069E-04	0.9601E-04

Table 7.5: Number, k, of pseudo-time steps required for convergence at time level t^n, and rms values of residuals at convergence. The computations were performed at Re = 250, $S = 25$ and $N = 19$ for 3-D analysis.

Number of time-step, N	Real (p)	Imaginary (p)	Amplitude (p)
15	-2.15938	1.03546	2.39481
19	-2.22727	0.97147	2.42991
25	-2.30500	0.92527	2.48378
30	-2.35245	0.90596	2.52087
40	-2.41788	0.88718	2.57550
50	-2.46030	0.87861	2.61248
60	-2.48993	0.87430	2.63897
70	-2.51150	0.87148	2.65840

Table 7.6: Real, Imaginary and pressure amplitude obtained for various values of time-steps N; 2-D analysis for $\epsilon = 0.1$, Re = 62.5, $\omega = 1$ and at $r = 4.965$, $\theta = 7.5°$; mean-position analysis.

n	k	rms (v)	rms (w)	rms (p)
3	36	0.9951E-04	0.4380E-04	0.5805E-05
4	29	0.9827E-04	0.4329E-04	0.5737E-05
5	37	0.9628E-04	0.4233E-04	0.5612E-05
6	38	0.8941E-04	0.3926E-04	0.5203E-05
7	38	0.9421E-04	0.4149E-04	0.5499E-05
8	38	0.9793E-04	0.4310E-04	0.5712E-05
9	39	0.8862E-04	0.3890E-04	0.5158E-05
10	39	0.8974E-04	0.3949E-04	0.5233E-05
11	39	0.9052E-04	0.3983E-04	0.5280E-05
12	39	0.9043E-04	0.3980E-04	0.5269E-05
13	39	0.8954E-04	0.3932E-04	0.5212E-05
14	38	0.9977E-04	0.4386E-04	0.5809E-05
15	38	0.9703E-04	0.4270E-04	0.5656E-05
16	38	0.9322E-04	0.4101E-04	0.5433E-05
17	38	0.8882E-04	0.3908E-04	0.5176E-05
18	37	0.9505E-04	0.4185E-04	0.5541E-05
19	37	0.8873E-04	0.3902E-04	0.5167E-05
20	36	0.9219E-04	0.4051E-04	0.5371E-05
21	35	0.9477E-04	0.4168E-04	0.5519E-05
22	34	0.9498E-04	0.4178E-04	0.5538E-05
23	33	0.9279E-04	0.4083E-04	0.5408E-05
24	31	0.9925E-04	0.4366E-04	0.5783E-05
25	30	0.8896E-04	0.3913E-04	0.5183E-05
26	27	0.9276E-04	0.4079E-04	0.5403E-05
27	23	0.9378E-04	0.4126E-04	0.5469E-05
28	16	0.8020E-04	0.3176E-04	0.4323E-05
29	17	0.8366E-04	0.3514E-04	0.4534E-05
30	25	0.9096E-04	0.3998E-04	0.5297E-05
31	28	0.8798E-04	0.3874E-04	0.5132E-05
32	30	0.9361E-04	0.4114E-04	0.5453E-05
33	32	0.9147E-04	0.4025E-04	0.5334E-05
34	33	0.9608E-04	0.4226E-04	0.5603E-05
35	34	0.9806E-04	0.4313E-04	0.5716E-05
36	35	0.9721E-04	0.4276E-04	0.5667E-05
37	36	0.9437E-04	0.4156E-04	0.5507E-05
38	37	0.9028E-04	0.3973E-04	0.5266E-05
39	37	0.9690E-04	0.4258E-04	0.5644E-05
40	38	0.9042E-04	0.3975E-04	0.5271E-05

Table 7.7: Number, k, of pseudo-time steps required for convergence at time level t^n, and rms values of residuals at convergence. The computations were performed at Re $= 62.5$, $S = 31.25$ and $N = 70$ for 2-D analysis (continued on next page).

n	k	rms (v)	rms (w)	rms (p)
41	38	0.9461E-04	0.4158E-04	0.5511E-05
42	38	0.9847E-04	0.4325E-04	0.5731E-05
43	39	0.8908E-04	0.3914E-04	0.5185E-05
44	39	0.9049E-04	0.3982E-04	0.5276E-05
45	39	0.9159E-04	0.4032E-04	0.5344E-05
46	39	0.9189E-04	0.4048E-04	0.5360E-05
47	39	0.9156E-04	0.4027E-04	0.5333E-05
48	39	0.9037E-04	0.3974E-04	0.5263E-05
49	39	0.8831E-04	0.3888E-04	0.5151E-05
50	38	0.9752E-04	0.4287E-04	0.5680E-05
51	38	0.9400E-04	0.4132E-04	0.5473E-05
52	38	0.8929E-04	0.3927E-04	0.5199E-05
53	37	0.9546E-04	0.4199E-04	0.5563E-05
54	37	0.8902E-04	0.3915E-04	0.5185E-05
55	36	0.9253E-04	0.4067E-04	0.5388E-05
56	35	0.9502E-04	0.4176E-04	0.5534E-05
57	34	0.9530E-04	0.4191E-04	0.5552E-05
58	33	0.9306E-04	0.4093E-04	0.5421E-05
59	31	0.9950E-04	0.4380E-04	0.5797E-05
60	30	0.8921E-04	0.3923E-04	0.5196E-05
61	27	0.9297E-04	0.4088E-04	0.5417E-05
62	23	0.9416E-04	0.4143E-04	0.5491E-05
63	16	0.8076E-04	0.3207E-04	0.4364E-05
64	17	0.8294E-04	0.3488E-04	0.4498E-05
65	25	0.9078E-04	0.3991E-04	0.5288E-05
66	28	0.8794E-04	0.3870E-04	0.5128E-05
67	30	0.9352E-04	0.4112E-04	0.5450E-05
68	32	0.9143E-04	0.4023E-04	0.5332E-05
69	33	0.9594E-04	0.4226E-04	0.5602E-05
70	34	0.9803E-04	0.4312E-04	0.5715E-05
71	35	0.9722E-04	0.4275E-04	0.5666E-05
72	36	0.9437E-04	0.4155E-04	0.5507E-05

n	k	rms (u)	rms (v)	rms (w)	rms (p)
3	62	0.9039E-05	0.1355E-04	0.3517E-04	0.9985E-04
4	12	0.4976E-04	0.9173E-04	0.3050E-04	0.7272E-04
5	48	0.1970E-04	0.1613E-04	0.3483E-04	0.9891E-04
6	34	0.1075E-04	0.1515E-04	0.3523E-04	0.9971E-04
7	13	0.2303E-04	0.7633E-04	0.3164E-04	0.8793E-04
8	13	0.2948E-04	0.7965E-04	0.2963E-04	0.8096E-04
9	13	0.3083E-04	0.7808E-04	0.3076E-04	0.8375E-04
10	13	0.2959E-04	0.7382E-04	0.3374E-04	0.9257E-04
11	17	0.2226E-04	0.3662E-04	0.3529E-04	0.9901E-04
12	26	0.1818E-04	0.1851E-04	0.3454E-04	0.9856E-04
13	27	0.1715E-04	0.1618E-04	0.3492E-04	0.9994E-04
14	31	0.1417E-04	0.1443E-04	0.3458E-04	0.9911E-04
15	29	0.1186E-04	0.1406E-04	0.3451E-04	0.9914E-04
16	29	0.1118E-04	0.1404E-04	0.3469E-04	0.9989E-04
17	31	0.1158E-04	0.1390E-04	0.3448E-04	0.9948E-04
18	32	0.1251E-04	0.1393E-04	0.3417E-04	0.9875E-04
19	32	0.1328E-04	0.1408E-04	0.3445E-04	0.9958E-04
20	34	0.1305E-04	0.1391E-04	0.3458E-04	0.9997E-04
21	35	0.1222E-04	0.1369E-04	0.3439E-04	0.9944E-04
22	35	0.1155E-04	0.1354E-04	0.3434E-04	0.9935E-04
23	36	0.1106E-04	0.1344E-04	0.3414E-04	0.9887E-04
24	35	0.1108E-04	0.1358E-04	0.3429E-04	0.9937E-04
25	36	0.1103E-04	0.1359E-04	0.3412E-04	0.9902E-04
26	35	0.1105E-04	0.1372E-04	0.3400E-04	0.9879E-04
27	34	0.1116E-04	0.1395E-04	0.3422E-04	0.9947E-04
28	34	0.1109E-04	0.1407E-04	0.3428E-04	0.9969E-04
29	33	0.1094E-04	0.1420E-04	0.3417E-04	0.9940E-04
30	31	0.1106E-04	0.1467E-04	0.3439E-04	0.9997E-04
31	31	0.1094E-04	0.1474E-04	0.3420E-04	0.9938E-04
32	28	0.1119E-04	0.1561E-04	0.3441E-04	0.9981E-04
33	28	0.1115E-04	0.1585E-04	0.3411E-04	0.9884E-04
34	24	0.1187E-04	0.1813E-04	0.3458E-04	0.9988E-04
35	24	0.1214E-04	0.1890E-04	0.3461E-04	0.9972E-04
36	22	0.1259E-04	0.2153E-04	0.3425E-04	0.9853E-04
37	19	0.1441E-04	0.2950E-04	0.3445E-04	0.9894E-04
38	18	0.1608E-04	0.3370E-04	0.3470E-04	0.9946E-04
39	17	0.1768E-04	0.3817E-04	0.3459E-04	0.9907E-04
40	16	0.1957E-04	0.4321E-04	0.3431E-04	0.9825E-04

Table 7.8: Number, k, of pseudo-time steps required for convergence at time level t^n, and rms values of residuals at convergence. The computations were performed at Re = 250, $S = 25$ and $N = 70$ for 3-D analysis (continued on next page).

n	k	rms (u)	rms (v)	rms (w)	rms (p)
41	15	0.2219E-04	0.5036E-04	0.3465E-04	0.9900E-04
42	16	0.2151E-04	0.4405E-04	0.3479E-04	0.9893E-04
43	17	0.2040E-04	0.3852E-04	0.3496E-04	0.9936E-04
44	20	0.1788E-04	0.2745E-04	0.3452E-04	0.9843E-04
45	21	0.1673E-04	0.2336E-04	0.3469E-04	0.9902E-04
46	23	0.1544E-04	0.1934E-04	0.3468E-04	0.9901E-04
47	23	0.1478E-04	0.1849E-04	0.3477E-04	0.9928E-04
48	24	0.1434E-04	0.1728E-04	0.3492E-04	0.9986E-04
49	26	0.1395E-04	0.1595E-04	0.3487E-04	0.9999E-04
50	28	0.1365E-04	0.1500E-04	0.3451E-04	0.9934E-04
51	29	0.1360E-04	0.1456E-04	0.3431E-04	0.9915E-04
52	31	0.1331E-04	0.1415E-04	0.3412E-04	0.9894E-04
53	32	0.1295E-04	0.1384E-04	0.3414E-04	0.9920E-04
54	33	0.1262E-04	0.1375E-04	0.3439E-04	0.9992E-04
55	35	0.1209E-04	0.1351E-04	0.3416E-04	0.9916E-04
56	34	0.1199E-04	0.1357E-04	0.3433E-04	0.9928E-04
57	35	0.1192E-04	0.1363E-04	0.3457E-04	0.9945E-04
58	35	0.1186E-04	0.1373E-04	0.3482E-04	0.9955E-04
59	35	0.1173E-04	0.1386E-04	0.3500E-04	0.9943E-04
60	35	0.1152E-04	0.1389E-04	0.3499E-04	0.9886E-04
61	34	0.1145E-04	0.1407E-04	0.3516E-04	0.9895E-04
62	34	0.1130E-04	0.1417E-04	0.3518E-04	0.9885E-04
63	33	0.1121E-04	0.1429E-04	0.3518E-04	0.9889E-04
64	32	0.1121E-04	0.1456E-04	0.3520E-04	0.9920E-04
65	31	0.1125E-04	0.1488E-04	0.3518E-04	0.9955E-04
66	30	0.1123E-04	0.1518E-04	0.3498E-04	0.9949E-04
67	28	0.1142E-04	0.1582E-04	0.3496E-04	0.9996E-04
68	28	0.1126E-04	0.1589E-04	0.3430E-04	0.9868E-04
69	24	0.1189E-04	0.1797E-04	0.3447E-04	0.9954E-04
70	24	0.1218E-04	0.1872E-04	0.3435E-04	0.9954E-04
71	22	0.1264E-04	0.2115E-04	0.3401E-04	0.9885E-04
72	19	0.1448E-04	0.2886E-04	0.3432E-04	0.9992E-04

Number of time-step, N	Amplitude (p)
10	0.53847
15	0.51170
19	0.50559
25	0.50572
35	0.50732
45	0.51024
55	0.51266
65	0.51485
70	0.51577

Table 7.9: Pressure amplitude obtained for various values of time-step N; 3-D analysis at $r = 9.926$, $\theta = 7.5^{o}$ for $\epsilon = 0.1$, Re =.250 and $S = 25$; mean-position analysis.

Number of time-step, N	Amplitude (p)
10	0.56264
15	0.52960
19	0.51956
30	0.50961
70	0.50423

Table 7.10: Pressure amplitude obtained for various values of time-step N; 3-D analysis at $r = 9.926$, $\theta = 7.5^{o}$ for $\epsilon = 0.1$, Re = 250 and $S = 25$; time-dependent-coordinate-transformation analysis.

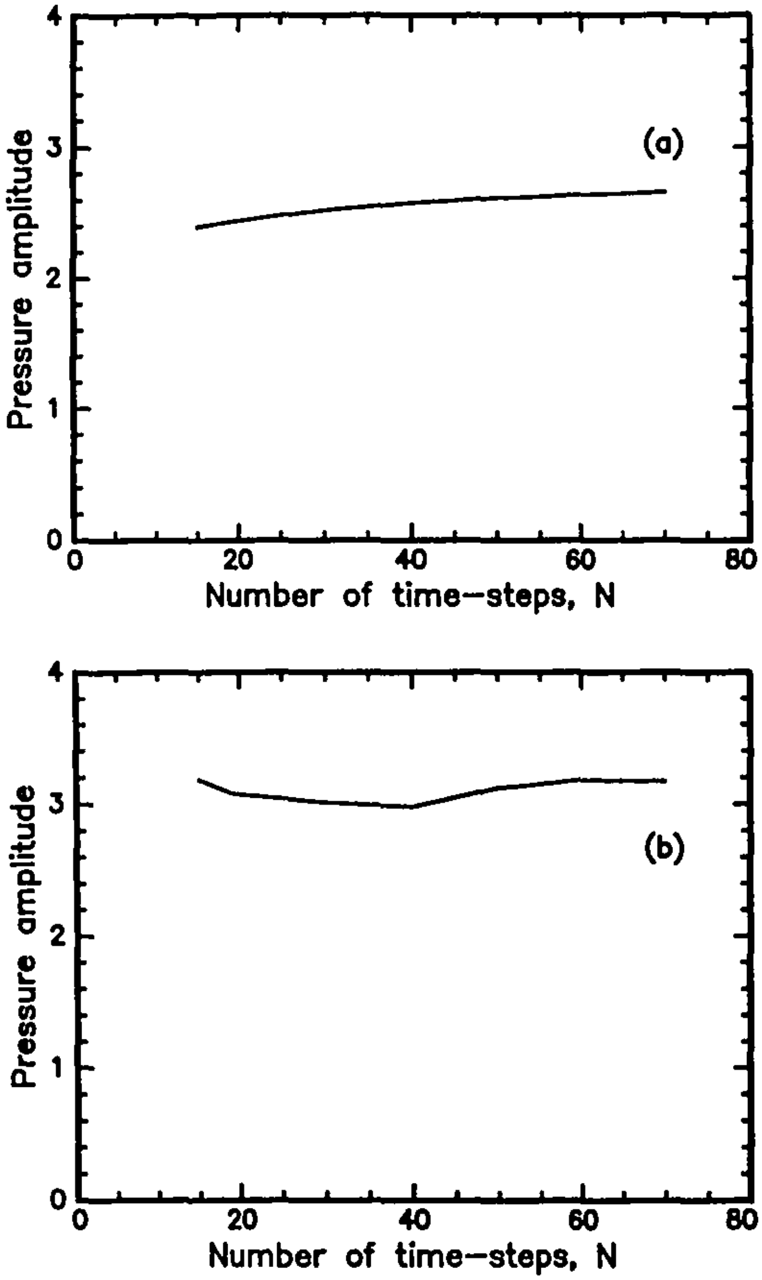

Figure 7.1: Unsteady pressure amplitude versus time-step N; 2-D analysis for $\epsilon = 0.1$, Re $= 62.5$ and $\omega = 1$: (a) mean-position analysis; (b) time-dependent-coordinate-transformation analysis.

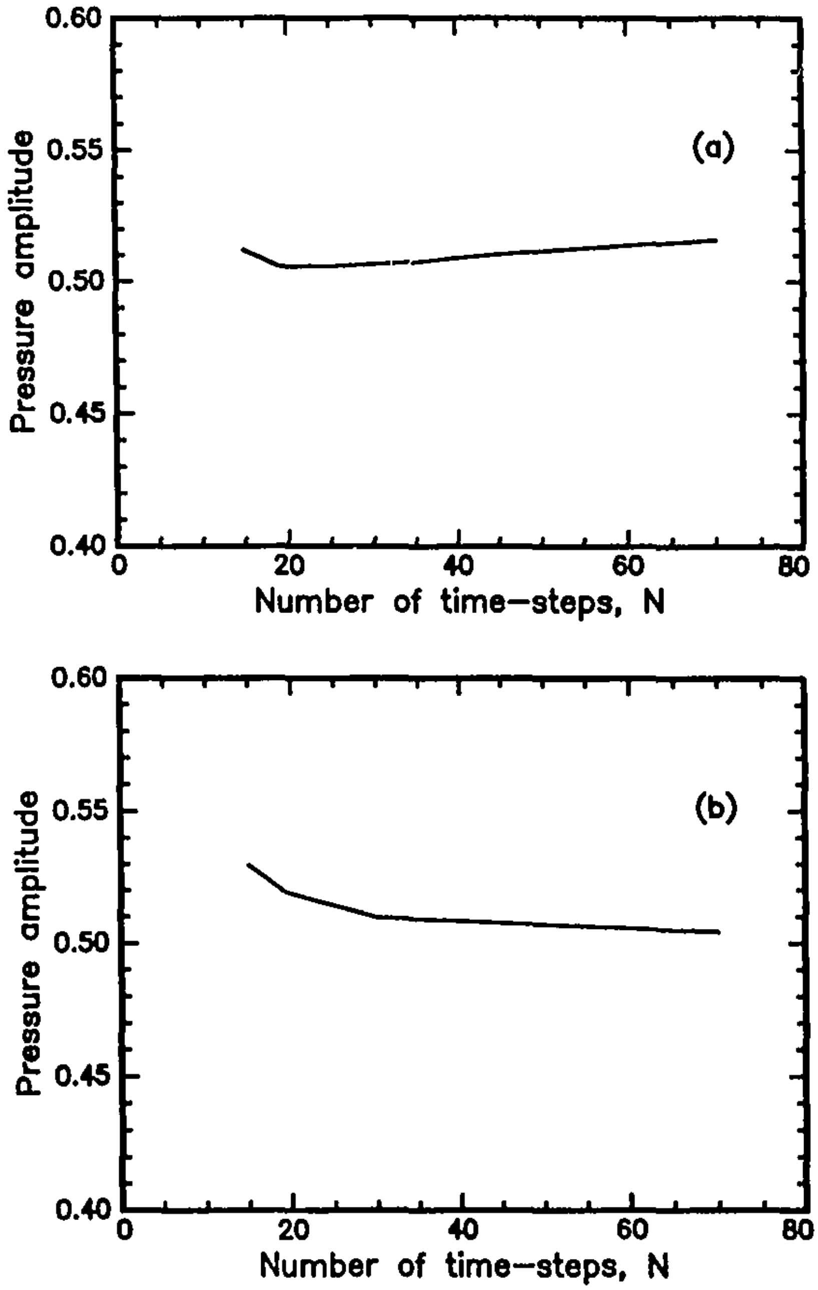

Figure 7.2: Unsteady pressure amplitude versus time-step N; 3-D analysis for $\epsilon = 0.1$, Re $= 250$ and $S = 25$: (a) mean-position analysis; (b) time-dependent-coordinate-transformation analysis.

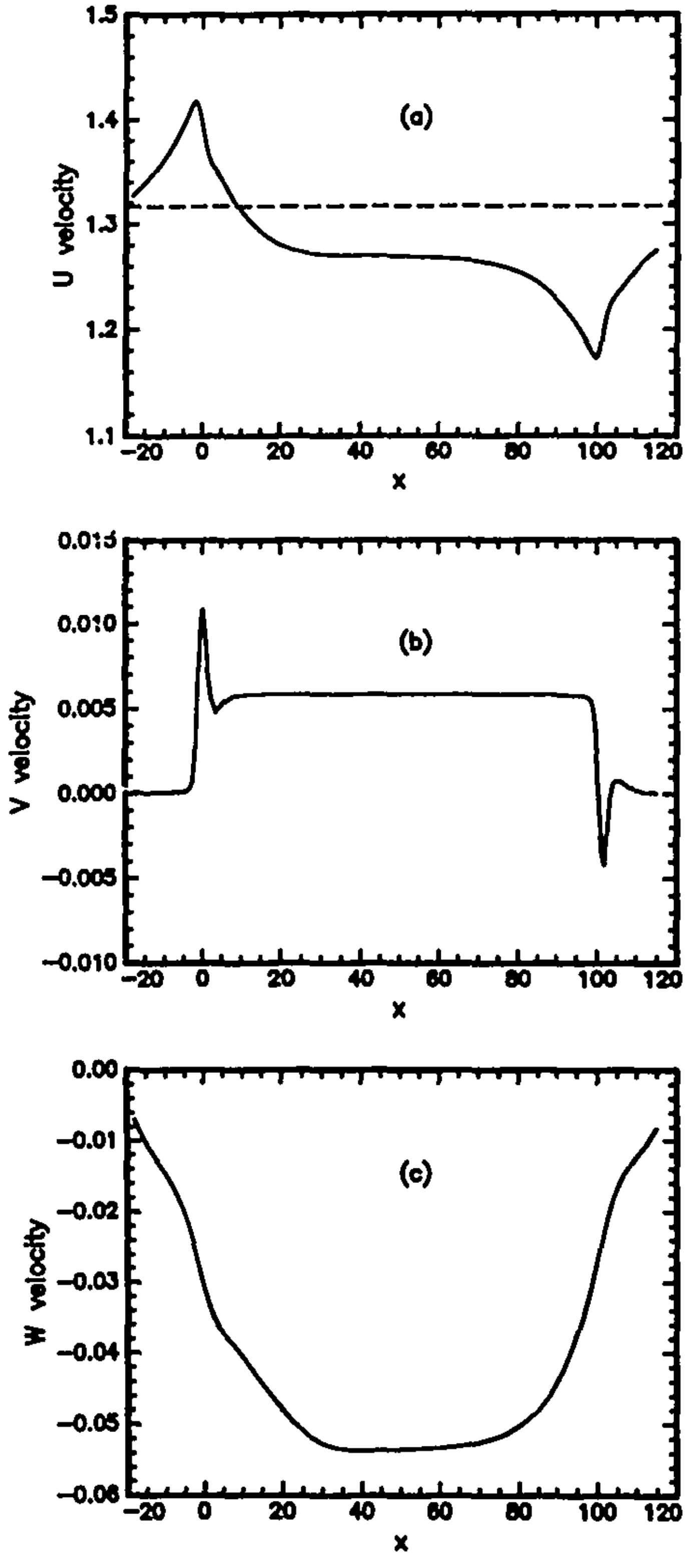

Figure 7.3: u, v and w velocity profiles along the x-axis at t^n, $n = 5$ and r_j, $j = 5$. —,steady plus unsteady values; - - -,steady value for u at r_j, $j = 5$.

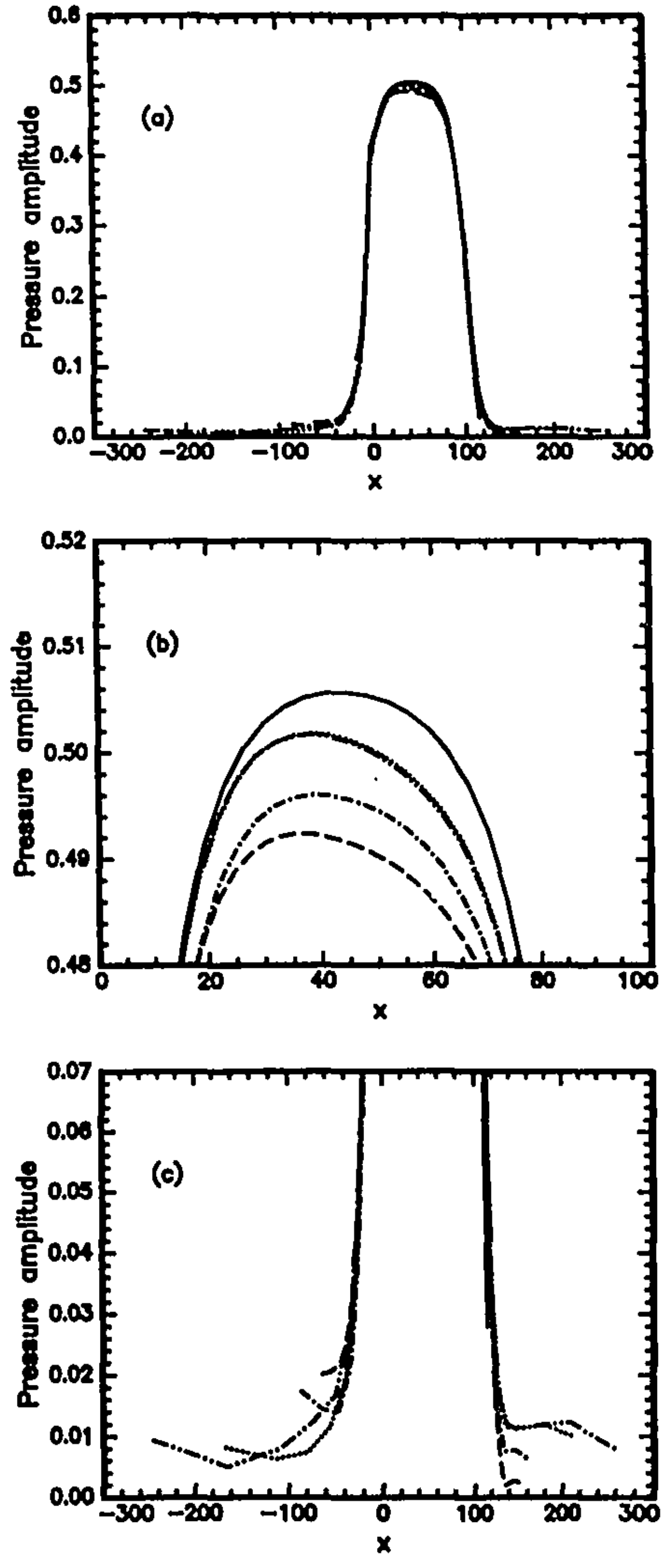

Figure 7.4: The effect of increasing the length of the upstream and downstream fixed portions on the unsteady pressure amplitude: (a) set of results; (b) magnified top portions of the curves in (a); (c) magnified bottom portions of the curves in (a). —,$L_1 = L_2 = 20$; - - -,60; -·-·-,100; · · ·,200 and -·····-,300.

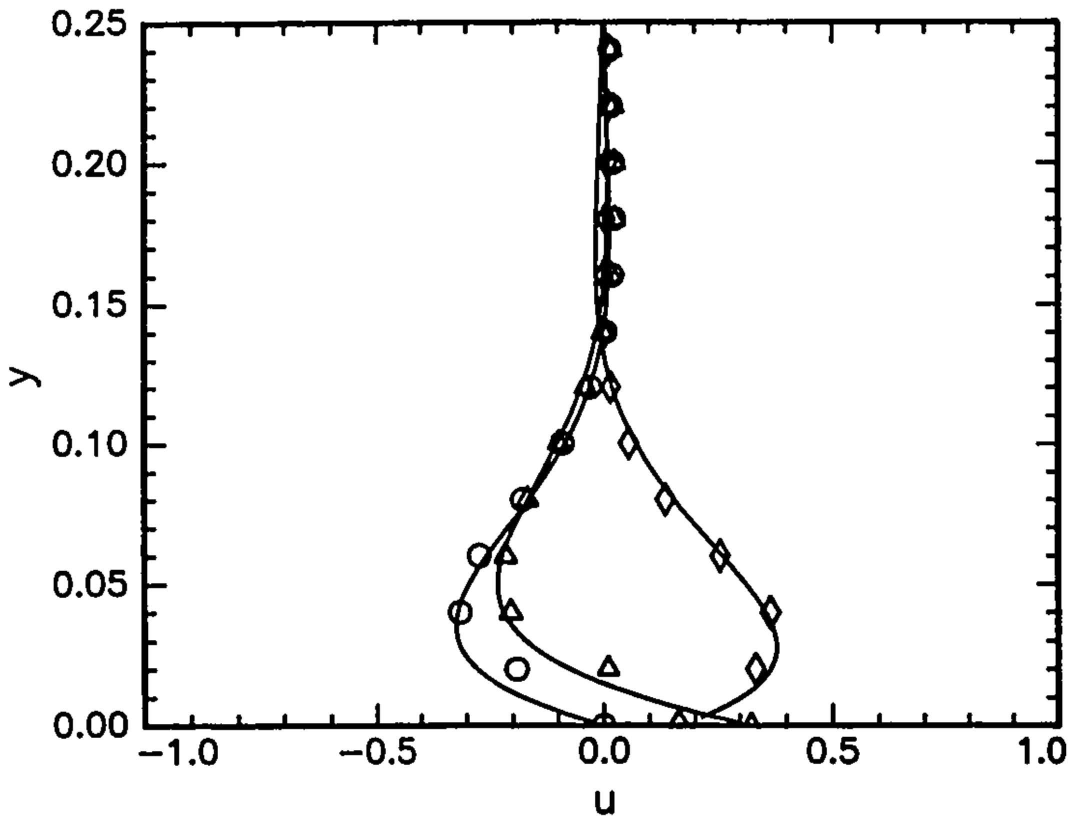

Figure 7.5: Variation with y in the x-component of velocity, u. The computations are for $S = 1000$, $J = 26$, $N = 19$, and three instants within the harmonic cycle have been represented. —,analytical solution; symbols, numerical solution.

Chapter 8

Experimental Investigation and Comparison with Theory

There are basically two methods which can be used to solve a problem in fluid mechanics and fluid-structure interactions as well as in most of the engineering and science problems: (i) experimental and (ii) theoretical, analytical or numerical. In the analytical method, simplifying assumptions are made in order to make the problem tractable. If possible a closed-form solution is sought. The big advantage of the analytical method is that "clean", general information can be obtained, in many cases from a simple formula, and reasonable answers can be obtained in a minimum amount of time. In the numerical method, a limited number of assumptions are made and a high-speed large-memory computer is required to solve the resulting governing, for instance in our case, fluid dynamic equations. The partial derivatives appearing in the governing equations are replaced, for example, by appropriate finite differences at each grid point. The resulting equations are then integrated to obtain the final results.

The greatest advantage of using the numerical method of attack, as compared to the experimental one, is its low cost; this may be orders of magnitude lower than the cost of a corresponding experimental investigation. The second advantage is the speed of computational investigation, plus the ability of providing the values of all the relevant variables (such as velocity, pressure, etc.) throughout the domain of interest. Unlike the situation in an experiment, there are few inaccessible locations for a computation, and there is no counterpart to the flow disturbances caused by the probes, bolts, support rods, etc. Obviously, no experimental study can be expected to measure the distribution of all variables over the entire domain. For this reason, even when an experiment is performed, there is great value in obtaining a companion computer solution to supplement the experimental information. In a computation, there exists the ability to simulate ideal conditions, for example, two-dimensionality, constant density, or laminar flow. On the other hand, even a very careful experiment can barely approximate such idealizations; instead, it obviously provides measurements corresponding to realistic conditions. In spite of all these advantages of computational solutions, a blind enthusiasm for any cause is undesirable.

As mentioned earlier, a computer analysis works out the implication of a mathematical model. The experimental investigation, in contrast, observes reality itself. The validity of the mathematical model, therefore, limits the usefulness of a computation. The user of a computer analysis receives an end product that depends on both the mathematical model and the numerical method. A mathematically well described problem (such as a laminar flow problem), if combined with a perfectly satisfactory numerical technique, will yield reliable results. Even in this case, however, depending on the complexity of the problem, an experimental study is sometimes superior to a computer solution. An optimal prediction effort should thus be a judicious combination of *computation* and *experiment*. The proportions of the two ingredients would depend on the nature of the problem, on the objectives of the prediction, and on the financial and other constraints of the situation.

In parallel to the foregoing numerical solutions of which the ultimate objective is to predict the unsteady flow fields in annular flow, the problem has also been studied experimentally in both the laminar and turbulent regimes. The experimental results obtained in the laminar regime are compared with the theoretical results of the previous chapters. For this special (FIV) problem, the need for experiments will probably remain for some time, in applications involving turbulent flow where it is presently both mathematically and economically not feasible to utilize computational models which are free of empiricism. Thus, the experimental results in the turbulent regime were obtained to be utilized in future extensions of this work.

The experimental measurements of the unsteady pressure in the annulus or unsteady forces applied either on the inner or outer cylinder have been done in the past for the purpose of design or validation of the proposed existing theoretical models (see Spurr & Hobson (1984), Parkin *et al.* (1987), Mateescu *et al.* (1988,1989), Hobson (1991)). Using an earlier experimental apparatus designed for concentric configurations, experimental investigations were made to study the flow field for later use in flow-induced vibration problems (Mateescu *et al.* 1989). In that set of experiments, the quantity measured was the unsteady pressure. In those tests, a rigid, cylindrical centre-body was forced to oscillate in rocking motion about a hinge with fluid flowing in the annulus, while the outer conduit was rigid and immobile. The experiments for this apparatus were characterized by high axial velocities, which permitted the validation of the approximate theory developed for turbulent flow in concentric annuli. In contrast, no experiments were conducted with that apparatus for unsteady laminar flows, which may be practically important especially in very narrow annuli.

In the present analysis, a new apparatus was constructed (Mekanik *et al.* 1994), the general layout of which is shown in Figure 8.1, with which the rocking and lateral (translational) motions would be equally feasible. In this design the following features were introduced: (a) the possibility of conducting experiments in eccentric arrangements, with the oscillation either in the plane of eccentricity or normal to it, which were not performed in experiments described here; (b) the facility of having very low velocity, so that the flow in the annulus could be either laminar or turbulent. This new apparatus has the possibility of having axial variations in the annular passage, either smooth such as a diffuser, or abrupt such as an annular passage with an axisymmetric backstep.

To accommodate all possibilities, it was found convenient to oscillate part of the outer cylinder conduit, while the centre-body remains immobile. To reduce viscous-flow related effects, such as flow separation and/or vortex shedding which are not considered in the present theory, a smooth transition between cylindrical and annular flow is assumed both upstream and downstream. This is ensured by connecting smooth ogives to the fixed centre-body at both ends, as shown in Figure 8.1. The constant cross-section, from the upstream ogive to the test section, where the pressure was measured, is long enough to obtain developed laminar flow, in the case where laminar flow experiments are undertaken. The tests have been conducted at low amplitudes of oscillation, characterized by an amplitude/gap ratio smaller than 0.2. For simplicity of design, the tests were performed in air rather than in water.

8.1 Experimental Apparatus

The test section consists of a rigid cylindrical centre-body with ogival ends in a cylindrical conduit (Figure 8.1). The ogives, together with an upstream meshed screen and a honeycomb help to make the annular flow as uniform as possible. As mentioned before, only the central portion of the outer cylinder is forced to oscillate, and hence, there will always be discontinuities at the boundaries between the oscillating portion of the outer cylinder and its immobile upstream and downstream extensions. Various flange designs were tried to study and reduce this effect (Figure 8.2), a discussion of which will be given later.

The unsteady pressure was measured using, in the latest experiments, eight PCB 103A11 and 103A12 pressure transducers (microphones) situated at $x/L = 0.263$, 0.342, 0.421, 0.500, 0.578, 0.657 and 0.763, in the vertical plane of oscillation, as shown in Figure 8.3. At the mid-point, two transducers were used diametrically opposite each other in order to compare the corresponding measured unsteady pressure; for instance, the phase difference between the two signals might be 180° for concentric configurations, when the cylinder executes either translational or rocking motion.

The sensitivity of these transducers was 72.51 mV/kPa. In earlier experiments, 10 less sensitive PCB 112A22 transducers were used. At each axial location, the new transducers were flush-mounted on the flat surface prepared inside the centre-body, facing small-diameter holes (0.8 mm, as compared with the manufacturer's recommendation of 3.175 mm, and 12.5 mm deep), to minimize the effect of the holes on the flow field used for measuring the pressure in the annulus.

The outer conduit was oscillated by means of a Brüel & Kjaer electrodynamic shaker. In the case of translational motion, the oscillatory motion was transmitted to the cylinder by a yoke made of two parallel plates, placed around the midpoint $X = x/L = 0.5$. For rocking motion, the oscillation about a "hinge" ($X = 0.237$) was transmitted via a flexible thin plate attached to the shaker at $X = 0.815$, Figure 8.4, which accommodated unavoidable small harmonic motion in the axial direction.

The possible vibration frequencies and amplitudes were limited by (a) the maximum shaker force rating of 445 N and peak-to-peak amplitude limit of 12.7 mm and (b) practical considerations associated with structural resonances, which gave an effective frequency range of 15-100 Hz. In practice, the amplitude was limited to half the maximum gap or 5.0 mm. The shaker was often used in its constant-frequency mode, while the frequency was being swept; for that purpose, an accelerometer mounted on the base plate of the shaker-head or on the outer pipe provided a feedback signal to the shaker controller as shown in Figure 8.5. The displacement of the oscillating cylinder as well as the phase angle between the unsteady pressure signal and the acceleration signal (from which the phase angle between the pressure and outer-cylinder displacement can be obtained) were measured by the same accelerometer.

The signals from the pressure transducers (one at a time) and the accelerometer, after suitable conditioning, were fed into a dual channel FFT digital spectrum analyzer, which can accept inputs as small as $1\mu V$. These signals could be postprocessed, as desired, with a PC486 computer as shown in Figure 8.5. The rms amplitude of the pressure and acceleration at the oscillation frequency were obtained from the corresponding spectra (typically with 16 averages). The phase difference of pressure to acceleration was determined when the analyzer was used in the transfer-function mode. It should be mentioned that, in most cases, the signals contained superharmonics (of smaller amplitude) of the basic frequency; in what is presented in this chapter a linear analysis is undertaken, and only the components at the principal frequency are considered.

The air flow was provided by either (i) a vacuum pump (used in suction), providing a laminar or low-velocity turbulent flow, or (ii) a large centrifugal blower for high, turbulent flow. When using the latter, an acoustic filter and a special noise attenuation plenum chamber were used to reduce the incident fluctuating noise. The flow velocity was measured by standard means.

Utilizing the present apparatus, we varied the following parameters were varied in the experiments: (a) oscillation frequency; (b) oscillation amplitude; (c) axial-flow velocity.

To describe the apparatus in detail, its different components are presented in the sub-sections that follow: the external conduit, including the oscillating outer cylinder; the fixed centre-body connected to the ogives; the "transmission" mechanism linking the shaker to the outer cylinder; the blower and the associated flow system.

8.1.1 The External Conduit

The external pipe consists of three main sections: the oscillating central portion, and the fixed parts upstream and downstream. The inner radius of the pipe is $R_i = 53.8$ mm, as shown in Figure 8.3, and its wall thickness is 3.2 mm. The central section, 965 mm long, executes one-degree-of-freedom oscillatory motion, as excited by the shaker.

The fixed cylindrical conduit of the same diameter as the moving portion continues on either side, and houses and supports the ogives as well as the fixed centre-body, as shown in Figures 8.1 and 8.3. These portions and the oscillatory part are made from aluminum with specific gravity of 2.785 gr/cm^3. The inlet axial flow was regularized with the aid of the several meshes and the ogive, to eventually obtain the developed laminar flow as mentioned before, or at high flow velocity, with the additional help of a honeycomb screen, an acoustic filter and a special noise attenuation plenum chamber, to obtain a uniform turbulent flow. These parts were secured on the vertical plates which were fixed on a long I-beam at a number of locations along the axial direction as shown in Figure 8.6. The system was horizontal.

A great deal of time was spent on the question of the discontinuity between the oscillating and stationary parts of the outer cylinder. The "obvious" solution of using flexible thin rubber sleeves to connect the two was found unsatisfactory, from the mechanical point of view: the sleeves had a bias either in shape or in locked-in stresses which affected the uniformity of motion in the case of transverse oscillation (by "pulling" at one extremity of the oscillating cylinder). With zero-mean-flow experiments, either of the arrangements in Figure 8.2(b,c) performed satisfactorily. With flow, however, especially at high velocities, the arrangement in Figure 8.2(a) with sponge-felt gaskets was by far the best. Unless otherwise remarked, in the results to be presented, the sponge felt was used.

8.1.2 The Fixed Centre-Body

The fixed centre-body comprised three parts: the central test section, facing the oscillating outer cylinder, and the upstream and downstream sections as shown in Figure 8.3. The centre-body was made from aluminum for uniform annular space and from steel for nonuniform (backstep and diffuser shaped) annular space. The pressure transducers were mounted in the central test section as shown in Figure 8.7(a-c) for different annular spaces. The fixed upstream and downstream sections were composed of two parts: an ogival part and a constant cross-section part. The constant cross-section part was connected to the test section. The ogival part was shaped to have a parabolic profile; it was designed to allow a smooth and uniform transition from cylindrical to annular flow, and vice-versa. Thus, fully developed annular flow in the test section is presumed to exist through the constant cross-section part.

The central test section of the centre-body was made up of two sections (split longitudinally to mount the pressure transducer inside the cylinder) and was connected to the upstream and downstream sections at both ends in sliding contact (male and female), to allow rotation of the central test section for measuring the unsteady pressures at various azimuthal locations if desired. An O-ring between the male and female parts prevented any air leakage into the hollow inner cylinder, as shown in Figure 8.8. Undesired rotations were prevented with the aid of a set of screws. The radius of the inner cylinder (apart from the ogives) was constant, $R_i = 44.5$ mm, in the case of a uniform annular space; $R_i = 44.5$ mm and $R_{id} = 35.2$ mm for nonuniform annular spaces. The dimensions of the whole system are shown in Figure 8.6. Based on the dimensions shown in this figure, it is clear that the constant cross-section parts of the annulus are long enough (500 mm) with respect to the annular gap width (9.3 mm) to insure developed laminar flow.

8.1.3 Shaker and Transmission

The harmonic oscillation was generated by a Brüel & Kjaer electromagnetic shaker (exciter body B&K 4801, with exciter head B&K 4812). The maximum peak-to-peak amplitude limit was 12.7 mm and the maximum force rating was 445 N, the possible frequency range was from 5 Hz to 10 kHz. In the present tests the frequency range chosen was 15-100 Hz and the amplitude of oscillation was kept below 5.0 mm peak-to-peak. The mass of the oscillating cylinder is 2.821 kg which indicates that the weight of the cylinder is much less than the maximum force rating.

The harmonic signals generated by the shaker controller (B&K exciter control type 1047) were fed into a power amplifier (B&K 2707) that amplified them to the levels appropriate to drive the shaker. The shaker controller controls the frequency and the displacement amplitude of the moving outer cylinder. A control accelerometer was mounted on the base plate of the shaker or on the oscillating outer cylinder. The signal from this accelerometer was processed to an effective sensitivity of 10 mV/g in the charge amplifier (B&K type 2624) and fed to the compressor circuit of the exciter control (1047) as shown in Figure 8.5. In this way, the acceleration level of the shaker system (and the oscillating outer cylinder) can be held constant throughout the frequency sweep.

The oscillatory motion of the outer cylinder is provided by a pair of vertical rigid plates parallel to each other, which were placed between the shaker and the cylinder at the mid-point of the cylinder ($X = 0.5$) as a yoke, to ensure purely transverse translation. These plates are 7% by weight of the oscillating cylinder, hence in the static situation (no motion of the cylinder) the central part of the outer cylinder always remains at the same horizontal level as the fixed portions at its extremities. For rocking motion about a hinge, the outer cylinder is kept fixed at $X = 0.237$ and is connected to the shaker at $X = 0.815$ via a flexible slender plate. Due to the rocking motion, there is a small axial displacement of the oscillating cylinder. The flexible slender plate renders this small movement negligible, especially for small-amplitude oscillations of the moving cylinder. Nevertheless, it generates secondary effects which should be taken into account for larger-amplitude oscillations.

8.1.4 Blower and the Associated Flow System

In the present work, the flow through the annulus was provided by two external air sources. A vacuum-cleaner type blower was used in the suction mode for generating laminar or low-velocity turbulent flow, as shown in Figure 8.1; a large fan (blower) was used for high velocities. The same fan can be used to provide low-velocity flow by utilizing a regulating valve and by smoothing the flow with special devices such as an acoustic filter and a noise-attenuation plenum chamber. The same devices were used during the experiments for turbulent flows, because the noise level generated by the blower was relatively large as compared to the expected pressure signal.

The flow rate was measured by means of several orifice plates (depending on the flow rate) with different sizes and the accuracy of readings; they were checked against one another using the appropriate equations, thus confirming that the orifice plates can be used with confidence. The orifice plate was mounted near the downstream end of a straight pipe (3 m long and 40 mm in diameter) which was connected at its other end to the downstream section of the outer pipe, as shown in Figure 8.1. This length is required to obtain fully developed flow near the inlet of the orifice plate.

When a vacuum-cleaner type blower is used for laminar-flow experiments, the flow rate was controlled by circumferential slot located at the downstream end near the vacuum pump and for high-velocity experiments by the slip valve located at the upstream end close to the outlet of the large blower.

Based on the usage of these devices and considering Figure 8.9, the Reynolds number is calculated from the following equations. To begin, the flow rate is obtained from (Miller 1989)

$$Q = 0.09970190 \frac{C_d Y d^2}{\sqrt{1-\gamma^4}} \sqrt{\frac{h_w}{\rho_f}}, \tag{8.1}$$

where Q is the volumetric flow rate of air in cubic feet per second, Y is the air expansion factor for the orifice, taken to be $Y = 1$ for small differential pressure, $\gamma = d/D$ and C_d is the coefficient of discharge for the orifice, given by

$$C_d = C_\infty + \frac{b}{\mathrm{Re}_D^n},$$

with $b = 91.71\gamma^{2.5}$, $n = 0.75$, $\mathrm{Re}_D = V_1 D/\nu$, V_1 being the velocity of air upstream of the orifice; C_∞ is given by

$$C_\infty = 0.5959 + 0.0312\gamma^{2.1} - 0.184\gamma^8 + 0.39\frac{\gamma^4}{1-\gamma^4} - 0.0158\gamma^3.$$

In equation (8.1), d and D are in inches, h_w is the differential air pressure in inches of water reading across the taps shown in Figure 8.9, and $\rho_f = 0.076$ lbm/ft^3 for air at standard temperature and pressure. It should be remarked that a kind of iteration procedure was used to calculate the true values of C_d, which is Reynolds-number dependent, for each orifice plate. The Reynolds number for the annulus is obtained as

$$\mathrm{Re} = \frac{2QH}{A_n \nu}, \tag{8.2}$$

where the annular gap width $H = 9.3$ mm, the kinematic viscosity of air $\nu = 1.62 \times 10^{-5}$ m^2/s, and $A_n = \pi(R_o^2 - R_i^2) = 2.87 \times 10^{-3}$ m^2 is the annular cross sectional area.

8.2 Instrumentation for Measurement

As mentioned before, the pressure as well as the phase and displacement were analyzed by means of signal processing through an FFT (Fast Fourier Transform) digital signal analyzer, from which the pressure amplitude and the phase angle with respect to the displacement could be obtained, as shown in Figure 8.5. In the present experiment the following instruments were used to obtain the required data: (i) eight highly sensitive microphone type pressure transducers; (ii) three accelerometers; (iii) one photonic sensor; (iv) one digital spectrum analyzer; (v) one inclined alcohol manometer. These are described in greater detail in what follows.

8.2.1 Microphone Type Pressure Transducers

At the heart of the measurements are the pressure transducers. The specifications of the transducers used will be outlined in the following paragraphs; their locations on the centre-bodies for different configurations of the annular space are shown in Figure 8.7(a-c). In these figures, most of the pressure transducers were installed at the top portion of the centre-body assuming that the whole system is symmetric with respect to the centre-line of the centre-body. However, to check this symmetry, at the mid-point, two transducers were used diametrically opposite each other.

Sound pressure microphones (of the PCB 103A type) feature a built-in amplifier and compensating accelerometer, and have ultra-high sensitivity (500 mV/psi). They can be used to measure transient events, turbulence, and other acoustic phenomena on a variety of test objects and models. This sophisticated sensor is available in two standard ranges and two configurations (pigtail and micro connector); this tiny instrument transfers dynamic and short-term static pressures into high-level, lowimpedance analog voltage signals. It is structured with ceramic crystal elements, a microelectronic amplifier and an accelerometer, to virtually cancel out vibration sensitivity. A thin, recessed Invar diaphragm and a bender-mode crystal element adapt it for very low pressure measurements in adverse shock, vibration and thermal environments. This model can be installed in several ways. Due to the necessity of relocating the transducers from one model of the annular configuration to the next, the servo-clamp mode of installing the pressure transducers was used as shown in Figure 8.10. Based on the inside configurations of the centre-body, the pressure transducers used have two configurations: pigtail and micro-connector, which are shown in Figure 8.11.

The main specifications of these pressure transducers (PCB 103A11 and PCB 103A12) are as follows:

Maximum pressure:	206.85 kPa (30 psi)
Resolution:	0.483 kPa (0.00007 psi)
Sensitivity(nominal):	0.07 mV/Pa (500 mV/psi)
Resonant Frequency:	13 kHz
Acceleration sensitivity:	3.45 Pa/g (0.0005 psi/g)
Vibration(max):	1000 g
Linearity:	±2 (%FS)
Size(dia×height):	9.53 × 5.59 (mm)

In this experiment, utilizing this pressure transducer, the steady (or static) component was undetectable and the signals had acceptable levels of dynamic pressure readings as will be discussed in the experimental results which follow.

8.2.2 Accelerometers

The displacement of the oscillating outer cylinder was measured by an accelerometer (B&K type 4381) with voltage sensitivity of 82.9 mV/g and charge sensitivity of 99.4 pC/g, where g=9.81 m/s^2. This accelerometer was mounted either on the shaker head or on the oscillating outer cylinder. The accelerometer signal was first fed into the charge amplifier (B&K type 2624). One of two-output signals from the charge amplifier was used for the constant-displacement control through the feedback loop of the shaker controller system, while the other was monitored by the spectrum analyzer, which gave the outer cylinder displacement, as shown in Figure 8.5.

Another accelerometer type (B&K 4338) was mounted inside the centre-body to make sure that during the experiment the centre-body did not vibrate sufficiently to affect the pressure readings. The centre-body vibration was less than 1% of the vibration of the outer cylinder for almost all of the experiments, especially for the cases of nonuniform centre-bodies which were made of steel. The uniform centre-body was made of aluminum.

To ensure that the outer cylinder always executes transverse oscillation in the plane of symmetry and does not move side-ways, and also to check that the two moving ends of the oscillating cylinder have the same acceleration as the middle part which is attached to the shaker through the yoke in translational motion, another accelerometer (B&K 4332) was attached to one and then the other end of the moving cylinder, either in the plane of translational motion or normal to it. It was found that the outer cylinder is rigid enough to have the same acceleration everywhere in the plane of oscillation and almost zero acceleration in the plane normal to it at both ends of the moving cylinder.

8.2.3 Spectrum Analyzer

A powerful dual-channel FFT digital spectrum analyzer (Hewlett-Packard 3582A) was used to monitor the signals from the pressure transducers and from the accelerometers. The frequency range of the dual-channel digital analyzer is 0.02 to 25 kHz. The instrument can measure inputs from +30 dB (31.62 V) down to -120 dB ($1\mu V$) noise level, without resorting to external signal conditioning. Its dynamic range is 70 dB. The use of this analyzer made it possible to obtain the transducer and accelerometer readings accurately in the frequency range of 20-50 Hz, in which the present experimental tests were performed. The analyzer is capable of performing the rms power spectrum averaging of the input signals. Normally, 16 averages were taken in the FFT analyzer readings to be presented.

The amplitude of either signal at the frequency of oscillation could be obtained from the power spectrum, while the phase difference between the pressure and the acceleration could similarly be obtained from the cross-spectrum of those quantities as well as coherence which is obtained directly. By measuring the coherence, one can make sure that the pressure signals obtained are due to the oscillation of the outer cylinder and are not due to the external sources such as acoustic noise or vibration of the centre-body. The information was available for each individual spectral component either by means of a cursor on the screen (CRT) of the FFT analyzer that can be positioned accordingly, or through the connection of the analyzer to a PC486 computer to collect the information for later postprocessing of the results.

The main advantage of using the FFT analyzer was that the signal due to secondary effects (*e.g.* the nonlinearity of the fluid motion, unexpected secondary motions of the cylinder as explained previously, the random noise from turbulence, and acoustic wave pressure components) can be adequately separated from the signal. The other advantage of this instrument is that it can accept signals down to 1 μV range without special signal conditioning, which was very useful. The signal levels could not be obtained directly without using a signal amplifier (PCB 483AO7), which receives the signals from the pressure transducers and amplifies them 70 times before they were fed into the analyzer, as shown in Figure 8.5.

8.2.4 Ancillary Equipment

To calculate the flow rate, the pressure drop across the orifice plate was measured by an inclined differential alcohol manometer, with a range of 0-200 mm of alcohol. Its two taps were connected upstream and downstream of the orifice plate. It must be remarked here that at large flow rates, especially in the turbulent regime, the range of the manometer was not large enough to read the pressure differences across the taps.

Therefore, when the readings were out of range, the orifice plate was replaced by the next larger size. All the orifice plates used were calibrated by using equation (8.1). Equation (8.2) was used to calculate the Reynolds numbers.

During the oscillation of the outer cylinder, the reading of the pressure transducer located at the bottom portion of the centre-body (see Figures 8.3 and 8.5) was different from the others. Besides the geometrical configuration in the annular space which contains some obstacles such as support rods, set screws, etc. which might have affected the pressure readings, there was also the possibility of nonsymmetric movement of the outer cylinder in its plane of oscillation which is due to the shaker not starting to shake the outer cylinder around its centre-line, but rather moving up when it is turned on and then shaking the cylinder. Two pieces of equipment and instrumentation were used to confirm that this is the case or not. The first one was a video-camera to see the motion visually and check any probable nonsymmetric movement of the cylinder. Due to the fast motion and low-amplitude vibration of the cylinder (determined by the undesirable induced vibration in the whole system which affects the readings), the difference between the up and down movements of the cylinder was difficult to recognize visually. Hence, the second instrument, which was a photonic sensor, was used for this purpose. The measurement of the up and down motions of the cylinder by this device indicates certain differences between these movements, as shown in Figure 8.12. This difference, along with the influence of the geometrical factors, might be the causes of discrepancies between the readings of the top and bottom pressure transducers in the mid-section of the centre-body.

It should be remarked that the spectrum analyzer can be remotely as well as manually controlled. For remote control, it should be equipped with a special interface card. Hence, another important step in this work, as compared to the earlier work of Mateescu *et al.* (1988), is the computerization of the data acquisition with the aid of a PC486 computer in which an HP-IB interface card was installed. In this manner, the results obtained after being processed by the analyzer are fed into the computer for later postprocessing and demonstration. As will be discussed in later sections, computerizing the data acquisition system helps reduce the time for collecting the large amount of data involved in this work; also, the final output may be presented in a very nice manner by the use of appropriate software.

8.3 Preliminary Experimental Work

8.3.1 Calibrations

To obtain signals with a desired accuracy, every aspect of the data acquisition process must be studied for each parameter to be measured. The measuring instruments must be appropriately calibrated before being used to assess the dynamical behaviour of the instrumentation with an accuracy relevant to the order of magnitude of the signals, and the factors affecting the readings such as the type of connection between the moving and fixed parts of the outer cylinder must be considered.

Hence, the pressure transducers and the accelerometer as well as the orifice plates must be calibrated. The pressure transducers were calibrated, one at a time, against a PCB 106B pressure transducer of known sensitivity (43.51 mV/kPa, with a resolution of 0.69 Pa) in a special chamber shown in Figure 8.13, excited by the shaker, over the frequency range of the experiments. Figure 8.13 shows the experimental apparatus for dynamic calibration, which consists of a plexiglas cylinder with one end covered by a rubber membrane and the other end with a rigid plexiglas cap, with two pressure transducer housing holes. The membrane is held tightly against the edge of the cylinder by means of screws in order to prevent air leakage. Two small circular plates on each side of the membrane and bolted together provide an oscillatory displacement of the membrane by means of a rod which is clamped to the base plate of the shaker (B&K 4801) in a horizontal configuration.

The reference pressure transducer was flush-mounted to the fixed end of the cylinder and the pressure transducer to be calibrated was mounted in another housing hole which had the same configuration as in the actual measurements on the centre-body. The signals from both pressure transducers are fed into the analyzer to be recorded and compared. Using the reference signal from PCB 106B, the sensitivities of the actual pressure transducers were found to be in the range of 53.9-93.7 mV/kPa. The individual calibration factors were compared with the calibration of the manufacturer; the agreement was fairly good. Nevertheless, the calibration factors as measured here were used in processing the results.

By considering the actual measurement configuration, the accelerometers were calibrated with the aid of an accelerometer calibration exciter (B&K 4294), the acceleration of which is fixed (10 m/s^2 at 159.2 Hz). To calibrate the accelerometers, they are mounted (one at a time) on the calibrator and then connected to the charge amplifier with the proper cable in the same arrangement as for actual measurements. The sensitivities of the accelerometers were found to be 0.623 mV/m^2, 1.686 mV/m^2 and 1.02 mV/m^2 for B&K 4332, B&K 4338 and B&K 4381, respectively.

There were several orifice plates with different orifice diameters d = 1.0, 1.125, 1.25, 1.375 and 2.68 in. to be used in the experiments for different flow rates. These orifices were calibrated against each other using equations (8.1) and (8.2). The calibration chart obtained was used to find the appropriate Reynolds number in the annulus for each flow velocity by having the related pressure drop across the designated orifice plate.

8.3.2 Experimental Procedure

Before each actual experiment began, it was necessary to prepare the experimental apparatus. For this purpose, the type of centre-body (uniform, backstep or diffuser with specific angle) was selected and installed carefully. Depending on the type of motion of the outer cylinder (translational or rocking motion), the outer cylinder was installed and the shaker position was determined appropriately. Then, the equipment, such as exciter control, power amplifier, charge amplifier, pressure signal amplifier and dual-channel spectrum analyzer must be warmed up to prevent any drift in the quantities they provide or measure such as the amplitude and the frequency of oscillation, etc. Also, depending on the type of experiment (with or without flow, laminar or turbulent, low flow or high flow in each regime), the end gaps (see Figure 8.2) were prepared appropriately, along with the preparation of the necessary piping and selection and installation of the appropriate orifice plate.

To check that the outer cylinder always oscillated in its plane of oscillation and not normal to it, and also to verify the rigidity of the outer cylinder during the experiments (*e.g.* the moving ends of the cylinder have the same acceleration as the mid-section which is attached to the shaker in the case of translational motion) for each actual experiment, a preliminary test was done in which the accelerations of the accelerometers attached to the side and top of the outer cylinder (each end and one side at a time) were checked and if they were found to be less than 1%, the actual experiments could then be started.

The experiment was started by first setting the amplitude of oscillation, for example 1 mm peak-to-peak, on the exciter control. Then, the frequency, for instance 20 Hz, was set. The shaker was turned on and the magnitude of the rms value of the pressure on the FFT analyzer was read for two pressure transducers, since the analyzer is dual-channel. To calculate the rms value, to avoid damage to the equipment (not becoming too hot for a long experiment before the experimental setting is changed for the next one) the number of averages chosen was 16. Then, the next two transducers were selected by using a selector switch and the readings were recorded by the computer. This procedure for all transducers was repeated until all transducer readings were recorded.

To measure the phase angle, one of the channels of the analyzer was connected to the accelerometer, while the other was connected to the selected pressure transducer via the selector switch. The mode of the analyzer was changed from the amplitude reading to phase reading. The phase angles for all the transducers were recorded in the same way as explained for pressure measurement. The coherences of the pressure signals with respect to the accelerometer signals were obtained by changing the mode of the analyzer from phase measurement to coherence measurement. The recording of the coherences was performed for all the transducers in the same manner.

Then, the next frequency of oscillation (30.4 Hz) was selected and the experiment was repeated for all the quantities measured. After the frequency sweep was finished, the amplitude of the oscillation was varied on the exciter control and the procedure of measurement was repeated for a new frequency sweep. It should be remarked that, for experiments with flow, the appropriate orifice readings were also recorded. Also, during each experiment, specially during the experiments with high-amplitude and/or high-frequency oscillations, the reading of the accelerometer mounted inside the centre-body was checked to ensure that the centre-body was not vibrating, which would affect the final readings.

The above procedure was repeated for the following cases: (a) uniform annular geometry, without and with flow (different flow rates in different regimes, laminar or turbulent), translational or rocking motion of the outer cylinder at various amplitudes and/or frequencies of oscillation; (b) nonuniform (backstep) geometry, with the same range of experiments as were performed for a uniform annulus; (c) nonuniform (diffusers with 6^o and 20^o half-angles, one at a time) again with the same range of experiments as for the other geometries.

For any individual experiment, if there was any doubt in the results or in the experimental environment, the experiment was repeated several times to obtain, as much as possible, the most accurate results under the best experimental conditions. Another important test to insure more accurate results was to interchange the pressure transducers. This eliminated the doubt that the readings of some of the transducers were influenced by the local geometrical configuration and by the mounting, set screws, support rods, pins, etc., which were used inside the annulus for rigidity.

8.4 Experimental Results

In this section, the experimental results are presented. The presentation begins with the results obtained for the uniform annular space, for the cases of translational and rocking motions of the outer cylinder. These include Figures 8.14-8.57. These figures represent sample data, chosen out of 6764 files of experimental data obtained for four different annular geometries, namely (i) uniform, (ii) backstep, (iii) diffuser with 6° half angle and (iv) diffuser with 20° half angle. Generally, the results shown in the figures are classified into two groups for each figure, unless otherwise mentioned in the captions: (a) the left panels are for no fluid flow, (b) the right panels are for fluid flow with Re = 2900. Normally, there are six panels in each figure. As mentioned in their appropriate captions, the panels from top to bottom of the figures are either for different (increasing) frequencies or amplitudes.

The figures (see Figures 8.14-8.57) present the following data: (1) the amplitude spectrum of the unsteady pressure for specific transducers; (2) the unsteady pressure versus distance along the cylinder, obtained by all pressure transducers; (3) the phase angle spectrum of the unsteady pressure with respect to the acceleration of the outer cylinder versus the frequency of oscillation for a specific pressure transducer; (4) the phase angle versus distance along the cylinder, obtained by all pressure transducers; (5) the coherence spectrum of the unsteady pressure with respect to the acceleration of the outer cylinder for specific pressure transducers; (6) a sample of the pressure spectra produced at a high Reynolds number without motion of the outer cylinder; (7) the unsteady pressure versus distance along the cylinder at high Reynolds numbers. All the aforementioned cases are for translational motion of the outer cylinder. Cases 1-5 and 7 are repeated for rocking motion of the cylinder and a uniform annular geometry. Similar figures are presented for nonuniform annular spaces.

Following these cases, the figures representing the comparison between the theoretical and experimental results are presented, which include the uniform annular space for translational or rocking motion of the outer cylinder. The next set of figures present the comparison between the theoretical results obtained both using time-dependent coordinate transformation and mean position analysis with the experimental results. Finally, the last figure presents the comparison between the theoretical and experimental results at different frequencies.

Figures 8.14, 8.21, 8.27, 8.33 and 8.39 present the unsteady pressure amplitudes (for uniform annular geometry when the outer cylinder is in translational motion, rocking motion, in translational motion with a backward facing step, with a diffuser section having half-angle $\alpha = 6°$ and with a diffuser section having $\alpha = 20°$, respectively), measured by individual pressure transducers through the spectrum analyzer, recorded and processed by the computer. The indicated pressure readings were then corrected by the calibration factors. Figures 8.15, 8.20, 8.22, 8.26, 8.28, 8.32, 8.34, 8.38, 8.40, 8.44-8.46 present the unsteady pressure amplitude along the axial distance of the centre-body for different annular geometries, in translational motion and for uniform annular geometry in rocking motion.

The discrepancy between the pressure readings for the two pressure transducers mounted at the midpoint of the centre-body diametrically opposite to each other is clearly seen in Figure 8.15; the reasons for these discrepancies were discussed before. Figure 8.20 is similar to the previous figure but was drawn for higher velocities (Re = 5000 and Re = 9000). In Figure 8.22, which is for uniform annular space and the outer cylinder in a rocking motion, the agreement between the pressure readings is much better than those of Figure 8.15. The hinge is located at $X = x/H = 18.5$. The pressure readings at the midpoint are also much better than in the case of translational motion of the outer cylinder. Figure 8.26 is similar to Figure 8.20 (turbulent regime), but for rocking motion of the outer cylinder. Figure 8.28 is similar to 8.15 but for annular geometry with a backstep. The pressure drop, obviously, indicates the wider space after the step and is due to the reduction in the unsteady flow velocity. Figure 8.32 is similar to Figure 8.20 (high Reynolds numbers) and was drawn for an annulus with a backstep. The generation of the vortices was seen after the step at Re = 9000, by sharp variations of the pressure after the step.

Figure 8.34 is similar to 8.28 and presents the unsteady pressure for a diffuser with 6° half-angle. The pressure readings are more uniform than those of backstep geometry. Figure 8.38 presents results similar to those shown in Figure 8.32 (turbulent regime). As expected, the pressure fluctuations were not seen downstream of the diffuser, which indicates that there was less vortex generation and the fluid flow behaved like a well streamlined flow, even at such a high Reynolds number. Figure 8.40 presents results similar to those shown in Figure 8.34. Here, the unsteady pressure behaved, more or less, the same way as in the backstep geometry (see Figure 8.28). Figure 8.44 is similar to Figure 8.38 (high Reynolds number). The pressure downstream of this type of diffuser behaved, somehow, in-between that for a backstep and a diffuser with $\alpha = 6^o$. Finally, Figure 8.45 presents the comparison between the pressure readings obtained for all nonuniform annular geometries and shown in the previous figures. A similar comparison is made for the turbulent range in Figure 8.46.

Figures 8.16, 8.23, 8.29, 8.35 and 8.41 present the phase angle of the unsteady pressure with respect to the acceleration of the outer cylinder, for uniform and nonuniform annular geometries, with the outer cylinder either in translational or rocking motion. In all the figures, the phase diagrams with flow were smoother than those without flow. Figures 8.17, 8.24, 8.30, 8.36 and 8.42 present the phase angle along the axis of the centre-body measured by all pressure transducers, for different geometries, and different motions of the outer cylinder. The phase angles for all geometries when the outer cylinder was in translational motion were nonzero but close to zero, which was obvious because the fluid is air.

Figures 8.18, 8.25, 8.31, 8.37 and 8.43 present the coherence between the unsteady pressure signals and the acceleration signals due to the motion of the outer cylinder. These figures are for uniform and nonuniform annular geometries when the outer cylinder is either in translational or rocking motion. The results presented indicate that the unsteady pressure was generated mostly by the oscillation of the outer cylinder (*i.e*, the magnitude of the coherence gets close to one) hence, the other extraneous factors have less effect on the magnitude of the measured pressure. Thus, the coherence measurement gives a measure of the accuracy of the measured quantities during experimentation. The coherence diagrams, also, show several peaks corresponding to the higher harmonics that cannot be easily seen in the pressure spectra.

Figures 8.47-8.50 present the comparison between the results obtained from the mean-position analysis and the experimental results, both for unsteady pressure and phase angle, during the translational motion of the outer cylinder, in uniform annular geometry. For such a small-amplitude oscillation, the agreement between both results is good.

Figures 8.51-8.54 present a similar comparison between the theoretical and experimental results, but for a rocking motion of the outer cylinder. It is seen that the agreement between the two is excellent. In fact, the main reason for this close agreement is that, in the rocking motion of the outer cylinder, the moving cylinder is fixed at one end through the hinge, and at the other end it is supported by the shaker, thus practically, the moving cylinder can not move side-ways nor is it free to move in any other direction except in the plane of symmetry. Therefore, the experimental results are more reliable than those obtained for translational motion of the outer cylinder.

Figures 8.55 and 8.56 present the comparison between the results obtained by theoretical models and the experimental results. The results show that, the time-dependent coordinate transformation, *vis à vis* the mean-position approach, provides closer agreement with experimental results and is more reliable. As shown in Figure 7.4, when much larger values of L_1 and L_2 are used, the results are within 3% of those for $L = 20$, hence, the theoretical values approach more the experimental values. Finally, Figure 8.57 was drawn to compare the theoretical and the average values of the experimental unsteady pressure at different frequencies. The agreement is good and the trend of the fitted curves indicates that the pressure is a quadratic function of the frequency (through the acceleration generating the unsteady pressure).

Regarding the results presented in the previous figures, the general conclusion is that the experimental results confirm the theoretical results for uniform annular space in both the translational and rocking motion of outer cylinder. The agreement is especially good for the rocking motions of the outer cylinder. It was found that the experimental results are in better agreement with the theoretical results obtained by time-dependent coordinate transformation analysis rather than those obtained by the mean-position analysis.

8.5 Experimental Error Analysis

Errors will creep into all experiments, regardless of the care exerted. An experimental error is an experimental error. If we knew what the error was, we would correct it and it would no longer be an error. The real errors in experimental data are those factors that are always vague to some extent and carry some amount of uncertainty. Our task is to determine just how uncertain a particular observation may be and to devise a consistent way of specifying the uncertainty in analytical form (in the form of an equation). It is better to speak of experimental uncertainty instead of experimental error because the magnitude of an error is always uncertain. But since the term error rather than uncertainty is used extensively, in this section we mostly use the former definition whenever we talk about uncertainty.

Some of the types of errors that may cause uncertainty in an experimental measurement are: first, the errors coming from the construction of the apparatus and instruments which may invalidate the results; second, there may be certain fixed or systematic errors which will cause repeated readings to be in error by roughly the same amount but for some unknown reason; third, there are random errors, which may be associated with the experimenter, random electronic fluctuations in the apparatus or instruments, various uncontrollable influences (*e.g.*, friction), *etc.*

These random errors usually follow a certain statistical distribution. We should use the theoretical methods based on the characteristics of the instruments and the conditions of experimentation to estimate the magnitude of a fixed error (Holman 1989).

Bias or systematic error is a fixed value re-occurring consistently every time the measurement is made. It is not susceptible to statistical analysis. Another type of error includes disturbances introducing errors of sufficient magnitude to hide the test information. Extreme vibration, mechanical shock of the equipment, or pickup of extraneous noise may be of sufficient magnitude to make the testing meaningless. In such cases the tests are stopped and the disturbing elements are eliminated.

There are precision errors in the measurand (particular physical parameter being observed and quantified) due to the observer not being consistent when estimating readings such as the amplitude or frequency on analog meters, or the process involved may include certain uncontrolled, or poorly controlled, variables that results in changing conditions (Beckwith & Marangoni 1990).

Most of the foregoing have occurred in this experimental investigation. Let us review the measures taken to reduce, to the extent possible, the error in the experiments. For each geometrical configuration (uniform or nonuniform annular spaces) the whole system must be disassembled and reassembled, hence, each time the adjustments of various parts to their original positions must be done, a time-consuming job, to prevent any misalignment in the system such as preventing eccentricity in a supposedly concentric arrangement. The pressure transducers were secured in their places as shown in Figure 8.10 with a rubber gasket to prevent any leakage of air from the gap between the transducer surface and the inner cylinder surface, thereby increasing the accuracy in pressure readings.

Although a sponge was used to fill the end gaps, it was squeezed enough to prevent air leakage from these gaps, which ultimately reduces the uncertainty in the pressure and velocity readings. During experimentation at high amplitudes and/or frequencies, there were vibrations induced in the whole system. These vibrations, as mentioned, are random in nature which introduces random errors in our results. To minimize this type of error, the mass of the whole system is increased by placing several bags of sand on the surface on which the apparatus is mounted; also, the frequency of experimentation is kept below 50 Hz (this explains the reason why most of the experiments were done in the range of $20 \leq f \leq 40$ Hz). Some measures were taken to eliminate the extraneous noise entering into the annular space, *e.g.*, by using an acoustic filter, in addition to a special noise-attenuation plenum chamber, during the experiments with flow as explained in the previous sections. Using these devices, we probably increased the accuracy of the readings.

The data obtained in this experimental investigation are single-reading data rather than multiple-reading data which are obtained in those instances where enough experiments are performed so that the reliability of the results can be assured statistically. The limitation of having more measuring devices (such as pressure transducers), the variety of experiments, and finally the time limitation prohibited the collection of multiple-reading data.

Suppose a set of measurements is made and these measurements are then used to calculate some desired results of the experiments. The result R can be given as a function of the primary measurements x_1, x_2, x_3, ..., x_n. Thus,

$$R = R(x_1, x_2, x_3, ..., x_n)\,. \tag{8.3}$$

If e_R is the uncertainty (error) in the results and e_1, e_2, e_3, ..., e_n is the uncertainties (errors) in the primary measurements, then, e_R is given by (Taylor 1982)

$$e_R = \left[\left(\frac{\partial R}{\partial x_1} e_1\right)^2 + \left(\frac{\partial R}{\partial x_2} e_2\right)^2 + \cdots + \left(\frac{\partial R}{\partial x_n} e_n\right)^2\right]^{1/2} . \tag{8.4}$$

The unsteady pressure produced by the oscillation of the outer cylinder is a function of acceleration of the cylinder; hence, for small-amplitude oscillations (0.5 mm, 1.0 mm and 1.5 mm) in this study the pressure is a linear function of amplitude of oscillation and a quadratic function of the frequency of oscillation, *i.e.*,

$$p = y(\epsilon, f^2) = y(\epsilon f^2)\,, \tag{8.5}$$

where ϵf^2 comes from the acceleration $\ddot{a} = \epsilon\omega^2 \sin\omega t$ when we have a harmonic sinusoidal oscillation of the outer cylinder. The error associated with equation (8.5) is

$$e_p = \left[\left(\frac{\partial y}{\partial \epsilon} e_\epsilon\right)^2 + \left(2\frac{\partial y}{\partial f} e_f\right)^2\right]^{1/2}. \tag{8.6}$$

Considering equation (8.1), the flow velocity in the annulus can be given by

$$U_o = z(C_d, d, D, h_w, \rho_f, R_o, R_i)\,. \tag{8.7}$$

The error associated with equation (8.7) using equation (8.4) is written as

$$e_u = \left[\left(\frac{\partial z}{\partial C_d} e_{C_d}\right)^2 + \left(\frac{\partial z}{\partial d} e_d\right)^2 + \left(\frac{\partial z}{\partial D} e_D\right)^2 + \left(\frac{\partial z}{\partial h_w} e_{h_w}\right)^2 + \left(\frac{\partial z}{\partial \rho_f} e_{\rho_f}\right)^2 \right.$$
$$\left. + \left(\frac{\partial z}{\partial R_o} e_{R_o}\right)^2 + \left(\frac{\partial z}{\partial R_i} e_{R_i}\right)^2\right]^{1/2}. \tag{8.8}$$

The physical measurable parameters influencing the accuracy of the experimental results obtained in this analysis with their appropriate uncertainties, and the uncertainties associated with the measuring equipment are as follows:

The manometer reading, $h_w = 7.3 \pm 2\%$ cm of alcohol (for Re = 2900).

the density of air, $\rho_f = 1.21 \pm 1\%$ kg/m^3;

the outer cylinder radius, $R_o = 5.38 \pm 0.2\%$ cm;

the inner cylinder radius, $R_o = 4.45 \pm 0.2\%$ cm;

the coefficient of discharge of the orifice plate, $C_d = 0.68 \pm 0.5\%$ (from calibration data);

the outer diameter of orifice plate, $D = 4.0 \pm 0.2\%$ cm;

the orifice diameter, $d = 2.54 \pm 0.2\%$ cm (one of the orifices);

the amplitude of oscillation, $\bar{\epsilon} = 10 \pm 4\%$ mm (obtained from the exciter controller);

The frequency of oscillation, $f = 20 \pm 4\%$ Hz (obtained from the exciter controller).

The instruments and equipment accuracies are as follows:

Fast Fourier Transform analyzer:

Amplitude accuracy (full scale, log) +0, -0.1 dB.

Frequency accuracy $\pm 0.003\%$ of the display centre frequency.

Display accuracy 3% of total height or width.

Transfer function accuracy (used for phase measurement) $\pm 5°$.

Coherence accuracy (marker resolution) 0.01.

Accelerometer calibrator accuracy 10 (rms)$\pm 3\%$ m/s^2.

Accelerometer B&K 4381 accuracy $82.9 \pm 2\%$ mV/g.

Exciter control accuracy 4% of meter reading.

There are certain other uncertainties, associated with some of the equipment, which were not available. These are: power amplifier calibration data, charge amplifier calibration data, calibration sheet for exciter head of the shaker.

Taking into account the most important uncertainties and using equations (8.4-8.8) in conjunction with equation (8.1), the uncertainties (errors) associated with the eight pressure transducers in Figure 8.7(a) for the case of fluid flow with Re = 2900 at $\bar{\epsilon} = 1$ mm amplitude corresponding to $\epsilon = 0.1075$ and $f = 20$ Hz are obtained and tabulated in Table 8.1.

The data presented in Table 8.1 is for the worst case of the results presented, *i.e.*, for Figure 8.48. The accuracy of $\pm 0.25 - 0.29$ Pa, which is less than 10% of the pressure readings, explains the absolute accuracy of each pressure transducer. For Figure 8.48, this accuracy does not include the discrepancies between the readings by different pressure transducers and, at most, is off by 5% of the reading of individual pressure transducer, while for Figures 8.47, 8.49 and 8.50, the accuracy shown in Table 8.1 also includes the latter.

The uncertainties of the phase angle are assumed to be the values given by the

	PT1	PT2	PT3	PT4	PT5	PT6	PT7	PT8
Pressure reading (Pa)	2.924	3.102	2.783	3.248	2.847	2.888	3.024	2.458
Accuracy (Pa)	±0.27	±0.28	±0.25	±0.29	±0.26	±0.26	±0.27	±0.22

Table 8.1: Uncertainties associated with measured unsteady pressures.

	PT1	PT2	PT3	PT4	PT5	PT6	PT7	PT8
Phase angle (deg)	177	183	183	-181	178	175	175	-12
Accuracy (deg)	±5	±5	±5	±5	±5	±5	±5	±5

Table 8.2: Uncertainties associated with measured phase angles.

accuracy of transfer function in the phase mode of the FFT analyzer, *i.e.*, $\pm 5^o$ for all phase angle measurements. For instance, for the pressure transducers shown in Figure 8.7(a), the phase angles at $\bar{\epsilon} = 1$ mm and $f = 20$ Hz are tabulated in Table 8.2.

Following the same analysis and using equations (8.1) and (8.8), the uncertainty pertinent to the flow velocity measurement for a specific orifice plate and manometer reading of $h_w = 7.3$ cm of alcohol with density $\rho_{al} = 0.7866$ gr/cm^3 is

$$U = 2.53 \pm 2.6\% \, \mathrm{m/s}\,.$$

Following the previous error analysis for most of the measurements, the experimental data presented in this chapter can be relied upon. Certain modifications in the apparatus and more precise measuring instruments would provide more accurate results. One of the most important factors affecting the experimental results is to have a firm foundation for the apparatus. The floor on which the whole system is mounted is not rigid enough to prevent transmission of vibration from the surroundings to the system or from the frame of the shaker to the inner cylinder via the supports of the apparatus. Also, developing other solutions for the problem of the end gaps would certainly improve the accuracy of the results.

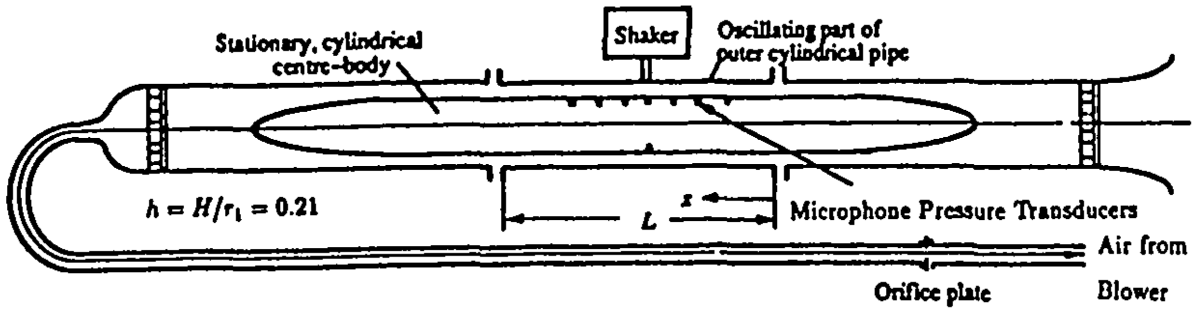

Figure 8.1: Schematic of the experimental apparatus in which either transverse or rocking motion of the central part of the outer cylinder can be imposed by the shaker.

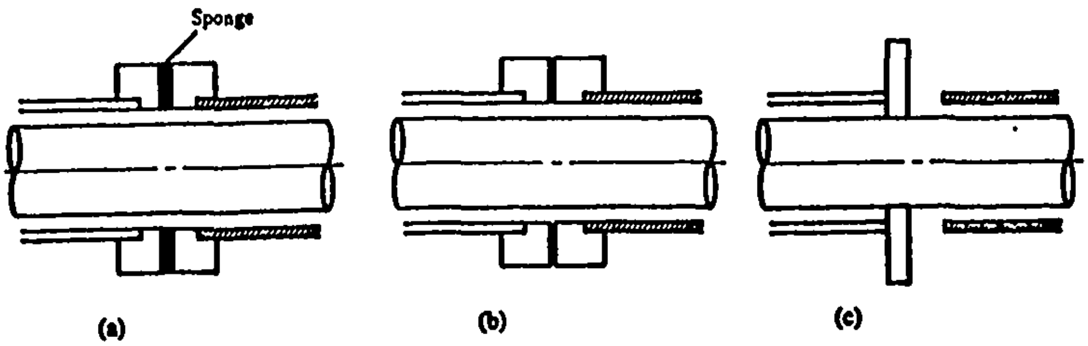

Figure 8.2: Sealing arrangements between the moving and fixed parts of the outer cylinder: (a) sponge-felt gaskets between the flanges; (b) close-fitting flanges; (c) flange with lubricated rubbing contact with the oscillating cylinder (for zero axial velocity only).

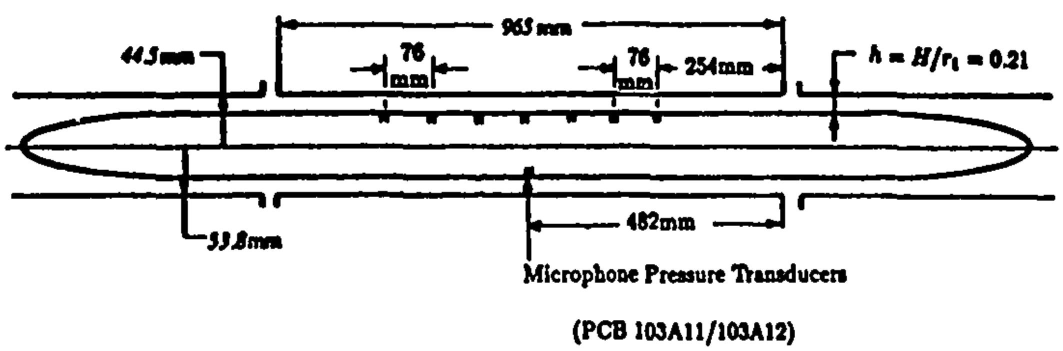

Figure 8.3: Schematic diagram of the central portion of the apparatus, showing dimensions and location of the pressure transducers.

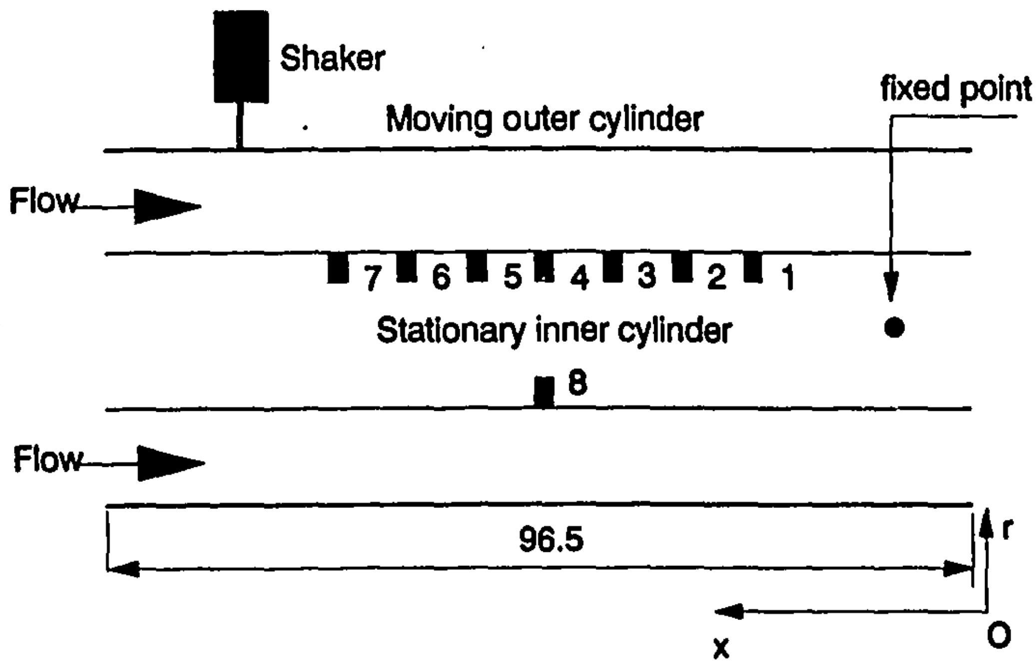

Figure 8.4: Schematic diagram of the centre-body, the outer cylinder, the shaker and the pressure transducers for rocking motion of the outer cylinder.

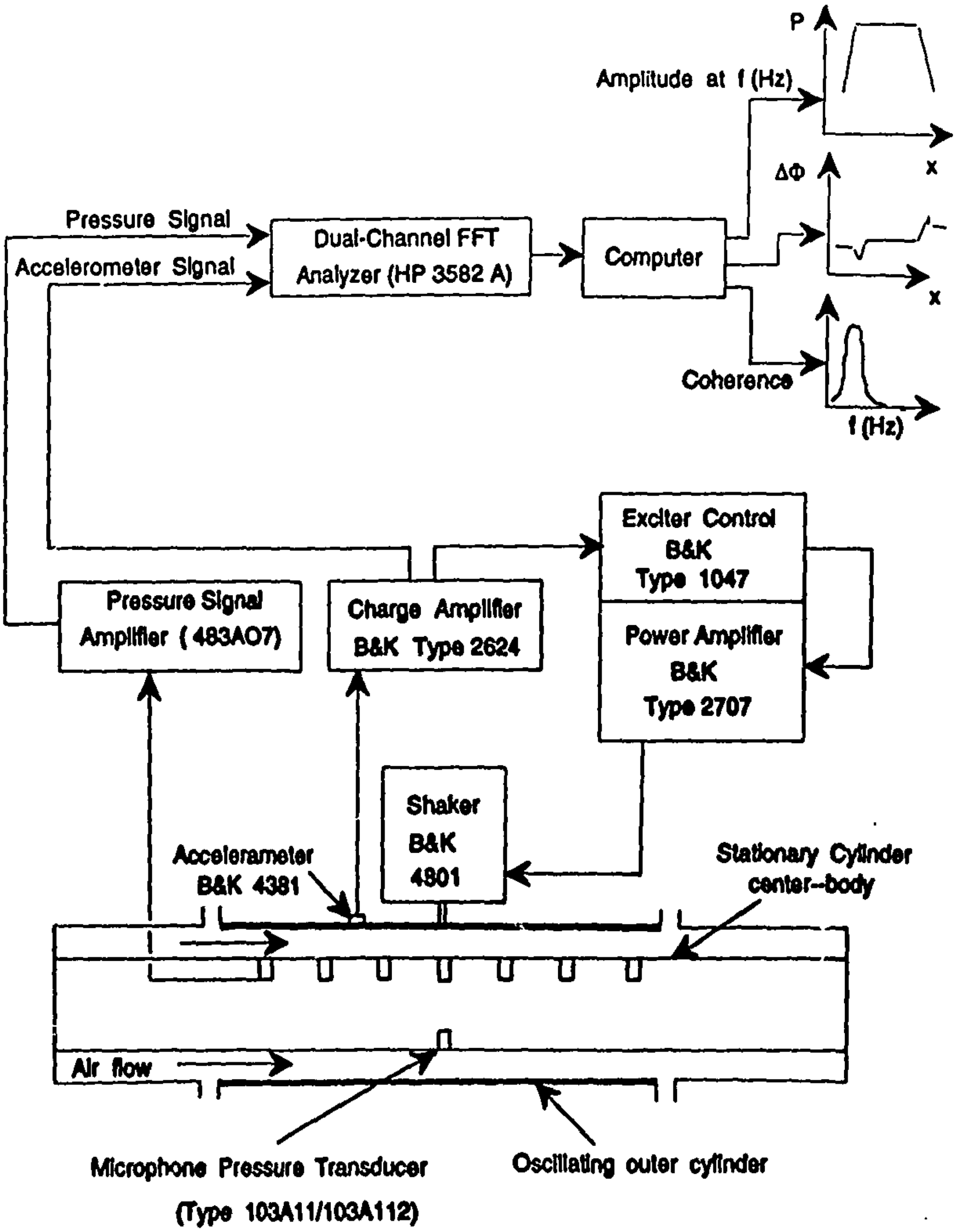

Figure 8.5: Schematic diagram of the experimental apparatus and its accessories.

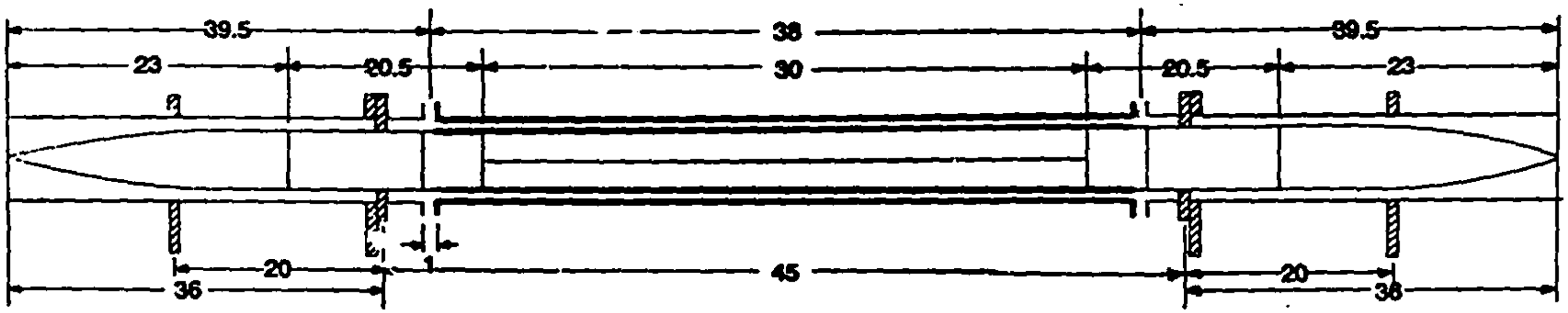

Figure 8.6: Schematic diagram of the centre-body, the outer cylinder and their supports with all dimensions in inches.

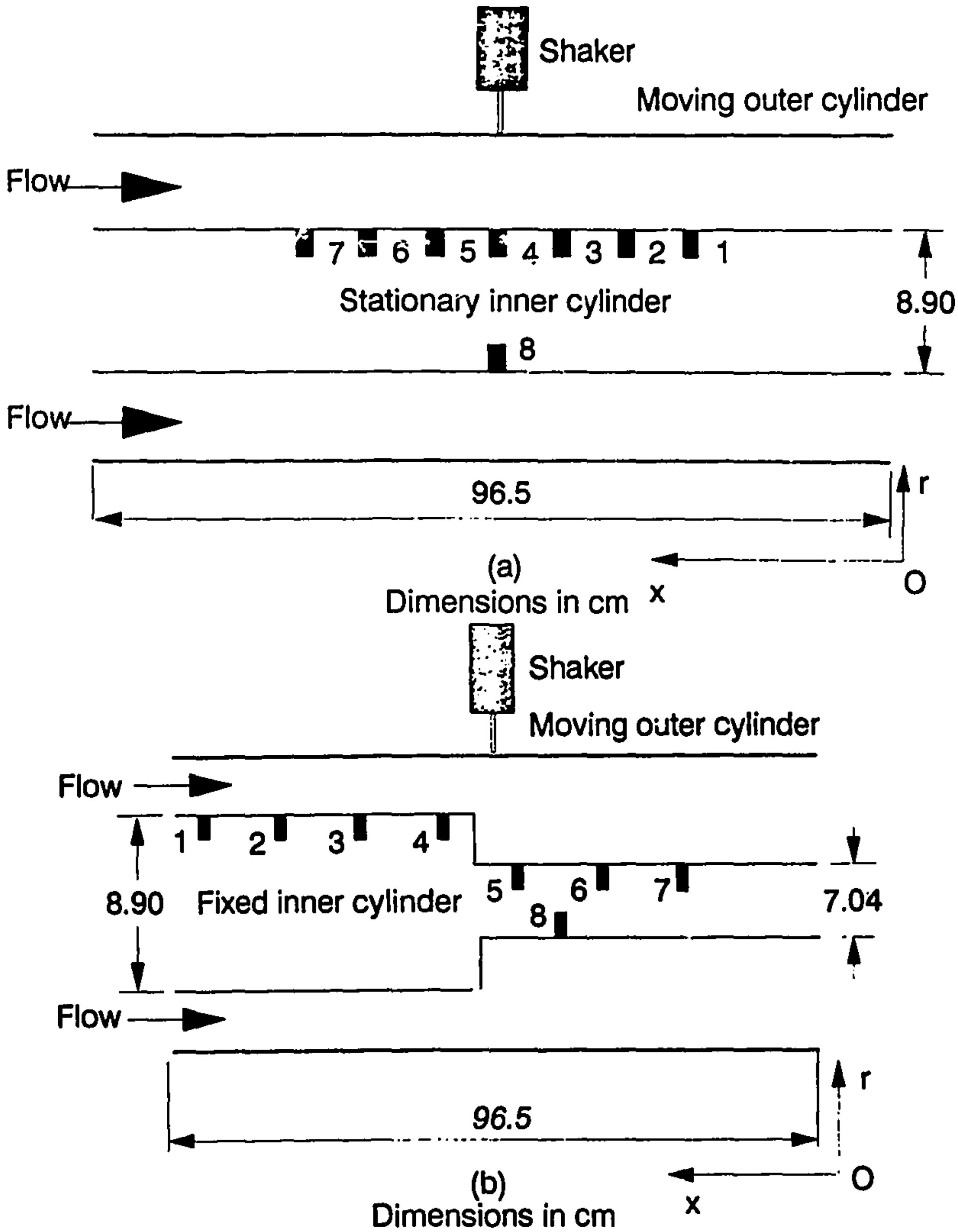

Figure 8.7: Schematic representation of the mounting of pressure transducers for three different annular spaces.

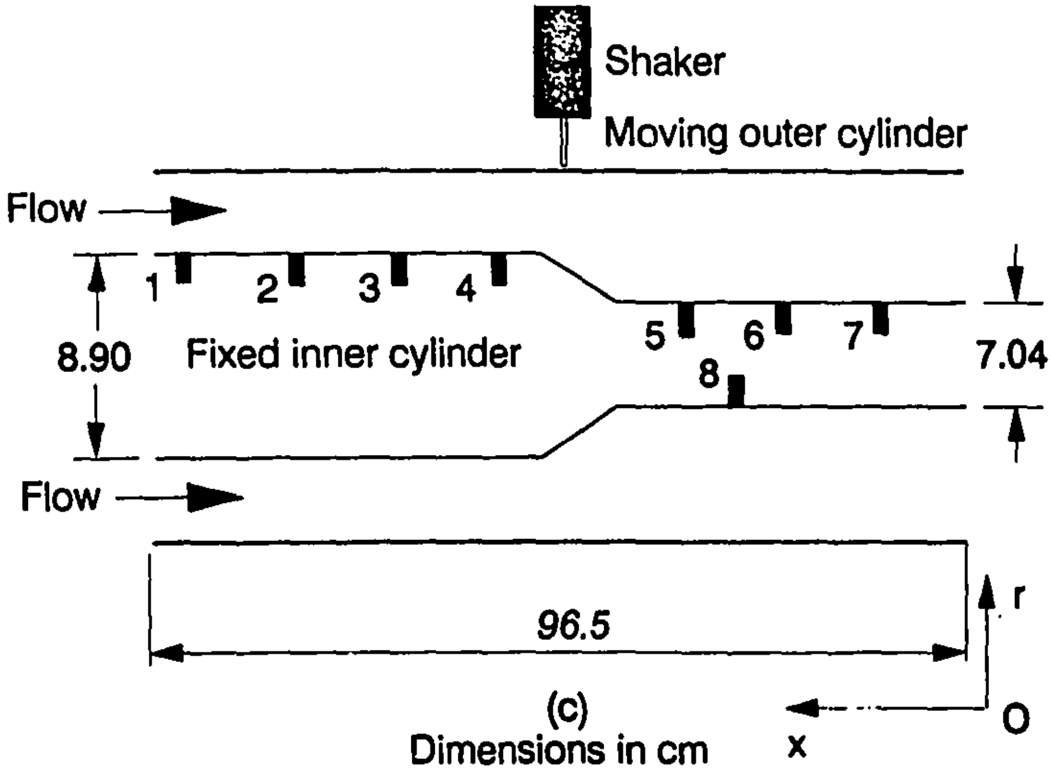

Figure 8.7: *continued*

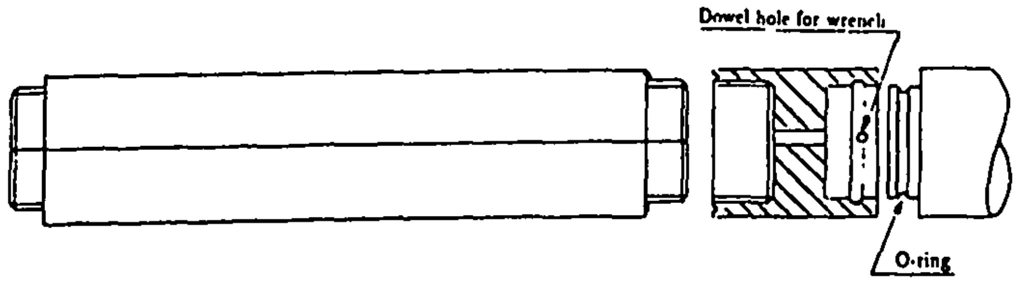

Figure 8.8: Expanded view of the centre-body and its end ring.

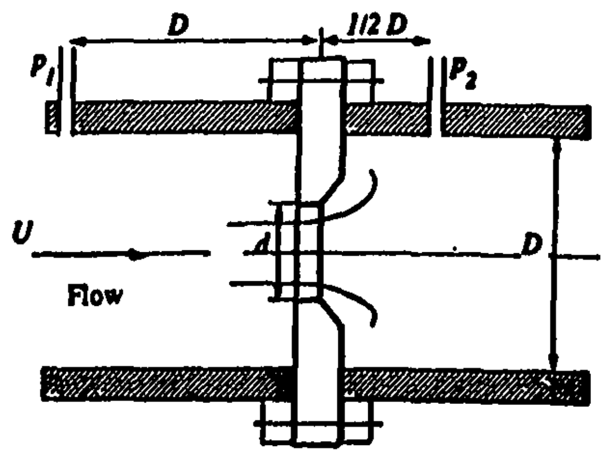

Figure 8.9: Schematic diagram of the orifice plate used in the experiments.

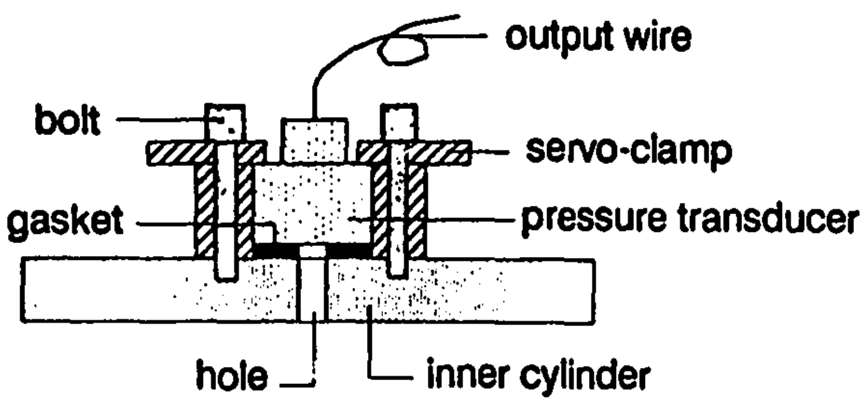

Figure 8.10: Schematic diagram of the arrangement for mounting the pressure transducer inside the centre-body.

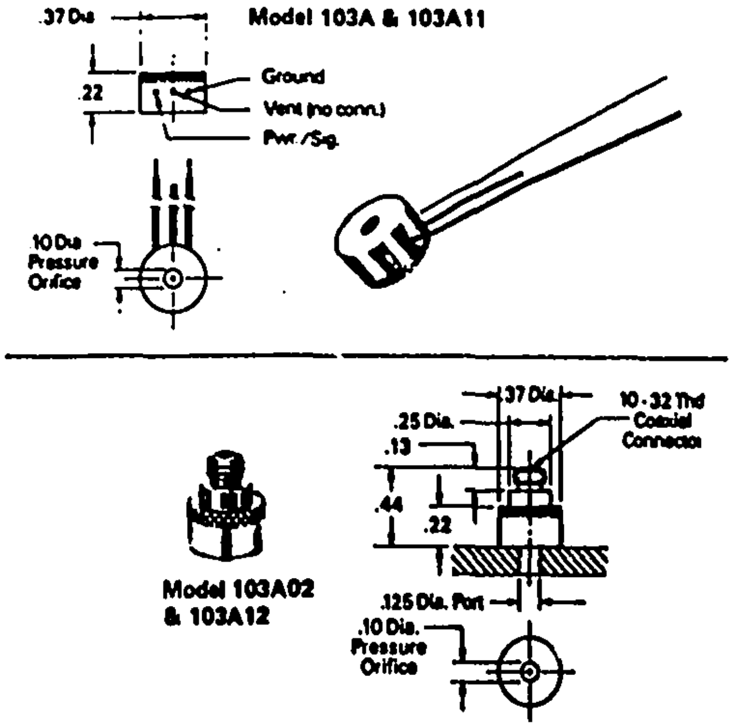

Figure 8.11: Schematic diagram of the microphone-type dynamic pressure transducers used in the experiments.

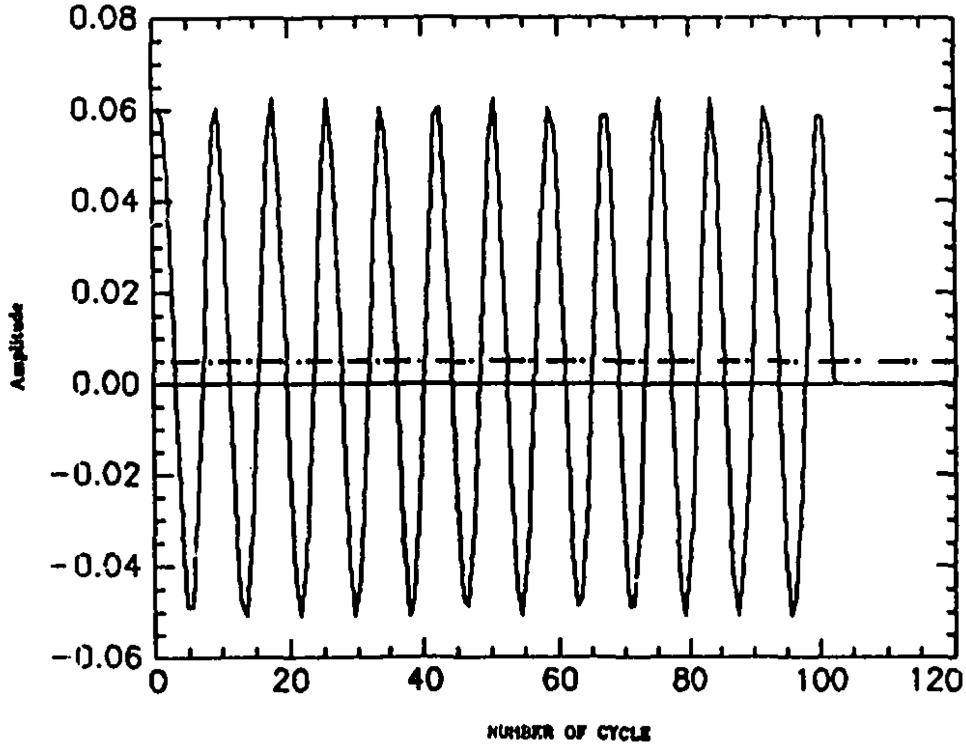

Figure 8.12: Amplitude of the moving outer cylinder detected by the photonic sensor for $\epsilon = 0.05375$.

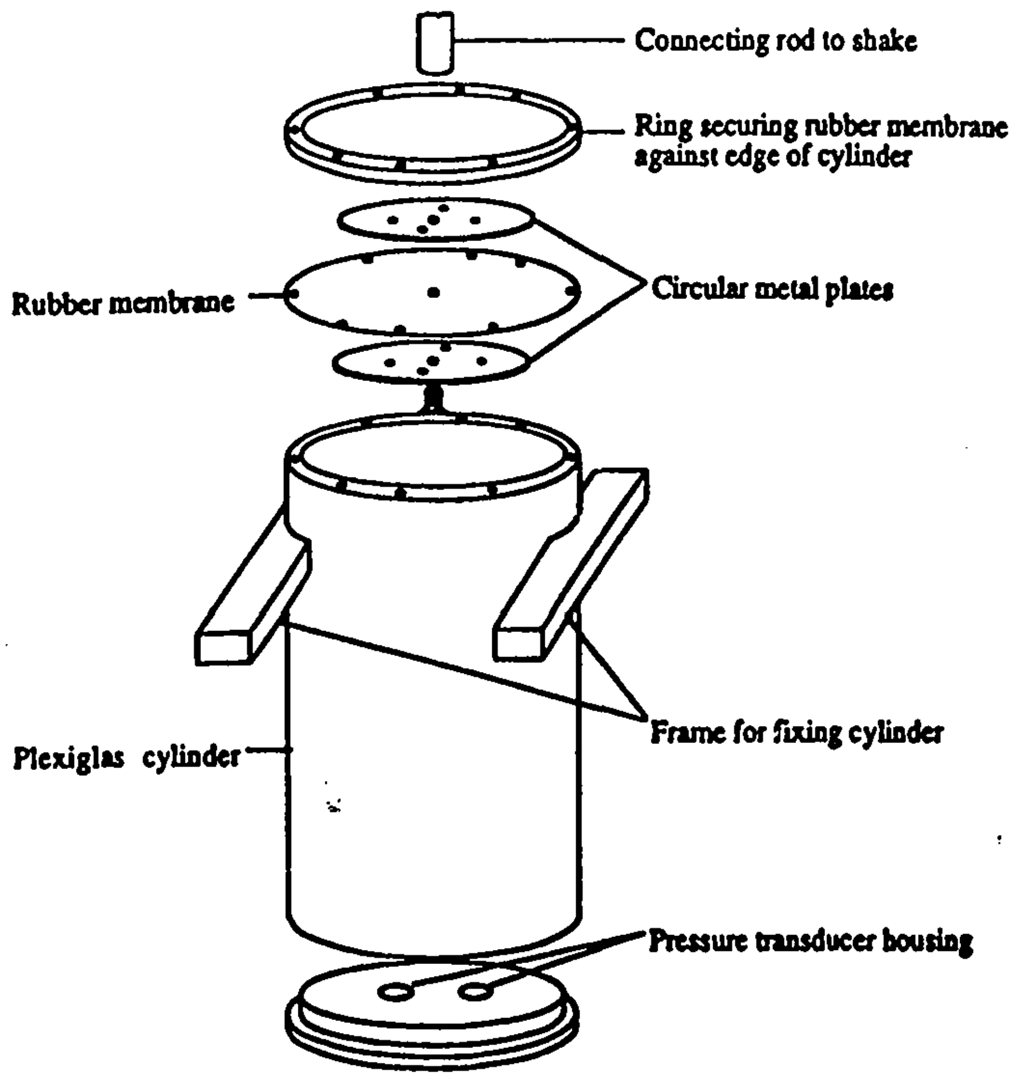

Figure 8.13: Schematic diagram of the chamber used for pressure-transducer calibration.

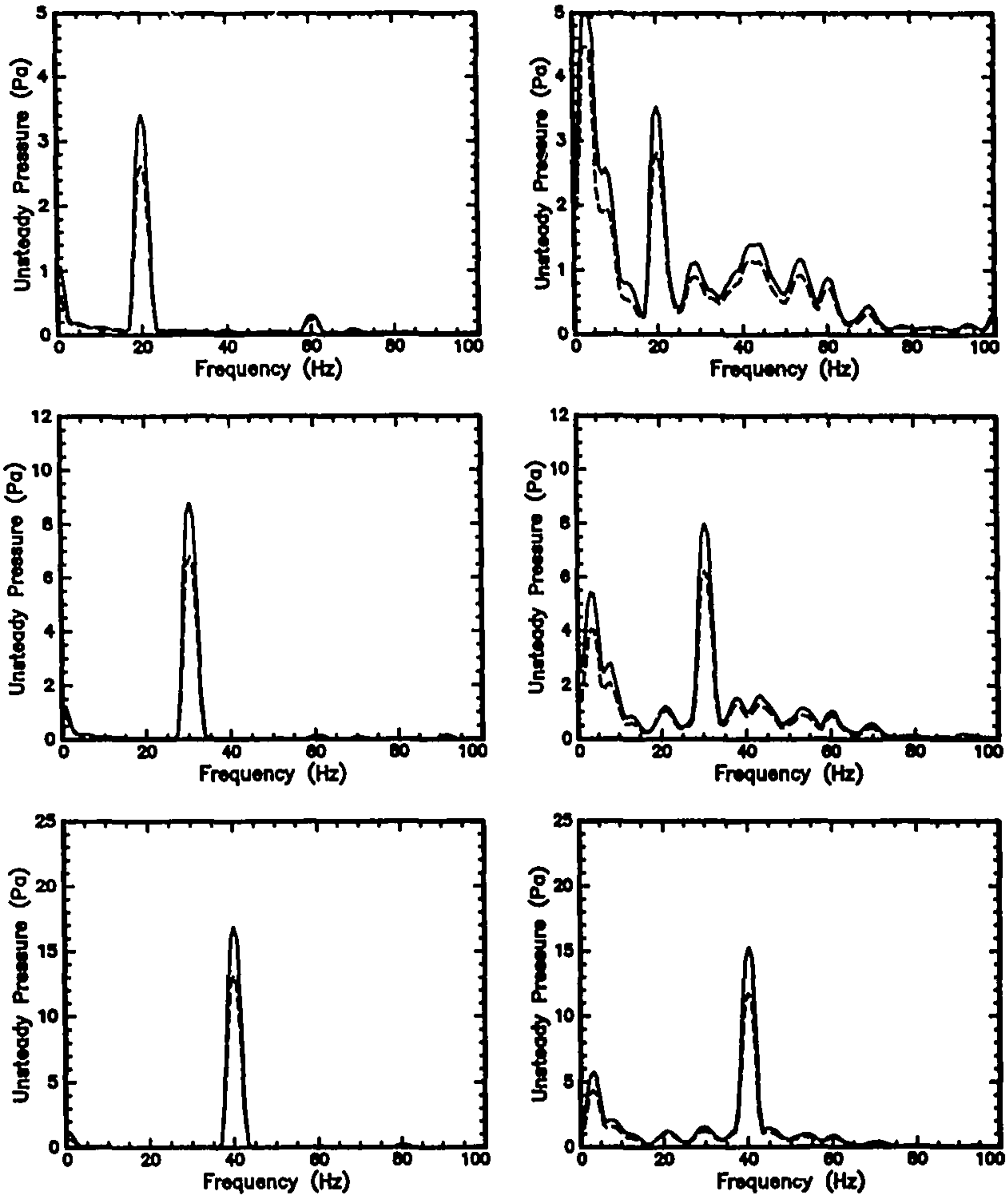

Figure 8.14: samples of amplitude spectra of the unsteady pressure from pressure transducers; —,No. 1; - - -,No. 2 shown in Figure 8.7(a) at different frequencies for amplitude of oscillation $\epsilon = 0.05375$. The outer cylinder is in translational motion. Left figures, no flow; right figures, Re = 2900.

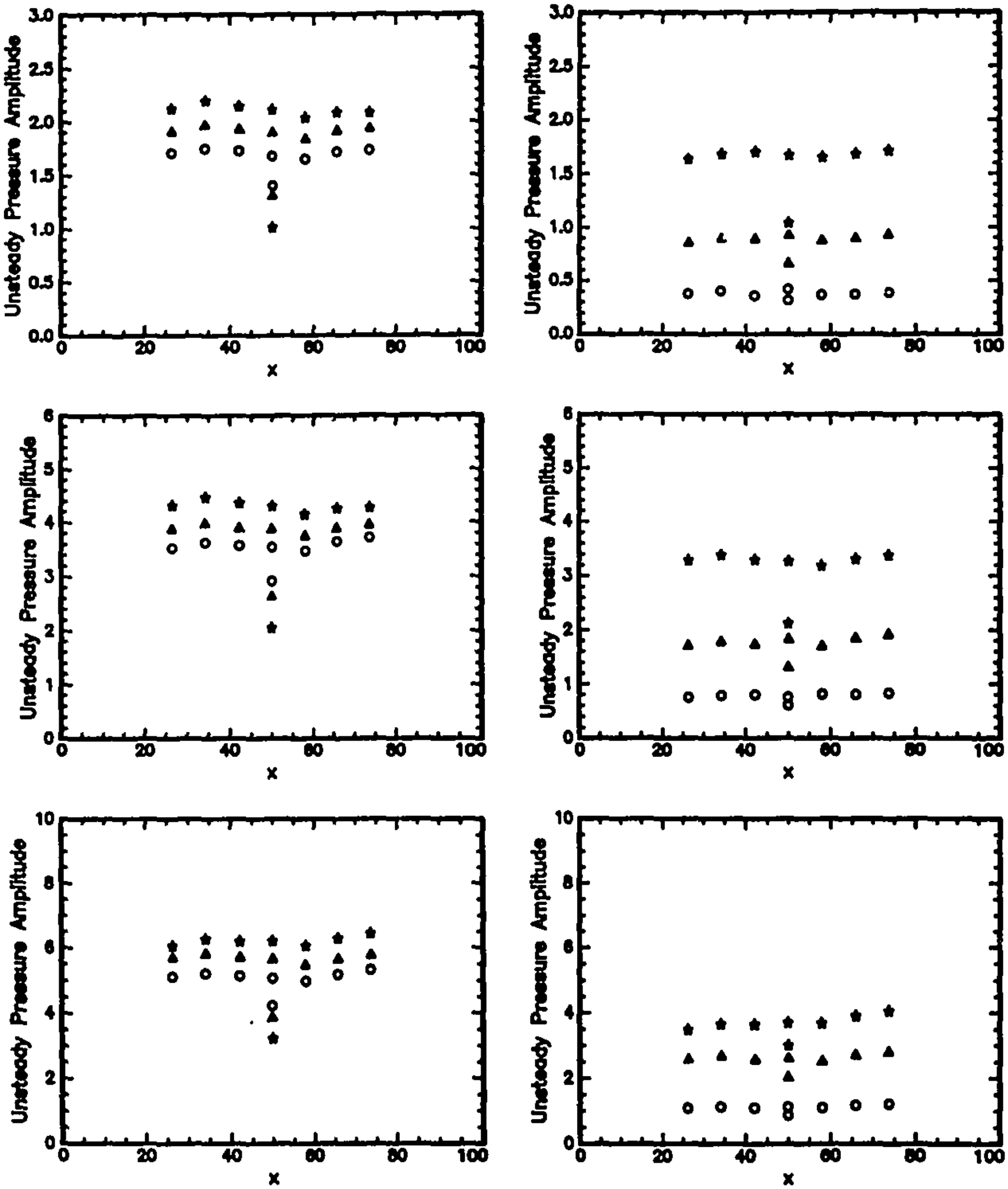

Figure 8.15: Nondimensional unsteady pressure versus length for translational motion of the outer cylinder. The amplitudes of oscillation from top to bottom are: $\epsilon = 0.05375$, $\epsilon = 0.1075$ and $\epsilon = 0.16125$ and the frequencies are: o, $f = 20$ Hz; Δ, $f = 30.4$ Hz; $*$, $f = 40$ Hz. Left figures, no flow; right figures, Re = 2900.

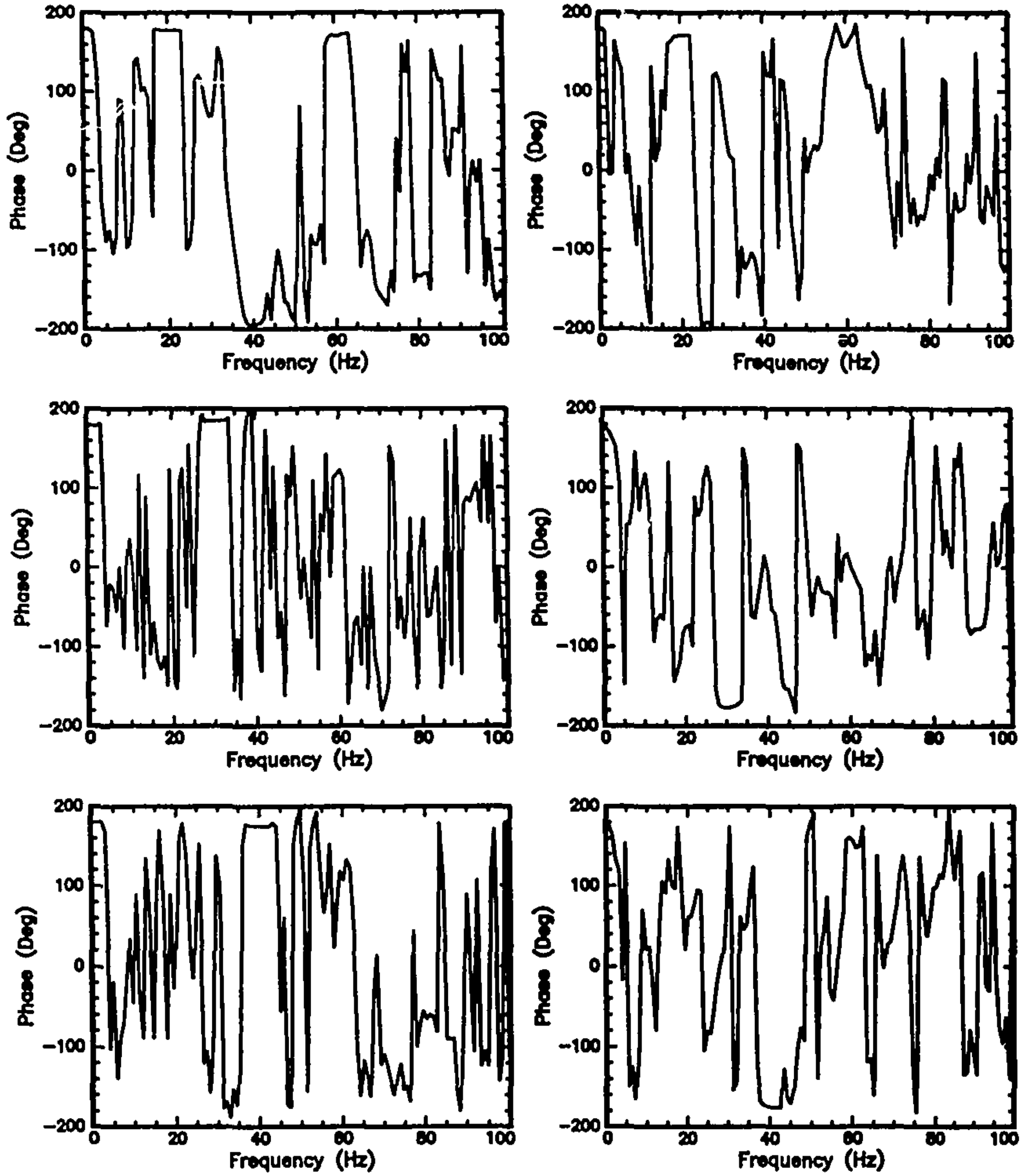

Figure 8.16: samples of phase angle spectra of the unsteady pressure with respect to the acceleration of the outer cylinder for pressure transducer No. 1 shown in Figure 8.7(a) at different frequencies for $\epsilon = 0.05375$; the outer cylinder is in translational motion. Left figures, no flow; right figures, Re = 2900.

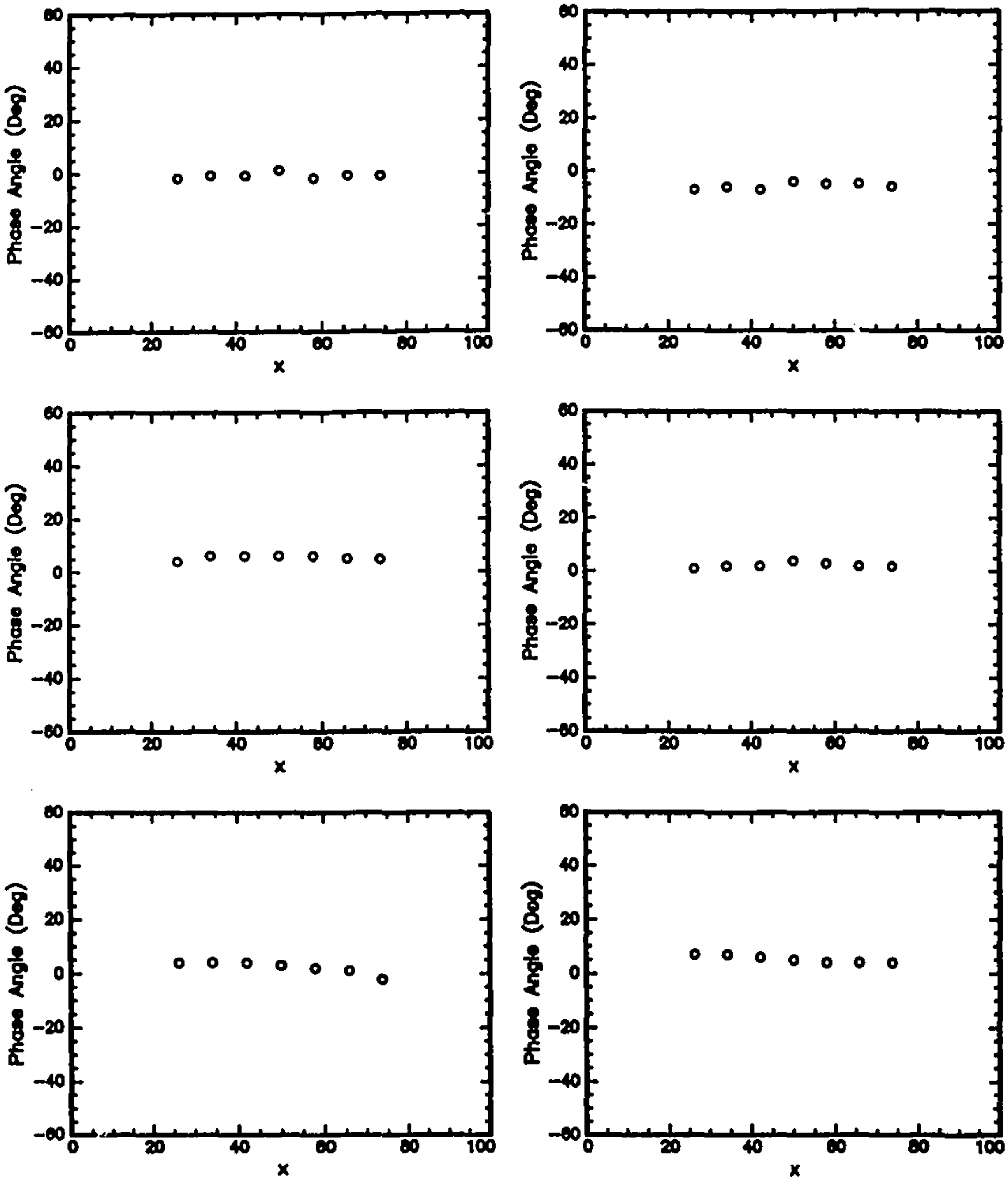

Figure 8.17: samples of phase angles of the unsteady pressure with respect to the displacement of the outer cylinder in translational motion for $\epsilon = 0.16125$. From top to bottom; f = 20 Hz, f = 30.4 Hz and f = 36 Hz. Left figures, no flow; right figures, Re = 2900. X is difined as x/H.

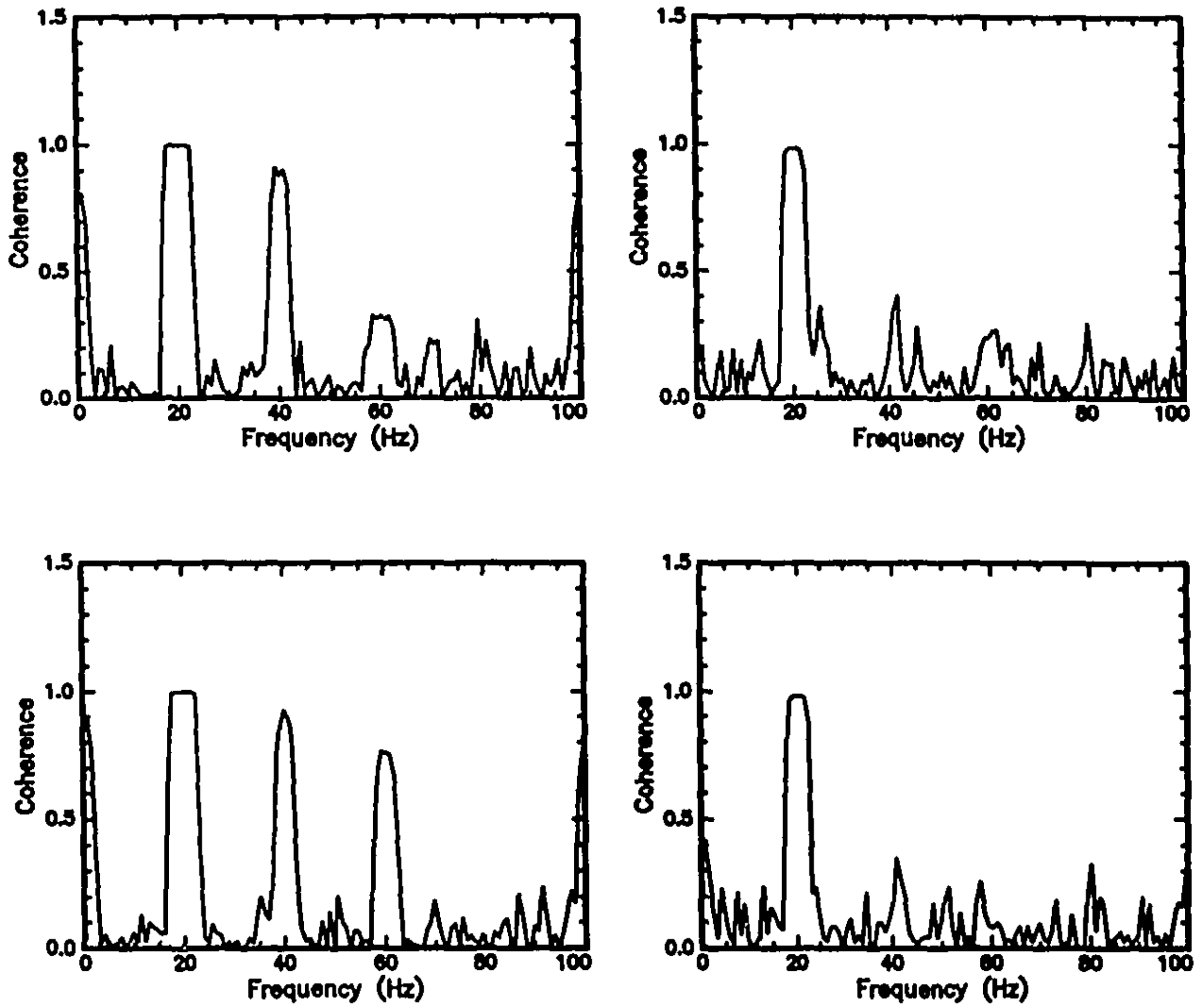

Figure 8.18: samples of coherence spectra of the unsteady pressure with respect to the acceleration of outer cylinder in translational motion from pressure transducers No. 3 (top) and No. 5 (bottom) shown in Figure 8.7(a) at $f = 20$ Hz and $\epsilon = 0.1075$; left figures, no flow; right figures, $Re = 2900$.

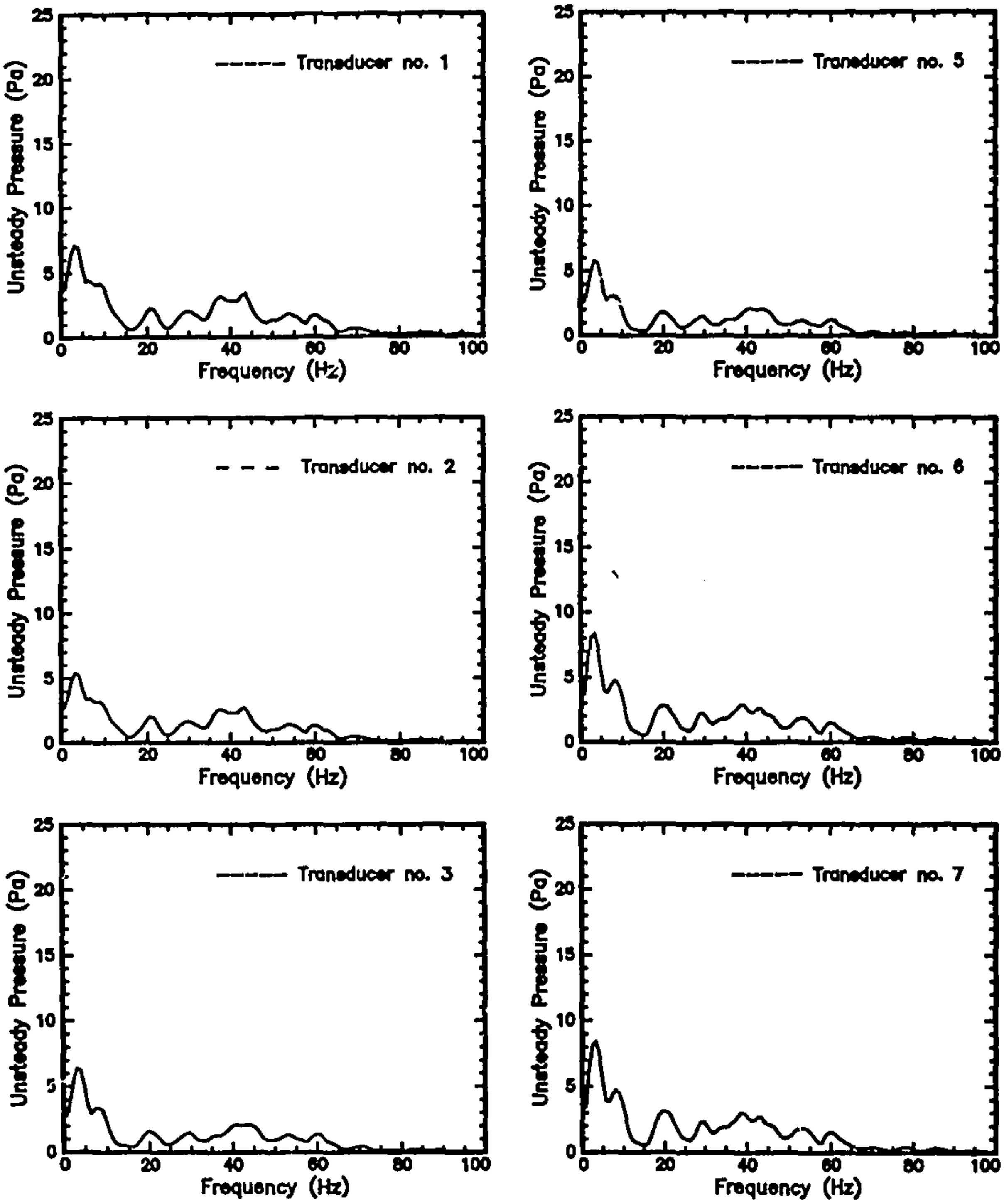

Figure 8.19: Unsteady pressure spectrum generated by high velocities, Re = 5000, without motion of the outer cylinder and measured by different pressure transducers.

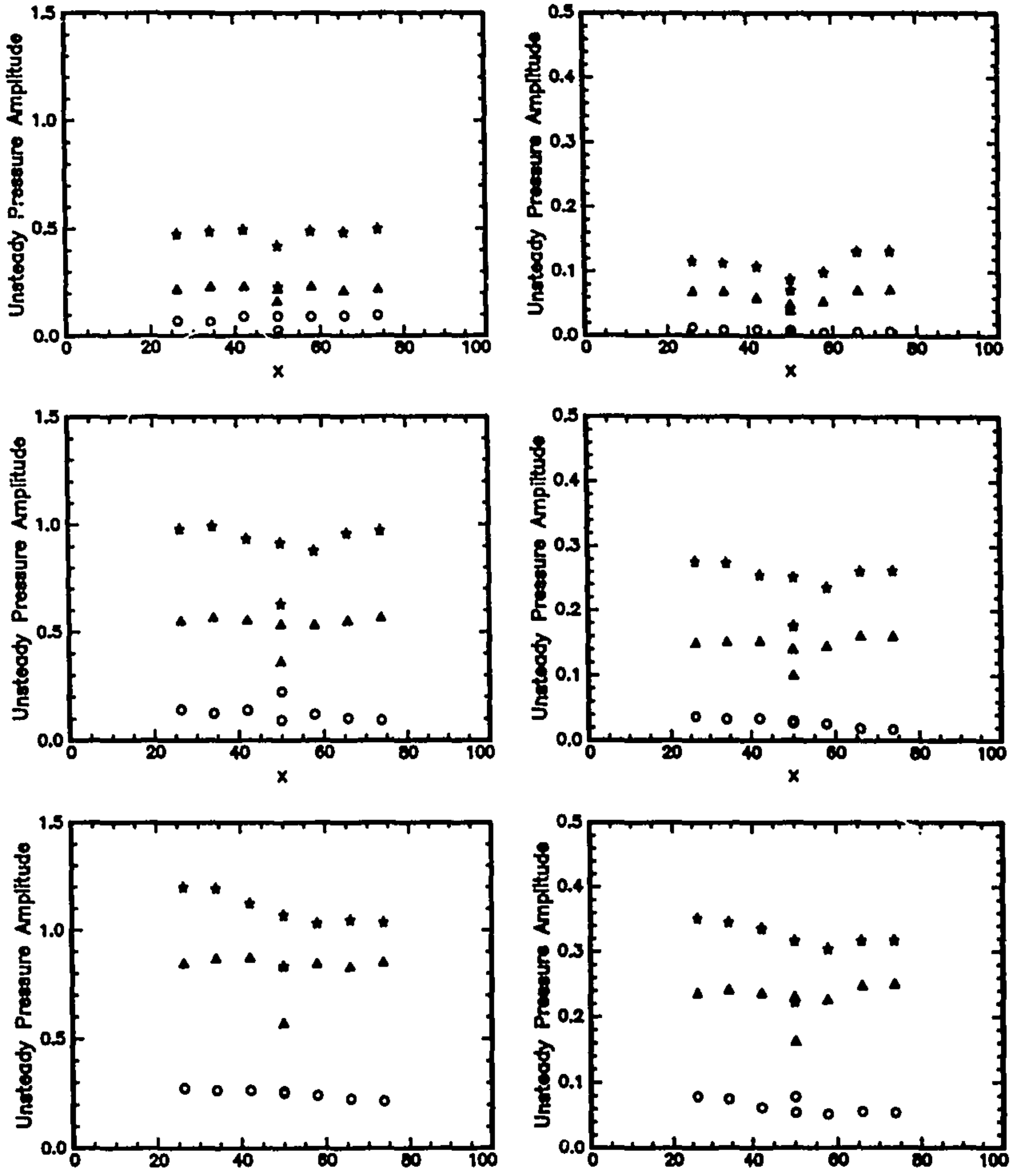

Figure 8.20: Nondimensional unsteady pressure versus length for translational motion of the outer cylinder. The amplitudes of oscillation from top to bottom are: $\epsilon = 0.05375$, $\epsilon = 0.1075$ and $\epsilon = 0.16125$ and the frequencies are: o, $f = 20$ Hz; Δ, $f = 30.4$ Hz; $*$, $f = 40$ Hz. Left figures, Re = 5000; right figures, Re = 9000.

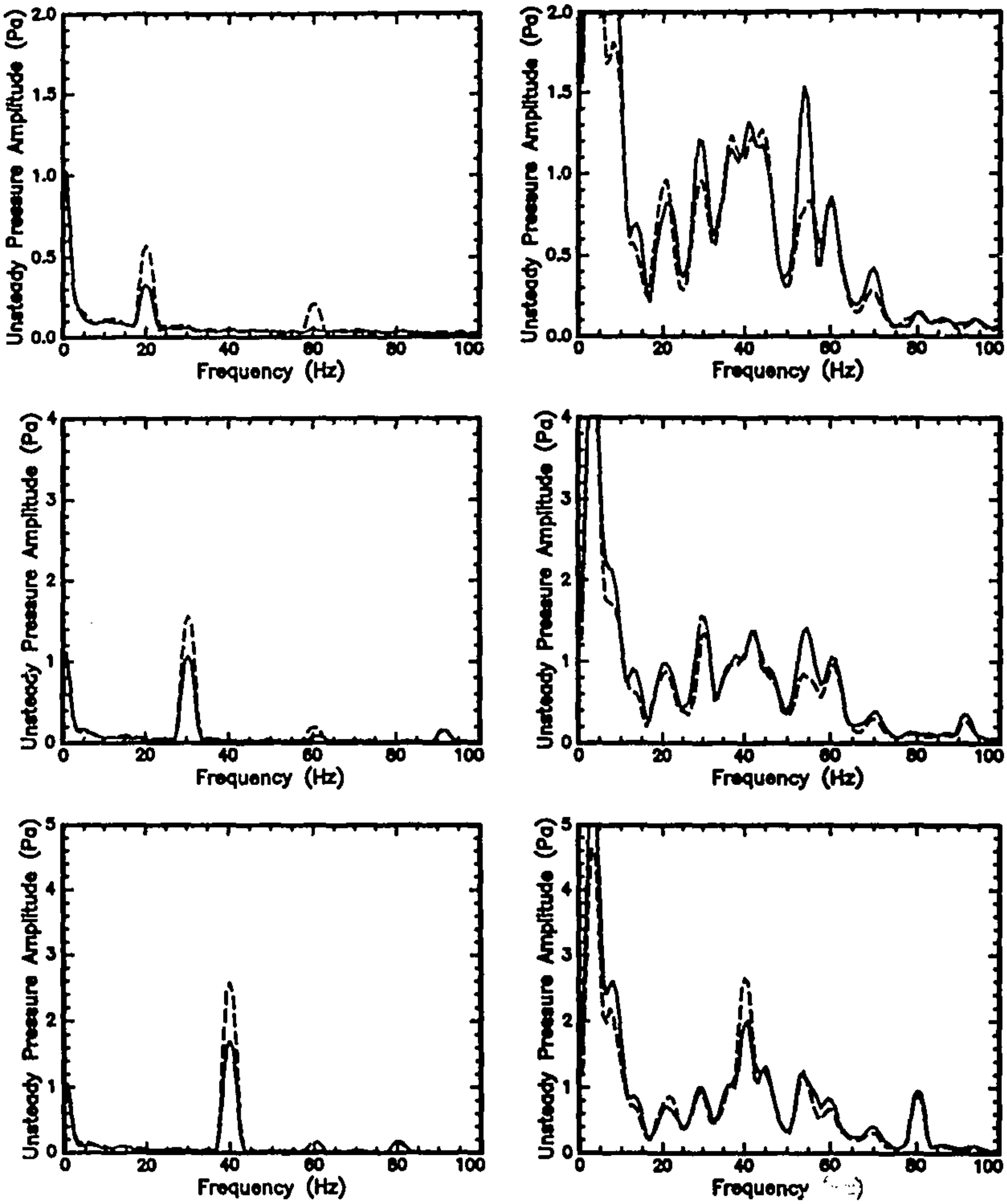

Figure 8.21: samples of amplitude spectra of the unsteady pressure from pressure transducers; —,No. 1; - - -,No. 2 shown in Figure 8.4 at different frequencies for $\epsilon = 0.05375$. The outer cylinder is in rocking motion. Left figures, no flow; right figures, Re = 2900.

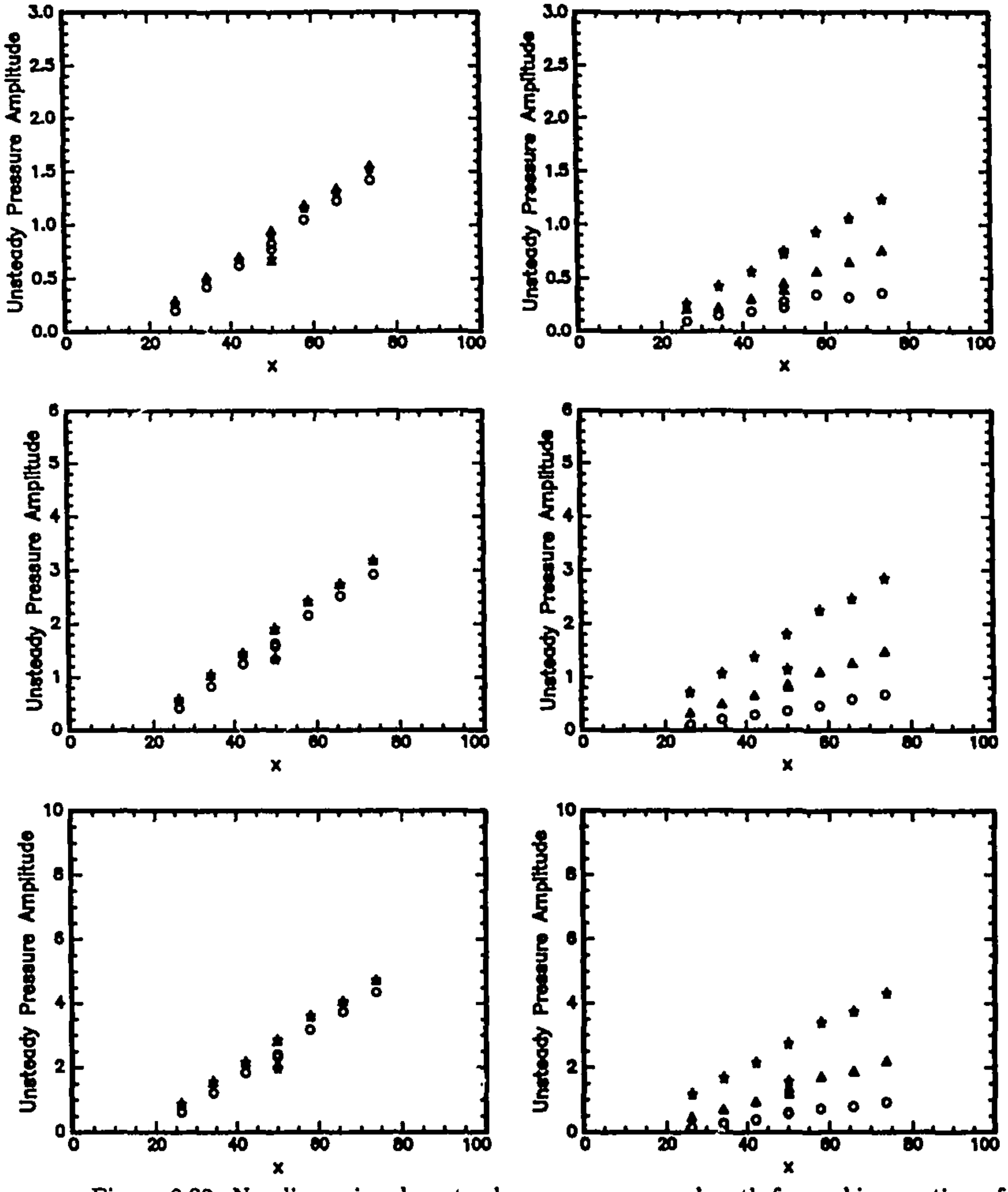

Figure 8.22: Nondimensional unsteady pressure versus length for rocking motion of the outer cylinder. The amplitudes of oscillation from top to bottom are: $\epsilon = 0.05375$, $\epsilon = 0.1075$ and $\epsilon = 0.16125$ and the frequencies are: $\circ$, $f = 20$ Hz; Δ, $f = 30.4$ Hz; $*$, $f = 40$ Hz. Left figures, no flow; right figures, Re = 2900.

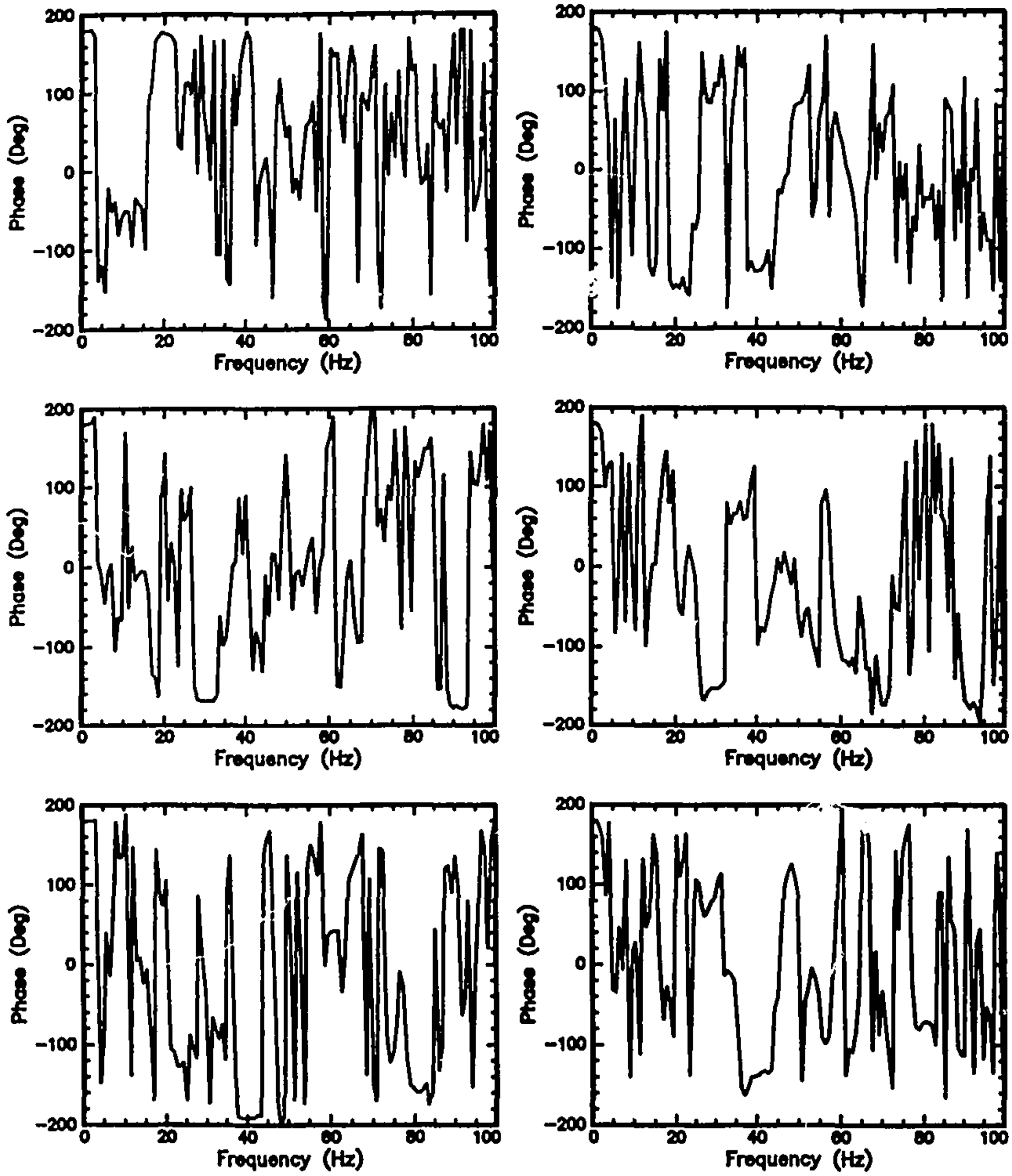

Figure 8.23: samples of phase angle spectra of the unsteady pressure with respect to the acceleration of outer cylinder for pressure transducer No. 1 shown in Figure 8.4 at different frequencies of oscillation for $\epsilon = 0.05375$; the outer cylinder is in rocking motion. Left figures, no flow; right figures, Re = 2900. Top, f = 20 Hz; middle, f = 30.4 Hz; bottom, f = 40 Hz.

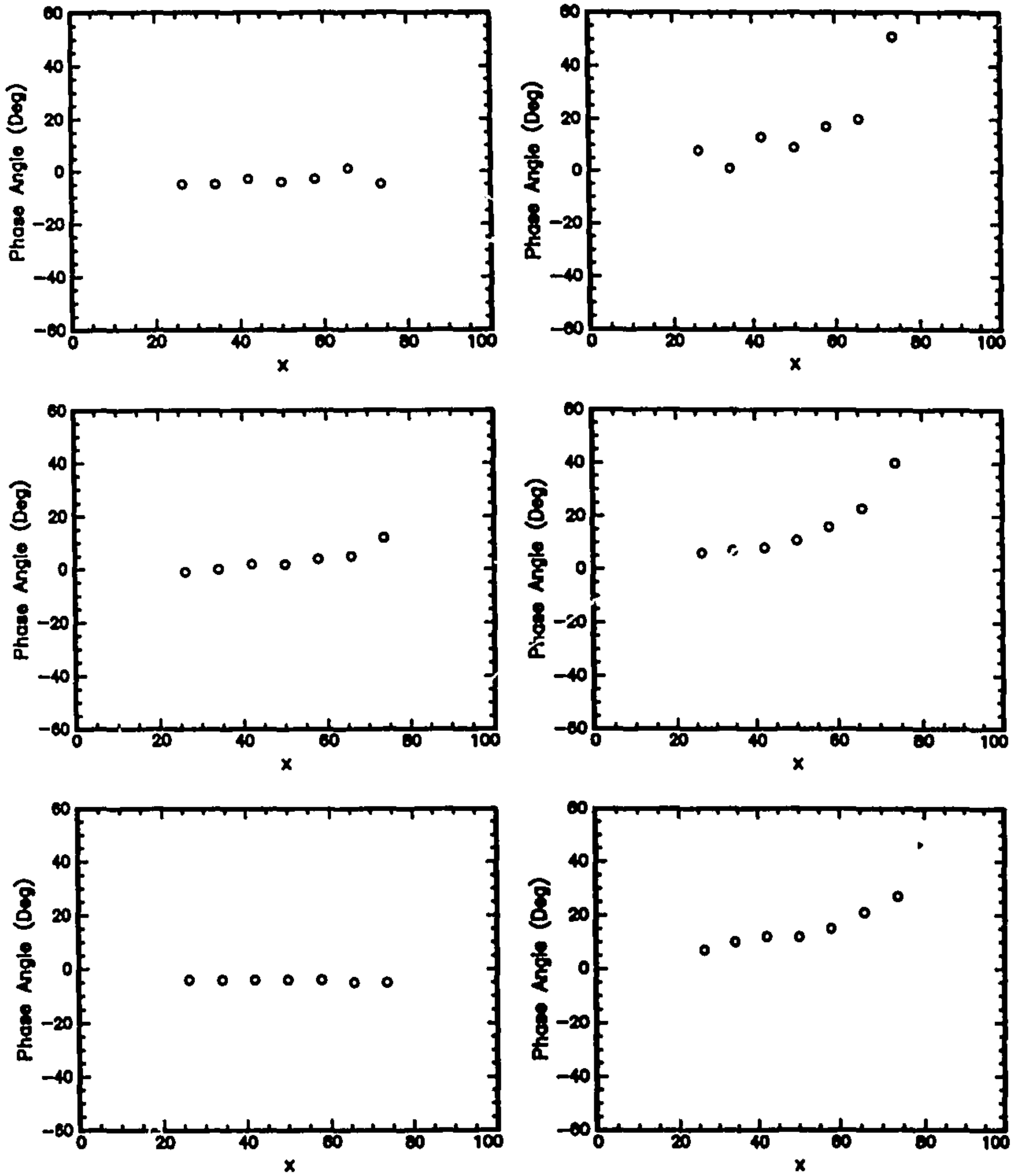

Figure 8.24: samples of phase angles of the unsteady pressure with respect to the displacement of the outer cylinder in rocking motion for $\epsilon = 0.16125$. From top to bottom; $f = 20$ Hz, $f = 30.4$ Hz and $f = 36$ Hz. Left figures, no flow; right figures, Re = 2900. X is difined as x/H.

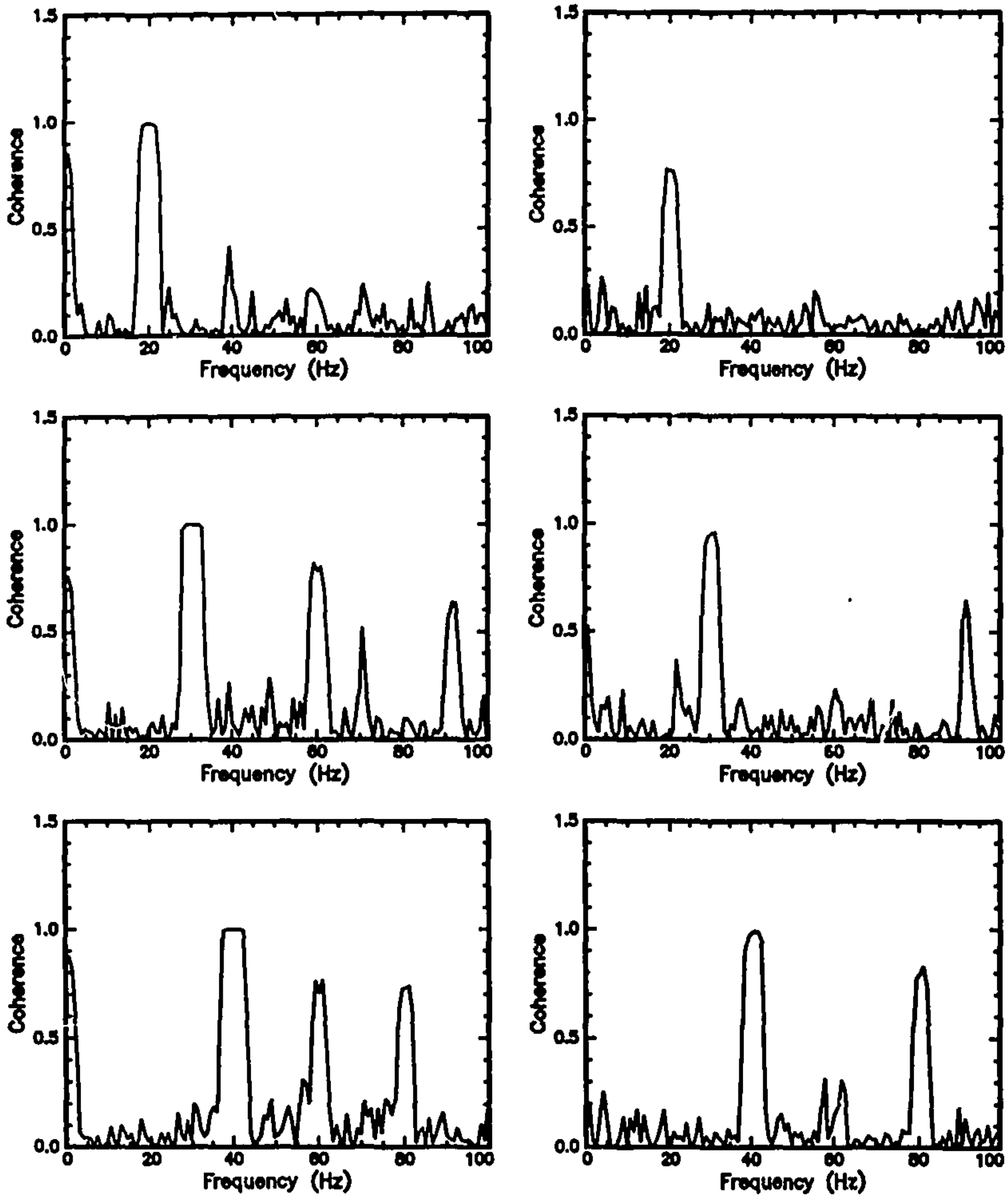

Figure 8.25: samples of coherence spectra of the unsteady pressure with respect to the acceleration of outer cylinder in rocking motion from pressure transducer No. 3 shown in Figure 8.4; top, $f = 20$ Hz; middle, $f = 30.4$ Hz; bottom, $f = 40$ Hz and $\epsilon = 0.05375$; left figures, no flow; right figures, Re $= 2900$.

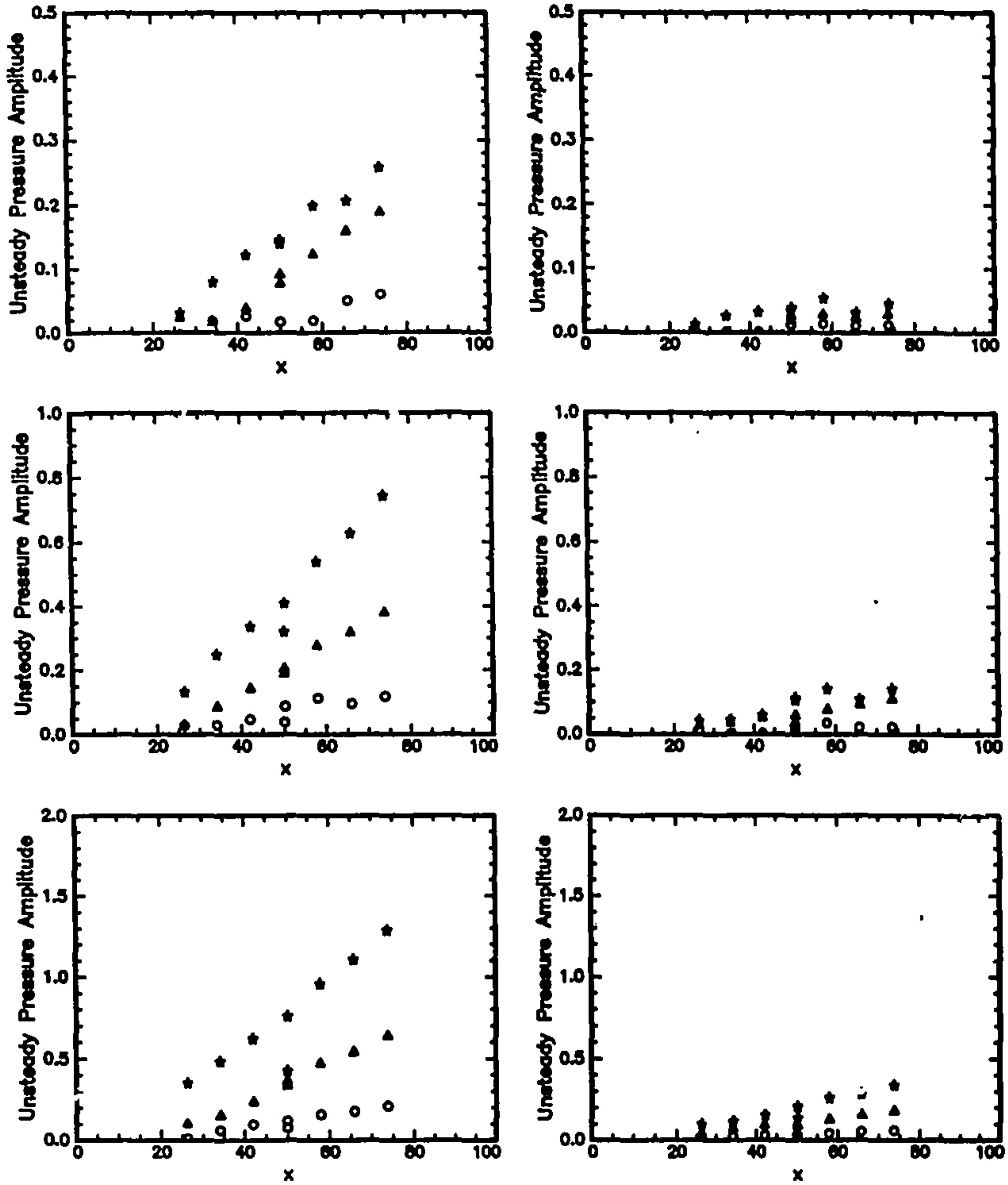

Figure 8.26: Nondimensional unsteady pressure versus axial distance for rocking motion of the outer cylinder. The amplitudes of oscillation from top to bottom are: $\epsilon = 0.05375$, $\epsilon = 0.1075$ and $\epsilon = 0.16125$ and the frequencies are o, $f = 20$ Hz; Δ, $f = 30.4$ Hz; $*$, $f = 40$ Hz. Left figures, Re = 5000; right figures, Re = 9000. The hinge is at $X = 18.5$, where $X = x/H$.

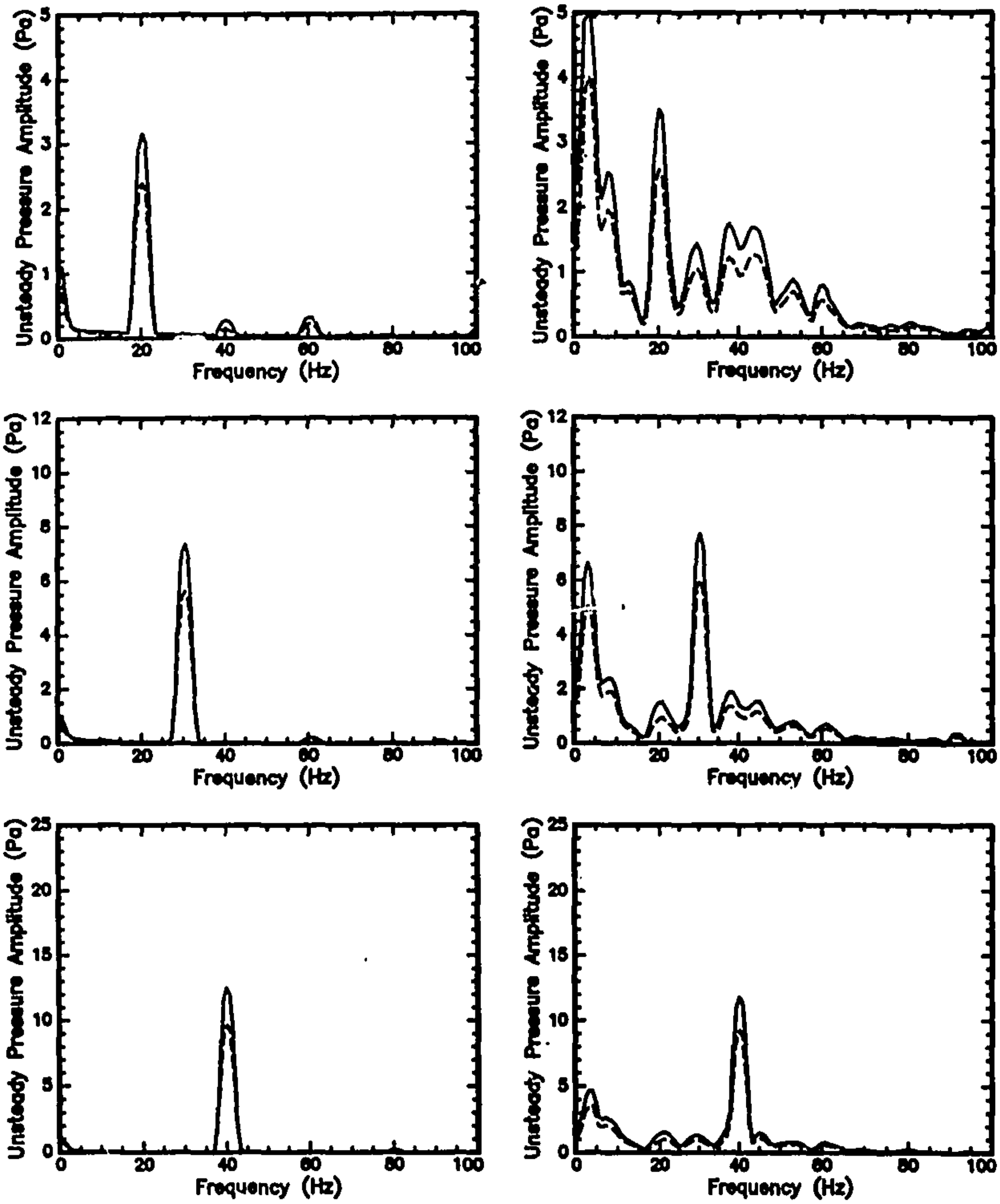

Figure 8.27: samples of amplitude spectra of the unsteady pressure from pressure transducers; —,No. 1; - - -,No. 2 shown in Figure 8.7(b) for backstep geometry at different frequencies for $\epsilon = 0.05375$. The outer cylinder is in translational motion. Left figures, no flow; right figures, Re = 2900.

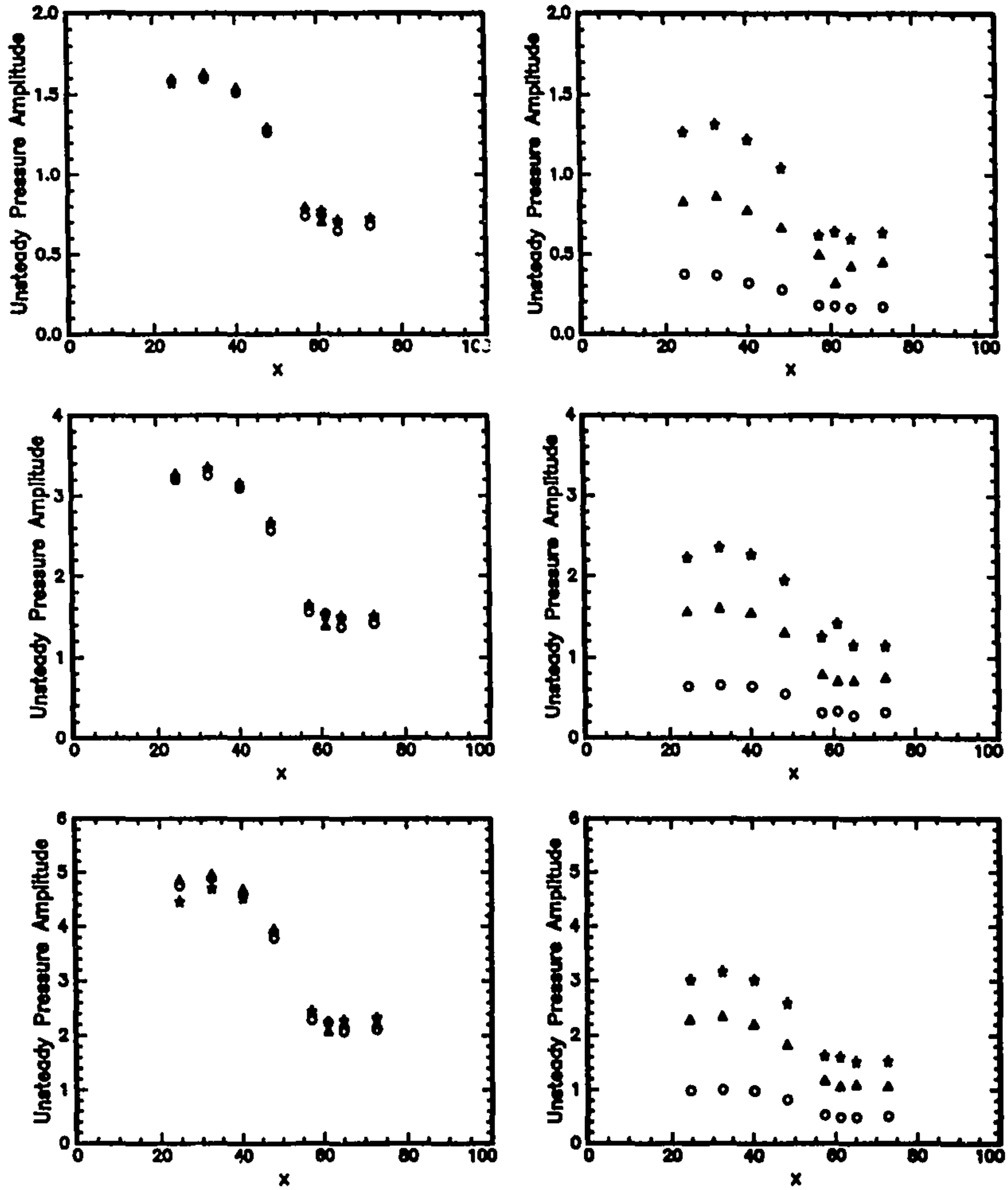

Figure 8.28: Nondimensional unsteady pressure versus axial distance for translational motion of the outer cylinder (backstep geometry). The amplitudes of oscillation from top to bottom are: $\epsilon = 0.05375$, $\epsilon = 0.1075$ and $\epsilon = 0.16125$ and the frequencies are o, f = 20 Hz; Δ, f = 30.4 Hz; $*$, f = 40 Hz. Left figures, no flow; right figures, Re = 2900.

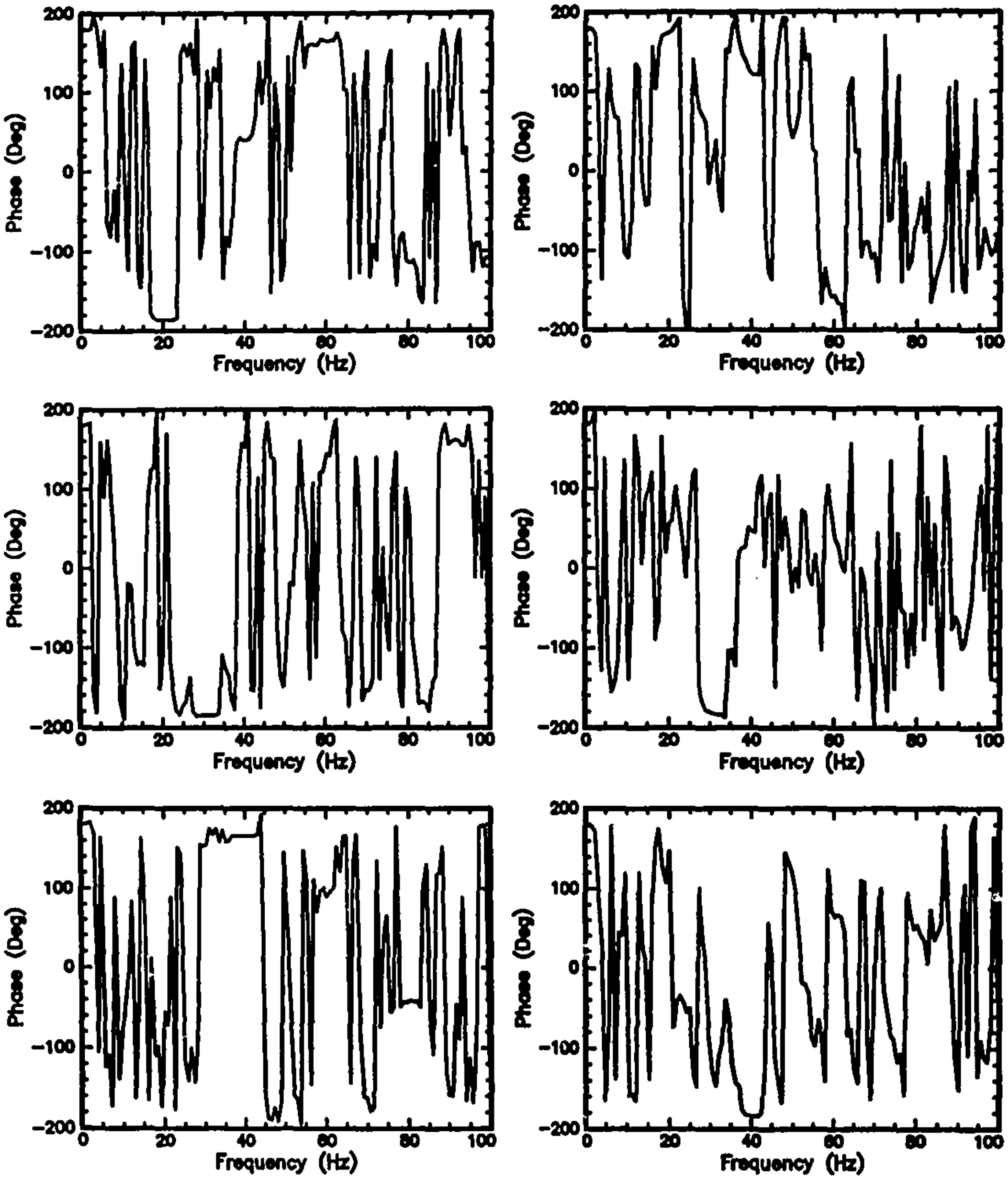

Figure 8.29: samples of phase angle spectra of the unsteady pressure with respect to the acceleration of the outer cylinder for pressure transducer No. 1 shown in Figure 8.7(b) for backstep geometry at different frequencies for $\epsilon = 0.05375$; the outer cylinder is in translational motion. Left figures, no flow; right figures, Re = 2900.

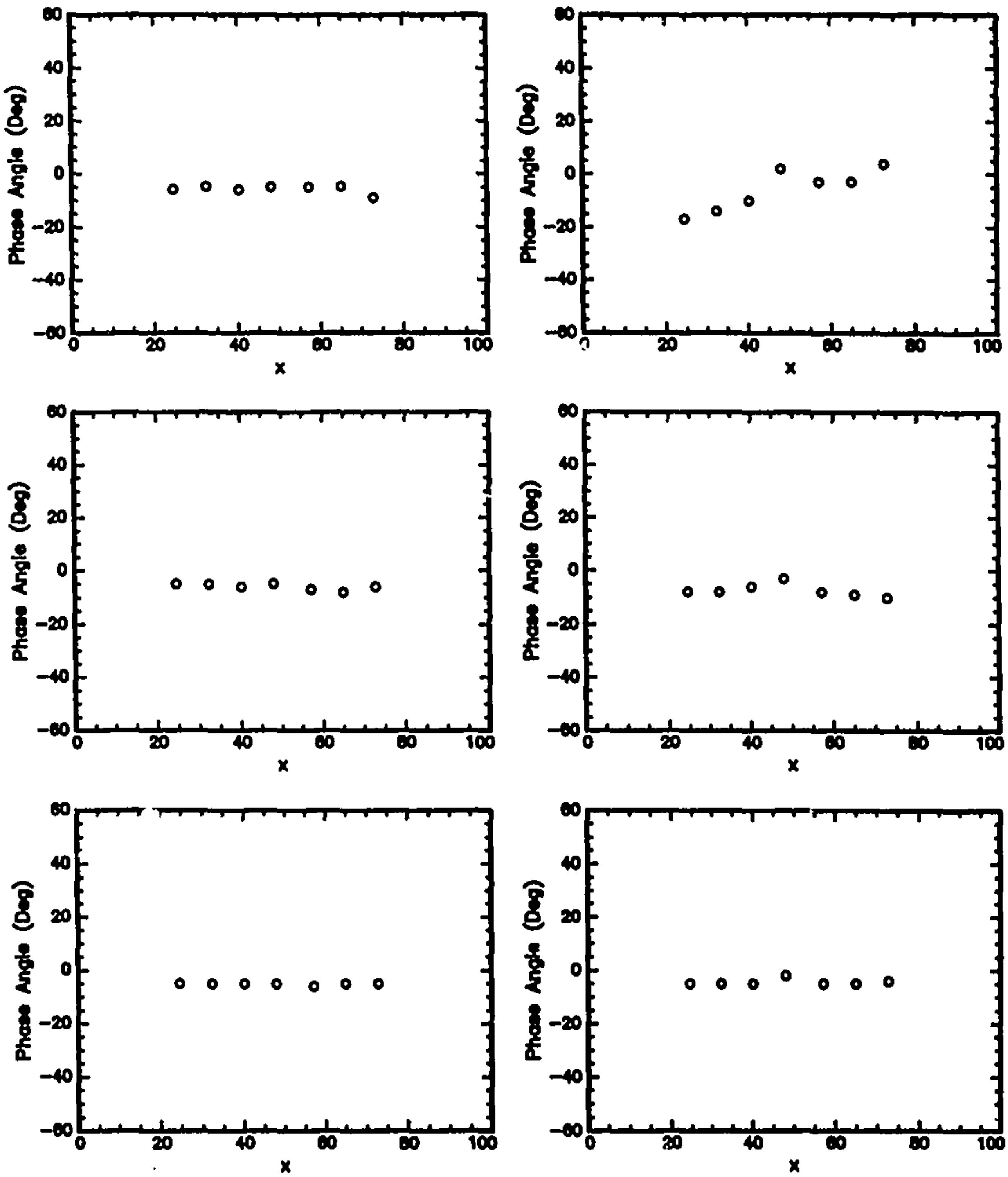

Figure 8.30: samples of phase angles of the unsteady pressure with respect to the displacemet of the outer cylinder in translational motion for backstep geometry and $\epsilon = 0.16125$. From top to bottom; $f = 20$ Hz, $f = 30.4$ Hz and $f = 36$ Hz. Left figures, no flow; right figures, Re = 2900. X is defined as x/H.

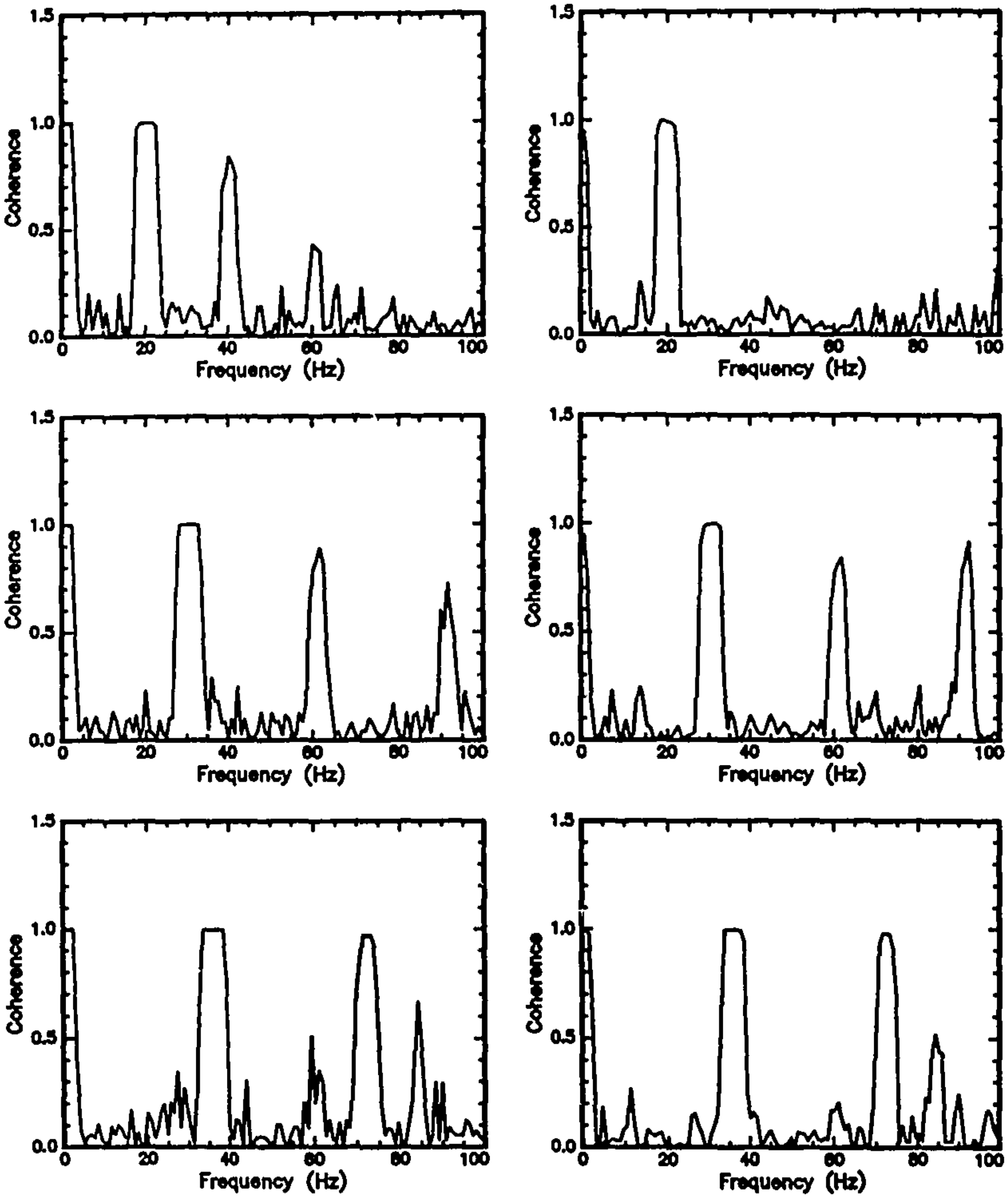

Figure 8.31: samples of coherence spectra of the unsteady pressure with respect to the acceleration of the outer cylinder in translational motion from pressure transducers No. 4 shown in Figure 8.7(b) for backstep geometry at different frequencies and $\epsilon = 0.16125$; left figures, no flow; right figures, Re = 2900.

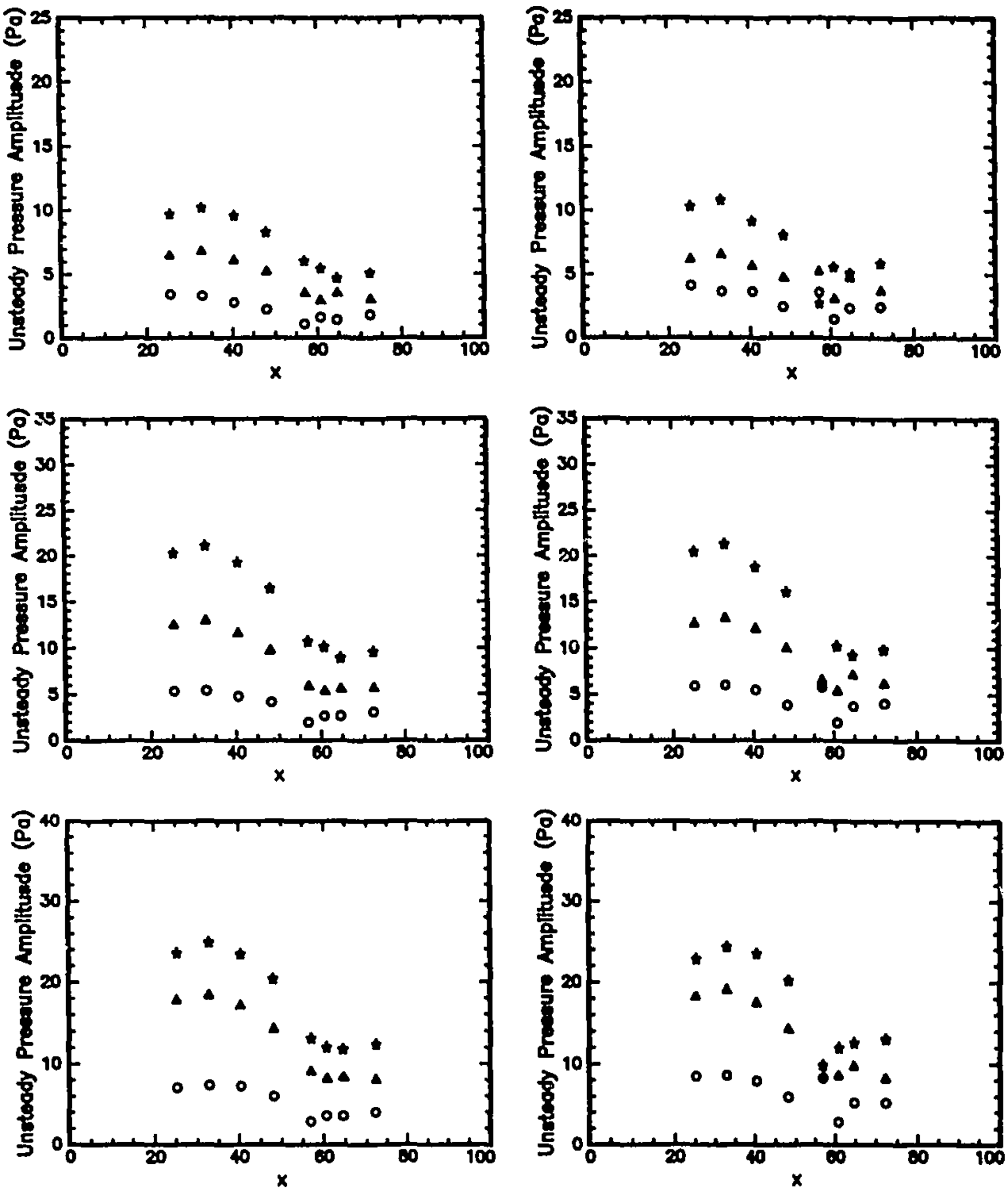

Figure 8.32: Nondimensional unsteady pressure versus axial distance for translational motion of the outer cylinder (backstep geometry). The amplitudes of oscillation from top to bottom are: $\epsilon = 0.05375$, $\epsilon = 0.1075$ and $\epsilon = 0.16125$ and the frequencies are o, $f = 20$ Hz; Δ, $f = 30.4$ Hz; $*$, $f = 40$ Hz. Left figures, Re = 5000; right figures, Re = 9000.

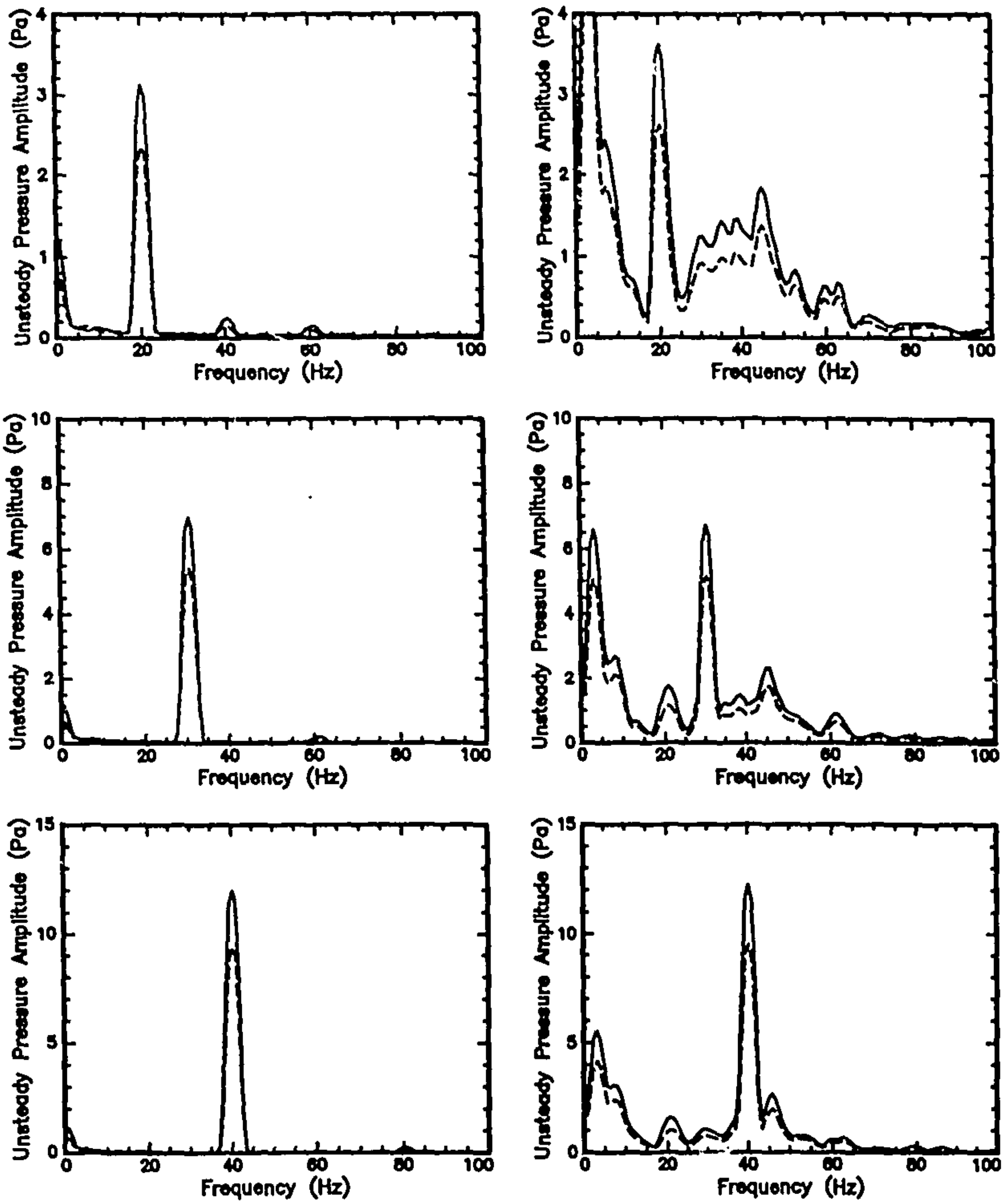

Figure 8.33: samples of amplitude spectra of the unsteady pressure from pressure transducers; —,No. 1; - - -,No. 2 shown in Figure 8.7(c) (diffuser geometry) for $\alpha = 6^o$ at different frequencies for $\epsilon = 0.05375$. The outer cylinder is in translational motion. Left figures, no flow; right figures, Re = 2900.

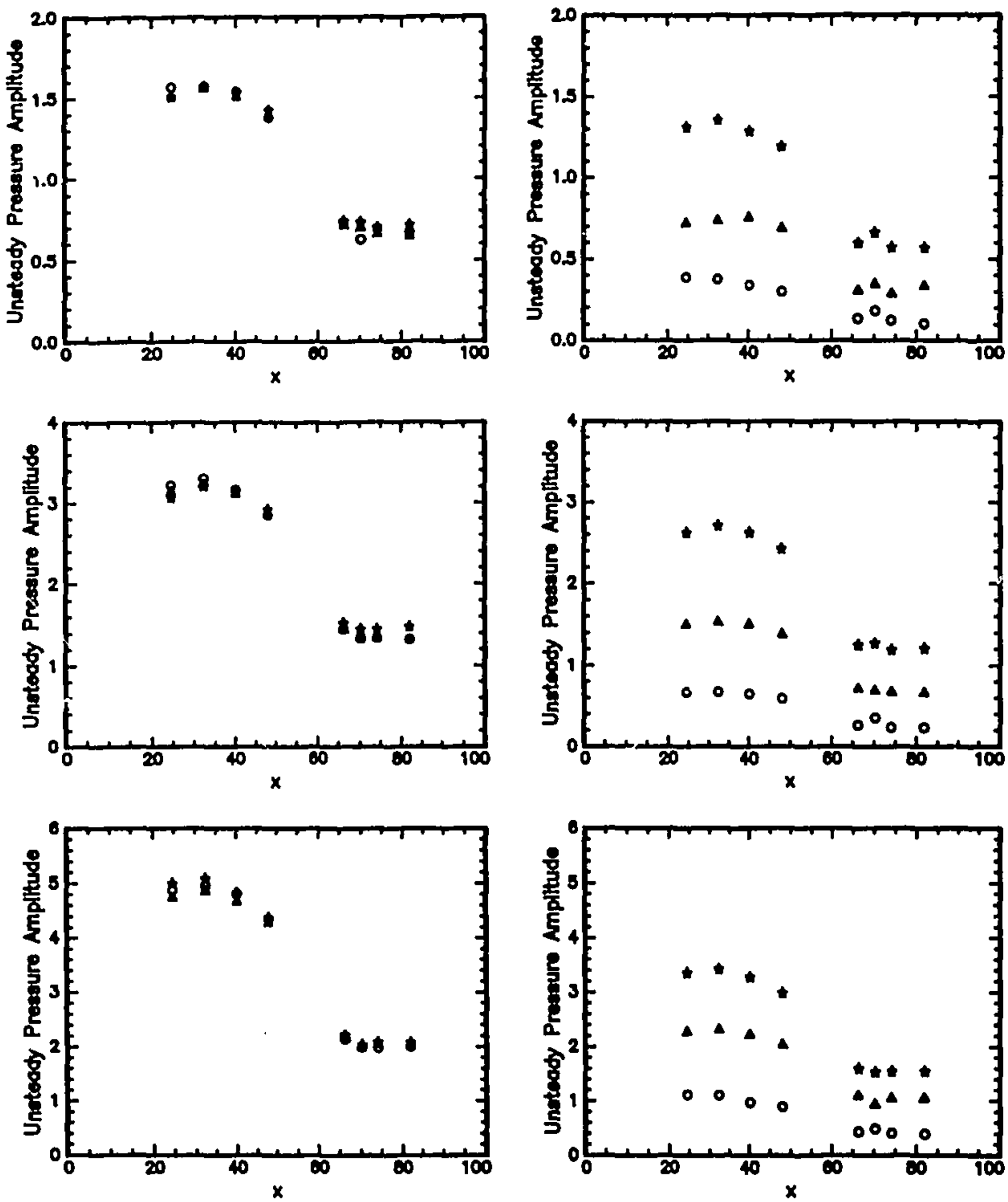

Figure 8.34: Nondimensional unsteady pressure versus axial distance for translational motion of the outer cylinder (diffuser geometry with $\alpha = 6°$). The amplitudes of oscillation from top to bottom are: $\epsilon = 0.05375$, $\epsilon = 0.1075$ and $\epsilon = 0.16125$ and the frequencies are: o, $f = 20$ Hz; Δ, $f = 30.4$ Hz; $*$, $f = 40$ Hz. Left figures, no flow; right figures, Re = 2900.

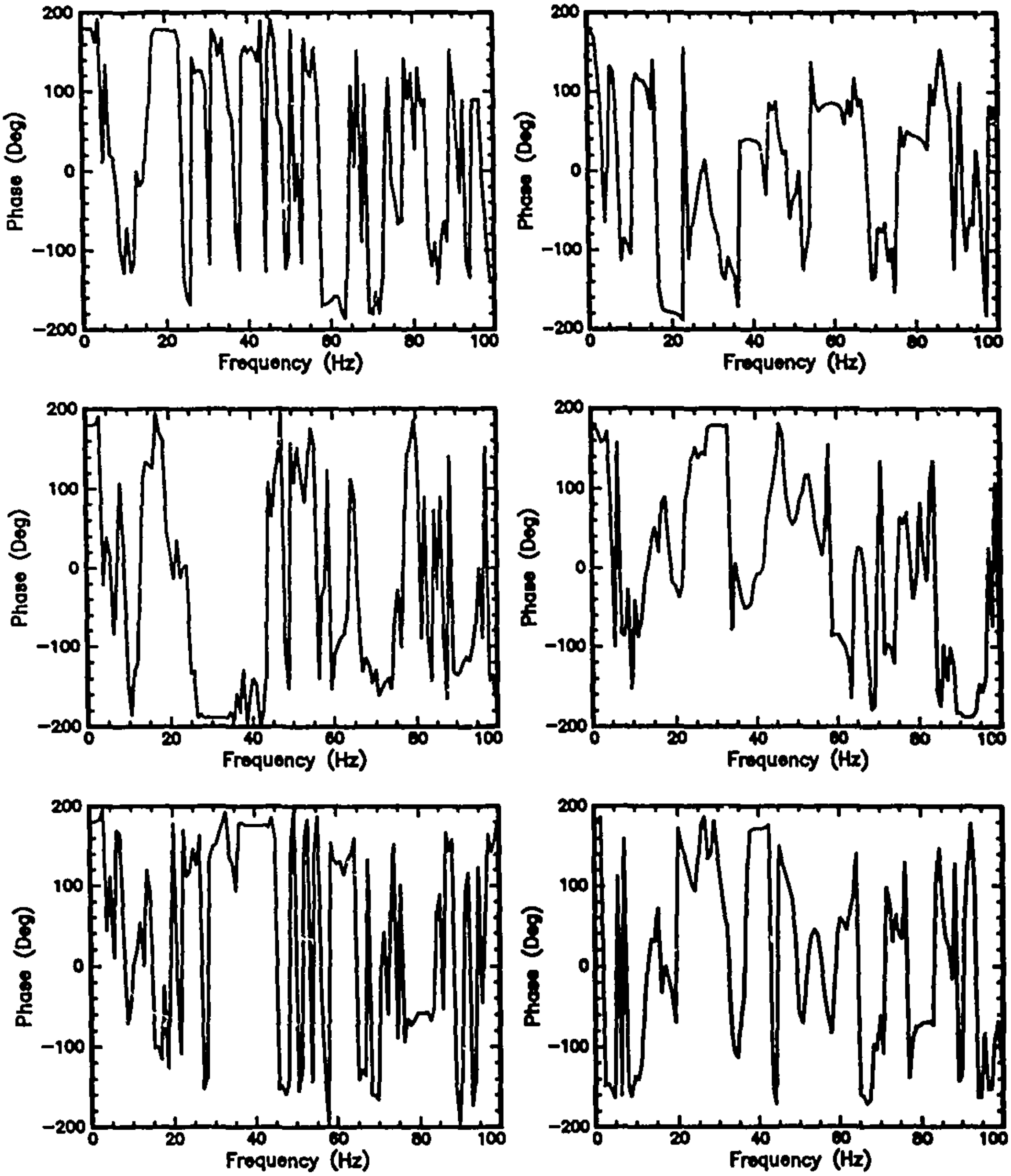

Figure 8.35: samples of phase angle spectra of the unsteady pressure with respect to the acceleration of outer cylinder for pressure transducer No. 1 shown in Figure 8.7(c) for diffuser geometry with $\alpha = 6^o$ at different frequencies for $\epsilon = 0.05375$; the outer cylinder is in translational motion. Left figures, no flow; right figures, Re = 2900.

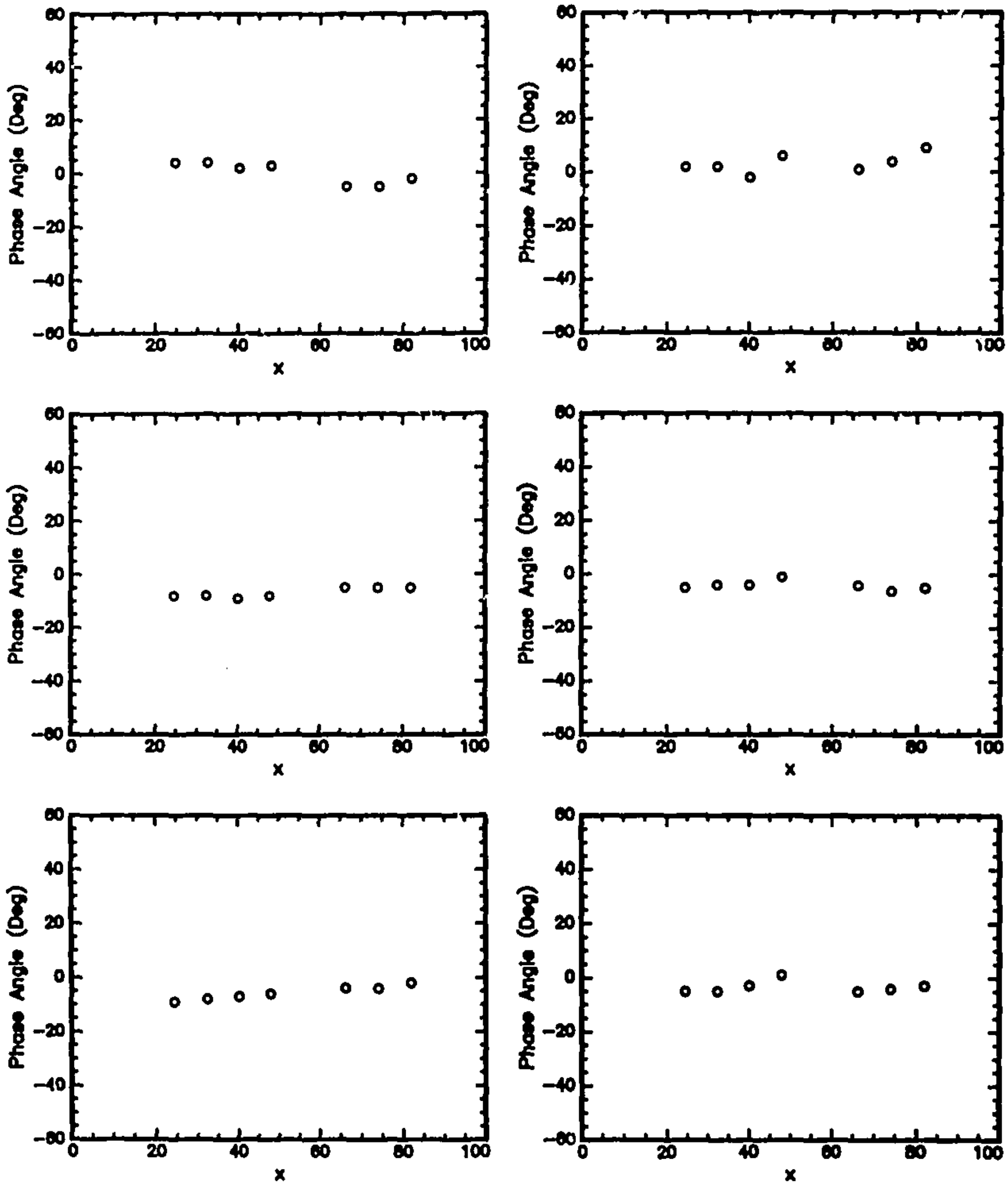

Figure 8.36: samples of phase angles of the unsteady pressure with respect to the displacemet of the outer cylinder in translational motion (diffuser geometry with $\alpha = 6^o$) for $\epsilon = 0.16125$. From top to bottom; $f = 20$ Hz, $f = 30.4$ Hz and $f = 36$ Hz. Left figures, no flow; right figures, Re = 2900. X is defined as x/H.

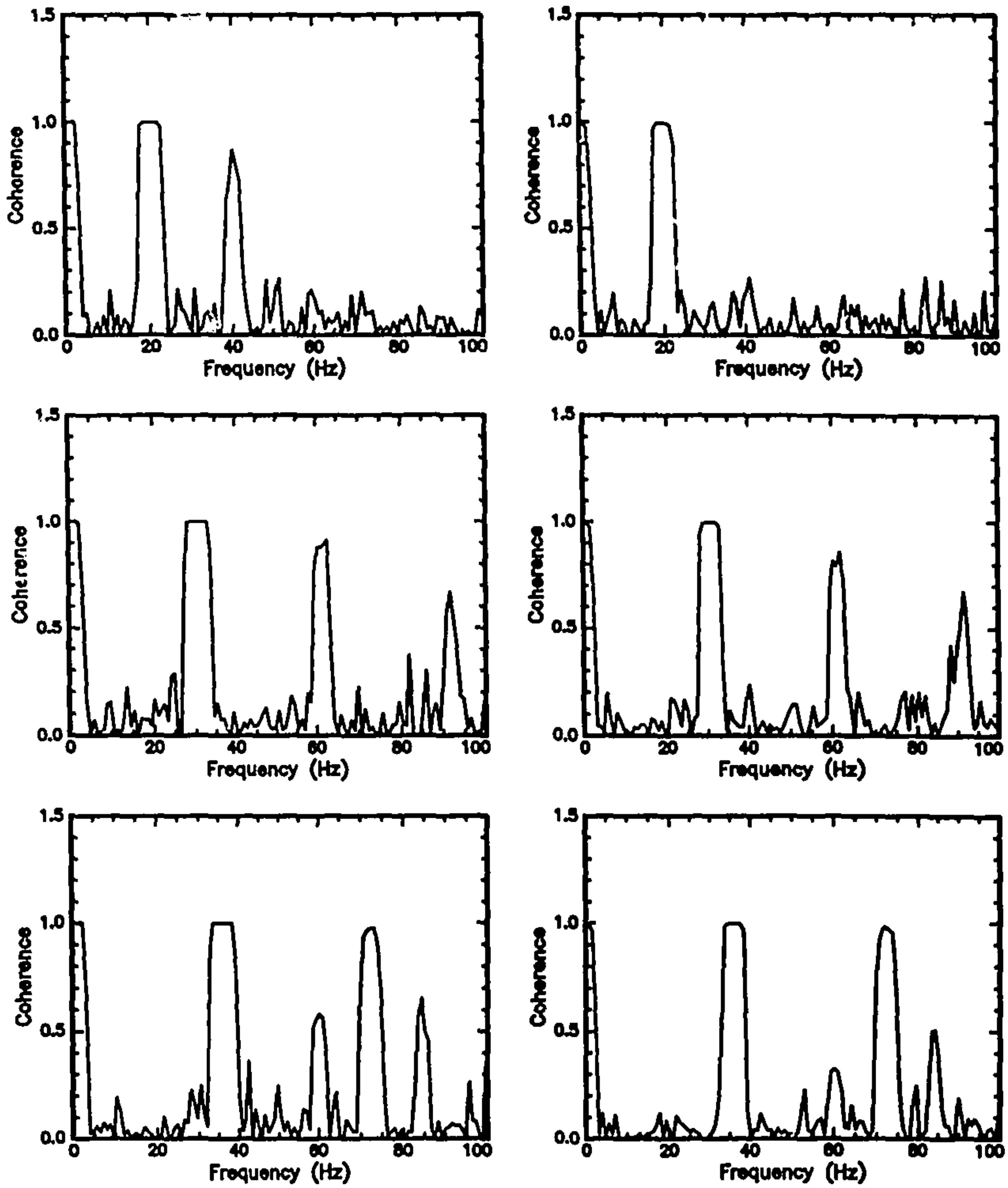

Figure 8.37: samples of coherence spectra of the unsteady pressure with respect to the acceleration of outer cylinder in translational motion from pressure transducers No. 4 shown in Figure 8.7(c) for diffuser geometry with $\alpha = 6^o$ at different frequencies and $\epsilon = 0.16125$; left figures, no flow; right figures, Re $= 2900$.

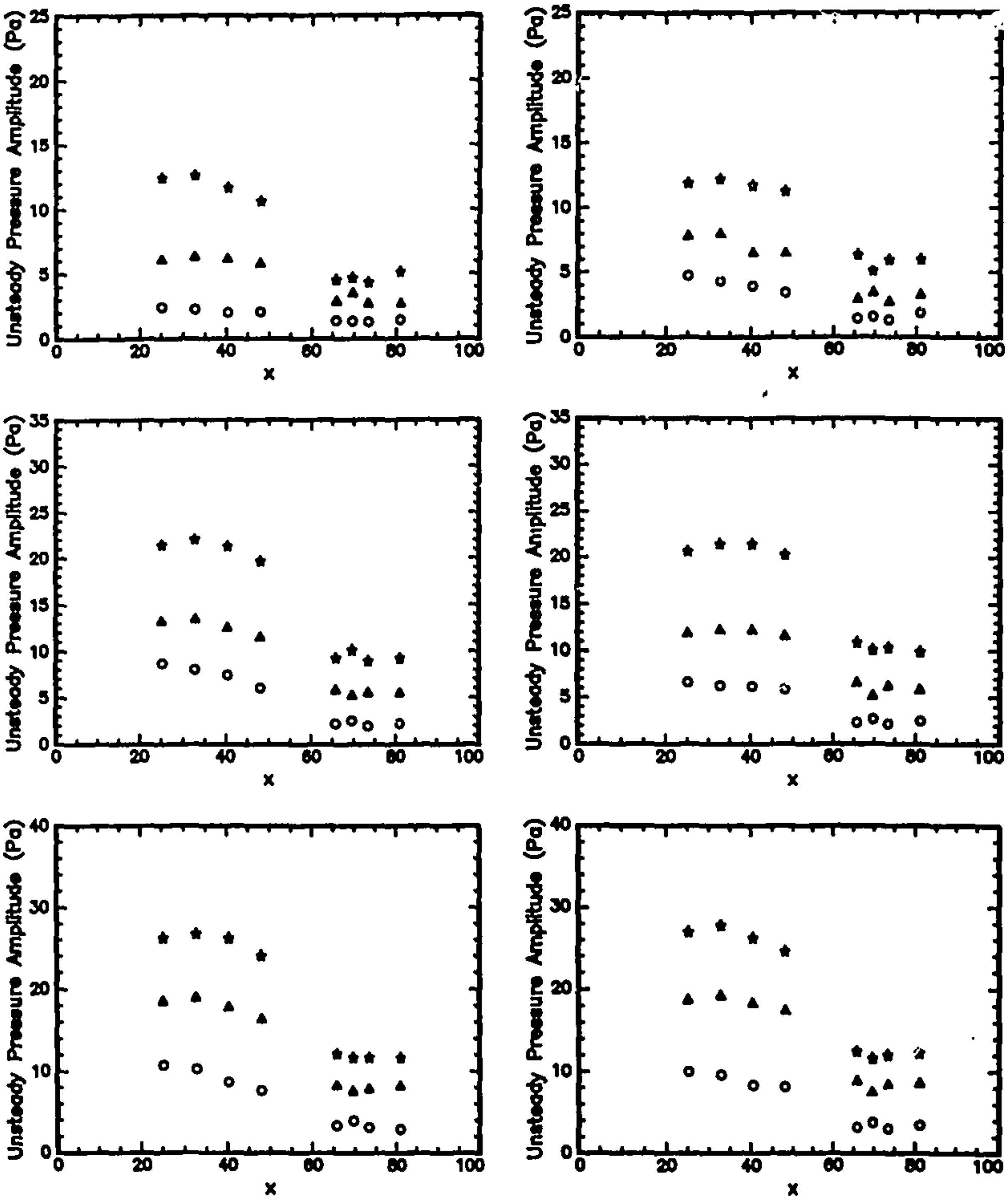

Figure 8.38: Nondimensional unsteady pressure versus axial distance for translational motion of the outer cylinder (diffuser geometry with $\alpha = 6^o$). The amplitudes of oscillation from top to bottom are: $\epsilon = 0.05375$, $\epsilon = 0.1075$ and $\epsilon = 0.16125$ and the frequencies are: o, $f = 20$ Hz; Δ, $f = 30.4$ Hz; $*$, $f = 40$ Hz. Left figures, Re = 5000; right figures, Re = 9000.

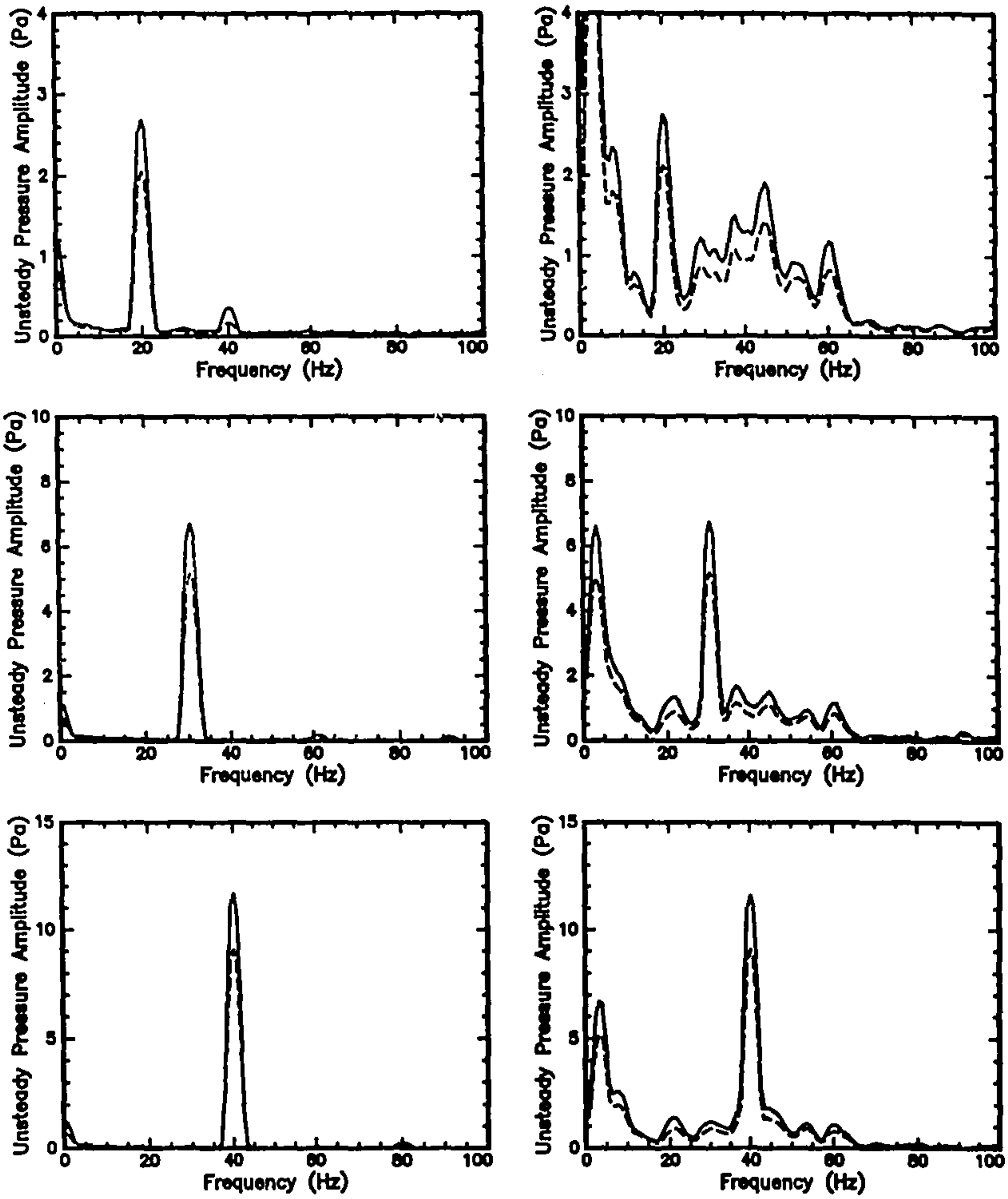

Figure 8.39: samples of amplitude spectra of the unsteady pressure from pressure transducers; —,No. 1; - - -,No. 2 shown in Figure 8.7(c) (diffuser geometry with $\alpha = 20^o$) at different frequencies for $\epsilon = 0.05375$. The outer cylinder is in translational motion. Left figures, no flow; right figures, $Re = 2900$.

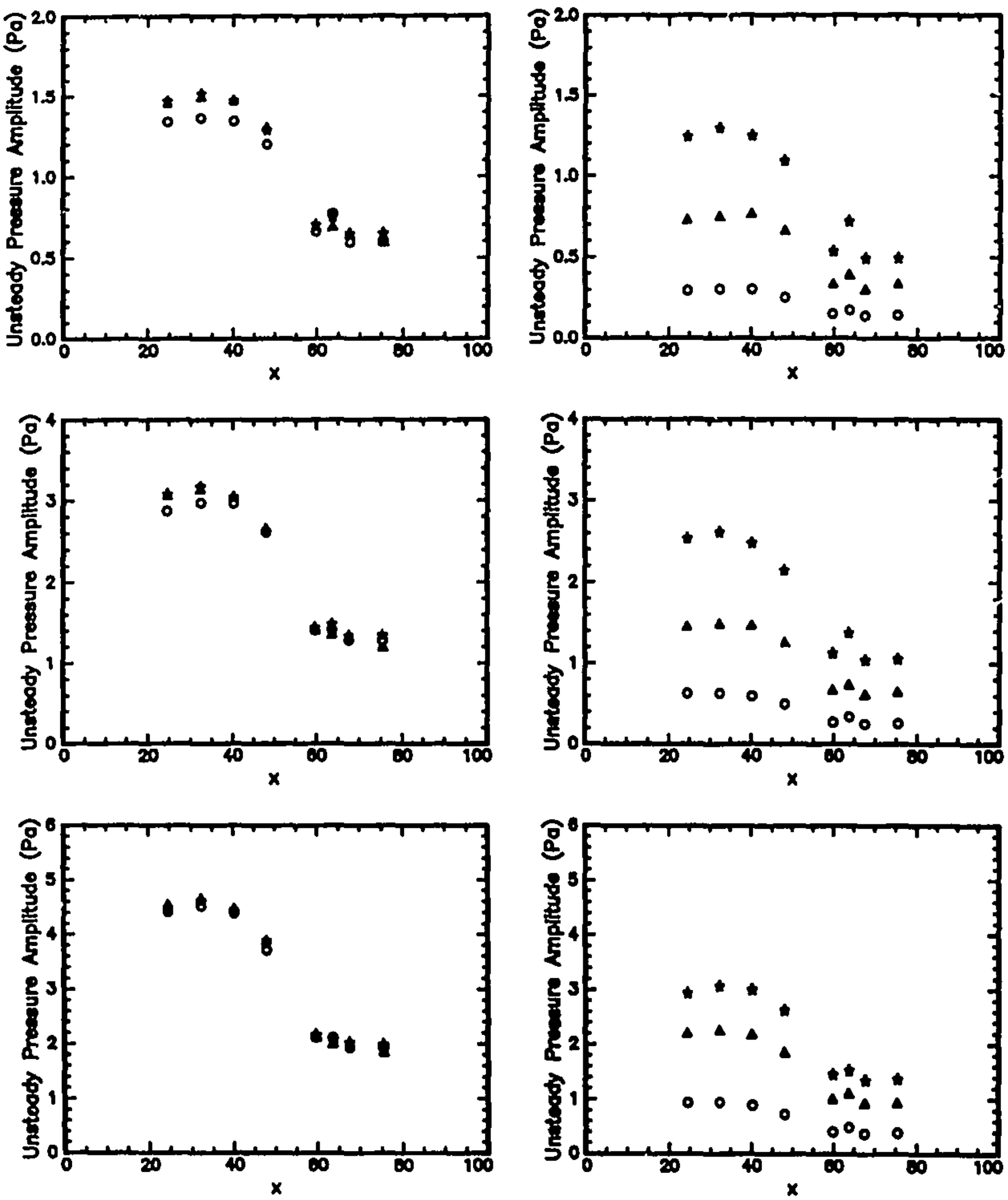

Figure 8.40: Nondimensional unsteady pressure versus axial distance for translational motion of the outer cylinder (diffuser geometry with $\alpha = 20^o$). The amplitudes of oscillation from top to bottom are: $\epsilon = 0.05375$, $\epsilon = 0.1075$ and $\epsilon = 0.16125$ and the frequencies are: o, $f = 20$ Hz; Δ, $f = 30.4$ Hz; $*$, $f = 40$ Hz. Left figures, no flow; right figures, Re = 2900.

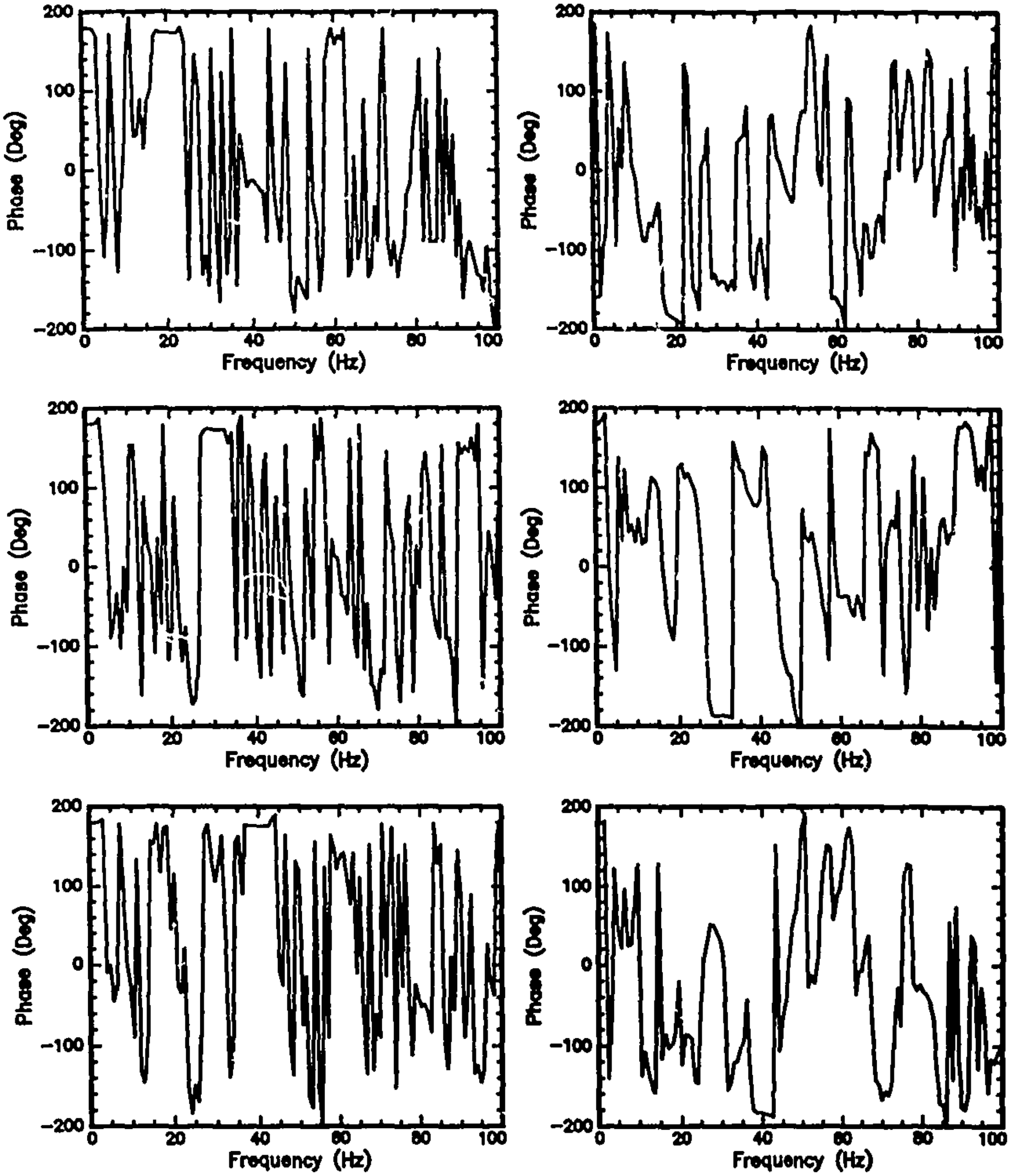

Figure 8.41: samples of phase angle spectra of the unsteady pressure with respect to the acceleration of outer cylinder for pressure transducer No. 1 shown in Figure 8.7(c) for diffuser geometry with $\alpha = 20^o$ at different frequencies for $\epsilon = 0.05375$; the outer cylinder is in translational motion. Left figures, no flow; right figures, Re = 2900.

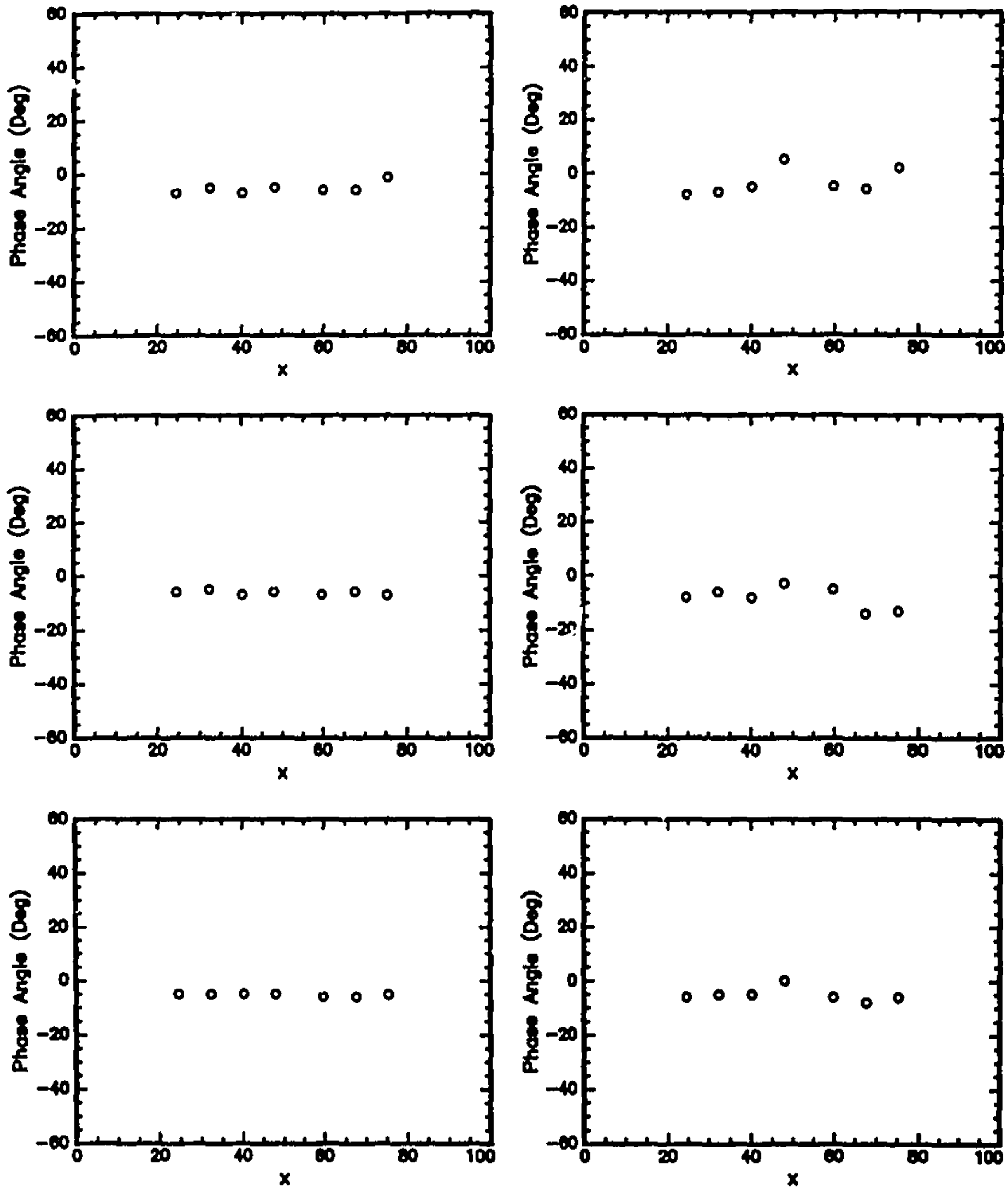

Figure 8.42: samples of phase angles of the unsteady pressure with respect to the displacemet of the outer cylinder in translational motion (diffuser geometry with $\alpha = 20°$) for $\epsilon = 0.16125$. From top to bottom; $f = 20$ Hz, $f = 30.4$ Hz and $f = 36$ Hz. Left figures, no flow; right figures, Re = 2900.

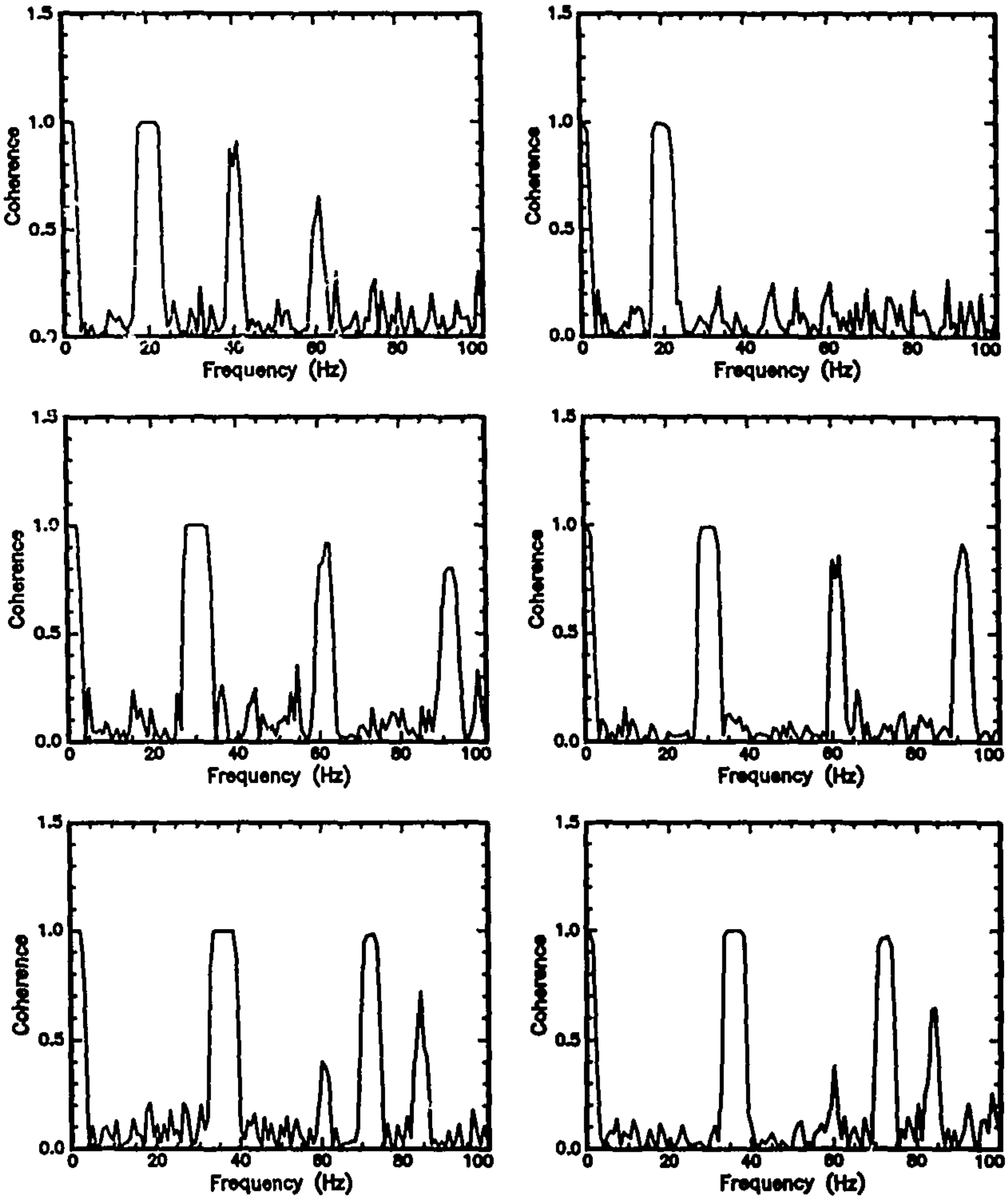

Figure 8.43: samples of coherence spectra of the unsteady pressure with respect to the acceleration of the outer cylinder in translational motion from pressure transducers No. 4 shown in Figure 8.7(c) for diffuser geometry with $\alpha = 20^o$ at different frequencies and $\epsilon = 0.16125$; left figures, no flow; right figures, Re = 2900.

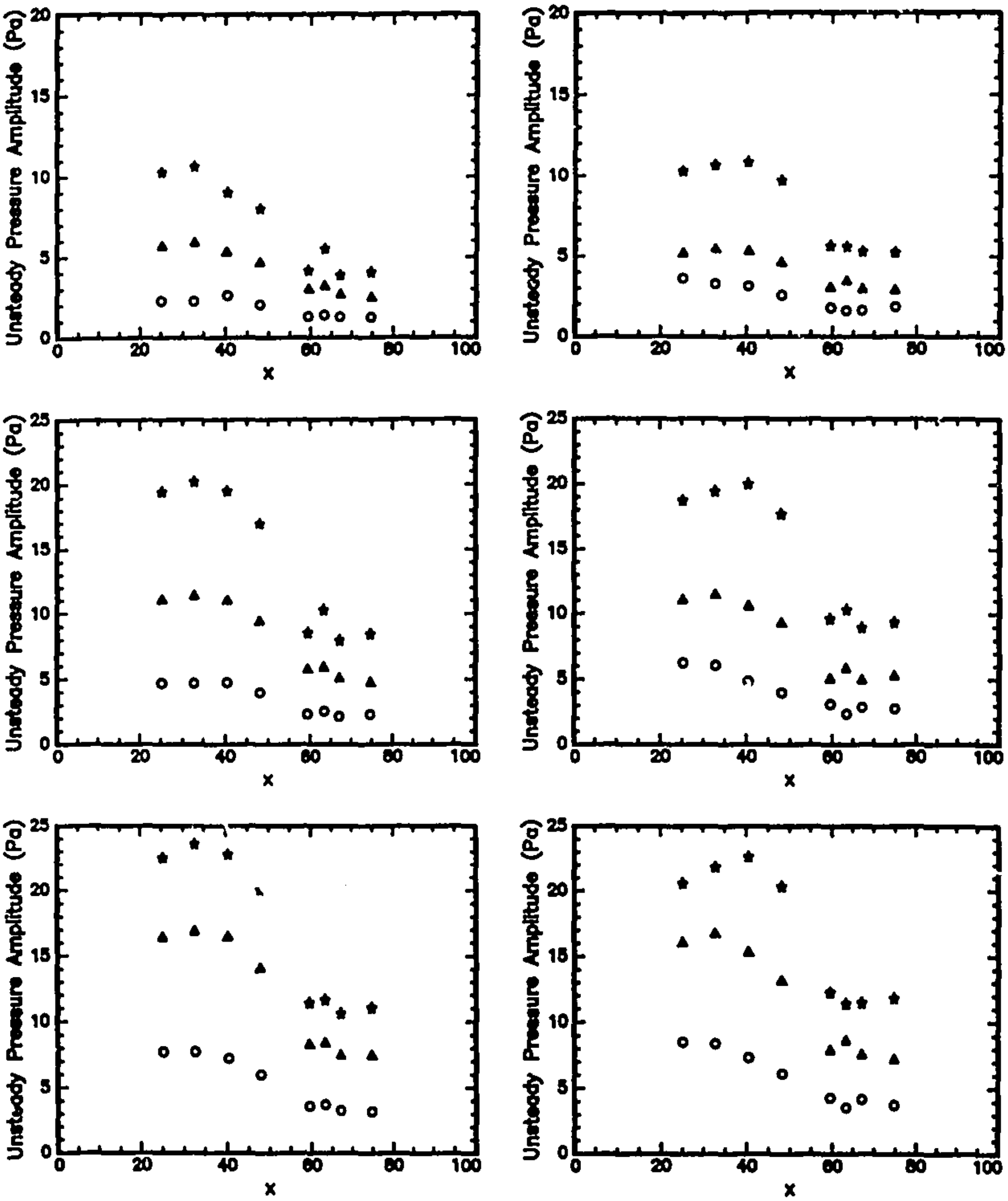

Figure 8.44: Nondimensional unsteady pressure versus axial distance for translational motion of the outer cylinder (diffuser geometry with $\alpha = 20°$). The amplitudes of oscillation from top to bottom are: $\epsilon = 0.05375$, $\epsilon = 0.1075$ and $\epsilon = 0.16125$ and the frequencies are: o, $f = 20$ Hz; Δ, $f = 30.4$ Hz; $*$, $f = 40$ Hz. Left figures, Re = 5000; right figures, Re = 9000.

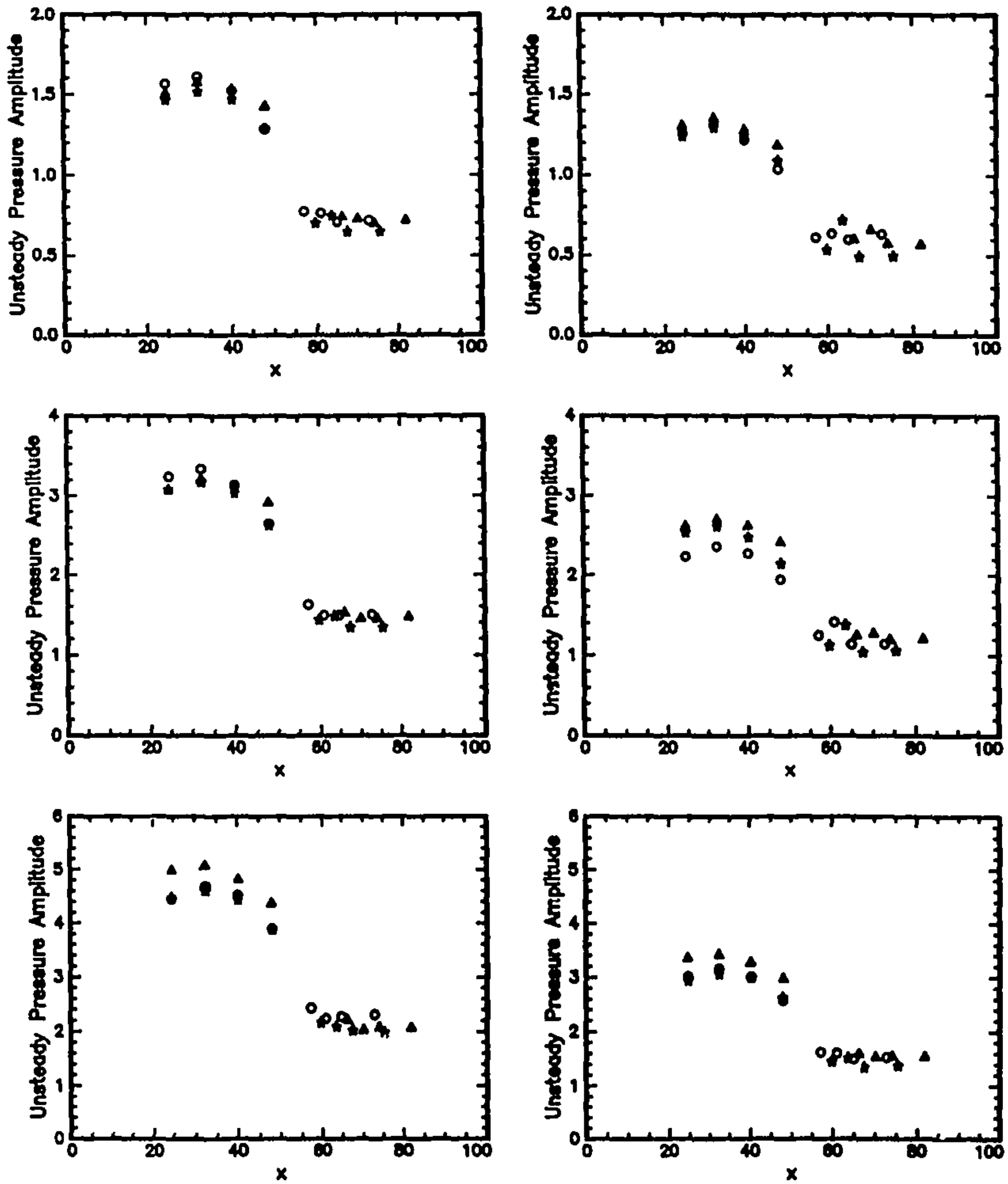

Figure 8.45: Nondimensional unsteady pressure versus axial distance for different geometries at f = 36 Hz. From top to bottom; $\epsilon = 0.05375$, $\epsilon = 0.1075$ and $\epsilon = 0.16125$.The symbols are; o, backstep; Δ, diffuser with 6^o half angle; $*$, diffuser with 20^o half angle. Left figures, no flow; right figures, Re = 2900.

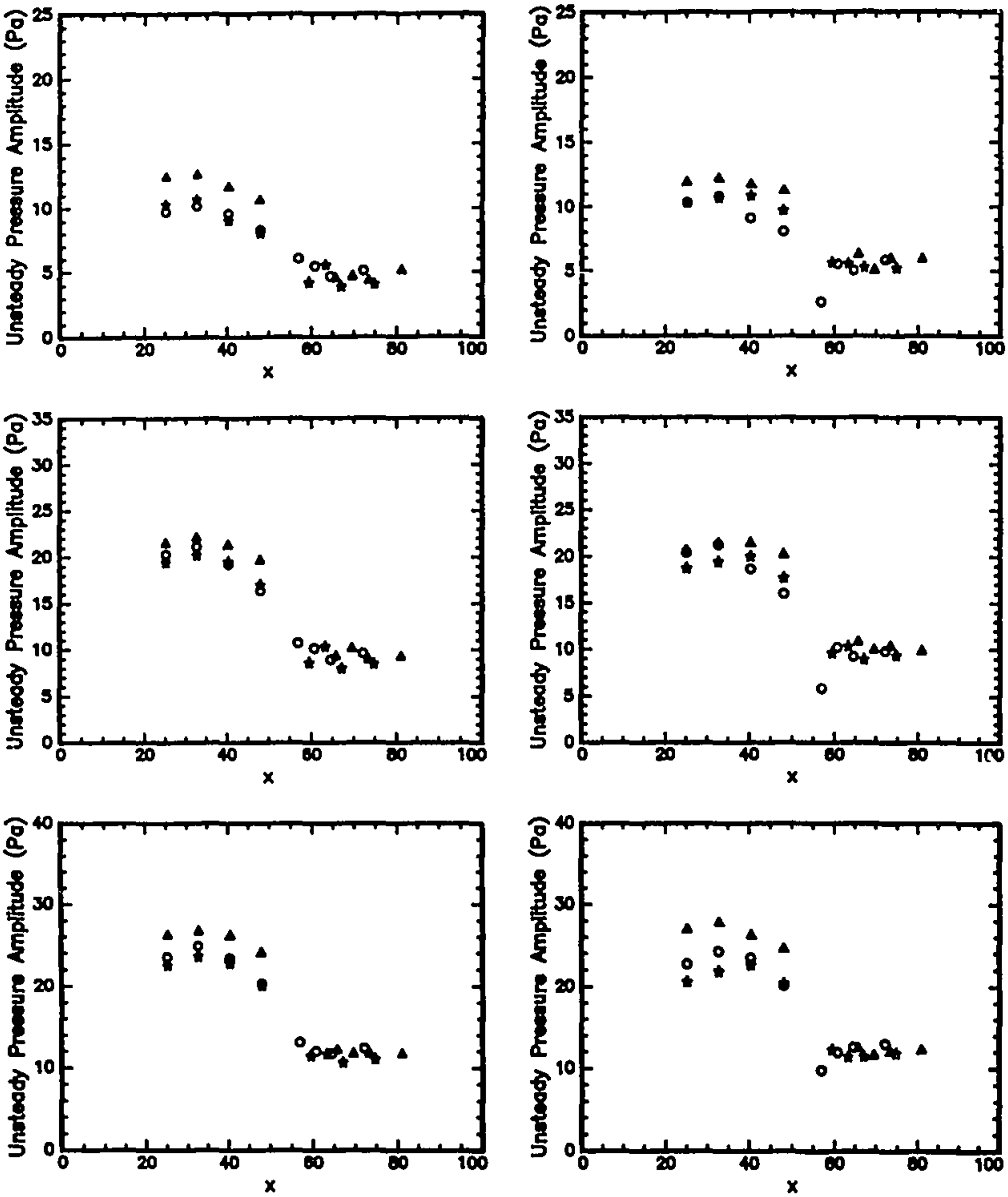

Figure 8.46: Nondimensional unsteady pressure versus axial distance for different geometries at $f = 36$ Hz. From top to bottom; $\epsilon = 0.05375$, $\epsilon = 0.1075$ and $\epsilon = 0.16125$.The symbols are; o, backstep; Δ, diffuser with 6^o half angle; $*$, diffuser with 20^o half angle. Left figures, Re = 5000 ; right figures, Re = 9000.

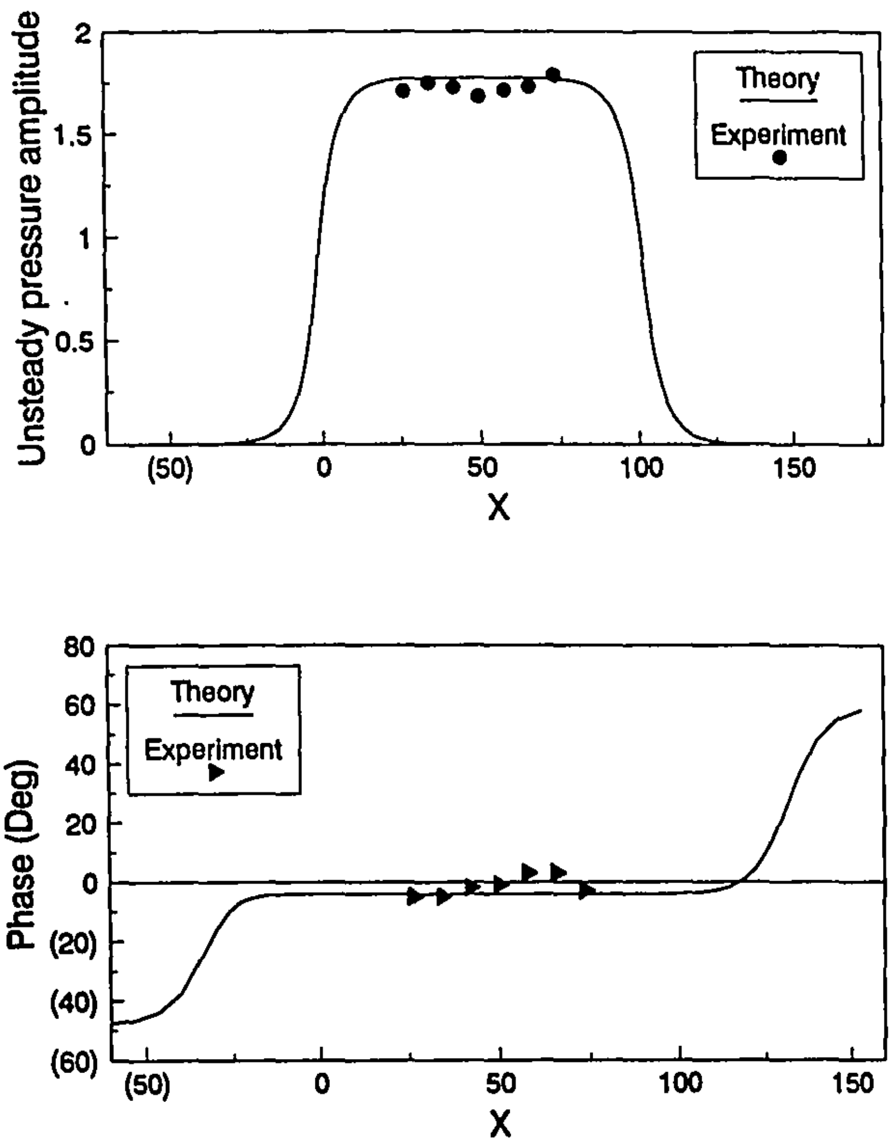

Figure 8.47: Nondimensional unsteady pressure amplitude and phase angle with respect to the displacement of the outer cylinder in translational motion. Comparison between theoretical (mean-position analysis) and experimental results for $\epsilon = 0.05375$, $f = 20$ Hz and no flow.

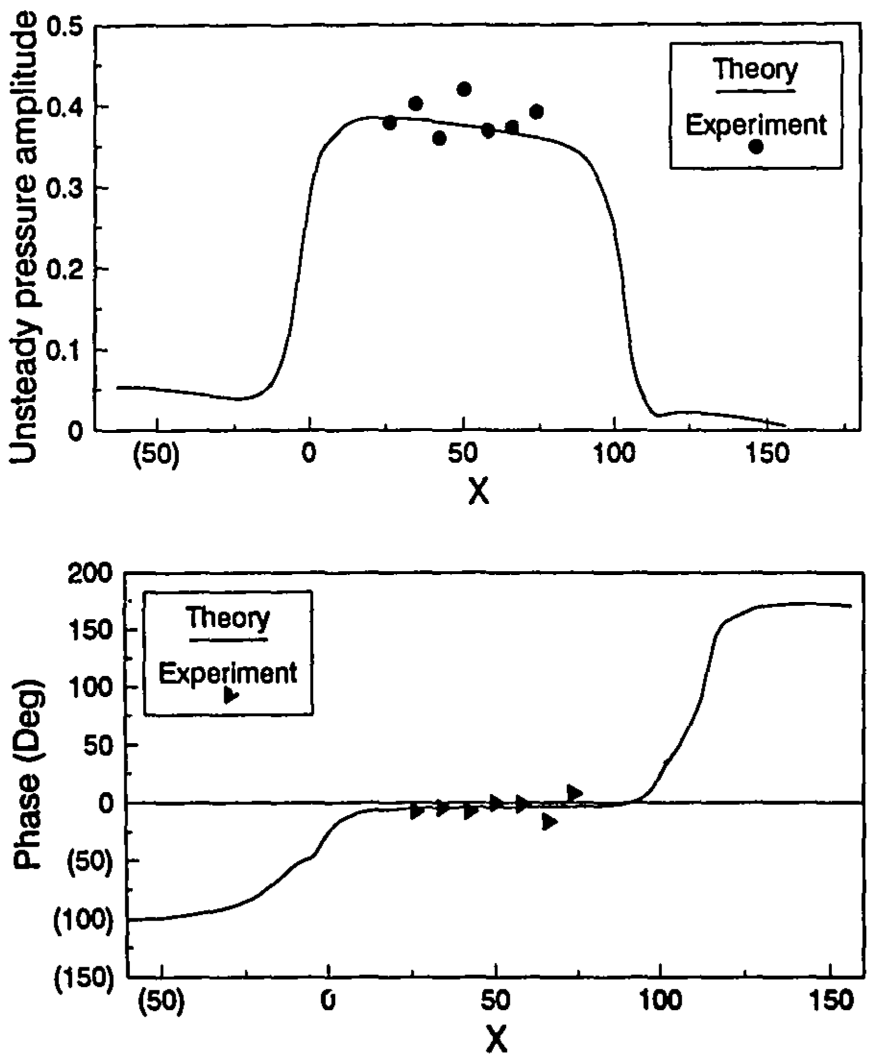

Figure 8.48: Nondimensional unsteady pressure amplitude and phase angle with respect to the displacement of the outer cylinder in translational motion. Comparison between theoretical (mean-position analysis) and experimental results for $\epsilon = 0.05375$, $f = 20$ Hz and Re $= 2900$.

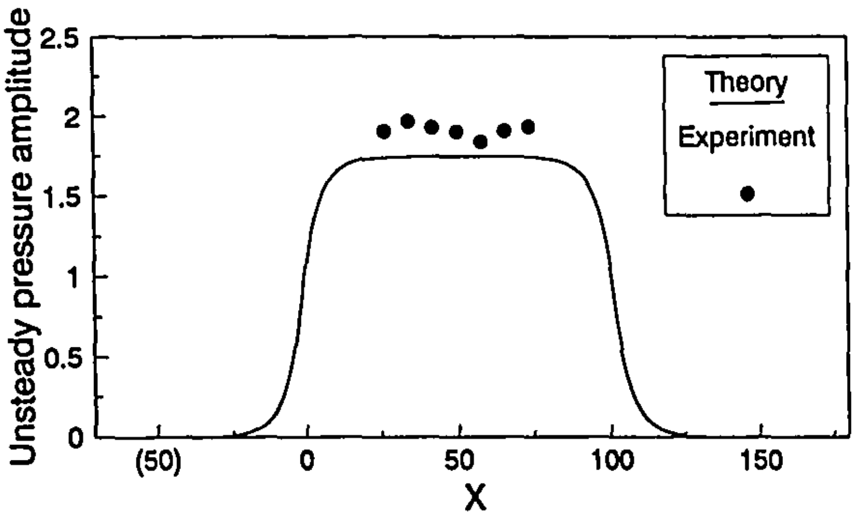

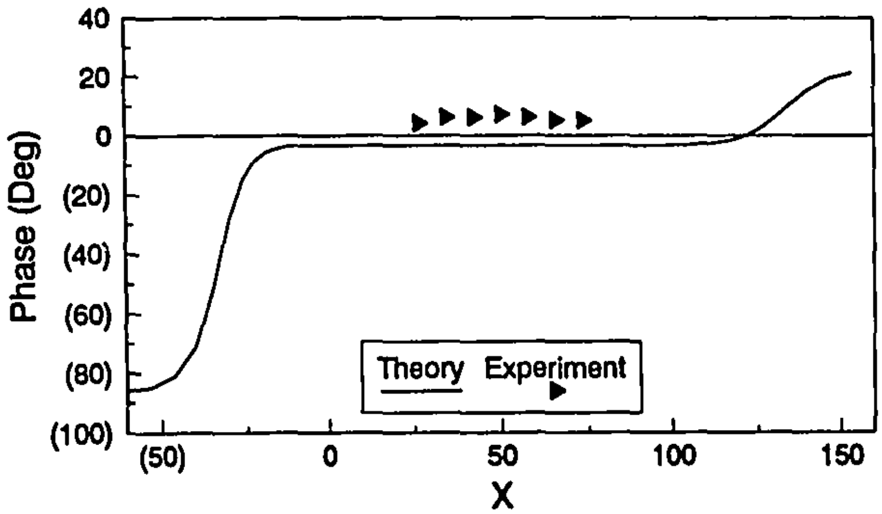

Figure 8.49: Nondimensional unsteady pressure amplitude and phase angle with respect to the displacement of the outer cylinder in translational motion. Comparison between theoretical (mean-position analysis) and experimental results for $\epsilon = 0.05375$, $f = 30.4$ Hz and no flow.

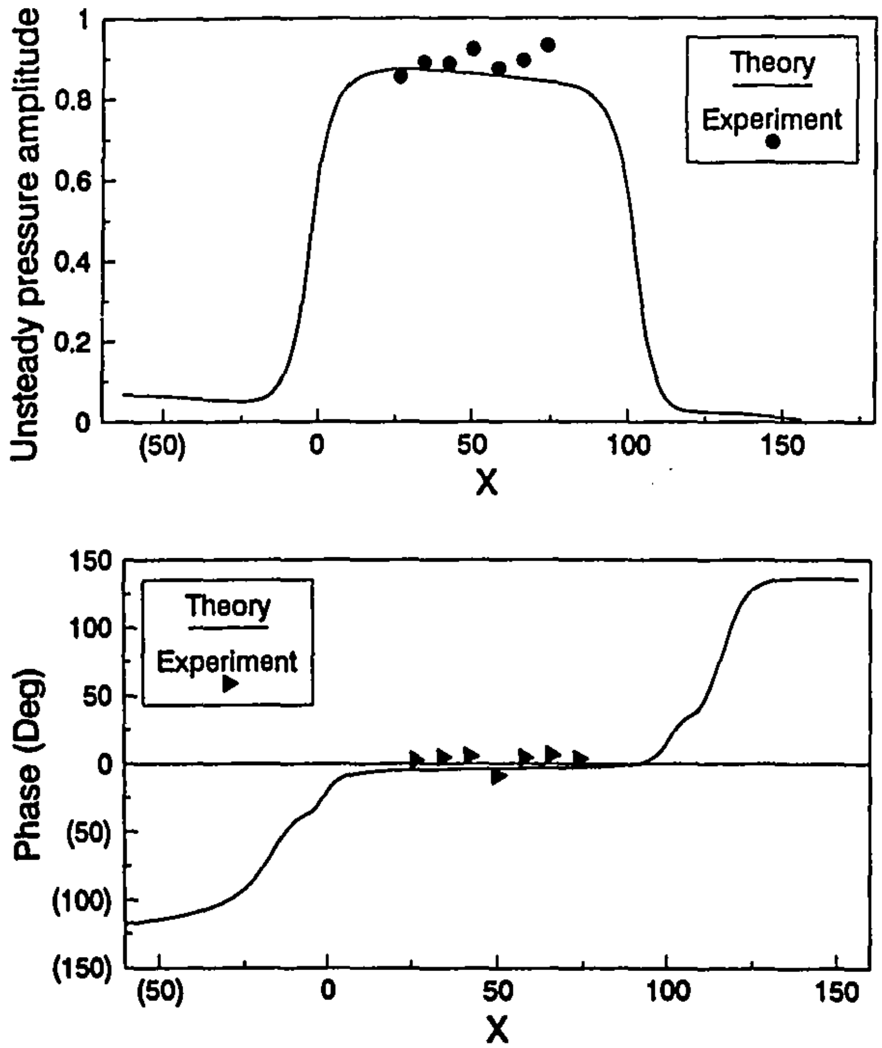

Figure 8.50: Nondimensional unsteady pressure amplitude and phase angle with respect to the displacement of the outer cylinder in translational motion. Comparison between theoretical (mean-position analysis) and experimental results for $\epsilon = 0.05375$, $f = 30.4$ Hz and Re = 2900.

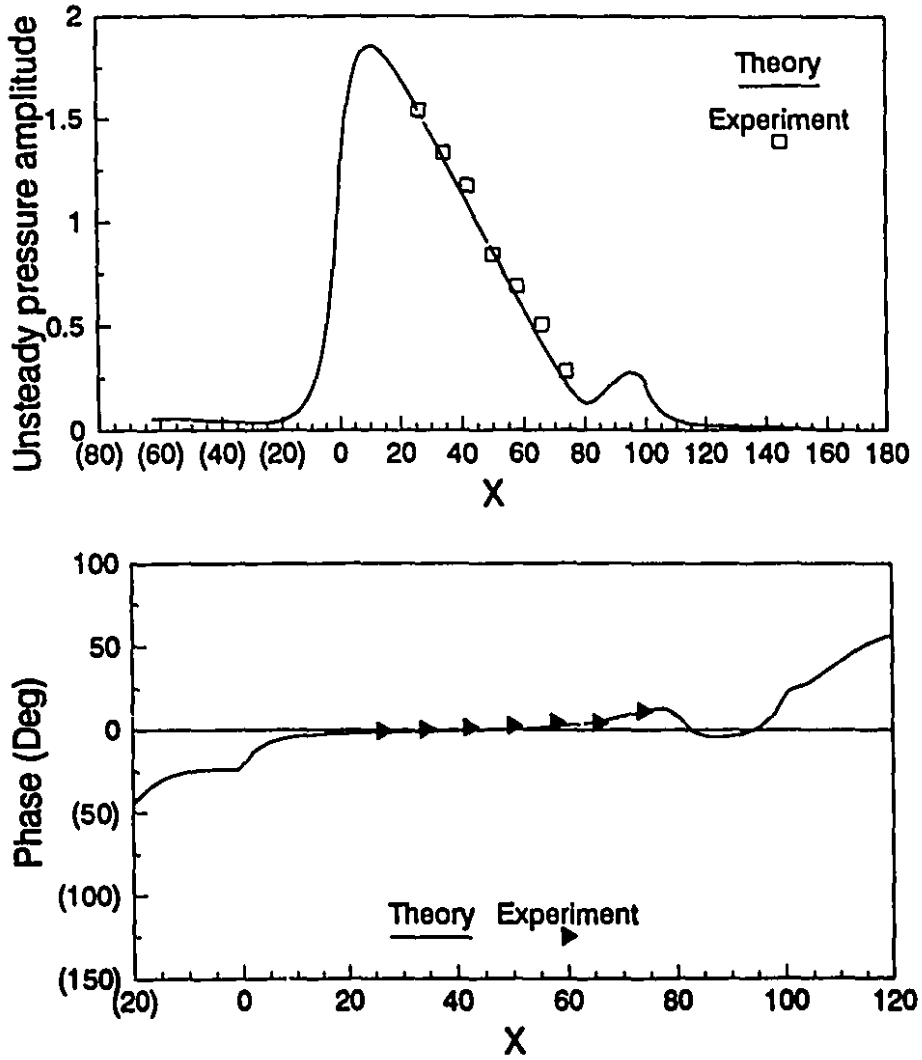

Figure 8.51: Nondimensional unsteady pressure amplitude and phase angle with respect to the displacement of the outer cylinder in rocking motion. Comparison between theoretical (mean-position analysis) and experimental results for $\epsilon = 0.05375$, $f = 30.4$ Hz and no flow.

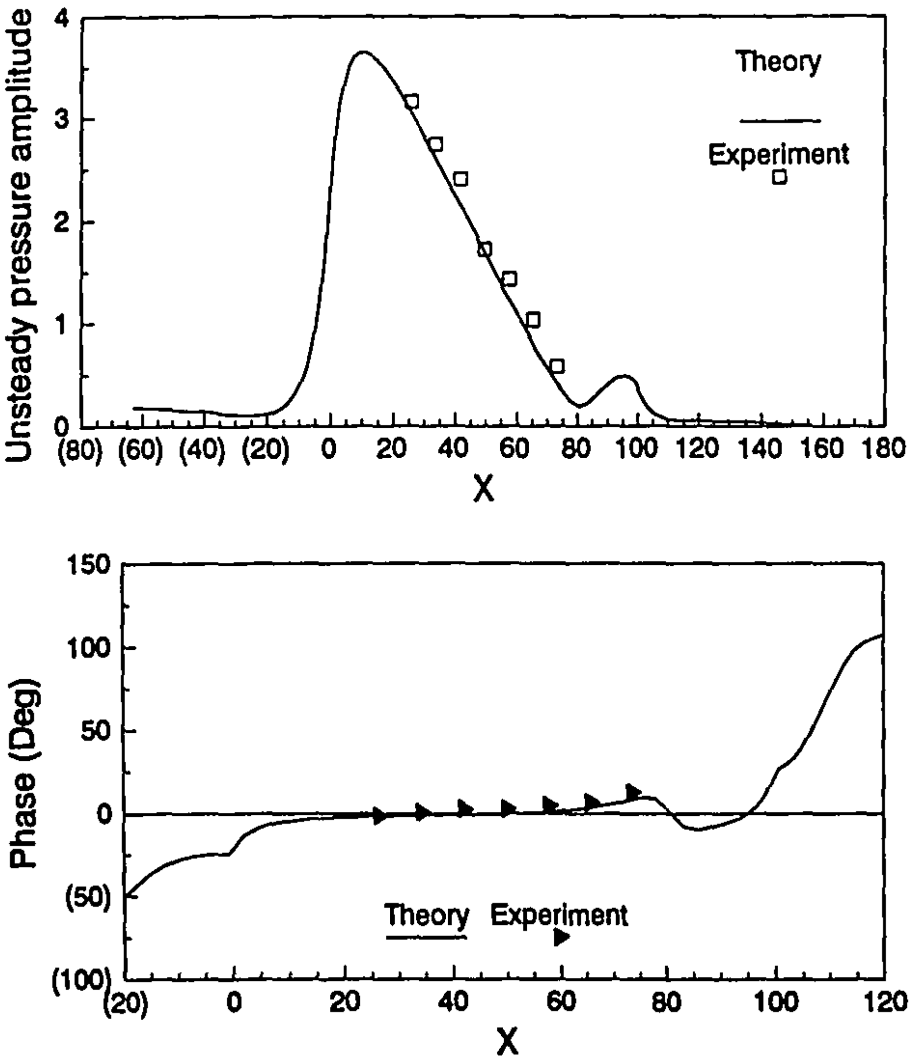

Figure 8.52: Nondimensional unsteady pressure amplitude and phase angle with respect to the displacement of the outer cylinder in rocking motion. Comparison between theoretical (mean-position analysis) and experimental results for $\epsilon = 0.1075$, $f = 30.4$ Hz and no flow.

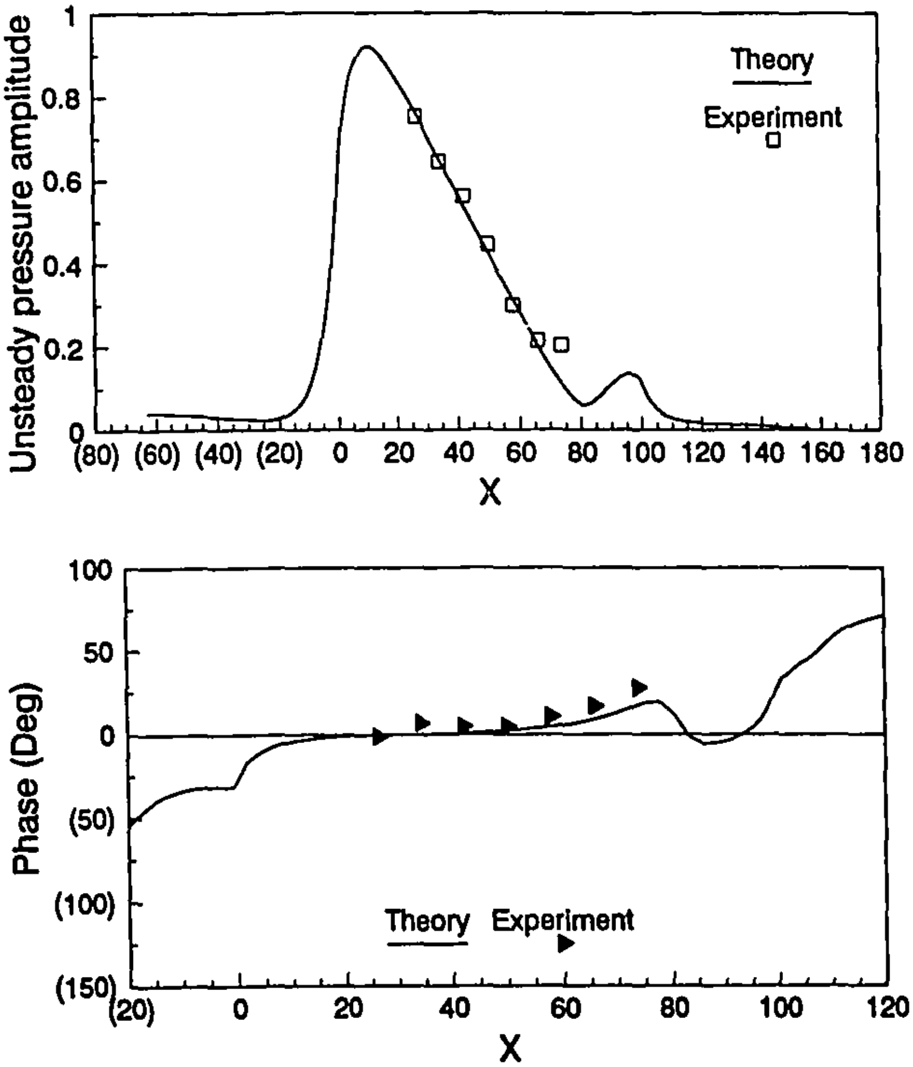

Figure 8.53: Nondimensional unsteady pressure amplitude and phase angle with respect to the displacement of the outer cylinder in rocking motion. Comparison between theoretical (mean-position analysis) and experimental results for $\epsilon = 0.053755$, $f = 30.4$ Hz and Re = 2900.

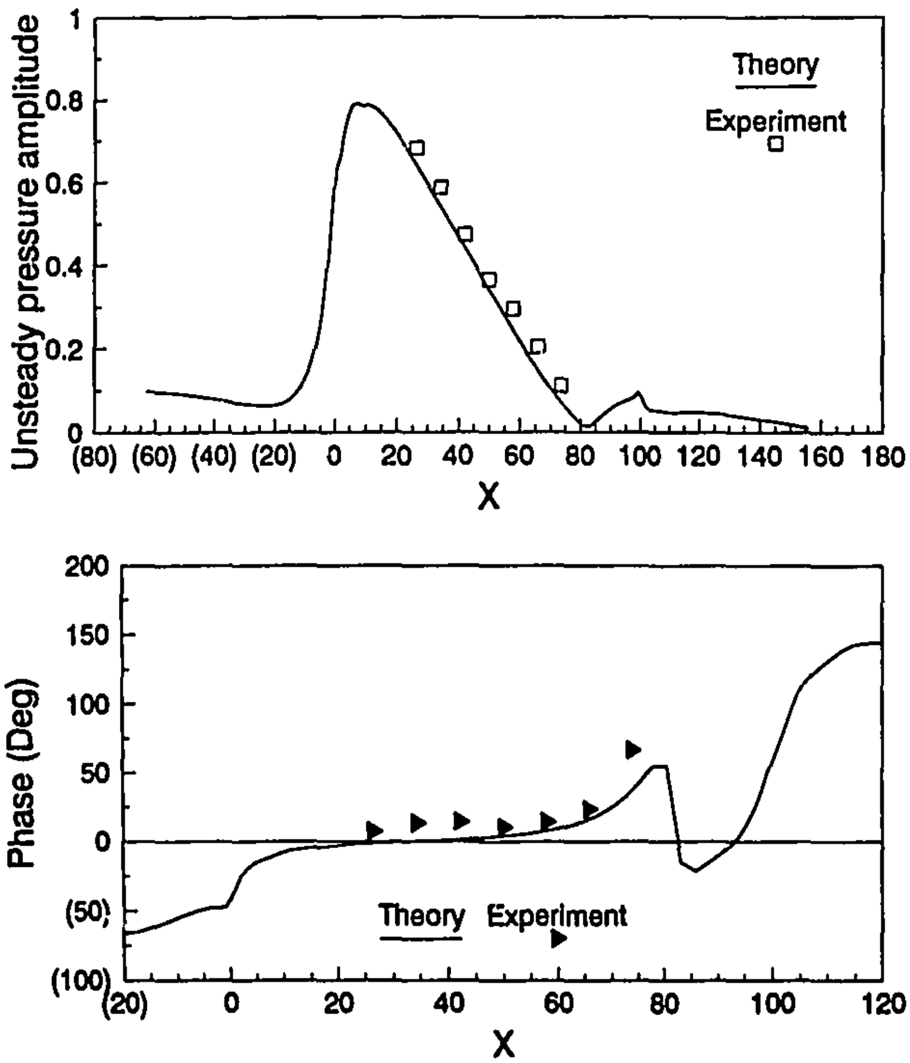

Figure 8.54: Nondimensional unsteady pressure amplitude and phase angle with respect to the displacement of the outer cylinder in rocking motion. Comparison between theoretical (mean-position analysis) and experimental results for $\epsilon = 0.1075$, $f = 20$ Hz and Re = 2900.

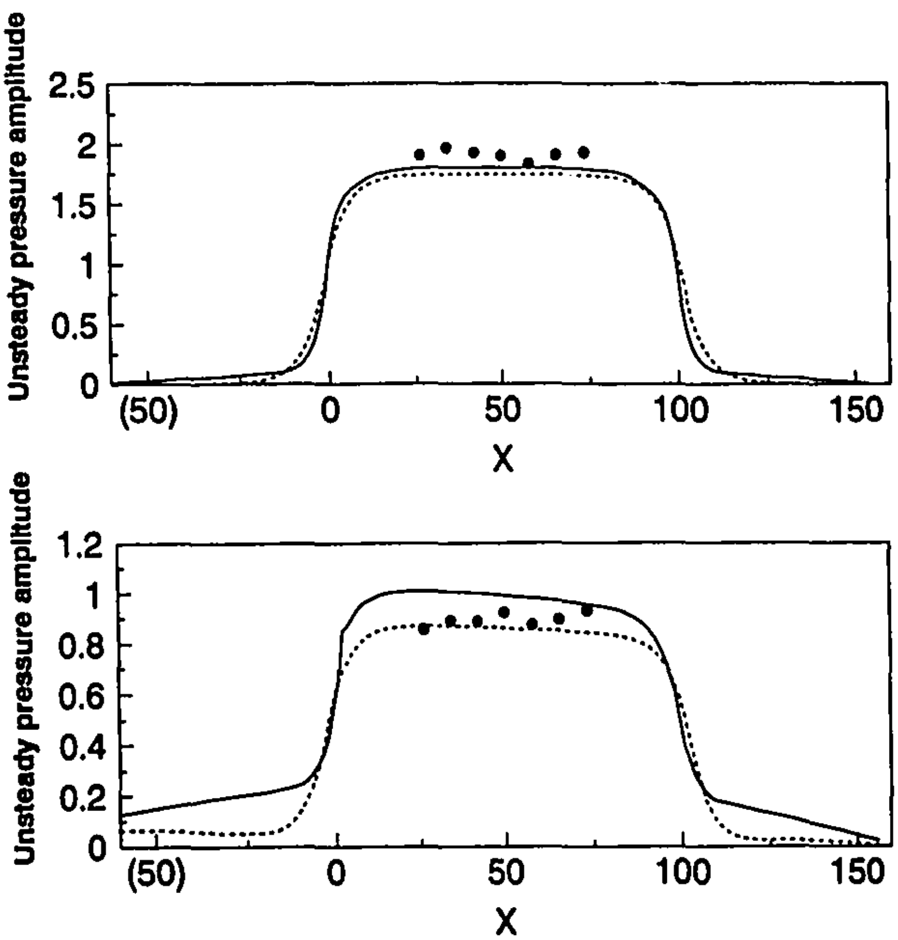

Figure 8.55: Nondimensional unsteady pressure amplitude versus axial distance of the outer cylinder in translational motion for $\epsilon = 0.05375$, $f = 30.4$ Hz. Comparison between:—, time-dependent-coordinate-transformation analysis; - - -, mean-position analysis; •, experimental results. Upper diagram, no flow; lower diagram, Re = 2900.

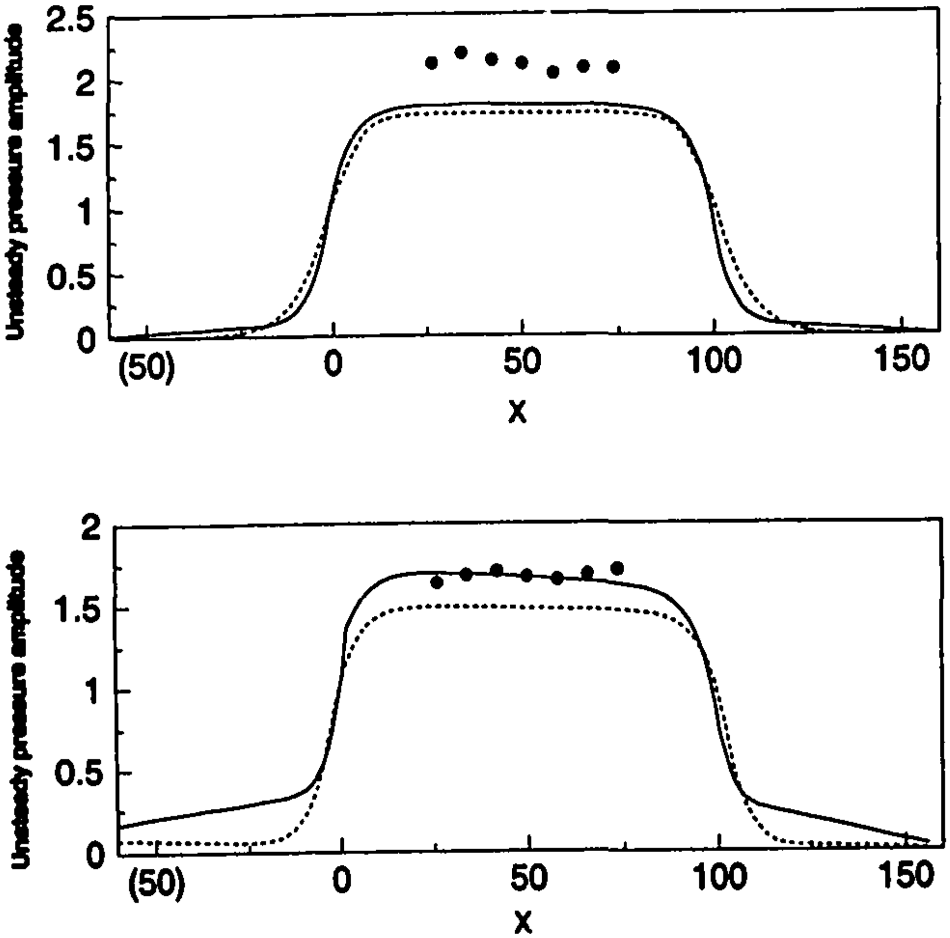

Figure 8.56: Nondimensional unsteady pressure amplitude versus axial distance of the outer cylinder in translational motion for $\epsilon = 0.05375$, $f = 36$ Hz. Comparison between:—, time-dependent-coordinate-transformation analysis; - - -, mean-position analysis; •, experimental results. Upper diagram, no flow; lower diagram, Re = 2900.

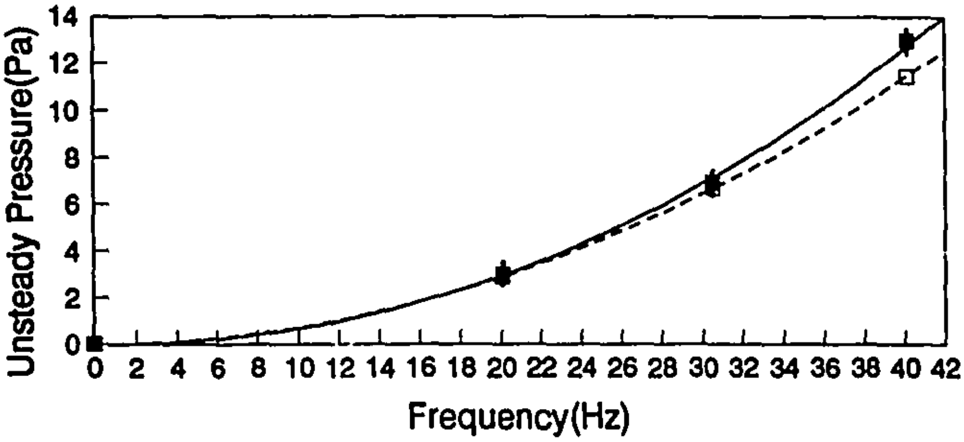

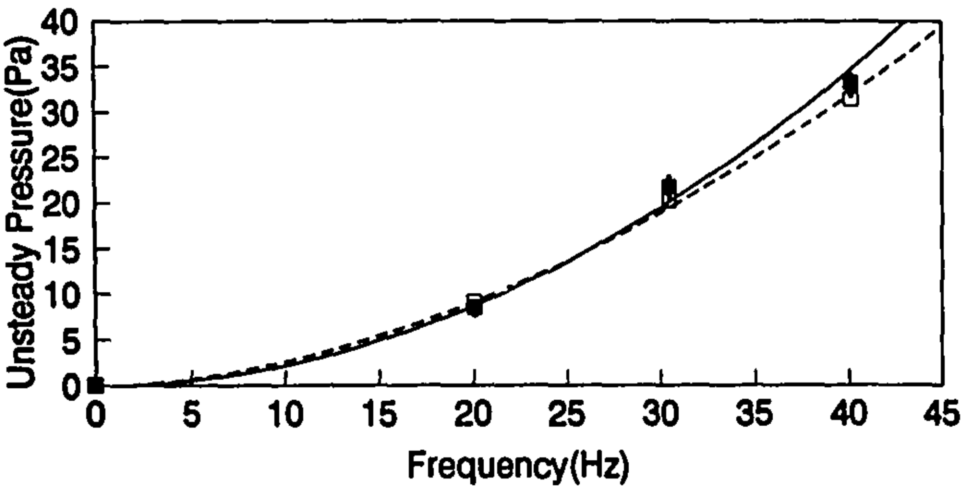

Figure 8.57: Unsteady pressure amplitude versus frequency of oscillation of the outer cylinder in translational motion for $\epsilon = 0.1075$ at different frequencies. Comparison between; - - -,theoretical and; —,the average values of experimental results. Upper diagram, no flow; lower diagram, Re = 2900.

Chapter 9

Time-Domain Study of Fluid-Structure Interaction and Stability Analysis

In the previous chapters, numerical solutions were obtained for the forced vibrations of the structure (outer cylinder) using mean-position and time-dependent coordinate-transformation analyses for both uniform and nonuniform annular geometries. In this chapter, the next important objective of this Thesis, namely, the stability of the structure under the influence of the fluid forces is investigated. In the previous chapters, the motion of the structural boundaries was assumed to be a function of time as given by equation (4.36) which is prescribed for all times.

As was shown in previous chapters, the boundary conditions required to solve the unsteady N-S equations were dependent on the method of solution. For the mean-position analysis it was sufficient to specify the velocity of the moving boundary (outer cylinder), whereas for the time-dependent coordinate transformation analysis both displacement and velocity of the moving boundary were specified. In this chapter both cases are considered. The unsteady time-dependent fluid force exerted on the wall of the outer cylinder executing forced vibration consists of pressure and viscous shearing forces. For the mean-position analysis, these forces are functions of only the velocity of the wall of the structure through the solution of the fluid equations which are dependent only on the structural wall velocity. On the other hand, in the time-dependent coordinate-transformation analysis, the unsteady fluid forces are functions of both the time-dependent displacement and velocity of the structure, *i.e.*, they depend on ϵ^{n+1} and $\mathbf{U_w}^{n+1}$ at time level t^{n+1}. In this chapter, the fluid-structure interaction problems are solved, whereby the motion of the structure is allowed to evolve in accordance with the forces acting on it, *i.e.*, the fluid forces.

The fluid-structure interaction involving the coupling of the fluid dynamic equations and the equation of structural motion was studied by Bélanger (1991), Païdoussis *et al.* (1992) and Bélanger *et al.* (1993) by using the linearized Navier-Stokes equations for small-amplitude oscillations (mean-position analysis) of the outer cylinder. A very simple explanation of the fluid-structure interaction phenomena is the following one (Bélanger 1991). Given a structure and a fluid flow about it, one displaces the structure by a small amount away from its equilibrium position, and then releases it. There are mechanical restoring and damping forces, as shown in Figure 9.1, which will act to return the structure to its equilibrium position. However, as it undergoes displacement toward equilibrium, fluid forces come into play and may render the fluid-structure system unstable, or add more damping or stiffness to it. The time-evolution of the displacement of the structure determines whether the system under consideration is stable or unstable. This is assessed by integrating the equation of motion of the structure under the combined mechanical and fluid forces, using either a predictor-corrector scheme or a fourth-order Runge-Kutta scheme.

The fluid-structure interaction cases considered in this chapter are divided into two groups. The first one involves the mean-position analysis of the fluid forces obtained in Chapter 4. The second group involves the time-dependent coordinate-transformation analysis of the fluid forces described in Chapter 6. For the first type of analysis, both uniform and nonuniform annular spaces are considered. For each annular geometry, translational motions of the outer cylinder are investigated; on the other hand, rocking motion of the outer cylinder is investigated only for the uniform annular geometry. For larger-amplitude oscillation, only translational motion of the outer cylinder for uniform and backstep annular geometries is considered. In addition to these 3-D fluid-structure interaction analyses, the cases of 2-D stability analysis of these systems for both types of theoretical analysis of Chapters 4 and 6 are also conducted.

9.1 Analytical Coupling of the Fluid Forces and Structural Dynamics

The cylindrical structures considered are shown in Figure 9.1. It is seen that this structure has one degree of freedom, $\epsilon(t)$, which is a generalized displacement. The structure (outer cylinder) has mass M, and is restrained by a mechanical spring K and a dashpot C; for rocking motion, the pertinent mass-moment of inertia about the hinge axis shown in Figure 8.4 is J; C_o and K_o are respectively the moment coefficients of the dashpot and rotational spring located at the hinge point (not shown in Figure 8.4). The equations of motion of the structure for translational and rocking motions are equations (2.19) and (2.20), respectively, which may be rewritten here as

$$M\ddot{y} + C\dot{y} + Ky = F(t)\,, \tag{9.1}$$

$$J\ddot{\theta} + C_o\dot{\theta} + K_o\theta = M_o(t)\,. \tag{9.2}$$

Considering the characteristic length, H, of the structure, and the characteristic velocity, U, of the fluid, one can write equation (9.1) in dimensionless form as

$$\ddot{\epsilon}(t) + 2\xi\omega_n\dot{\epsilon}(t) + \omega_n^2\epsilon(t) = \sigma\mathcal{F}(\epsilon,\dot{\epsilon})\,, \tag{9.3}$$

where

$$t = \frac{U}{H}t^*\,, \qquad \omega_n = \sqrt{\frac{K}{M}}\frac{H}{U} = \Omega_n\frac{H}{U}\,, \qquad \xi = \frac{C}{2\sqrt{KM}}\,, \qquad \sigma = \frac{\rho H^3}{M}\,, \tag{9.4}$$

and $\mathcal{F}$ represents the nondimensional fluid dynamic forces exerted on the cylinder.

The equation of motion of the structure in rocking motion can similarly be written in nondimensional form as

$$\ddot{\theta}(t) + 2\xi\omega_{nR}\dot{\theta}(t) + \omega_{nR}^2\theta(t) = \sigma\mathcal{M}_o(\theta,\dot{\theta})\,, \tag{9.5}$$

where

$$\omega_{nR} = \sqrt{\frac{K_o H^2}{J}}\frac{H}{U} = \Omega_{nR}\frac{H}{U}, \qquad \xi = \frac{C_o H}{2\sqrt{K_o J}}, \qquad \sigma = \frac{\rho H^5}{J}; \tag{9.6}$$

θ is the angular displacement, and $\mathcal{M}_o$ is the nondimensional moment of the fluid-dynamic forces exerted on the cylinder.

In equations (9.3) and (9.5), t, ω_n, ω_{nR} and ξ are the dimensionless time, frequency and damping ratio, respectively, while σ is a dimensionless factor weighting the relative contribution of the fluid and mechanical forces; t^* is the dimensional time, Ω_n or Ω_{nR} is the dimensional radian natural frequency of the structure, and ρ is the dimensional fluid density. The nondimensional fluid force $\mathcal{F}$ is a function of $\epsilon(t)$, $\dot{\epsilon}(t)$ and $\ddot{\epsilon}(t)$ through the added stiffness, added damping and added mass effects, respectively, but $\ddot{\epsilon}(t)$ is not needed explicitly in the numerical evaluation of the fluid forces [$\epsilon(t)$ is also not needed explicitly when we consider small amplitude analysis of the fluid forces]. The nondimensional fluid moment $\mathcal{M}_o$ is, equivalently, a function of $\theta(t)$, $\dot{\theta}(t)$ and $\ddot{\theta}(t)$.

9.2 Numerical Solution of the Coupled Equations

To integrate equation (9.3), we suppose at the beginning that the time level t^n has been reached, where all the quantities necessary to describe the structural motion are known (Païdoussis *et al.* 1992): the displacement, ϵ, the velocity, $\dot{\epsilon}$, and the acceleration, $\ddot{\epsilon}$, of the structure, and the fluid forces acting on it, $\mathcal{F}(\epsilon^n, \dot{\epsilon}^n) \equiv \mathcal{F}^n$. For the rocking motion, the proper quantities in equation (9.5) are assumed to be known. As mentioned in the previous chapters, these quantities are known at all previous time levels t^k, $k \le n$, and the solution is advanced to t^{n+1}. For structural motion analysis, this is done using a second-order Runge-Kutta scheme, defined by the sequence

Predictor step:

$$\epsilon^{n+1/2} = \epsilon^n + \frac{\Delta t}{2}\dot{\epsilon}, \qquad \dot{\epsilon}^{n+1/2} = \dot{\epsilon} + \frac{\Delta t}{2}\ddot{\epsilon}^n, \tag{9.7,9.8}$$

$$\mathcal{F}^{n+1/2}=\mathcal{F}(\epsilon^{n+1/2},\dot{\epsilon}^{n+1/2})\,,\qquad \ddot{\epsilon}^{n+1/2}=-2\xi\omega_n\dot{\epsilon}^{n+1/2}-\omega_n^2\epsilon^{n+1/2}+\sigma\mathcal{F}^{n+1/2}\,;\tag{9.9,9.10}$$

Corrector step:

$$\epsilon^{n+1}=\epsilon^n+\Delta t\dot{\epsilon}^{n+1/2}\,,\qquad \dot{\epsilon}^{n+1}=\dot{\epsilon}^n+\Delta t\,\ddot{\epsilon}^{n+1/2}\,,\tag{9.11,9.12}$$

$$\mathcal{F}^{n+1}=\mathcal{F}(\epsilon^{n+1},\dot{\epsilon}^{n+1})\,,\qquad \ddot{\epsilon}^{n+1}=-2\xi\omega_n\dot{\epsilon}^{n+1}-\omega_n^2\epsilon^{n+1}+\sigma\mathcal{F}^{n+1}\,.\tag{9.13,9.14}$$

In the predictor step, the intermediate values for displacement and velocity are first determined at the intermediate time level $t^{n+1/2}=t^n+\Delta t/2$, *i.e.*, $\epsilon^{n+1/2}$ and $\dot{\epsilon}^{n+1/2}$. Once $\epsilon^{n+1/2}$ and $\dot{\epsilon}^{n+1/2}$ are so obtained, they serve for imposing boundary conditions to integrate the N-S equations up to $t^{n+1/2}$, which allows the calculation of the fluid force $\mathcal{F}^{n+1/2}$ at $t^{n+1/2}$. The acceleration, $\ddot{\epsilon}^{n+1/2}$, of the structure is then calculated from equation (9.10), and the solution can proceed on to the corrector step, which is solved in the same manner for the variables ϵ^{n+1}, $\dot{\epsilon}^{n+1}$, $\mathcal{F}^{n+1}$ and $\ddot{\epsilon}^{n+1}$.

The same solution can be obtained through a fourth-order Runge-Kutta scheme (Bélanger 1991), summarized in the following table as

$\mathcal{T}_1=t^n$	$\mathcal{X}_1=\epsilon^n$	$\mathcal{V}_1=\dot{\epsilon}^n$	$\mathcal{A}_1=\ddot{\epsilon}(\mathcal{X}_1,\mathcal{V}_1)$
$\mathcal{T}_2=t^n+\frac{\Delta t}{2}$	$\mathcal{X}_2=\epsilon^n+\frac{\Delta t}{2}\mathcal{V}_1$	$\mathcal{V}_2=\dot{\epsilon}^n+\frac{\Delta t}{2}\mathcal{A}_1$	$\mathcal{A}_2=\ddot{\epsilon}(\mathcal{X}_2,\mathcal{V}_2)$
$\mathcal{T}_3=t^n+\frac{\Delta t}{2}$	$\mathcal{X}_3=\epsilon^n+\frac{\Delta t}{2}\mathcal{V}_2$	$\mathcal{V}_3=\dot{\epsilon}^n+\frac{\Delta t}{2}\mathcal{A}_2$	$\mathcal{A}_3=\ddot{\epsilon}(\mathcal{X}_3,\mathcal{V}_3)$
$\mathcal{T}_4=t^n+\Delta t$	$\mathcal{X}_4=\epsilon^n+\Delta t\mathcal{V}_3$	$\mathcal{V}_4=\dot{\epsilon}^n+\Delta t\mathcal{A}_3$	$\mathcal{A}_4=\ddot{\epsilon}(\mathcal{X}_4,\mathcal{V}_4)$

Table 9.1: Runge-Kutta scheme applied to the integration of the equation of the structure.

The quantities $\mathcal{T}_i$, $\mathcal{X}_i$, $\mathcal{V}_i$, and $\mathcal{A}_i$ are variables of time, displacement, velocity and acceleration, respectively. After they have been calculated through the process outlined in Table 9.1, the time level is advanced to t^{n+1} as

$$\epsilon^{n+1}=\epsilon^n+\frac{\Delta t}{6}(\mathcal{V}_1+\mathcal{V}_2+\mathcal{V}_3+\mathcal{V}_4)\,,\qquad \dot{\epsilon}^{n+1}=\dot{\epsilon}^n+\frac{\Delta t}{6}(\mathcal{A}_1+\mathcal{A}_2+\mathcal{A}_3+\mathcal{A}_4)\,,\tag{9.15,9.16}$$

where $\mathcal{F}^{n+1}$ and $\ddot{\epsilon}^{n+1}$ are obtained by equations (9.13) and (9.14).

The sequence of calculations is similar to the predictor-corrector steps outlined previously. In both cases, the main point is that the displacements $\epsilon^{n+1/2}$, ϵ^{n+1}, and the velocities $\dot{\epsilon}^{n+1/2}$, $\dot{\epsilon}^{n+1}$, obtained from equations (9.7) and (9.11) (9.8) and (9.12) may be used as boundary conditions to integrate the N-S equations and calculate the fluid forces $\mathcal{F}^{n+1/2}$ and $\mathcal{F}^{n+1}$.

As shown in equations (9.7)-(9.10) and Table 9.1, the solution is sought at intermediate time level $t^{n+1/2}$. In such circumstances, the three-level real time discretization given by equation (3.2) and used in the previous chapters cannot be applied. Hence, the following semi-discretization is used for the N-S equations:

$$\frac{8\mathbf{V}^{n+1/2} - 9\mathbf{V}^{n} + \mathbf{V}^{n-1}}{3\Delta t} + \mathbf{Q}^{n+1/2} = 0 \,, \qquad (9.17)$$

which is also a three-time-level, second order accurate implicit scheme, written in terms of velocity at time levels t^{n-1}, t^{n} and $t^{n+1/2}$. Equations (3.3) and (3.4) can be expressed as

$$\mathbf{V}^{n+1/2} + \beta \mathbf{Q}^{n+1/2} = \mathbf{E}^{n} \,, \qquad \nabla \cdot \mathbf{V}^{n+1/2} = 0 \,, \qquad (9.18, 9.19)$$

where

$$\beta = \frac{3}{8}\Delta t \,, \qquad \mathbf{E}^{n} = \frac{1}{8}(9\mathbf{V}^{n} - \mathbf{V}^{n-1}) \,,$$

and $\mathbf{Q}^{n+1/2}$ is similar to $\mathbf{Q}^{n+1}$ defined in Chapter 3 except that it is evaluated at time $t^{n+1/2}$ instead of t^{n+1}.

Equations (9.18) and (9.19) are solved in the same manner for the quantities $\mathbf{V}^{n+1/2}$ and $p^{n+1/2}$, as was done for quantities $\mathbf{V}^{n+1}$ and p^{n+1} in Chapter 3. Thus, according to the notations of Chapter 3, in order to solve equations (9.18) and (9.19), we need to impose as boundary condition the wall velocity $\mathbf{U}_{w}^{n+1/2}$, which is given in Table 9.1 by $\mathcal{V}_2$ and $\mathcal{V}_3$, in steps 2 and 3, respectively. Step 4 in Table 9.1, and the final updating of the solution, equation (9.14), which both project the solution to $t^{n} + \Delta t$, can use the time differencing equation (3.2). From now on, all the numerical steps taken in Chapter 3 are followed, including the pseudo-time discretization of the N-S and continuity equations in delta forms as given by equations (3.9) and (3.10), application of the approximate factorization to the equations which results in equation (3.24), and solution of the resulting equations based on the ADI scheme using equations (3.26-3.28).

As mentioned before, depending on the method of solution (mean-position or time-dependent coordinate-transformation analysis), the solution obtained for the N-S equations and applied for the stability analysis will be different in terms of the fluid forces obtained, but the final output, *i.e.*, the displacement and the velocity of the moving boundary are always imposed as boundary conditions for obtaining the fluid force $\mathcal{F}$.

In order to start the numerical integration of the coupled equations, the displacement of the outer cylinder at t^1 and t^2 is set equal to $\epsilon(t^1) = \epsilon(t^2) = \epsilon_o$, away from its equilibrium position. This displacement could be small or large, depending on the method of solution. The other quantities, namely, velocity, acceleration and fluid force, are all equal to zero. This means that the outer cylinder is stationary at the first two time steps and there are no unsteady perturbations in the fluid flow. Then the structure is released, and the time integration is started. By imposing this two-time-level displacement, the solution would follow exactly the same three-time-level scheme described in the previous chapters. For small displacements imposed as boundary conditions to the cylinder, as well as for large displacements, it is assumed that the mean flow which exists before releasing the cylinder will remain the same as that which exists in the equilibrium position of the cylinder, for $\epsilon = 0$.

9.3 Numerical Results for 2-D Annular Geometry

For the stability analysis of 2-D annular geometries, we assume that the two cylinders are concentric, infinite in extent and of constant cross-section; the inner radius of the annulus is r_i and the outer one r_o. The outer cylinder has one degree of freedom in translational motion; *i.e.*, its axis always remains parallel with the axis of the inner cylinder which is fixed.

Equation (9.1) can now be used to investigate the motion of the outer cylinder in 2-D annular flow; for convenience M is replaced by m, C by c, K by k and $\mathcal{F}$ by $\breve{\mathcal{F}}$, where the lower case letters and $\check{\mathcal{F}}$ stand for quantities defined per unit length of the cylinder. The fluid force $\check{\mathcal{F}}$ can be obtained from equation (2.16). For the 2-D stability analysis, the same procedure as in Chapter 4 is applied in determining the unsteady pressure and the velocity gradients given by equations (2.17) and (2.18). Also, since no fluid flow is considered, the characteristic flow velocity used to nondimensionalize equation (9.1) will be $\Omega_n H$, the dimensional natural frequency Ω_n is defined by $\Omega_n = \sqrt{k/m}$ and, as in Chapter 4, the Reynolds number used for numerical integration of the fluid equations is given by $\mathrm{Re} = S = \Omega_n H^2/\nu$.

Given the characteristic length and velocity, equation (9.1) becomes

$$\ddot{\epsilon} = -2\xi\dot{\epsilon} - \epsilon + \sigma\check{\mathcal{F}}(\epsilon, \dot{\epsilon}) \,, \tag{9.20}$$

and equation (9.4) becomes

$$\omega_n = \sqrt{\frac{k}{m}}\frac{H}{\Omega_n H} = 1 \,, \qquad \xi = \frac{c}{2\sqrt{km}} \,, \qquad \sigma = \frac{\rho H^2}{m} \,, \tag{9.21}$$

To make the effect of fluid damping clearly and easily visible, the structural damping ratio ξ is taken equal to zero. As initial condition, $\epsilon_o = 0.1$ was taken; the calculations were conducted with $\Delta t = 2\pi/19$, and only the narrow annular space with $r_o = 10$ was considered. The unit of time for all figures presented in this chapter will be the natural period, T_n, of the system, which is given by $T_n = 2\pi/\omega_n$.

One of the important factors influencing the stability analysis through the solution of, for example, equation (9.20) and similar ones, is the determination of the value of σ. Linearized potential flow theory provides the per unit length nondimensional added mass, σ_m, for the geometry under consideration (Gibert 1986; Fritz 1972). This parameter is expressed as

$$\sigma_m = \frac{\rho H^2}{m_a} = \frac{1}{\pi r_o^2}\frac{\mathcal{E}^2 - 1}{\mathcal{E}^2 + 1} \,, \tag{9.22}$$

where m_a is the dimensional fluid-added mass and $\mathcal{E} = r_o/r_i$. Using equation (9.22) and the value for σ from equation (9.21), one obtains

$$\frac{\sigma_m}{\sigma} = \frac{m}{m_a} \,, \tag{9.23}$$

which indicates the ratio of structural mass to fluid-added mass.

To start the stability analysis, either this ratio must be known in advance, or it must be chosen in such a way that a reasonable structural behaviour is obtained. Practically, if the fluid is, for instance, water or another high density fluid, the fluid-added mass can become very important as compared to the mass of the cylinder. When the fluid-added mass exceeds the structural mass, numerical difficulties may arise. In this analysis, we consider only cases where the fluid-added mass does not exceed the mass of the structure; thus, the value of σ in (9.20) is selected to be equal to $\sigma = \sigma_m/2.0$, corresponding to a structural mass m equal to twice the fluid-added mass m_a determined by potential flow theory.

Figure 9.2(a) presents the time-domain history of the motion of the outer cylinder for different Reynolds numbers, and for potential flow as well, when the mean position analysis is used. The structure is displaced by $\epsilon = 0.1$ and then released. For the potential flow results, equation (9.20) was solved in which the fluid forces were determined by linearized potential flow theory. In fact, the potential flow theory result was used to ensure the validity of the procedure adapted for solving the coupled N-S and structural equations; by employing potential flow theory, one can obtain an analytical solution, which in fact compares well with the present numerical solution, for the motion of the structure immersed in fluid.

In Figure 9.2(a), we see that at a very low Reynolds number, Re = 4, viscosity dominates the solution and the cylinder motion is so highly damped that no oscillations are possible: the system is overdamped; the cylinder monotonically regains its equilibrium position, $\epsilon = 0$. As the Reynolds number increases, Re = 200 and Re = 20,000, damped oscillation develops. As the Reynolds number becomes larger, the viscous solution gets closer to the potential flow solution (zero dissipation, and hence zero fluid damping).

In Figure 9.2(b), comparison is made between the results obtained from mean position analysis (MPA) and time-dependent coordinate-transformation analysis (TD-

CTA). There are a number of points to be remarked upon in this comparison. First of all, as mentioned before, the fluid force in MPA is velocity dependent *vis-à-vis* the fluid force in TDCTA which is both displacement and velocity dependent. This is reflected in the fact that the frequency of the coupled fluid-structure according to TDCTA is increased *vis-à-vis* the frequency obtained from MPA; *i.e.*, the added fluid-stiffness is positive. This can be verified (using Figure 9.2(b)) by calculating the ratio of the natural damping frequencies, $(\omega_n)_{TDCTA}/(\omega_n)_{MPA} = 1.3$, as compared with the ratio of damping ratios $(\xi)_{TDCTA}/(\xi)_{MPA} = 0.182$. It is also noted that the MPA results indicate more damping due to fluid action than the TDCTA results; in the case of TDCTA, the structure has the opportunity to really move and the fluid to accommodate structural motion, which may explain why the effect of viscous damping is less pronounced *vis-à-vis* the frequency increment. The results shown in Figure 9.2(b) indicate the importance of taking into consideration the movement of the boundaries when investigating the stability of the fluid-structure systems even for small amplitude oscillations.

9.4 Numerical Results for 3-D Annular Geometries

The geometries that we consider in 3-D consist of uniform and nonuniform annular shapes shown in Figure 2.3. In translational motion, the configuration of Figure 2.4 (withot hinge) is used for stability analysis. The equation of motion of the system and the associated numerical results are first presented for the uniform annular geometry, when the outer cylinder is in translational motion in the plane of symmetry. Equations (2.16-2.18) and (9.3-9.4) are used to study the time-domain behaviour of the structure. As in 2-D analysis, the reduced mechanical damping, ξ, is neglected. The Reynolds number appearing in the equations of fluid motion is given by $\mathrm{Re} = 2UH/\nu$. Now, the value of σ should be determined before solving the equation of motion of the structure. In potential flow theory, the equation of motion of the oscillating cylinder can be written as (Mateescu & Païdoussis 1985)

$$(1 + \sigma q_2)\ddot{\epsilon} + (2\xi\omega_n + \sigma q_1)\dot{\epsilon} + (\omega_n^2 + \sigma q_o)\epsilon = 0 \ , \tag{9.24}$$

where q_2, q_1 and q_o are the nondimensional added mass, added damping and added stiffness, respectively. These parameters are given by

$$q_2 = \frac{M_a}{\rho H^3} , \qquad q_1 = \frac{C_a H}{MU} , \qquad q_o = \frac{K_a H^2}{MU^2} , \tag{9.25}$$

where M_a, C_a and K_a are dimensional added mass, added damping and added stiffness. Then, for 3-D potential flow, one can find σ from equations (9.4) and (9.24) as

$$\sigma q_2 = \frac{\rho H^3}{M} \frac{M_a}{\rho H^3} = \frac{M_a}{M} \ . \tag{9.26}$$

Once again, the mass ratio is selected to be $M/M_a = 2.0$, and to find σ the added mass q_2 must be known. For this purpose, the coupled structural and potential flow equations, similar to equation (9.24) but without the damping term, are solved (Bélanger *et al.* 1993).

For rocking motion of the outer cylinder, considering small amplitude motion, the fluid force acting on the outer cylinder is not given by equation (2.16); rather, it is obtained from

$$F(t) = \int_o^{2\pi} \left(\tau_{rr}|_{r=R_o} \cos\theta - \tau_{r\theta}|_{r=R_o} \sin\theta + \tau_{rx}|_{r=R_o} \frac{d\epsilon(t,x)}{dt} \right) R_o d\theta \ , \tag{9.27}$$

where τ_{rx} is given by equation (2.15) as

$$\prod\nolimits_{13} = \tau_{rx} = \mu \left(\frac{\partial u}{\partial r} + \frac{\partial v}{\partial x} \right) \ , \tag{9.28}$$

and $d\epsilon(t,x)/dt$ is obtained from equation (4.41). The moment of the fluid force is denoted by M_o in equation (9.2), or in nondimensional form by $\mathcal{M}_o$ in equation (9.5); it can be obtained by calculating the moment about the hinge point of the distributed fluid force along the cylinder axis.

Equation (9.5) can be written in the same form as equation (9.24). Thus, for rocking motion of the outer cylinder, the final equation to be solved reads (Mateescu

& Païdoussis 1985,1987)

$$(1+\sigma q_2)\ddot{\theta}+(2\xi\omega_n+\sigma q_1)\dot{\theta}+(\omega_n^2+\sigma q_o)\theta=0\ , \tag{9.29}$$

where

$$q_2=\frac{J_a}{\rho H^5}\ , \qquad q_1=\frac{C_a H^3}{JU}\ , \qquad q_o=\frac{K_a H^4}{JU^2}\ , \tag{9.30}$$

and as in equation (9.25), J_a, C_a and K_a stand for the added moment of inertia, added damping and added stiffness of the fluid force, respectively.

To solve equation (9.29), one needs to determine σ. By the same method used for translational motion of the cylinder, we can define $\sigma q_2 = J_a/J$. Thus, by preliminary calculation, q_2 is obtained using potential flow theory (Mateescu & Païdoussis 1987).

The stability analysis for annular geometries other than uniform (such as backstep- and diffuser-shaped) are implemented in the same manner, but for translational motion of the outer cylinder. For the annular geometry with a backstep, both the MPA and TDCTA are used to calculate the fluid forces. For diffuser shaped annular geometries, only MPA is used. The results for all three-dimensional analyses are shown in Figures (9.3-9.5).

Figure 9.3(a) shows the time-evolution solutions for the displacement of the vibrating outer cylinder for uniform annular geometry via MPA and TDCTA, when $\omega_n = 0.1$ and Re = 200. The same behaviour of the structure is seen in Figure 9.3(a) as was shown in Figure 9.2(b) for 2-D analysis, but there is more damping of the motion due to fluid flow and shear stresses along the cylinder axis. Once again, the natural frequency of the coupled fluid-structure system is increased in TDCTA *vis-à-vis* MPA. Figure 9.3(b) presents the behaviour of the system when the backstep geometry is used, for $\omega = 0.1$ and Re = 200. Comparison between the MPA and TDCTA results in Figure 9.3(b) indicates that, as for uniform annular regions, TDCTA predicts less damping and a fluid stiffenning effect in the system for the same imposed frequency and Reynolds number. Comparison between Figures 9.3(a) and 9.3(b) indicates that the system with backstep is less damped than for the uniform annular space, no matter whether using MPA or TDCTA; this is because the flow confinement in the former case is smaller over a portion of the system. Also, when TDCTA is used, the natural frequency of the coupled system is increased more in the uniform annular geometry than in the backstep one, for the same reason.

Figure 9.4(a) presents the behaviour of the system during rocking motion of the outer cylinder, for $\omega = 0.1$ and Re = 250, for a uniform annular geometry. It is seen that, the system initially appears to diverge, by falling from an angular displacement $\theta = 0.5729^o$ to $\theta = -5.0^o$, but it recovers its motion and then oscillates with almost constant frequency, showing tendency toward oscillating about the horizontal axis. The behaviour of the system in Figure 9.4(a) shows that after the cylinder is released, initially undergoes a transient oscillation around an axis other than the horizontal axis; however, it is seen that this is a short term behaviour and the cylinder approaches a limite-cycle of oscillation.

In this respect, it should be noted that linearized (N-S) analysis can only predict linear stability; *i.e.*, either damping or divergent motion (oscillatory or static); since the nonlinear N-S equations are solved here, we can have nonlinear behaviour predicted: in this case, a limit cycle.

Figure 9.4(b) presents the behaviour of the system when diffuser shaped annular geometries are used. It is seen that, the coupled system is more stable and its natural frequency is reduced when $\alpha = 6^o$ than the system with $\alpha = 20^o$. This, however, might not be so for other flow and geometrical conditions of the system than those investigated here. Figure 9.5 presents a comparison between the stability analysis results obtained for translational motion, for all types of annular geometries mentioned when $\omega = 0.1$ and Re = 200. It is seen, that the most stable (most highly damped) system is the uniform annular system and the least stable is that involving a backward step.

The final points that should be remarked are that the results obtained are for a specific natural frequency of the structure, as well as for a specific Reynolds number and annular gap width. Also, the effect of the fine or coarse mesh on the solution of the N-S equations needs special attention. In the 3-D analysis, the results presented were for cases where extension of the extremities of the fixed upstream and downstream cylinders were not considered. It is obvious that the behaviour of the systems would be different when each one or the combination of the parameters mentioned is changed, *e.g.* through equations (9.4,9.6,9.21,9.25,9.30). This task needs a comprehensive parameter study, which is beyond the scope of this Thesis; can be considered as a possible extension of this work in the future.

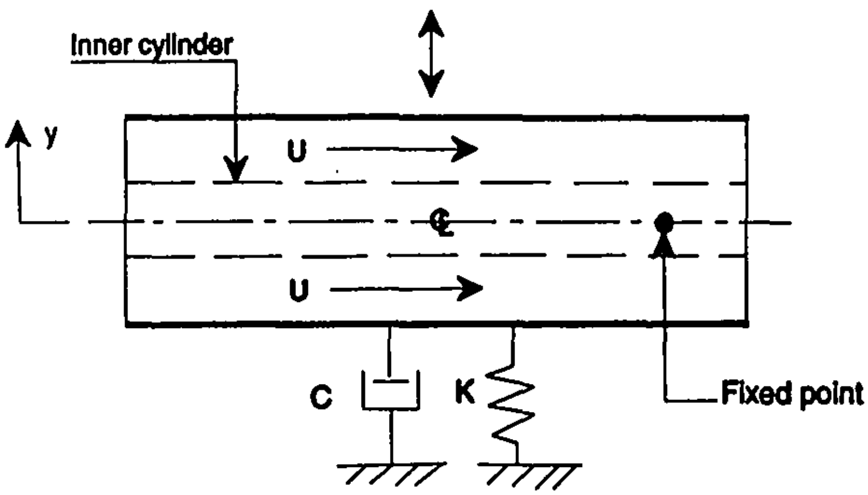

Figure 9.1: Schematic diagram showing the system considered for stability analysis.

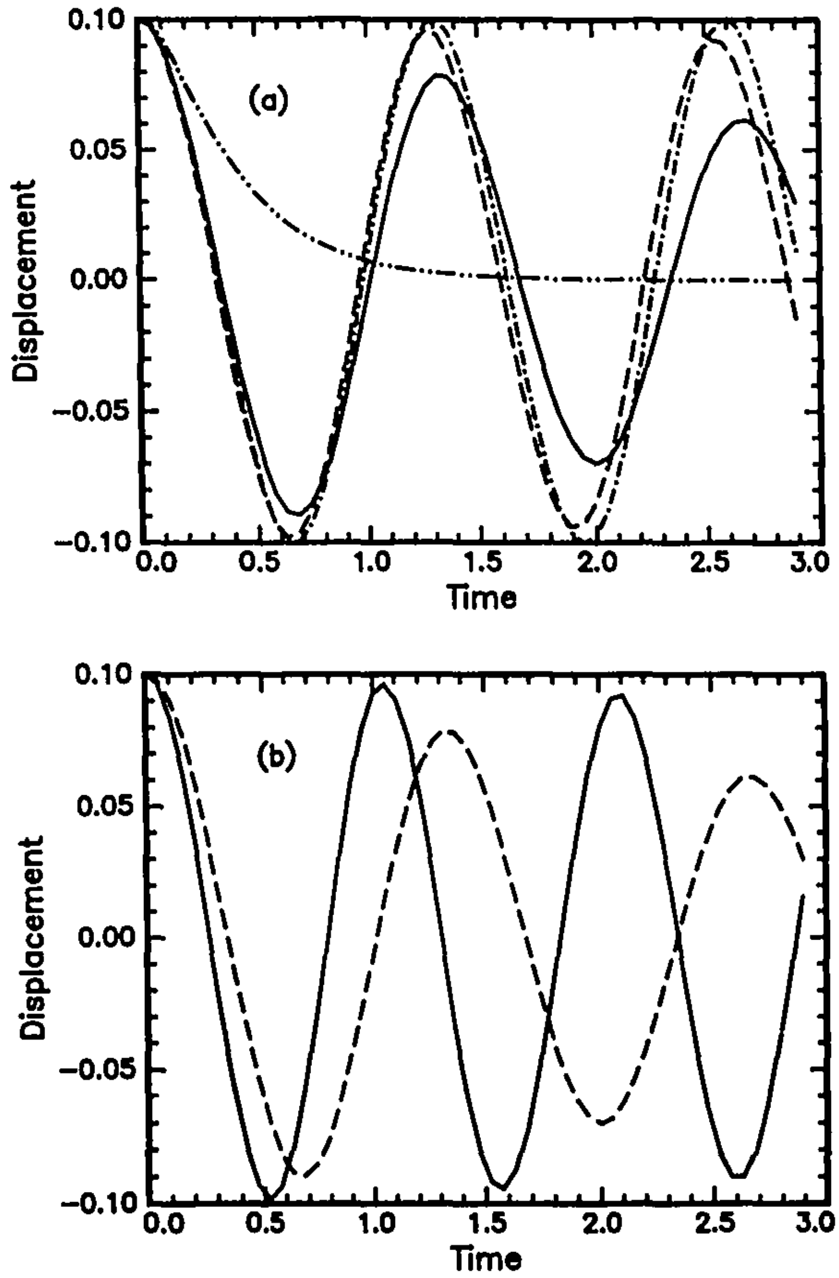

Figure 9.2: (a) Displacement, ϵ, of the outer cylinder in translational motion versus time, $T_n = 2\pi/\omega_n$, with $\omega_n = 1$ for 2-D; ·········,Re = 4; —,Re = 200; - - -,Re = 20,000; -··-·-,Potential flow. (b) Comparison between the displacements of the outer cylinder for Re = 200: - - -,MP analysis; —,TDCT analysis.

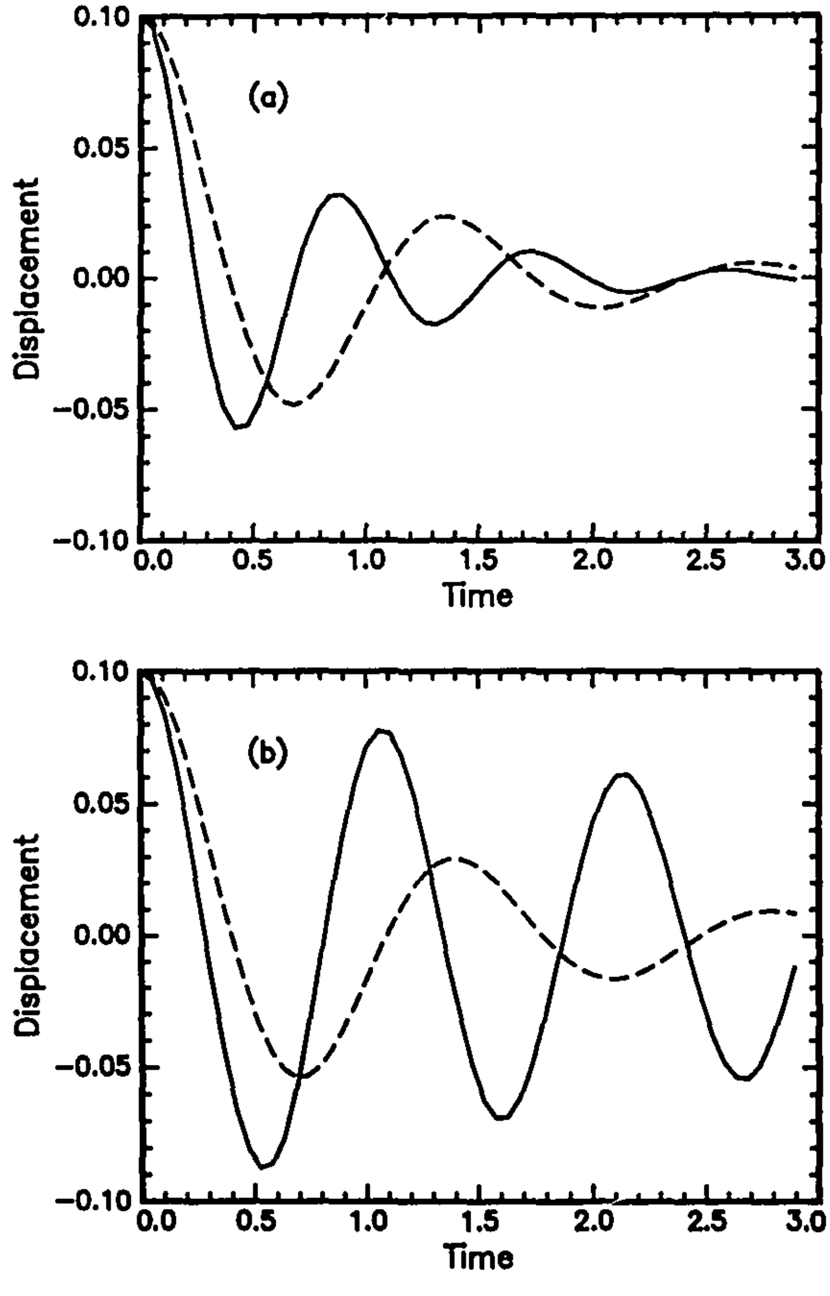

Figure 9.3: Displacement, ϵ, of the outer cylinder in translational motion versus time, $T_n = 2\pi/\omega_n$, for $\omega_n = 0.1$ and Re = 200: (a) for uniform annular geometry, (b) for annular geometry with backstep; - - -,MP analysis; —,TDCT analysis.

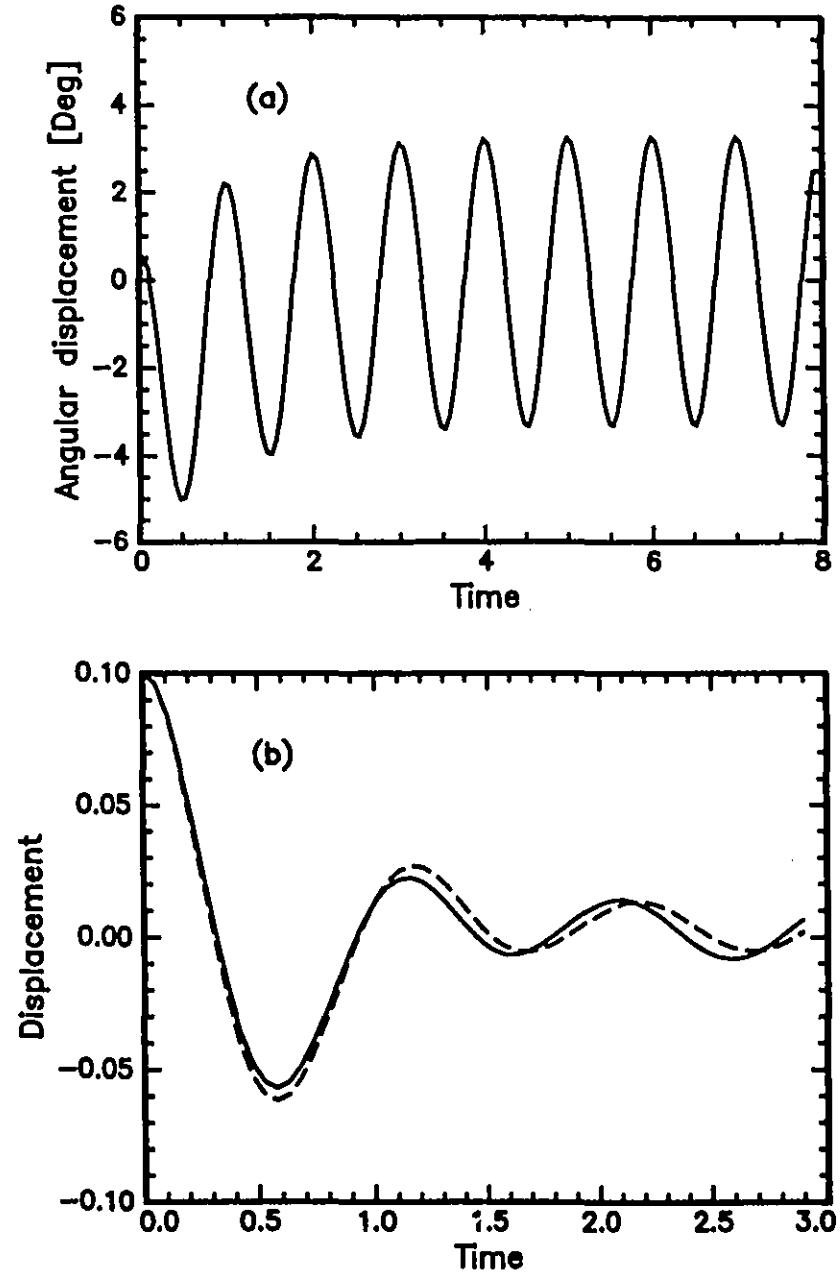

Figure 9.4: Displacement, θ and ϵ, versus time, $T_n = 2\pi/\omega_n$, for $\omega_n = 0.1$: (a) uniform annular geometry with rocking motion of the outer cylinder, Re = 250, hinge point at $X = x/H = 90$; (b) diffuser shaped annular geometry with translational motion of the outer cylinder, Re = 200; —,diffuser half-angle $\alpha = 6^o$; - - -,diffuser half-angle $\alpha = 20^o$.

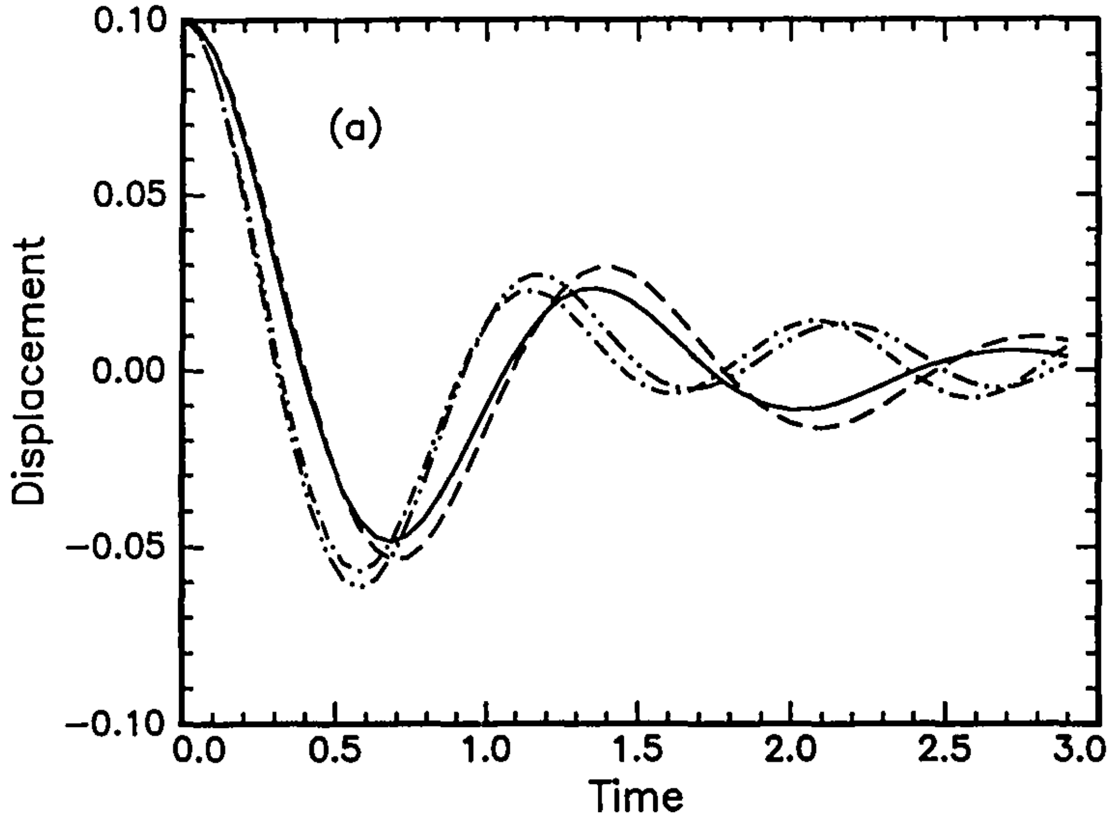

Figure 9.5: Comparison between the behaviour of the system in translational motion for different geometries at $\omega = 0.1$ and Re = 200; —,uniform; - - -,backstep; -·-·- ,diffuser with $\alpha = 6^o$; -··-··-,diffuser with $\alpha = 20^o$.

Chapter 10

Conclusion

10.1 General Conclusions

This Thesis takes several major steps in the solution of annular flow-induced vibration problems. The main step in the theoretical investigation was the development of the numerical method of solution of the full nonlinear Navier-Stokes equations for laminar flows based on a *time-dependent coordinate transformation*, in different annular geometries. The second step, was the numerical solution of the fluid equations in axially variable annular geometries (diffuser type). The third step was the carrying out of a comprehensive set of experiments to validate the theories developed, again for different annular geometries, with quiescent fluid or fluid flow in the laminar regime. Experiments were also conducted in the turbulent regime, which will be useful when the theory is extended to deal with turbulent flows. The last step was the time-domain study of the fluid-structure interaction and stability analysis for all annular geometries considered in this Thesis.

The most important contributions of this Thesis are presented in Chapter 6, where the *time-dependent coordinate transformation* analysis was introduced in this work. To solve the flow-induced vibration problems in annular regions, the moving domain was transformed to a fixed computational domain by using appropriate transformation equations. Then, the time-integration of the incompressible laminar N-S and the continuity equations was effected by using the method of artificial compressibility in conjunction with a three-point backward implicit *real-time* differencing scheme on a fixed domain. After the semi-discretization, artificial *pseudo-time* derivative terms were added to the equations, including artificial compressibility in the continuity equation, and the solution was advanced from one real (physical) time level to the next by integrating in pseudo-time until steady state was reached. The equations were cast in delta-form after differencing the pseudo-time derivatives by using an Euler scheme. The solution was effected by using the Approximate Factorization and ADI techniques, and finite differences were used in which the spatial differential operators were written on stretched staggered grids.

Introducing the idea of *time-dependent coordinate transformation* in FIV analysis of annular geometries having either uniform or nonuniform annular passages enables handling of different modes of the motion of the outer (or inner) cylinder (including shell motion, which of course was not the topic of this research). When the limitation imposed on the motion of the structure is removed by a *time-dependent coordinate transformation*, the flexibility of performing better and more extensive studies on the subject of FIV is enhanced. The results obtained by using the *time-dependent coordinate transformation* analysis for both uniform and nonuniform annular geometries were more realistic, and hence in better agreement with experiment, than those obtained from mean-position analysis. The unsteady pressures obtained were appreciably higher than those predicted by mean-position analysis, and the phase angles of the unsteady pressure with respect to the displacement of the outer cylinder are clearly different in the *time-dependent coordinate transformation* analysis than in the mean-position analysis, specially when the flow velocity is high (in the laminar range).

Another basic objective of this research was fulfilled in Chapter 5 which was dedicated to the study of axially-variable geometries, which can develop flow-induced vibrations; it is recalled that several such problems have been encountered in different industries. The annular geometries with diffuser sections of half-angle 6° and 20°, which are of interest to researchers, were studied. The unsteady pressures obtained by the present numerical solution in the annular space after the diffuser section, which predicts pressure recovery, were in good agreement with the findings of other investigators. It was shown that, the pressure recovery is more pronounced for diffusers with small half- angles than those with larger ones as well as for the backstep geometry. This pressure recovery, as discussed previously, is a major factor in the stability of the system.

The next important objective of this Thesis was the implementation of a comprehensive experimental study of the system, which were successfully performed and the results obtained were presented in Chapter 8. The primary concern regarding experimental investigations was the validation of the numerical results obtained from two approaches (mean-position and moving-boundary). This chapter, also, presents another important step taken toward the future extension of this work by presenting the collected data in the turbulent regime. The set of data obtained (both laminar and turbulent) were processed and analyzed. The comparison was made between the experimental results for different nonuniform annular geometries, which clearly indicated different trends of the unsteady pressure in various annular shapes and regions. The final conclusion about this comparison is that the time-dependent coordinate transformation analysis agrees better with the experimental results and is therefore recommended for future FIV analyses in annular configurations. Also, the theoretical rocking motion results are in excellent agreement with the experimental results both in terms of unsteady pressure and phase angle.

In all cases considered, the solution of the full nonlinear N-S equations provides the opportunity of obtaining more accurate unsteady pressure and phase angle than could be obtained otherwise by linearized solution of these equations. The extension of the range of Reynolds number from 250 to 2900 (laminar regime) was another outcome of using the full N-S equations. For time-dependent coordinate transformation, mean-position and annular flow with axially variable geometry analyses, the boundary conditions were modified in such a way as to reduce the pressure and velocity perturbations (to the extent possible) emerging from the extremities of the system, specially when there is no fluid flow.

The numerical procedure was applied, for the first time by the present method of solution, to the rocking motion of the outer cylinder. The results obtained were gratifying, specially since they were in excellent agreement with the experimental results which was referred to in the associated paragraph. It is concluded that the mean-position analysis can be used in rocking motion study of the annular flow, provided that the amplitude of oscillation is appropriately small. Also, for the nonuniform annular geometry (backstep), the rocking motion results predict favourably well the behaviour of the unsteady pressure in the annular space.

Of course, as shown in Chapter 7, some of the results presented are not fully convergent, because of practical difficulties. Nevertheless, the work in that chapter shows that the discrepancy is not large enough (for instance, less than 3% as shown in Figures 7.2 and 7.4) to invalidate any of the results presented.

Finally, the theoretical models presented were used to predict the behaviour of the structure (outer cylinder) when it is set in motion from rest. The coupling of the unsteady flow and structural equations was performed through a fourth-order Runge-Kutta scheme to integrate the equation of the structure under the combined action of mechanical forces and fluid forces. The fluid forces were obtained by solving the N-S equations by two approaches: mean-position and *time-dependent coordinate transformation* analyses. The stability of the system was analyzed for: (i) translational or rocking motion of the outer cylinder; (ii) in different annular geometries. It was shown that, the behaviour of the outer cylinder using *time-dependent coordinate transformation* analysis can be physically more deterministic (since the displacement of the outer cylinder is considered during stability analysis) than that predicted by mean position analysis. The same conclusion was reached when the annular geometry involves a backward facing step.

For the cases, where the annular space is uniform and the outer cylinder moves in rocking motion, it was shown that for the specific conditions imposed on the system, the structure initially has a transient motion around an axis different from the horizontal axis. After several cycles of oscillation, this behaviour of the structure is changed and the cylinder continues oscillating around the horizontal axis, indicating flutter and the establishment of limite-cycle motion. In the study of the stability of the system containing the diffuser shaped annuli, it was found that the structure with small-angle diffuser is more stable than the one with large-angle diffuser. Lastly, another important point was reached in the stability analysis when comparison was made between different annular geometries. It was shown that for translational motion of the outer cylinder, among the geometries considered and under the imposed initial and boundary conditions, the most stable system (relatively) is the one having uniform annular geometry and the least stable one is the geometry having a backstep.

10.2 Contribution to Knowledge

This work could be used to launch future investigations in the field of FIV with annular (or even axial internal or external) flows. It was shown that the foundation is firm and reliable; however, like any such work, it does not cover all aspects of the problems defined in this field of interest. This Thesis has made the following major contributions to knowledge:

(a) Development and implementation of the method of solution for fluid flow equations (full nonlinear Navier-Stokes equations) based on the *time-dependent coordinate transformation* for laminar flow in annular geometries.

(b) Unsteady flow solutions have been obtained for axially-variable geometries by integrating the Navier-Stokes equations using a mean-position analysis.

(c) Extensive experimental investigations of forced vibration of the structure in order to obtain the unsteady pressure and its phase angle to be compared with the theoretical results, and also the collection of the experimental data in the turbulent regime.

(d) Study of the dynamical behaviour of the structure, under the influence of the fluid-structure interaction, based on the theoretical models developed, and a case of limit-cycle motion was found.

Other contributions are:

(e) Modification of the mean-position analysis by considering the full nonlinear Navier-Stokes equations in order to obtain more accurate solutions for small-amplitude oscillations (translational or rocking motion) and/or larger Reynolds numbers.

10.3 Future Extension of this Research and Some Recommendations

As one notices in the previous section, the originality of the work done in this Thesis provides the opportunity of extending the formulation and the results of the experiments presented here to the other FIV problems. Clearly, more work is necessary on any individual topic in order to make it applicable to the wide range of problems encountered in science, engineering and other fields (*e.g.*, in medicine) involving fluid-structure interactions. The following topics which could be the continuation of this research were classified as follows.

Theoretical Work

(i) The numerical procedure presented here can be used with different boundary conditions representing practical interest;

(ii) the numerical model (*time-dependent coordinate transformation*) can be used to solve shell motion in FIV problems;

(iii) the numerical models can be modified to predict the unsteady pressure for nonuniform annular geometries with fluid flows of higher Reynolds number (which could not be implemented in this research);

(iv) the numerical models can be used for parametric studies such as the effects of the mesh size and the number of grid points as well as the number of real-time steps (to investigate and improve convergence), Reynolds number, annular gap width, the length of the oscillating cylinder, length of the fixed upstream and downstream portions, higher amplitudes of oscillation, higher frequencies of oscillation, rocking motion with different position of the hinge point, annular regions with different geometries or combination of the geometries, eccentric cylinders instead of concentric ones, combination of translational and rocking motion of the outer cylinder, etc., on the solution of the N-S equations in the annular region;

(v) modification of the numerical model to minimize the pressure perturbation at the fixed portions as well as using large memory and faster computers to obtain more converged solutions;

(vi) theoretical stability analysis of the systems can be done for different annular gap width, Reynolds number, amplitudes of oscillation of the outer cylinder, frequencies of oscillation of the cylinder, different mesh sizes, different positions of the hinge point (in rocking motion) and different geometries.

Experimental work

(i) Experiments with nonuniform annular geometries in rocking motion;

(ii) experiments with uniform or nonuniform annular geometries having eccentric cylinders for both translational or rocking motion of the outer cylinder;

(iii) experiments for the combination of the nonuniform annular geometries;

(iv) experiments for circumferential measurements of the unsteady pressure at different circumferential angle, θ, for both concentric and eccentric cylinders, using either uniform or nonuniform annular spaces;

(v) experimental studies for all the cases mentioned with more pressure transducers to be mounted along the centre-body in order to obtain more experimental data, and if possible implementation of the experiment with water by modification of the present apparatus appropriate for that purpose;

(vi) more studies regarding the end gaps between the moving and fixed cylinders;

(vi) experimentation with better facilities for fluid flow measurements (in such a narrow annular space), and on a much more solid foundation (free from mechanical vibration) to have more accurate results free from extraneous factors;

(vii) finally, implementation of flow visualization by using appropriate equipment to see the patterns of the fluid flow in such narrow annular spaces during motion of the outer cylinder.

References

Anderson, D.A., Tannehill, J.C. and Pletcher, R.H., 1984, *Computational Fluid Mechanics and Heat Transfer*, Hemisphere Publishing Corporation, New York.

Asaithambi, N.S., 1988, "On a Variable Time-Step Method for the One-Dimensional Stefan Problem", *Computer Methods in Applied Mechanics and Engineering*, Vol. 71, pp. 1-13.

Ashurts, W.T. and Durst, F., 1980, "Studies of Flow Instabilities in Two-Dimensional Test Sections with Sudden Expansions", *Practical Experiences with Flow-Induced Vibrations*, Eds Naudascher, E., and Rockwell, D., pp. 801-808.

Beam, R.M. and Warming, R.F., 1978, "An Implicit Factored Scheme for the Compressible Navier-Stokes Equations", *AIAA Journal*, Vol. 16, No. 4, pp. 393-402.

Beckwith, T.G. and Marangoni, R.D., 1990, *Mechanical Measurement*, 4th Edition, Addison-Wesley.

Bendat, J.S. and Piersol, A.G., 1971, *Random Data: Analysis and Measurement Procedures*, Wiley-Interscience, New York.

Benocci, C., Bellomi, P. and Michelassi, V., 1987, "Comparison of Cartesian and Curvilinear Grids for Incompressible Flow Around Steps", *Numerical Methods in Laminar and Turbulent Flows*, Eds Taylor, C., Habashi, W.G. and Hafez, M.M., Vol. 5, Part 1, pp. 584-594.

Bélanger, F., 1991, "A Numerical Method for Confined Unsteady Flows Related to Fluid-Structure Interaction", Ph.D. Thesis, Department of Mechanical Engineering, McGill University.

Bélanger, F., De Langre, E., Axisa, F., Païdousis, M.P. and Mateescu, D., 1993, "Dynamics of Coaxial Cylinders in Laminar Annular Flow by Simultaneous Integration of the Navier-Stokes and Structural Equations, *Journal of Fluids and Structures*, (in press).

Blevins, R.D., *Flow-Induced Vibration*, 1990, 2nd Edition, Van Nostrand Reinhold, New York.

Braaten, M. and Shyy, W., 1986, "A Study of Ricirculating Flow Computation Using Body-Fitted Coordinates: Consistency Aspects and Mesh Skewness", *Numerical Heat Transfer*, Vol. 9, pp. 559-574.

Canuto, C., Hussaini, M.Y., Quarteroni, A. and Zang, T.A., 1987, *Spectral Methods in Fluid Dynamics*, Springer-Verlag, New York.

Chen, S.S., 1987, *Flow-Induced Vibration of Circular Cylindrical Structures*, Hemisphere Publication Corporation, Washington.

Chorin, A.J., 1967, "A Numerical Method for Solving Incompressible Viscous Flow Problems", *Journal of Computational Physics*, Vol. 2, pp. 12-26.

Chorin, A.J., 1968, "Numerical Solution of the Navier-Stokes Equations", *Mathematics of Computation*, Vol. 22, pp. 745-762.

Cooley, J.W., Lewis, P.A.W. and Welch, P.D., 1969, "The Finite Fourier Transform", *IEEE Transaction on Audio and Electronics*, Vol. AU-17, pp. 77-85.

Djomehri, M.J. and George, J.H., 1988, "Application of the Moving Finite Element Method to Moving Boundary Stefan Problems", *Computer Methods in Applied Mechanics and Engineering*, Vol. 71, pp. 125-136.

Demirdzic, I. and Peric, M., 1990, "Finite Volume Method for Prediction of Fluid Flow in Arbitrarily Shaped Domains with Moving Boundaries", *International Journal for Numerical Methods in Fluids*, Vol. 10, pp. 771-790.

Domaradzki, J.A. and Metcalfe, R.W., 1987, "Stabilization of Laminar Boundary Layers by Compliant Membranes", *Physics of Fluids*, Vol. 30, pp. 695-705.

Duda, J.L., Malone, M.F. and Notter, R.H., 1975, "Analysis of Two-Dimensional Diffusion-Controlled Moving Boundary Problems", *International Journal of Heat and Mass Transfer*, Vol. 18, pp. 901-910.

Faghri, M., Sparrow, E.M. and Prata, A.T., 1984, "Finite-Difference Solutions of Convection-Diffusion Problems in Irregular Domains, Using a Nonorthogonal Coordinate Transformation", *Numerical Heat Transfer*, Vol. 7, pp. 183-209.

Fritz, R.J., 1972, "The Effect of Liquids on the Dynamic Motions of Immeresed

Solids", *Journal of Engineering for Industry*, pp. 167-173.

Gartling, D.K., 1990, "A Test Problem for Outflow Boundary Conditions – Flow Over a Backward-Facing Step", *International Journal for Numerical Methods in Fluids*, Vol. 11, pp. 953-967.

Gibert, R.J., 1988, *Vibrations des Structures*, Éditions Eyrolles, Paris.

Gupta, R.S. and Kumar, A., 1984, "Variable Time-Step Method with Coordinate Transformation", *Computer Methods in Applied Mechanics and Engineering*, Vol. 44, pp. 91-103

Harlow, F.H. and Welch, J.E., 1965, "Numerical Computation of Time-Dependent Viscous Incompressible Flow of Fluid with Free Surface", *Physics of Fluids*, Vol. 8, pp. 2182-2189.

Hobson, D.E., 1982, "Fluid-elastic Instabilities Caused by Flow in an Annulus", in *Proceedings of* 3rd *International Conference on Vibration of Nuclear Plant*, Keswick, U.K., pp. 440-463.

Hobson, D.E., 1984, "Instabilities of the AGR Fuel Assembly During On-Load Refuelling", *ASME Symposium on Flow-Induced Vibration, Vol. 4: Vibration Induced by Axial and Annular Flows* (eds M. P. Païdoussis and M. K. Au-Yang), pp. 25-39.

Hobson, D.E., 1991, "Measurement of Damping Forces Caused by Flow Between Two Concentric Cylinders", Flow-Induced Vibration, *Proceeding of the Institution of Mechanical Engineers*, 1991-6, 459-471.

Hobson, D.E. and Jedwab, M., 1990, "Investigation of the Effect of Eccentricity on the Unsteady Fluid Forces on the Centrebody of an Annular Diffuser", *Journal of Fluids and Structures*, Vol. 4, pp. 155-169.

Hoffmann, K.A., 1989, *Computational Fluid Dynamics for Engineers*, A Publication of Engineering Education Systems, Austin, Texas.

Holman, J.P., 1989, *Experimental Methods for Engineers*, 5th Edition, McGraw-Hill, New York.

Hsu, C.F., Sparrow, E.M. and Patankar, S.V., 1981, "Numerical Solution of

Moving Boundary Problems by Boundary Immobilization and A Control-Volume-Based Finite-Difference Scheme", *International Journal of Heat and Mass Transfer*, Vol. 24, pp. 1335-1343.

Inada, F. and Hayama, S., 1990, "A Study on Leakage-Flow-Induced Vibrations. Part I: Fluid-Dynamic Forces and Moments Acting on the Walls of a Narrow Tapered Passage", *Journal of Fluids and Structures*, Vol. 4, pp. 395-412.

Inada, F. and Hayama, S., 1990, "A Study on Leakage-Flow-Induced Vibrations. Part II: Stability Analysis and Experiments for Two-Degree-of-Freedom Systems Combining Translational and Rotational Motions", *Journal of Fluids and Structures*, Vol. 4, pp. 413-428.

Karki, K.C., 1986, "A Calculation Procedure for Viscous Flows at All Speeds in Complex Geometries", Ph.D. Thesis, University of Minnesota.

Kansa, E.J., 1988, "Shock Computations with Adaptive Mesh Refinement and Moving Grids", *Computers and Mathematics with Applications*, Vol. 15, pp. 623-634.

Kreyszig, E., 1964, *Differential Geometry*, University of Toronto Press.

Mateescu, D., Mekanik, A. and Païdoussis, M.P., 1994, "Computational Solutions for Unsteady Annular Flows with Oscillating Boundaries Based on Time-dependent Coordinate Transformations", pp. 51-58, *Proceedings of Second Annual Conference of the CFD Society of Canada (CFD 94)*, University of Toronto, Toronto, Ont., Canada.

Mateescu, D. and Païdoussis, M.P., 1985, "The Unsteady Potential Flow in an Axially Variable Annulus and its Effect on the Dynamics of the Oscillating Rigid Centre-Body", *Journal of Fluids Engineering*, Vol. 107, pp. 421-427.

Mateescu, D. and Païdoussis, M.P., 1987, "Unsteady Viscous Effects on the Annular-Flow-Induced Instabilities of a Rigid Cylindrical Body in a Narrow Duct", *Journal of Fluids and Structures*, Vol. 1, 197-215.

Mateescu, D., Païdoussis, M.P. and Bélanger, F., 1988, "Unsteady Pressure Measurements on an Oscillating Cylinder in a Narrow Annular Flows", *Journal of*

Fluids and Structures, Vol. 2, pp. 615-628.

Mateescu, D., Païdoussis, M.P. and Bélanger, F., 1989, "A Theoretical Model Compared with Experiments for the Unsteady Pressure on a Cylinder Oscillating in Turbulent Annular Flow", *Journal of Sound and Vibration*, Vol. 135, pp. 487-498.

Mateescu, D., Païdoussis, M.P. and Bélanger, F., 1991, "Computational Solutions Based on a Finite Difference Formulation for Unsteady Internal Flows", *AIAA Paper No. 91-0724*.

Mateescu, D., Païdoussis, M.P. and Bélanger, F., 1994, "Unsteady Annular Viscous Flows Between Oscillating Cylinders. Part I: Computational Solutions Based on a Time-integration Method", *Journal of Fluids and Structures*, Vol. 8, pp. 489-507.

Mateescu, D., Païdoussis, M.P. and Mekanik, A., submitted 1994, "Analysis of 3-D unsteady Annular Flows Based on Time-dependent Coordinate Transformation", to be presented in *PACAM IV in Buenos Aires*, January 1995.

Mateescu, D., Païdoussis, M.P. and Sim, W.-G., 1994, "A Spectral Collocation Method for Confined Unsteady Flows with Oscillating Boundaries", *Journal of Fluids and Structures*, Vol. 8, pp. 157-181.

Mekanik, A., Mateescu, D. and Païdoussis, M.P., 1993, "Computational Solution of Navier-Stokes Equations for Annular Flows with Moving Boundaries", pp. 243-244, *Proceedings of* 14th *Canadian Congress of Applied Mechanics*, Queen's University, Kingston, Ont., Canada.

Mekanik, A., Païdoussis, M.P. and Mateescu, D., 1994, "Pressure Measurements in Unsteady Flows Between Concentric Cylinders in Translation and Rotation", pp. 345-353, *Proceedings of the 12th Symposium on Engineering Applications of Mechanics*, McGill University, Montreal, Qc., Canada.

Merkle, C.L. and Athavale, M., 1987, "Time-Accurate Unsteady Incompressible Flow Algorithms Based on Artificial Compressibility", *AIAA Paper No. 87-1137.*

Miller, R.W., 1989, *Flow Measurement Engineering Handbook*, 2nd Edition, McGraw-Hill, New York.

Mulcahy, T.M., 1983, "A Review of Leakage-Flow-Induced Vibration of Reactor Components", *Argonne National Laboratory Report ANL-83-43.*

Mulcahy, T.M., 1988, "One-Dimensional Leakage-Flow Vibration Instabilities", *Journal of Fluids and Structures*, Vol. 2, pp. 383-403.

Ogawa, S., and Ishiguro, T., 1987, "A Method for Computing Flow Fields Around Moving Bodies", *Journal of Computational Physics*, Vol. 69, pp. 49-68.

Païdoussis, M.P., 1980, "Flow-Induced Vibration in Nuclear Reactors and Heat Exchangers: Practical Experiences and State of Knowledge", *Practical Experinces with Flow-Induced Vibrations*, (eds E. Naudascher and D. Rockwell), Springer, Berlin, pp. 1-81.

Païdoussis, M.P., 1983, "A Review of Flow-Induced Vibrations in Reactors and Reactor Components", *Nuclear Engineering and Design*, Vol. 74, pp. 31-60.

Païdoussis, M.P., 1987, "Flow-Induced Instabilities of Cylindrical Structures", *Applied Mechanics Reviews*, Vol. 40, No. 2, pp. 163-175.

Païdoussis, M.P., 1993, "1992 Calvin Rice Lecture: Some Curiosity-Driven Research in Fluid Structure Interactions and Its Current Applications", *ASME Journal of Pressure Vessel Technology*, Vol. 115, pp. 2-14.

Païdoussis, M.P. and Au-Yang, M.K. (Eds), 1984, *Symposium on Flow-Induced Vibrations*; Vol. 4: Vibration Induced by Axial and Annular Flows, ASME, New York.

Païdoussis, M.P. and Au-Yang, M.K. (Eds), 1988, *Symposium on Flow-Induced Vibrations; Vol. 4: Vibration Induced by Axial and Annular Flows*, ASME, New York.

Païdoussis, M.P. and Au-Yang, M.K. (Eds), 1992, *International Symposium on Flow-Induced Vibration and Noise; Vol. 5: Axial and Annular Flow-Induced Vibration and Instabilities*, ASME, New York.

Païdoussis, M.P., Chan, S.P. and Misra, A.K., 1985, "Dynamics and Stability of Coaxial Cylindrical Shells Containing Flowing Fluid", *Journal of Sound and Vibration*, Vol. 97, pp. 201-235.

Païdoussis, M.P., Mateescu, D. and Sim, W.-G., 1990, "Dynamics and Stability of Flexible Cylinder in a Narrow Coaxial Cylindrical Duct Subjected to Annular Flow", *Journal of Applied Mechanics*, Vol. 57, pp. 232-240.

Païdoussis, M.P., Mateescu, D. and Bélanger, 1992, "A Computational Method for the Dynamics of Cylindrical Structures Subjected to Annular Flows by Simultaneous Integration of the Navier-Stokes and Structural Equations", *International Symposium on Flow-Induced Vibration and Noise; Vol. 5: Axial and Annular Flow-Induced Vibration and Instabilities*, ASME, New York.

Païdoussis, M.P., Misra, A.K., and Chan, S.P., 1985, "Dynamics and Stability of Coaxial Cylindrical Shells Conveying Viscous Fluid", *Journal of Applied Mechanics*, Vol. 52, pp. 389-396.

Païdoussis, M.P. and Ostoja-Starzewski, M., 1981, "Dynamics of a Flexible Cylinder in Subsonic Axial Flow", AIAA Journal, Vol. 19, pp. 1467-1475.

Païdoussis, M.P. and Pettigrew, M.J., 1979, "Dynamics of Flexible Cylinders in Axisymmetrically Confined Axial Flow", *Journal of Applied Mechanics*, Vol. 46, pp. 37-44.

Parkin, M.W. and Watson, C.P., 1984, "Reduction of Vibration Caused by Flow in an Annular Diffuser", *ASME Symposium on Flow-Induced Vibration, Vol. 4: Vibration Induced by Axial and Annular Flows* (eds M. P. Païdoussis and M. K. Au-Yang), pp. 1-14.

Patankar, S.V., 1980, *Numerical Heat Transfer and Fluid Flow*, Hemisphere Publishing Corporation, New York.

Peaceman, D.W. and Rachford, H.H., 1955, "The Numerical Solution of Parabolic and Elliptic Differential Equations", *Journal of the Society of Industrial and Applied Mathematics*, Vol. 3, pp. 28-41.

Peyret, R. and Taylor, T.D., 1983, *Computational Methods for Fluid Flows*, Springer-Verlag, New York.

Press, W.H., Flannery, B.P., Teukolsky, S.A. and Vetterling, W.T., 1988, *Numerical Recipes: The Art of Scientific Computing*, Cambridge University Press.

Rai, M.M. and Anderson, D.A., 1982, "Application of Adaptive grids to Fluid-Flow Problems with Asymptotic Solutions", *AIAA Journal*, Vol. 20, No. 4, pp. 496-502.

Ralph, M.E. and Pedley, T.J., 1988, "Flow in a Channel with Moving Indentation", *Journal of Fluid Mechanics*, Vol. 190, pp. 87-112.

Rogers, S.E. and Kwak, D., 1990, "Upwind Differencing Scheme for the Time-Accurate Incompressible Navier-Stokes Equations", *AIAA Journal*, Vol. 28, pp. 253-262.

Rosenfeld, M., Kwak, D. and Vinokur, M., 1991, "A Fractional Step Solution Method for the Unsteady Incompressible Navier-Stokes Equations in Generalized Coordinate Systems", *Journal of Computational Physics*, Vol. 94, pp. 102-137.

Saitoh, T., 1978, "Numerical Method for Multi-Dimensional Freezing Problems in Arbitrary Domains", *Journal of Heat Transfer*, Vol. 100, pp. 294-299.

Shames, I.H., 1982, *Mechanics of Fluids*, 2nd Edition, McGraw-Hill Book Company, New York.

Shyy, W., 1985, "A Numerical Study of Annular Dump Diffuser Flows" , *Computer Methods in Applied Mechanics and Engineering*, Vol. 53, pp. 47-65.

Shyy, W., 1988, "Computation of Complex Fluid Flows Using an Adaptive Grid Method", *International Journal for Numerical Methods in Fluids*, Vol. 8, 475-489.

Soh, W.Y., 1987, "Time-marching Solution of Incompressible Navier-Stokes Equations for Internal Flows", *Journal of Computational Physics*, Vol. 70, pp. 232-252.

Soh, W.Y. and Goodrich, J.W., 1988, "Unsteady Solution of Incompressible Navier-Stokes Equations", *Journal of Computational Physics*, Vol. 79, pp. 113-134.

Southworth, R.W. and Deleeuw, S.L., 1965, *Digital Computation and Numerical*

Methods, McGraw-Hill Book Company.

Spurr, A. and Hobson, D.E., 1984, "Forces on the Vibrating Centrebody of an Annular Diffuser", *ASME Symposium on Flow-Induced Vibration, Vol. 4: Vibration Induced by Axial and Annular Flows* (eds M. P. Païdoussis and M. K. Au-Yang), pp. 41-52.

Taylor, J.R., 1982, *An Introduction to Error Analysis*, University Science Books, Mill Valley, California.

Thames, F.C., Thompson, J.F., Wayne Mastin, C. and Walker, R.L., 1977, "Numerical Solutions for Viscous and Potential Flow about Arbitrary Two-Dimensional Bodies Using Body-Fitted Coordinate Systems", *Journal of Computational Physics*, Vol. 24, pp. 245-273.

Thomas, P.D. and Lombard, C.K., 1979, "Geometric Conservation Law and Its Application to Flow Computations on Moving Grids", *AIAA Journal*, Vol. 17, No. 10, pp. 1030-1037.

Thomson, W.T., 1981, *Theory of Vibration with Applications*, 2nd Edition, Prentice-Hall.

Thompson, J.F., Thames, F.C. and Wayne Mastin, C., 1974, "Automatic Numerical Generation of Body-Fitted Curvilinear Coordinate System for Field Containing Any Number of Arbitrary Two-Dimensional Bodies", *Journal of Computational Physics*, Vol. 15, 299-319.

Thompson, J.F., Thames, F.C. and Wayne Mastin, C., 1977, "TOMCAT-A Code for Numerical Generation of Boundary-Fitted Curvilinear Coordinate Systems of Fields Containig Any Number of Arbitrary Two-Dimensional Bodies", *Journal of Computational Physics*, Vol. 24, 274-302.

Thompson, J.F., Warsi, Z.U.A. and Wayne Mastin, C., 1982, "Boundary-Fitted Coordinate Systems for Numerical Solution of Partial Differential Equations — A Review", *Journal of Computational Physics*, Vol. 47, pp. 1-108.

Thompson. J.F., Warsi, Z.U.A. and Wayne Mastin, C., 1985, *Numerical Grid*

Generation: Foundations and Applications, Elsevier Science, New York.

Vinokur, M., 1983, "On One-Dimensional Stretching Functions for Finite-Difference Calculations", *Journal of Computational Physics*, Vol. 50, pp. 215-234.

Warsi, Z.U.A., 1981, "Conservation form of the Navier-Stokes Equations in General Nonsteady Coordinates", *AIAA Journal*, Vol. 19, No. 2, pp. 240-242.

Yeoh, G.H., Behnia, M., De Vahl Davis, G. and Leonardi, E., 1990, "A Numerical Study of Three-Dimensional Natural Convection During Freezing of Water", *International Journal for Numerical Methods in Engineering*, Vol. 30, pp. 899-914.

Appendix A

Discretization of the Navier-Stokes and Continuity Equations in 2-D and 3-D on a Staggered Mesh

With reference to Figures 4.8 and 4.9 and using equations (3.13) and (3.15), the discretized form of the N-S and continuity equations can be written on a staggered mesh. For 2-D problems, Figure 4.9 applies, whereas for 3-D problems both figures are used. Note that if the 2-D solutions in the r- and x-directions are required, then Figure 4.8 must be used instead of 4.9 for defining Δ and ∇. In this analysis, the 2-D equations are discretized in the r- and θ-directions.

By looking at Figure 4.9 (or Figure 3.2), the central Δ and backward ∇ difference operators are defined for the 2-D problem as

$$\begin{aligned} \Delta r_j^w &= r_j^v - r_{j-1}^v\,, & \Delta r_j^v &= r_{j+1}^w - r_j^w\,, \\ \nabla r_j^w &= r_j^w - r_{j-1}^v\,, & \nabla r_j^v &= r_j^v - r_j^w\,. \end{aligned} \tag{A.1}$$

The discretized forms of $(Q_v)_{j,k}$, $(Q_w)_{j,k}$ and $(\nabla\cdot\mathbf{V})_{j,k}$ using these operators are given by equations (3.21-3.23), where the linear interpolates of the velocity components on the staggered mesh are defined by

$$v_v^{ru} = \frac{\nabla r_{j+1}^v\; v_{j,k} + \nabla r_{j+1}^w\; v_{j+1,k}}{\Delta r_{j+1}^w} \quad , \quad v_v^{rd} = \frac{\nabla r_j^v\; v_{j-1,k} + \nabla r_j^w\; v_{j,k}}{\Delta r_j^w}\,, \tag{A.2}$$

$$v_v^{\theta f} = \frac{v_{j,k} + v_{j,k+1}}{2} \quad , \quad v_v^{\theta b} = \frac{v_{j,k} + v_{j,k-1}}{2} \, , \tag{A.3}$$

$$v_w^{ru} = \frac{v_{j,k} + v_{j,k+1}}{2} \quad , \quad v_w^{rd} = \frac{v_{j-1,k} + v_{j-1,k+1}}{2} \, , \tag{A.4}$$

$$v_w^{\theta f} = \frac{\nabla r_j^v \, v_{j-1,k+1} + \nabla r_j^w \, v_{j,k+1}}{\Delta r_j^w} \quad , \quad v_w^{\theta b} = \frac{\nabla r_j^v \, v_{j-1,k} + \nabla r_j^w \, v_{j,k}}{\Delta r_j^w} \, , \tag{A.5}$$

$$w_v^{\theta f} = \frac{\nabla r_{j+1}^w \, w_{j,k} + \nabla r_j^v \, w_{j+1,k}}{\Delta r_j^v} \quad , \quad w_v^{\theta b} = \frac{\nabla r_{j+1}^w \, w_{j,k-1} + \nabla r_j^v \, w_{j+1,k-1}}{\Delta r_j^v} \, , \tag{A.6}$$

$$w_w^{ru} = \frac{\nabla r_{j+1}^w \, w_{j,k} + \nabla r_j^v \, w_{j+1,k}}{\Delta r_j^v} \quad , \quad w_w^{rd} = \frac{\nabla r_j^w \, w_{j-1,k} + \nabla r_{j-1}^v \, w_{j,k}}{\Delta r_{j-1}^v} \, , \tag{A.7}$$

$$w_w^{\theta f} = \frac{w_{j,k+1} + w_{j,k}}{2} \quad , \quad w_w^{\theta b} = \frac{w_{j,k} + w_{j,k-1}}{2} \, . \tag{A.8}$$

The terms v_w and w_v appearing in equations (3.22) and (3.23) are given by

$$\begin{aligned} v_w &= \frac{1}{2}\left[\frac{\nabla r_j^v}{\Delta r_j^w}\left(v_{j-1,k} + v_{j-1,k+1}\right) + \frac{\nabla r_j^w}{\Delta r_j^w}\left(v_{j,k} + v_{j,k+1}\right)\right] \, , \\ w_v &= \frac{1}{2}\left[\frac{\nabla r_j^v}{\Delta r_j^v}\left(w_{j+1,k} + w_{j+1,k-1}\right) + \frac{\nabla r_{j+1}^w}{\Delta r_j^v}\left(w_{j,k} + w_{j,k-1}\right)\right] \, . \end{aligned}$$

The symmetry boundary conditions applied at $\theta = 0$ and $\theta = \pi$ and mentioned in Chapter 4 for 2-D analysis can easily be seen in Figure A.1.

$$\begin{array}{cccccc} \Diamond v_{j,1} & & \Diamond v_{j,2} & & \Diamond v_{j,3} & \\ & & & & & \\ \bigcirc p_{j,1} & \square w_{j,1} & \bigcirc p_{j,2} & \square w_{j,2} & \bigcirc p_{j,3} & \square w_{j,3} \\ | & | & | & | & | & | \\ \theta_1^v & \theta_1^w & \theta_2^v & \theta_2^w = 0 & \theta_3^v & \theta_3^w \end{array}$$

Figure A.1: Diagram showing the symmetry boundary conditions applied at $\theta = 0$.

Having obtained all these tools, now the discretized forms of the momentum and continuity equations are written for different sweeps.

The r-, θ-momentum and continuity equations in the r-sweep:

The r-momentum equation (4.25) can be written in differenced form as

$$
\begin{aligned}
(1+\Delta\tau)\overline{\Delta v}_{j,k} \quad + \quad & \frac{\beta\Delta\tau}{r_j^v \Delta r_j^v}\left\{ r_{j+1}^w v_v^{ru}\overline{\Delta v}_v^{ru} - r_j^w v_v^{rd}\overline{\Delta v}_v^{rd} + r_j^v\left(\overline{\Delta p}_{j+1,k} - \overline{\Delta p}_{j,k}\right)\right. \\
& \left. - \frac{1}{\mathrm{Re}}\left[\frac{r_{j+1}^w(\overline{\Delta v}_{j+1,k} - \overline{\Delta v}_{j,k})}{\Delta r_{j+1}^w} - \frac{r_j^w(\overline{\Delta v}_{j,k} - \overline{\Delta v}_{j-1,k})}{\Delta r_j^w}\right] - \frac{\overline{\Delta v}_{i,j,k}}{r_j^{v2}}\right\} \\
= \quad & \Delta\tau(E_v^n - \hat{v}^\mu - \beta\hat{Q}_v^\mu)_{j,k}\,, \qquad \text{(A.9)}
\end{aligned}
$$

with the following expressions for $\overline{\Delta v}$'s and $\overline{\Delta p}$'s

$$
\overline{\Delta v}_v^{ru} = \frac{\nabla r_{j+1}^v \overline{\Delta v}_{j,k} + \nabla r_{j+1}^w \overline{\Delta v}_{j+1,k}}{\Delta r_{j+1}^w}\,, \qquad \text{(A.10)}
$$

$$
\overline{\Delta v}_v^{rd} = \frac{\nabla r_j^v \overline{\Delta v}_{j-1,k} + \nabla r_j^w \overline{\Delta v}_{j,k}}{\Delta r_j^w}\,, \qquad \text{(A.11)}
$$

$$
\overline{\Delta p}_{j,k} = -\frac{\Delta\tau}{\delta}\nabla\cdot\mathbf{V}_{j,k} - \frac{\Delta\tau}{\delta r_j^w \Delta r_j^w}\left(r_j^v\overline{\Delta v}_{j,k} - r_{j-1}^v\overline{\Delta v}_{j-1,k}\right)\,, \qquad \text{(A.12)}
$$

$$
\overline{\Delta p}_{j+1,k} = -\frac{\Delta\tau}{\delta}\nabla\cdot\mathbf{V}_{j+1,k} - \frac{\Delta\tau}{\delta r_{j+1}^w \Delta r_{j+1}^w}\left(r_{j+1}^v\overline{\Delta v}_{j+1,k} - r_j^v\overline{\Delta v}_{j,k}\right)\,.
$$

The equation obtained from equation (A.9) using equations (A.2), (A.10) and (A.11) is equation (4.31). Proceeding as with the r-momentum equation in the r-sweep we can write the θ-momentum equation (4.26) in differenced form as

$$
\begin{aligned}
\overline{\Delta w}_{j,k} \quad + \quad & \frac{\beta\Delta\tau}{r_j^w \Delta r_j^w}\left\{ r_j^v v_w^{ru}\overline{\Delta w}_w^{ru} - r_{j-1}^v v_w^{rd}\overline{\Delta w}_w^{rd} + v_w\Delta r_j^w\overline{\Delta w}_{j,k}\right. \\
& \left. - \frac{1}{\mathrm{Re}}\left[\frac{r_j^v\left(\overline{\Delta w}_{j+1,k} - \overline{\Delta w}_{j,k}\right)}{\Delta r_j^v} - \frac{r_{j-1}^v\left(\overline{\Delta w}_{j,k} - \overline{\Delta w}_{j-1,k}\right)}{\Delta r_{j-1}^v}\right] - \frac{\beta\Delta\tau\overline{\Delta w}_{j,k}}{\mathrm{Re} r_j^{w2}}\right\} \\
= \quad & \Delta\tau\left(E_w^n - \hat{w}^\mu - \beta\hat{Q}_w^\mu\right)_{j,k}\,, \qquad \text{(A.13)}
\end{aligned}
$$

with the following expressions for the $\overline{\Delta w}$'s:

$$
\overline{\Delta w}_w^{ru} = \frac{\nabla r_{j+1}^w \overline{\Delta w}_{j,k} + \nabla r_j^v \overline{\Delta w}_{j+1,k}}{\Delta r_j^v}\,, \qquad \text{(A.14)}
$$

$$
\overline{\Delta w}_w^{rd} = \frac{\nabla r_j^w \overline{\Delta w}_{j-1,k} + \nabla r_{j-1}^v \overline{\Delta w}_{j,k}}{\Delta r_{j-1}^v}\,; \qquad \text{(A.15)}
$$

with the help of (A.4), after rearranging the terms one obtains equation (4.32).

The r-, θ-Momentum and continuity equations in the θ-sweep:

The solution in the θ-sweep will be done in similar manner as in the r-sweep. The r-momentum equation (4.28) in the θ-sweep can be written in differenced form as

$$\Delta v_{j,k} + \frac{\beta\Delta\tau}{r_j^v\Delta\theta}\left[w_v^{\theta f}\Delta v_v^{\theta f} - w_v^{\theta b}\Delta v_v^{\theta b}\right.$$

$$\left. - \frac{1}{\mathrm{Re}}\left(\frac{\Delta v_{j,k+1} + \Delta v_{j,k-1} - 2\Delta v_{j,k}}{r_j^v\Delta\theta} + \frac{2r_j^v}{\mathrm{Re}}\frac{\partial(\Delta w_{j,k+1} - w_{j,k})}{r_j^{v2}}\right)\right] = \overline{\Delta v}_{j,k}, \quad \text{(A.16)}$$

with the following expressions for the Δv's:

$$\Delta v_v^{\theta f} = \frac{\Delta v_{j,k} + \Delta v_{j,k+1}}{2}, \qquad \Delta v_v^{\theta b} = \frac{\Delta v_{j,k} + \Delta v_{j,k-1}}{2};$$

rearranging the terms to obtain the corresponding coefficients for Δv's in the tridiagonal matrix solver, one obtains equation (4.33). Progressing as with the θ-momentum equation in the r-sweep explained in the previous section, the θ-momentum and continuity equations (4.29-4.30) are written in differenced form as

$$(1+\Delta\tau)\,\Delta w_{j,k} + \frac{\beta\Delta\tau}{r_j^w\Delta\theta}\left[w_w^{\theta f}\Delta w_w^{\theta f} - w_w^{\theta b}\Delta w_w^{\theta b} + \left(\Delta p_{j,k+1} - \Delta p_{j,k}\right)\right.$$

$$\left. - \frac{\Delta w_{j,k+1} + \Delta w_{j,k-1} - 2\Delta w_{j,k}}{\mathrm{Re}r_j^w\Delta\theta} - \frac{2r_j^w}{\mathrm{Re}}\frac{\partial(\Delta v_{j,k+1} - v_{j,k})}{r_j^{v2}}\right] = \overline{\Delta w}_{j,k}, \qquad \text{(A.17)}$$

with the following equations for the Δw's and Δp's:

$$\Delta w_w^{\theta f} = \frac{\Delta w_{j,k+1} + \Delta w_{j,k}}{2}, \qquad \text{(A.18)}$$

$$\Delta w_w^{\theta b} = \frac{\Delta w_{j,k} + \Delta w_{j,k-1}}{2}, \qquad \text{(A.19)}$$

$$\Delta p_{j,k} = \overline{\Delta p}_{j,k} - \frac{\Delta\tau}{\delta}\frac{\Delta w_{j,k} - \Delta w_{j,k-1}}{r_j^w\Delta\theta}, \qquad \text{(A.20)}$$

$$\Delta p_{j,k+1} = \overline{\Delta p}_{j,k+1} - \frac{\Delta\tau}{\delta}\frac{\Delta w_{j,k+1} - \Delta w_{j,k}}{r_j^w\Delta\theta}.$$

Rearranging the terms in equation (A.17) will provide equation (4.34). All these equations are obtained with the help of equations (A.2-A.8).

For 3-D solution of the problems, the central Δ and backward ∇ difference operators, using Figures 4.8 and 4.9, are defined as

$$\Delta x_i^u = x_{i+1}^v - x_i^v \,, \qquad \Delta x_i^v = x_i^u - x_{i-1}^u \,, \tag{A.21}$$

$$\Delta r_j^u = r_j^v - r_{j-1}^v \,, \qquad \Delta r_j^v = r_{j+1}^u - r_j^u \,, \tag{A.22}$$

$$\nabla x_i^u = x_i^u - x_i^v \,, \qquad \nabla x_i^v = x_i^v - x_{i-1}^u \,, \tag{A.23}$$

$$\nabla r_j^u = r_j^u - r_{j-1}^v \,, \qquad \nabla r_j^v = r_j^v - r_j^u \,. \tag{A.24}$$

Equations (4.42-4.45) are thus discretized as follows where we have, first for $Q_u(u, v, w, p)$

$$\begin{aligned}
(Q_u)_{i,j,k} \;=\; & \frac{1}{\Delta x_i^u}\Bigg[u_u^{xf}\, u_u^{xf} - u_u^{xb}\, u_u^{xb} \\
&+ p_{i+1,j,k} - p_{i,j,k} - \frac{1}{\mathrm{Re}}\left\{ \frac{u_{i+1,j,k} - u_{i,j,k}}{\Delta x_{i+1}^v} - \frac{u_{i,j,k} - u_{i-1,j,k}}{\Delta x_i^v} \right\}\Bigg] \\
&+ \frac{1}{r_j^u\, \Delta r_j^u}\Bigg[r_j^v v_u^{ru}\, u_u^{ru} - r_{j-1}^v v_u^{rd} u_u^{rd} \\
&- \frac{1}{\mathrm{Re}}\left\{ \frac{r_j^v}{\Delta r_j^v}\left(u_{i,j+1,k} - u_{i,j,k}\right) - \frac{r_{j-1}^v}{\Delta r_{j-1}^v}\left(u_{i,j,k} - u_{i,j-1,k}\right) \right\}\Bigg] \\
&+ \frac{w_u^{\theta f}\, u_u^{\theta f} - w_u^{\theta b}\, u_u^{\theta b}}{r_j^u \Delta\theta} - \frac{u_{i,j,k+1} + u_{i,j,k-1} - 2\, u_{i,j,k}}{\mathrm{Re}\,(r_j^u)^2 (\Delta\theta)^2} \,,
\end{aligned} \tag{A.25}$$

with the interpolates defined by

$$u_u^{xf} = \frac{\nabla x_{i+1}^u\; u_{i,j,k} + \nabla x_{i+1}^v\; u_{i+1,j,k}}{\Delta x_{i+1}^v} \;,\; u_u^{xb} = \frac{\nabla x_i^u\; u_{i-1,j,k} + \nabla x_i^v\; u_{i,j,k}}{\Delta x_i^v} \,, \tag{A.26}$$

$$u_u^{ru} = \frac{\nabla r_{j+1}^u\; u_{i,j,k} + \nabla r_j^v\; u_{i,j+1,k}}{\Delta r_j^v} \;,\; u_u^{rd} = \frac{\nabla r_j^u\; u_{i,j-1,k} + \nabla r_{j-1}^v\; u_{i,j,k}}{\Delta r_{j-1}^v} \,, \tag{A.27}$$

$$u_u^{\theta f} = \frac{1}{2}\left(u_{i,j,k+1} + u_{i,j,k}\right) \;,\; u_u^{\theta b} = \frac{1}{2}\left(u_{i,j,k} + u_{i,j,k-1}\right) \,, \tag{A.28}$$

$$v_u^{ru} = \frac{\nabla x_{i+1}^v\; v_{i,j,k} + \nabla x_i^u\; v_{i+1,j,k}}{\Delta x_i^u} \;,\; v_u^{rd} = \frac{\nabla x_{i+1}^v\; v_{i,j-1,k} + \nabla x_i^u\; v_{i+1,j-1,k}}{\Delta x_i^u} \,, \tag{A.29}$$

$$w_u^{\theta f} = \frac{\nabla x_i^u\; w_{i+1,j,k} + \nabla x_{i+1}^v\; w_{i,j,k}}{\Delta x_i^u} \;,\; w_u^{\theta b} = \frac{\nabla x_i^u\; w_{i+1,j,k-1} + \nabla x_{i+1}^v\; w_{i,j,k-1}}{\Delta x_i^u} \,. \tag{A.30}$$

The term $Q_v(u, v, w, p)$ is given by

$$
\begin{aligned}
(Q_v)_{i,j,k} &= \frac{1}{\Delta x_i^v} \left[u_v^{xf}\, v_v^{xf} - u_v^{xb}\, v_v^{xb} \right. \\
&- \left. \frac{1}{\mathrm{Re}} \left\{ \frac{v_{i+1,j,k} - v_{i,j,k}}{\Delta x_i^u} - \frac{v_{i,j,k} - v_{i-1,j,k}}{\Delta x_{i-1}^u} \right\} \right] \\
&+ \frac{1}{r_j^v\, \Delta r_j^v} \left[r_{j+1}^u\, (v_v^{ru})^2 - r_j^u\, (v_v^{rd})^2 \right. \\
&- \left. \frac{1}{\mathrm{Re}} \left\{ \frac{r_{j+1}^u}{\Delta r_{j+1}^u} (v_{i,j+1,k} - v_{i,j,k}) - \frac{r_j^u}{\Delta r_j^u} (v_{i,j,k} - v_{i,j-1,k}) \right\} \right] \\
&+ \frac{p_{i,j+1,k} - p_{i,j,k}}{\Delta r_j^v} + \frac{1}{r_j^v} \left[\frac{w_v^{\theta f}\, v_v^{\theta f} - w_v^{\theta b}\, v_v^{\theta b}}{\Delta\theta} - (w_v)^2 \right] \qquad \text{(A.31)} \\
&- \frac{1}{\mathrm{Re}\, (r_j^v)^2} \left[\frac{v_{i,j,k+1} + v_{i,j,k-1} - 2\, v_{i,j,k}}{(\Delta\theta)^2} - 2\, \frac{w_v^{\theta f} - w_v^{\theta b}}{\Delta\theta} - v_{i,j,k} \right],
\end{aligned}
$$

where the following interpolates were used

$$
v_v^{xf} = \frac{\nabla x_{i+1}^v\; v_{i,j,k} + \nabla x_i^v\; v_{i+1,j,k}}{\Delta x_i^u}\,,\; v_v^{xb} = \frac{\nabla x_i^v\; v_{i-1,j,k} + \nabla x_{i-1}^u\; v_{i,j,k}}{\Delta x_{i-1}^u}, \qquad \text{(A.32)}
$$

$$
v_v^{ru} = \frac{\nabla r_{j+1}^v\; v_{i,j,k} + \nabla r_{j+1}^u\; v_{i,j+1,k}}{\Delta r_{j+1}^u}\,,\; v_v^{rd} = \frac{\nabla r_j^v\; v_{i,j-1,k} + \nabla r_j^u\; v_{i,j,k}}{\Delta r_j^u}, \qquad \text{(A.33)}
$$

$$
v_v^{\theta f} = \frac{v_{i,j,k} + v_{i,j,k+1}}{2}\,,\; v_v^{\theta b} = \frac{v_{i,j,k} + v_{i,j,k-1}}{2}, \qquad \text{(A.34)}
$$

$$
u_v^{xf} = \frac{\nabla r_{j+1}^u\; u_{i,j,k} + \nabla r_j^v\; u_{i,j+1,k}}{\Delta r_j^v}\,,\; u_v^{xb} = \frac{\nabla r_{j+1}^u\; u_{i-1,j,k} + \nabla r_j^v\; u_{i-1,j+1,k}}{\Delta r_j^v}, \qquad \text{(A.35)}
$$

$$
w_v^{\theta f} = \frac{\nabla r_{j+1}^u\; w_{i,j,k} + \nabla r_j^v\; w_{i,j+1,k}}{\Delta r_j^v}\,,\; w_v^{\theta b} = \frac{\nabla r_{j+1}^u\; w_{i,j,k-1} + \nabla r_j^v\; w_{i,j+1,k-1}}{\Delta r_j^v}; \qquad \text{(A.36)}
$$

and $Q_w(u,v,w,p)$ is computed as

$$
\begin{aligned}
(Q_w)_{i,j,k} &= \frac{1}{\Delta x_i^v}\left[u_w^{xf}\,w_w^{xf} - u_w^{xb}\,w_w^{xb}\right.\\
&- \left.\frac{1}{\mathrm{Re}}\left(\frac{w_{i+1,j,k}-w_{i,j,k}}{\Delta x_i^u} - \frac{w_{i,j,k}-w_{i-1,j,k}}{\Delta x_{i-1}^u}\right)\right]\\
&+ \frac{1}{r_j^u\,\Delta r_j^u}\left[r_j^v\,v_w^{ru}w_w^{ru} - r_{j-1}^v\,v_w^{rd}w_w^{rd}\right.\\
&- \left.\frac{1}{\mathrm{Re}}\left\{\frac{r_j^v}{\Delta r_j^v}\left(w_{i,j+1,k}-w_{i,j,k}\right) - \frac{r_{j-1}^v}{\Delta r_{j-1}^v}\left(w_{i,j,k}-w_{i,j-1,k}\right)\right\}\right]\\
&+ \frac{1}{r_j^u}\left[\frac{(w_w^{\theta f})^2 - (w_w^{\theta b})^2 + p_{i,j,k+1} - p_{i,j,k}}{\Delta\theta} + v_w\,w_{i,j,k}\right] \qquad \text{(A.37)}\\
&- \frac{1}{\mathrm{Re}\,(r_j^u)^2}\left[\frac{w_{i,j,k+1}+w_{i,j,k-1}-2\,w_{i,j,k}}{(\Delta\theta)^2} + 2\,\frac{v_w^{\theta f}-v_w^{\theta b}}{\Delta\theta} - w_{i,j,k}\right],
\end{aligned}
$$

with the help of the following interpolates

$$w_w^{xf} = \frac{\nabla x_{i+1}^v\ w_{i,j,k} + \nabla x_i^u\ w_{i+1,j,k}}{\Delta x_i^u} \quad , \quad w_w^{xb} = \frac{\nabla x_i^v\ w_{i-1,j,k} + \nabla x_{i-1}^u\ w_{i,j,k}}{\Delta x_{i-1}^u} \qquad \text{(A.38)}$$

$$w_w^{ru} = \frac{\nabla r_{j+1}^u\ w_{i,j,k} + \nabla r_j^v\ w_{i,j+1,k}}{\Delta r_j^v} \quad , \quad w_w^{rd} = \frac{\nabla r_j^u\ w_{i,j-1,k} + \nabla r_{j-1}^v\ w_{i,j,k}}{\Delta r_{j-1}^v} \qquad \text{(A.39)}$$

$$w_w^{\theta f} = \frac{w_{i,j,k+1} + w_{i,j,k}}{2} \quad , \quad w_w^{\theta b} = \frac{w_{i,j,k} + w_{i,j,k-1}}{2}, \qquad \text{(A.40)}$$

$$v_w^{ru} = \frac{v_{i,j,k} + v_{i,j,k+1}}{2} \quad , \quad v_w^{rd} = \frac{v_{i,j-1,k} + v_{i,j-1,k+1}}{2}, \qquad \text{(A.41)}$$

$$v_w^{\theta f} = \frac{\nabla r_j^u\ v_{i,j,k+1} + \nabla r_j^v\ v_{i,j-1,k+1}}{\Delta r_j^u} \quad , \quad v_w^{\theta b} = \frac{\nabla r_j^u\ v_{i,j,k} + \nabla r_j^v\ v_{i,j-1,k}}{\Delta r_j^u}, \qquad \text{(A.42)}$$

$$u_w^{xf} = \frac{u_{i,j,k} + u_{i,j,k+1}}{2} \quad , \quad u_w^{xb} = \frac{u_{i-1,j,k} + u_{i-1,j,k+1}}{2}; \qquad \text{(A.43)}$$

finally, the continuity equation $\nabla\cdot\mathbf{V}$ in discretized form is obtained as

$$(\nabla\cdot\mathbf{V})_{i,j,k} = \frac{u_{i,j,k} - u_{i-1,j,k}}{\Delta x_i^v} + \frac{r_j^v\,v_{i,j,k} - r_{j-1}^v\,v_{i,j-1,k}}{r_j^u\,\Delta r_j^u} + \frac{w_{i,j,k} - w_{i,j,k-1}}{r_j^u\,\Delta\theta}. \qquad \text{(A.44)}$$

In equations (A.31) and (A.37) the terms v_w and w_v are given by

$$v_w = \frac{1}{2}\left[\frac{\nabla r_j^v}{\Delta r_j^u}\left(v_{i,j,k} + v_{i,j,k+1}\right) + \frac{\nabla r_j^u}{\Delta r_j^u}\left(v_{i,j-1,k} + v_{i,j-1,k+1}\right)\right],$$

$$w_v = \frac{1}{2}\left[\frac{\nabla r_j^v}{\Delta r_j^v}\left(w_{i,j+1,k} + w_{i,j+1,k-1}\right) + \frac{\nabla r_{j+1}^u}{\Delta r_j^v}\left(w_{i,j,k} + w_{i,j,k-1}\right)\right] .$$

The solution of Navier-Stokes equations can be obtained by introducing difference expressions like those of (A.25), (A.31) and (A.37) in the left-hand sides of equations (4.46-4.57) to obtain the discretized forms of r-,θ- and x-momentum and continuity equations in the r-, θ-, and x-sweeps. The discretized forms of the equations are similar to those obtained for 2-D discretization, except that now we have additional equations in the x-sweep which gives the final values for Δu. The method of solution using the discretized equations was described in Chapter 4 and the discretized equations in the form of tridiagonal matrices are given here as

The x-momentum equation in r-sweep:

$$\widetilde{\Delta u}_{i,j-1,k}\left\{\frac{\beta\Delta\tau}{r_j^u\Delta r_j^u}\left(-r_{j-1}^v v_u^{rb}\frac{\nabla r_j^u}{\Delta r_{j-1}^v} - \frac{r_{j-1}^v}{\mathrm{Re}\Delta r_{j-1}^v}\right)\right\}$$

$$+\widetilde{\Delta u}_{i,j,k}\left\{\frac{\beta\Delta\tau}{r_j^u\Delta r_j^u}\left[r_j^v v_u^{rf}\frac{\nabla r_{j+1}^u}{\Delta r_j^v} - r_{j-1}^v v_u^{rb}\frac{\nabla r_{j-1}^v}{\Delta r_{j-1}^v} + \frac{1}{\mathrm{Re}}\left(\frac{r_j^v}{\Delta r_j^v} + \frac{r_{j-1}^v}{\Delta r_{j-1}^v}\right)\right]\right\}$$

$$+\widetilde{\Delta u}_{i,j+1,k}\left\{\frac{\beta\Delta\tau}{r_j^u\Delta r_j^u}\left(r_j^v v_u^{rf}\frac{\nabla r_j^u}{\Delta r_j^v} - \frac{r_j^v}{\mathrm{Re}\Delta r_j^v}\right)\right\}$$

$$= \Delta\tau\left(E_u^n - \hat{u}^\mu + \beta\hat{Q}_u^\mu\right)_{i,j,k} ; \qquad \text{(A.45)}$$

the r-momentum equation in r-sweep:

$$\widetilde{\Delta v}_{i,j-1,k}\left[\frac{\beta\Delta\tau}{r_j^v\Delta r_j^v}\left\{-r_j^u v_v^{rd}\frac{\nabla r_j^v}{\Delta r_j^u} - \frac{r_j^u}{\mathrm{Re}\Delta r_j^u}\right\} - \frac{\beta\Delta\tau^2 r_{j-1}^v}{\delta r_j^u\Delta r_j^u\Delta r_j^v}\right]$$

$$+\widetilde{\Delta v}_{i,j,k}\left[1.0 + \Delta\tau + \frac{\beta\Delta\tau}{r_j^v\Delta r_j^v}\left\{r_{j+1}^u v_v^{ru}\frac{\nabla r_{j+1}^v}{\Delta r_{j+1}^u} - r_j^u v_v^{rd}\frac{\nabla r_j^u}{\Delta r_j^u}\right.\right.$$

$$\left.\left.+\frac{1}{\mathrm{Re}}\left(\frac{r_{j+1}^u}{\Delta r_{j+1}^u} + \frac{r_j^u}{\Delta r_j^u} + \frac{\Delta r_j^v}{r_j^v}\right) + \frac{\Delta\tau r_j^{v2}}{\delta r_j^u\Delta r_j^u} + \frac{\Delta\tau r_j^{v2}}{\delta r_{j+1}^u\Delta r_{j+1}^u}\right\}\right]$$

$$+\widetilde{\Delta v}_{i,j+1,k}\left[\frac{\beta\Delta\tau}{r_j^v\Delta r_j^v}\left(r_{j+1}^u v_v^{ru}\frac{\nabla r_{j+1}^u}{\Delta r_{j+1}^u} - \frac{r_{j+1}^u}{\mathrm{Re}\Delta r_{j+1}^u}\right) - \frac{\beta\Delta\tau^2 r_{j+1}^v}{\delta r_{j+1}^u\Delta r_{j+1}^u\Delta r_j^v}\right]$$

$$= \Delta\tau\left(E_v^n - \hat{v}^\mu - \beta\hat{Q}_v^\mu\right)_{i,j,k} + \frac{\beta\Delta\tau^2}{\delta\Delta r_j^v}\left(\nabla\cdot\mathbf{V}_{i,j+1,k} - \nabla\cdot\mathbf{V}_{i,j,k}\right) ; \qquad \text{(A.46)}$$

the θ-momentum equation in r-sweep:

$$
\begin{aligned}
&\widetilde{\Delta w}_{i,j-1,k}\left\{\frac{\beta\Delta\tau}{r_j^u\Delta r_j^u}\left[-r_{j-1}^v v_w^{rd}\frac{\nabla r_j^u}{\Delta r_{j-1}^v}-\frac{r_{j-1}^v}{\mathrm{Re}\Delta r_{j-1}^v}\right]\right\} \\
&+\widetilde{\Delta w}_{i,j,k}\left\{1.0+\frac{\beta\Delta\tau v_w}{r_j^u}+\frac{\beta\Delta\tau}{r_j^u\Delta r_j^u}\left[r_j^v v_w^{ru}\frac{\nabla r_{j+1}^u}{\Delta r_j^v}-r_{j-1}^v v_w^{rd}\frac{\nabla r_{j-1}^v}{\Delta r_{j-1}^v}\right.\right. \\
&\qquad\left.\left.+\frac{1}{\mathrm{Re}}\left(\frac{r_j^v}{\Delta r_j^v}+\frac{r_{j-1}^v}{\Delta r_{j-1}^v}\right)\right]+\frac{\beta\Delta\tau}{\mathrm{Re}r_j^{u2}}\right\} \\
&+\widetilde{\Delta w}_{i,j+1,k}\left\{\frac{\beta\Delta\tau}{r_j^u\Delta r_j^u}\left[r_j^v v_w^{ru}\frac{\nabla r_j^v}{\Delta r_j^v}-\frac{r_j^v}{\mathrm{Re}\Delta r_j^v}\right]\right\} \\
&=\Delta\tau\left(E_w^n-\hat{w}^\mu-\beta\hat{Q}_w^\mu\right)_{i,j,k}\,;
\end{aligned}
\tag{A.47}
$$

the continuity equation in r-sweep:

$$
\widetilde{\Delta p}_{i,j,k}=-\frac{\Delta\tau}{\delta}\nabla\cdot\mathbf{V}_{i,j,k}-\frac{\Delta\tau}{\delta r_j^u\Delta r_j^u}\left(r_j^v\widetilde{\Delta v}_{i,j,k}-r_{j-1}^v\widetilde{\Delta v}_{i,j-1,k}\right).
\tag{A.48}
$$

The x-momentum equation in θ-sweep:

$$
\begin{aligned}
&\overline{\Delta u}_{i,j,k-1}\left\{\frac{\beta\Delta\tau}{r_j^u\Delta\theta}\left[-w_u^{\theta-}\left(\frac{1}{2}\right)-\frac{1}{\mathrm{Re}r_j^u\Delta\theta}\right]\right\} \\
&+\overline{\Delta u}_{i,j,k}\left\{1+\frac{\beta\Delta\tau}{r_j^u\Delta\theta}\left[w_u^{\theta+}\left(\frac{1}{2}\right)-w_u^{\theta-}\left(\frac{1}{2}\right)+\frac{2}{\mathrm{Re}r_j^u\Delta\theta}\right]\right\} \\
&+\overline{\Delta u}_{i,j,k+1}\left\{\frac{\beta\Delta\tau}{r_j^u\Delta\theta}\left[w_u^{\theta+}\left(\frac{1}{2}\right)-\frac{1}{\mathrm{Re}r_j^u\Delta\theta}\right]\right\}=\widetilde{\Delta u}_{i,j,k}\,;
\end{aligned}
\tag{A.49}
$$

the r-momentum equation in θ-sweep:

$$
\begin{aligned}
&\overline{\Delta v}_{i,j,k-1}\left\{\frac{\beta\Delta\tau}{r_j^v\Delta\theta}\left[-w_v^{\theta-}\left(\frac{1}{2}\right)-\frac{1}{\mathrm{Re}r_j^v\Delta\theta}\right]\right\} \\
&+\overline{\Delta v}_{i,j,k}\left\{1+\frac{\beta\Delta\tau}{r_j^v\Delta\theta}\left[w_v^{\theta+}\left(\frac{1}{2}\right)-w_v^{\theta-}\left(\frac{1}{2}\right)+\frac{2}{\mathrm{Re}r_j^v\Delta\theta}\right]\right\} \\
&+\overline{\Delta v}_{i,j,k+1}\left\{\frac{\beta\Delta\tau}{r_j^v\Delta\theta}\left[w_v^{\theta+}\left(\frac{1}{2}\right)-\frac{1}{\mathrm{Re}r_j^v\Delta\theta}\right]\right\}=\widetilde{\Delta v}_{i,j,k}-\frac{2}{\mathrm{Re}}\frac{\left(\Delta w_{i,j,k+1}-\Delta w_{i,j,k}\right)}{r_j^u\Delta\theta}\,;
\end{aligned}
\tag{A.50}
$$

the θ-momentum equation in θ-sweep:

$$
\overline{\Delta w}_{i,j,k-1}\left\{\frac{\beta\Delta\tau}{r_j^u\Delta\theta}\left[-w_w^{\theta-}\left(\frac{1}{2}\right)-\frac{\Delta\tau}{\delta}\frac{1}{r_j^u\Delta\theta}-\frac{1}{\mathrm{Re}r_j^u\Delta\theta}\right]\right\}
$$

$$+\overline{\Delta w}_{i,j,k}\left\{1+\Delta\tau+\frac{\beta\Delta\tau}{r_j^u\Delta\theta}\left[w_w^{\theta+}\left(\frac{1}{2}\right)-w_w^{\theta-}\left(\frac{1}{2}\right)+\frac{2}{\mathrm{Re}r_j^u\Delta\theta}+\frac{\Delta\tau}{\delta}\frac{2}{r_j^u\Delta\theta}\right]\right.$$

$$\left.+\frac{\beta\Delta\tau}{\mathrm{Re}r^{u2}_j}+\frac{\beta\Delta\tau}{r_j^u}v_w\right\}$$

$$+\overline{\Delta w}_{i,j,k+1}\left\{\frac{\beta\Delta\tau}{r_j^u\Delta\theta}\left[w_w^{\theta+}\left(\frac{1}{2}\right)-\frac{\Delta\tau}{\delta}\frac{1}{r_j^u\Delta\theta}-\frac{1}{\mathrm{Re}r_j^u\Delta\theta}\right]\right\}$$

$$=\widetilde{\Delta w}_{i,j,k}-\frac{\beta\Delta\tau}{r_j^u\Delta\theta}\left(\widetilde{\Delta p}_{i,j,k+1}-\widetilde{\Delta p}_{i,j,k}\right)+\frac{2}{\mathrm{Re}}\frac{\left(\Delta v_{i,j,k+1}-\Delta v_{i,j,k}\right)}{r_j^v\Delta\theta}\,; \tag{A.51}$$

the continuity equation in θ-sweep:

$$\overline{\Delta p}_{i,j,k}=\widetilde{\Delta p}_{i,j,k}-\frac{\Delta\tau}{\delta}\frac{\overline{\Delta w}_{i,j,k}-\overline{\Delta w}_{i,j,k-1}}{r_j^v\Delta\theta}\,. \tag{A.52}$$

The x-momentum equation in x-sweep:

$$\Delta u_{i-1,j,k}\left\{\frac{\beta\Delta\tau}{\Delta x_i^u}\left[-u_u^{xb}\frac{\nabla x_i^u}{\Delta x_i^v}-\frac{1}{\mathrm{Re}\Delta x_i^v}-\frac{\Delta\tau}{\delta\Delta x_i^v}\right]\right\}$$

$$+\Delta u_{i,j,k}\left\{1+\Delta\tau+\frac{\beta\Delta\tau}{\Delta x_i^u}\left[u_u^{xf}\frac{\nabla x_{i+1}^u}{\Delta x_{i+1}^v}-u_u^{xb}\frac{\nabla x_i^v}{\Delta x_i^v}+\frac{1}{\mathrm{Re}}\left(\frac{1}{\Delta x_i^v}+\frac{1}{\Delta x_{i+1}^v}\right)\right.\right.$$

$$\left.\left.+\frac{\Delta\tau}{\delta}\left(\frac{1}{\Delta x_i^v}+\frac{1}{\Delta x_{i+1}^v}\right)\right]\right\}$$

$$+\Delta u_{i+1,j,k}\left\{\frac{\beta\Delta\tau}{\Delta x_i^u}\left[u_u^{xf}\frac{\nabla x_{i+1}^u}{\Delta x_{i+1}^v}-\frac{1}{\mathrm{Re}\Delta x_{i+1}^v}-\frac{\Delta\tau}{\delta\Delta x_{i+1}^v}\right]\right\}$$

$$=\overline{\Delta u}_{i,j,k}-\frac{\beta\Delta\tau}{\Delta x_i^u}\left(\overline{\Delta p}_{i+1,j,k}-\overline{\Delta p}_{i,j,k}\right)\,; \tag{A.53}$$

the r-momentum equation in x-sweep:

$$\Delta v_{i-1,j,k}\left\{\frac{\beta\Delta\tau}{\Delta x_i^v}\left[-u_v^{xb}\frac{\nabla x_i^v}{\Delta x_{i-1}^u}-\frac{1}{\mathrm{Re}\Delta x_{i-1}^u}\right]\right\}$$

$$+\Delta v_{i,j,k}\left\{1+\frac{\beta\Delta\tau}{\Delta x_i^v}\left[u_v^{xf}\frac{\nabla x_{i+1}^v}{\Delta x_i^u}-u_v^{xb}\frac{\nabla x_{i-1}^u}{\Delta x_{i-1}^u}+\frac{1}{\mathrm{Re}\Delta x_i^u}+\frac{1}{\mathrm{Re}\Delta x_{i-1}^u}\right]\right\}$$

$$+\Delta v_{i+1,j,k}\left\{\frac{\beta\Delta\tau}{\Delta x_i^v}\left[u_v^{xf}\frac{\nabla x_i^u}{\Delta x_i^u}-\frac{1}{\mathrm{Re}\Delta x_i^u}\right]\right\}=\overline{\Delta v}_{i,j,k}\,; \tag{A.54}$$

the θ-momentum equation in x-sweep:

$$\Delta w_{i-1,j,k}\left\{\frac{\beta\Delta\tau}{\Delta x_i^v}\left[-u_w^{xb}\frac{\nabla x_i^v}{\Delta x_{i-1}^u}-\frac{1}{\mathrm{Re}\Delta x_{i-1}^u}\right]\right\}$$

$$+\Delta w_{i,j,k}\left\{1+\frac{\beta\Delta\tau}{\Delta x_i^v}\left[u_w^{xf}\frac{\nabla x_{i+1}^v}{\Delta x_i^u}-u_w^{xb}\frac{\nabla x_{i-1}^u}{\Delta x_{i-1}^u}+\frac{1}{\mathrm{Re}\Delta x_i^u}+\frac{1}{\mathrm{Re}\Delta x_{i-1}^u}\right]\right\}$$

$$+\Delta w_{i+1,j,k}\left\{\frac{\beta\Delta\tau}{\Delta x_i^v}\left[u_w^{xf}\frac{\nabla x_i^u}{\Delta x_i^u}-\frac{1}{\mathrm{Re}\Delta x_i^u}\right]\right\}=\overline{\Delta w}_{i,j,k}\,; \qquad \text{(A.55)}$$

the continuity equation in x-sweep:

$$\Delta p_{i,j,k}=\overline{\Delta p}_{i,j,k}-\frac{\Delta\tau}{\delta}\frac{1}{\Delta x_i^v}\left(\Delta u_{i,j,k}-\Delta u_{i-1,j,k}\right)\,. \qquad \text{(A.56)}$$

Appendix B

Discretization of 3-D Equations in Time-dependent Coordinate Transformation Solution

In the following discretized equations the rearranged form of the transformation equation (6.1) to define r^* in the physical domain is

$$r^* = r\Phi(\theta, t) + R_i \, .$$

This equation is used to define the following equations at each computational point $r^u = r^w$ and r^v in the staggered mesh as

$$RU_j = r^u\Phi(\theta, t) + R_i \, , \qquad RV_j = r^v\Phi(\theta, t) + R_i \, , \tag{B.1,B.2}$$

where $\Phi(\theta, t)$ was defined in chapter 6. Note that in all the following derivations of equations the superscript has been deleted from the terms for simplicity, and it should be borne in mind that the equations are written in pseudo-time.

Then, the continuity equation (6.11) is discretized as

$$-\frac{\Delta\tau}{\delta}(\nabla \cdot \mathbf{V})_{i,j,k} = -\frac{\Delta\tau}{\delta}\left[\frac{(u_{i,j,k} - u_{i-1,j,k})}{\Delta x_i^u} + \frac{A\,(RV_j v_{i,j,k} - RV_{j-1} v_{i,j-1,k})}{RU_j \Delta r_j^u} + \frac{Br_{j-1}^v\,(w_{i,j,k} - w_{i,j-1,k})}{RV_{j-1}\Delta r_{j-1}^v} + \frac{(w_{i,j,k} - w_{i,j,k-1})}{RU_j \Delta\theta}\right], \tag{B.3}$$

and the r-momentum equation (6.17) is discretized to implement the radial sweep for

$v_{i,j,k}$ as

$$(1+\Delta\tau)\,\widetilde{\Delta v}_{i,j,k} + \frac{\beta\Delta\tau}{RV_j\Delta r_j^v}\left[A\left(RU_{j+1}v_v^{ru}\widetilde{\Delta v}_v^{ru} - RU_j v_v^{rd}\widetilde{\Delta v}_v^{rd}\right)\right.$$

$$\left.+r_j^v B\left(w_v^{ru}\widetilde{\Delta v}_v^{ru} - w_v^{rd}\widetilde{\Delta v}_v^{rd}\right)\right] + \frac{\beta\Delta\tau r_j^u C}{\Delta r_j^u}\left(\widetilde{\Delta v}_{i,j,k} - \widetilde{\Delta v}_{i,j-1,k}\right)$$

$$-\frac{A^2\beta\Delta\tau}{\mathrm{Re}RV_j\Delta r_j^v}\left[\frac{RU_{j+1}\left(\widetilde{\Delta v}_{i,j+1,k} - \widetilde{\Delta v}_{i,j,k}\right)}{\Delta r_{j+1}^u} - \frac{RU_j\left(\widetilde{\Delta v}_{i,j,k} - \widetilde{\Delta v}_{i,j-1,k}\right)}{\Delta r_j^u}\right]$$

$$-\frac{(B^2+D)\beta\Delta\tau r_j^u\left(\widetilde{\Delta v}_{i,j,k} - \widetilde{\Delta v}_{i,j-1,k}\right)}{\mathrm{Re}RU_j^2\Delta r_j^u}$$

$$-\frac{B^2\beta\Delta\tau r_j^{u2}}{\mathrm{Re}RV_j^2\Delta r_j^v}\left[\frac{\left(\widetilde{\Delta v}_{i,j+1,k} - \widetilde{\Delta v}_{i,j,k}\right)}{\Delta r_{j+1}^u} - \frac{\left(\widetilde{\Delta v}_{i,j,k} - \widetilde{\Delta v}_{i,j-1,k}\right)}{\Delta r_j^u}\right]$$

$$-\frac{B\beta\Delta\tau r_j^u}{\mathrm{Re}RV_j^2\Delta\theta}\left[\frac{\left(\widetilde{\Delta v}_{i,j,k} - \widetilde{\Delta v}_{i,j-1,k}\right)}{\Delta r_j^u} - \frac{\left(\widetilde{\Delta v}_{i,j,k-1} - \widetilde{\Delta v}_{i,j-1,k-1}\right)}{\Delta r_j^u}\right]$$

$$+\frac{2B\beta\Delta\tau r_{j-1}^v}{\mathrm{Re}RV_j^2\Delta r_{j-1}^v}\left(\widetilde{\Delta w}_{i,j,k} - \widetilde{\Delta w}_{i,j-1,k}\right) + \frac{\beta\Delta\tau\widetilde{\Delta v}_{i,j,k}}{\mathrm{Re}RV_j^2}$$

$$+\frac{A\beta\Delta\tau}{\Delta r_j^v}\left(\widetilde{\Delta p}_{i,j+1,k} - \widetilde{\Delta p}_{i,j,k}\right) = \Delta\tau\left(E_v{}^n - v - \beta Q_v\right)_{i,j,k}\,. \tag{B.4}$$

The terms $\widetilde{\Delta v}_v^{ru}$, and $\widetilde{\Delta v}_v^{rd}$ appearing in this equation are evaluated as

$$\widetilde{\Delta v}_v^{ru} = \frac{\nabla r_{j+1}^v\widetilde{\Delta v}_{i,j,k} + \nabla r_{j+1}^u\widetilde{\Delta v}_{i,j+1,k}}{\Delta r_{j+1}^u}\,, \quad \widetilde{\Delta v}_v^{rd} = \frac{\nabla r_j^v\widetilde{\Delta v}_{i,j-1,k} + \nabla r_j^u\widetilde{\Delta v}_{i,j,k}}{\Delta r_j^u}\,,$$

while the terms $\widetilde{\Delta p}_{i,j,k}$ and $\widetilde{\Delta p}_{i,j+1,k}$ are obtained from continuity equation (6.19) as

$$\widetilde{\Delta p}_{i,j,k} = -\frac{\Delta\tau}{\delta}\nabla\cdot\mathbf{V}_{i,j,k} - \frac{A\Delta\tau}{\delta RU_j\Delta r_j^u}\left(RV_j\widetilde{\Delta v}_{i,j,k} - RV_{j-1}\widetilde{\Delta v}_{i,j-1,k}\right)$$

$$-\frac{B\Delta\tau r_{j-1}^v}{\delta RV_{j-1}\Delta r_{j-1}^v}\left(\widetilde{\Delta w}_{i,j,k} - \widetilde{\Delta w}_{i,j-1,k}\right)\,, \tag{B.5}$$

$$\widetilde{\Delta p}_{i,j+1,k} = -\frac{\Delta\tau}{\delta}\nabla\cdot\mathbf{V}_{i,j+1,k} - \frac{A\Delta\tau}{\delta RU_{j+1}\Delta r_{j+1}^u}\left(RV_{j+1}\widetilde{\Delta v}_{i,j+1,k} - RV_j\widetilde{\Delta v}_{i,j,k}\right)$$

$$-\frac{B\Delta\tau r_j^v}{\delta RV_j\Delta r_j^v}\left(\widetilde{\Delta w}_{i,j,k} - \widetilde{\Delta w}_{i,j,k}\right)\,; \tag{B.6}$$

finally the component $-\beta\Delta\tau Q_v$ of the vector $\mathbf{Q}$ in equation (3.11), considering (3.12), is discretized as

$$
\begin{aligned}
(-\beta\Delta\tau Q_v)_{i,j,k} = & -\frac{\beta\Delta\tau}{\Delta x_i^v}\left[u_v^{xf}v_v^{xf} - u_v^{xb}v_v^{xb} - \frac{1}{\mathrm{Re}}\left\{\frac{v_{i+1,j,k}-v_{i,j,k}}{\Delta x_i^u} - \frac{v_{i,j,k}-v_{i-1,j,k}}{\Delta x_{i-1}^u}\right\}\right] \\
& -\frac{C\beta\Delta\tau r_j^u}{\Delta r_j^u}(v_{i,j,k}-v_{i,j-1,k}) - \frac{\beta\Delta\tau}{RV_j\Delta r_j^v}\Big[A\cdot RU_{j+1}v_v^{ru2} - A\cdot RU_j v_v^{rd2} \\
& -\frac{A^2}{\mathrm{Re}}\left\{\frac{RU_{j+1}}{\Delta r_{j+1}^u}(v_{i,j+1,k}-v_{i,j,k}) - \frac{RU_j}{\Delta r_j^u}(v_{i,j,k}-v_{i,j-1,k})\right\}\Big] - \frac{A\beta\Delta\tau}{\Delta r_j^v}(p_{i,j+1,k}-p_{i,j,k}) \\
& -\frac{B\beta\Delta\tau r_j^u}{RV_j\Delta r_j^v}\left(w_v^{ru}v_v^{ru} - w_v^{rd}v_v^{rd}\right) + \frac{\beta\Delta\tau}{\mathrm{Re}}\Bigg[\frac{(B^2+D)r_j^u(v_{i,j,k}-v_{i,j-1,k})}{RU_j^2\Delta r_j^u} \\
& +\frac{B^2 r_j^{v2}}{RV_j^2\Delta r_j^v}\left(\frac{v_{i,j+1,k}-v_{i,j,k}}{\Delta r_{j+1}^u} - \frac{v_{i,j,k}-v_{i,j-1,k}}{\Delta r_j^u}\right) \\
& +\frac{Br_j^u}{RV_j^2\Delta\theta}\left(\frac{v_{i,j,k}-v_{i,j-1,k}}{\Delta r_j^u} - \frac{v_{i,j,k-1}-v_{i,j-1,k-1}}{\Delta r_j^u}\right) \\
& +\frac{1}{RV_j^2}\Bigg(\frac{v_{i,j,k+1}+v_{i,j,k-1}-2v_{i,j,k}}{\Delta\theta^2} - 2\frac{w_v^{\theta f}-w_v^{\theta b}}{\Delta\theta} - v_{i,j,k} \\
& -2\frac{Br_{j-1}^v}{\Delta r_{j-1}^v}(w_{i,j,k}-w_{i,j-1,k})\Bigg)\Bigg] - \frac{\beta\Delta\tau}{RV_j}\left(\frac{w_v^{\theta f}v_v^{\theta f} - w_v^{\theta b}v_v^{\theta b}}{\Delta\theta} - {w_v}^2\right), \qquad \text{(B.7)}
\end{aligned}
$$

where

$$
w_v = \frac{1}{2}\left[\frac{\nabla r_j^v}{\Delta r_j^v}(w_{i,j+1,k}+w_{i,j+1,k-1}) + \frac{\nabla r_{j+1}^u}{\Delta r_j^v}(w_{i,j,k}+w_{i,j,k-1})\right].
$$

Now, using equation (B.5) and (B.6), equation (6.17) in discretized tridiagonal form can be written as

$$
\begin{aligned}
& \widetilde{\Delta v}_{i,j-1,k}\Bigg[-\frac{A^2\beta\Delta\tau RU_j}{\mathrm{Re}RV_j\Delta r_j^v\Delta r_j^u} + \frac{(B^2+D)\beta\Delta\tau r_j^u}{\mathrm{Re}RU_j^2\Delta r_j^u} - \frac{B^2\beta\Delta\tau r_j^{v2}}{\mathrm{Re}RV_j^2\Delta r_j^v\Delta r_j^u} - \frac{A^2\beta\Delta\tau^2 RV_{j-1}}{\delta RU_j\Delta r_j^u\Delta r_j^v} \\
& +\frac{\beta\Delta\tau}{RV_j\Delta r_j^v}\left(-A\cdot RU_j v_v^{rd}\frac{\nabla r_j^v}{\Delta r_j^u} - Br_j^v w_v^{rd}\frac{\nabla r_j^v}{\Delta r_j^u}\right) - \frac{\beta\Delta\tau r_j^u C}{\Delta r_j^u}\Bigg] \\
& +\widetilde{\Delta v}_{i,j,k}\Bigg[\frac{A^2\beta\Delta\tau RU_{j+1}}{\mathrm{Re}RV_j\Delta r_j^v\Delta r_{j+1}^u} + \frac{A^2\beta\Delta\tau RU_j}{\mathrm{Re}RV_j\Delta r_j^v\Delta r_j^u} - \frac{(B^2+D)\beta\Delta\tau r_j^u}{\mathrm{Re}RU_j^2\Delta r_j^u} + 1.0 + \Delta\tau \\
& +\frac{B^2\beta\Delta\tau r_j^{v2}}{\mathrm{Re}RV_j^2\Delta r_j^v\Delta r_{j+1}^u} + \frac{B^2\beta\Delta\tau r_j^{v2}}{\mathrm{Re}RV_j^2\Delta r_j^v\Delta r_j^u} + \frac{\beta\Delta\tau}{\mathrm{Re}RV_j^2} + \frac{A^2\beta\Delta\tau^2 RV_j}{\delta RU_j\Delta r_j^u\Delta r_j^v} + \frac{A^2\beta\Delta\tau^2 RV_j}{\delta RU_{j+1}\Delta r_{j+1}^u\Delta r_j^v}
\end{aligned}
$$

$$+\frac{\beta\Delta\tau}{RV_j\Delta r_j^v}\left(A\cdot RU_{j+1}v_v^{ru}\frac{\nabla r_{j+1}^v}{\Delta r_{j+1}^u}+Br_j^v w_v^{ru}\frac{\nabla r_{j+1}^v}{\Delta r_{j+1}^u}-A\cdot RU_j v_v^{rd}\frac{\nabla r_j^u}{\Delta r_j^u}-Br_j^v w_v^{rd}\frac{\nabla r_j^u}{\Delta r_j^u}\right)$$

$$+\left.\frac{C\beta\Delta\tau r_j^u}{\Delta r_j^u}\right]$$

$$+\widetilde{\Delta v}_{i,j+1,k}\left[-\frac{A^2\beta\Delta\tau RU_{j+1}}{\mathrm{Re}RV_j\Delta r_j^v\Delta r_{j+1}^u}-\frac{B^2\beta\Delta\tau r_j^{v2}}{\mathrm{Re}RV_j^2\Delta r_j^v\Delta r_{j+1}^u}-\frac{A^2\beta\Delta\tau^2 RV_{j+1}}{\delta RU_{j+1}\Delta r_{j+1}^u\Delta r_j^v}\right.$$

$$\left.+\frac{\beta\Delta\tau}{RV_j\Delta r_j^v}\left(A\cdot RU_{j+1}v_v^{ru}\frac{\nabla r_{j+1}^u}{\Delta r_{j+1}^u}+Br_j^v w_v^{ru}\frac{\nabla r_{j+1}^u}{\Delta r_{j+1}^u}\right)\right]$$

$$=\Delta\tau(E_v^n-v-\beta Q_v)_{i,j,k}+\frac{A\beta\Delta\tau^2}{\delta\Delta r_j^v}(\nabla\cdot\mathbf{V}_{i,j+1,k}-\nabla\cdot\mathbf{V}_{i,j,k})$$

$$+\frac{A\cdot B\beta\Delta\tau^2}{\delta\Delta r_j^v}\left[\frac{r_j^v}{RV_j\Delta r_j^v}\widetilde{\Delta w}_{i,j+1,k}+\frac{r_{j-1}^v}{RV_{j-1}\Delta r_{j-1}^v}\widetilde{\Delta w}_{i,j-1,k}\right.$$

$$\left.-\left(\frac{r_j^v}{RV_j\Delta r_j^v}+\frac{r_{j-1}^v}{RV_{j-1}\Delta r_{j-1}^v}\right)\widetilde{\Delta w}_{i,j,k}\right]-\frac{2B\beta\Delta\tau r_{j-1}^v}{\mathrm{Re}RV_j^2\Delta r_{j-1}^v}\left(\widetilde{\Delta w}_{i,j,k}-\widetilde{\Delta w}_{i,j-1,k}\right)$$

$$+\frac{B\beta\Delta\tau r_j^u}{\mathrm{Re}RV_j^2\Delta\theta\Delta r_j^u}(\widetilde{\Delta v}_{i,j,k}-\widetilde{\Delta v}_{i,j-1,k}-\widetilde{\Delta v}_{i,j,k-1}+\widetilde{\Delta v}_{i,j-1,k-1})\,. \tag{B.8}$$

The discretized r-momentum equation (6.21) in the θ-sweep, using the results of equation (B.8), provides

$$\overline{\Delta v}_{i,j,k}+\frac{\beta\Delta\tau}{RV_j\Delta\theta}\left[w_v^{\theta f}\overline{\Delta v}_v^{\theta f}-w_v^{\theta b}\overline{\Delta v}_v^{\theta b}\right.$$

$$\left.-\frac{1}{\mathrm{Re}}\left(\frac{\overline{\Delta v}_{i,j,k+1}+\overline{\Delta v}_{i,j,k-1}-2\overline{\Delta v}_{i,j,k}}{RV_j\Delta\theta}\right)\right]=\widetilde{\Delta v}_{i,j,k}\,, \tag{B.9}$$

where the terms $\overline{\Delta v}^{\theta f}$ and $\overline{\Delta v}^{\theta b}$ are obtained from

$$\overline{\Delta v}_v^{\theta f}=\frac{\overline{\Delta v}_{i,j,k}+\overline{\Delta v}_{i,j,k+1}}{2}\,,\quad \overline{\Delta v}_v^{\theta b}=\frac{\overline{\Delta v}_{i,j,k}+\overline{\Delta v}_{i,j,k-1}}{2}\,.$$

Therefore, equation (B.9) in tridiagonal form is written as

$$\overline{\Delta v}_{i,j,k-1}\left\{\frac{\beta\Delta\tau}{RV_j\Delta\theta}\left[-w_v^{\theta b}\left(\frac{1}{2}\right)-\frac{1}{\mathrm{Re}RV_j\Delta\theta}\right]\right\}$$

$$+\overline{\Delta v}_{i,j,k}\left\{1+\frac{\beta\Delta\tau}{RV_j\Delta\theta}\left[w_v^{\theta f}\left(\frac{1}{2}\right)-w_v^{\theta b}\left(\frac{1}{2}\right)+\frac{2}{\mathrm{Re}RV_j\Delta\theta}\right]\right\}$$

$$+\overline{\Delta v}_{i,j,k+1}\left\{\frac{\beta\Delta\tau}{RV_j\Delta\theta}\left[w_v^{\theta f}\left(\frac{1}{2}\right)-\frac{1}{\mathrm{Re}RV_j\Delta\theta}\right]\right\}=\widetilde{\Delta v}_{i,j,k}\,. \tag{B.10}$$

The discretization of r-momentum equation (6.25) in the x-sweep, using the results of equation (B.10), yields

$$\Delta v_{i,j,k} + \frac{\beta\Delta\tau}{\Delta x_i^u}\left\{u_v^{xf}\Delta v_v^{xf} - u_v^{xb}\Delta v_v^{xb}\right.$$

$$\left. - \frac{1}{\mathrm{Re}}\left[\frac{\Delta v_{i+1,j,k} - \Delta v_{i,j,k}}{\Delta x_i^u} - \frac{\Delta v_{i,j,k} - \Delta v_{i-1,j,k}}{\Delta x_{i-1}^u}\right]\right\} = \overline{\Delta v}_{i,j,k}, \quad \text{(B.11)}$$

where the terms Δv_v^{xf} and Δv_v^{xb} are obtained from

$$\Delta v_v^{xf} = \frac{\nabla x_{i+1}^v \Delta v_{i,j,k} + \nabla x_i^u \Delta v_{i+1,j,k}}{\Delta x_i^u}, \quad \Delta v_v^{xb} = \frac{\nabla x_i^v \Delta v_{i-1,j,k} + \nabla x_{i-1}^u \Delta v_{i,j,k}}{\Delta x_{i-1}^u}.$$

Hence, equation (B.11) in tridiagonal form is written as

$$\Delta v_{i-1,j,k}\left\{\frac{\beta\Delta\tau}{\Delta x_i^v}\left[-u_v^{xb}\frac{\nabla x_i^v}{\Delta x_{i-1}^u} - \frac{1}{\mathrm{Re}\Delta x_{i-1}^u}\right]\right\}$$

$$+\Delta v_{i,j,k}\left\{1 + \frac{\beta\Delta\tau}{\Delta x_i^v}\left[u_v^{xf}\frac{\nabla x_{i+1}^v}{\Delta x_i^u} - u_v^{xb}\frac{\nabla x_{i-1}^u}{\Delta x_{i-1}^u} + \frac{1}{\mathrm{Re}\Delta x_i^u} + \frac{1}{\mathrm{Re}\Delta x_{i-1}^u}\right]\right\}$$

$$+ \Delta v_{i+1,j,k}\left\{\frac{\beta\Delta\tau}{\Delta x_i^v}\left[u_v^{xf}\frac{\nabla x_i^u}{\Delta x_i^u} - \frac{1}{\mathrm{Re}\Delta x_i^u}\right]\right\} = \overline{\Delta v}_{i,j,k}. \quad \text{(B.12)}$$

The same procedure is applied to discretize the θ-, x-momentum, and continuity equations (6.18, 6.22, 6.26) and (6.16, 6.20, 6.24), respectively. The discretized equations are given here without further explanation.

<u>Discretized θ-momentum equation in the r-sweep:</u>

$$\widetilde{\Delta w}_{i,j,k} + \frac{\beta\Delta\tau}{RU_j\Delta r_j^v}\left[A\left(RV_j v_w^{ru}\widetilde{\Delta w}_w^{ru} - RV_{j-1}v_w^{rd}\widetilde{\Delta w}_w^{rd}\right)\right.$$

$$\left.+Br_j^v\left(w_w^{ru}\widetilde{\Delta w}_w^{ru} - w_w^{rd}\widetilde{\Delta w}_w^{rd}\right)\right] + \frac{C\beta\Delta\tau r_{j-1}^v}{\Delta r_{j-1}^v}\left(\widetilde{\Delta w}_{i,j,k} - \widetilde{\Delta w}_{i,j-1,k}\right) + \frac{\beta\Delta\tau v_w\widetilde{\Delta w}_{i,j,k}}{RU_j}$$

$$-\frac{(B^2+D)\beta\Delta\tau r_{j-1}^v}{\mathrm{Re}RV_{j-1}^2\Delta r_{j-1}^v}\left(\widetilde{\Delta w}_{i,j,k} - \widetilde{\Delta w}_{i,j-1,k}\right) - \frac{2B\beta\Delta\tau r_j^u}{\mathrm{Re}RU_j^2\Delta r_j^u}\left(\widetilde{\Delta v}_{i,j,k} - \widetilde{\Delta v}_{i,j-1,k}\right)$$

$$-\frac{B^2\beta\Delta\tau r_j^{u2}}{\mathrm{Re}RU_j^2\Delta r_j^u}\left(\frac{\widetilde{\Delta w}_{i,j+1,k} - \widetilde{\Delta w}_{i,j,k}}{\Delta r_j^v} - \frac{\widetilde{\Delta w}_{i,j,k} - \widetilde{\Delta w}_{i,j-1,k}}{\Delta r_{j-1}^v}\right)$$

$$-\frac{B\beta\Delta\tau r_{j-1}^v}{\mathrm{Re}RU_j^2\Delta\theta}\left(\frac{\widetilde{\Delta w}_{i,j,k} - \widetilde{\Delta w}_{i,j-1,k}}{\Delta r_j^v} - \frac{\widetilde{\Delta w}_{i,j,k-1} - \widetilde{\Delta w}_{i,j-1,k-1}}{\Delta r_{j-1}^v}\right)$$

$$-\frac{A^2\beta\Delta\tau}{\mathrm{Re}RU_j\Delta r_j^u}\left[\frac{RV_j\left(\widetilde{\Delta w}_{i,j+1,k}-\widetilde{\Delta w}_{i,j,k}\right)}{\Delta r_j^v}-\frac{RV_{j-1}\left(\widetilde{\Delta w}_{i,j,k}-\widetilde{\Delta w}_{i,j-1,k}\right)}{\Delta r_{j-1}^v}\right]$$

$$+\frac{\beta\Delta\tau\widetilde{\Delta w}_{i,j,k}}{\mathrm{Re}RU_j^2}+\frac{B\beta\Delta\tau}{RV_j\Delta r_j^v}\left(\widetilde{\Delta p}_{i,j+1,k}-\widetilde{\Delta p}_{i,j,k}\right)=\Delta\tau\left(E_w^n-w-\beta Q_w\right)_{i,j,k}\ ; \quad \text{(B.13)}$$

$$\widetilde{\Delta w}_w^{ru}=\frac{\nabla r_{j+1}^v\widetilde{\Delta w}_{i,j,k}+\nabla r_j^v\widetilde{\Delta w}_{i,j+1,k}}{\Delta r_j^v}\ ,\qquad \widetilde{\Delta w}_w^{rd}=\frac{\nabla r_j^u\widetilde{\Delta w}_{i,j-1,k}+\nabla r_{j-1}^v\widetilde{\Delta w}_{i,j,k}}{\Delta r_{j-1}^v}\ ,$$

where

$$\left(-\beta\Delta\tau Q_w\right)_{i,j,k}=-\frac{\beta\Delta\tau}{\Delta x_i^v}\left[u_w^{xf}w_w^{xf}-u_w^{xb}w_w^{xb}-\frac{1}{\mathrm{Re}}\left(\frac{w_{i+1,j,k}-w_{i,j,k}}{\Delta x_i^u}-\frac{w_{i,j,k}-w_{i-1,j,k}}{\Delta x_{i-1}^u}\right)\right]$$

$$-\frac{C\beta\Delta\tau r_{j-1}^v}{\Delta r_{j-1}^v}\left(w_{i,j,k}-w_{i,j-1,k}\right)-\frac{\beta\Delta\tau}{RU_j\Delta r_j^u}\Big[A\cdot RV_jv_w^{ru}w_w^{ru}-A\cdot RV_{j-1}v_w^{rd}w_w^{rd}$$

$$-\frac{A^2}{\mathrm{Re}}\left\{\frac{RV_j}{\Delta r_j^v}\left(w_{i,j+1,k}-w_{i,j,k}\right)-\frac{RV_{j-1}}{\Delta r_{j-1}^v}\left(w_{i,j,k}-w_{i,j-1,k}\right)\right\}\Big]$$

$$-\frac{B\beta\Delta\tau r_j^v}{RV_j\Delta r_j^v}\left(p_{i,j+1,k}-p_{i,j,k}\right)-\frac{B\beta\Delta\tau r_j^v}{RU_j\Delta r_j^u}\left(w_w^{ru2}-w_w^{rd2}\right)$$

$$-\frac{\beta\Delta\tau}{RU_j}\left[\frac{w_w^{\theta f2}-w_w^{\theta b2}+p_{i,j,k+1}-p_{i,j,k}}{\Delta\theta}+v_ww_{i,j,k}\right]$$

$$+\frac{\beta\Delta\tau}{\mathrm{Re}}\left\{\frac{(B^2+D)r_{j-1}^v}{RV_{j-1}^2\Delta r_{j-1}^v}\left(w_{i,j,k}-w_{i,j-1,k}\right)+\frac{B^2r_j^{u2}}{RU_j^2\Delta r_j^u}\left(\frac{w_{i,j+1,k}-w_{i,j,k}}{\Delta r_j^v}-\frac{w_{i,j,k}-w_{i,j-1,k}}{\Delta r_{j-1}^v}\right)\right.$$

$$+\frac{Br_{j-1}^v}{RU_j^2\Delta\theta}\left(\frac{w_{i,j,k}-w_{i,j-1,k}}{\Delta r_{j-1}^v}-\frac{w_{i,j,k-1}-w_{i,j-1,k-1}}{\Delta r_{j-1}^v}\right)$$

$$\left.\frac{1}{RU_j^2}\left[\frac{w_{i,j,k+1}+w_{i,j,k-1}-2w_{i,j,k}}{\Delta\theta^2}+2\frac{v_w^{\theta f}-v_w^{\theta b}}{\Delta\theta}-w_{i,j,k}\right]+2\frac{Br_j^u}{RU_j^2\Delta r_j^u}\left(v_{i,j,k}-v_{i,j-1,k}\right)\right\}\ , \quad \text{(B.14)}$$

in which

$$v_w\ =\ \frac{1}{2}\left[\frac{\nabla r_j^v}{\Delta r_j^u}\left(v_{i,j,k}+v_{i,j,k+1}\right)+\frac{\nabla r_j^u}{\Delta r_j^u}\left(v_{i,j-1,k}+v_{i,j-1,k+1}\right)\right]\ .$$

With the aid of equations (B.5) and (B.6) one obtains

$$\widetilde{\Delta w}_{i,j-1,k}\left\{-\frac{C\beta\Delta\tau r_{j-1}^v}{\Delta r_{j-1}^v}+\frac{(B^2+D)\beta\Delta\tau r_{j-1}^v}{\mathrm{Re}RV_{j-1}^2\Delta r_{j-1}^v}\right.$$

$$-\frac{B^2\beta\Delta\tau r_j^{v2}}{\mathrm{Re}RU_j^2\Delta r_j^u\Delta r_{j-1}^v}-\frac{A^2\beta\Delta\tau RV_{j-1}}{\mathrm{Re}RU_j\Delta r_j^u\Delta r_{j-1}^v}-\frac{B^2\beta\Delta\tau^2r_j^vr_{j-1}^v}{\delta RV_j\Delta r_j^vRV_{j-1}\Delta r_{j-1}^v}$$

$$+\frac{\beta\Delta\tau}{RU_j\Delta r_j^u}\left[-A\cdot RV_{j-1}v_w^{rd}\frac{\nabla r_j^u}{\Delta r_{j-1}^v}-Br_j^v w_w^{rd}\frac{\nabla r_j^u}{\Delta r_{j-1}^v}\right]$$

$$+\widetilde{\Delta w}_{i,j,k}\left\{\frac{C\beta\Delta\tau r_{j-1}^v}{\Delta r_{j-1}^v}-\frac{(B^2+D)\beta\Delta\tau r_{j-1}^v}{\mathrm{Re}RV_{j-1}^2\Delta r_{j-1}^v}\right.$$

$$+\frac{B^2\beta\Delta\tau r_j^{v2}}{\mathrm{Re}RU_j^2\Delta r_j^u}\left(\frac{1}{\Delta r_j^v}+\frac{1}{\Delta r_{j-1}^v}\right)+1.0+\frac{\beta\Delta\tau v_w}{RU_j}+\frac{\beta\Delta\tau}{\mathrm{Re}RU_j^2}$$

$$+\frac{A^2\beta\Delta\tau}{\mathrm{Re}RU_j\Delta r_j^u}\left(\frac{RV_j}{\Delta r_j^v}+\frac{RV_{j-1}}{\Delta r_{j-1}^v}\right)+\frac{B^2\beta\Delta\tau^2 r_j^v}{\delta RV_j\Delta r_j^v}\left(\frac{r_j^v}{RV_j\Delta r_j^v}+\frac{r_{j-1}^v}{RV_{j-1}\Delta r_{j-1}^v}\right)$$

$$\left.+\frac{\beta\Delta\tau}{RU_j\Delta r_j^u}\left(A\cdot RV_j v_w^{ru}\frac{\nabla r_{j+1}^u}{\Delta r_j^v}-A\cdot RV_{j-1}v_w^{rd}\frac{\nabla r_{j-1}^v}{\Delta r_{j-1}^v}+Br_j^v w_w^{ru}\frac{\nabla r_{j+1}^u}{\Delta r_j^v}-Br_j^v w_w^{rd}\frac{\nabla r_{j-1}^v}{\Delta r_{j-1}^v}\right)\right\}$$

$$+\widetilde{\Delta w}_{i,j+1,k}\left\{-\frac{B^2\beta\Delta\tau r_j^{v2}}{\mathrm{Re}RU_j^2\Delta r_j^u\Delta r_j^v}-\frac{B^2\beta\Delta\tau^2 r_j^{v2}}{\delta RV_j^2\Delta r_j^{v2}}\right.$$

$$\left.+\frac{\beta\Delta\tau}{RU_j\Delta r_j^u}\left(A\cdot RV_j v_w^{ru}\frac{\nabla r_j^v}{\Delta r_j^v}+Br_j^v w_w^{ru}\frac{\nabla r_j^v}{\Delta r_j^v}\right)-\frac{A^2\beta\Delta\tau RV_j}{\mathrm{Re}RU_j\Delta r_j^u\Delta r_j^v}\right\}$$

$$=\Delta\tau\left(F_w^n-\hat{w}^\mu-\beta\hat{Q}_w^\mu\right)_{i,j,k}+\frac{B\beta\Delta\tau^2 r_j^v}{\delta RV_j\Delta r_j^v}\left(\nabla\cdot\mathbf{V}_{i,j+1,k}-\nabla\cdot\mathbf{V}_{i,j,k}\right)$$

$$+\frac{A\cdot B\beta\Delta\tau^2 r_j^v}{\delta RV_j RU_{j+1}\Delta r_j^v\Delta r_{j+1}^u}\left(RV_{j+1}\widetilde{\Delta v}_{i,j+1,k}-RV_j\widetilde{\Delta v}_{i,j,k}\right)$$

$$-\frac{A\cdot B\beta\Delta\tau^2 r_j^v}{\delta RV_j RU_j\Delta r_j^v\Delta r_j^u}\left(RV_j\widetilde{\Delta v}_{i,j,k}-RV_{j-1}\widetilde{\Delta v}_{i,j-1,k}\right)+\frac{2B\beta\Delta\tau r_j^u\left(\widetilde{\Delta v}_{i,j,k}-\widetilde{\Delta v}_{i,j-1,k}\right)}{\mathrm{Re}RU_j^2\Delta r_j^u}$$

$$+\frac{B\beta\Delta\tau r_{j-1}^v}{\mathrm{Re}RU_j^2\Delta\theta\Delta r_{j-1}^v}\left(\widetilde{\Delta w}_{i,j,k}-\widetilde{\Delta w}_{i,j-1,k}-\widetilde{\Delta w}_{i,j,k-1}+\widetilde{\Delta w}_{i,j-1,k-1}\right). \qquad \text{(B.15)}$$

Discretized θ-momentum and continuity equations in the θ-sweep:

$$(1+\Delta\tau)\,\overline{\Delta w}_{i,j,k}+\frac{\beta\Delta\tau}{RU_j\Delta\theta}\left[w_w^{\theta f}\overline{\Delta w}_w^{\theta f}-w_w^{\theta b}\overline{\Delta w}_w^{\theta b}-\frac{\overline{\Delta w}_{i,j,k+1}+\overline{\Delta w}_{i,j,k-1}-2\overline{\Delta w}_{i,j,k}}{\mathrm{Re}RU_j\Delta\theta}\right]$$

$$+\frac{\beta\Delta\tau}{RU_j}\left[+\frac{\overline{\Delta p}_{i,j,k+1}-\overline{\Delta p}_{i,j,k}}{\Delta\theta}\right]=\widetilde{\Delta w}_{i,j,k}\,, \qquad \text{(B.16)}$$

$$\overline{\Delta w}_w^{\theta f}=\frac{\overline{\Delta w}_{i,j,k+1}+\overline{\Delta w}_{i,j,k}}{2}\,,\qquad \overline{\Delta w}_w^{\theta b}=\frac{\overline{\Delta w}_{i,j,k}+\overline{\Delta w}_{i,j,k-1}}{2}\,,$$

and with the aid of equation (6.23)

$$\overline{\Delta p}_{i,j,k}=\widetilde{\Delta p}_{i,j,k}-\frac{\Delta\tau}{\delta}\frac{\overline{\Delta w}_{i,j,k}-\overline{\Delta w}_{i,j,k-1}}{RU_j\Delta\theta}\,,$$

$$\overline{\Delta p}_{i,j,k+1} = \widetilde{\Delta p}_{i,j,k+1} - \frac{\Delta\tau}{\delta}\frac{\overline{\Delta w}_{i,j,k+1} - \overline{\Delta w}_{i,j,k}}{RU_j\Delta\theta} ;$$

hence, one obtains

$$\overline{\Delta w}_{i,j,k-1}\left\{\frac{\beta\Delta\tau}{RU_j\Delta\theta}\left[-w_w^{\theta b}\left(\frac{1}{2}\right) - \frac{\Delta\tau}{\delta}\frac{1}{RU_j\Delta\theta} - \frac{1}{\mathrm{Re}RU_j\Delta\theta}\right]\right\}$$
$$+\overline{\Delta w}_{i,j,k}\left\{1 + \Delta\tau + \frac{\beta\Delta\tau}{RU_j\Delta\theta}\left[w_w^{\theta f}\left(\frac{1}{2}\right) - w_w^{\theta b}\left(\frac{1}{2}\right) + \frac{2}{\mathrm{Re}RU_j\Delta\theta} + \frac{\Delta\tau}{\delta}\frac{2}{RU_j\Delta\theta}\right]\right\}$$
$$+\overline{\Delta w}_{i,j,k+1}\left\{\frac{\beta\Delta\tau}{RU_j\Delta\theta}\left[w_w^{\theta f}\left(\frac{1}{2}\right) - \frac{\Delta\tau}{\delta}\frac{1}{RU_j\Delta\theta} - \frac{1}{\mathrm{Re}RU_j\Delta\theta}\right]\right\}$$
$$= \widetilde{\Delta w}_{i,j,k} - \frac{\beta\Delta\tau}{RU_j\Delta\theta}\left(\widetilde{\Delta p}_{i,j,k+1} - \widetilde{\Delta p}_{i,j,k}\right) . \qquad \text{(B.17)}$$

Discretized θ-momentum equation in the x-sweep:

$$\Delta w_{i,j,k} + \frac{\beta\Delta\tau}{\Delta x_i^v}\left\{u_w^{xf}\Delta w_w^{xf} - u_w^{xb}\Delta w_w^{xb} - \frac{1}{\mathrm{Re}}\left[\frac{\Delta w_{i+1,j,k} - \Delta w_{i,j,k}}{\Delta x_i^u} - \frac{\Delta w_{i,j,k} - \Delta w_{i,j-1,k}}{\Delta x_{i-1}^u}\right]\right\} , \qquad \text{(B.18)}$$

$$\Delta w_w^{xf} = \frac{\nabla x_{i+1}^v \Delta w_{i,j,k} + \nabla x_i^u \Delta w_{i+1,j,k}}{\Delta x_i^u} , \quad \Delta w_w^{xb} = \frac{\nabla x_i^v \Delta w_{i-1,j,k} + \nabla x_{i-1}^u \Delta w_{i,j,k}}{\Delta x_{i-1}^u} .$$

Then,

$$\Delta w_{i-1,j,k}\left\{\frac{\beta\Delta\tau}{\Delta x_i^v}\left[-u_w^{xb}\frac{\nabla x_i^v}{\Delta x_{i-1}^u} - \frac{1}{\mathrm{Re}\Delta x_{i-1}^u}\right]\right\}$$
$$+\Delta w_{i,j,k}\left\{1 + \frac{\beta\Delta\tau}{\Delta x_i^v}\left[u_w^{xf}\frac{\nabla x_{i+1}^v}{\Delta x_i^u} - u_w^{xb}\frac{\nabla x_{i-1}^u}{\Delta x_{i-1}^u} + \frac{1}{\mathrm{Re}\Delta x_i^u} + \frac{1}{\mathrm{Re}\Delta x_{i-1}^u}\right]\right\}$$
$$+ \Delta w_{i+1,j,k}\left\{\frac{\beta\Delta\tau}{\Delta x_i^v}\left[u_w^{xf}\frac{\nabla x_i^u}{\Delta x_i^u} - \frac{1}{\mathrm{Re}\Delta x_i^u}\right]\right\} = \overline{\Delta w}_{i,j,k} . \qquad \text{(B.19)}$$

Discretized x-momentum equation in the r-sweep:

$$\widetilde{\Delta u}_{i,j,k} + \frac{\beta\Delta\tau}{RU_j\Delta r_j^u}\left[A\left(RV_j v_u^{ru}\widetilde{\Delta u}_u^{ru} - RV_{j-1}v_u^{rd}\widetilde{\Delta u}_u^{rd}\right)\right.$$
$$\left.+Br_j^v\left(w_u^{ru}\widetilde{\Delta u}_u^{ru} - w_u^{rd}\widetilde{\Delta u}_u^{rd}\right)\right] - \frac{(B^2+D)\beta\Delta\tau r_{j-1}^v}{\mathrm{Re}RV_{j-1}^2\Delta r_{j-1}^v}\left(\widetilde{\Delta u}_{i,j,k} - \widetilde{\Delta u}_{i,j-1,k}\right)$$
$$-\frac{B^2\beta\Delta\tau r_j^{u2}}{\mathrm{Re}RU_j^2\Delta r_j^u}\left(\frac{\widetilde{\Delta u}_{i,j+1,k} - \widetilde{\Delta u}_{i,j,k}}{\Delta r_j^v} - \frac{\widetilde{\Delta u}_{i,j,k} - \widetilde{\Delta u}_{i,j-1,k}}{\Delta r_{j-1}^v}\right)$$
$$-\frac{B\beta\Delta\tau r_{j-1}^v}{\mathrm{Re}RU_j^2\Delta\theta}\left(\frac{\widetilde{\Delta u}_{i,j,k} - \widetilde{\Delta u}_{i,j-1,k}}{\Delta r_{j-1}^v} - \frac{\widetilde{\Delta u}_{i,j,k-1} - \widetilde{\Delta u}_{i,j-1,k-1}}{\Delta r_{j-1}^v}\right)$$

$$
-\frac{A^2\beta\Delta\tau}{\mathrm{Re}RU_j\Delta r_j^u}\left[\frac{RV_j}{\Delta r_j^v}\left(\widetilde{\Delta u}_{i,j+1,k}-\widetilde{\Delta u}_{i,j,k}\right)-\frac{RV_{j-1}}{\Delta r_{j-1}^v}\left(\widetilde{\Delta u}_{i,j,k}-\widetilde{\Delta u}_{i,j-1,k}\right)\right]
$$

$$
+\frac{C\beta\Delta\tau r_{j-1}^v}{\Delta r_{j-1}^v}\left(\widetilde{\Delta u}_{i,j,k}-\widetilde{\Delta u}_{i,j-1,k}\right)=\Delta\tau\left(E_u^n-u-\beta Q_u\right)_{i,j,k}\ , \qquad \text{(B.20)}
$$

$$
\widetilde{\Delta u}_u^{ru}=\frac{\nabla r_{j+1}^u\widetilde{\Delta u}_{i,j,k}+\nabla r_j^v\widetilde{\Delta u}_{i,j+1,k}}{\Delta r_j^v}\ ,\qquad \widetilde{\Delta u}_u^{rd}=\frac{\nabla r_j^u\widetilde{\Delta u}_{i,j-1,k}+\nabla r_{j-1}^v\widetilde{\Delta u}_{i,j,k}}{\Delta r_{j-1}^v}\ ,
$$

$$
w_u{}^{ru}=\frac{\nabla r_{j+1}^u\left(w_u\right)_{i,j,k}+\nabla r_j^v\left(w_u\right)_{i,j+1,k}}{\Delta r_j^v}\ ,\qquad w_u{}^{rd}=\frac{\nabla r_j^u\left(w_u\right)_{i,j-1,k}+\nabla r_{j-1}^v\left(w_u\right)_{i,j,k}}{\Delta r_{j-1}^v}\ ,
$$

where

$$
(w_u)_{i,j-1,k}=\frac{1}{2}\left[\left(\frac{\nabla x_{i+1}^v}{\Delta x_i^u}w_{i,j-1,k}+\frac{\nabla x_i^u}{\Delta x_i^u}w_{i+1,j-1,k}\right)+\left(\frac{\nabla x_{i+1}^v}{\Delta x_i^u}w_{i,j-1,k-1}+\frac{\nabla x_i^u}{\Delta x_i^u}w_{i+1,j-1,k-1}\right)\right]\ ,
$$

$$
(w_u)_{i,j,k}=\frac{1}{2}\left[\left(\frac{\nabla x_{i+1}^v}{\Delta x_i^u}w_{i,j,k}+\frac{\nabla x_i^u}{\Delta x_i^u}w_{i+1,j,k}\right)+\left(\frac{\nabla x_{i+1}^v}{\Delta x_i^u}w_{i,j,k-1}+\frac{\nabla x_i^u}{\Delta x_i^u}w_{i+1,j,k-1}\right)\right]\ ,
$$

$$
(w_u)_{i,j+1,k}=\frac{1}{2}\left[\left(\frac{\nabla x_{i+1}^v}{\Delta x_i^u}w_{i,j+1,k}+\frac{\nabla x_i^u}{\Delta x_i^u}w_{i+1,j+1,k}\right)+\left(\frac{\nabla x_{i+1}^v}{\Delta x_i^u}w_{i,j+1,k-1}+\frac{\nabla x_i^u}{\Delta x_i^u}w_{i+1,j+1,k-1}\right)\right]\ ,
$$

with

$$
(-\beta\Delta\tau Q_u)_{i,j,k}=-\frac{\beta\Delta\tau}{\Delta x_i^u}\left\{u_u^{xf}u_u^{xf}-u_u^{xb}u_u^{xb}+p_{i+1,j,k}-p_{i,j,k}\right.
$$

$$
\left.-\frac{1}{\mathrm{Re}}\left[\frac{u_{i+1,j,k}-u_{i,j,k}}{\Delta x_{i+1}^v}-\frac{u_{i,j,k}-u_{i-1,j,k}}{\Delta x_i^v}\right]\right\}-\frac{C\beta\Delta\tau r_{j-1}^v}{\Delta r_{j-1}^v}\left(u_{i,j,k}-u_{i,j-1,k}\right)
$$

$$
-\frac{\beta\Delta\tau}{RU_j\Delta r_j^u}\left\{A\left(RV_jv_u^{ru}u_u^{ru}-RV_{j-1}v_u^{rd}u_u^{rd}\right)\right.
$$

$$
\left.-\frac{A^2}{\mathrm{Re}}\left[\frac{RV_j}{\Delta r_j^v}\left(u_{i,j+1,k}-u_{i,j,k}\right)-\frac{RV_{j-1}}{\Delta r_{j-1}^v}\left(u_{i,j,k}-u_{i,j-1,k}\right)\right]\right\}
$$

$$
-\frac{B\beta\Delta\tau r_j^v}{RU_j\Delta r_j^u}\left(w_u^{ru}u_u^{ru}-w_u^{rd}u_u^{rd}\right)-\frac{\beta\Delta\tau}{RU_j}\left(\frac{w_u^{\theta f}u_u^{\theta f}-w_u^{\theta b}u_u^{\theta b}}{\Delta\theta}\right)
$$

$$
+\frac{\beta\Delta\tau}{\mathrm{Re}}\left[\frac{(B^2+D)r_{j-1}^v}{RV_{j-1}^2\Delta r_{j-1}^v}\left(u_{i,j,k}-u_{i,j-1,k}\right)+\frac{B^2r_j^{u2}}{RU_j^2\Delta r_j^u}\left(\frac{u_{i,j+1,k}-u_{i,j,k}}{\Delta r_j^v}-\frac{u_{i,j,k}-u_{i,j-1,k}}{\Delta r_{j-1}^v}\right)\right.
$$

$$
\left.+\frac{\left(u_{i,j,k+1}+u_{i,j,k-1}-2u_{i,j,k}\right)}{RU_j^2\Delta\theta^2}+\frac{Br_{j-1}^v}{RU_j^2\Delta\theta}\left(\frac{u_{i,j,k}-u_{i,j-1,k}}{\Delta r_{j-1}^v}-\frac{u_{i,j,k-1}-u_{i,j-1,k-1}}{\Delta r_{j-1}^v}\right)\right]\ ; \qquad \text{(B.21)}
$$

hence, one obtains

$$
\widetilde{\Delta u}_{i,j-1,k}\left\{-\frac{C\beta\Delta\tau r_{j-1}^v}{\Delta r_{j-1}^v}+\frac{(B^2+D)\beta\Delta\tau r_{j-1}^v}{\mathrm{Re}RV_{j-1}^2\Delta r_{j-1}^v}-\frac{B^2\beta\Delta\tau r_j^{v2}}{\mathrm{Re}RU_j^2\Delta r_j^u\Delta r_{j-1}^v}\right.
$$

$$-\frac{A^2\beta\Delta\tau RV_{j-1}}{\mathrm{Re}RU_j\Delta r_j^u\Delta r_{j-1}^v}+\frac{\beta\Delta\tau}{RU_j\Delta r_j^u}\left(-A\cdot RV_{j-1}v_u^{rd}\frac{\nabla r_j^u}{\Delta r_{j-1}^v}-Br_j^v w_u^{rd}\frac{\nabla r_j^u}{\Delta r_{j-1}^v}\right)\Bigg\}$$

$$+\widetilde{\Delta u}_{i,j,k}\left\{\frac{C\beta\Delta\tau r_{j-1}^v}{\Delta r_{j-1}^v}-\frac{(B^2+D)\beta\Delta\tau r_{j-1}^v}{\mathrm{Re}RV_{j-1}^2\Delta r_{j-1}^v}+\frac{B^2\beta\Delta\tau r_j^{v2}}{\mathrm{Re}RU_j^2\Delta r_j^u}\left(\frac{1}{\Delta r_j^v}+\frac{1}{\Delta r_{j-1}^v}\right)\right.$$

$$+\frac{A^2\beta\Delta\tau}{\mathrm{Re}RU_j\Delta r_j^u}\left(\frac{RV_j}{\Delta r_j^v}+\frac{RV_{j-1}}{\Delta r_{j-1}^v}\right)$$

$$\left.+\frac{\beta\Delta\tau}{RU_j\Delta r_j^u}\left[A\left(RV_jv_u^{ru}\frac{\nabla r_{j+1}^u}{\Delta r_j^v}-RV_{j-1}v_u^{rd}\frac{\nabla r_{j-1}^v}{\Delta r_{j-1}^v}\right)+B\left(r_j^vw_u^{ru}\frac{\nabla r_{j+1}^u}{\Delta r_j^v}-r_j^vw_u^{rd}\frac{\nabla r_{j-1}^v}{\Delta r_{j-1}^v}\right)\right]\right\}$$

$$+\widetilde{\Delta u}_{i,j+1,k}\left\{-\frac{B^2\beta\Delta\tau r_j^{v2}}{\mathrm{Re}RU_j^2\Delta r_j^u\Delta r_j^v}-\frac{A^2\beta\Delta\tau RV_j}{\mathrm{Re}RU_j\Delta r_j^u\Delta r_j^v}\right.$$

$$\left.+\frac{\beta\Delta\tau}{RU_j\Delta r_j^u}\left(A\cdot RV_jv_u^{ru}\frac{\nabla r_j^v}{\Delta r_j^v}+Br_j^vw_u^{ru}\frac{\nabla r_j^v}{\Delta r_j^v}\right)\right\}$$

$$=\Delta\tau\left(E_u^n-u-\beta Q_u\right)_{i,j,k}+\frac{B\beta\Delta\tau r_{j-1}^v}{\mathrm{Re}RU_j^2\Delta\theta\Delta r_{j-1}^v}\left(\widetilde{\Delta u}_{i,j,k}-\widetilde{\Delta u}_{i,j-1,k}-\widetilde{\Delta u}_{i,j,k-1}+\widetilde{\Delta u}_{i,j-1,k-1}\right). \tag{B.22}$$

Discretized x-momentum equation in the θ-sweep:

$$\overline{\Delta u}_{i,j,k}+\frac{\beta\Delta\tau}{RU_j\Delta\theta}\left[w_u^{\theta f}\overline{\Delta u}_u^{\theta f}-w_u^{\theta b}\overline{\Delta u}_u^{\theta b}\right.$$

$$\left.-\frac{1}{\mathrm{Re}}\left(\frac{\overline{\Delta u}_{i,j,k+1}+\overline{\Delta u}_{i,j,k-1}-2\overline{\Delta u}_{i,j,k}}{RU_j\Delta\theta}\right)\right]=\widetilde{\Delta u}_{i,j,k}\,, \tag{B.23}$$

$$\overline{\Delta u}_u^{\theta f}=\frac{\overline{\Delta u}_{i,j,k+1}+\overline{\Delta u}_{i,j,k}}{2}\,,\quad \overline{\Delta u}_u^{\theta b}=\frac{\overline{\Delta u}_{i,j,k}+\overline{\Delta u}_{i,j,k-1}}{2}\,;$$

then

$$\overline{\Delta u}_{i,j,k-1}\left\{\frac{\beta\Delta\tau}{RU_j\Delta\theta}\left[-w_u^{\theta b}\left(\frac{1}{2}\right)-\frac{1}{\mathrm{Re}RU_j\Delta\theta}\right]\right\}$$

$$+\overline{\Delta u}_{i,j,k}\left\{1+\frac{\beta\Delta\tau}{RU_j\Delta\theta}\left[w_u^{\theta f}\left(\frac{1}{2}\right)-w_u^{\theta b}\left(\frac{1}{2}\right)+\frac{2}{\mathrm{Re}RU_j\Delta\theta}\right]\right\}$$

$$+\overline{\Delta u}_{i,j,k+1}\left\{\frac{\beta\Delta\tau}{RU_j\Delta\theta}\left[w_u^{\theta f}\left(\frac{1}{2}\right)-\frac{1}{\mathrm{Re}RU_j\Delta\theta}\right]\right\}=\widetilde{\Delta u}_{i,j,k}\,. \tag{B.24}$$

Discretized x-momentum and continuity equations in the x-sweep:

$$(1+\Delta\tau)\,\Delta u_{i,j,k}+\frac{\beta\Delta\tau}{\Delta x_i^u}\left[u_u^{xf}\Delta u_u^{xf}-u_u^{xb}\Delta u_u^{xb}\right.$$

$$-\frac{1}{\mathrm{Re}}\left(\frac{\Delta u_{i+1,j,k}-\Delta u_{i,j,k}}{\Delta x^{v}_{i+1}}-\frac{\Delta u_{i,j,k}-\Delta u_{i,j-1,k}}{\Delta x^{v}_{i}}\right)+\Delta p_{i+1,j,k}-\Delta p_{i,j,k}\Bigg]=\overline{\Delta u}_{i,j,k}\,, \tag{B.25}$$

$$\Delta u^{xf}_{u}=\frac{\nabla x^{u}_{i+1}\Delta u_{i,j,k}+\nabla x^{v}_{i+1}\Delta u_{i+1,j,k}}{\Delta x^{v}_{i+1}}\,,\quad \Delta u^{xb}_{u}=\frac{\nabla x^{u}_{i}\Delta u_{i-1,j,k}+\nabla x^{v}_{i}\Delta u_{i,j,k}}{\Delta x^{v}_{i}}\,,$$

and with the aid of equation (6.27)

$$\Delta p_{i,j,k}+\frac{\Delta\tau}{\delta}\frac{1}{\Delta x^{v}_{i}}\left(\Delta u_{i,j,k}-\Delta u_{i-1,j,k}\right)=\overline{\Delta p}_{i,j,k}\,,$$

$$\Delta p_{i+1,j,k}+\frac{\Delta\tau}{\delta}\frac{1}{\Delta x^{v}_{i+1}}\left(\Delta u_{i+1,j,k}-\Delta u_{i,j,k}\right)=\overline{\Delta p}_{i+1,j,k}\,;$$

hence, one obtains

$$\begin{aligned}
&\Delta u_{i-1,j,k}\left\{\frac{\beta\Delta\tau}{\Delta x^{u}_{i}}\left[-u^{xb}_{u}\frac{\nabla x^{u}_{i}}{\Delta x^{v}_{i}}-\frac{1}{\mathrm{Re}\Delta x^{v}_{i}}-\frac{\Delta\tau}{\delta\Delta x^{v}_{i}}\right]\right\}\\
&+\Delta u_{i,j,k}\left\{1+\Delta\tau+\frac{\beta\Delta\tau}{\Delta x^{u}_{i}}\left[u^{xf}_{u}\frac{\nabla x^{u}_{i+1}}{\Delta x^{v}_{i+1}}-u^{xb}_{u}\frac{\nabla x^{v}_{i}}{\Delta x^{v}_{i}}\right.\right.\\
&\left.\left.+\frac{1}{\mathrm{Re}}\left(\frac{1}{\Delta x^{v}_{i}}+\frac{1}{\Delta x^{v}_{i+1}}\right)+\frac{\Delta\tau}{\delta}\left(\frac{1}{\Delta x^{v}_{i}}+\frac{1}{\Delta x^{v}_{i+1}}\right)\right]\right\}\\
&+\Delta u_{i+1,j,k}\left\{\frac{\beta\Delta\tau}{\Delta x^{u}_{i}}\left[u^{xf}_{u}\frac{\nabla x^{u}_{i+1}}{\Delta x^{v}_{i+1}}-\frac{1}{\mathrm{Re}\Delta x^{v}_{i+1}}-\frac{\Delta\tau}{\delta\Delta x^{v}_{i+1}}\right]\right\}\\
&=\overline{\Delta u}_{i,j,k}-\frac{\beta\Delta\tau}{\Delta x^{u}_{i}}\left(\overline{\Delta p}_{i+1,j,k}-\overline{\Delta p}_{i,j,k}\right)\,.
\end{aligned} \tag{B.26}$$

We recall that the terms containing Δ and ∇ indicate the central and backward difference operators applied to the grid point coordinates, and 34 interpolates such as v^{ru}_{v}, v^{rd}_{v}, w^{ru}_{v}, w^{rd}_{v}, ...etc are evaluated by the relations given in Appendix A.